1992
Topical Meeting on Advances in Reactor Physics

March 8-11, 1992
Charleston Sheraton Hotel
Charleston, S. C.

DISCLAIMER

CONF-920308--Vol.2

DE92 009763

Proceedings of the 1992 Topical Meeting on Advances in Reactor Physics

March 8 - 11, 1992

Charleston Sheraton, Charleston, SC, USA

Sponsored by the American Nuclear Society Savannah River Section,
Reactor Physics Division, and
Mathematics and Computations Division

Co-sponsored by the U. S. Department of Energy, and
The Atomic Energy Society of Japan

MEETING PERSONNEL

GENERAL CHAIRMAN
Henry C. Honeck
Computer Application Technology

TECHNICAL CHAIRMAN
Mel R. Buckner
Westinghouse Savannah River Co.

ASSISTANT GENERAL CHAIRMAN
William R. Ferrara
Westinghouse Savannah River Co.

ASSISTANT TECHNICAL CHAIRMAN
Christa E. Boman
Westinghouse Savannah River Co.

PUBLICATIONS CHAIRMAN
Andrew O. Smetana
Westinghouse Savannah River Co.

REGISTRATION
John R. Chandler
Westinghouse Savannah River Co.

ARRANGEMENTS
Dave C. Losey
Westinghouse Savannah River Co.

FINANCE
Kevin R. O'Kula
Westinghouse Savannah River Co

PUBLICITY
E. Fitz Trumble
Westinghouse Savannah River Co.

AUDIO/VISUAL
Nina Baxter
Westinghouse Savannah River Co.

DOE LIAISON
Paul S. Shieh
U. S. Department of Energy

EXHIBITS
Chuck M. Voldness
Westinghouse Savannah River Co

GUEST PROGRAM
Deborah Henrikson
Westinghouse Savannah River Co.

TECHNICAL PROGRAM COMMITTEE

Courtney Apperson
Westinghouse SRC
Lee Dodds
Univ of Tennessee
Mike Gregory
Westinghouse SRC
Dale Lancaster
Georgia Institute of Tech
Massimo Salvatores
Centre d'Etudes Nucleaires
Skip Kahler
Westinghouse Electric Corp
Paul Wyatt
Westinghouse SRC
Mike Westfall
Oak Ridge National Lab

Christa Boman
Westinghouse SRC
Thomas Downar
Purdue University
Henry Honeck
Computer Applications Tech.
Ron Pevey
Westinghouse SRC
Paul Shieh
US Dept of Energy (SRS)
Roger Webb
Westinghouse SRC
Russ Mosteller
Los Alamos National Lab
Wolfgang Werner
Gesellschaft für Reaktorsicherheit

Mel Buckner
Westinghouse SRC
William Ziegler
Carolina Power & Light
Harry Hootman
Westinghouse SRC
Paul Turinsky
NC State University
Alain Valee
Framatome
Klaus Koebke
Kraftwerkunion
Hussein Khalil
Argonne National Lab

SESSIONS BY DAY

Monday 1 30 - 3·10
1 1 Code Benchmarks & Validation I
1 2 Fuel Management I
1 3 Nodal Methods for Diffusion Theory I

Monday 3 25 - 5 30
6 1 Transport Theory I
6 2 Fast Reactors I
6 3 Plant Analyzers & Core Simulators

Tuesday 8 30 - 10 10
2 1 Criticality Safety & Applications and Waste
2 2 Core Computational Systems I

Tuesday 10 20 - 12 00
7 1 Integral Experiments
7 2 Core Computational Systems II

Tuesday 2 00 - 3 40
3 1 Nuclear Data
3 2 Reactor Physics I
3 3 Fuel Management II

Tuesday 3 50 - 5 30
8 1 Monte Carlo
8 2 Reactor Physics II
8 3 Reactor Physics III

Wednesday 8 30 - 10 10
4 1 Safety Aspects of D_2O Reactors I
4 2 Space-Time Core Kinetics I

Wednesday 10 20 - 12 00
9 1 Safety Aspects of D_2O Reactors II
9 2 Space-Time Core Kinetics II

Wednesday 1 30 - 3 10
5 1 Code Benchmarks & Validation II
5 2 Nodal Methods for Diffusion Theory II

Wednesday 3 25 - 5 30
10 1 Transport Theory II
10 2 Fast Reactors II

TABLE OF CONTENTS

Volume 1

AUTHOR INDEX

Volume 2

Session 8.1 Monte Carlo

Session 8.2 Reactor Physics II

Session 8.3 Reactor Physics III

Session 10.2 Fast Reactors II

AUTHOR INDEX

COLLISION IMPORTANCE FUNCTION IN REACTOR CELL CALCULATION

V. V. Tebin
Kurchatov Institute of Atomic Energy
Moscow

ABSTRACT

A method for calculation of the reactor cells using collision importance function is described. The collision probability equation is formulated which differs from conventional one. It is assumed that spatial, angular and energy variables are not separated and neutron collision importance function is introduced, which is found by solving adjoint to neutrons collision density equation. This method has been used for development of generalized subgroup approach, which is implemented in SAPFIR code package. The numerical results are given.

INTRODUCTION

The cell calculation is an important step in modeling neutron-physical processes in nuclear reactors. Usually, the cell calculation means solution of kinetic equation for neutrons in given subvolume of reactor with the a priori determined sources and boundary conditions. There are many codes solving this problem. It is possible to distinguish two types of them: deterministic codes (APOLLO, EPRI-CELL, SRAC, WIMS) and are statistical codes based on Monte-Carlo method (MCNP, MCU, SAME-CE). First-type codes are characterized by small run-time, by use of equivalence theorem of homogeneous and heterogeneous media and by presence of free parameters for results adjustment. Second-type codes are characterized by big run-time, universal geometry and by using exact operators in kinetic equation. The cell-calculating part MBC-1.5(B20) of neutron-physical code SAPFIR, developed during 80-th, is neither of two these types. CPU-time need for MBC-1.5(B20) is 2-3 time greater than for deterministic codes and significantly less than for statistical codes. Though MBC-1.5(B20) is deterministic code, its error can be estimated in the course of cell calculation. The operators of

equations solved are consistent with details of neutron data. The calculation techniques have no adjustment parameters.

The method underlying MBC-1.5(B20) was developed for generalized subgroup approach to resonance absorption calculation[1]. But in code package SAPFIR this method is used not only for resonance absorption calculation. The method is based on collision importance function application directly in the calculations.

The adjoint function to neutron flux is used widely in the perturbation theory for differential form of kinetic equation. Sometimes the adjoint equation to the integral kinetic equation is considered[2]. The difference between adjoint equations of differential and integral forms of kinetic equations is discussed in Ref.[3] In works[4,5] the properties of this function, which is solution of adjoint equation to collision probability equation are noted.

COLLISION IMPORTANCE FUNCTION

The inhomogeneous equation for collision density of neutrons in point $\mathbf{r}$, moving with the velocity $v = |\mathbf{v}|$, in direction $\Omega = \mathbf{v} / |\mathbf{v}|$ has the form (we use notations of Ref.[3-5]):

$$\Psi(\mathbf{r},\mathbf{v}) = \int d\mathbf{r}' T(\mathbf{v},\mathbf{r}'|\mathbf{r}) \Sigma(\mathbf{r},\mathbf{v}) \left[\int d\mathbf{v}' \chi(\mathbf{r}',\mathbf{v}'\to\mathbf{v}) \frac{\Sigma_s(\mathbf{r}',\mathbf{v}')}{\Sigma(\mathbf{r}',\mathbf{v}')} \Psi(\mathbf{r}',\mathbf{v}') + Q(\mathbf{r}',\mathbf{v}) \right] . \quad (1)$$

The adjoint to equation (1) has the form:

$$\Psi^+(\mathbf{r},\mathbf{v}) = \frac{\Sigma_s(\mathbf{r},\mathbf{v})}{\Sigma(\mathbf{r},\mathbf{v})} \int d\mathbf{v}'' \chi(\mathbf{r},\mathbf{v}\to\mathbf{v}'') \int d\mathbf{r}'' T(\mathbf{v}'',\mathbf{r}|\mathbf{r}'',) \Sigma(\mathbf{r}'',\mathbf{v}'') \Psi^+(\mathbf{r}'',\mathbf{v}'') + Q^+(\mathbf{r},\mathbf{v}) . \quad (2)$$

The function $\Psi^+(\mathbf{r},\mathbf{v})$ can be named the collision importance function in reference to $\Sigma(\mathbf{r},\mathbf{v})Q^+(\mathbf{r},\mathbf{v})$. It can be shown that for equations (1) and (2) the next statements are valid:

1^0 If the solution of the equation (1) exists, then the unique solution of the equation (2) exists for each real adjoint source $Q^+(\mathbf{r},\mathbf{v})$. (Else exists nonzero solution of equation (1) with $Q(\mathbf{r},\mathbf{v}) \equiv 0$.)

2^0 The reciprocity theorem for two points of phase volume corresponding to successive collisions stems directly from kernels symmetry of equations (1) and (2)

3^0 If $Q^+(\mathbf{r},\mathbf{v})=\Sigma_a(\mathbf{r},\mathbf{v})/\Sigma(\mathbf{r},\mathbf{v})$ and

$$\int d\mathbf{v}''\chi(\mathbf{r},\mathbf{v}\to\mathbf{v}'') = 1 ,$$

$$\int d\mathbf{r}''T(\mathbf{v}'',\mathbf{r}|\mathbf{r}'')\ \Sigma(\mathbf{r}'',\mathbf{v}'') = 1 ,$$

then solution of equation (2) is:

$$\Psi_a^+(\mathbf{r},\mathbf{v}) \equiv 1 . \qquad (3)$$

4^0 If we solve an equation (2) for all

$$Q_{kx}^+(\mathbf{r},\mathbf{v})=\frac{\Sigma_{kx}(\mathbf{r},\mathbf{v})}{\Sigma(\mathbf{r},\mathbf{v})},$$

where x - nonscattering processes (c,f) ,
k - number of isotope (k=1,2,...K),
then

$$0 \le \Psi_{kx}^+(\mathbf{r},\mathbf{v}) \le 1 ,$$
$$\sum_k \sum_x \Psi_{kx}^+(\mathbf{r},\mathbf{v}) \equiv 1 \qquad (4)$$

will be correct.

The most important for practical application is the statement 3^0. The identity (3) in some sense can be named "the particular solution" of the equation (1), since for the correct calculation of reactor integral parameters it is enough to know solution only of the equations (1) or (2). Physical sense of identity (3) is clear. Really, in cell with total reflection boundary condition after all collisions neutron in the end will be absorbed in same or another point of phase volume considered.

As example of application of equations (1),(2) and statements 1^0-4^0 let us consider two traditional problem of neutron-physical reactor calculation which can be solved by many other methods also:

- how can we come from exact kinetic equation to collision probability equation by Chernick;
- how to calculate the criticality of benchmark assembly if the buckling in its asymptotic region is known.

COLLISION PROBABILITY EQUATION

The problem of formulation of collision probability equation consists of the search of optimal way for determination piecewise-constant operators and cross sections at the minimal errors of calculation for selected functionals.

Let us divide phase volume U = {R,V} on M elementary volumes $\Delta U_m = \{\Delta R_i, \Delta V_n, \Delta\Omega_l\}$,

where: $\Delta U_m \in U$,

$i=1,2...I$ - number of geometrical regions,

$n=1,2...N$ - number of energy groups or subgroups,

$l=1,2...L$ - number of direction.

Let the functionals, which we take into account, be chosen is

$$Q^{+}_{kx} = < Q^{+}_{kx}(\mathbf{r},\mathbf{v})\ \Psi(\mathbf{r},\mathbf{v}) >_m \quad ,$$

where: brackets $< >_m$ represent an integral by elementary phase volume m.

Multiplying equation (1) by Ψ^{+} and equation (2) by Ψ and carrying out integration in each m. Introduce the following notation:

Column matrices:

$$\vec{\Psi} = \left(\frac{\int d\mathbf{r} \int d\nu \int d\Omega \Psi(\mathbf{r},\nu,\Omega)}{\Delta R_i\ \Delta\nu_i\ \Delta\Omega_l} \right) = \left(\frac{< \Psi(\mathbf{r},\mathbf{v}) >_m}{\Delta U_m} \right) ;$$

$$\vec{\Psi}^{+}_{kx} = \left(\Psi^{+}_{kx}(\mathbf{r}_i,\mathbf{v}_{nl}) \right) ;$$

$$\vec{Q} = \left(\left\langle Q(\mathbf{r}_i,\mathbf{v}) \right\rangle_{nl} \right) ;$$

$$\vec{Q}^{+}_{kx} = \left(\frac{\left\langle \frac{\Sigma_{kx}(\mathbf{r},\mathbf{v})}{\Sigma(\mathbf{r},\mathbf{v})} \Psi(\mathbf{r},\mathbf{v}) \right\rangle_m}{\left\langle \Psi(\mathbf{r},\mathbf{v}) \right\rangle_m} \right) \quad ;$$

Square matrix of order M:

$$\vec{W} = \left\| \frac{\left\langle \chi(\mathbf{r}_i',\mathbf{v}' \rightarrow \mathbf{v}) \frac{\Sigma_s(\mathbf{r}',\mathbf{v}')}{\Sigma(\mathbf{r}',\mathbf{v}')} \psi(\mathbf{r}_{i'},\mathbf{v}') \right\rangle_{n'i'ni}}{\left\langle \Psi(\mathbf{r}_{i'},\mathbf{v}') \right\rangle_{n',i'}} * \right.$$

$$\left. * \frac{\left\langle T(\mathbf{v}_{ni},\mathbf{r}'|\mathbf{r}) \Sigma(\mathbf{r},\mathbf{v}_{ni}) \Psi^{+}_{kx}(\mathbf{r},\mathbf{v}_{ni}) \right\rangle_{ii'}}{\left\langle \Psi^{+}_{kx}(\mathbf{r},\mathbf{v}_{ni}) \right\rangle_i} \right\|$$

Diagonal matrices:

$$\hat{K} = \left\| \frac{\left\langle \psi(\mathbf{r}_i,\mathbf{v}) \right\rangle_{n,i}}{\left\langle \psi(\mathbf{r},\mathbf{v}) \right\rangle_m} \Delta R_i \, \delta_{mm'} \right\|$$

$$\hat{K}^{+}_{kx} = \left\| \frac{\left\langle \Psi^{+}_{kx}(\mathbf{r},\mathbf{v}_{ni}) \right\rangle_i}{\Psi^{+}_{kx}(\mathbf{r}_{i'},\mathbf{v}_{ni}) \Delta R_i} \delta_{mm'} \right\|$$

Here $\mathbf{r}_l$, $\mathbf{v}_{nl}$ - have arbitrary values inside elementary phase volume m.

It is possible by using above introduced notations and statements 2^0 to formulate collision probability equation in the form:

$$\vec{\Psi} = \hat{k}^{+}_{kx} \hat{W} \hat{k} \vec{\Psi} + \hat{k}^{+}_{kx} \vec{Q} \quad , \tag{5}$$

$$\vec{\Psi}^{+}_{kx} = \hat{k} \hat{W}^{+} \hat{k}^{+}_{kx} \vec{\Psi}^{+}_{kx} + \vec{Q}^{+}_{kx} \quad . \tag{6}$$

Elementary phase volumes and points $(\mathbf{r}_l, \mathbf{v}_{nl})$ can be chosen for each kx, separately, therefore we will have $2KX$ or in general case $2KXM$ equations.

If functions $\Psi(\mathbf{r},\mathbf{v})$ and $\Psi^{+}_{kx}(\mathbf{r},\mathbf{v})$ are a priori unknown, then for determination $\hat{W}$, $\hat{k}$, $\hat{k}^{+}_{kx}$, $\vec{Q}^{+}_{kx}$ it is needed to introduce some hypothesis about their behavior. In difference with Chernick's equations we can test the quality of hypothesis by using the statement 4^0 and the fact that neutron flux must be the same for different kx in intersecting elementary phase volumes.

For example in course of realization of subgroup generalized approach[1], subgroups for each isotope were chosen from behavior analysis function $\Psi^{+}_{kx}(\mathbf{r},\mathbf{v})$ in cells typical for thermal and intermediate reactors. It was assumed that collision density is lethargy-independent in each subgroup. The spatial-angular division of phase volume was chosen to minimize the difference of group isotope fluxes (group isotope flux is $\Phi^{g}_{kx} = \Psi^{g}_{kx} / \Sigma^{g}_{kx}$).

Numerical results obtained with MBC-1.5(B20) for tests from Ref.[6] are shown in Tables 1. and 2. These tests are numerical benchmark for the Doppler coefficient of reactivity in light water reactor square cell. In Table 1. are shown k-infinite at temperature of 600K. In Table 2. are shown the Doppler defect in k-infinite from 600K to 900K:

$$\Delta\rho_{Dop} = \frac{k_{\infty}^{600} - k_{\infty}^{900}}{k_{\infty}^{600}\, k_{\infty}^{900}}$$

In these tables also results from Ref.[6] calculated with the MCNP-3A and CELL-2 codes using data taken from ENDF/B-V nuclear data library are shown . The MBC-1.5(B20) calculation has been made in two regimes:

SAPG - square outer boundary and reflecting boundary condition;
SAPS - circular outer boundary (equivalent cell radius) and isotropicall reflecting boundary condition.

Results of four calculations are in good agreement, despite the fact that we used our nuclear data. Excellent agreement of SAPS and CELL-2 results is most probably accidental, since errors of cylinderization for SAPS and CELL-2 differ in sign.

ANALYSIS OF BENCHMARK EXPERIMENTS.

Usually, the critical deterministic calculations of benchmark experiments is carried out in two steps. The first one - the spectrum for cell in asymptotic region of lattice and the group diffusion parameters are calculated using known buckling. The second step - using diffusion code the criticality of lattice is evaluated.

We will carry out critical calculation of benchmark experiments using the collision importance function. 26-group effective cross sections were obtained by MBC-1.5(B20) for pin cell and reflector without leakage, since leakage have small influence on the value of 26-group constants. For taking leakage into account let us return to Eq.(6), which may be written with leakage term.

$$\vec{\Psi}^{+} = \hat{k}\ \hat{W}^{+}\ \hat{k}^{+}_{a+Z}\ \vec{\Psi}^{+}_{a+Z} + \vec{Q}^{+}_{a} + \vec{Z} \qquad (7)$$

Where Z_m - element of the vector $\vec{Z}$, which is equal to probability that neutron leaves the elementary phase volume m.

In the P_1-approximation Z_m averaged per one collision in m is (B^2 - bucling):

$$Z_m = \frac{B^2}{3(\Sigma^2_m - \mu_m \Sigma_{s_m} \Sigma_m)} . \qquad (8)$$

If we substitute exact Z_m in Eq.(2), then it is possible to prove that statement 3^0 is correct also in this case.

Thus, Eq. (6) reduces to:

$$\vec{E} = \hat{W}^{+} \hat{k}^{\bullet} \vec{E} + \vec{Q}_{a}^{+} + \vec{Z} , \qquad (9)$$

where $\vec{E}$ - unit column matrix.

Left $\hat{W}^{+}$ be unit normalized, then elements of unknown diagonal matrix $\hat{k}^{\bullet}$ may be interpreted as probability for neutron after collisions in all m' and subsequent transfer in m to stay in the lattice.

Till now we analyzed the inhomogeneous equations. For critical calculations let us assume that leakage probability for the neutron of source also may be taken into account by using $k^{\bullet}$

Then Eq. (5) reduces to:

$$\vec{\Psi} = \hat{k}^{\bullet} \hat{W} \vec{\Psi} + \hat{k}^{\bullet} \vec{Q} . \qquad (10)$$

where $\hat{k}^{\bullet}$ - is the solution of Eq.(9)

Solving Eq.(10) we obtain the quantity of secondary neutrons on one absorbed neutron. This quantity we determine as the criticality.

In the model offered the reflector influence on the criticality can be taken into account. It can be done by using surface currents of neutrons, which are proportional to $(1-k_m)$, core-reflector surface and anisotropy correction for surface current. The anisotropy correction may be easily calculated in P_1-approximation, if position of surface and direction of leakage are known.

The model described is implemented in MBC-1.5(B50) code from code package SAPFIR. The MBC-1.5(B50) code is used for preparation of reactor diffusion parameters.

Benchmark experiments[7] TRX and BAPL were calculated using SAPFIR's codes and some results are presented in Table 3. In Table 3. following notation are used:

k_{∞}^{B20} - k-infinite by MBC-1.5(B20) pin cell without taking leakage into account;

k_{as}^{B50} - the criticality by MBC-1.5(B50) without taking into account the surface current;

k_0^{B50} - the criticality by MBC-1.5(B50) taking into account the isotropic surface current;

k_1^{B50} - the criticality by MBC-1.5(B50) taking into account the surface current in P_1-approximation.

As is seen from the Table 3. there is an overestimation of calculated criticality for all lattices except TRX-1. More wide analysis shows that overestimation is mostly because off our nuclear data and that TRX-1 lattice is not quite correctly cylindrized.

CONCLUSIONS.

The method presented is used in code package SAPFIR for solving different neutron - physical problems from nuclear data library verification to practical reactor problems. As a rule, total expenditure on solving the problem from formulation stage to final results with its uncertainty estimation is smaller than with other methods.

REFERENCES

1. V.V. Tebin, "A Generalized Subgroup Approach to Calculating Resonance Absorption of Neutrons in Nuclear Reactors," IAEA - TECDOC-491, (1989), p 79.

2. J. Lewins "Importance The Adjoint Function," Pergamon Press, (1965).

3. M.A.Robkin, M,J. Clarc "Integral Reactor Theory: Orthogonality and Importance," Nucl. Sci. & Eng.,8 (1960), p 437.

4. F Storrer at al., "Heterogeneity Calculation for Fast Reactors by a Perturbation Method," Nucl. Sci. & Eng., 24 (1966), p 153.

5. J. Lewins "Collision Probability Theory" in "Advances in Nuclear Science and Technology," 4 (1968), p 318.

6. R.D. Mosteller "Benchmark Calculations for the Doppler Coefficient of Reactivity," Nucl. Sci. & Eng., 107 (1991), p 265.

7. Cross Section Evaluation Working Group Benchmark Specifications BNL-19302(ENDE-202).

Table 1. k_∞ for fuel temperature = 600K

Fuel Enrich. (wt%)	MCNP 3A	MBC-1.5(B20) SAPG	MBC-1.5(B20) SAPS	CELL-2
0.711	0.6638 ±.0006	0.6665	0.6651	0.6652
1.6	0.9581 ±.0006	0.9621	0.9604	0.9605
2.4	1.0961 ±.0007	1.1004	1.0984	1.0989
3.1	1.1747 ±.0007	1.1786	1.1794	1.1773
3.9	1.2379 ±.0007	1.2420	1.2397	1.2404

Table 2. $\Delta\rho_{Dop}$ for ΔT=900-600 K

Fuel Enrich. (wt%)	MCNP 3A	MBC-1.5(B20) SAPG	MBC-1.5(B20) SAPS	CELL-2
0.711	0.0163 ±.0023	0.0168	0.0174	0.0168
1.6	0.0108 ±.0009	0.0103	0.0107	0.0107
2.4	0.0081 ±.0008	0.0084	0.0087	0.0089
3.1	0.0078 ±.0007	0.0075	0.0077	0.0080
3.9	0.0071 ±.0006	0.0071	0.0074	0.0074

Table 3. k_{eff} for benchmark experiments TRX and BAPL

k_{eff}	TRX-1	TRX-2	BAPL-1	BAPL-2	BAPL-3
k_{∞}^{B20}	1.1775	1.1694	1.1415	1.1473	1.1354
k_{as}^{B50}	0.9899	0.9959	0.9998	1.0005	1.0021
k_{0}^{B50}	1.0011	1.0060	1.0045	1.0062	1.0071
k_{1}^{B50}	0.9993	1.0041	1.0040	1.0052	1.0062

DEVELOPMENT OF A HEXAGONAL ASSEMBLY TRANSPORT CODE

Y.Tahara, M.Nakano, H.Wakiyama
Mitsubishi Atomic Power Industries, Inc.
4-1 Shibakouen 2-chome, Minato-ku, Tokyo, Japan
M.Yamasaki, N.Ushio, T.Takeda
Osaka University, Department of Nuclear Engineering
2-1 Yamadaoka, Suita, Osaka, Japan

ABSTRACT

A two-dimensional, multi-group hexagonal transport code, HARPY, has been developed to improve the calculational accuracy of physics characteristics of cores with hexagonal assemblies such as HCPWRs and nuclear reactors for cancer therapy. Pin power distributions and K_∞'s were calculated by HARPY and compared to those obtained by the Monte Carlo code GMVP. Good agreement between the two sets of results was found. This verifies the accuracy of HARPY.

INTRODUCTION

The High Conversion PWR (HCPWR) has been studied to utilize surplus plutonium effectively and save uranium resources. A hexagonal assembly with hexagonal cells has been employed in HCPWRs in order to enhance the conversion ratio by hardening the neutron spectrum by means of the reduction of moderator to fuel volume ratio. Recently, a study was carried out to produce a reactor concept suitable for Boron Neutron Capture Therapy. Hexagonal assemblies are also employed in this reactor to obtain a high intensity of epi-thermal neutrons. Although there are some codes which can treat hexagonal assemblies, they are not suitable for the nuclear design of the cores due to their long computer times. Thus, we have developed a hexagonal transport code HARPY as a design tool to improve the calculational accuracy of the physics characteristics of such cores. HARPY is a two-dimensional, multi-group transport theory code for treating assemblies with hexagonal cells.

HARPY employs a well known methodology ,which is a combination of the nodal method for pin cell coupling and the Sn method. The results of the HARPY code have been compared with those obtained by the Monte Carlo code GMVP[1] developed at JAERI. These comparisons have shown that the pin power distributions and K∞'s are in good agreement between the two codes.

METHODOLOGY

The HARPY code consists of two major programs. The first is a nodal code for pin cell coupling in hexagonal geometry and the second is a hexagonal mesh discrete ordinates transport code. The calculational flow scheme of HARPY is shown in Fig.1, and is similar to that of the PHOENIX-P code[2] for assemblies with square cells. The combination of these codes provides accurate solutions of the infinite multiplication factor and power distribution in hexagonal assemblies.

NODAL METHOD FOR HEXAGONAL PIN-CELL COUPLING

The pin cell coupling method[3] has been applied to an assembly with hexagonal cells. The nodal code calculates the microgroup microregion (pellet,clad,moderator) fluxes of the cells in a hexagonal assembly. The total partial current from node N to K which is shown in Fig.2, is expressed as follows

$$J_{NK} = \frac{1}{6} R_N + \frac{1}{6}(1-\Gamma_N -5\rho_N) \sum_{M} J_{MN} + \rho_N \sum_{M \neq N} J_{MN} \qquad (1)$$

where

R_N source neutrons that escape from node N
Γ_N removal blackness
ρ_N first-flight transmission probability ($\rho_N = (1-\gamma_N)/5$)
γ_N first-flight blackness

The first term of the right-hand side is the total number of neutrons that escape from node N to k. The second term is the contribution from those incoming neutrons that have scattered at least once. The last term represents the first-flight passages from the other nodes except node k. The nodal variable M_N is defined by

$$M_N = R_N + \mu_N \bar{J}_N \qquad (2)$$

where J_N^- is the total partial in-current into node N

$$J_N^- = \sum_K J_{KN} \tag{3}$$

and the coefficient is given by

$$\mu_N = 1 - \Gamma_N + \rho_N \tag{4}$$

Then M_N is transformed to the following expression

$$M_N = \frac{R_N + \frac{\mu_N}{6} \sum_K \frac{M_K}{1-\rho_K \rho_N}}{1 + \frac{\mu_N}{6} \sum_K \frac{\rho_K}{1-\rho_K \rho_N}} \tag{5}$$

By introducing the coefficients A_{KN} , λ_N and B_N, one can obtain the following set of equations

$$M_N = \sum_K A_{KN} M_K + B_N \tag{6a}$$

$$A_{KN} = \frac{1}{6} \frac{\lambda_N \mu_N}{1 - \rho_K \rho_N} \tag{6b}$$

$$\lambda_N = \left[1 + \frac{\mu_N}{6} \sum_K \frac{\rho_K}{1-\rho_K \rho_N}\right]^{-1} \tag{6c}$$

$$B_N = \lambda_N R_N \tag{6d}$$

M_N can be solved iteratively and the microgroup microregion fluxes Φ_{Ni} are calculated by means of the following equations using current response fluxes Y_{Ni} ,source response fluxes X_{Ni}^J and the converged nodal variables M_N

$$J_N^- = \frac{1}{\mu_N} (M_N - \Gamma_N) \tag{7a}$$

$$\Phi_{Ni} = \sum_J Q_{N,J} X_{Ni}^J + J_N^- Y_{Ni} \tag{7b}$$

Few-group homogenized cross-sections of the pin cells are generated using the fluxes. The flux-volume weighted cross-sections do not preserve the reaction rates and the partial currents at the surface of the homogenized regions, simultaneously.
The interaction between two adjacent regions cannot be properly

described by the homogenized cross-sections alone. Therefore, false sources[3] have been introduced to restore the surface-integrated partial currents from the nodal solution. The false sources are used in the iteration process in the following Sn code.

Sn METHOD FOR A HEXAGONAL MESH

The hexagonal mesh Sn code calculates the flux distribution in a hexagonal assembly using the few-group cross-sections and false sources, which are obtained from the nodal calculation. Angular fluxes are defined at vertices of a hexagonal mesh as shown in Fig.3 and the fluxes are obtained by solving a finite difference transport equation by means of the diamond difference scheme and an Sn quadrature set for a hexagonal geometry which is modified from that in square geometry. The descretized transport equation has the following form for hexagonal meshes

$$\sum_{K} \mu_K \ (\phi_{K+} - \phi_{K-}) + \frac{3}{2} h_p \Sigma_t \phi = \frac{3}{2} h_p S. \tag{8}$$

where $\phi_{k\pm}$ is the surface average angular flux(k=x,u,v); ϕ is the cell-average angular flux; hp is the hexagonal cell pitch; μ_k is the directional cosine with respect to the k-axis. The surface average angular fluxes of a particular surface are defined to be the average of the two adjoining vertex fluxes of that surface. To solve the equation, the following diamond difference equations are assumed,

$$\phi_1 + \phi_4 = 2\phi \tag{9a}$$
$$\phi_2 + \phi_5 = 2\phi \tag{9b}$$
$$\phi_3 + \phi_6 = 2\phi \tag{9c}$$

Using Eq.(9), the cell-average flux is given by

$$\phi = \frac{2\{\mu_x(\phi_2+\phi_3)+\mu_u(\phi_3+\phi_4)+\mu_v(\phi_1+\phi_2)\}+3h_p S}{4(\mu_x+\mu_u+\mu_v)+3h_p \Sigma_t} \tag{10}$$

In the cell shown in Fig.3 inflow fluxes ϕ_1, ϕ_2, ϕ_3, and ϕ_4 are known and the cell-average flux can be determined from Eq.(10) and the outflow vertex fluxes ϕ_5 and ϕ_6 can then be determined from Eq.(9b) and Eq.(9c). The water gap is treated as a number of hexagonal cells which contain the same amount of water as the actual narrow water gap and have the same size as the fuel cells.

The above equations are solved with reflective conditions. In the calculation, hexagonal meshes, in other words, coarse meshes are used. Therefore, to eliminate space truncation errors, cell average fluxes are recalculated by means of the following weighted diamond difference scheme[4] using the surface fluxes.

$$\bar{\phi}_x = \{(1-\alpha_x)\,\phi_{x-}+(1-\alpha_x)\,\phi_{x+}\}/2 \tag{11a}$$

$$\bar{\phi}_u = \{(1-\alpha_u)\,\phi_{u-}+(1-\alpha_u)\,\phi_{u+}\}/2 \tag{11b}$$

$$\bar{\phi}_v = \{(1-\alpha_v)\,\phi_{v-}+(1-\alpha_v)\,\phi_{v+}\}/2 \tag{11c}$$

$$\bar{\phi} = (\bar{\phi}_x+\bar{\phi}_u+\bar{\phi}_v)/3 \tag{12}$$

where

$$\alpha_x = \frac{3}{16}\,\frac{\beta}{\mu_x}\,h_p \quad , \quad \alpha_u = \frac{3}{16}\,\frac{\beta}{\mu_u}\,h_p$$

$$\alpha_v = \frac{3}{16}\,\frac{\beta}{\mu_v}\,h_p \quad , \quad \beta = \Sigma_t - \frac{S}{\phi}$$

The pin power distribution and K_∞ of the assembly are calculated by using the cell average fluxes $\bar{\phi}$.

PROGRAM QUALIFICATION

In order to check the accuracy of the HARPY code, it was applied to a small assembly shown in Fig.4. The fuel assembly contains 12 control rod guide thimble cells and 73 fuel cells with 6.2 w/o Pu-fis MOX fuel rods. The water to fuel volume ratio of the cell is 1.0. B4C control rods with 90% B10 are inserted into the thimbles. The multi-group Monte Carlo code GMVP was used as a reference to avoid any uncertainties associated with modeling in the calculation except statistical errors. Cross-sections of the microregions in each cell were generated by the SRAC code[5] in 20 energy groups and supplied to both codes. The calculational flow scheme is shown in Fig.5. In the HARPY calculation, 20 energy groups were used in the nodal calculation and these were collapsed into 9 energy groups for the following S4 calculation. The water gap was represented by hexagonal cells which preserve the amount of water contained in the actual narrow water gap. Calculations were performed for assemblies with and without control rods. The comparisons of the microgroup neutron spectra in pellet regions calculated by the nodal code in HARPY and GMVP are shown in Fig.6 and Fig.7. Figure 6 shows the neutron spectrum

in a fuel pellet of a fuel cell at the vertex of the assembly. Figure 7 shows the spectrum in a B4C pellet of a control rod cell which is in the third row from the center of the assembly. Neutron spectra calculated by both codes are in good agreement. This demonstrates the adequacy of the nodal method for pin cell coupling in hexagonal geometry incorporated into the HARPY code. Results of K_∞ and rod worth are presented in Table 1. The values calculated by HARPY agree with those by GMVP within about 1% ΔK for both the rodded and unrodded cases. The rod worth agrees with the reference value within 3.3 percent difference. Thus, good agreements are found for K_∞ and rod worth. The comparisons of power distributions are shown in Fig.8 and Fig.9 for the unrodded case and rodded case respectively. The maximum difference is 1% for the unrodded case and 3% for the rodded case. Thus, good agreement is also found between the two power distributions in each case.

CONCLUSION

A two-dimensional,multi-group transport code in hexagonal geometry has been developed to improve the calculational accuracy of the nuclear design of cores such as HCPWRs and nuclear reactors for cancer therpy. The capability of predicting pin power distribution and k_∞ has been tested by comparing the results obtained by HARPY and Monte Carlo code GMVP. The good agreement between HARPY and GMVP has verified the adequacy of the nodal method and the Sn method incorporated into the HARPY code.

ACKNOWLEDGMENTS

The authors wish to acknowledge the contributions and support of K.Okumura of JAERI. He provided us with the reference solutions and it is highly appreciated.

REFERENCES

1 M.Nakagawa,et al.,"Development of Monte-Carlo Code for Particle Transport Calculations on Vector Processors",Proc. of International Conference on Supercomputing in Nuclear Applications, Mito,Japan,March12-16,(1990).

2 A.J.Harris,et al.,"A Description of The Nuclear Design and Analysis Programs for Boiling Water Reactors", WCAP-10106, (1982).

3 R.J.J.Stammler and M.J.Abbate,Methods of Steady-State Reactor Physics in Nuclear Design,Academic Press (1988).

4 T.Takeda,et al.,"An Weighted Diamond Difference Approximation for Improving 3-D Coarse Mesh Sn Calculations", the ANS 1992 Topical Meeting on Advances in Reactor Physics March 8-11 1992.

5 K.Tsuchihashi,et al.,"Revised SRAC Code System",JAERI1302, September 1986.

Table 1. Comparisons of K_∞ and Rod Worth Between HARPY and GMVP

CODE	K_∞		Rod WORTH(%$\Delta\rho$)
	RODDED	UNRODDED	
HARPY	1.1936	0.6152	78.8
GMVP	1.2010	0.6266	76.3

Figure 1 Calculational Flow Scheme of HARPY

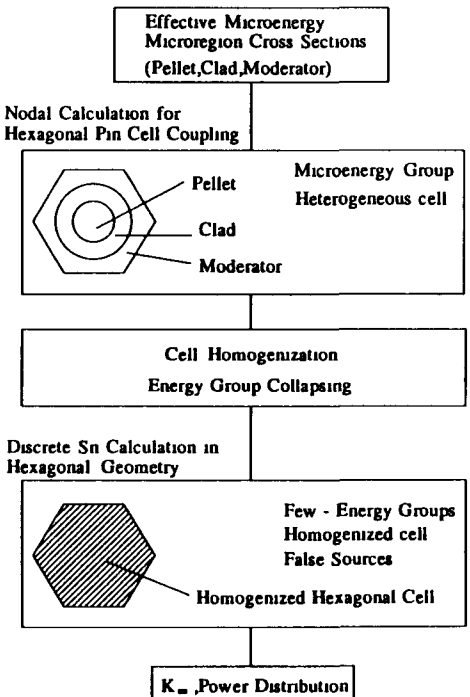

Figure 2 Partial Currents Between Nodes N and K

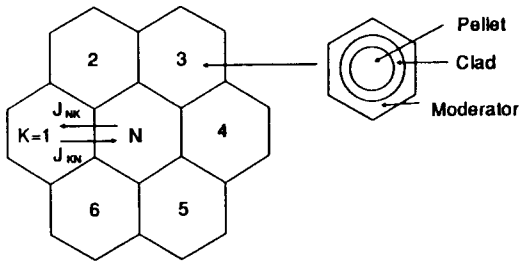

Figure3 Coordinates and Fluxes for S_N Calculation

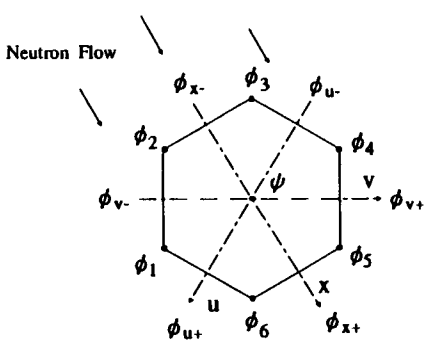

Figure 4. Fuel Assembly Used in the Calculations

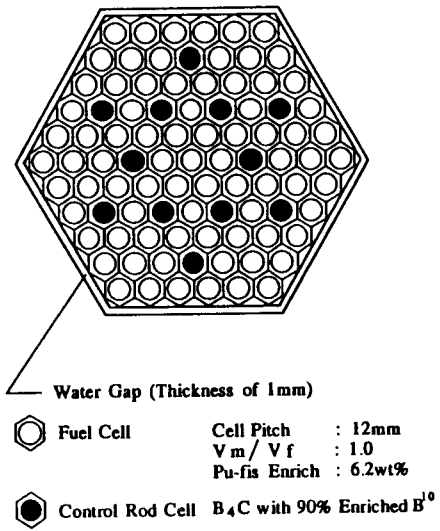

Figure 5. Calculational Flow Scheme for HARPY verification

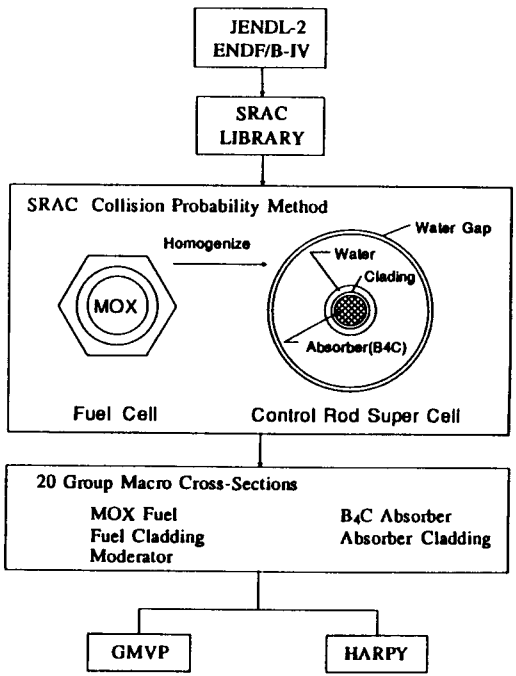

Figure 6. Comparison of Neutron spectra calculated by HARPY and GMVP for a fuel pellet in the rodded case

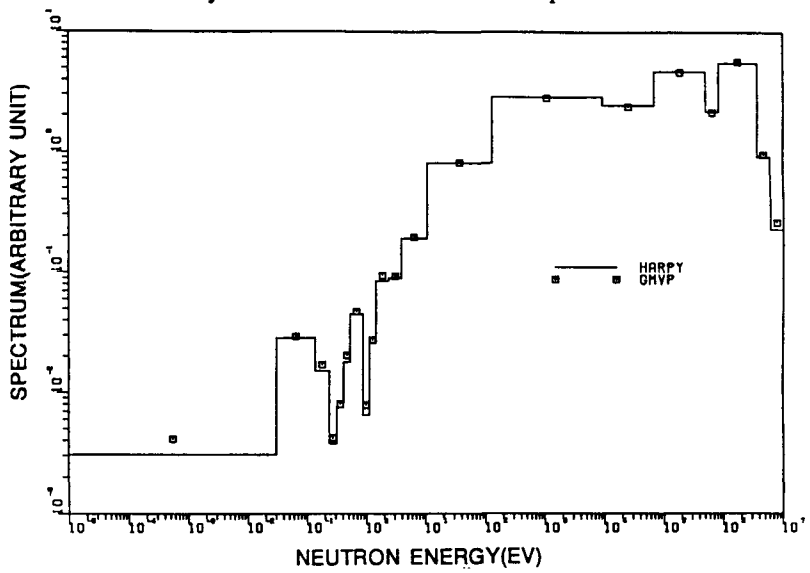

Figure 7. Comparison of Neutron spectra calculated by HARPY and GMVP for a B_4C pellet in the rodded case

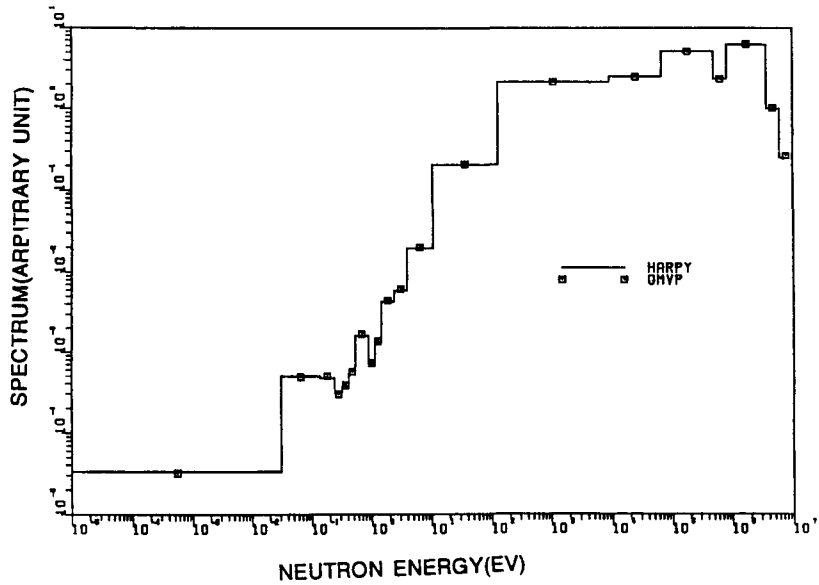

Figure 8. Pin Power Distribution Comparison for Unrodded Case.

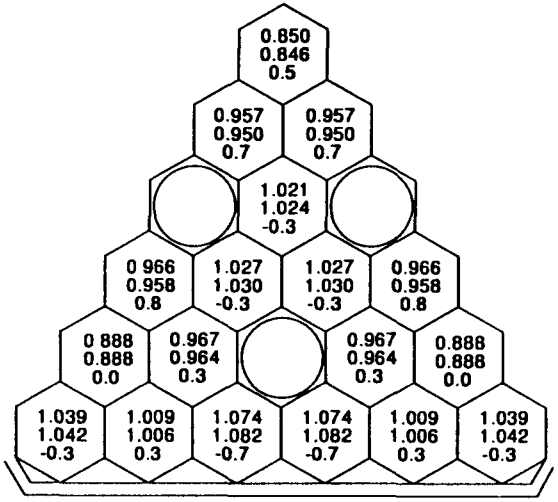

Figure 9. Pin Power Distribution Comparison for Rodded Case.

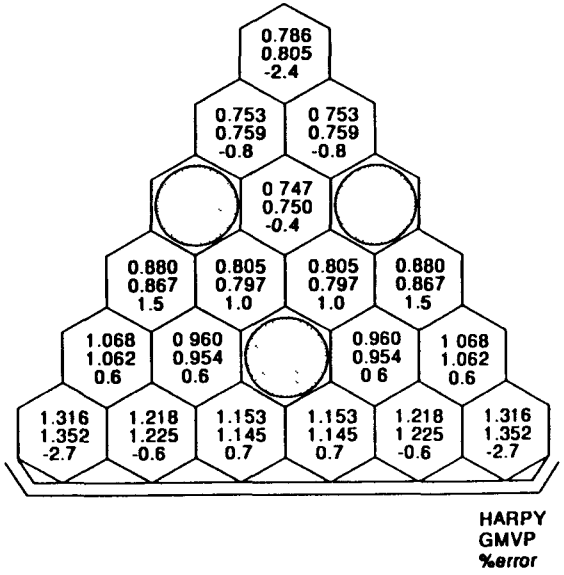

COLLISION PROBABILITY CALCULATIONS WITH FINITE-ORDER OF ANISOTROPY

R. Roy, G. Marleau, A. Hébert and D. Rozon
Groupe d'Analyse Nucléaire
Institut de Génie Énergétique, École Polytechnique de Montréal
Montréal (Québec), Canada H3C 3A7

ABSTRACT

The integral transport equation with anisotropic scattering is solved in general 2-D Cartesian geometries in the case where specular boundary conditions are taken into account. Using selected quadrature sets, the cyclic tracking procedure is first applied in order to follow the infinite path of neutrons in a regular 2-D lattice. Collision probabilities (CP) of any order of anisotropy are then computed as linear combinations of closed-form contributions resulting from the infinite line integration on these cyclic tracks. Numerical results for two-group problems are presented.

1. INTRODUCTION

The cyclic tracking procedure was developed originally for the calculation of collision probabilities (CP) on 2-D square cells where specular boundary conditions must be taken into account. These boundary conditions were accounted for by following the neutron paths on the lattice covering the whole 2-D space and made of the original reflected cell repeated with a coherent mirror-like rotation-inversion process. Numerical results for problems with isotropic scattering and sources have already been presented using these CP calculations.[1] Basically, the cyclic tracking procedure consists of selecting a numerical quadrature which requires the tracks to be "cyclic" in the sense that a track finishes where it has started after a finite number of crossings of the cell under investigation. The computation of angle-dependent CP factors is then performed by adding closed-form contributions resulting from infinite line integration on all cyclic tracks corresponding to the same angle. A model for anisotropic collision probability calculations based on these angle-dependent factors has been developed for 1-D slab and 2-D XY lattices[2] and numerical results for some multigroup anisotropic problems will now be presented. We will show here that this technique can be used to reconstruct the CPs up to any anisotropic order.

In section 2, we will introduce some notations and we will describe how anisotropic CPs can be computed using cyclic tracks. Section 3 is devoted to a short study of the Green functions involved for a directional source transported along a cyclic track. In section 4, we will apply our technique on two 2-D test problems, one being a forward-scattering mock-up of original isotropic data, the other being a problem with P_3 scattering cross-sections. Finally, we will describe future work and draw some conclusions.

2. COMPUTATION OF ANISOTROPIC COLLISION PROBABILITIES

Consider the basic domain D of a 2-D Cartesian lattice and assume that specular boundary conditions associated with the external faces are given; this basic domain is extended to fill up the whole 2-D space using mirror-like replication. The angular flux $\Phi(\vec{r},\vec{\Omega})$ is solution of the one-group neutron transport equation:

$$\mathcal{L}\Phi(\vec{r},\vec{\Omega}) = \vec{\Omega}\cdot\vec{\nabla}\Phi(\vec{r},\vec{\Omega}) + \Sigma(\vec{r})\,\Phi(\vec{r},\vec{\Omega}) = Q(\vec{r},\vec{\Omega}) \quad \text{for} \quad \vec{r}\in D,\ \vec{\Omega}\in S_{4\pi}, \qquad (1a)$$

with angular souces of the form:

$$Q(\vec{r},\vec{\Omega}) = \int_{4\pi} d^2\Omega'\ \Sigma_s(\vec{r},\vec{\Omega}\cdot\vec{\Omega}')\,\Phi(\vec{r},\vec{\Omega}') + S(\vec{r},\vec{\Omega})\ , \qquad (1b)$$

where $\Sigma(\vec{r})$ and $\Sigma_s(\vec{r},\vec{\Omega}\cdot\vec{\Omega}')$ are the total and transfer cross-sections respectively (the angular part of the transfer function is assumed to depend only on the scalar product $\mu_0 \equiv \vec{\Omega}\cdot\vec{\Omega}'$). We are thus interested in solving this system subject to boundary conditions given by:

$$\Phi(\vec{r}_s,\vec{\Omega}) = \beta(\vec{r}_s)\,\Phi(\vec{r}_s,\vec{\Omega}_{\text{refl}}) = \beta(\vec{r}_s)\,\Phi(\vec{r}_s,\vec{\Omega} - 2\,(\vec{\Omega}\cdot\vec{N}_{\vec{r}_s})\,\vec{N}_{\vec{r}_s}\ ), \qquad (1c)$$

where $\vec{r}_s \in \partial D$ and the albedo $\beta(\vec{r}_s)$ is a regular function defined all over the external boundary ∂D; here, $\vec{\Omega}_{\text{refl}}$ and $\vec{N}_{\vec{r}_s}$ are respectively the reflected angle and the outward normal at the point $\vec{r}_s$.

Let us partition the original domain D into I zones; each zone has volume V_i and is defined such that it has homogeneous material properties. We now assume that the infinite transfer expansion is truncated to the Legendre order L in anisotropy for the problem to be solved in domain D and expand the flux and the transfer cross-section as follows:

$$\Phi(\vec{r},\vec{\Omega}) = \sum_{l=0}^{L}\frac{(2l+1)}{4\pi}\sum_{m=-l}^{l}\psi^{lm}(\vec{r})\,R^{lm}(\vec{\Omega})$$

and

$$\Sigma_s(\vec{r},\mu_0) = \sum_{l=0}^{L}\frac{(2l+1)}{4\pi}\Sigma_s^l(\vec{r})P_l^0(\mu_0)\ ,$$

and we define spatially averaged (flat flux) values for the flux and source coefficients in zone $1 \le i \le I$ and for angular mode lm as

$$\phi_i^{lm} = \frac{1}{V_i} \int_{V_i} d^3r \int_{4\pi} d^2\Omega \; R^{lm}(\vec{\Omega}) \; \Phi(\vec{r}, \vec{\Omega}) \; ,$$

$$q_i^{lm} = \frac{(2l+1)}{V_i} \int_{V_i} d^3r \int_{4\pi} d^2\Omega \; R^{lm}(\vec{\Omega}) \; S(\vec{r}, \vec{\Omega}) \; ,$$

where the orthogonal real spherical harmonic functions are defined as

$$R^{lm}(\vec{\Omega}) = R^{lm}(\varphi, \mu) = \begin{cases} \sqrt{2\frac{(l-|m|)!}{(l+|m|)!}} \; P_l^{|m|}(\mu) \; \cos|m|\varphi & \text{for } 0 < m \le l, \\ P_l^0(\mu) & \text{for } m = 0, \\ \sqrt{2\frac{(l-|m|)!}{(l+|m|)!}} \; P_l^{|m|}(\mu) \; \sin|m|\varphi & \text{for } -l \le m < 0, \end{cases} \tag{2}$$

for $l + m$ even and $l \le L$ the maximum order of anisotropy considered The neutron angular direction $\vec{\Omega}$ is described here by $\mu = \cos\theta$ where θ is the polar angle measured from the z-axis, and by φ the azimuthal angle measured from the x-axis From 2 D symmetry, the contributions from the $l+m$ odd modes vanish With these zone-averaged coefficients, the one-group transport equation (1) is converted into the linear system

$$V_j \phi_j^{l'm'} = \sum_{i=1}^{I} \sum_{l=0}^{L} \sum_{m=-l}^{l} P_{j \leftarrow i}^{l'm' \leftarrow lm} \{ \Sigma_{s_i}^l \phi_i^{lm} + q_i^{lm} \} \; , \tag{3}$$

where $\Sigma_{s_i}^l = 2\pi(2l+1) \int_{-1}^{1} d\mu_0 \; P_l^0(\mu_0) \Sigma_s(\vec{r}, \mu_0)$ for $\vec{r} \in V_i$, solutions to these one-group linear equations can be easily found after calculation of a scattering-reduced matrix or using an iterating within-group scattering process

The anisotropic CPs from zone i to zone j are defined as [2]

$$P_{j \leftarrow i}^{l'm' \leftarrow lm} = \int_0^{\pi/2} \frac{d\varphi}{2\pi} \int_0^1 \frac{d\mu}{\sqrt{1-\mu^2}} \; R^{l'm'}(\varphi, \mu) R^{lm}(\varphi, \mu)$$

$$\times \sum_{o'=1}^{4} \sum_{o=1}^{4} I_{o'}^{m'} \; I_o^m \int_{\perp(\varphi)} dr' F_{ji}^{o'o}(\varphi, \mu, r') \; , \tag{4}$$

where dr' stands for a line element perpendicular to the angle φ The principal value of an angle $\varphi \in [0, \pi/2]$ is defined in the first quadrant, associated with this principal value, we also define four *quadrant modes* and four quadrant sign functions by

$$\begin{aligned} \varphi_1 &= \varphi \quad \text{with} \quad I_1^m = +1 \; , \\ \varphi_2 &= \pi - \varphi \quad \text{with} \quad I_2^m = \text{sign}\, m \; (-)^m \; , \\ \varphi_3 &= \pi + \varphi \quad \text{with} \quad I_3^m = \text{sign}\, m \; , \\ \varphi_4 &= 2\pi - \varphi \quad \text{with} \quad I_4^m = (-)^m \; , \end{aligned}$$

with sign m equal to $+1$ for $m \geq 0$ and equal to -1 for $m < 0$ Since the functions defined in equation (2) are affected only by sign changes for any kind of specular reflexions (that is, changing the quadrant mode from φ_k to φ_l), it is possible to limit our analysis to the principal quadrant

In equation (4), discrete values for (φ, r') will be used to define 2 D tracks that intersect different zones in the lattice Should the μ integration of equation (4) be performed, the usual formulation of CP using various order of Bickley functions is obtained In that case however, the multiplicative property of the exponential function is lost and boundary conditions need to be approximated to some extent using surface currents [3] For a particular track, the factors $F_{j_1}^{o'o}(\varphi, \mu, r')$ collect all the contributions from segments of zone i to segments of zone j according to sixteen (4×4) possible combinations of the starting and ending quadrant modes that are associated to the tracking direction (φ, μ) All these factors are also added up for a given track density $\Delta r'$ and, because the principal angular direction is not changed, factors of the form

$$\mathcal{F}_{j_1}^{o'o}(\vec{\Omega}) = \int_{\perp(\varphi)} dr' F_{j_1}^{o'o}(\varphi, \mu, r')$$

can be computed prior to performing CP reconstruction using quadrant sign functions

The numerical integration of the CPs in equation (4) is performed using a set of angles and weights respectively defined by

$$\vec{\Omega}_{k'k} = (\varphi_{k'}, \mu_k) \quad \text{and} \quad \omega_{k'k} = W_{k'} \times w_k$$

such that[1 2]

1) a set of angles and weights $\{\varphi_{k'}, W_{k'}\}$ where the angles must be chosen so that they generate cyclic tracks and the corresponding positive weights are calculated in order to preserve even moments of the angular flux,
2) a set of Gauss points and weights $\{\mu_k, w_k\}$ is used in the interval $[0, 1]$ for the μ integration with a compatible order of accuracy,
3) an user-input density $\Delta r'$, in tracks/cm, required for track separation and automatically adjusted for every angle to the nearest possible cyclic track separation in order to perform the integration of $\mathcal{F}$-factors using equally spaced intervals

After setting the angular quadrature and the minimal track separation, the equation (4) is converted into the discretized form

$$P_{j \leftarrow i}^{l'm' \leftarrow lm} \approx \sum_{k'k} \omega_{k'k} \frac{R^{l'm'}(\vec{\Omega}_{k'k}) R^{lm}(\vec{\Omega}_{k'k})}{\sqrt{1-\mu_k^2}} \sum_{o'=1}^{4} \sum_{o=1}^{4} I_{o'}^{m'} \; I_{o}^{m} \; \mathcal{F}_{j_1}^{o'o}(\vec{\Omega}_{k'k}) \,, \qquad (5)$$

which is the basis of all our anisotropic CP computations In all cases, these CP matrices are full, thus, an efficient scattering-reduced, or direct, transport solution can be obtained only in problems for which not too many zones are involved Further simplifications can be obtained for isotropic problems.[1]

3. DIRECTIONAL TRANSPORT ON A CYCLIC TRACK

The factors F_{ij} of equation (4) collect the flux contributions for a particular track from all segments in zone i to zone j,[1] these can be expressed as double line integrals of the Green functions corresponding to a point source (the source being smooth in angle) In order to describe these periodic Green functions, we will consider here a simplified form of the one group transport problem described in equations (1a) (1c), with specular boundary conditions We define the phase space X and two subspaces ∂X^+ and ∂X^- describing the neutron paths respectively leaving and entering the domain as

$$X = \{x = (\vec{r}, \vec{\Omega}),\ \vec{r} \in D,\ \vec{\Omega} \in \mathcal{S}_{4\pi}\},$$
$$\partial X^{\pm} = \{x = (\vec{r}_s, \vec{\Omega}),\ \vec{r}_s \in \partial D,\ \pm\vec{\Omega}\ \ N_{\vec{r}_s} \geq 0\}$$

The problem to find a Green function $g(x) = G(x' \rightarrow x)$, solution of the one-group formulation for an unit directional point source, can be written in the following form

$$\mathcal{L}g(x) = \vec{\Omega}\ \ \vec{\nabla}g(x) + \Sigma(\vec{r})g(x) = \delta(x' - x) \quad , \qquad \text{for } x \in X, \tag{6a}$$
$$g(x^-) = \beta(\vec{r}_s)\ g(x^+_{\text{refl}}) \quad , \qquad \text{for } x^- \in \partial X^- \tag{6b}$$

where $x^+_{\text{refl}} = (\vec{r}_s, \vec{\Omega}_{\text{refl}})$ is the phase point obtained after reflexion on the boundary of the corresponding $x^- = (\vec{r}_s, \vec{\Omega})$ point and $\delta(x' - x) = \delta(\vec{r}' - \vec{r})\ \delta_2(\vec{\Omega}'\ \ \vec{\Omega})$ is the usual delta measure [4] The adjoint kernel $g^*(x) = G^*(x' \rightarrow x)$ will be solution of the problem

$$\mathcal{L}^*g^*(x) = -\vec{\Omega}\ \ \vec{\nabla}g^*(x) + \Sigma(\vec{r})g^*(x) = \delta(x - x') \quad , \qquad \text{for } x \in X, \tag{7a}$$
$$g^*(x^+) = \beta(\vec{r}_s)\ g^*(x^-_{\text{refl}}) \quad , \qquad \text{for } x^+ \in \partial X^+ \tag{7b}$$

These two problems could also be formulated on an infinite domain, using periodic delta measures attenuated to take into account the lattice behaviour of the sources

Using the weak form associated with problems (6) and (7), it can be easily proved that

$$G^*(x \rightarrow x') = G(x' \rightarrow x) = G(x_I \rightarrow x'_I)$$

where the phase points $x_I = (\vec{r}, -\vec{\Omega})$ and $x'_I = (\vec{r}', -\vec{\Omega}')$ have same the spatial coordinates as x and x', but reverse angular direction The last equality relation is the usual *reciprocity relation*, a basic theorem due to the invariance of optical paths between two phase points in one-speed transport From now on, we will only consider a discrete set of directions $\{\vec{\Omega}_n^{\text{per}} \in \mathcal{S}_{4\pi}, n = 1, N\}$, where all neutron paths are cyclic In order to study the directional transport along a cyclic track, we will choose a specific tracking line of period t and we will also simplify the form of the kernel problem to get rid of the albedo factors along the tracking line This idealized problem will be completely periodic and can be written in a form similar to the periodic transport problem with plane symmetry that looks like

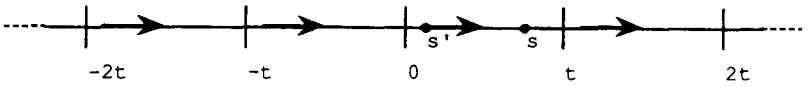

where only two directions $\mu = \cos\theta = \pm 1$ (θ is the angle taken from the track) are available for the sources Consider a forward source along the tracking line at $s' \in [0\ t]$ this source has a periodic behaviour and, in order to compute the Green function that we are looking for, we solve the transport equation written in the local coordinate system of the track

$$\frac{dg}{ds}(s,\mu) + \Sigma(s)g(s,\mu) = \delta^{\text{per}}(s'-s)\ \delta(1-\mu) \tag{8}$$

where the function δ^{per} is a spatially periodic delta measure described by

$$\delta^{\text{per}}(s'-s) = \sum_{k=-\infty}^{+\infty} \delta(s'-s+kt)$$

Equation (8) can be solved for the whole infinite cyclic line, since the solution $g(s,\mu)$ is also periodic It can be defined for $s \in [0,t]$ as

$$g(s,\mu) = \begin{cases} \dfrac{\exp(-\tau_{s's})}{1-\exp(-\tau_{0t})}\ \delta(1-\mu) & \text{for } s > s', \\ \dfrac{\exp(-\tau_{s't}-\tau_{0s})}{1-\exp(-\tau_{0t})}\ \delta(1-\mu) & \text{for } s < s', \end{cases} \tag{9}$$

where $\tau_{s's}$ is the optical path on the tracking line between s' and s Here, the value $\{1-\exp(-\tau_{0t})\}^{-1}$ is constant for any source point chosen on the track and is called the total cyclic factor of the track, it has to be computed only once, and it is used to factorize the periodic source Note that for a cyclic track in complete void ($\Sigma(s) = 0$), the total cyclic factor is infinite and so will be the neutron flux

Although the idealized problem is highly simplified, it can be used to compute the Green function on any cyclic track, which can cross the domain in various reflected angular directions with proper albedo attenuation after each external crossing Using the notations introduced in reference 1, it is possible to write a simplified expression for the general Green functions introduced in the beginning of this section for two phase points x and x' on a cyclic track

$$g(x) = G(x' \to x) = \delta_2(\vec{\omega}_{s'}\ \ \vec{\Omega}')\alpha^{\infty}(x')\frac{\beta(\vec{r}',\vec{r})\exp(-\tau(\vec{r}',\vec{r}))}{|s'-s|^2}\delta_2(\vec{\omega}_s\ \ \vec{\Omega}) \tag{10}$$

where $\alpha^{\infty}(x') = \{1-\beta_c(x')\exp[-\tau_c(x')]\}^{-1}$ is the cyclic factor of the track and where $\beta(\vec{r}',\vec{r})$ and $\tau(\vec{r}',\vec{r})$ are the total attenuation factor and the total optical path, respectively, on the track between $\vec{r}'$ and $\vec{r}$ Here, s' and s respectively represent the local coordinates of $\vec{r}'$ and $\vec{r}$ on the cyclic track while $\vec{\omega}_{s'}$ and $\vec{\omega}_s$ are respectively the angles defined by the track at locations s' and s We see that, in this general formulation, the

neutron flux can be infinite if the original lattice is both purely reflected ($\beta_c(x') = 1$) and the track chosen crosses only void zones

4. NUMERICAL RESULTS

The cyclic tracking procedure described above was used to generate tracks and integrate anisotropic CPs in the module INTPN, as part of a development version of the lattice code DRAGON[6] In order to show the precision of the cyclic tracking procedure, we will present here two-group problems, one-group problems were already investigated in reference 2 All tests were performed on an IBM ES 9000 computer with single precision arithmetics except for CP double precision accumulators The two problems examined here are

(i) a forward-scattering source problem,

(ii) a two-group P_3 XY source problem,

All of the geometric dimensions in these problems are given in cm and all of the cross-sections are in cm^{-1}, in source problems, fixed sources are given in $cm^{-3}s^{-1}$ The four external faces are labeled X_-, X_+, Y_- and Y_+, and these respectively refer to lines $y = y_{min}$, $y = y_{max}$, $x = x_{min}$ and $x = x_{max}$ User input to the cyclic tracking procedure is given by two parameters a prime number p to generate angles and a minimal track density d in tracks/cm To illustrate the angular quadratures that will be used in this section, we give in Figure 1 a polar plot of angles and weights $\{(\varphi_{k'}, W_{k'}), k' = 0, p\}$, as they were obtained for a square cell with prime numbers $p = 11$ Angles are concentrated near the $x-$ and $y-$ axes, so the corresponding weights are minimal near the axes

A last remark before going into the test cases Our flux solutions to the transport equation are piece-wise constant (flat-flux approximation) over 2 D zones for any anisotropic component of the flux, these flat fluxes are useful to homogenize or to compute integral values, such as reaction rates, but they can not easily be compared to point fluxes obtained by other methods

4 1 Forward-scattering source problem

We will now study approximations to a standard two group isotropic test case [7] The geometry of this two-group problem is a square $[0,2] \times [0,2]$ domain with a unit source in the first group located in $[0,1] \times [0,1]$, reflective boundaries are present on the two faces X_- and Y_-, and vacuum boundaries on X_+ and Y_+ Figure 2 gives a sketch of this domain The original homogeneous set of cross-sections throughout the domain is given in Table 1 with label ISOTC The isotropic fluxes obtained using these cross-sections were already computed using various mesh splitting in the specular cyclic tracking module[1] EXCELL and will be labeled *ISOTC* here A forward-scattering problem, which is a mock-up of this isotropic problem, was obtained as follows we superimpose over the domain a constant pure forward scattering cross-section

$$\Sigma_s(\mu, E' \rightarrow E) = \frac{\delta(1-\mu)}{4\pi}\, \delta(E' - E) \quad ,$$

this process should be indistinguishable from no scattering As can be seen from Table 1, the cross-sections were changed by adding the cross section $\Sigma_{sl}^{g\to g'} = 0\ 50\ \delta_{gg'}$ everywhere in the domain, this also resulted in total cross-sections of $\Sigma_t = 1\ 25$ in both groups We now construct a sequence of problems using a truncated expansion of this scattering law, and the resulting test cases are labeled successively $\{P_n, n = 0, 3\}$ Using the cyclic tracking parameters $p = 11$ and $d = 20$ tracks/cm, we performed anisotropic CP calculations after splitting the domain into 8×8 equally space mesh intervals

In Table 3, we present the flux errors in both groups of P_n with respect to *ISOTC* for calculations that were done with this regular decomposition of the domain The P_1 results have errors greater than 3%, suggesting that P_1 truncated cross sections are insufficient to treat the forward problem The P_3 fit is much better, with respective volume averaged errors of 0 64% and 0 44% CPU times are also given for these various calculations, which were done in full geometry without using the diagonal symmetry In Figure 3, we plot the flux distributions at the edge of the domain The solid line indicates the reference fluxes of the *ISOTC* test case, the dashed lines are for P_n results As one can see, the edge flux in group 2 is almost stabilized for P_1 results, this can be explained by the very large P_0-scattering cross-section in Group 2

4 2 Two-group P_3 *XY* source problem

Our second problem has been introduced initialy to have a direct comparison between the finite element method and discrete ordinates codes [8] The geometry of this problem is again described by Figure 2 Macroscopic cross sections for this P_3 scattering problem are given in Table 2 Using cyclic tracking parameters and domain splitting similar to the previous problem, we performed the anisotropic CP calculations The CPU times for this problem are 0 45 s for tracking, 74 55 s for computing the CPs and 8 60 s to achieve the flux solution Because there are 10 flux coefficients in every zone for a P_3-scattering development, the dimensions of CP matrices in each group are 40960×40960 While the S_4 flux solution (and even the S_{16} solution, to a lesser extent) reported in reference 8 exhibit oscillations (ray effects), our integral flux solution given in Figure 4 is smoothly decreasing from the origin to the boundary of the cell In this figure, we have shown piece-wise constant mean flux distributions as they are obtained by our code These averaged fluxes could not be compared with those given in reference 8, since they appear only in graphic form, but fluxes are similar at the edge of the domain

5. SUMMARY AND CONCLUSIONS

Multigroup numerical results have shown that it is possible to use the cyclic tracking procedure to obtain accurate solutions to the integral transport equation with anisotropic scattering The most important features of the cyclic tracking procedure are that no approximation is made to include the boundary conditions and that it can easily be applied even in void regions For middle size problems (not too optically large domains split into not more than a few hundred regions), we conclude that this integral method is accurate for an adequate choice of the tracking parameters As a part of the Canadian

lattice code DRAGON, the code development described above could provide adequate integral solutions for standard lattices In order to provide a global deterministic package, 3 D computations are the next step, this development will be carried out using the same concept for the directional tracking and the angular integration of the CPs

Finally, there are other possible uses for this tracking method For example, by tak ing into account the streaming effects due to coolant or moderator voiding in a lattice explicitly, the cyclic tracking method should also offer the opportunity to investigate the heterogeneous B_1 method and make it usable for practical situations (perfectly reflected unit cell or square lattice) with few approximations Such a method would offer a consistent way to determine the reactivity effect due to voiding, directional diffusion coefficients could be computed to represent the leakage on the unit cell and used by diffusion reactor codes to study the neutronics of loss of coolant accident in a PWR, in a CANDU or in a fast breeder reactor

Acknowledgements—This work has been carried out partly with the help of grants from Hydro-Quebec and the Natural Science and Engineering Research Council of Canada, for which I wish to express my appreciation

REFERENCES

[1] R ROY, G MARLEAU, A HEBERT and D ROZON, "A Cyclic Tracking Procedure for Collision Probability Calculations in 2 D Lattices," Top Meet on Adv in Mathematics, Computations, and Reactor Physics, April 28 - May 2, Pittsburgh, Pennsylvania (1991)

[2] R ROY, *Ann nucl Energy*, **18**, 511 (1991) see also *Ann nucl Energy*, **17**, 379 (1990)

[3] J L VUJIC and W R MARTIN, "Two-Dimensional Collision Probability Method with Anisotropic Scattering for Vector and Parallel Processing," Conf PHYSOR 90, Marseilles, France (1990)

[4] R SANCHEZ and N J McCORMICK, *Nucl Sci Eng*, **80**, 481 (1982)

[5] R SANCHEZ, "Schemas approches de resolution de l'equation integrale du transport a deux dimensions", CEA-N-2123, Commissariat a l'Energie Atomique, France (1979)

[6] G MARLEAU, R ROY, A HEBERT, "New Computational Methods Used in the Lat tice Code DRAGON," this meeting, see also G MARLEAU, A HÉBERT and R ROY, "DRAGON A Collision Probability Transport Code for Cell and Multicell Calculations," Report IGE 100, Ecole Polytechnique de Montreal (1990)

[7] W F MILLER and W H REED, *Nucl Sci Eng*, **62**, 391 (1977), this problem was also studied in A K ZIVER and A J H GODDARD, *Ann nucl Energy*, **8**, 689 (1981)

[8] J G ISSA, N S RIYAIT, A J H GODDARD, G STOTT, *Prog Nucl Eng*, **18**, 251 (1986)

Table 1. Problem 4.1 cross-sections

Cross-section	Group 1 (cm^{-1})	Group 2 (cm^{-1})
(ISOTC) Σ_t	0.75	0.75
(ISOTC) $\Sigma_{s0}^{g\to g}$	0.40	0.74
(ISOTC) $\Sigma_{s0}^{g\to g+1}$	0.10	—
Σ_t	1.25	1.25
$\Sigma_{s0}^{g\to g}$	0.90	1.24
$\Sigma_{s0}^{g\to g+1}$	0.10	—
$\Sigma_{s1}^{g\to g}$	0.50	0.50
$\Sigma_{s2}^{g\to g}$	0.50	0.50
$\Sigma_{s3}^{g\to g}$	0.50	0.50
Source ($cm^{-3}s^{-1}$)	1.00	0.00

Table 2. Problem 4.2 cross-sections

Cross-section	Group 1 (cm^{-1})	Group 2 (cm^{-1})
Σ_t	0.75	1.00
$\Sigma_{s0}^{g\to g}$	0.50	0.80
$\Sigma_{s0}^{g\to g+1}$	0.20	—
$\Sigma_{s1}^{g\to g}$	0.20	0.30
$\Sigma_{s1}^{g\to g+1}$	0.10	—
$\Sigma_{s2}^{g\to g}$	0.12	0.15
$\Sigma_{s2}^{g\to g+1}$	0.08	—
$\Sigma_{s3}^{g\to g}$	0.08	0.10
$\Sigma_{s3}^{g\to g+1}$	0.05	—
Source ($cm^{-3}s^{-1}$)	1.00	0.00

Table 3. Percentage maximum [and mean] flux errors for Problem 4.1. Reference is *ISOTC* test case with isotropic data.

Group	P_0 results	P_1 results	P_2 results	P_3 results
$g = 1$	25.75 [9.08]	7.91 [4.23]	3.16 [1.61]	1.42 [0.64]
$g = 2$	43.65 [31.77]	7.34 [3.02]	1.47 [0.60]	1.12 [0.44]
CPU time*	2.8 s	9.9 s	33.5 s	89.4 s

* (tracking takes 0.5 s)

Figure 1. Angular quadrature (for square domain with $p = 11$).

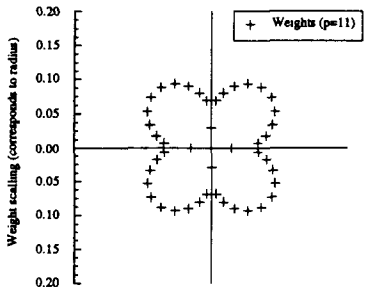

Figure 2. Geometry and boundary conditions for problems 4.1 and 4.2.

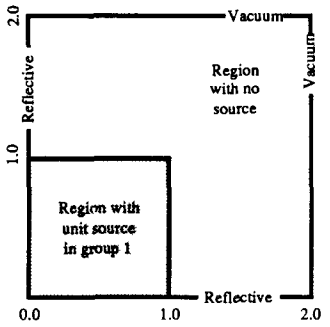

Figure 3. Comparison of the two-group edge flux (at X=1 875cm) for Problem 4 1

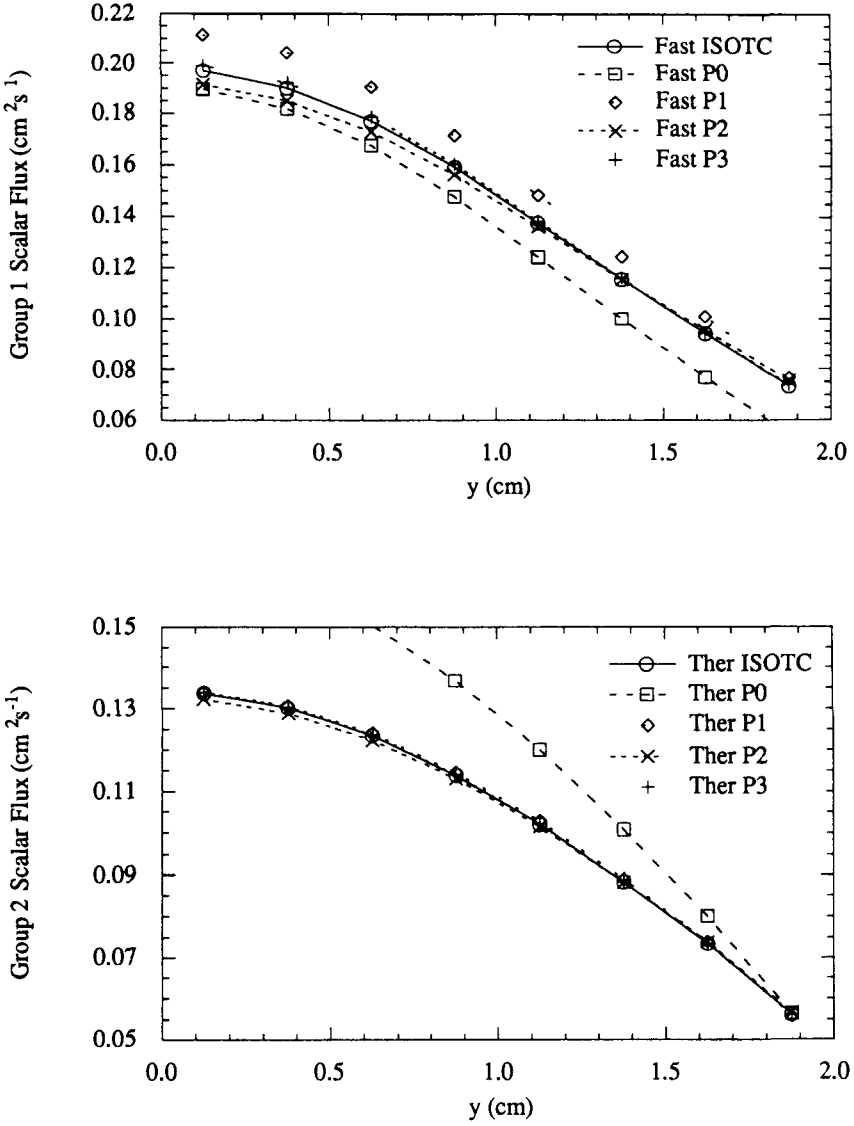

Figure 4. Two-group mean flux distribution for P3 XY problem.

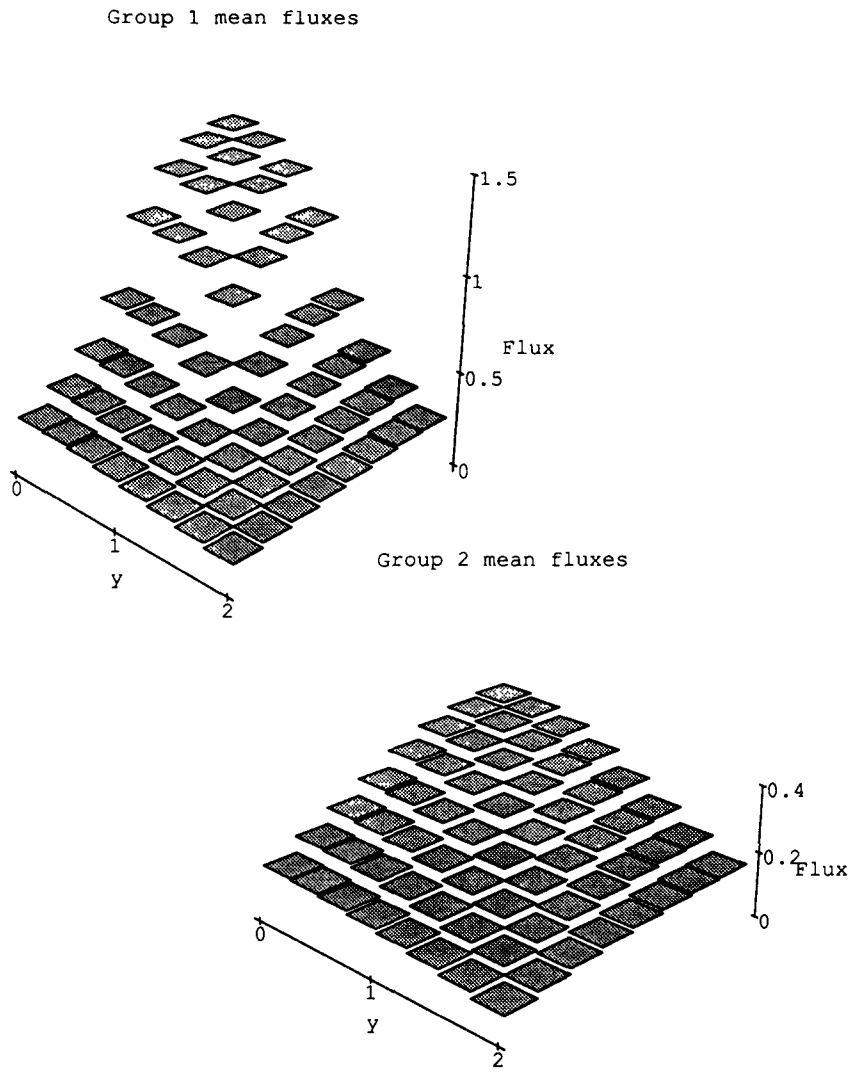

A NODAL SOLUTION OF THE INTERFACE PARTIAL CURRENT EQUATIONS

W R Joubert
Reactor Theory Program, Building P-1900
Atomic Energy Corporation of South Africa Ltd
P O Box 582, Pretoria 0001, R S A.

Z J Weiss
Buro fur Angewandte Mathematik,
Meisenweg 16, D-6458 Rodenbach, Germany

ABSTRACT

A method is presented that utilizes non-linear feedback in order to convert the Interface Current equations to a nodal form This leads to a saving in CPU time due to a decrease in the number of simultaneous equations that has to be solved Also, in contrast to the IC method where acceleration methods are not well developed, the nodal equations are written in the form of the mesh-centred FD diffusion equations, where a multitude of acceleration techniques exists Exhaustive numerical testing shows that the non-linear feedback introduced into the coefficients matrix does not compromise the convergence properties of the iterative solution process

1. INTRODUCTION

Due to the increasing complexity in fuel assembly design, Interface Current (IC) methods (both low and high order) are becoming more popular for assembly calculations However, the penalty in computing time may be an obstacle to the general use of these more accurate methods for industrial application, even in a low order approximation Thus there exists an incentive to find cost-effective alternatives to the solution of the standard IC equations

In a previous paper[1] we described a direct inversion method that can be applied to high or low order IC methods, and saves CPU time by eliminating inner iterations In this paper the low order (only two unknowns per interface) IC equations are converted to a nodal form, gaining the advantage of a reduced number of unknowns This method (here called the *Advanced Nodal Pin-Cell Coupling* (ANPC) method) differs in two

aspects from a similar technique known as the Nodal Pin-Cell Coupling method[2,3] (also called Heterogeneous Response method[4]) Firstly, the restriction to synthetic response matrices is overcome by utilizing non-linear feedback corrections The method also lends itself to the incorporation of higher order effects into the low order model through non-linear feedback Secondly, the nodal equations are written in a *neutron conservation form* similar to the finite difference (FD) diffusion equations This implies that a wide range of acceleration techniques, developed for this form of equations, may be found to be directly applicable

The Interface Current equations for a node consisting of NR internal regions and NS surface segments can be written as

$$\underline{J}^{+} = \hat{R}\underline{J}^{-} + \hat{L}\underline{q} \tag{1}$$

$$\underline{\Phi} = \hat{Y}\underline{J}^{-} + \hat{X}\underline{q} \tag{2}$$

with

$\underline{\Phi}$	≡	NRx1 vector of average region fluxes
$\underline{q}$	≡	NRx1 vector of region source densities
$\underline{J}^{+}$	≡	NSx1 vector of partial outcurrents
$\underline{J}^{-}$	≡	NSx1 vector of partial incurrents
$\hat{\mathbf{X}}$	≡	NRxNR matrix of source response fluxes*
$\hat{\mathbf{Y}}$	≡	NRxNS matrix of current response fluxes*
$\hat{\mathbf{L}}$	≡	NSxNR matrix of escape probabilities
$\hat{\mathbf{R}}$	≡	NSxNS matrix of transfer probabilities (response matrix)

In this notation, bold typeface and a hat ($\hat{\mathbf{R}}$) denotes a matrix, while underlined variables ($\underline{\Phi}$) will be used for vectors All other variables in an equation are scalars

In a group-by-group solution of the IC equations, Eqs (1), written for all the nodes, are solved simultaneously for the global coupling between nodes (the so-called *inner iterations*), while the fine structure of the flux within nodes is kept frozen in the source distribution $\underline{q}$ Thereafter Eq (2) is used node by node to retrieve regionwise average fluxes $\underline{\Phi}$ from the known inwards directed partial currents and microregion source densities This form part of the so-called *outer iterations* which can also include an eigenvalue (k-effective) calculation This work is only concerned with the solution of Eq (1), since the outer iteration strategy is identical for the IC equations and for the Nodal equations The biggest disadvantage in solving Eq (1) directly, as is done in standard IC methods, is the large number of unknowns (two per interface in the low order model) that has to be solved for simultaneously Also, existing acceleration methods do not seem to be very successful[5,6]

---

*Flux and current response matrices in annular geometry were introduced by Stamm'ler in reference 3, Chapter IV 10

In order to reduce the number of unknowns, a suggestion of Weiss[2] to rigorously synthesize response matrices by using non-linear feedback is followed, enabling a nodal formulation of Eq (1) However, instead of starting from a given geometry (rectangular) and explicitly changing the response matrix elements, as it was done in references 2 and 3, the non-linear feedback is incorporated into the equation system Furthermore, neutron balance is explicitly enforced and, in order to utilize proven solution techniques developed for FD diffusion methods, the one-group nodal equations are written in the form

$$\sum_K d_{NK} (S_{NK}\varphi_N - S_{KN}\varphi_K) + C_{N0}\varphi_N = C_{Nq}Q_N \qquad (3)$$

where the summation runs over all the neighbors of node N and φ is the nodal variable, corresponding to the average flux in the diffusion equations Note that Eq (3) replaces Eq (1) only in the iterative process in order to reduce the number of simultaneous equations to be solved Although Eq (3) is solved for the nodal variable φ, the real unknowns are still the partial currents It is therefore also necessary to obtain *expansion relations* (see Section 2) that express the partial currents in terms of the nodal variables of neighboring nodes In order to retain the structure of the FD equations, we require that the coupling coefficients d_{NK} are symmetric in N and K, while S_{NK}, C_{N0} and C_{Nq} depend only on the properties of node N and not on the properties of neighboring nodes However, non-linear feedback is incorporated in Eq (3) by allowing the coefficients S_{NK}, C_{N0} and C_{Nq} to depend also on the partial currents entering node N Furthermore, S_{NK} may be direction-dependent, as indicated by the subscript NK

2. ESSENTIALS OF CONVERSION TO A NODAL FORM

In order to obtain a nodal formulation as postulated in Eq (3), it is first necessary to define a parameter that can be identified as a nodal variable φ The conversion of the IC equations to a nodal form is based on extracting from the IC equations a relation containing the two partial currents across an interface on one side of the relation and a "compound" term of incurrents from all faces on the other side of the relation The compound term is then taken as the nodal variable

This relation can be obtained by writing the response matrix $\hat{\mathbf{R}}$ as

$$\hat{R} = \hat{P} + \hat{T} \qquad (4)$$

where $\hat{\mathbf{P}}$ is a diagonal matrix and $\hat{\mathbf{T}}$ is a full matrix Assume

$$P_{\nu\nu} = R_{\nu\nu} - \sum_{\mu\neq\nu} R_{\nu\mu} c_{\mu\nu} \qquad \nu = 1,2, \ldots NS \qquad (5)$$

where $c_{\mu\nu}$ are some constants and $R_{\nu\mu}$ is the transmission probability from face μ to face ν

The choice of the constants c in the decomposition is arbitrary and can be used to optimize the iterative convergence of the final equation system However, numerical experimentation with different choices of c revealed that the convergence properties are rather insensitive to them An exception is when all c's are taken to be zero Although convergence was always reached, the speed of convergence was very slow in many cases For this choice the matrix $\hat{\mathbf{T}}$ has zero's on the diagonal, leading to a 'compound" term that does not include all incurrents (see Eqs (7) and (10)) In this work the following choice was made for the element $P_{\nu\nu}$ (traditionally denoted by ρ_ν) corresponding to face ν of a node.

$$P_{\nu\nu} = R_{\nu\nu} - R_{\nu\mu} \quad \text{if a unique opposite face } \mu \text{ can be identified}$$

$$P_{\nu\nu} = R_{\nu\nu} - \frac{1}{NS - 1} \sum_{\mu \neq \nu} R_{\nu\mu} \quad \text{if a unique opposite face cannot be identified}$$

Using decomposition (4) of the response matrix $\hat{\mathbf{R}}$ the relation between partial currents, Eq (1), can be written as

$$\underline{J}^{+} - \hat{P}\underline{J}^{-} = \hat{T}\underline{J}^{-} + \hat{L}\underline{q} \tag{6}$$

Since $\hat{\mathbf{P}}$ is diagonal, the term to the left defines components per face, one at a time, while the term to the right involves in each row, all incoming current components and all source densities However, it does not involve outcoming currents i e , it is completely defined by 'input" vectors $\underline{J}$ and $\underline{q}$ In this respect it is similar in structure to the right side of Eq (2) which was shifted to the post-processing part of the algorithm

Recall, that the decoupling of Eqs (1) and (2) was achieved by treating the leakage current due to the source, $\hat{\mathbf{L}}\underline{q}$, in a non-linear feedback manner, by writing it as $Q\underline{L}$, where Q is the total source in the node, while

$$\underline{L} = \frac{1}{Q}\hat{L}\underline{q} \tag{7}$$

can be interpreted as a vector of leakage probabilities, having as components the probabilities that a neutron born anywhere in the node will leak through a specific face These probabilities are dependent on the source distribution inside the node and are updated during the outer iterations

In the derivation of the ANPC method the instreaming term, $\hat{\mathbf{T}}\underline{J}^{-}$, is treated in the same way, by writing it as $J^{in}\underline{T}$ where J^{in} is the total incurrent into the node, while

$$\underline{T} = \frac{1}{J^{in}} \hat{T} \underline{J}^{-} \tag{8}$$

The v-th component of $\underline{T}$ can be described as the average probability that a neutron entering the node through any of its faces will leak out through the v-th face These probabilities, dependent on the distribution of the incurrents on the node boundary, are also treated as non-linear feedback and are updated during outer iterations

The Interface Current equation (6) can finally be written in the form

$$\underline{J}^{+} - \hat{P} \underline{J}^{-} = \underline{M} \tag{9}$$

where

$$\underline{M} = J^{in} \underline{T} + Q \underline{L} \tag{10}$$

can be interpreted as the global variable

Once the form of $\underline{M}$ has been defined, the procedure to obtain explicit expressions for the partial currents at interfaces, the *expansion relations*, can be followed exactly like it was done earlier for the synthetic response matrices[3,7] Eq (9) is written for the partial currents across the common interface of two neighboring nodes By equating the outcurrent of one to the incurrent of the other (and vice versa), the partial currents are obtained in terms of the components of the vectors $\underline{M}$ of the two nodes that correspond to the common interface

It is also possible to proceed, in the same way as was done by Weiss[7] and Stamm'ler[3] for the Nodal Pin-Cell Coupling method, to a generalized tensorial formulation (the number of unknowns per node is equal to the number of faces of the node) Coupling equations can be obtained by substituting the expansion relations into the definition of $\underline{M}$ However, we prefer to strictly impose neutron balance

$$\sum_{v} J_{v}^{net} + A = Q \tag{11}$$

where A is the removal rate, Q is the neutron source and J_v^{net} is the net neutron current through its v-th face The next step is then to find expressions for the net neutron current and the removal rate

3. THE BALANCE FORM OF THE NODAL EQUATIONS

An expression for the net current between two neighboring nodes N and K is obtained by subtraction of the partial currents given by the expansion relations After some mathematical manipulation the expression is obtained in a form similar to the FD equations

$$J_{Nv}^{net} = d_{NK} (\varphi_{Nv} - \varphi_{Kv}) \tag{12}$$

where

$$\varphi_{Nv} = M_{Nv}/(1 - \rho_{Nv}) \tag{13}$$

$$d_{NK} = \frac{(1 - \rho_{Nv})(1 - \rho_{Kv})}{1 - \rho_{Nv}\rho_{Kv}} \tag{14}$$

In these equations v defines the common interface between nodes N and K and the subscript Nv is used to indicate the element of a vector defined for node N corresponding to that face The vector $\underline{\varphi}$ with components defined by Eq (13) has been introduced to make d_{NK} symmetric in N and K. Equation (12) is still in terms of components of a vector, and is now converted to a scalar form *purely on the basis of non-linear feedback* to give

$$J_{Nv}^{net} = d_{NK} (S_{Nv}\varphi_N - S_{Sv}\varphi_K) \tag{15}$$

where

$$\varphi_N = \sum_v \varphi_{Nv} \tag{16}$$

$$S_{Nv} = \frac{\varphi_{Nv}}{\varphi_N} \tag{17}$$

and φ is the desired single nodal variable per node

As far as the removal rate in a node is concerned, it can be written in terms of the average blackness γ and total leakage probability L of the node

$$A = \gamma J^{in} + Q(1 - L) \tag{18}$$

The first term on the right represents neutrons which entered the node from outside and have then been removed in that node (after any number of collisions) The second term

represents neutrons which have been born in the node and were then removed The total leakage probability is just the sum of the leakage probabilities through all the faces, given by Eq (7), and is thus dependent on the source distribution inside the node The average blackness on the other hand is dependent on the distribution of the incurrents on the node boundary Define the probability that a neutron entering the node through face ν will be removed in the node, by γ_ν The average blackness constitutes the final non-linear feedback and is given by

$$\gamma = \frac{1}{J^{in}} \sum_{\nu} \gamma_\nu J_\nu^- \tag{19}$$

It remains to express A in terms of the nodal variable φ By adding the components of Eq (10), the total incurrent J^{in} can be written as

$$J^{in} = \frac{M - QL}{T}$$

where (see Eqs (7) and (8))

$$M = \sum_{\nu} M_\nu$$

$$L = \sum_{\nu} L_\nu$$

$$T = \sum_{\nu} T_\nu$$

Using Eq (13), this is written in terms of φ and substituted in Eq (18) with the definition $\omega = \gamma/T$ to give

$$A = \omega \varphi \sum_{\nu} (1 - \rho_\nu) S_\nu + Q[1 - L(1 + \omega)] \tag{20}$$

At this stage all the necessary ingredients for setting up the ANPC equations are available Introducing Eqs (15) and (18) into the nodal balance equation (Eq (11)) and taking all terms proportional to Q to the right hand side, the nodal equation system is obtained

$$\sum_{K} d_{NK} (S_{NK} \varphi_N - S_{KN} \varphi_K) + C_{N0} \varphi_N = C_{Nq} Q_N \tag{21}$$

with

$$C_{N0} = \omega_N \sum_v (1 - \rho_{Nv}) S_{Nv}$$

$$C_{Nq} = L_N (1 + \omega_N)$$

Eq (21) is equivalent to the IC Eq (1) with low order, but otherwise quite general, response matrices describing the nodes Moreover, nodes are allowed to have an arbitrary internal substructure defined by their $\hat{\mathbf{X}}$ and $\hat{\mathbf{Y}}$ matrices

Notice that in the special case of synthetic response matrices no feedback is involved and the non-linear parameters (Eqs (5), (8), (17) and (19)) are all constants

4. DIAGONAL DOMINANCE OF THE COEFFICIENTS MATRIX

The convergence of the FD diffusion equation system is guaranteed due to the physical nature of the entries of its coefficients matrix Such a property can also be shown for the ANPC method for the particular case of synthetic response matrices However, when non-linear feedback is introduced, the existence of diagonal dominance can no longer be rigorously proved The convergence properties of the ANPC method were tested by using a 40x40 node test case, corresponding roughly to a 2x2 PWR assembly color set calculation Response matrices were randomly generated for each node, preserving the physical neutron conservation relations The results for 400 1-group fixed source calculations, with the source in each node also randomly generated, are summarized in Table 1 The Table shows the minimum and maximum number of inner and outer iterations needed for convergence of the flux, as well as the minimum and maximum values obtained for two of the feedback parameters All cases converged within a rather narrow range of outer iterations, although the ranges of the primary feedback mechanisms indicate that very severe cases were encountered It can thus be said with confidence that convergence of the ANPC method is not destroyed by the non-linear feedback

5. NUMERICAL RESULTS

To test the performance of the ANPC method, two programs were written IC - to solve the Interface Current equations in a standard way and RED - to solve the same equations using the nodal approach of Eq (3) The outer iterations are unaccelerated in both programs In the IC program, scattering and albedo pre-conditioning[6] of the transmission matrices is used to accelerate the inner iterations The first of these is just a normal property of the Integral Transport program that is used to calculate

transmission matrices In the RED program, successive overrelaxation (with $\omega = 1.3$) and normalization of the flux after the first inner iteration is used

Two test cases were compared, both eigenvalue calculations for a typical 17x17 array of square nodes The first case is a one energy group calculation and has heterogeneous nodes for which synthetic response matrices were calculated All non-linear feedback parameters are therefore constant, but are nevertheless periodically recalculated by the program This serves as a test of the effectiveness of the reduction in the number of simultaneous equations to be solved In the second case, ten energy groups were used and response matrices for homogeneous nodes were randomly generated, resulting in substantial feedback corrections In both cases, feedback parameters were recalculated after each outer iteration The convergence of microregion fluxes was used to terminate outer iterations In all cases the k-effective and final fluxes of RED and IC were compared to confirm that true convergence was reached In Table 2 the CPU times and number of outer iterations needed to obtain convergence are tabulated against the inner convergence criteria The CPU times are for the iteration process and exclude data preparation and editing times

Clearly, for RED it is better to have fairly tight convergence in the inner iterations in order to limit the number of outer iterations, and thus also the number of times that the feedback parameters are recalculated For IC it is better to have less stringent inner convergence, since the total number of iterations decreases although the number of outer iterations increases It is also interesting to note that the performance of RED is very similar between test case 1 (no non-linear feedback) and test case 2 (substantial non-linear feedback) Obviously the feedback does not disturb the convergence of the iterative process significantly

A variety of further test cases gave results similar to those quoted in Table 2 In all of them the CPU time of RED varies between two and four times faster than that of IC

6. CONCLUSIONS

The Advanced Nodal Pin-Cell Coupling method utilizes non-linear feedback in order to convert the Interface Current equations to a nodal form The reduction in the number of simultaneous equations to be solved leads to a saving in CPU time of a factor of about 3 when only very rudimentary acceleration techniques are used for both methods However, in contrast to the IC method where acceleration methods are not well developed, the nodal equations are written in the form of the FD diffusion equations, where a multitude of acceleration techniques exists In subsequent investigations it was found that the non-linear feedback parameters tend monotonically towards their final values, implying that standard extrapolation methods can be applied to them Since no restrictions are placed on the form of the low order response matrices, the ANPC method lends itself to inclusion of higher order effects into the low order model through non-linear feedback

Some interesting auxiliary observations resulted from this study. It was numerically shown that for synthetic response matrices the ANPC equations are equivalent to the Nodal Pin-Cell Coupling equations, including identical eigenvalues of the iteration matrices. This would confirm the observation[3] that the Nodal Pin-Cell Coupling equations converge for all practical cases, even though diagonal dominance of the coefficients matrix, a sufficient but not necessary condition for convergence, can not be proved. It is also possible to cast the ANPC equations in the same form as in the well-known TRILUX[8] equations. This means that the heuristically defined TRILUX coefficients can be given clear definitions in terms of the response matrix entries of a node.

REFERENCES

1 Weiss, Z. and Joubert, W.R. Alternative Methods of Solving Response Matrix Equations, Proceedings of the International Topical Meeting on Advances in Mathematics, Computations and Reactor Physics, Pittsburgh, Pennsylvania, USA, April 28 - May 2, 1991

2 Weiss, Z. Some Basic Properties of the Response Matrix Equations, Nucl. Sci. Eng., **63**, 457-492 (1977)

3 Stamm'ler, R.J.J. and Abbate M.J. Methods of Steady-State Reactor Physics in Nuclear Design, Academic Press (1983), Chapter VII

4 Villarino, E.A. and Stamm'ler, R.J.J. The Heterogeneous Response Method in Slab Geometry, Ann. Nucl. Energy, Vol. 11, No. 9, 429-440 (1984)

5 Sanchez, R. An Acceleration Procedure for the Iterative Solution of the Flux-Current Equations in the APOLLO II Code, Proceedings of the International Conference on the Physics of Reactors: Operation, Design and Computation, Marseille, France, April 23-27, 1990, Vol 3, page IV-74

6 Marleau, A. et al Acceleration Strategies for the Interface Current Method, Proceedings of the Second International Conference on Simulation Methods in Nuclear Engineering, Montreal, Canada, October 14-16, 1986

7 Weiss, Z. Nodal Equations Derived from Invariant Imbedding Theory, Nucl. Sci. Eng., **48**, 235-247 (1972)

8 Goldstein, L. et al Calculation of Fuel-Cycle Burnup and Power Distribution of Dresden-1 Reactor with the TRILUX Fuel Management Program, Trans. Am. Nucl. Soc., **10**, 300 (1967)

Table 1: Stability of Feedback Mechanism in the ANPC Method

	Minimum	Maximum	Average
Number of inner iterations	59	98	70
Number of outer iterations	11	18	12
S_v [Eq. (17)]	0.0080	0.7756	
T_v [Eq. (8)]	0.0030	0.6693	

Table 2: Number of Outer Iterations and CPU Times Needed by Interface Current and ANPC Nodal Formulations to Reach Convergence

Program	RED	RED	IC	IC
Inner convergence	10^{-5}	10^{-6}	10^{-5}	10^{-6}
Test Case 1:				
Number of Outer Iterations	64	43	67	47
CPU Time in Arbitrary Units	143	117	355	457
Test Case 2:				
Number of Outer Iterations	92	59	96	52
CPU Time in Arbitrary Units	3986	2956	8981	12409

AN WEIGHTED DIAMOND DIFFERENCE APPROXIMATION FOR IMPROVING 3-D COARSE MESH S_N CALCULATIONS

Toshikazu TAKEDA, Masatoshi YAMASAKI
and Hideaki IKEDA
Osaka University, Faculty of Engineering,
Department of Nuclear Engineering
Yamadaoka 2-1, Suita, Osaka
JAPAN

ABSTRACT

An improved coarse-mesh 3-D (hexagonal-Z) discrete ordinates transport calculation method has been developed. This method employs an weighted diamond difference approximation, the weight in which is a function of neutron direction and scaler flux, and can be easily incorporated into conventional discrete ordinates transport codes. Results obtained from hexagonal fuel assembly calculations of high conversion reactors and fast reactor core calculations indicate that the errors of k_{eff} and power distribution are remarkably reduced by the present method.

INTRODUCTION

In order to accurately predict neutronic performance parameters in fast and thermal reactors, we made a three-dimensional (XYZ) S_N code TRITAC[1] which solves the multigroup transport equation by the diffusion synthetic acceleration (DSA) method. TRITAC was utilized to evaluate the transport effect of large fast critical assemblies ZPPR-9, 10, 13, 17, 19[2]. With the transport effect a consistency was obtained between calculation and experiment for k_{eff} of these cores.[2]

To treat hexagonal cells and/or assemblies of fast reactors and high-conversion reactors, we have implemented a hexagonal-Z geometry option to TRITAC. We have applied the TRITAC hexagonal-Z option to the NEACRP 3-D Neutron Transport Benchmarks[3]. For the Model 4 of the Benchmark, TRITAC largely underestimated k_{eff} and control rod worth because a hexagon mesh interval was rather large and a large error in fluxes in control rods was produced. In order to eliminate this truncation error due to coarse meshes we have derived an improved coarse mesh S_N method using weighted diamond difference approximation.

A coarse-mesh is divided into two submeshes in each direction for X-Y-Z geometry and into 7 submeshes for hexagonal-Z geometry and the subsidiary fluxes in submeshes are eliminated using a neutron conservation equation. This coarse mesh method is equivalent to a weighted diamond difference equation. In the next chapters we describe the improved coarse-mesh X-Y-Z and hexagonal-Z discrete ordinates transport method, and show numerical results and conclusions.

IMPROVED COARSE-MESH METHOD IN X-Y-Z AND HEXAGONAL-Z GEOMETRY

Let us start with a finite difference form in slab geometry. **Fig. 1** shows one-dimensional submeshes in the slab geometry. A coarse-mesh is divided into two submeshes and

they are denoted by I and II. The finite difference transport equation in the submesh I is

$$\frac{2\mu}{h_i}(\psi^S_{m,i} - \psi^S_{m,i-1/2}) + \Sigma_{t,i}\psi^V_{m,i-1/4} = S^V_{m,i-1/4}, \quad (1)$$

where m :Neutron direction
$\psi^S_{m,i}$:Angular flux on surface i
$\psi^V_{m,i}$:Volume average angular flux in submesh I
$S^V_{m,i-1/4}$:Neutron source in submesh I
μ :Direction cosine with respect to X-axis
h_i :Mesh spacing

Similarly the difference equation in the submesh II is

$$\frac{2\mu}{h_i}(\psi^S_{m,i+1/2} - \psi^S_{m,i}) + \Sigma_{t,i}\psi^V_{m,i+1/4} = S^V_{m,i+1/4}. \quad (2)$$

The subscript 'm' is omitted hereafter. We use the commonly used diamond difference approximations for the submeshes:

$$2\psi^V_{i-1/4} = \psi^S_i + \psi^S_{i-1/2}, \quad (3)$$
$$2\psi^V_{i+1/4} = \psi^S_{i+1/2} + \psi^S_i. \quad (4)$$

The volume averages of angler flux and source in the coarse-mesh are defined by

$$2\psi^V_i = \psi^V_{i-1/4} + \psi^V_{i+1/4}, \quad (5)$$
$$2S^V_i = S^V_{i-1/4} + S^V_{i+1/4}. \quad (6)$$

Adding Eqs. (1) and (2), and using Eqs. (5) and (6), we obtain the following difference equation in a coarse-mesh :

$$\frac{2\mu}{h_i}(\psi^S_{i+1/2} - \psi^S_{i-1/2}) + \Sigma_{t,i}\psi^V_i = S^V_i \quad (x_{i-1/2} < x < x_{i+1/2}). \quad (7)$$

This equation corresponds to the commonly used finite difference equation. However, it is noted that

$$\psi^V_i \neq (\psi^S_{i+1/2} + \psi^S_{i-1/2})/2.$$

A relation between ψ^V_i, $\psi^S_{i+1/2}$ and $\psi^S_{i-1/2}$ is obtained by adding Eqs. (3) and (4) and using Eq. (5):

$$4\psi^V_i = \psi^S_{i-1/2} + 2\psi^S_i + \psi^S_{i+1/2}. \quad (8)$$

We subtract Eq. (1) from Eq. (2) to obtain

$$\frac{2\mu}{h_i}(\psi^S_{i+1/2} - 2\psi^S_i + \psi^S_{i-1/2}) = -\left(\Sigma_{t,i} - \frac{S^V_{i+1/4} - S^V_{i-1/4}}{\psi^V_{i+1/4} - \psi^V_{i-1/4}}\right)(\psi^V_{i+1/4} - \psi^V_{i-1/4}). \quad (9)$$

Here we assume that the ratio $S(x)/\psi(x)$ is constant over the coarse-mesh and the neutron flux is isotropic. Then the second term in the first bracket is approximated by

$$\frac{S^V_{i+1/4} - S^V_{i-1/4}}{\psi^V_{i+1/4} - \psi^V_{i-1/4}} = \frac{S^V_i}{\Phi^V_i} \tag{10}$$

where Φ^V_i is the scalar flux.

We eliminate $\psi^V_{i-1/4}$ and $\psi^V_{i+1/4}$ from Eq. (9) using Eqs. (3) and (4), and use Eq. (8) to obtain the following diamond difference approximation :

$$2\psi^V_i = (1 - \alpha_i)\psi^S_{i-1/2} + (1 + \alpha_i)\psi^S_{i+1/2} \tag{11}$$

where $\alpha_i = \frac{h_i}{8\mu}(\Sigma_{t,i} - \frac{S^V_i}{\psi^V_i})$.

This weighted diamond difference approximation is similar to the conventional weighted diamond difference approximation, but there is a difference in that α is a function of μ and ψ. The conventional weight is not a function of ψ. In the 3-D (XYZ) geometry, we use the above method in each direction.

In hexagonal-Z geometry, we divided a hexagon into seven submeshes as shown in **Fig. 2.** These submeshes are numerated from I to VII. Using the difference transport equations in submeshes I - VII, an weighted diamond difference equation is obtained.

$$\begin{aligned} 2\psi^V &= (1 + \alpha_x)\psi^S_{+x} + (1 - \alpha_x)\psi^S_{-x}, \\ &= (1 + \alpha_u)\psi^S_{+u} + (1 - \alpha_u)\psi^S_{-u}, \\ &= (1 + \alpha_v)\psi^S_{+v} + (1 - \alpha_v)\psi^S_{-v}, \\ &= (1 + \alpha_z)\psi^S_{+z} + (1 - \alpha_z)\psi^S_{-z}, \end{aligned} \tag{12}$$

where $\alpha_x = (3/16)\beta_{i,j,k}(h_p/\mu_x)$, $\alpha_u = (3/16)\beta_{i,j,k}(h_p/\mu_u)$, $\alpha_v = (3/16)\beta_{i,j,k}(h_p/\mu_v)$,
$\alpha_z = (1/8)\beta_{i,j,k}(h_p/\xi)$, $\beta_{i,j,k} = \Sigma_{t,i,j,k} - S_{i,j,k}/\psi_{i,j,k}$.

Here x, u and v indicate directions shown in **Fig. 2.** The coefficients of α in the $x-$, $u-$ and $v-$directions are different from that of α in $z-$direction. The former is 3/16, and the latter is 1/8 and the same as in the XYZ geometry.

FINITE DIFFERENCE SCHEME IN HEXAGONAL-Z GEOMETRY

Let us now derive explict finite difference formulas in hexagonal-Z geometry. The treatment in $z-$direction is straightfowards. Therefore we consider finite difference formulas only in hexagonal geometry.

A mesh center angular flux and surface angular fluxes (or vertex angular fluxes) are calculated using incoming angular fluxes. In **Fig. 3** the incoming angular fluxes ψ_{-x}, ψ_{-u}, ψ_{-v} are assumed to be given, and we consider the following three finite difference schemes:

1) Scheme 1

In this scheme we consider the angular fluxes at six surfaces on the hexagon. Using the conventional diamond approximation,

$$\psi = \frac{1}{2}(\psi_{+x} + \psi_{-x}),$$

$$\psi = \frac{1}{2}(\psi_{+u} + \psi_{-u}), \tag{13}$$

and $\psi = \frac{1}{2}(\psi_{+v} + \psi_{-v})$,

the center flux ψ is given by

$$\psi = \frac{2\mu_x\psi_{-x} + 2\mu_u\psi_{-u} + 2\mu_v\psi_{-v} + \frac{3}{2}\frac{h_p}{h_z}\mu_z\psi_{-z} + \frac{3}{2}h_p\Sigma^V_t}{2\mu_x + 2\mu_u + 2\mu_v + \frac{3}{2}\frac{h_p}{h_z}\mu_z + 3\frac{3}{2}h_pS^V} \tag{14}$$

where h_p is the pitch of hexagon node, and h_z is the axial mesh interval.

ψ_{+x}, ψ_{+u}, ψ_{+v} are calculated by Eq. (14). This is the commonly used scheme. In the 2-D (X,Y) geometry the diamond approximation is used in $x-$ and $y-$ directions. The use of diamond approxiamtion in three directions per node in hexagonal geometry may gives us large errors compared to X-Y geometry.

2) Scheme 2

We consider the angular fluxes at vertices and assume that the fluxes at points 1, 2, 3, and 4 are given (See **Fig. 3**).

Using the relations

$$\psi = \frac{1}{2}(\psi_2 + \psi_5),$$
$$\psi = \frac{1}{2}(\psi_3 + \psi_6), \tag{15}$$

we obtain

$$\psi = \frac{2\mu_x(\psi_2+\psi_3) + \mu_u(-\psi_1+2\psi_3+\psi_4) + \mu_v(\psi_1+2\psi_2-\psi_4) + 3\frac{h_p}{h_z}\mu_z\psi_{+z} + 3h_p\Sigma^V_t}{4\mu_x + 4\mu_u + 4\mu_v + 3\frac{h_p}{h_z}\mu_z + 3h_pS^V}. \tag{16}$$

In this scheme the four angular fluxes are assumed to be given, and two unknown angular fluxes at vertices are calculated. Two diamond approximations are used instead of 3 for the scheme 1.

3) Scheme 3

The angular fluxes at vertices are also used and the discontinuity of fluxes at point 1 and 4 is considered. The angular fluxes ψ_1 and ψ_4 are assumed to be given, and the angular fluxes ψ_1' and ψ_4' (See **Fig. 3**) are calculated from the the diamond approximations

$$\psi = \frac{1}{2}(\psi_1 + \psi_4'),$$
$$\psi = \frac{1}{2}(\psi_4 + \psi_1'),$$

$$\psi = \frac{1}{2}(\psi_2 + \psi_5), \tag{17}$$

and $$\psi = \frac{1}{2}(\psi_3 + \psi_6).$$

Eliminating ψ_4' and ψ_1', the center flux is given by

$$\psi = \frac{2\mu_x(\psi_2+\psi_3) + 2\mu_u(\psi_3+\psi_4) + 2\mu_v(\psi_1+\psi_2) + 3\frac{h_p}{h_z}\mu_z\psi_{-z} + 3h_p\Sigma^V_t}{4\mu_x + 4\mu_u + 4\mu_v + 3\frac{h_p}{h_z}\mu_z + 3h_pS^V}. \tag{18}$$

This equation corrsponds to Eq. (14), if we assume that

$$\psi_{-x} = \frac{1}{2}(\psi_2 + \psi_3),$$

$$\psi_{-u} = \frac{1}{2}(\psi_3 + \psi_4),$$

and $$\psi_{-v} = \frac{1}{2}(\psi_1 + \psi_2).$$

The above three schemes were incorporated into the TRITAC code. The improved coarse mesh method, Eq. (12), is also implemented.

NUMERICAL RESULTS

The calculational accuracy of the present 3-D improved coarse-mesh method has been checked by applying it to two hexagonal models. One is a hexagonal-Z fast reactor core model shown in **Fig. 4** which corresponds to the Model 4 of the NEACRP international benchmark problems[3]. The other is a hexagonal fuel assembly which simulates a high conversion light water reactor assembly shown in **Fig. 5**.

Table 1 lists k_{eff} values for the 3-D fast reactor core. All transport calculations were done with the 4-group cross sections given in Ref(3) for the two control rod patterns, rod-out, and rod-in cases. The reference value is the average of Monte-Carlo calculations performed by Wehmann with MOCA[4], Bryzgalov with MCU[5], Seifert with OMEGA[6], and Nakagawa with GMVP[7]. The $1/\sigma_i^2$ weight was used in the averaging, where σ_i is variance of individual results.

The standard deviation of the reference k_{eff} is about 0.04%Δk, and the reference is very reliable. All S_N calculations were done using 169 meshes in radial direction and 38 meshes in axial direction. For the rod-out case all the schemes produced k_{eff} within 1.0%Δk accuracy from the reference. For the rod-in case, however, the scheme 1 overestimated k_{eff} by -6%, and produced unreasonable flux distribution as will be shown later. The scheme 2 with the conventional coarse mesh method underestimated k_{eff} by 2%, and the flux did not converge when the present improved coarse mesh method was incorporated. The scheme 3 is stable, and the error of k_{eff} was -0.7%Δk for the conventional coarse mesh method and -0.3%Δk for the present improved method. This scheme produced rod worth of 23.5%Δk/kk', which well agrees with the reference value of 22.3%Δk/kk'.

Table 2 lists region-averaged group fluxes calculated by Monte-Carlo method, and

the conventional and present improved methods with the scheme 1, 2 and 3, for the rod-in case The scheme 1 largely overestimated the 3rd and 4th group fluxes of the test zone, and underestimated all group fluxes in the control rod The incorporation of the improved method to this scheme worsened the 4th group flux in the control rod The underestimation of the control rod fluxes produced the large k_{eff} overestimation as seen in **Table 1** The scheme 2 overestimated the fluxes in the axial blanket The neutron leakage from the core region was therefore overestimated, and the k_{eff} value was underestimated The scheme 3 gave us reasonable flux in the axial blanket Therefore the neutron leakage is well predicted compared to the scheme 1 and 2 The neutron spectrum is ,however, largely hardened in the test zone In the control rod the use of the present coarse mesh method improved the accuracy of the lower energy fluxes Then k_{eff} value was improved by 0 4% for the rod-in case

Next let us compare the results for the high convergion fuel assembly **Table 3** lists k_{∞} values calculated by the reference Monte-Carlo method and the S_N methods using the schemes 1, 2 and 3 Calculations were carried out in 7 groups for the rod-in and rod-out cases The reference calculation was carried out usivg GMVP code[7]

The improved coarse mesh method was applied only to the scheme 3 For the rod-out case, all the S_N methods produces k_{∞} error within 0 5% The improved coarse mesh method worsened k_{∞} value, but the difference between the conventional and the improved methods was very small For the rod-in case, convergence was not obtained for the scheme 1 The scheme 2 produced rather accurate k_{∞} value The power distribution was however not well predicted by this scheme as will be shwon later The scheme 3 with the conventional coarse mesh method largely underestimated k_{∞} This is due to the flux overestimation in the rod region The use of of the present coarse mesh method remarkably improved this k_{∞} underestimation **Fig. 6** show the assembly power distribution for the reference calculation, the scheme 2 calculation with the conventional coarse mesh method, and the scheme 3 calculation with the present method For the latter two cases the percent difference from the reference calculation is shown For the both rod-in and rod-out cases, the percent difference is rather large at the center fuel The scheme 2 produced 2-4% maximum error near the assembly periphery where the power is large The present method incorporated into the scheme 3 improved this error remarkably

CONCLUSION

We have developed an improved coarse mesh method for 3-D (X-Y-Z and hexagonal-Z) discrete ordinates transport calculations This method employes an weighted diamond difference approximation As the finite difference form in hexagonal-Z geometry we considered three schemes

The applicability of the improved coarse mesh method was investigated using the three finite difference schemes The eigenvalue and flux distribution in the hexagonal-Z geometry fast reactor core and the high conversion core fuel assembly were calculated by the present method, and compared with the reference Monte-Carlo method As the result it was found that the present improved coarse mesh method with the finite difference scheme 3 produced accurate results

REFERENCES

(1) M BANDO et al , J Nuclear Sci Technol , 22, 841, (1985)

(2) T YAMAMOTO et al , J Nuclear Sci Technol , 849, (1986)

(3) T TAKEDA and H IKEDA, *"3-D Neutron Transport Benchmarks"*,

NEACRP-L-330, (1991).

(4) J. LIEBEROTH, "*A Monte-Carlo Technique to Solve the Static Eigenvalue Problem of the Boltzmann Transport Equation*", Nukleonik 11, 213-219, (1968)

(5) L. N. MAIOROV and M. S. YUDKEVICH, Vopr. Atom. Nauk. i Techn. (Fiz. i Techn. Nucl. React.), N7 1985, p.54

(6) E. SEIFERT, "*The Monte-Carlo Criticality Code OMEGA*",ZfK-report, 364, (1978)

(7) M. NAKAGAWA et al., "*Deveropment of Monte-Carlo Code for Paticle Transport Calculation Calculations on Vector Processors*", Proc. of International Conference on Supercomputing in Nuclear Applications, Mito, Japan, March 12-16, (1990)

Table 1. K_{eff} values for 3-D fast reactor core calculated by verious methods

Method	Rod-out	Rod-in	Control rod worth (%)
Monte-Carlo	1.0951 ±0.0004	0.8799 ±0.0003	22.3 ± 0.1
Finite Difference			
Scheme 1 (conventional)	1.1033(+0.8)[a]	0.9355(+5.6)	16.3
(present)	1.1182(+2.3)	0.9355(+5.6)	17.5
Scheme 2 (conventional)	1.0888(-0.6)	0.8584(-2.2)	24.7
Scheme 3 (conventional)	1.1038(+0.9)	0.8723(-0.8)	24.0
(present)	1.1034(+0.8)	0.8768(-0.3)	23.5

a : Percent difference from Monte-Carlo result

Table 2. Region-averaged group fluxes for 3-D fast reactor core by various methods (Rod-in case)

Method	Group	Test Zone	Axial Blanket	Driver with Moderator	Control Rod
Monte-Carlo	1G	1.60E-04	4.07E-05	7.50E-05	9.55E-05
		0.11%[a]	0.24%	0.10%	0.10%
	2G	1.17E-04	5.18E-05	5.19E-05	6.93E-05
		0.14%	0.23%	0.10%	0.11%
	3G	2.18E-05	2.36E-05	2.70E-05	1.34E-05
		0.29%	0.36%	0.11%	0.21%
	4G	1.17E-06	9.85E-06	1.34E-05	9.53E-07
		0.41%	0.43%	0.13%	0.40%
Finite Difference					
Scheme 1	1G	1.59E-04	3.90E-05	7.06E-05	8.40E-05
(conventional)	2G	1.14E-04	5.03E-05	5.02E-05	6.02E-05
	3G	2.30E-05	2.32E-05	2.58E-05	1.01E-05
	4G	2.14E-06	9.76E-06	1.31E-05	6.39E-07
(present)	1G	1.60E-04	3.90E-05	7.06E-05	8.34E-05
	2G	1.14E-04	5.03E-05	5.04E-05	5.97E-05
	3G	2.37E-05	2.33E-05	2.57E-05	1.02E-05
	4G	2.10E-06	9.77E-06	1.31E-05	4.68E-07
Scheme 2	1G	1.69E-04	4.17E-05	7.63E-05	1.06E-05
(conventional)	2G	1.18E-04	5.29E-05	5.26E-05	7.54E-05
	3G	2.04E-05	2.34E-05	2.66E-06	1.46E-05
	4G	9.82E-05	9.56E-06	1.32E-05	7.85E-07
Scheme 3	1G	1.67E-04	4.09E-05	7.45E-05	1.04E-05
(conventional)	2G	1.18E-04	5.25E-05	5.23E-05	7.54E-05
	3G	2.04E-05	2.35E-05	2.63E-05	1.51E-05
	4G	1.04E-06	9.68E-06	1.32E-05	1.16E-07
(present)	1G	1.66E-04	4.05E-05	7.51E-05	1.02E-05
	2G	1.17E-04	5.20E-05	5.27E-05	7.41E-05
	3G	2.12E-05	2.35E-05	2.64E-05	1.47E-05
	4G	1.06E-06	9.64E-06	1.32E-05	9.74E-07

a : Standard deviation

Table 3. K_∞ values for 2-D hexagoal fuel assembly calculated by verious methods

Method	CR-out	CR-in	CR worth (%)
Monte-Carlo	1.1616	0.7866	41.0
	±0.0003	±0.0004	± 0.1
Finite Difference			
Scheme 1 (conventional)	1.1640(+0.5)[a]	Not converged	
Scheme 2 (conventional)	1.1658(+0.4)	0.7920(-0.5)	40.5
Scheme 3 (conventional)	1.1610(-0.1)	0.7687(-1.8)	44.0
(present)	1.1592(-0.2)	0.7836(-0.5)	41.3

a : Percent difference from Monte-Carlo result

Fig 1 One-dimensional mesh in slab geometry

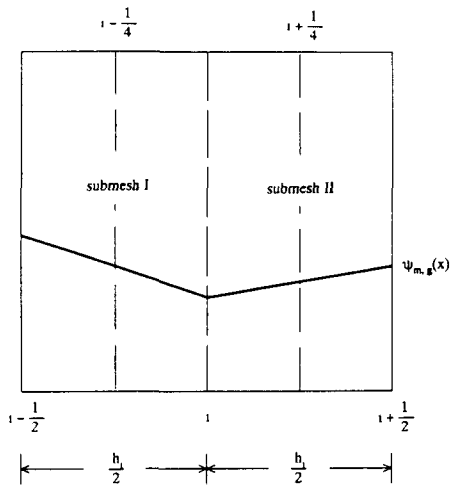

Fig 3 Relation between surface fluxes and vertex fluxes

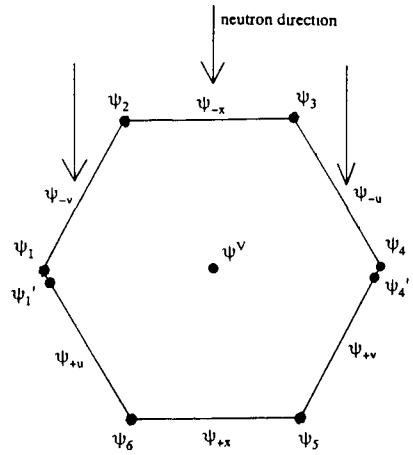

Fig. 2 Seven submeshes in a hexagonal node

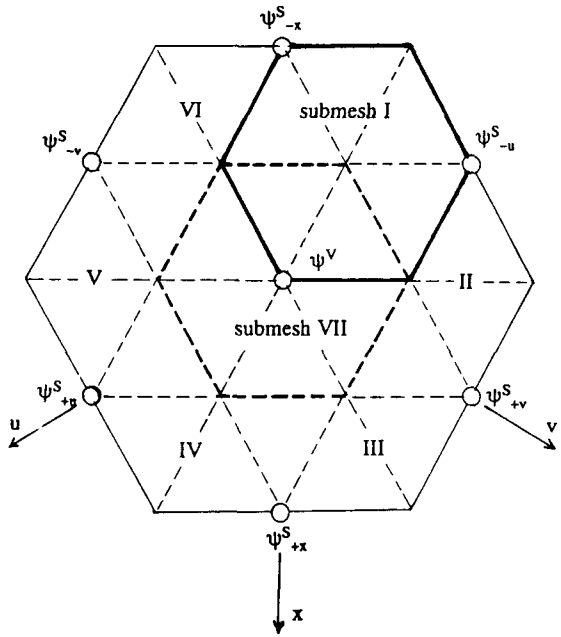

Fig. 4 Calculational model of fast reactor core

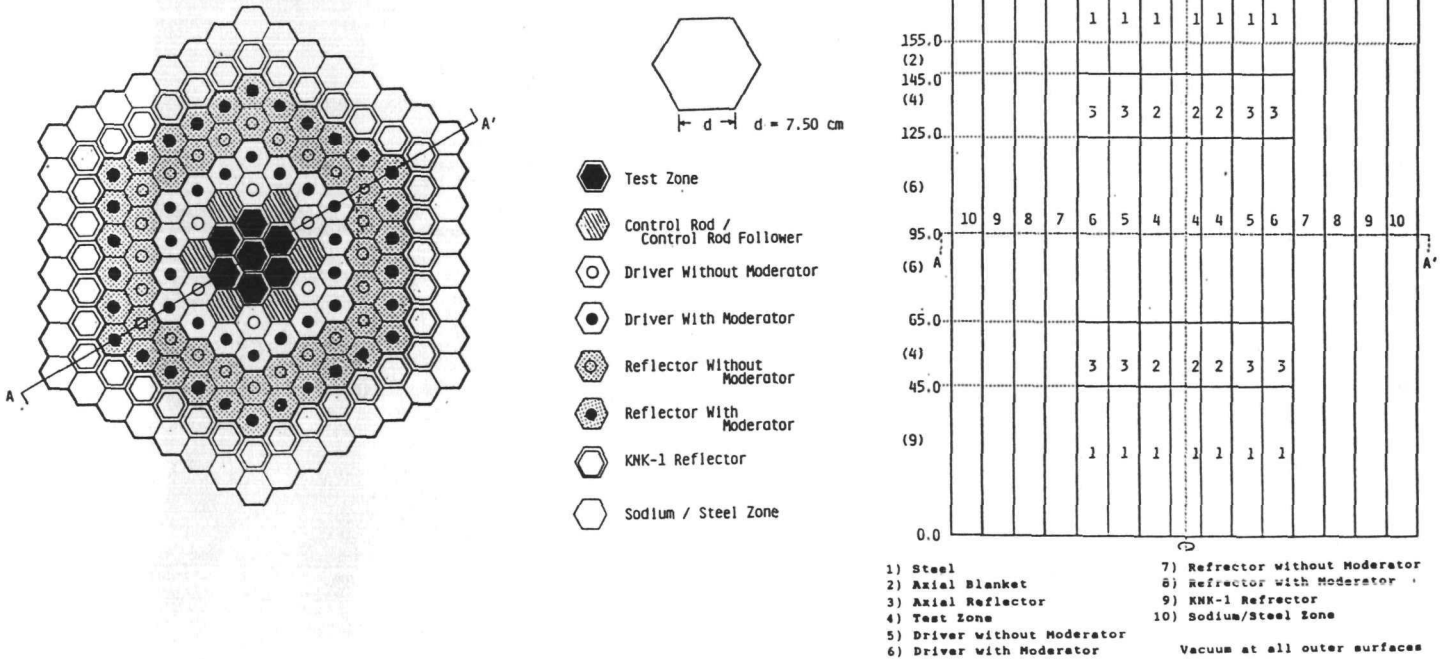

Fig. 5 Calculational model of high conversion fuel assembly

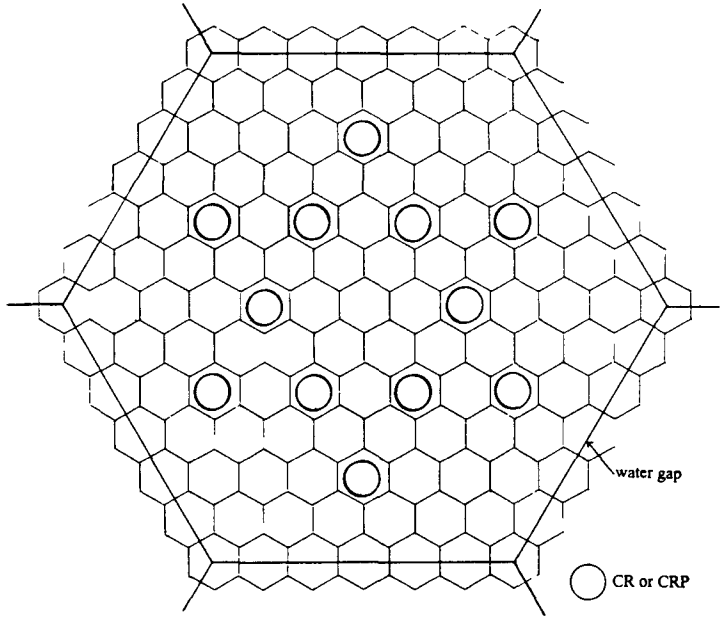

Fig. 6 Power Distribution of hexagonal fuel assembly calculation

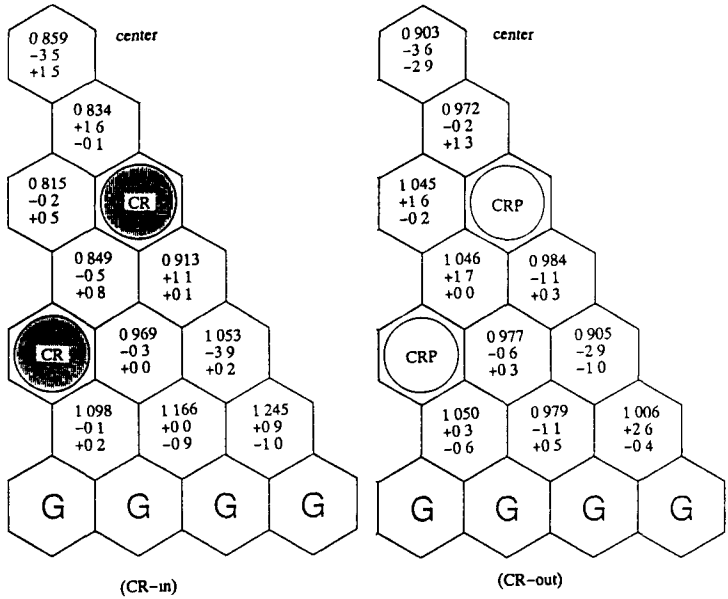

Reference
Scheme 2 (%error from reference)
Scheme 3 (with present method) (%error from reference)

EVALUATION OF INTEGRAL MEASUREMENTS FOR THE SP-100 SPACE REACTOR

Peter J Collins, Steven E Aumeier* and Gary L Grasseschi
Argonne National Laboratory - West
P O Box 2528, Idaho Falls, ID 83403-2528

ABSTRACT

Experiments in support of the SP-100 space reactor were done in ZPPR-20 Biases in calculations were found for criticality predictions and control worths Although the biases were on the conservative side for SP-100 design, the more general question of the reasons for the calculational errors is important for design optimization and for other fast space reactor designs A data sensitivity analysis has been made for the ZPPR-20 results using the GMADJ code Results for ZPPR-20 are used in conjunction with a wide database of fast reactor parameters It is shown that calculations of criticality for the reference core, for a core simulating water immersion and for the control rod worths are consistent with all other benchmark data and that differences in prediction are within uncertainties in nuclear data The results from ZPPR-20 can be used with confidence for prediction of calculational bias factors and uncertainties in SP-100 and related designs The most effective use of the ZPPR-20 data would be to create a sensitivity file for SP-100 and use the GMADJ system to reduce biases and uncertainties

INTRODUCTION

The nuclear reactor power source for the SP-100 space system was designed with the requirements of minimum mass, high operational reliability and safety response to launch accidents[1] Experiments for two systems were carried out at Argonne National Laboratory (ANL) in Idaho to validate the physics calculations of a 100 kilowatt-electric design and were jointly coordinated by ANL, the GE Astro Division and Westinghouse Advanced Energy Systems Division (WAESD) The experiments, in ZPPR-20 modelled the Nuclear Assembly Test (NAT), intended for testing on the ground, and the Reference Flight System (RFS) for use in space The test system mock-up included structure surrounding the core and shields while the RFS simulated conditions in space by a natural-lithium hydride shield which eliminated "room-return" effects in the experiments A description of the ZPPR-20 measurements is given by McFarlane et al[2] A cross section of the mock-up of the NAT configuration and its relation to the ground test is shown in Figure 1 By necessity, the experiments used the square tubular matrix and materials available at the Zero Power Physics Reactor (ZPPR) to model the fuel pins, hexagonal subassemblies and conical regions of the test design However, the experiments represented the sizes and zone compositions quite accurately Calculations for both the design and the mock-up used the MCNP Monte Carlo code[3] with very detailed modelling so that the differences were accurately taken into account

The fuel of ZPPR-20 used uranium plates of 93% enrichment and in combination with depleted uranium to form a second enrichment zone Rhenium and niobium were used as fuel pin liners and in a core vessel to provide extra shutdown reactivity in the water flooded condition The coolant was ^{7}Li canned in stainless steel BeO was used for the reflector-control segments and for the B_4C control rod followers The Be/lithium-hydride/tungsten shield was included in the experiments, but the core plenum used sodium

---

* Department of Nuclear Engineering, University of Michigan

in place of lithium The steel vacuum vessel, the fiberglass insulation and the steel/water facility shield were included in the NAT tests The principal mismatches in the mock-up were lack of nitrogen in the uranium nitride fuel and the inclusion of undesirable steel due to the ZPPR structure

Analysis of the experiments using the MCNP code and the project data, which was based on ENDF/B-V established two significant bias factors (ratios of calculation to experiment or C/E) These were

- Overprediction of criticality (k-eff) by about 1%
- Underprediction of the worth of boron shutdown rods by about 10%

The same criticality bias was applicable to all phases reflectors closed, reflectors open, both the NAT and the RFS, water-immersed and sand-buried states Reaction rate distributions were well predicted within the Monte Carlo statistics An uncertainty remained in interpretation of reflector-control worths due either to systematic errors in the experiment or calculation problems[2] However, the criticality predictions with reflectors open and closed were consistent

The ZPPR-20 experiments were sufficient to provide validation of the SP-100 design Where calculational biases existed, they were on the conservative side However, the reasons for the errors in calculation are important for future design optimization and for other fast space reactor designs Because of the detailed Monte Carlo calculations used, calculation methods are not in question and problems can be attributed to nuclear data errors and uncertainties For this reason, a detailed sensitivity analysis for space reactors has been made using the GMADJ code at ANL-W[4] This analysis uses an extensive database for fast reactors with many different measured parameters Since independent measurements from different laboratories and experiments employing different techniques, are used simultaneously, the GMADJ analysis provides a powerful check against possible systematic errors in the ZPPR-20 experiments

The sensitivity analysis is discussed in some detail in the paper and data adjustments required to give the best fit to all integral data for fast reactors are described It is claimed that this method provides the most reliable uncertainty estimates from use of all available integral measurements

THE GMADJ CODE AND DATABASE

The GMADJ code uses generalized least-squares fitting procedures A detailed description of the method and application to LMR predictions is given in reference 4 Basically, additional information from integral experiments is combined with a pre-evaluated data library by way of the sensitivity coefficients The system is overdetermined and the unbiased estimator of any integral parameter is provided by the least squares fit Covariances of differential data parameters and of integral measurements are included The fit is driven by the higher accuracy of integral measurements, particularly for k-eff The data adjustments result in a strongly correlated set of cross sections which gives the best fit to the experimental results After fitting, the code can be used to give biases and uncertainties for parameters that are not directly measurable

The database for GMADJ, before adding the data for space reactors, includes about 250 integral measurements This includes assemblies built at ANL-W, ANL-E, LANL and in the UK and a diverse range of parameters[4] The code has proved valuable in the LMR field in resolving different criticality predictions for ^{239}Pu and ^{235}U fuel, in accounting for mispredictions of spatial parameters in decoupled cores and predicting errors and uncertainties in burn-up calculations[5]

In order to focus on nuclear data errors, the reactor calculations must be as accurate as possible to minimize uncertainties Calculated values in the database were obtained with one, two or three dimensional S_n and nodal transport codes as appropriate or, in some cases, Monte Carlo Completely detailed models were used and, in some cases, older benchmark specifications were considerably revised Sensitivities were calculated with variational methods by diffusion theory and, in a few sensitive cases, by

direct variations with S_n calculations A two-dimensional transport sensitivity code is under development at ANL and is intended for use in configurations involving strong leakage effects

SPACE REACTOR DATA

A number of measurements for space reactors were added to the GMADJ database These were

(1) ZPPR-20B k-eff The NAT reference with reflectors closed and control rods withdrawn The calculated k-eff was consistent with that for ZPPR-20A with reflectors open and with that for the flight system simulation in ZPPR-20C

(2) ZPPR-20D k-eff The water flooded and immersed simulation The core was subcritical with the control rods inserted

(3) The control rod bank worth in ZPPR-20B The prediction of rod worth was consistent with that for the weighted average using six measured results in 20B and using six measurements in 20A

(4) Subsequent measurements in ZPPR-21 were done to study the criticality of metallic fuel for Argonne's Integral Fast Reactor (IFR) These covered six fuel mixtures, from all Pu fuel in ZPPR-21A to all ^{235}U fuel in 21F[6] Spectra were similar to that in the SP-100 core and the criticality was strongly correlated to ZPPR-20

(5) A useful addition to the data was the k-eff of a much earlier space reactor core built by the Pratt and Whitney Aircraft Company[7] The assembly used here, called PWAC, had a core of 93%-enriched uranium and 103 kg fissile mass with carbon, niobium and aluminum and with BeO reflectors Unfortunately, the data were not reported to present-day accuracy requirements but this is an important addition because the measurements are completely independent of those in ZPPR

BENCHMARK AND LMR DATA

Apart form ZPPR-21, most other data have spectra which are harder or softer than in the SP-100 An integral data correlation coefficient[8], with values between ±1, is calculated in GMADJ to give a simple parameter which quantifies the impact of one parameter on the prediction of another An example for the SP-100 is shown in Table VI of reference 2

Benchmark data most relevant to criticality in ZPPR-20 are Godiva, a bare sphere of uranium with 93% enrichment and FLATTOP-25, an enriched sphere of uranium with a depleted uranium reflector Uranium cores with lower enrichment but having a fairly hard spectrum are LANL's BIG-10 ANL's U9 and a European benchmark SCHERZO-556 (see reference 4)

The LMR data have softer spectra and are closer to that in the water-flooded ZPPR-20D Basic studies for the IFR with metallic fuel were done in ZPPR-15 ZPPR-15D had 90% ^{235}U fuel with a correlation of 0 4 to ZPPR-20 Control rod worths in ZPPR-15 are relevant to that in ZPPR-20B (correlation 0 6) Boron sample worths in ZPPR-15, BIG-10, U9 and other cores, and measurements of helium production in boron and ß-eff are also connected to the space reactor data The criticality in oxide fuel (ZPR-6/6A) is related to that for metal fuel in ZPPR-15D (correlation 0 96) Spectra in GODIVA, ZPPR-20 and the IFR are shown in Figure 2

Priorities of the LMR program meant that many integral measurements were made in plutonium oxide rather than uranium fuel Integral parameters measured in plutonium cores are relevant for some

parameters such as boron worths, ^{235}U to ^{239}Pu fission ratios, by the ^{238}U in the fuel, the oxygen in the BeO reflectors, through the Pu and U data covariances and as general check on the experimental techniques The GMADJ code is capable of treating all data simultaneously

NUCLEAR DATA COVARIANCES

The starting point for the cross section covariances in the GMADJ Library was the ENDF/B-V files processed through the NJOY code[9] Considerable extensions were made by Poenitz[4] Data for the fission spectra used the parameters defining the spectra in ENDF/B-V (Watt or Madland-Nix) The delayed neutron yields were used for sensitivities of worths and subcritical reactivity For the space reactor materials, Nb, ^{185}Re, ^{187}Re, W, covariance data did not exist in the files and estimates of uncertainties were taken from a 1986 survey by ANL For example, 1σ uncertainties for Re used were 25% (n,n), 50% (n,n^1), 30% (n,γ) and 100% (n,2n) Uncertainties for Nb were taken to be 5% (n,n), 20% (n,n^1) and 10% (n,γ)

A positive-definite covariance matrix is required to give positive variances in the GMADJ fitting This is not guaranteed in the files and a routine in GMADJ is used to make random variations within prescribed limits to assure this condition

RESULTS OF THE LEAST-SQUARES FITTING

The fitting of LMR data has been reported in some detail[4] When the space reactor and IFR criticality data are added, the LMR results do not change significantly The measured k-eff results for ZPPR-20 and ZPPR-21 were accurate to better than 0 1% (uncertainty due principally to knowledge of the fuel mass) The measured uncertainty for the ZPPR-20B control rod worth was estimated as 1 9% Uncertainties in the calculated k-eff's by Monte Carlo statistics were close to 0 1% and the uncertainty for the control worth of 19$ was 1% Total uncertainties for k-eff in most other assemblies (combination of measurement and calculation) were about 0 2% The principal adjustments to nuclear data impacting the space reactors are summarized in Table 1

Results for the critical eigenvalues are shown in Table 2 With ENDF/B-V data, the biases are about 1% in ZPPR-20 and PWAC These are much larger than in some benchmark cores (GODIVA, FLATTOP and ZPPR-21) and in the opposite sense to those in the LMR cores (ZPPR-15D and ZPR-6/6A), but are similar to those in the low-enrichment benchmarks, BIG-10 and ZPR-U9 One might speculate that the differences may be due to "unusual" materials in the space reactors - Nb, Re, Li and BeO While the error of one percent might not seem particularly large, this represents up to six standard deviations of the uncertainty and consequently has a high weight in the GMADJ fit

The k-effs for ZPPR-20 and PWAC are extremely well treated with the adjusted data (compare A/E-1 with C/E-1 in Table 2) After the fitting, discrepancies with other data do not exist Uncertainties of 1% to 3% with ENDF data are reduced to between 0 1% and 0 3%, a factor of ten The fit for PWAC shows an uncertainty of 0 4% and indicates that the estimated input uncertainty of 0 4% was a realistic

The results of the ZPPR-20B control rod worth and some of the other relevant data are given in Table 3 Note that ZPPR-20D was near critical with the control bank inserted The underprediction of rod worth in 20B by 12% is reduced to 2% in the fit with a 2% uncertainty This result, in conjunction with the control rod worths in ZPPR-15D and ZPPR-13C and boron sample worths in BIG-10 provides confidence in the quality of the data for ZPPR-20B

The effectiveness of the space reactor measurements can be shown by excluding these data from the GMADJ fit and predicting their results using all other data This is the same procedure that would be used (with space reactor measurements included) to predict the biases and uncertainties for a target SP-100 design The results are shown in Table 4, with the ENDB-V and adjusted results included for

comparison Without ZPPR-20 and PWAC data in the fit, the k-eff bias is reduced by 0 5% (by 0 8% in the flooded core) and the control rod bias is reduced from 12% to 5% Uncertainties in the predictions are only a little reduced unless the space reactor measurements are included We will indicate in the next section which material adjustments permit the good results for the space reactors

DATA ADJUSTMENTS PROJECTED FOR THE SPACE REACTORS

The individual data adjustments are rarely significant as is shown by the marginal reduction in uncertainties after the GMADJ fit The improvements in prediction of integral parameters result from the induced set of correlations of the cross sections after the fitting However, it is of interest to see which items of data adjustments lead to the excellent results Remember that the same adjustments are applied to all data and the changes in different integral parameters are due to sensitivity coefficients

Contributions of different data adjustments for a number of parameter are given in Figure 3 in histogram form Percentage contributions to the positive and negative adjustments are shown with the totals given in boxes above the plots A few of the more relevant sensitivities are shown in Figure 4

The k-effs for ZPPR-20 and PWAC are overpredicted by about 1% with ENDF/B-V, in comparison with the good predictions for GODIVA and ZPPR-21 Figure 3 shows that the good predictions for the space reactors after fitting are due to ^{235}U capture and inelastic scattering (positive) and ^{235}U fission and oxygen elastic scattering (negative) In GODIVA, there is no oxygen The components from ^{235}U balance and result in a small net adjustment In PWAC there is a negative adjustment due mostly to oxygen scattering In ZPPR-20B oxygen is again important, but less so than in PWAC, and components due to steel, Re and Nb contribute PWAC has niobium but no rhenium The fit to the uranium fuelled IFR core (ZPPR-15D) is dominated by adjustment to ^{238}U capture followed by ^{235}U capture and fission

The large positive adjustment for the ZPPR-20 control rod worth results mainly from an increase in $^{10}B(n,\alpha)$ and offset by smaller components for the delayed neutron yield, ^{238}U and steel This is also true for the smaller adjustment required in ZPPR-15D (4% versus 11%) Similar adjustments (with results in the opposite sense) are important in fitting the k-eff of ZPPR-20D, which was near critical with the control rods inserted

Most of the adjustments required to fit the space reactor data and other data are less than one standard deviation of the nuclear data uncertainties and combine in a complex way in the fit The exception is $^{10}B(n,\alpha)$ in the 100 KeV to 1 MeV range, which is increased by 5% to 16% with input uncertainties of 2% to 10% (see Table 1) This indicates that a re-evaluation of the high-energy ^{10}B data in ENDF/B-V may be necessary

SUMMARY

Two unexpected results of the sensitivity analysis were the importance of the high energy oxygen scattering data in the BeO reflectors and the low errors projected for rhenium and niobium data This indicates that anisotropic scattering in oxygen should be given extra care but that ENDF/B data for the refractory materials was more accurate than supposed Measurements of rhenium capture cross sections which postdate the ENDF/B-V evaluation show much lower uncertainties[10] Measurements of $^{10}B(n,\alpha)$ inside a boron control rod support the need for increases of the high-energy data[11]

It is concluded that the ZPPR-20 data are highly reliable and can be used with confidence for the SP-100 and related designs The most effective use of the data would be through a code such as GMADJ This takes into account all relevant measurements and provides a guard against systematic errors Mismatches in composition and the presence of unwanted materials such as steel in the experiments would be accurately taken into account

ACKNOWLEDGEMENTS

The experiments on ZPPR-20 were coordinated by David N Olsen and much of the data processing was done by Dale M Smith This work was supported by the U S Department of Energy under contract No W-31-109-END-38

REFERENCES

1 C L Cowan et al , "SP-100 Nuclear Reactor Design," Proc of the 1988 International Reactor Physics Conference, Jackson Hole, Wyoming, Sept 18-22, 1988, Vol IV p 315 (1988)

2 H F McFarlane et al , "Analysis and Evaluation of ZPPR Critical Experiments for a 100 kilowatt Electric Space Reactor," Proc International Conference on the Physics of Reactors Operation, Design, and Computation, Marseille, France, April 23-27, 1990, Vol 3, p 292, (1990)

3 J F Briesmeister, Editor, MCNP - A General Monte Carlo Code for Neutron and Photon Transport, Version 3A, Los Alamos National Laboratory Report LA-7396-M, Rev 2, (September 1986)

4 W P Poenitz and P J Collins, "Utilization of Experimental Integral Data for the Adjustment and Uncertainty Evaluation of Reactor Design Quantities," Proc of the NEACRP Specialist Meeting, Jackson Hole, Wyoming, Sept 23-24, 1988, NEACRP-L-307 (1988)

5 H Khalil and J J Downer, "Uncertainty in the Burnup Reactivity Swing of Fast Reactors,", Reference 4, p 187 (1988)

6 D N Olsen, P J Collins and S G Carpenter, "Experiments for IFR Fuel Criticality in ZPPR-21," ICNC '91 International Conference on Nuclear Criticality Safety, Oxford UK, September 9-13, (1991)

7 P J Collins et al , "Fast Critical Experiment Data for Space Reactors," Space Nuclear Power Systems, 1986, Chapter 33, M S El-Genk and M D Hoover, eds , Orbit Book Co , Malabar, Florida, pp 343-356, (1988)

8 P J Collins et al , "Integral Data for Fast Reactors," Proc of the Conf on Nuclear data for Science and Technology, Mito, Japan, May 1988, Seikon Publ Co , p 31 (1988)

9 R E McFarlane, "The NJOY Nuclear Data Processing System, Volume 1 Users Manual," Los Alamos National Laboratory Report, LA-9303-M, Vol 1 (ENDF-324), (May 1982)

10 R L Macklin and P G Young, "Neutron Capture Cross Sections of Rhenium from 3 to 1900 keV " Nucl Sci Eng 97, 239-244 (1987)

11 S B Brumbach et al , "Measurements and Calculations of $^{10}B(n,He)$ and $^{235}U(n,f)$ Reaction Rates in a Control Rod Mockup in ZPPR," Proc Topical Meeting on Reactor Physics and Safety, Saratoga Springs, NY, Sept 17-19, 1986 NUREG/CP-0080 Vol 2, p 1145, (1986)

Table 1 Summary of the Principal Data Adjustments Used to Fit SP 100 Experiments

Material	Adjustment (Input Uncertainty) %*		
^{235}U	nf 1 to 2 (2 to 3)	nγ 6 to 11 (10 to 60)	nn 5 to 30 (15 to 30)
	ν 0 1 to 0 2 (0 5 to 1)	delayed ν 0 4 (2 5)	chi (parametric) <1/2 σ
^{238}U	nf 0 to 3 (2 to 3)	nγ 5 (5)	nn 7 to 7 (5 to 15)
	delayed ν 2 4 (2 5)		
^{6}O	nn -3 (4)		
^{9}Be	nn <1 (3)	nα < 1 (10)	n2n <1 (20)
^{93}Nb	nγ <1 (10)	nn <1 (5)	
^{85}Re	nγ <1 (40)	nn <2 (25)	nn <1 (40)
^{87}Re	nγ <2 (40)	nn 2 to -3 (25)	nn < 1 (40)
^{10}B	nα 5 to 16 (2 to 10)		

* The larger adjustments above 100 KeV are shown with input uncertainties in parentheses

Table 2 Results of LS Fitting of ZPPR 20 k effectives and Other Relevant Data

			ENDF/B-V 2 Data			Adjusted Data		
Assembly	Experimental Value, E	Uncertainty %*	Calculation, C	(C/E 1) %	Data Uncertainty %	A	(A/E 1) %	Uncertainty %
ZPPR 20B	1 0021	0 23	1 0110	0 89	2 00	1 0023	0 02	0 23
ZPPR 20D	0 9524	0 31	0 9630	1 11	3 41	0 9524	0 01	0 31
PWAC CCA7	1 0000	0 44	1 0112	1 12	2 18	0 9993	-0 07	0 41
ZPPR 21F	1 0006	0 26	0 9984	-0 21	1 66	0 9991	-0 15	0 20
ZPPR 21E	1 0009	0 25	1 0007	-0 02	1 45	1 0009	0 00	0 17
ZPPR 21D	1 0014	0 22	1 0026	0 12	1 38	1 0021	0 07	0 15
ZPPR 21C	0 9993	0 21	1 0010	0 17	1 60	0 9990	-0 02	0 14
GODIVA	1 0000	0 14	0 9971	-0 29	1 61	1 0008	0 08	0 13
FLATTOP 25	1 0000	0 14	1 0036	0 36	1 20	0 9990	-0 10	0 11
ZPPR 15D	1 0007	0 30	0 9936	-0 71	1 14	1 0007	0 00	0 16
ZPPR-6/6A	1 0016	0 32	0 9895	1 21	1 21	1 0002	-0 14	0 19
ZPR U9	1 0014	0 30	1 0152	1 38	2 18	1 0049	0 35	0 13
BIG10	0 9960	0 32	1 0118	1 59	2 04	0 9973	0 13	0 17

* Combined uncertainty due to experiment and calculation method excluding nuclear data uncertainty

Table 3 Results of LS Fitting of ZPPR-20B Control Rod Worths and Other Relevant Data

			ENDF/B-V 2 Data			Adjusted Result		
Measurement	Experimental Value, E	Uncertainty, %[a]	Calculation, C	(C/E-1), %	Data Uncertainty, %[b]	A	(A/E-1) %	Uncertainty %[b]
Z20B CRS	-28 97$	2 35	-25 46$	-12 12	4 53	-28 38$	-2 02	2 06
Z20D k-eff	0 9524	0 31	0 9630	1 11	3 41	0 9524	0 01	0 31
Z15D Central CR	-1 389$	3 16	-1 295$	-6 77	2 68	-1 373$	1 17	0 85
Z15D Pnm CRs	-9 580$	3 16	-8 966$	-6 10	2 52	-9 36$	2 29	0 80
Z15D All 13 CRs	-19 14$	3 16	-18 42$	-3 76	2 48	-19 13$	-0 02	0 77
Z15D Worth ^{10}B	-1 289-2	2 93	-1 163-2	-9 78	3 71	1 272-2	-1 31	1 19
Z15D Worth ^{238}U	5 856-4	2 93	5 925-4	1 18	2 57	5 917-4	1 04	0 73
ZU9 Worth ^{10}B	-3 87-2	4 28	-3 22-2	-16 8	7 46	-3 649-2	-5 71	1 27
ZU9 ß-eff	7 061-3	1 64	7 006-3	-0 78	1 78	7 099-3	0 53	0 65
BIG10 Worth ^{10}B	-7 354-2	2 73	-6 596-2	-10 31	7 88	-7 528-2	2 36	1 36
BIG10 (n,He)	0 9840	1 94	0 8518	-13 43	3 24	0 9409	-4 38	1 29
BIG10 ß-eff	7 222-3	1 32	7 147-3	-1 04	1 77	7 244-3	0 31	0 66
Z13C 4CRsX	-6 940$	3 14	-7 200$	+3 75	3 99	-7 004$	+0 92	0 77
Z13C 4CRsY	-1 178$	3 14	-1 126$	-4 41	4 23	-1 175$	-0 22	0 90

[a] Combined uncertainty due to experiment and calculation method, excluding nuclear data uncertainty
[b] Delayed neutron data uncertainty is included for control rod and sample worths through the yield sensitivities

Table 4 The Improvement in Space Reactor Data Due to ZPPR-20 and PWAC Experiments

		ENDF/B V 2 Data		Predicted Result Space Reactors Excluded[a]		Adjusted Result Space Reactors Included[a]	
Parameter	Uncertainty, %	No Fit C/E-1 , %	Data Uncertainty, %	P/E-1, %	Uncertainty %	A/E-1, %	Uncertainty %
PWAC k-eff	0 44	1 12	2 18	0 64	1 71	-0 07	0 41
ZPPR-20B k-eff	0 23	0 89	2 00	0 48	1 42	0 02	0 23
ZPPR-20D k-eff	0 31	1 11	3 41	0 33	2 55	0 01	0 31
ZPPR-20B CR Worth	2 35	-12 12	4 53	-4 98	3 25	-2 02	2 06

[a] Data for all benchmarks and LMR cores included, PWAC and ZPPR-20 excluded
[b] All integral data, including PWAC and ZPPR-20, used in adjustment

Figure 1. ZPPR-20 Mockup of the Nuclear Assembly Test (NAT) Configuration

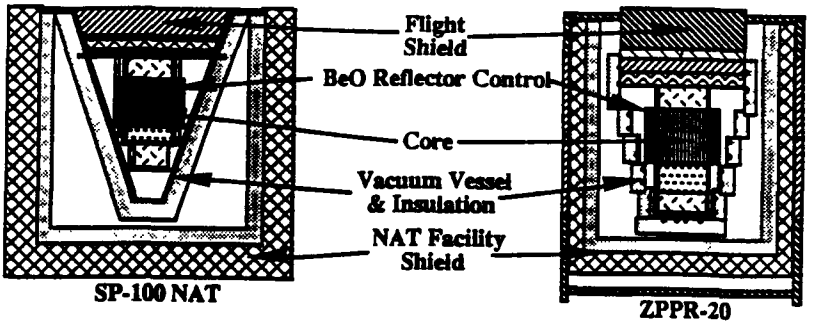

Figure 2. Spectra in GODIVA, ZPPR-20 and the IFR

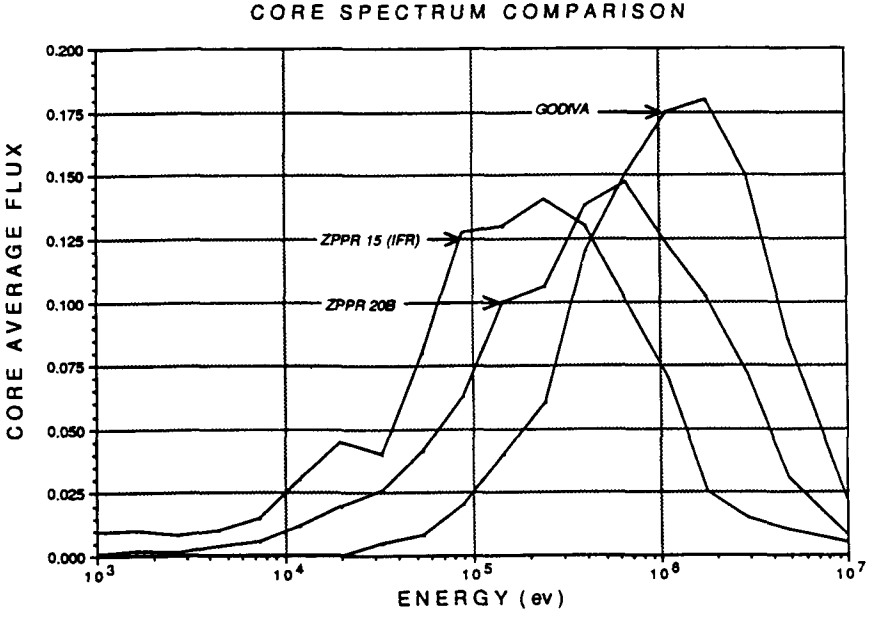

Figure 3 Components of Integral Parameter Adjustments

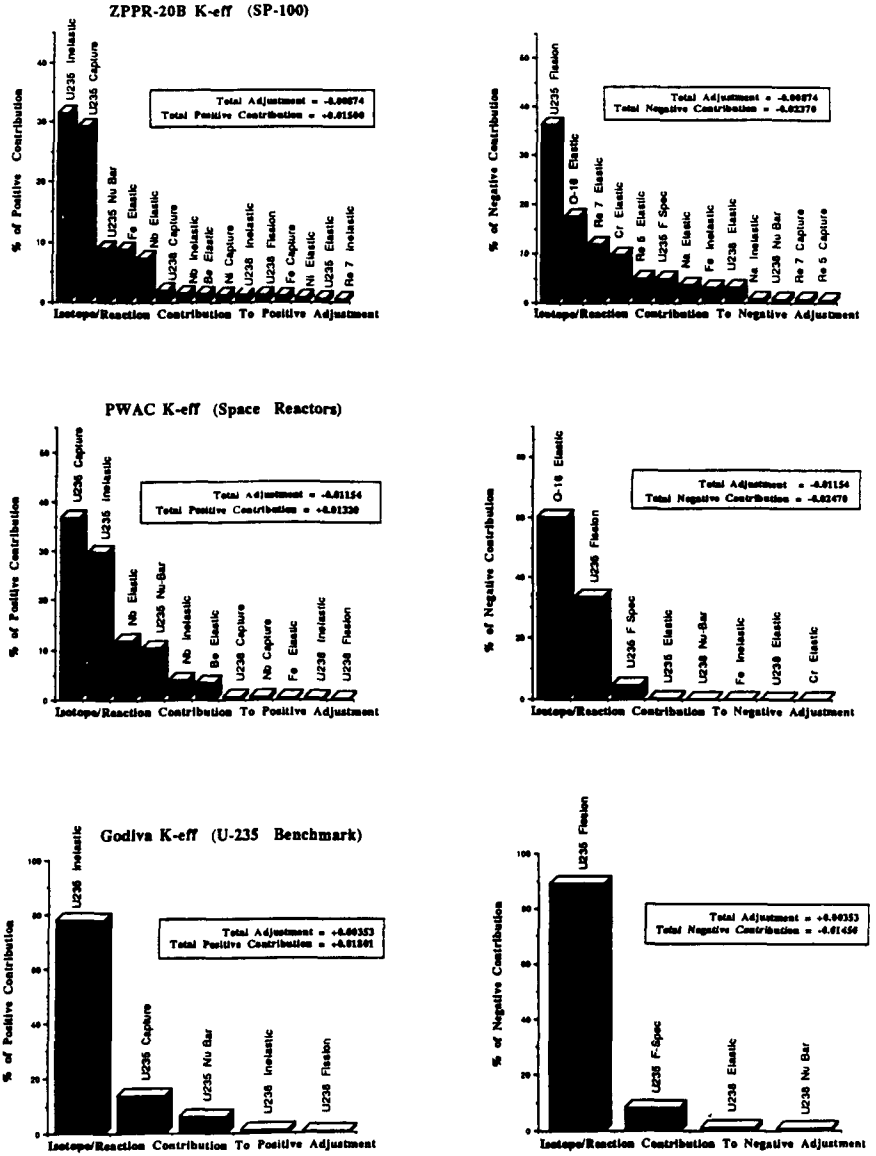

Figure 3. Components of Integral Parameter Adjustments (Continued)

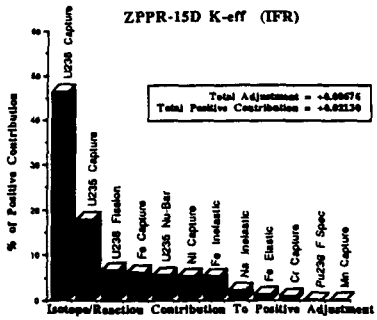

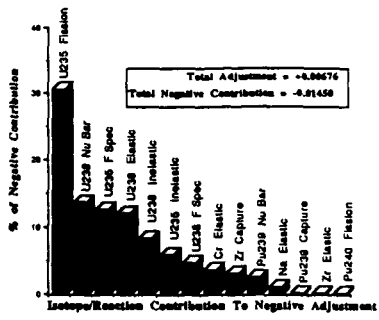

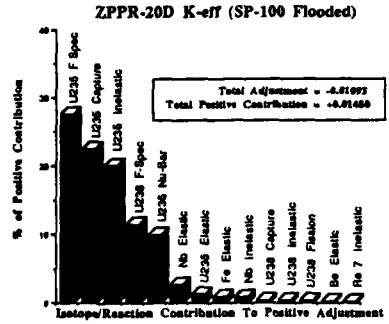

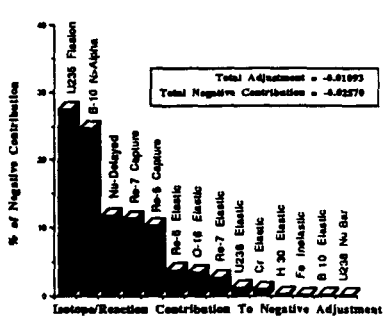

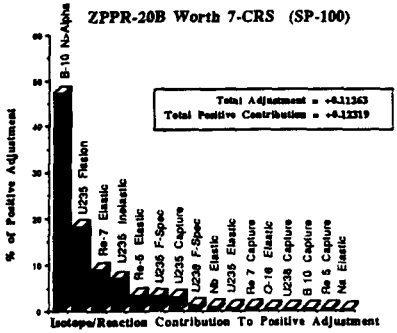

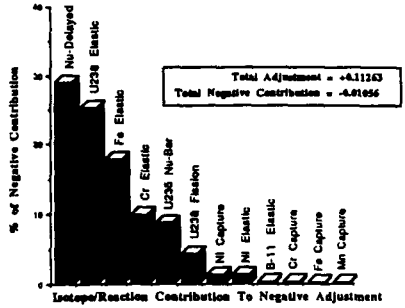

Figure 3 Components of Integral Parameter Adjustments (Continued)

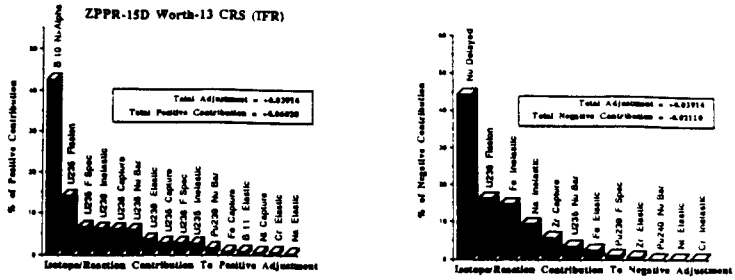

Figure 4 Some Sensitivities for Space Reactor Materials

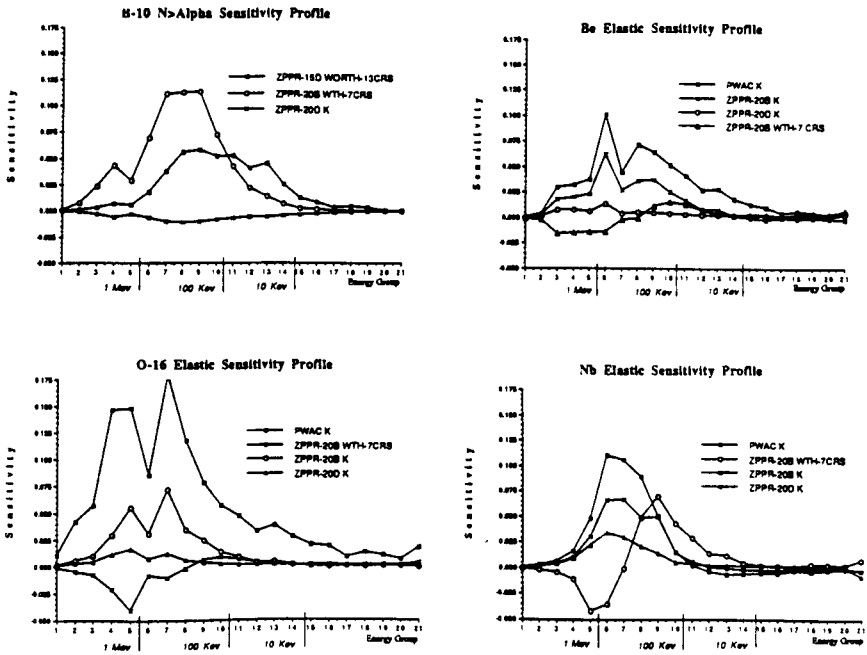

VALIDATION OF THE REBUS-3/RCT METHODOLOGIES FOR EBR-II CORE-FOLLOW ANALYSIS

R D McKnight
Argonne National Laboratory
Argonne, Illinois 60439

ABSTRACT

Operations and material control and accountancy requirements for the Fuel Cycle Facility will demand accurate prediction of the mass flow from EBR-II into the facility This will require validated calculational tools that can predict the burnup and isotopic distribution in irradiated binary- and ternary-fueled Mark III, Mark IV, and Mark V assemblies The present study demonstrates that the REBUS-3/RCT methodologies can meet these requirements Validation is achieved via a two-step procedure First, a set of detailed core-follow depletion calculations using the REBUS-3/RCT codes is performed for an extensive series of EBR-II runs Second, the results of this analysis are compared with experimental determinations of burnup and U and Pu isotopic weight fractions that have been measured in IFR fueled test assemblies irradiated in EBR-II The results of these comparisons are very good and indicate that mass flow predictions based on the methods and models used in this study are adequate for operational and MCA requirements in FCF

INTRODUCTION

A design objective for the Integral Fast Reactor (IFR) is self-sufficiency of the fuel cycle, that is, no outside source of fissile make-up is required when the reactor is coupled to a small collocated reprocessing plant [1,2] The IFR uses a pyrometallurgical process to remove fission products and recover plutonium from discharged core and blanket assemblies This process uses compact, inexpensive equipment that can be easily scaled to the anticipated deployment of LMRs collocated with the fuel cycle plant

One of the many tasks to be completed over the next year regarding IFR fuel cycle closure at EBR-II/FCF is to develop and install the systems to be used for fissile material accountancy and control The IFR fuel cycle and pyrometallurgical process scheme determine the degree of actinide buildup in the reload fuel assemblies Inventories of curium, americium and neptunium in the fuel will affect the radiation and thermal environmental conditions at the fuel fabrication stations, the chemistry of reprocessing, and the neutronic performance of the core Thus, it is important that validated calculational tools be put in place for accurately determining isotopic mass and neutronic inputs to FCF for both operational and material control and accountancy purposes

The current fuel management methodology used by the EBR-II division has focused on uranium-fueled cores This methodology treats the higher plutonium isotopes and minor actinides coarsely, if they are included at all. However, determining the concentration of the transuranic isotopes will be important in an integral reprocessing system with recycling uranium or mixed-(U,Pu) fuels The primary goal of this work is to validate the REBUS-3/RCT codes[3,4] as tools which can adequately compute the burnup and isotopic distribution in binary- and ternary-fueled Mark-III, Mark-IV, and Mark-V drivers, and all anticipated experimental fuel assembly loadings (i e., mixed fuel element assemblies, fabrication test experiments, etc.) The validation procedure is based on comparing EBR-II burnup calculations with experimentally measured burnup indicators, including destructive assay of EBR-II assemblies.

Although the initial fissile loadings of fresh driver subassemblies are always known, details of the actual EBR-II reactor composition (that is, the quantity and distribution of isotopes in irradiated driver, test, and control assemblies) have, in general, been neither measured nor calculated and therefore are unknown The validation procedure chosen for this study has involved obtaining the available loading information for an EBR-II configuration which sufficiently preceded the runs of EBR-II into which were loaded driver/test assemblies that were ultimately analyzed for discharge compositions. Detailed REBUS-3 modeling of the core loading and core power level history for that EBR-II run is used to calculate the burnup history. This process is then extended through a series of all subsequent EBR-II runs, where input to the REBUS-3 burnup calculations utilizes the known heavy metal loadings for freshly-loaded subassemblies and the calculated (REBUS-3) number densities for the remainder of the subassemblies This procedure should approximate the energy and spatial distribution of the neutron flux for the freshly-loaded subassemblies Therefore, after a series of EBR-II runs have been analyzed, the effect of the initial conditions (i e , the coarse initial reactor loading data) should diminish Depletion analysis for a series of EBR-II runs is then repeated for specific experimental test subassemblies using the RCT code to obtain local values (e.g., values for an axial segment of a single element within a subassembly) of the burnup and isotopic compositions. Validation of these analytical methods and procedures is then determined via comparison of calculated element discharge compositions with experimentally measured burnup indicators (such as ^{139}La and ^{148}Nd measurements and U and Pu isotopic ratio measurements)

METHODOLOGY

One of the principal goals of this series of depletion calculations or core-follow analyses for EBR-II is to compare calculated fuel burnup values and element discharge compositions with measured values for binary-and ternary-fueled IFR subassemblies. The experimental database consists primarily of measurements on the three lead IFR experimental subassemblies X419, X420 and X421, which had been introduced into EBR-II in Run 133A (February, 1985). The core-follow analyses for this study begin with Run 130A (August, 1984), i.e., they begin three runs (or 9 reactor sub-runs) prior to the initial loading of the lead IFR experiments into the reactor

Cross sections for this study are based on the ENDF/B Version V 2 nuclear data files Region-dependent multigroup cross sections in 9 broad energy groups have been generated using the MC^2-2/SDX cell homogenization codes[5,6] for each of

the following EBR-II cell types: Mark-II (U-5Fs) driver, Mark-III (U-10Zr) driver, internal blanket, stainless steel reflector, and depleted uranium blanket. The SDX one-dimensional reactor model included the following seven collapsing regions: internal blanket, Mark-II inner core driver, Mark-III inner core driver, Mark-II outer core driver, Mark-III outer core driver, stainless steel reflector, and outer radial blanket. Cross sections have also been generated for lumped fission products which did not include the burnup indicators ^{139}La and ^{148}Nd, which have been treated individually and included explicitly in the depletion analysis. The depletion chain used in the REBUS-3 calculations includes 19 "active" (or depletable) isotopes, ranging from ^{234}U through ^{246}Cm.

REBUS-3 Methods and Models

EBR-II contains 16 rows of hexagonal assemblies within the reactor vessel. The core is contained within the first seven rows (central 127 subassemblies). The pitch of the hexagonal subassemblies is 2.32 inches (5.8928 cm) and the effective core radius is approximately 12* inches (~32 cm). The active length of the (cold, unirradiated) fueled subassemblies is 13.5 inches (34 29 cm). The active core length in the REBUS-3 model is 14.43 inches (36.66cm). The increase (~7%) represents the combined effects of temperature expansion and irradiation growth.

The core contains two Row 3 safety rods and from eight to ten Row 5 control rods. All the control rods and safety rods are fueled (that is, they reside in the core in their normal operating position and they are withdrawn to remove reactivity). In a typical core, there is only one normal control rod; the remainder of the control rods are High-Worth Control Rods (HWCRs). The HWCRs contain B_4C followers which are above the core in the rods-inserted position.

In the normal operation of EBR-II, the safety rods are banked together over the operating cycle, as are all but one of the control rods--that one being used as a reactivity shim When the shim rod reaches its normal limit of insertion, it is repositioned outward and the remaining bank of control rods are notched inward. For the neutronics calculations, an attempt has been made to have the control rods and the safety rods each modeled in the average rod bank position at the beginning-of-cycle and at the end-of-cycle.

Rows 8-10 (and portions of Row 7) contain stainless steel reflector assemblies which are 55 inches (139.70 cm) long. Rows 11-16 (Rows 15 and 16 are incomplete) contain depleted uranium blanket assemblies. The length of the blanket assemblies is also 55 inches (139.70 cm), except for new blanket assemblies, which are only 33 inches (83.82 cm) long.

The REBUS-3 reactor model of EBR-II is a three-dimensional (hexagonal-Z) full core model which explicitly models each hexagonal subassembly through Row 16. An additional row of hexagons (Row 17) is included in the REBUS-3 model representing the sodium pool. The reactor model includes three axial depletion regions in each of the core and blanket subassemblies. The neutronics solution uses DIF3D nodal diffusion theory.[7] The control rods and safety rods are modeled explicitly with time-dependent positions.

The REBUS-3 calculation for each EBR-II run is a single burn step non-equilibrium calculation in which all loading changes from the preceding reactor run have been modeled. The power is assumed to be constant over the burn

step (and taken to be the total MWDays for the run divided by the number of days in the run). The series of EBR-II runs analyzed for this study (Run 130A through Run 154F) includes 67 reactor sub-runs, that is, analysis of these runs requires 67 separate REBUS-3 non-equilibrium calculations

Each of these calculations has the following characteristics The full core model contains approximately 33x33x25 mesh intervals and about 1400 zones Each REBUS-3 input deck contains ~20,000 lines and the neutronics input processing alone requires ~5 minutes of CPU on the ANL CRAY-XMP Each complete calculation uses 3 megawords of memory and requires ~30 minutes of CPU on the CRAY Approximately 1360 of the 1400 zones are "burn" zones with ~240 burn zones in the core and ~1120 burn zones in the radial blanket. Reduction of the number of axial burn zones in each radial blanket subassembly from 3 to 1 reduces the total number of burn zones by ~55%, but reduces the total CPU time by only ~35% This is because ~75% of the CPU time is spent in the neutronics solution, and reducing the number of burn zones (without reducing the number of spatial mesh) does not impact the neutronics solution Simplifying the blanket model would complicate treatment of blanket fuel management, more than offsetting the small saving in computer time

RCT Methods and Models

Because all three of the lead IFR test subassemblies (X419, X420, and X421) are mixed fuel types, direct comparison cannot be made between the REBUS-3 results and the analytical chemistry measurements of burnup and U and Pu isotopic fractions for these three subassemblies. That is, the compositions of the different element types in these subassemblies have been homogenized within the node (hexagon) in the REBUS-3 analysis Furthermore, the depletion in REBUS-3 has been zone or block depletion, thereby lacking point values And finally, the not uncommon procedure of reconstitution and further irradiation of many test assemblies (including these three experimental assemblies) is well beyond the standard abilities of REBUS-3. The RCT code has been developed to reconstruct the intra-nodal distributions of power density, burnup, nuclide densities, group fluxes, and fast and total fluences from nodal-diffusion/depletion calculations performed in hexagonal-Z geometry using REBUS-3/DIF3D. Several important capabilities have been implemented in RCT to permit its application to a wide range of core designs and fuel management strategies. Specifically, the burnup characteristics can be explicitly calculated for user-defined "special pins" by point depletion using interpolated fluxes at the center of each fuel element The radioactive decay during the shutdown period between reactor runs or during out-of-core storage is also accounted for in the nuclide density calculation Rotation of assemblies is allowed (in integer multiples of 60 degrees), and to permit assembly reconstitution, pin-by-pin shuffling is allowed for the special pins. Multi-cycle reconstruction calculations are performed as a sequence of single cycle RCT calculations

COMPARISON OF CALCULATIONS WITH EXPERIMENTAL DATA

The EBR-II experimental data available for comparison with REBUS-3/RCT calculations include burnup measurements, U and Pu isotopic fraction measurements, and gamma scan data.

Burnup Measurements on IFR Metal Fuel

The current study focuses only on chemistry measurements performed by personnel of the Argonne-West Analytical Laboratory on metal fuel. This limits the database, at this time, to measurements on six experimental assemblies, namely, the three lead IFR test assemblies X419, X420, and X421, and the experimental assemblies X425, X444, and XC-1. Assembly X425 contains 61 new HT9 clad IFR metal fuel elements with as-built fissile loadings designed to closely match those of X419, X420, and X421. Assembly X444 is a standard Mark-III driver subassembly containing 61 D9 clad binary fuel elements. Assembly XC-1 contains 61 Mark IIC/Mark IICS binary fuel elements used in the fueled safety rods and control rods.

The burnup measurements are based on Isotope Dilution Mass Spectroscopic (IDMS) analysis of fission products ^{139}La and ^{148}Nd. The accuracy of performing these burnup measurements in metallic fuel is dependent on:

1. the precision of the weight of the sample, namely a measurement of the U and Pu,
2. the precision and accuracy of performing a hot-cell separation of La and Nd without external contamination,
3. the accuracy of the La and Nd spike calibration,
4. the precision of the mass spectrometric measurement of La and Nd,
5. the stability and uniformity of La and Nd in the fuel,
6. the accuracy of the fast fission yield for La and Nd in U and Pu, and
7. the accuracy of calculated relative fission rates in the isotopes of U and Pu.

The overall accuracy of the Analytical Laboratory's determination of burnup on irradiated IFR fuel (U-10Zr or U-xPu-10Zr) up to 20 atom percent burnup is estimated to be ±4% provided the diffusion of La and Nd is only in the radial (and not axial) direction. Furthermore, there is an absolute uncertainty of 4% in the measurement of the power level of EBR-II. Because the power level is a direct normalization to the burnup values obtained in the REBUS-3/RCT analysis, the 4% uncertainty in the reactor power contributes a 4% uncertainty to the calculated values in addition to other nuclear data, methods, and modeling uncertainties. Therefore, agreement between calculated and experimental burnup values within about 6% should be considered good. Comparison between the current burnup calculations and the experimental values follows.

Summary of Burnup Measurement Results

There are two sets of burnup measurements which cannot be used, namely the measurements for X419A (at ~0.8% burnup) and X421 (at ~10% burnup). Both sets of measurements are for ternary fuel elements, and in both cases the Analytical Laboratory has noted their suspicion of the data. These data shed no information on the agreement with calculations. Their value is in alerting the Analytical Laboratory to the difficulty in executing this experimental procedure for the ternary elements, particularly in regard to the dissolution of the sample. However, the results for X425A, which also are for a U-8Pu-10Zr ternary element, are very good. These measurements were performed about three years after the X421 measurements, and they do not exhibit anomalous trends.

With regard to the remaining measured burnup values, there are data for 28 samples -- each measured with La and Nd burnup monitors. These data are summarized in Table 1. As discussed earlier, agreement between calculated and measured burnup values within about 6% should be considered acceptable In that sense, the agreement between the calculated and measured burnup values for the IFR metal fuel is very good. The mean value ±1σ spread of all 56 C/E values is 1.044±0.030. This 1σ value is not the 1σ uncertainty in the C/E values (though related to it) It is simply a measure of the spread or dispersion in the values. The range of the 56 C/E values is from 0.960 to 1 087, these extreme values being La burnup measurements of two samples of the same U-8Pu-10Zr ternary pin in X419 at ~1.9%. The mean and 1σ spread in the C/E values according to fuel type are shown below.

	Burnup C/E's Mean Value ±1σ
	==========
U-10Zr	1.050 ± 0.023
U-8Pu-10Zr	1.027 ± 0.039
U-19Pu-10Zr	1 041 ± 0.035

The slight differences in the mean C/E values according to fuel type are not significant. In fact, there are no significant trends in the C/E biases The set of six C/E values for the binary pin in X419 at ~1.8% burnup are the best and most consistent set (i.e., closest to unity and to each other). However, the best C/E's for a single sample are for the U-19Pu-10Zr ternary pin in X419B at ~12% burnup, which is the highest burnup measured.

Summary of Gamma Scan Measurements

Burnup data are available at different axial positions for only five elements of IFR metal fuel, namely, for elements T167, T013, and T119 of test assembly X419 and elements A352 and A451 of assembly X444. For the three elements of assembly X419, the C/E value is lower near the top of the fuel column than at the middle and bottom. It is natural to question (i) whether this distributional bias is real, and (ii) does it portend a misprediction in the axial flux or power profile. Because these C/E values all agree within ±6%, the first question cannot be answered unequivocably without additional data (i.e., more comparisons of measured burnup distributions). However, one can still consider the second question. Many of the irradiated IFR fuel elements have been analyzed with a precision gamma scanner. Energy dependent activity measurements are taken every one or two mils along the entire length of the fuel elements. Although some of the fission products migrate and redistribute within the fuel element, other fission products, such as ^{95}Nb, appear to remain fixed in the fuel matrix. Therefore, the gamma scan for ^{95}Nb approximates the fission distribution or burnup profile along the fuel element. The ^{95}Nb gamma scan measurement in the U-19Pu-10Zr element T167 of assembly X419 is shown in Figure 1. The REBUS-3/RCT calculated values of axial power density and burnup for this fuel element are also shown in Figure 1. Each of these curves have been normalized to have a peak value of unity The calculated distributions are more convex or "buckled" than the measured data, that is, the calculated values are lower at both the top and bottom of the fuel column. However, it must again be noted that the differences are small (<4%) relative to overall uncertainties.

Measurements of U and Pu Isotopic Fractions

U and Pu isotopic analyses have also been performed by the Analytical Laboratory on four of the same IFR test assemblies discussed above. The determinations are again obtained from mass spectrometer measurements The achievable accuracy of determining the actinide isotopic fractions on irradiated IFR fuel is dependent on:

1. the precision of the mass spectrometer to repetitively perform an isotopic measurement, and
2. the certified uncertainty of the standard reference material used to calibrate the mass spectrometer.

The overall accuracy of performing isotopic measurements on irradiated IFR fuel with the mass spectrometer used for all the measurements discussed in the current study is estimated to be ~0.2% for ^{235}U, ^{238}U, and ^{239}Pu, and ~1.0% for ^{234}U, ^{236}U, and ^{240}Pu.

In the case of X419, X420, and X421, isotopic data have been measured from radial drilling of the irradiated samples. As might be expected, the radial variation within the samples was determined to be quite small. The experimental values quoted here represent average values for the entire axial section of the samples. Comparison of calculated and measured values of the U and Pu isotopic fractions has been made as a function of burnup for U-10Zr, U-8Pu-10Zr, and U-19Pu-10Zr IFR fuel In all cases where measured data are available for the Pu isotopics, the calculated values of the ^{241}Pu weight fractions have been decay-corrected to the date of the experimental determination using a decay constant of 1.494×10^{-9} sec $^{-1}$. In most cases, data were measured in at least three axial locations· top, center, and bottom. The REBUS-3/RCT values reported as top, center, and bottom correspond to 0.25-inch axial sections taken 12.25-12 50 inches, 6.25-6 50 inches, and 1 25-1.50 inches from the bottom of the fuel column, respectively. The variation in isotopic fractions with axial position is very small. The agreement between measured and calculated values is quite good.

U and Pu isotopic fractions have also been measured for the two burnup samples of element T456 (U-8Pu-10Zr) in test assembly X425A. These data are compared with calculated values in Table 2. As mentioned above, the calculated ^{241}Pu weight fractions have been decay-corrected to the date of the experimental determination. For the X425A data the decay time was slightly more than two years and the corrections were ~10%. Again, agreement is quite good, except for ^{242}Pu which represents a very small component of the Pu in element T456. One of the two C/E values for the ^{242}Pu weight fraction is ~9% high and the other ~27% low. The measurements in X419, X420, and X421 did not report the ^{242}Pu weight fractions.

CONCLUSIONS AND RECOMMENDATIONS

Before reviewing the conclusions from the above comparisons, one important question should be answered. It is, in fact, the very point of the current study, namely, "Are the REBUS-3/RCT methodologies adequate to predict the material flow of irradiated IFR fuel from EBR-II into FCF?" The answer is YES.

In the above discussion it was noted that the burnup measurements have a 1σ uncertainty of ±4% and that the measurement of the reactor power also has a 1σ uncertainty of ±4%, and therefore, the "agreement" between calculated and experimental values of burnup cannot be discerned finer than ~6% That is, if the calculational methods (including nuclear data) and models were refined and/or adjusted by whatever means, there would still remain a limit of ~6% uncertainty on the C/E value for burnup The results of the present study have demonstrated that the predicted burnup values based on the REBUS-3/RCT methodology (as applied herein) do consistently agree with experimental values within 6%.

The conclusion that a 6% uncertainty in burnup prediction is not limiting for operational or MCA purposes in FCF is based on the following argument. The heavy metal mass uncertainties for material flows into FCF have a component based on their pre-irradiation uncertainties and a component based on burnup uncertainties. The impact of the uncertainty component due to the burnup calculation is largely mitigated by the fact that only about 10% of the heavy metal atoms in a fuel element undergo fission. That is, if the pre-irradiation uncertainty is assumed to be 1%, then for a typical fuel cycle the post-irradiation uncertainties are increased only slightly to ~1.06%.

The principle conclusions from the present study are:

1. REBUS-3 analysis using nodal diffusion theory with a three-dimensional hexagonal-Z full core model and ENDF/B-V.2 nuclear data can adequately follow EBR-II fuel management and depletion.

2. Details of nuclide density, burnup, power density, and fluence within the node or hexagonal subassembly can adequately be reconstructed using the RCT code

3. Comparisons have been made of REBUS-3/RCT analyses with experimental values, including the analysis of mixed fuel type test assemblies that have had complex irradiation histories (such as multiple reconstitutions, multiple core insertions/removals, and multiple core locations and subassembly orientation)

4. Results of these comparisons for burnup and U and Pu isotopic fractions are quite good (i.e., generally within experimental uncertainties).

REFERENCES

1. D. C. Wade and Y. I. Chang, "The Integral Fast Reactor (IFR) Concept: Physics of Operation and Safety," Proc. Intl. Topical Meeting on Advances in Reactor Physics, Mathematics and Computation, Paris, France, Vol. 1, pp. 311-336 (April 27-30, 1987).

2. Y. I. Chang, "The Integral Fast Reactor," Nucl. Tech., **88**, 129 (November 1989).

3. B. J. Toppel, "A User's Guide to the REBUS-3 Fuel Cycle Analysis Capability," Argonne National Laboratory Report ANL-83-2 (March 1983).

4. W. S. Yang, P. J. Finck, and H. Khalil, "Reconstruction of Pin Burnup Characteristics from Nodal Calculations in Hexagonal Geometry," Proc. of Intl. Conf. on the Physics of Reactors: Operation, Design and Computation, Marseille, France, Vol. 2, VIII-22 (April 23-27, 1990).

5. H. Henryson II, B. J. Toppel, and C. G. Stenberg, "MC^2-2: A Code to Calculate Fast Neutron Spectra and Multigroup Cross Sections," Argonne National Laboratory Report ANL-8144 (ENDF-239), (1976).

6. W. M. Stacey, Jr. et al., Trans. Am. Nucl. Soc., 15, 292 (1972).

7. R. D. Lawrence, "The DIF3D Nodal Neutronics Option for Two- and Three-Dimensional Diffusion Theory Calculations in Hexagonal Geometry," Argonne National Laboratory Report ANL-83-1 (March 1983).

Figure 1. Comparison of Nb Gamma Scan Data and Calculated Power Density and Burnup Profiles for Test Assembly X419

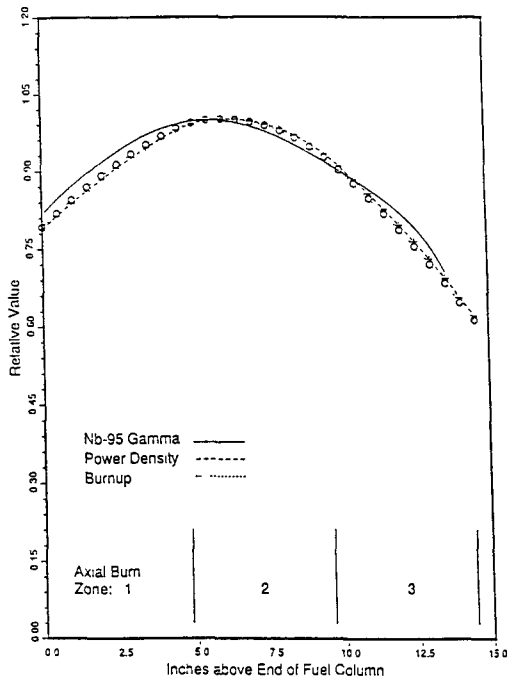

Table 1. Burnup Measurements from IFR Test Assemblies

Distance above Bottom of Fuel (inches)	Measured Burnup (atom-percent) La-139	Nd-148	REBUS/RCT Calculation (atom-percent)	Calc/Exper Relative to La-139	Nd-148
S/A: **X419** Element: **T167** **(U-19Pu-Zr)**					
1.25 - 1.50	1.571	1.624	1.69722	1.080	1.045
6.00 - 6.25	1.828	1.834	1.96534	1.075	1.072
12.25 -12.50	1.426	1.486	1.49521	1.049	1.006
S/A: **X419** Element: **T013** **(U-8Pu-Zr)**					
1.25 - 1.50	1.628	1.665	1.69471	1.041	1.018
6.00 - 6.25	1.791	1.831	1.94689	1.087	1.063
12.25 -12.50	1.550	1.544	1.48817	0.960	0.964
S/A: **X419** Element: **T119** **(U-10Zr)**					
1.25 - 1.50	1.645	1.615	1.67817	1.020	1.039
6.00 - 6.25	1.848	1.872	1.92038	1.039	1.026
12.25 -12.50	1.454	1.467	1.47511	1.015	1.006
S/A: **X419B** Element: **T112** **(U-19Pu-Zr)**					
5.50 - 5.75	12.53	12.17	12.3459	0.985	1.014
S/A: **X419B** Element: **T141** **(U-10Zr)**					
5.50 - 5.75	11.65	12.14	12.0857	1.037	0.996
S/A: **X420** Element: **T096** **(U-8Pu-Zr)**					
6.00 - 6.25	5.339	5.679	5.60506	1.050	0.987
S/A: **X425A** Element: **T456** **(U-8Pu-Zr)**					
6.25 - 6.50	10.69	10.71	10.9600	1.025	1.023
6.50 - 6.75	10.47	10.34	10.9419	1.045	1.058
S/A: **X444** Element: **A352** **(U-10Zr)**					
1.25 - 1.50	7.990	7.697	8.3968	1.051	1.091
12.50 -12.75	7.048	6.913	7.2791	1.033	1.053
S/A: **X444** Element: **A303** **(U-10Zr)**					
7.00 - 7.25	8.980	8.885	9.4764	1.055	1.067
S/A: **X444** Element: **A398** **(U-10Zr)**					
7.00 - 7.25	8.774	8.675	9.3808	1.069	1.081
S/A: **X444** Element: **A424** **(U-10Zr)**					
7.25 - 7.50	9.068	8.808	9.3737	1.034	1.064

Table 1. Burnup Measurements from IFR Test Assemblies (Continued)

Distance above Bottom of Fuel (inches)	Measured Burnup (atom-percent) La-139	Nd-148	REBUS/RCT Calculation (atom-percent)	Calc/Exper Relative to La-139	Nd-148
S/A: **X444** Element: **A355** (U-10Zr)					
7.00 - 7.25	9.101	8.828	9.3374	1.026	1.058
S/A: **X444** Element: **A451** (U-10Zr)					
7.00 - 7.25	9.009	8.924	9.2433	1.026	1.036
12.50 -12.75	6.736	6.748	7.0834	1.052	1.050
S/A: **X444** Element: **A473** (U-10Zr)					
7.00 - 7.25	8.446	8.444	9.0621	1.073	1.073
S/A: **X444** Element: **A410** (U-10Zr)					
7.00 - 7.25	8.583	8.386	8.8621	1.032	1.057
S/A: **XC-1A** Element: **R287** (U-10Zr)					
6.50 - 6.75	7.86	7.69	8.2996	1.056	1.079
S/A: **XC-1A** Element: **P003** (U-10Zr)					
6.75 - 7.00	7.51	7.49	8.0859	1.077	1.080
S/A: **XC-1A** Element: **A503** (U-10Zr)					
6.75 - 7.00	7.85	7.77	8.3356	1.062	1.073
S/A: **XC-1A** Element: **A493** (U-10Zr)					
6.75 - 7.00	7.72	7.54	8.1239	1.052	1.077

Table 2. Neutron Induced Isotopic Changes in Test Assembly X425

Element: T456
Grid Position: 59
Fuel Type: U-8Pu-10Zr

Sample Elevation (Inches from End of Fuel Column)		Burnup (at-%)	Uranium Isotopic Fractions (wt-%) ^{234}U	^{235}U	^{236}U	^{238}U
As Cast		0.00000	0.46	63.80	0.29	35.44
6.25-6.50	Exper.	10.70	0.487	58.9	2.21	38.40
	Calc.	10.960	0.472	58.75	2.182	38.60
	C/E	1.024	0.969	0.997	0.987	1.005
6.50-6.75	Exper.	10.40	0.487	58.95	2.20	38.36
	Calc.	10.942	0.472	58.76	2.179	38.59
	C/E	1.052	0.968	0.997	0.990	1.006

Sample Elevation (Inches from End of Fuel Column)		Burnup (at-%)	Plutonium Isotopic Fractions (wt-%) ^{239}Pu	^{240}Pu	^{241}Pu	^{242}Pu
As Cast		0.00000	93.84	5.72	0.37	0.07
6.25-6.50	Exper.	10.70	91.77	7.78	0.38	0.08
	Calc.	10.960	91.86	7.58	0.408	0.087
	C/E	1.024	1.001	0.974	1.073	1.089
6.50-6.75	Exper.	10.40	91.71	7.78	0.39	0.12
	Calc.	10.942	91.86	7.58	0.405	0.087
	C/E	1.052	1.002	0.974	1.038	0.726

Note:
Experimental burnup values are average of La and Nd measurements.

SENSITIVITY THEORY FOR LMFBR IN-VESSEL SHIELDING ANALYSIS

V.V.Bolyatko, Yu.I.Balashov, M.A.Berzonis, A.V.Kyachin
Moscow Engineering Physics Institute, USSR

ABSTRACT

The paper is devoted to the sensitivity analysis application to the investigation of neutron and gamma functionals, error estimation for LMFBR in-vessel calculations. By use sensitivity analysis and spatial channel theory practical recommendations of the shield developments are worked out. New code ZAKAT-2.2 developed in the USSR for sensitivity analysis application to the investigation of neutron and gamma functionals in radiation shielding and core is described. Code is written for calculating the sensitivity coefficients of linear and fractionlinear functionals of the radiation field to cross-sections and other input parameters, contributon current and contributon flux of spatial channel theory. Selection of energy group structure and weighting spectra as well as introduction of spatial dependence of cross-sections are pointed out in paper. Error estimation, taking into account nonlinear effects are provided.

INTRODUCTION

Recently sensitivity and uncertainty analysis has become wide-spread in usage for reactor shielding calculations[1,2]. Two-dimensional benchmark model of LMFBR is investigated[3]. Model represents LMFBR in-vessel composition for BN-600 type of fast power reactor (Figure 1). Material mixtures and nuclide atom densities of different zones are presented in Table 1. The following functionals were selected for calculations: sodium activation rate in intermediate heat exchanger, radiation damage of steel and carbon, radiation heating for steel and carbon in different material mixtures of in-vessel shield.

CALCULATIONS

Two-dimensional transport calculations in R-Z geometry of forward and adjoint fluxes are carried out with discrete ordinates codes KASKAD-1[4] and DOT-III[5]. The sensitivity analysis and channel theory have been realized in code ZAKAT-2.2 for transport code KASKAD-1 and in code ZAKAT-3[6] for transport code DOT-III. P_3S_8, P_3S_6, P_3S_4 angular approximations were chosen. The agreement in calculations for such angular approximations is within 10%. Spatial mesh chosen for two-dimensional calculations (120×190 mesh intervals for 595×895cm R-Z dimensions) had provided in one-dimensional calculations of all functionals error within 30%. Besides, for separate calculation of central part of the model more dense spatial mesh was chosen (130×100 mesh intervals for 390×415cm dimensions).

LMFBR in-vessel shielding analysis includes four stages:

1.Generating of application-dependent cross-section library for calculations.

2.Two-dimensional transport calculations of forward and adjoint fluxes, neutron and gamma functionals of interest in different zones of in-vessel shield.

3.Calculations of sensitivity coefficients, contributon current and contributon flux for neutron and gamma functionals.

4.Determination of main spatial channels of functional formation, error estimation, practical recommendations of the in-vessel shield developments.

An application-dependent cross section libraries have become wide-spread in usage for different type reactor shielding calculations. Fine-group cross-section libraries, which are restricted in utilization for multi-dimensional calculations by a large expense of computing time, are usually the basis for generating such libraries. Wide-spread fine-group library VITAMIN-C was taken as a basis for deriving problem-dependent cross-section library BN28+15 (28n,15γ). Space dependent 43 group library BN28+15 was collapsed from VITAMIN-C to be used in two-dimensional calculations. BN28+15 energy group structure is very close to energy group structure of Russian ABBN library. The derivation of BN28+15 library was made by use AMPX-II modular code system[7] on a basis of three mutually supplemented one-dimensional spherical models of LMFBR in-vessel composition. They represent core, blanket, fuel storage and activation shields: the shield in radial direction, the shield in the direction of sodium transfusion area (upper shield) and the shield in the direction of heat exchanger bottom (lower shield)[3]. Ratio computing time/accuracy for different cross section sets were ananlyzed during derivation of BN28+15 library.

Besides BN28+15, fine group library EURLIB-IV (100n,20γ) and Russian broad-group library ABBN were used in calculations of

central part of model. There was made the comparison of spatial (R,Z) distributions of following neutron and gamma functionals: fast neutron flux $\varphi^n_{0.1}$, total neutron flux φ^n_t, total gamma flux φ^g_t, total energy gamma flux φ^g_E. Figure 2-4 illustrate ratio of neutron fluxes calculated by use broad group libraries to neutron fluxes calculated by use fine-group library EURLIB. Obtained results demonstrate obvious advantage of use space dependent library BN28+15. BN28+15 fast fluxes overestimate EURLIB fluxes within 20%, then ABBN fast fluxes overestimate EURLIB fluxes more then ten times. Discrepancies between fine-group and broad group total neutron flux calculations are within 100%. The same discrepancies are obtained for gamma functionals. Discrepancy between fine-group and broad-group ABBN calculations is increasing with the distance from the core as a result of neutron spectrum deformation in the extended LMFBR in-vessel shielding.

SENSITIVITY AND UNCERTAINTY ANALYSIS

The transport calculations of forward and adjoint fluxes for sensitivity analysis are carried out utilizing application-dependent BN28+15 cross-section library. Sensitivity coefficients of sodium activation rate in heat exchanger due to total cross-section of different zone material mixtures in radial direction are presented in Table 2. It is evident that steel shield (zone 4) and carbon shield (zone 5) contribute main input to total sensitivity coefficient.
Figure 5 depicts spatial dependence of contributon current for radiation damage of steel ($\varphi^n_{0.1}$) in the lower part of steel shield as three dimensional plot and as an isolines (there transfered 10% of total contribution between neighbouring isolines). The main spatial channel of contribution is evident in this figure. Study of formation of sodium activation rate in intermediate heat exchanger is performed using the sensitivity coefficients and spatial dependence of contributon current and contributon flux. There are three main spatial channels of sodium activation rate formation, which correspond to three one-dimensional spherical models of LMFBR in-vessel composition chosen. Over 90% of contributon flux correspond to the sodium transfusion area direction, some percents correspond to the radial direction and less then 1% correspond to the direction of heat exchanger bottom. One of the possibilities of secondary sodium activation rate in intermediate heat exchanger reduction is connected with inserting of supplementary shielding materials to the sodium transfusion area.
Shield development is one of application of sensitivity theory. In this case using $\langle\varphi^*,\varphi\rangle$ data for the initial shield structure we obtain spatial dependence of sodium activation sensitivity as a function of concentrations of main and possible supplementary shielding materials. Efficiency of using supplementary materials or

structure changes for LMFBR in-vessel composition was estimated analyzing spatial dependence of sodium activation sensitivity as a function of concentration of main and supplementary materials and ratio of sensitivity coefficients obtained. The most effective way of sodium activation rate reduction is adding B_4C in sodium transfusion area, less effective way is adding borated steel. The effective way of shield developments in radial direction is adding B_4C in sodium near heat exchanger or altering expansion of "carbon shield" zone to "steel shield" zone.

Sensitivity coefficients are also used to estimate uncertainties in responses due to uncertainties in cross-sections. Comparison of evaluated uncertainties and requirements to them shows that recent accuracy of cross-sections does not allow to calculate sodium activation rate in transfusion area with the required accuracy. Besides, average magnitudes of cross-sections $\bar{\Sigma}$ are usually used in calculations. From the other side result of calculation is a function of not only average magnitudes but its probability distribution (arises from the statistical nature of cross-section knowledge). Therefore for deep penetration problem average of response differs from response of averages[2]. For this case statistical correction factor is introduced $\omega_R=\overline{R(\Sigma)}/R(\bar{\Sigma})$, where $\overline{R(\Sigma)}$ is average of response, $R(\bar{\Sigma})$ is response for averages. For radiation transport problems $\omega_R>1$. The following expression is obtained $\omega_R=\exp\left[\frac{1}{2}\sigma_R^2\right]$, where σ_R - uncertainty of response within the accuracy of linear perturbation theory. Calculation of statistical correction factor is performed using code ZAKAT-2.2. Thus, uncertainty of sodium activation rate calculation in sodium transfusion area equals to 50%, and $\omega_R=1.2$.

CONCLUSIONS

LMFBR in-vessel composition was investigated in paper using sensitivity theory. Multigroup application-dependent library BN28+15 was developed for design LMFBR in-vessel calculations. By use contributon currents reactor shielding areas responsible for main contribution to functionals of interest were determined. Spatial dependence of functional sensitivity as a function of concentrations of main and possible supplementary shielding materials was obtained for the initial shield structure. Efficiency of using supplementary materials or structure changes was estimated. Thus, study of different flux functionals formation in LMFBR in-vessel shielding is performed using sensitivity theory, and practical recommendations of the reactor developments are presented.

REFERENCES

1. V.V.Bolyatko, M.Yu.Vyrsky, A.I.Ilyushkin, et al., "Error Estimation in Reactor Shielding Calculations", American Institute of Physics. Translation Series. New York, 1987.

2. Yu.I.Balas h ov, V.V.Bolyatko, V.P.Mashkovich, et al., Atomic Energy, Mo s cow, 59(1985), p.101.

3. M.A.Berzonis, V.V.Bolyatko, V.I.Savitsky, Problems of Atomic Science and Technology. Nuclear Data Series, 2(1990), p.65.

4. A.M.Voloschenko, A.V.Shwetsov, "The KASKAD-1 Two- Dimensional Discrete Ordinates Nodal Transport Code". Proceedings of International Topical Meeting Advances in Mathematics, Computations, and Reactor Physics. Pittsburgh, USA, 1991.

5. F.R.Mynatt, et al. DOT-III. Two- dimensional Discrete Ordinates Radiation Transport Code System. ORNL-TM-4280, 1973.

6. M.A.Berzonis, V.V.Bolyatko, Atomic Energy, Moscow, 66(1989), p.287.

7. AMPX-II. Modular Code System for Generating Coupled Multigroup Neutron-Gamma-Ray Cross Sections from Data in ENDF Format, ORNL, PSR-63, 1978.

Table 1. Material Mixtures and Nuclide Atom Densities, 10^{24} atoms/cm^3

Element / Zone number; T,K	1 900	2 900	3 900	4 700	5 700
Pu-239	7.46-4				
U-238	7.40-3	1.27-2	9.55-3		
Oxygen	1.71-2	2.54-2	1.91-2		
Sodium	7.20-3	5.50-3	7.20-3	4.44-3	4.88-3
Iron	1.24-2	8.42-3	1.24-2	4.83-2	1.03-2
Cromium	3.21-3	2.19-3	3.21-3	1.30-2	2.75-3
Nickel	2.66-3	1.81-3	2.66-3	6.83-3	1.36-3
Carbon					4.74-2

Element / Zone number; T,K	6 700	7 700	8 700	9 700	10 700
Sodium	2.22-2	1.89-2	7.20-3	8.88-3	1.51-2
Iron		9.06-3	1.24-2	3.62-2	1.93-2
Cromium		2.43-3	3.21-3	9.72-3	5.20-3
Nickel		1.20-3	2.66-3	4.80-3	2.55-3

Table 2. Sodium Activation Sensitivity in Heat Exchanger Due to Total Cross Sections for Zone Materials Mixtures in Radial Direction

Zone number	Sensitiviy coefficient
1	-1.78-1
2	-2.24-1
4	-2.21
5	-2.96
6	-4.33-1
7	-7.86-1

Figure 1. Geometry of two-dimensional benchmark model of LMFBR in-vessel composition. In radial direction: 1-core, 2-3-blankets, 4-steel shield, 6-sodium, 7-heat exchanger.

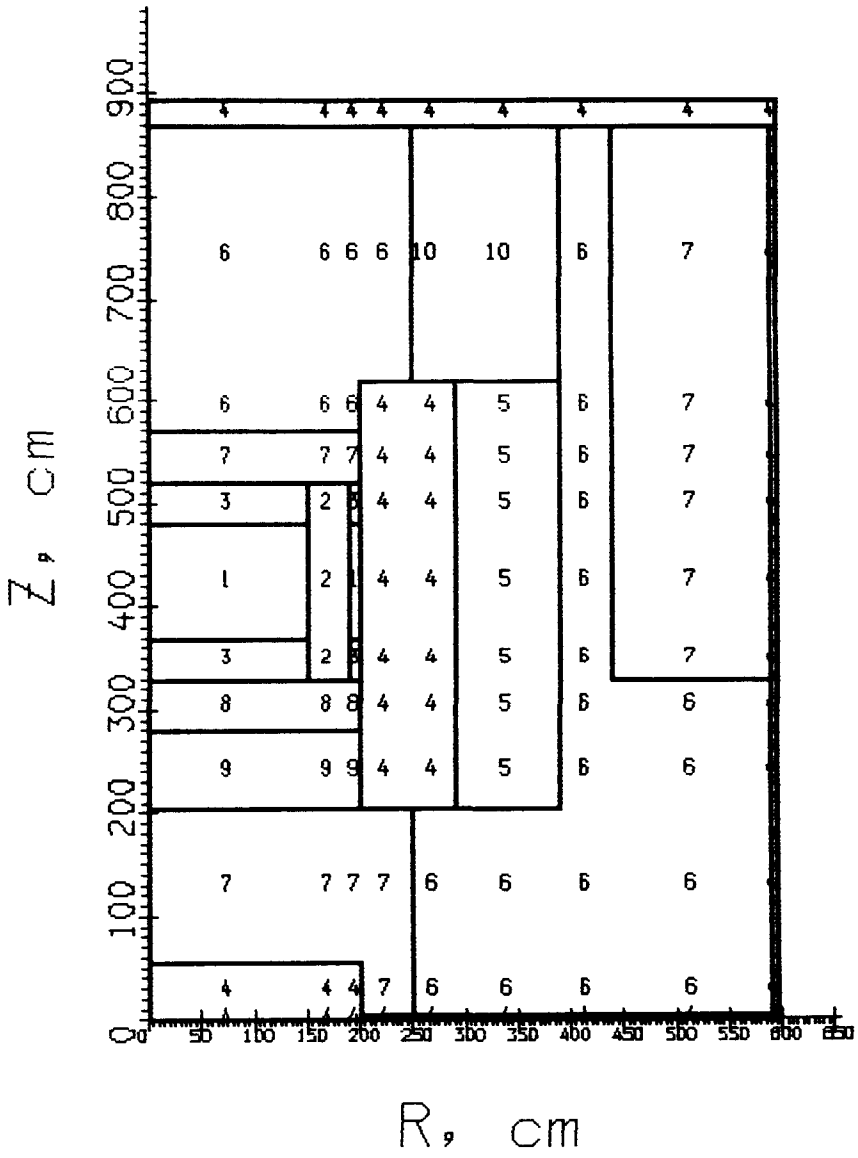

Figure 2. Fast neutron flux ratio (BN28+15/EURLIB)
for centre part of model.

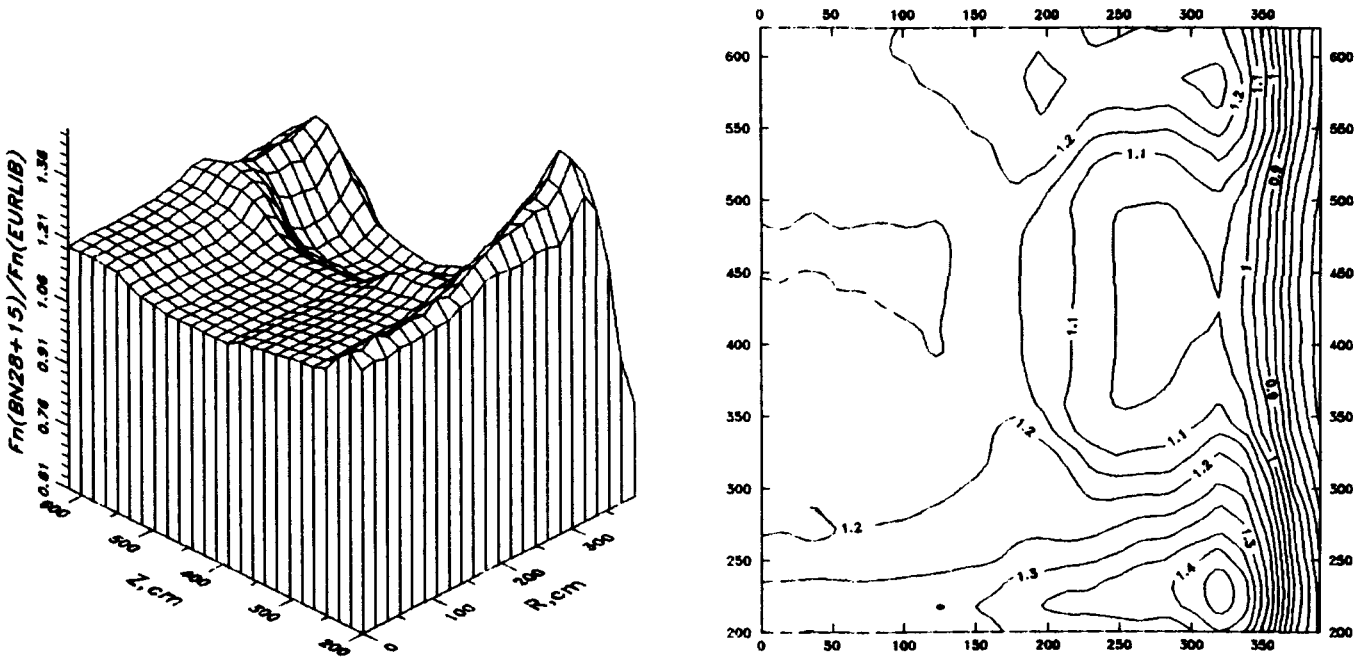

Figure 3. Fast neutron flux ratio (ABBN/EURLIB)
for centre part of model.

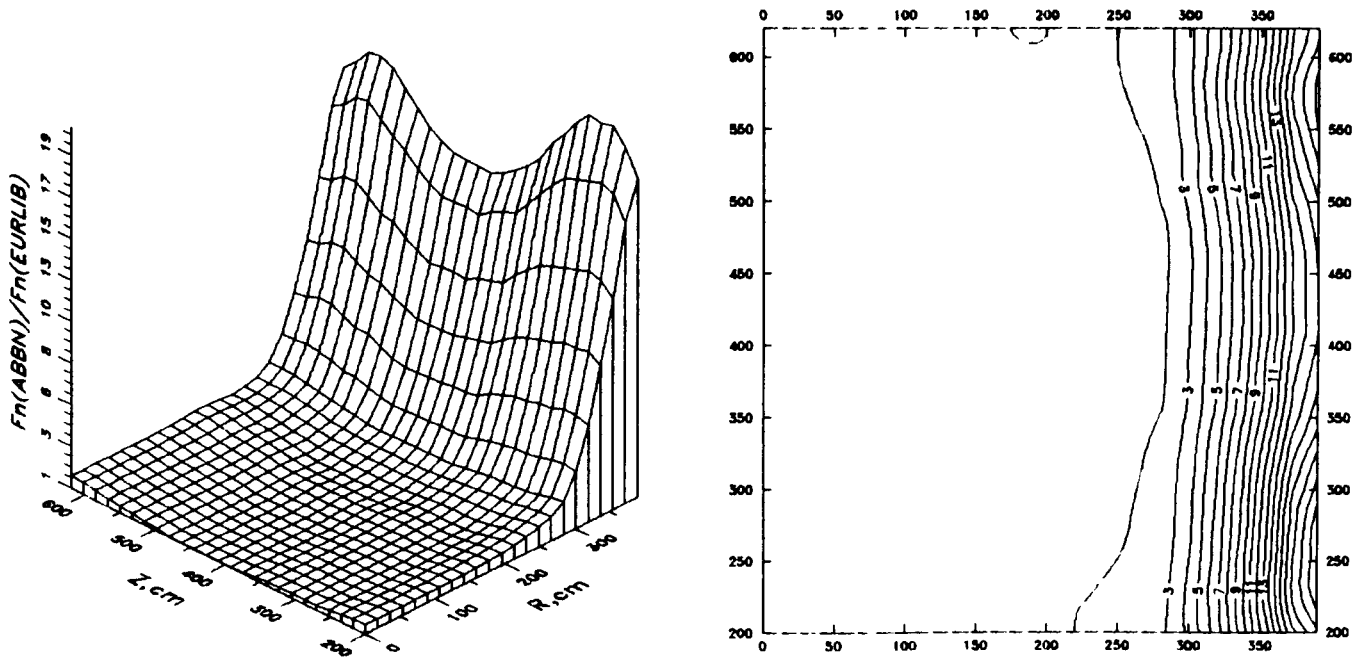

Figure 4. Total neutron flux ratio (BN28+15/EURLIB)
for centre part of model.

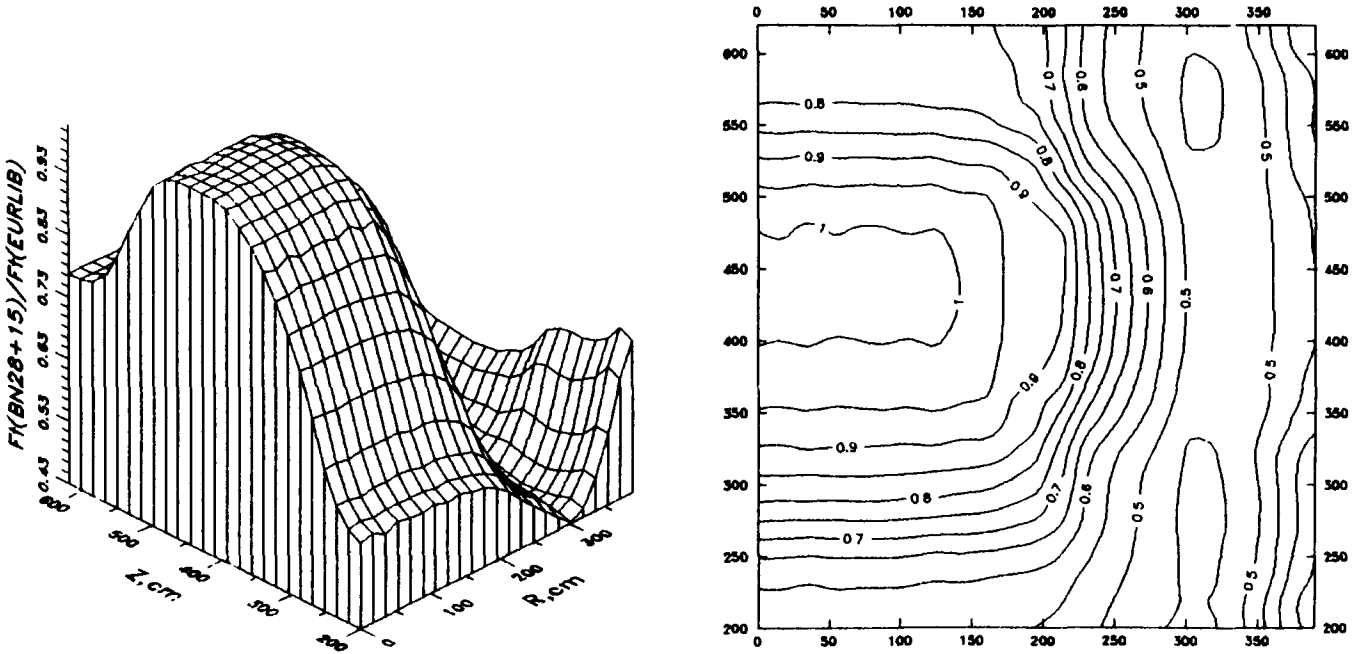

Figure 5. Contributon current spatial distribution and contributon channels $\varphi^{n}_{0.1}$ in steel shield.

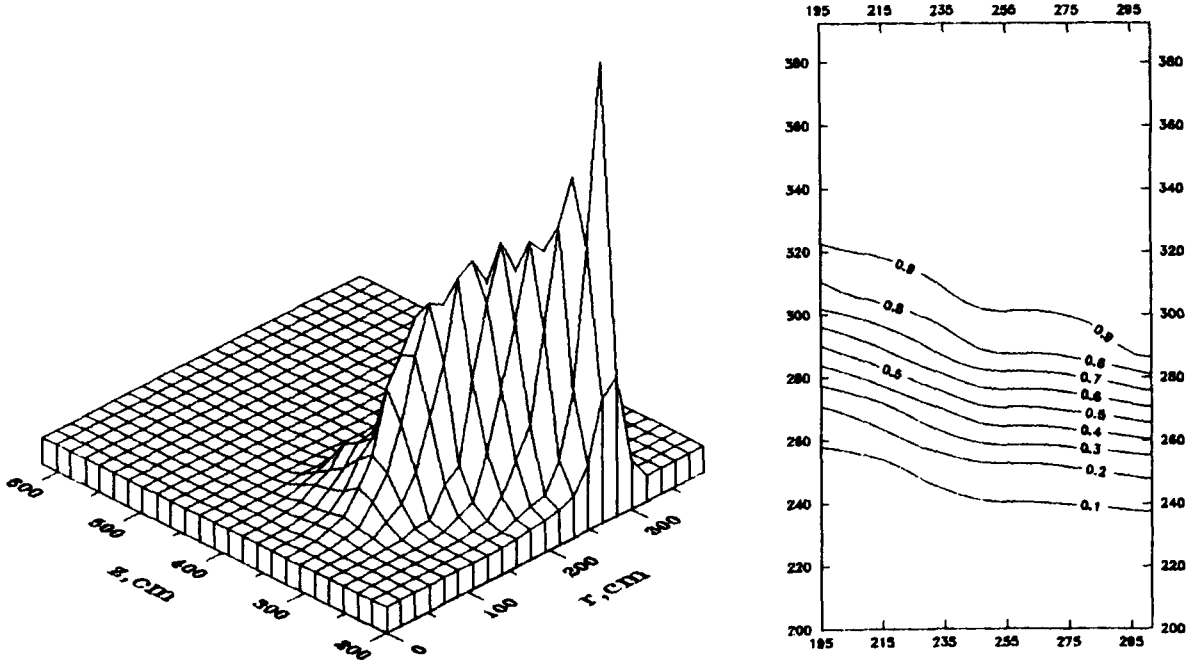

Benchmark Physics Experiment of Metallic-Fueled LMFBR at FCA

S. Iijima, H. Oigawa, and A. Ohno

Japan Atomic Energy Research Institute,
Tokai-mura, Ibaraki-ken, 319-11

and

M. Bando

Energy Research Laboratory, Hitachi, Ltd.
Hitachi-shi, Ibaraki-ken, 316

ABSTRACT

Results of the benchmark physics experiments of a metallic-fueled LMFBR are described. A clean, two-zone, cylindrical mockup core was built at JAERI's Fast Critical Assembly(FCA). Reactivity feedback physics parameters such as Doppler, sodium void, fuel expansion and B_4C control rod worth were measured in FCA assembly XVI-1. Analysis was made with two- and three-dimensional diffusion calculation and JENDL-2 cross section library. Calculation accuracy was evaluated for the reactivity feedback parameters.

INTRODUCTION

The benchmark physics experiments of a metallic-fueled LMFBR are conducted on JAERI's Fast Critical Assembly (FCA) facility in order to test calculated predictions of physics parameters in a design of metallic-fueled core. The two mockup cores, which consist of metallic fuel composition and have different neutron spectrum each other, were built in the experiment. The following physics parameters have been measured to investigate typical physics characteristics of a metallic-fueled core.

1) parameters related to reactivity feedback
   - Doppler reactivity worth
   - sodium void worth
   - control rod worth
   - fuel expansion and bowing reactivity worths
2) parameters related to breeding performance
   - reaction rate ratios.

The experiment in the FCA assembly XVI-1, which was the first core in the experimental program, was continued since October 1989 to November 1990. The reactivity feedback parameters were mainly measured in the assembly. In this paper the experimental results of the assembly XVI-1 are described and calculation ac-

curacy of reactivity feedback parameters is examined for the metallic-fueled core.

The second mockup core FCA XVI-2 was built in December 1990. We intend to do the measurement up to November 1991.

ASSEMBLY DESCRIPTION

FCA assembly XVI-1 is a clean and cylindrical two-zone core and its core size is in a range of 100~ 150MWe metallic-fueled LMFBR. A diameter of the inner and outer core are 68cm and 91cm and a core height is 91cm. A cross-sectional view of assembly XVI-1 is shown in Fig. 1, and its r-z model is presented in Fig. 2. Axial blanket of 20cm thick (natural uranium block) is placed at the upper and lower parts of the core. A radial blanket (depleted uranium block) is placed outside of the core.

Fuel drawers simulating metallic-fueled composition are loaded in the inner and outer core. Cell plate loading patterns of the drawers are shown in Fig. 3. Because of inventory limit constrained plutonium, mixed fuel of plutonium and enriched uranium is used in the inner and outer core. Natural uranium metal plate is inserted in the fuel drawer. Plutonium and ^{235}U enrichments are 10% and 5% in the inner core and 10% and 9% in the outer core. Zirconium is added at ~ 7 wt% in the fuel drawer. Since a bonding sodium is filled in a fuel pin of a metallic-fueled LMFBR, amount of sodium in the fuel drawer is increased by ~ 20% as compared with that of a mockup core of conventional oxide-fueled LMFBR.

MEASUREMENT AND ANALYSIS

Calculation Method

The experiments are analyzed using the cross-section library JENDL-2[1] and JAERI's standard calculation system for fast reactor neutronics. The JFS-3-J2 group constant set[2] with a 70 energy group structure (0.25 lethargy width) has been generated from JENDL-2. Infinite-medium cell calculations are made by using the JFS-3-J2; for the core cells, a buckling search to critical is introduced. These basically involve two steps- resonance shielding for heavy isotopes by the "table lookup" method and calculation of the flux fine structure by the collision probability method. Cell averaged group constants are prepared by flux-volume weighting to preserve the reaction rates of the heterogeneous cell. Anisotropic diffusion coefficients are also prepared by Benoist's formula[3]. These calculation are made using the calculation code SLAROM[4].

A diffusion calculation by the CITATION-FBR code[5] is made in r-z geometry and in 70-energy groups. The cell averaged group constants of 70-groups are collapsed to 25-groups using the region-averaged spectra calculated in r-z geometry.

Criticality

The diffusion calculation using anisotropic diffusion coeffi-

cients was made in x-y-z geometry modeling the reference core configuration(shown in Fig.1) and in 25-groups. Transport and mesh-size corrections were applied to the k_{eff}. The transport correction is taken from transport and diffusion calculations in r-z geometry. The S_n calculation is made by the TWOTRAN-II code[8]; order of n is eight and a correction factor $(1-\bar{\mu})$ is applied to elastic scattering cross section. The result of k_{eff} is given in Table 1.

The calculated-to-experiment (C/E) value for k_{eff} of assembly XVI-1 is 1.002; this is similar to the results of oxide-fueled mockup cores in FCA (assembly XI-1, etc.).

Doppler Reactivity

Doppler reactivity was measured with cylindrical small heated metallic sample (natural uranium(NU); 25mm ϕ and 150mm in length). Same size oxide sample(NUO_2) was also used as a tie to past experimental results. The reactivity worths were measured at three temperature points 300, 550 and 800℃ .

Resonance self-shielded cross sections for the Doppler samples were prepared for the reference and each elevated temperatures of the sample using pin-cell modeling in SLAROM. An r-z diffusion calculation of 70-groups was used in the evaluation of the Doppler reactivity. This model has the Doppler sample and its surrounding capsule region at the core center. The first order perturbation calculations were done by replacing the reference temperature cross sections with the elevated temperature cross sections. The results for Doppler reactivity are given in Table 2. Averaged C/E of the NU sample is 0.83; this is ~ 10% lower than those of oxide-fueled cores.

The additional calculations have been made to investigate the discrepancies on the Doppler reactivity. The result was described in detail in the reference 7. In JENDL-2 cross section library, resonance parameters of ^{238}U are not contained in an energy range above 50 keV. Since the assembly XVI-1 has hard spectrum of metallic-fueled core, contribution above some ten keV is fairly large in the Doppler reactivity. In order to evaluate the contribution of higher energy neutrons to Doppler reactivity, capture cross sections of ^{238}U in energy range from 40.9keV to 143keV were generated from ENDF/B-VI which contained the resonance parameters up to 149keV.

The contribution above 40.9keV was evaluated to be 13% in the Doppler reactivity of assembly XVI-1, while to be only 4% in the oxide-fueled core. The C/E of Doppler reactivity is improved to be 0.93 by considering the contribution above 40.9keV.

Sodium Void Worth

The sodium void worth was measured in an upper half of the assembly. The central 9-drawer zone in the inner core was voided at three steps. The voided zone was axially extended from the midplane toward the upper core edge.

The sodium void worths were predicted by first order perturbation method based on diffusion theory. Results are shown in Table 3. The C/E values for first and second step worths are similar to the oxide core results, i.e., ~ 10% above unity, while

the channel void worth(step 3), which include leakage-dominated zone, shows different trend in C/E value In order to evaluate uncertainty of the channel void worth calculated by the first order perturbation method, the direct calculation was performed Its result become ~ 7% lower than the first order perturbation method The improved C/E value of the channel void worth is 1 24

Control Rod Worth

The central material worth for B_4C sample was measured is fundamental data for control rod characteristics The reactivity for inserting two B_4C plates (~ 22g boron) into the center cell was measured by substitution method The B_4C plates with 20% 40%, 60% and 90% ^{10}B enrichment were prepared in the experiment

In the calculation for B_4C sample worths, exact perturbation method was performed as standard calculation, because the results by first order perturbation method showed ~ 10% discrepancy in the C/E values of the 20% and the 90% sample The exact perturbation calculation based on diffusion theory was made in r-z geometry and in 70-groups The results is shown in Table 4 The C/E values for B_4C sample worths of metallic-fueled core are ~ 5% lower than those of oxide-fueled cores

In a reference core of control rod worth measurement, the central fuel drawer was replaced to the sodium follower drawer filled with sodium plates The four mockup control rods having different ^{10}B enrichment were prepared using 20%, 40%, 60% and 90% B_4C plates and sodium plates A plate arrangement of the mockup control rod is shown in Fig 4 The reactivity for replacing the sodium follower drawer to the mockup control rod was measured by modified neutron source multiplication method

The control rod worth measurements were analyzed using core calculation based on diffusion theory in r-z geometry and in 70-groups The rod worth was defined as $(k_2-k_1)/k_1k_2$, where k_1 is k_{eff} of the core with the sodium follower in and k_2 is k_{eff} with the B_4C rod in Results are shown in Table 5 The C/E of rod worths are ~ 0 94 and show the similar trend to those of the B_4C sample worths The transport correction was evaluated for 90% rod worth The correction factor $f_{T/D}$ is 0 98

Fuel Expansion and Bowing Reactivity

A reactivity for radial bowing and axial expansion were measured as important reactivity feed back parameters in a metallic-fueled core

Uniform radial expansion was simulated by shifting fuel within the drawers The fuel movement was made in the zone shown in Fig 5 The zone was radially symmetric about the y-axis Prior to the fuel expansion measurement, the fuel cells in the zone were replaced to special plate arrangement cells Illustration for plate arrangement is shown in Fig 5 The reactivity for fuel shift of 3 mm and 6 mm in the vertical three drawers was measured as changing the radial position at $\pm$ 6R $\pm$ 7R and $\pm$ 8R

The radial expansion measurements were analyzed using a material worth map calculated by first order perturbation method based on diffusion theory in x-y-z geometry and in 25-groups Data between flux points was interpolated The reactivity worths

by shifting the fuel, structure material and sodium plates were sum up as radial expansion reactivity worth Results are shown in Table 6 The radial expansion reactivity were reasonably well predicted. The C/E's are in the range of 0 98 to 1 11

Prior to the axial expansion measurement the full-size zirconium plate(2"-2"-1/16") was replaced to two half-size zirconium plates(2"-1"-1/16") in the central 25-drawers, two full-size plates in the unit cell of the IC1 drawer were replaced to four half-size plates The axial expansion was simulated by taking out the two half-size zirconium plates from the unit cell and inserting them to front and back of the cell The number of zirconium plate was same in the reference and the axial expansion core. Illustrations for the axial expansion measurements are shown in Fig. 6. The core fuel in the drawer was moved ~ 6% in an axial direction. The fuel expansion zone was extended radially in the four steps; the reactivity for 1-drawer, 5-drawers, 9-drawers and 25-drawers were measured.

The axial expansion reactivity was calculated by exact perturbation method based on diffusion theory because of taking account of flux change near the axial core edge. The results for axial expansion measurements are shown in Table 7 The axial expansion experiments were reasonably well calculated The C/E's are 1 05± 2%.

SUMMARY

The physics parameters related to reactivity feedback of a metallic-fueled LMFBR have been measured in FCA assembly XVI-1 The calculations have been performed by using the standard calculation system and JENDL-2 cross section library

In a prediction of Doppler reactivity of metallic-fueled core, it is important to take into account the resonance in the energy region above 50 keV. The C/E is improved to be 0 93 by considering the contribution of high energy region.

The C/E's of the sodium void worths are in the range of 1 10 to 1 24.

In the measurement of B_4C control rod worths with different ^{10}B enrichment, the C/E's are ~ 0.94.

The calculation reasonably well predicts the fuel expansion and bowing reactivity.

ACKNOWLEDGMENTS

The authors wish to express their thanks to the FCA staff for support in the experiment and calculations. They also thank to M. Nakano(JAERI) for advice in the experiment.

REFERENCE

(1) Nakagawa T. : "Summary of JENDL-2 general purpose file",

JAERI-M 84-103 (1984)
(2) Takano H et al "JFS-3-J2 fast reactor group constants library, JAERI-memo 8823 (in Japanese) (1980)
(3) Benoist P Streaming effects and collision probabilities on lattices, Nucl Sci Eng 34(1968)285
(4) Nakagawa M and Tuchihashi K SLAROM JAERI-1294(1984)
(5) Iijima S et al 'CITATION FBR and PERKY code system to be published in JAERI-M
(6) Lathrop K and Brinkley F TWOTRAN-II LA 4848-MS (1973)
(7) Oigawa H Contribution of higher energy neutrons to Doppler effect of ^{238}U in metal fueled reactor J Nucl Sci Tech nol 28(11) (1991)

Table 1 Result of Criticality

Experiment	1 0038± 0 0001
Base Calculation	1 00034
Correction	
Transport	0 00673
Mesh	-0 00119
Corrected	1 00588
C/E	1 002

Table 2 Result of Doppler Reactivity Worth

Sample	Temperature (℃)	Experiment (10^{-4} Δ k/k)	Calculation	C/E
Nb(metal)	20 - 300	-4 65± 0 20	-3 986	0 86
(U, 1347 g)	20 - 550	-7 42± 0 21	-6 272	0 85
	20 - 800	-9 64± 0 19	-7 954	0 83
NbO_2 (U, 605 g)	20 - 800	-4 35± 0 18	-3 609	0 83

Table 3 Result of Sodium Void Worth

Step	Void Region (mm)[a]	Experiment (10^{-4} Δ k/k)	Calculation	C/E
1	0 0 to 101 6	1 519± 0 022	1 675	1 102
2	0 0 to 304 8	2 810± 0 022	3 150	1 121
3	0 0 to 457 2	1 452± 0 022	1 913	1 317[b]
			1 8	1 24 [c]

(a) distance from midplane(upper half was voided)
(b) first order perturbation calculation
(c) direct calculation

Table 4 Result of B_4C Sample Worth

B_4C Sample	Experiment (10^{-4} Δ k/k)	Calculation	C/E
20%	-1.998± 0.022	-1.881	0.941
40%	-3.686± 0.022	-3.464	0.940
60%	-5.131± 0.022	-4.871	0.949
90%	-7.172± 0.022	-6.870	0.958

Table 5 Result of Control Rod Worth

Rod Type	Experiment (10^{-3} Δ k/k)	Calculation	C/E
20%	-2.191± 0.013	-2.028	0.926
40%	-3.846± 0.044	-3.582	0.931
60%	-5.130± 0.061	-4.815	0.939
90%	-6.853± 0.093	-6.532	0.953

Table 6 Result of Radial Expansion Reactivity

Model	Experiment (10^{-4} Δ k/k)	Calculation	C/E
± 6R 6mm shift	-1.146± 0.022	-1.272	1.110
± 7R 6mm shift	-1.398± 0.022	-1.497	1.071
± 8R 6mm shift	-1.668± 0.022	-1.629	0.977
± 7R and ± 8R 6mm shift	-3.129± 0.022	-3.126	0.999
± 6R ~ ± 8R 6mm shift	-4.311± 0.022	-4.399	1.020
± 8R 3mm shift	-0.795± 0.022	-0.804	1.011

Table 7 Result of Axial Expansion Reactivity

Model	Experiment (10^{-6} Δ k/k)	Calculation	C/E
1-drawer	-0.60± 0.022	-0.61	1.03
5-drawers	-2.76± 0.022	-2.93	1.06
9-drawers	-4.85± 0.022	-5.11	1.05
25-drawers	-12.77± 0.022	-13.42	1.05

Fig. 1 Cross-sectional View of FCA Assembly XVI-1

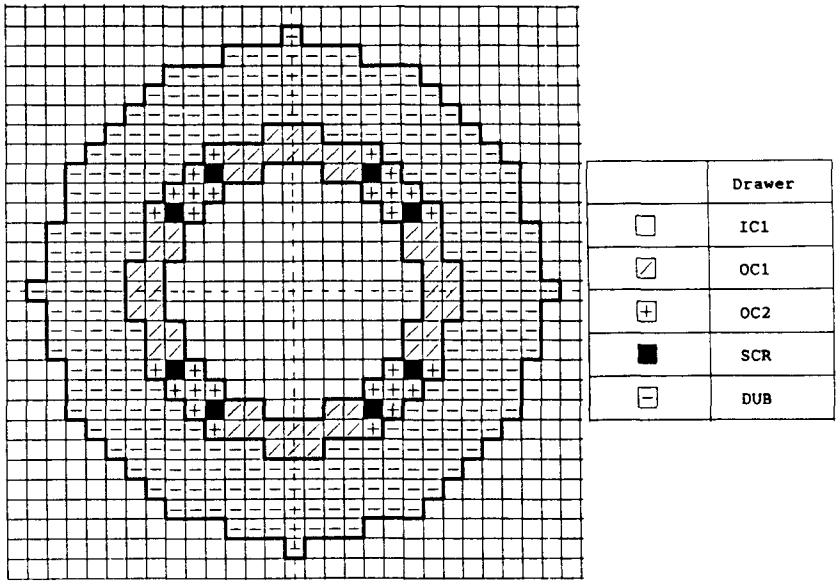

Fig. 2 The R-Z Configuration of Assembly XVI-1

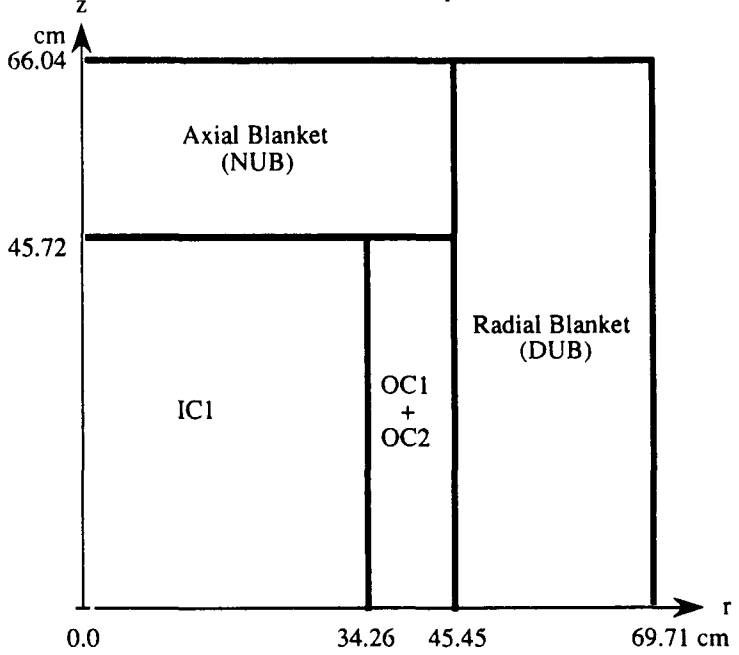

Fig. 3 Drawer Loading Pattern Used in Assembly XVI-1

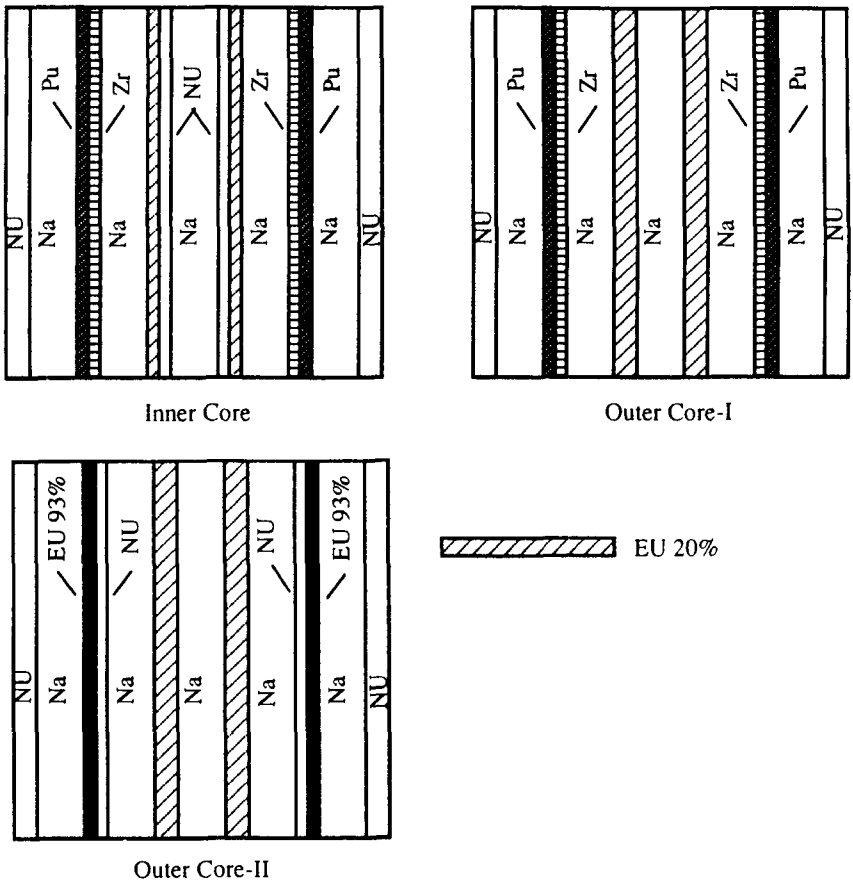

Fig. 4 Plate Arrangement of B_4C Mockup Rod

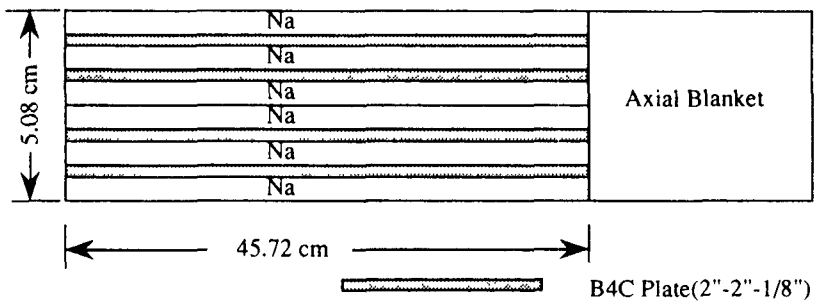

Fig. 5 Illustration for Radial Expansion Measurement

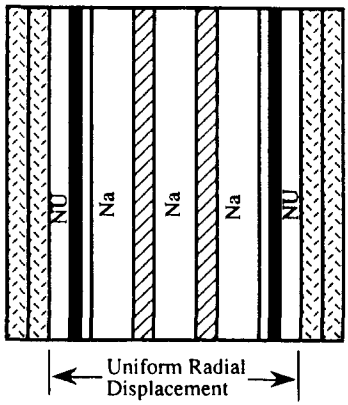

Reference for Radial Expansion

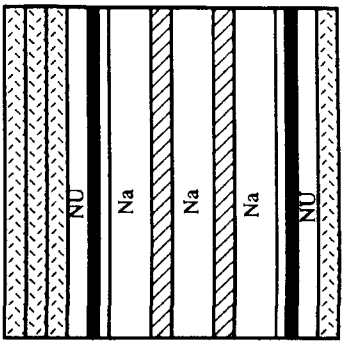

3mm Shift Cell

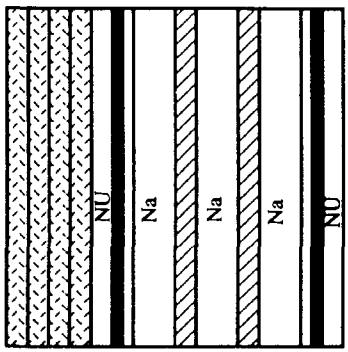

6mm Shift Cell

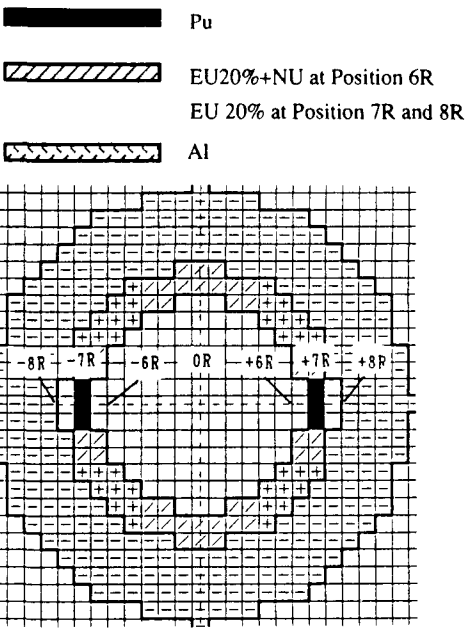

Fig. 6 Illustration for Axial Expansion Measurement

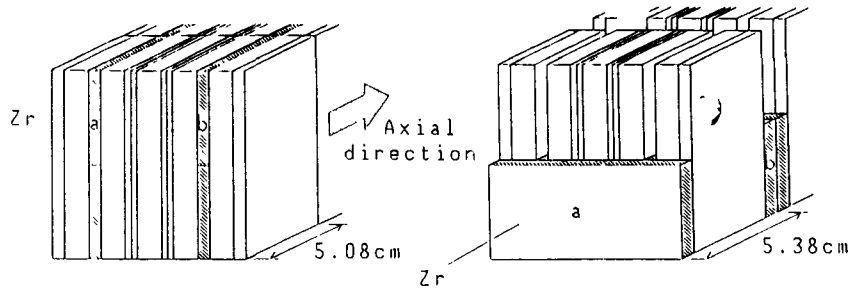

Standard Cell

Axial Expansion Cell

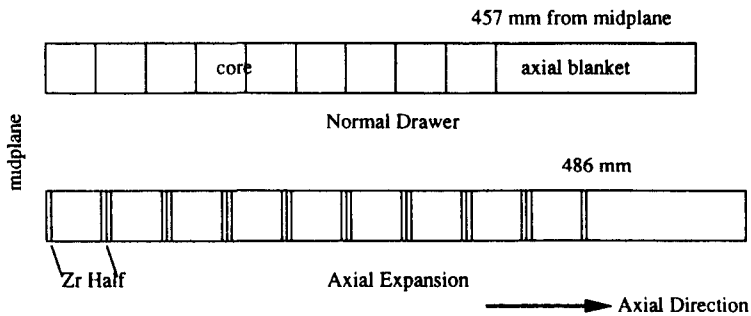

AN EVALUATION OF MULTIGROUP FLUX PREDICTIONS IN THE EBR-II CORE

R N Hill T H Fanning*, and P J Finck
Argonne National Laboratory
9700 S Cass Ave
Argonne, Illinois 60349-4842 USA

*Permanent Address
Dept of Nuclear Engineering and Engineering Physics
University of Wisconsin, Madison

ABSTRACT

The unique physics characteristics of EBR-II which are difficult to model with conventional neutronic methodologies are identified, the high neutron leakage fraction and importance of neutron reflection cause errors when conventional calculational approximations are utilized In this paper various conventional and higher-order group constant evaluations and flux computation methods are compared for a simplified R Z model of the EBR-II system Although conventional methods do provide adequate predictions of the flux in the core region significant mispredictions are observed in the reflector and radial blanket regions Calculational comparisons indicate that a fine energy group structure is required for accurate predictions of the eigenvalue and flux distribution greater detail is needed in the iron resonance scattering treatment Calculational comparisons also indicate that transport theory with detailed anisotropic scattering treatment is required

I. INTRODUCTION

Experimental Breeder Reactor No 2 (EBR-II) and its adjoining fuel cycle facility were originally designed and operated to provide a small plant demonstration of a sodium-cooled fast breeder power plant with an integral fuel cycle Following successful demonstration of the plant EBR-II has been utilized for many fast neutron irradiation and materials testing experiments Meanwhile significant improvements have been developed for metal fuel reprocessing, various process changes including the use of electrorefining, have reduced the heavy metal losses from 5-10% to less than 1% and virtually eliminated the noble metals from the heavy metal product This new reprocessing technique is the basis for the Integral Fast Reactor (IFR) fuel cycle concept The behavior of IFR metal fuel has been investigated using irradiation experiments in EBR-II and a key milestone of the IFR program is to demonstrate closure of the IFR fuel cycle at EBR-II

Operation of this closed fuel cycle requires an accurate tracking of all materials during both in-core and ex core phases It is particularly important to trace actinide isotopes, since fissile material recovery is the primary objective in fuel reprocessing Chemical and isotopic analyses of the discharged fuel are impractical on a large scale Therefore accurate core depletion calculations are necessary to specify the material composition of the spent fuel

Methodological improvements for depletion calculations were proposed in references 1 and 2 using nodal equivalence theory significant improvements in the depletion calculations were observed Nodal equivalence theory provides additional degrees of freedom ("discontinuity factors") to the standard diffusion equations allowing nodal schemes to reproduce any higher order solution For EBR-II applications higher order multigroup flux solutions are calculated by a series (R-Z and planar) of two dimensional transport calculations the results are used to create few group cross section data and a set of few group discontinuity factors This approach allows a few-group nodal diffusion calculation (as used in the depletion computation) to account for the higher-order effects, however, any errors present in the higher-order multigroup solutions will be reproduced in the nodal solution In this paper the primary goal is to evaluate the accuracy of various higher-order methods for generation of EBR-II multigroup flux solutions

Some unique physics characteristics of the EBR-II system are identified in Section II these characteristics cause calculational difficulties which must be accounted for in accurate higher order solutions Many physics phenomena (i e axial streaming) are discussed in Section II however the evaluation of detailed geometric effects is beyond the scope of this paper In this paper the analyses focus on a simplified R-Z model of EBR-II where a minimal number of homogeneous material compositions are specified Accurate physics predictions are difficult even in this simplified model the high leakage probability causes a breakdown of the basic assumptions applied in many conventional neutronic methods In this paper, EBR-II flux predictions using various methodologies for generating multigroup cross section data and for evaluating the neutron flux distribution are evaluated The generation of group constants for EBR-II flux predictions is addressed in Section III, and different calculational methods (i e diffusion or transport theory) are evaluated in Section IV

II. PHYSICS CHARACTERISTICS OF EBR-II

EBR-II is a small sodium cooled fast reactor system with a power rating of 62 5 MWt A simplified R Z model of the reactor is shown in Figure 1 in the simplified model only eight distinct material regions are specified The core is composed of high enrichment (~70% U-235) U-10% Zr metal fuel the reflector and grid regions are composed primarily of stainless steel The blanket region is composed of thick metal fuel pins which contain about 0 05% Pu-239 from prior burnup As shown in Fig 1 the core height is ~35 cm with a core radius of 35 cm, thus the H/D ratio is ~1/2 indicating a pancaked core geometry Both the small core size and geometric spoiling lead to a high neutron leakage fraction about 60% of the neutrons produced leak out of the core The high neutron leakage fraction leads to the large discrepancies between diffusion and transport theory as discussed in Section IV

*The ex-core configuration of EBR-II creates additional physics complications First, in the axial direc*tion there is a plenum region above the core and a reflector below the core (note that the pancaked design makes axial leakage dominant in the core) This leads to an axial power tilt toward the lower portion of the core The severity of this tilt depends upon the relative importance of upper and lower leakage

1 In the upper plenum, there is a significant streaming path within the pin which may lead to inaccuracies for a homogenized treatment

2 In the lower reflector there is significant reflection back into the core this requires an accurate modeling of directional change through scattering This treatment is further complicated by the dominance of resonance scattering in the steel reflector (see discussion below)

Thus it is difficult to obtain accurate predictions of the axial profile even with higher order methods

The radial configuration of EBR II is particularly unique As shown in Fig 1 the radial reflector is adjacent to the core and is surrounded by several rows of radial blanket, in conventional designs the radial blanket is adjacent to the core and surrounded by a reflector/shield zone Because of the high

leakage fraction, the EBR-II core relies heavily on neutron reflection to maintain criticality thus, an accurate evaluation of the reflection rate is necessary for accurate predictions of the core multiplication factor Prediction of neutron reflection is especially complex because the reflection involves scattering reactions which change a neutron's angle **and** energy Radial transmission predictions are also crucial because the radial blanket assemblies produce roughly 5% of the reactor power during normal operation Thus, accurate flux predictions in the radial blanket are essential for evaluating the local coolant outlet temperature and local fast fluence level

Flux predictions in the ex-core regions must evaluate the transmission of neutrons through the subcritical reflector and blanket zones, physics predictions in these radial transition zones are especially difficult As discussed in reference 3, discrepancies between predictions and experiments increase with penetration in a uniform blanket zone, in reference 4, these errors are attributed to directional effects on the transitional resonance spectra and group constants Similar effects may occur in the iron resonances within the radial reflector this phenomena is particularly important because resonance scattering is a principal mechanism for the reflection of neutrons back into the core Many of the important iron resonances can be accurately modeled by refining the energy group structure however, the narrow iron resonances and most high energy actinide resonances cannot be represented by multiple energy groups in any prac tical group structure

In summary, accurate multigroup flux predictions in EBR-II are complicated by several physical phenomena Because of the asymmetric axial profile and importance of radial transmission between the core and radial blanket, three-dimensional flux solutions are necessary Because of errors in leakage treatment, diffusion theory is likely inadequate for this small core In addition, a detailed energy group structure may be required for modeling the neutron reflection

III. ANALYSIS OF GROUP CONSTANT GENERATION

As discussed above, accurate modeling of the reflection of neutrons in EBR-II may require refinements of the neutron energy group structure because of the high leakage fraction, the core multiplication factor is particularly sensitive to the reflection rate In addition, the prediction of radial and axial flux distributions requires an accurate modeling of the neutron transmission and reflection To assess the importance of group structure, eigenvalue calculations for a wide variation of energy group distributions are compared

For this analysis, fine group neutron cross sections are generated using the MC^2-2 code [5] In MC^2-2, an infinite medium spectrum is calculated for a 2082 energy group structure with resonance reaction rates evaluated within each group using the narrow resonance approximation, combining the multigroup and resonance contributions, group constants are generated for a specified energy structure Fine group constants were generated for three compositions (representative of the core, radial reflector and radial blanket in EBR-II) in various energy group structures, the radial reflector group constants were also used in the plenum, grid, and axial reflector zones The infinite medium calculation for the core composition utilized a buckling search to criticality, whereas the reflector and blanket calculations utilized a fixed source representative of the incoming leakage source in each region

In MC^2-2, the infinite medium spectra can be evaluated using a consistent P_1 or B_1 evaluation of the extended transport equation [5] P_1 infinite medium calculations allow an accurate representation of the first moment of the scattering cross section, whereas B_1 schemes account for the curvature (second moment of the flux) produced by a given buckling Thus, P_1 group constants are more accurate when anisotropic scattering is important and B_1 calculations are preferable for high leakage cores The two generation techniques can lead to significant differences in the transport cross section For high leakage geometries, the transport cross sections are significantly higher for the B_1 evaluation (indicating a smaller diffusion

coefficient) however all other group constants are virtually unchanged Since only the transport cross section is modified calculational differences between P_1 and B_1 group constant sets were only observed for diffusion calculations transport theory predictions with higher-order scattering are nearly identical for the two methods

Diffusion theory eigenvalue predictions for the P_1 and B_1 group constant sets are compared in Table I the eigenvalues are shown for infinite medium, one-dimensional (with constant group-independent buckling), and two dimensional calculations As shown in Table I large differences are observed in the infinite medium evaluations (the B_1 material buckling is 6% larger) however, these differences decrease to 2 5% and 1 0% respectively in the one- and two-dimensional calculations This behavior is caused by the different diffusion coefficients The smaller diffusion coefficients in the B_1 group constant set allow fewer neutrons to leak, but also create a larger curvature Therefore, when the $D\nabla^2\phi$ leakage term is evaluated, the differences between the P_1 and B_1 sets tend to compensate Conversely the leakage term is DB^2 when a fixed buckling is applied and the B_1 set allows significantly less leakage because the curvature difference is not modeled The ~1 0% eigenvalue increase observed using B_1 group constants does not compensate for the large errors in diffusion predictions which are shown in Section IV, and the diffusion core flux predictions are observed to be more accurate for the smaller curvature P_1 group constants (see Section IV)

The effect of group structure on transport calculation eigenvalue predictions was evaluated by comparing the flux calculation predictions for a wide range of energy detail As a starting point, consistent P_1 infinite medium calculations were utilized to generate 230 energy group constants for the core, reflector, and blanket Using the transport theory code *TWODANT*[6], the flux distribution (S_8P_1) was calculated for the simplified R-Z model of EBR-II shown in Fig 1 Using the 230 group R-Z flux solution, the fine energy group constants were then collapsed in detailed spatial zones Nine 21 50 and 68 energy group constants were calculated for 225 spatial zones the collapsing mesh utilized 15 axial regions (including 5 core zones) and 15 radial regions (including 7 core zones)

In Table II, the computed eigenvalues for the various group constant sets are compared to a continuous energy Monte Carlo solution (generated using the *VIM*[7] code) note that the VIM and *MC*^{2}-2 cross section libraries are both generated from ENDF/B-V As shown in Table I, the eigenvalue varies by 1% Δk between 9 group and 230 group solutions the difference decreases to 0 2% Δk if 68 energy groups are used However the 230 group solution is 0 9% Δk higher than the continuous energy VIM solution Thus, several additional refinements to the group constant generation method were also investigated Because of the "resonance like" structure of the iron scattering cross section above the resolved resonance range, important self-shielding effects may be neglected in the conventional 2082 energy group *MC*^{2}-2 library As shown in Table II, when these self-shielding effects are modeled the eigenvalue is 0 4% Δk lower Use of a 274 energy group structure with particular detail in the high-energy iron resonances was also analyzed Using the 274 energy group structure and the specialized self-shielding treatment of the high-energy iron cross section the eigenvalue decreases by another 0 3% Δk as shown in Table I

An eigenvalue discrepancy of 0 2% Δk remains between the Monte Carlo and fine group transport solutions Consistency between the Monte Carlo and transport evaluations was demonstrated by comparing multigroup Monte Carlo and transport predictions utilizing identical group constants, errors of less than 1σ were observed for Monte Carlo runs with a standard deviation (σ) of ~ 0 01% Δk Thus, the remaining discrepancy is most likely caused by differences between the continuous energy and fine group structures Ongoing analyses are investigating the consistency of the VIM and multigroup cross section libraries, preliminary results indicate that some discrepancies are still present in the evaluation of scattering cross sections in the radial reflector

In Table II the eigenvalue predictions for various energy group structures are evaluated however for core power mapping and depletion calculations, the critical parameter is the flux distribution not the eigenvalue In Figure 2 the total flux levels of the 9, 230, 230* (special treatment of high-energy iron cross sections), and 274* group calculations are compared for a radial traverse at the core axial midplane The 9 and 230 group flux solutions are 1-2% lower than the more detailed 274* solution in the core region However, larger differences are observed in the outer regions The 230 group solution agrees well with the 274 group solution in the radial reflector but decreases to a 5% lower level in the outer regions of the radial blanket, smaller differences are observed for the 230* group constant set The 9 group solution (note that the group constants are based on a spatial collapse of the 230 group solution) overpredicts the flux level in the middle of the radial reflector by 5% and then progressively underpredicts the neutron transmission leading to a 10% lower level in the outer blanket These deviations are caused by the complex physical phenomena which complicate group condensation in these outer zones it is difficult to accurately model the reflection and transmission in a coarse group structure

In a similar manner axial traverses of the 9 230 230*, and 274* energy group flux solutions are compared in Figure 3 Again, the flux solutions agree very well in the core region and differences are observed in the outer regions Errors in the 9 group solution of 5% are observed in the upper and lower reflector zones (once again the 9 group flux is higher in the reflector region) and the 230 group solutions agree well with the 274* group solution The errors in the axial profile appear to be smaller than the radial profile differences (see Fig 2) This behavior is likely caused by the fact that the flux level at the axial edges is attenuated by about 1 order of magnitude and at the radial edge by about 2 orders of magnitude (as compared to the core center), thus, the radial transmission problem is more severe

In summary, it appears that accurate prediction of the eigenvalue requires a very fine energy group structure with a detailed treatment of self-shielding effects in iron with a tailored 274 energy group structure, differences of 0 2% Δk are still observed between continuous energy and multigroup solutions For practical applications few-group structures are obviously desirable Thus methods for reducing the number of energy groups while retaining computational accuracy (i e specialized group structures) must be developed In addition the application of nodal equivalence theory to account for group condensation errors is a promising alternative

IV. ANALYSIS OF FLUX COMPUTATION METHODS

Given a set of multigroup cross sections, various methods can be used to compute the flux distribution Because of the high neutron leakage fraction in EBR-II, large discrepancies between diffusion and transport theory calculations are expected Since diffusion theory tends to overpredict the neutron leakage, large underpredictions of the eigenvalue and significant errors in the radial and axial profiles can be expected

In this paper, the accuracy of diffusion theory and various approximations in discrete ordinates transport theory are compared by analyzing flux prediction in the simplified R-Z model Using the spatially collapsed nine group cross sections described in Section III, neutron flux calculations for the simplified R-Z model of the EBR-II core (see Fig 1) were performed using the DIF3D [8] diffusion theory code and the *TWODANT*[6] transport theory code The eigenvalue predictions are compared in Table III Each calculation in Table III utilized an identical spatial mesh spatial mesh convergence was verified for the S_8 solution As expected, the transport eigenvalue is significantly (5 5% Δk) higher than the diffusion eigenvalue, thus, the transport effects are very significant for the small EBR-II core The anisotropic scattering treatment is also observed to be crucial The S_4P_0 result is about 9% Δk too high and the transport-corrected S_4P_0 (in which the transport solution uses the transport cross section instead of the total cross section) eigenvalue is 2 5% Δk below the $S_{16}P_1$ solution Low levels of angular quadrature appear to be sufficient the S_4P_1 eigenvalue is only 0 3% Δk too high and the S_8P_1 value is within 0 05% Δk of the $S_{16}P_1$ result

In Table III, the eigenvalue predictions for various flux calculation methods are evaluated however for core power mapping and depletion calculations, the critical parameter is the flux distribution not the eigenvalue Thus, the total flux levels of the diffusion, S_4P_0* S_8P_1, and $S_{16}P_1$ calculations are compared in Figure 4 for a radial traverse at the core axial midplane The diffusion and transport results agree well (within 2% for total flux) in the core however significant deviations (up to 15%) are observed in the radial blanket Note that the B_1 group constants described in Section III generate more curvature in the core flux distribution and lead to larger errors in the diffusion flux prediction at the core center The diffusion calculation overpredicts the neutron leakage from the core (giving the lower eigenvalue result shown in Table III) and this causes overpredictions of the flux level which steadily increase in the outer regions The diffusion calculation will significantly overpredict (>10%) the power and fluence levels in the radial blanket Because the diffusion solution gives adequate predictions of the flux in the core region critical safety parameters and depletion effects can be calculated with reasonable accuracy utilizing conventional diffusion methods, however transport solutions are obviously necessary for accurate predictions in the radial reflector and blanket zones The transport-corrected S_4P_0 solution also exhibits significant errors in calculated flux distribution as shown in Fig 4 the computed total fluxes are 3% too high at the core center, 5% too low in the radial reflector and increase to 10% too high in the radial blanket (as compared to the $S_{16}P_1$ solution) The S_8P_1 solution agrees well with the more detailed $S_{16}P_1$ solution throughout

A comparison of the axial flux profiles for the diffusion, S_4P_0* S_8P_1, and $S_{16}P_1$ calculations is shown in Fig 5 As discussed in Section II, the axial flux is tilted toward the lower core because of the unequal axial reflection (plenum above the core and reflector below) The differences in total flux indicate that the axial tilt is more severe in the diffusion prediction, the B_1 group constants described in Section III would further magnify the axial tilt in the diffusion calculation by increasing the flux curvature As discussed in Section III, the flux attenuation is less severe in the axial direction of this model thus smaller overpredictions are observed for the diffusion evaluation in the outer axial regions The S_4P_0* results show similar trends to the radial comparison (see Fig 4) the flux is underpredicted in reflector zones and overpredicted in the core (as compared to the $S_{16}P_1$ solution) Once again the S_8P_1 solution agrees well with the reference solution

The comparison of transport solutions indicates that simplified anisotropic scattering treatment (the S_4P_0* results) create significant errors in the eigenvalue and flux solutions Therefore the effect of higher-order Legendre expansions was evaluated Since the accuracy of higher-order Legendre cross sections generated with the MC^2-2/SDX package has not been validated, higher-order Legendre scattering matrices were generated using the continuous energy VIM code [7] For a two-region reflected sphere (with a core volume similar to EBR-II), P_5 scattering matrices were generated in the core and reflector regions, to give reasonable statistical accuracy in the individual group constant values, a coarse 9 group structure is utilized The calculated eigenvalues for P_0 through P_5 scattering expansions are summarized in Table IV Similar to the R-Z results a 10% eigenvalue difference is observed between eigenvalue predictions utilizing P_0 and P_1 scattering expansions the P_0 results grossly overpredict the multiplication factor For the P_0 evaluation, all scattering reactions lead to an isotropic outgoing neutron distribution However the angular flux distribution in the ex-core regions will be tilted away from the core because of the dominance of core leakage, for scattering reactions with an anisotropic scattering treatment the outgoing neutrons will tend to maintain this angular bias Therefore the P_0 treatment overpredicts the reflection rate The results in Table IV also indicate a 0 4% Δk difference between P_1 and P_3 predictions a higher eigenvalue is calculated when higher-order scattering matrices are utilized The P_3 through P_5 eigenvalue predictions are virtually identical thus P_3 scattering expansions appear to be adequate in this calculation It is important to recognize that the errors incurred in anisotropic scattering treatment may vary for different group structures, if finer group structure are utilized, the anisotropic scattering effects must be evaluated for the detailed energy structure

In summary, large eigenvalue discrepancies (~5 5% Δk) are observed between diffusion and transport theory predictions Although diffusion theory does provide adequate predictions of the flux level in

the core region, large discrepancies (up to 15%) are observed in the flux predictions for the reflector and blanket regions Simplified anisotropic scattering treatments can cause significant errors in the transport theory predictions Transport-corrected P_0 results indicate a 2 5% Δk underprediction of the eigenvalue and 5-10% errors in the flux level In addition preliminary results indicate a 0 4% Δk difference between P_1 and P_3 predictions Because of the computational complexity and expense of transport calculations with detailed anisotropic scattering treatment the application of nodal equivalence theory to account for these effects, within the framework of a diffusion code is a promising alternative

V. SUMMARY AND CONCLUSIONS

Because of the unique physics characteristics of EBR-II it is difficult to obtain accurate multigroup flux predictions The high neutron leakage fraction and importance of neutron reflection cause errors when conventional methods are utilized In this paper, various conventional and higher-order group constant evaluations and flux computation methods are compared for a simplified R-Z model of the EBR-II system Although conventional methods (diffusion theory with coarse group structure) do provide adequate predictions of the flux in the core region discrepancies are observed in the reflector and radial blanket regions Thus, to achieve accurate predictions in the outer zones transport effects must be modeled (discrete ordinates solution or nodal equivalence diffusion solution)

Flux predictions for energy group structures ranging from 9 to 274 energy groups were evaluated Group structures with particular detail in the high-energy iron resonance range yield superior results Some discrepancies between continuous-energy and detailed multigroup results are still observed Comparisons of calculational results also indicate that detailed anisotropic scattering treatment is required for accurate transport theory predictions transport-corrected P_0 scattering matrices are clearly inferior and P_3 expansions may be required

REFERENCES

1 P J Finck, R N Hill, and S Sakamoto, "Improvements in EBR-II Core Depletion Calculations," Proc Intl Conf on Fast Reactor and its Fuel Cycles Kyoto October 1991

2 P J Finck and K L Derstine "The Application of Nodal Equivalence Theory to Hexagonal Geometry Lattices," Proc Intl Topical Mtg on Advances in Mathematics Computations, and Reactor Physics, Pittsburgh, April 1991

3 R N Hill and K O Ott, "Advanced Methods Comparisons of Reaction Rates in the Purdue Fast Breeder Blanket Facility," *Nuclear Science and Engineering* **103** 12 (1989)

4 R N Hill, K O Ott, and J D Rhodes, "Directional Effects in Transitional Resonance Spectra and Group Constants," *Nuclear Science and Engineering*, **103** 25 (1989)

5 H Henryson II, B J Toppel, and C G Stenberg, "MC^2-2 A Code to Calculate Fast Neutron Spectra and Multigroup Cross Sections," ANL-8144 Argonne National Laboratory (June 1976)

6 R E Alcouffe, F W Brinkley, D R Marr and R D O'Dell, "User's Guide for TWODANT A Code Package for Two-Dimensional, Diffusion-Accelerated Neutral-Particle Transport," LA-10049-M Los Alamos National Laboratory (March 1984)

7 R N Blomquist, "VIM Users Guide " Applied Physics Division, Argonne National Laboratory (1987)

8 K L Derstine, "DIF3D A Code to Solve One-, Two-, and Three-Dimensional Finite-Difference Diffusion Theory Problems," ANL-82-64, Argonne National Laboratory (April 1984)

Table I. Eigenvalue Comparison for P_1 and B_1 Group Constants

Model	P_1	B_1
Infinite Medium Material Buckling, B_m^2 (cm^{-2})	6 19E-3	6 55E-3
One-Dimension,[a] k_{eff}	1 0000	1 0242
Two-Dimension,[b] k_{eff}	0 9536	0 9638

[a]radial model with constant axial buckling

[b]regional depleted R-Z model

Table II. Group Structure Comparison for Simplified EBR-II R-Z Model

No of Groups	k_{eff}
9	1 2343
21	1 2296
50	1 2282
68	1 2257
230	1 2236
230[a]	1 2195
274[a]	1 2168
VIM[b]	1 215

[a]with self-shielding of high energy iron cross sections

[b]continuous-energy Monte Carlo calculation (see Ref 7)

Table III. Flux Method Comparison for Simplified EBR-II R-Z Model

Flux Method	k_{eff}
Diffusion	1 1782
S_4P_0	1 3218
S_4P_0[a]	1 2083
S_4P_1	1 2367
S_8P_1	1 2343
$S_{12}P_1$	1 2341
$S_{16}P_1$	1 2340

[a]transport corrected P_0

Table IV. Legendre Scattering Order Comparison for Spherical Model

Legendre Order	k_{eff}
P_0	1 2803
P_1	1 1827
P_2	1 1869
P_3	1 1867
P_4	1 1867
P_5	1 1867

All eigenvalues are calculated using S_8P_1 transport theory and nine energy groups in a reflected sphere.
Group constants are generated using VIM (Ref 7)

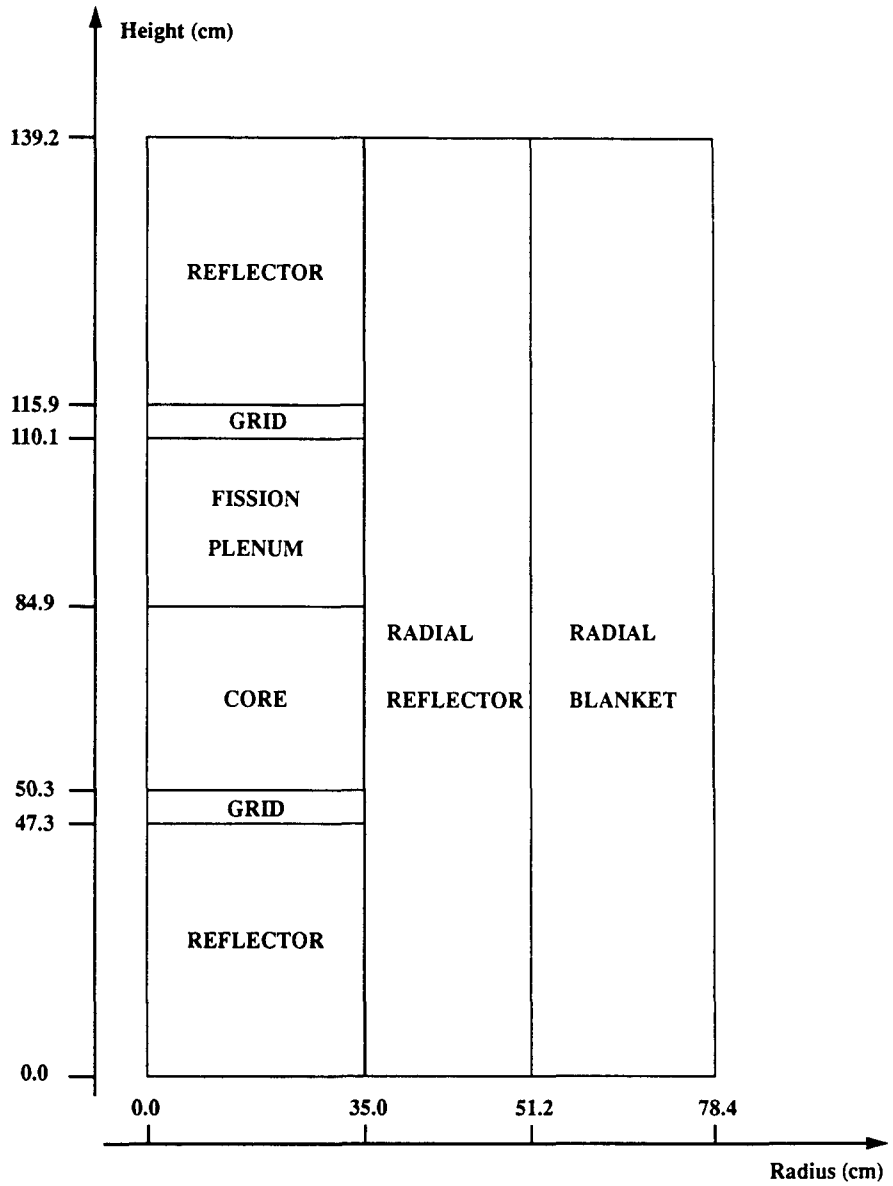

Figure 1. Simplified R-Z Model of EBR-II Reactor

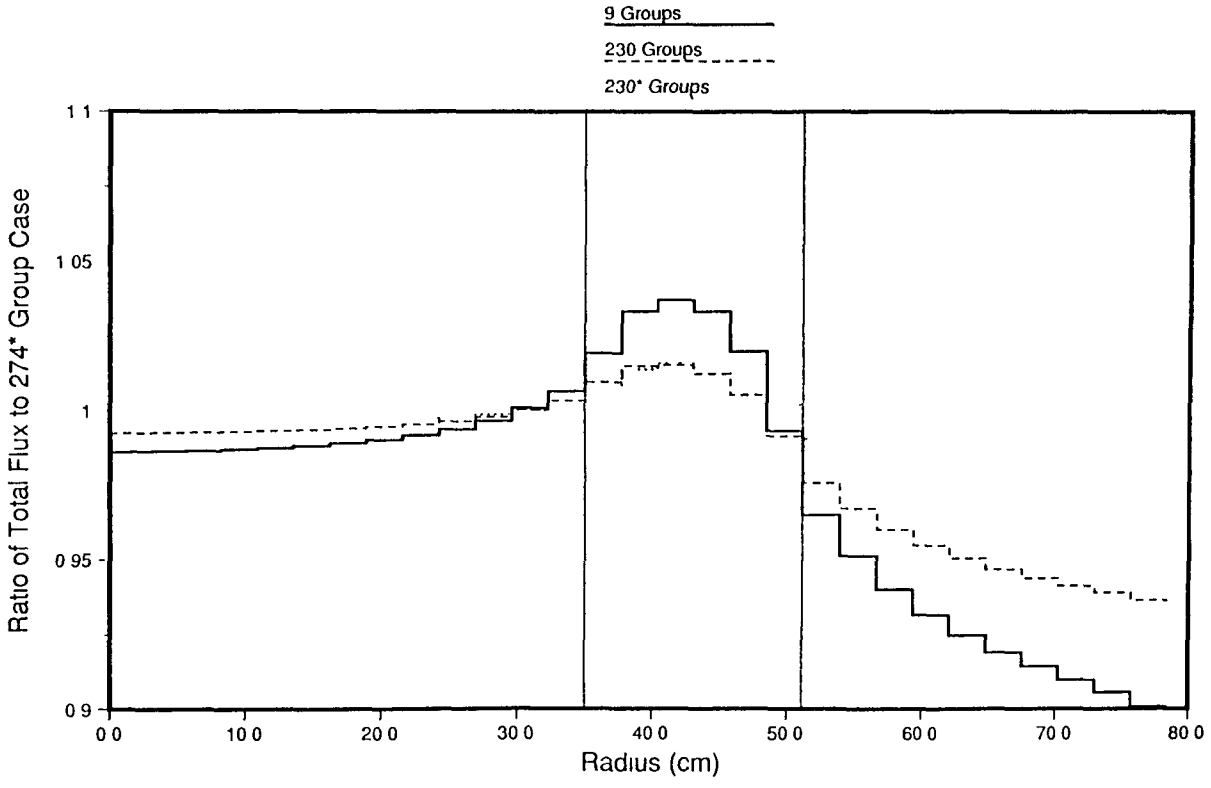

Figure 2 Comparison of Total Flux Predictions using Four Different Group Structures for a Radial Traverse at the Core Axial Midplane

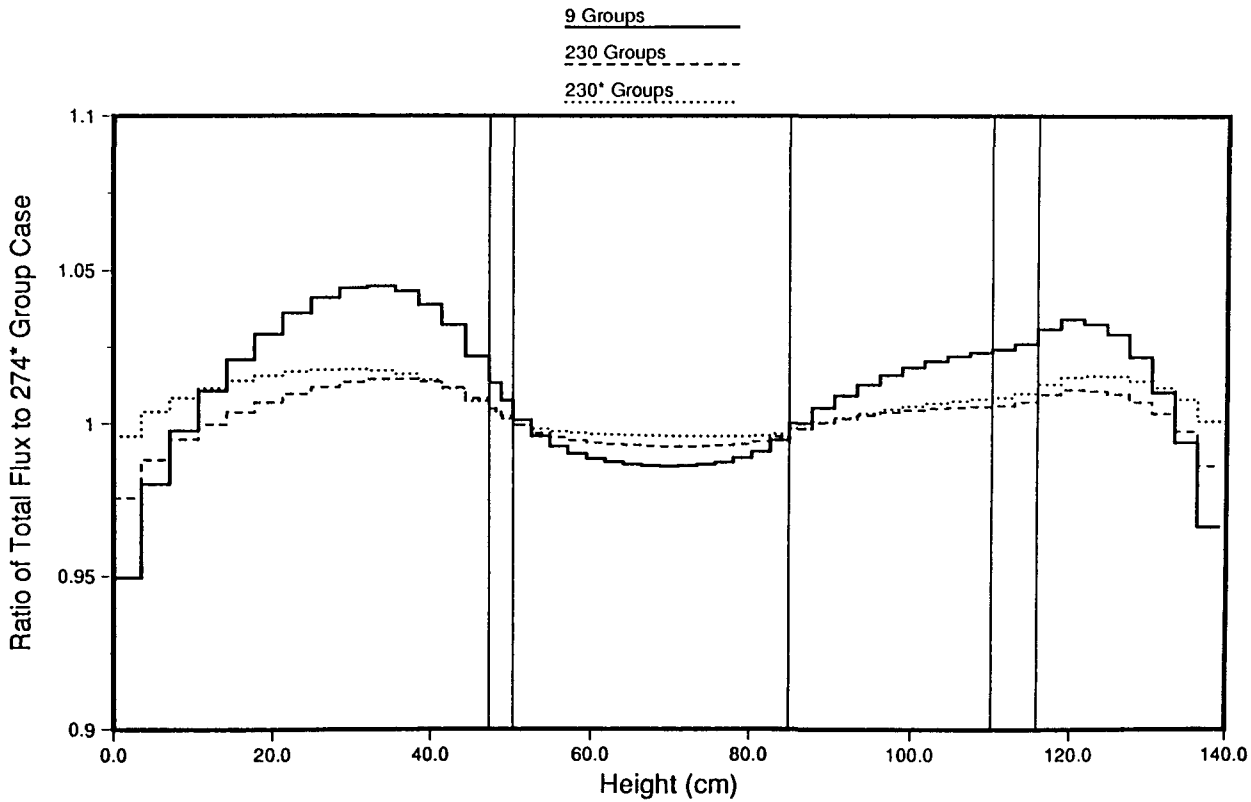

Figure 3. Comparison of Total Flux Predictions using Four Different Group Structures for an Axial Traverse at the Core Center

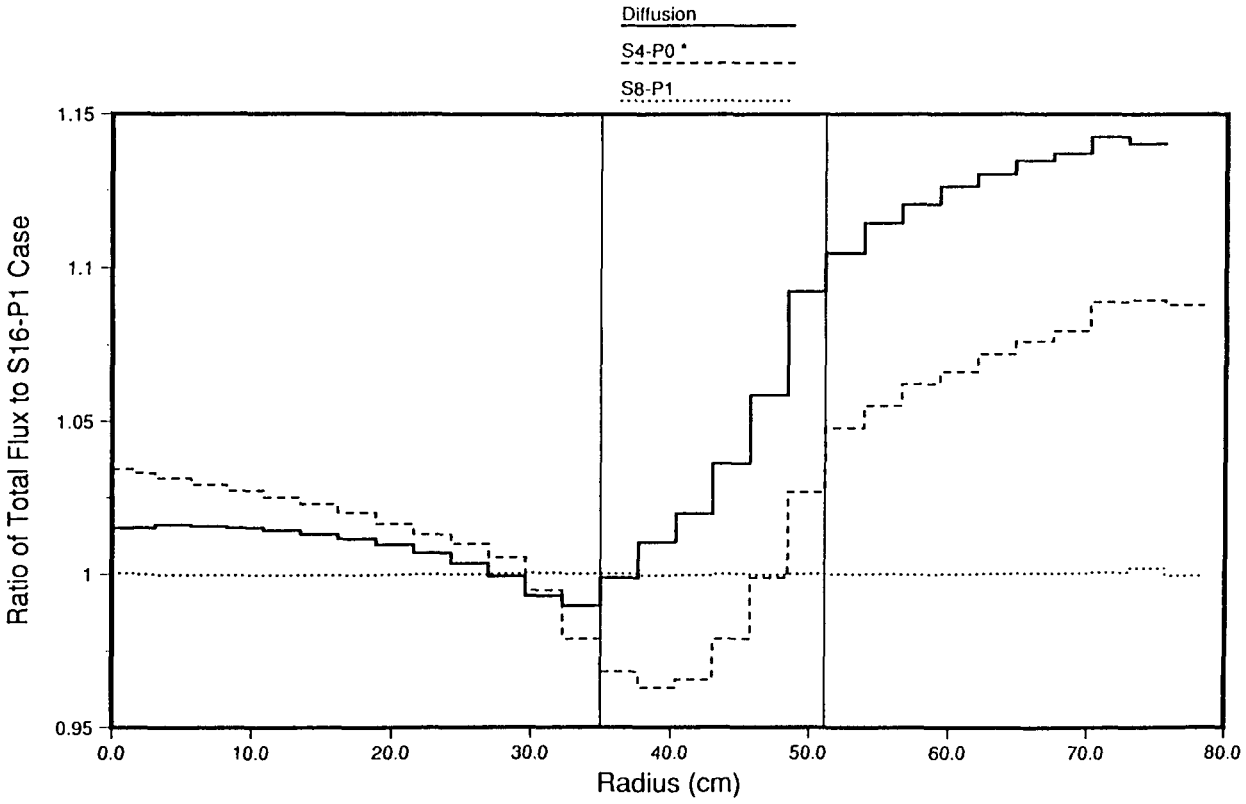

Figure 4. Comparison of Total Flux Predictions using Four Different Flux Calculation Methods for a Radial Traverse at the Core Axial Midplane

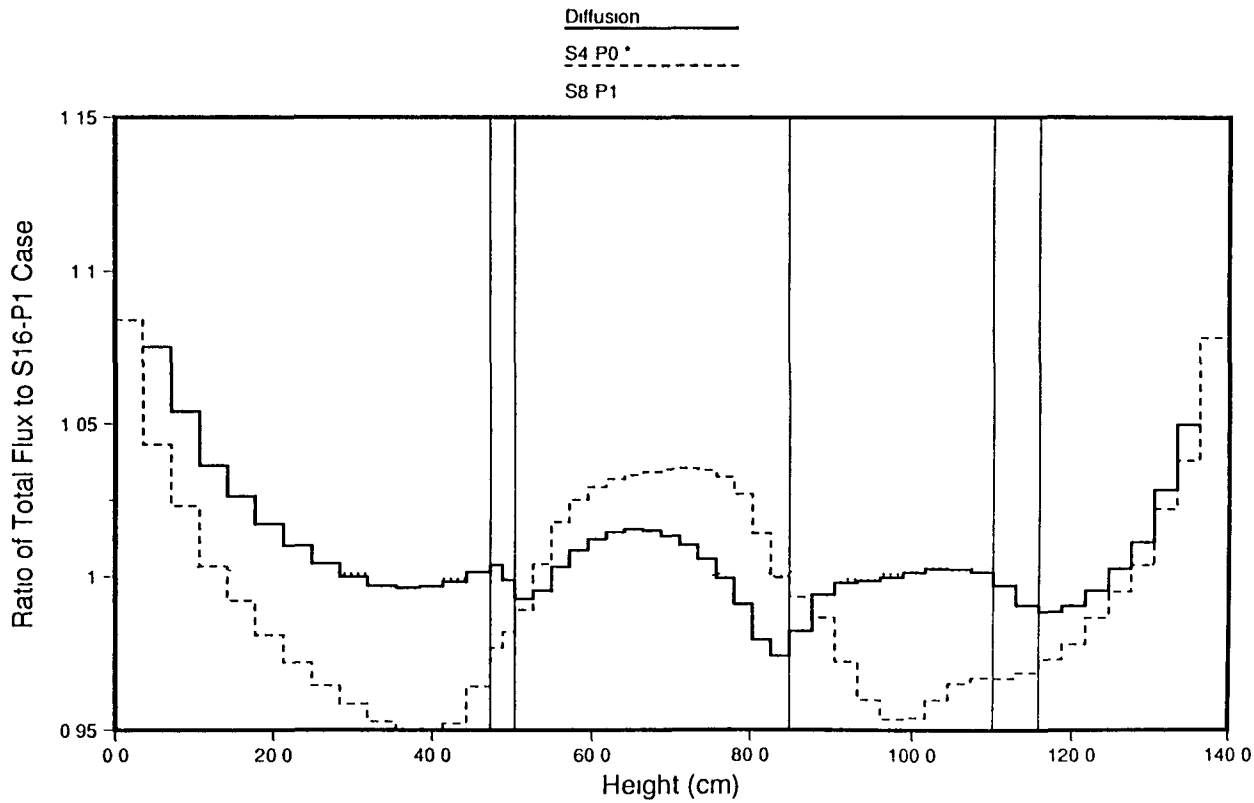

Figure 5. Comparison of Total Flux Predictions using Four Different Flux Calculation Methods for an Axial Traverse at the Core Center

Design of a Multi-Tiered, Digital Controller for the Supervisory, Global, and Local Control of a Pressurized Water Reactor

Brian N Aviles,[1,2] David D Lanning,[2] and John A Bernard[3]
[2]Department of Nuclear Engineering
and [3]Nuclear Reactor Laboratory
Massachusetts Institute of Technology
Cambridge, MA 02139

ABSTRACT

A closed-loop digital controller has been developed for reactor cores exhibiting spatially-dependent kinetics The proposed digital controller is multi-tiered, with supervisory, global and local control algorithms that employ real time core neutronic and thermal-hydraulic models for parameter estimation The supervisory level ensures that core neu tronic and primary loop thermal power are kept within a predetermined conservative operating envelope The global level computes a control rod speed and direction in order to meet a specified secondary load response The local level computes and monitors three-dimensional safety related parameters and interrupts control rod motion if any local limit is violated The digital controller has been evaluated in simulation for a typical commercial PWR and is successful in maneuvering reactor power and primary loop average temperature safely and efficiently during operational transients

INTRODUCTION

Recent advances in computer technology have made it possible for fully-coupled, three dimensional core reactor physics and thermal-hydraulics models to be used both as real-time plant estimators and as the basis of closed loop digital control strategies for reactor cores exhibiting spatial kinetics In this regard, a real-time analytic plant estimation code has been designed and evaluated via simulation at the Massachusetts Institute of Technology (MIT) as part of an on-going program to develop and demonstrate advanced instrumentation and control techniques for nuclear power plants This code has been given the acronym POPSICLE for POwer Plant SImulator and ControlLEr [1] POPSICLE's core neutronics model is based on a quasi-static transient solution of the analytic nodal diffusion equations [2,3] A multi-assembly nodal geometry is employed with thermal-hydraulic feedback accomplished through adjustments in the macroscopic nodal cross sections The core thermal-hydraulics nodal model, which employs multi channel control volumes of the fuel and primary coolant, allows for subcooled nucleate boiling and changes in fuel rod properties from thermal effects [4] In addition, a one-dimensional model of the primary loop is included so that PWR operational transients may be simulated Dynamics of the secondary system are provided by steam and feedwa ter flows through the steam generator

---

1 Present Address Knolls Atomic Power Laboratory
P O Box 1072
Schenectady, NY 12301

POPSICLE may be used as either a plant estimator or a controller When functioning as the latter, it provides supervi sory, global, and local control in order to ensure that there are no challenges to the safety system, that both core power and temperature can be adjusted efficiently, and that no DNB-related local limits are violated This hierarchical approach to controller design is recommended because it permits plant-specific control laws (the global level) to be combined with generic concepts that ensure the safety of the core (the supervisory and local levels) Such an approach simplifies control system design Also it may facilitate the licensing of digital controllers because the super visory algorithms are based on first principles and hence are applicable to many reactor types

The objective of this paper is to describe POPSICLE's multi-tiered design with emphasis on the contribution that real time, accurate reactor physics and thermal hydraulic models can make to reactor control

POPSICLE MULTI-TIERED CONTROLLER STRUCTURE

Figure 1 is a simplified diagram of the POPSICLE digital control algorithm The controller's structure is multi tiered and includes (1) a supervisory level which ensures that core neutronic and thermal power transients caused by actions of the digital controller will not challenge the reactor safety systems, (2) a bank of plant-specific control laws respon sible for the global (total) control of reactor power and primary coolant temperature, and (3) a routine for local power shaping in which three-dimensional power, heat flux, and temperature distributions are monitored and controlled to avoid operation that might approach DNB conditions Inputs to the controller include validated signals from the instrumentation systems as well as data from real-time analytic models of the core The availability of the calculated information is of course a major advantage to the digital approach The output from the controller consists of control rod bank(s) speed and direction

The controller tiers are separate and are prioritized according to their importance to reactor safety Thus, the supervi- sory and local power shaping controllers have the capability to override the actions of the global controller if an approach to an unsafe condition is detected Also, the proposed digital controller is completely separate from the nuclear safety system This ensures that the safety system could not be compromised by the actions of the digital con- troller If an input signal is common to both the safety system and the digital controller, isolation devices are used to prevent possible feedback from the digital controller that might adversely affect the safety system Also, fault-tolerant equipment should be used This proposed digital controller has the capability to evaluate the safety of its own actions This is an advantage relative to current analog automatic PWR control systems which rely on a set of safety system control rod interlocks that are in turn based on both current reactor conditions and the dynamic behavior of the aver age primary coolant temperature The proposed controller adds another level of safety conservatism by performing an on-line check of both the prompt neutronic and time-delayed thermal behavior of the reactor This is done to prevent the control system from implementing control actions that might challenge a set of predetermined safety limits a some future time The specific functions of the three controller tiers are discussed in the following three sections

SUPERVISORY CONTROL LEVEL

The purpose of the supervisory control level is to prevent the digital controller from calculating and implementing control rod motion that would place the reactor in an undesirable region of operation such that the reactor safety sys- tem might be challenged or operating limits violated The supervisory mission is accomplished by applying a reactiv- ity constraint derived from few-group diffusion theory, and a primary loop thermal power constraint derived from thermodynamic first principles [5,6] The supervisory reactivity constraint restricts core neutronic power to a prede- termined envelope by limiting the time-delayed contribution of the delayed neutrons to a level that can be negated by an induced change in prompt neutron population through an appropriate control device Similarly, the supervisory constraint on thermal power restricts the time-delayed effects of thermal inertia in the primary loop to a level that can be negated by a change in core neutronic power before an overshoot of the thermal power delivered to the steam gen- erators can occur In effect, *the supervisory constraints restrict the core neutronic power and primary loop thermal* power to a safe envelope by limiting the time-delayed contribution of the system dynamics to that which can be offset by forced changes in those components of the system that are directly controllable Simulation studies of the POPSI- CLE controller showed that both the neutronic and thermal power were kept from overshooting or undershooting their target values even when non-optimal global control laws were utilized [6] This important capability makes the use of supervisory control indispensable to the design of closed-loop digital controllers for large power reactors Ref- erence [6] contains a detailed description of the supervisory level of the proposed digital controller

GLOBAL CONTROL LEVEL

The second level of the multi-tiered controller is for global operation of the reactor At this level, the controller performs a task equivalent to that of analog controllers in current-generation Westinghouse-type PWRs, namely to maneuver reactor power and average primary coolant temperature so as to meet a demanded secondary steam load The global control algorithm functions beneath the safety umbrella of the supervisory controller It calculates an actuator signal at every time step but is allowed to implement that signal only if the supervisory constraints on neutronic and/or thermal power and the local constraints on DNB-related parameters are satisfied The inputs to the global controller are the reference temperature, the primary coolant temperature, the core neutronic power, and the first stage turbine impulse pressure The first and fourth are specified as a function of load The second and third are provided by instrumentation and the real-time analytic models. The outputs are the control rod bank(s) speed and direction Figure 2 is a block diagram of the proposed digital global controller. Its logic closely resembles that of existing analog controllers. The principal difference is the incorporation of real-time models for use in computing various reactor parameters As with the analog controller, two error signals are used to produce a control signal The first error signal is the difference between the average primary coolant temperature and the reference temperature with the former being obtained from either the narrow range temperature sensors or an analytic model, and the latter being generated from the load map. The second error signal is a power rate mismatch which is obtained by comparing the rates of change of turbine and neutronic power. This error signal is then converted to an equivalent temperature error so that it may be summed directly with the error in the average temperature and sent to the control rod speed and direction program The rod speed and direction unit converts the total equivalent temperature error to a control rod speed and direction signal based on the magnitude and sign of the temperature error The two error signals provide complimentary control in that the temperature error is inherently slow while the power rate mismatch anticipates changes in the average primary coolant temperature.

LOCAL POWER CONTROL LEVEL

The availability of real-time analytic models of spatially-dependent reactor cores makes it possible to calculate, monitor, and control neutron flux and fuel rod surface heat flux. This capability is a major advantage of digital controllers relative to the current analog ones in which in-core safety parameters are monitored on-line using estimates provided by the ex-core flux and temperature detection systems and with the only in-core information coming from periodic flux maps

The three-dimensional neutron flux, temperature, and wall heat flux maps calculated by real-time core models allow on-line calculation of DNB-related parameters such as DNBR, linear heat generation rate, heat flux hot channel factor, and the nuclear enthalpy rise hot channel factor. Also, core flux shape peaking parameters such as the axial flux difference (AFD) can be computed and monitored. This local controller will override the global level if such action is necessary to ensure that the reactor is not guided into regions of unsafe operation A description of the safety parameters that are calculated and monitored by the local control level is now presented

Departure from Nucleate Boiling Ratio (DNBR)

Departure from nucleate boiling (DNB) results in a change from an efficient nuclear boiling heat transfer mechanism to film boiling for which the heat transfer coefficient is significantly reduced DNB may induce damaging temperature transients in fuel rods and ultimately lead to fuel failure. The margin to DNB is quantified as DNBR which is the ratio of the calculated local DNB heat flux to the actual fuel rod surface heat flux at a particular axial location in the core The critical DNB heat flux can be estimated using the W-3 correlation [7]. On-line DNBR calculations entail computing the DNBR for each node in the core, identifying the minimum DNBR, and modifying this value with an appropriate correction factor that accounts for the approximations inherent in POPSICLE's multi-assembly nodalization. If the minimum DNBR falls below the setpoint, the digital controller intercedes and inserts the control rods to reduce the core power. This intervention continues until the minimum DNBR once again satisfies the controller limit.

Linear Heat Generation Rate (LHGR)

Another important safety parameter that is monitored to ensure fuel integrity is the linear fuel rating, expressed as a linear heat generation rate (LHGR). LHGR limits are design-specific, and conservative allowances must be made for the uncertainty in POPSICLE's multi-assembly calculation The local tier of the controller calculates the LGHR for each of the nodal channels using data from the real-time core model. If the LHGR limit is violated, the local control-

ler interrupts the global control signal and inserts the control rods until the core maximum LHGR is again at an acceptable value

Hot Channel Factors

The DNBR and LHGR limits are expressed in absolute terms by comparing core conditions to limits set by conservative experimental results after allowance for uncertainty There are also thermal operating limits that monitor relative axial and radial power peaking within the core These thermal limits, the nuclear heat flux hot channel factor and the nuclear enthalpy rise hot channel factor, are designed to maintain the relative axial and radial power peaking within bounds that do not challenge either the DNB or LHGR limits

The nuclear heat flux hot channel factor is defined as the ratio of the maximum local heat flux on the surface of a fuel rod at the axial location of the peak power to the average fuel rod heat flux The heat flux hot channel factor is therefore a measure of the axial power peaking in a nodal channel The nuclear enthalpy rise hot channel factor is defined as the ratio of the integrated linear power along the rod with the highest channel enthalpy rise to the core average rod power It is therefore a measure of the relative radial power peaking in the core Limits for both hot channel factors are plant-specific. Given real-time estimates of nodal power densities, heat flux and enthalpy rise hot channel factors can now be calculated on-line and monitored by the digital controller If either hot channel factor limit is breached, action is initiated from the local tier of the controller to insert the control rods until the initiating condition has cleared As regards priority, the DNBR and LHGR limits are evaluated first and any corrective actions required by those limits have precedence

Axial Power Shaping

The axial power shape in the current generation of PWR's is monitored on-line using information from the upper and lower quadrant ex-core detectors to estimate the axial flux difference (AFD), which is a measure of the axial power tilt in the core The axial flux difference is monitored in order to control axial peaking factors as well as to control axial power oscillations caused by thermal feedback and fission product poisons Plant specific technical specifications limit the allowed degree of power tilt at a particular power level

The availability of real-time models for three-dimensional in-core power calculations means that improved estimates of true power shape are possible The axial flux difference can be computed directly from the node-averaged power in the upper and lower halves of the core This is a major advantage over the present approach which relies on ex-core measurements that are calibrated periodically against in-core flux maps

CONTROLLER EVALUATION VIA SIMULATION

Simulation studies were conducted to evaluate the performance of the proposed digital controller A 3411 MWt Westinghouse-type PWR was chosen as the reactor type to be modelled because the reactor embodies the complex three-dimensional core behavior and the time-lagged dynamic response between system components necessary to evaluate the control strategies, and a reactor physics and thermal-hydraulic database corresponding to a generic Westinghouse type PWR has been assembled for this research

The two operational transients presented in this paper are typical examples of the controller behavior The first transient involves a +10% step increase in load from 90% to 100% nominal reactor power This transient demonstrates the interaction between the supervisory and global controller levels The second transient is a ramp increase in load from 20% power to 100% power at a rate of 5% per minute The second transient demonstrates the importance of the local controller level in maintaining the core power shape within safe bounds

90% to 100% Step Increase in Load

This simulation assumed that the reactor was initially in a steady-state condition at 90% power with the controlling bank of rods (bank D) positioned 1/3 the distance from the top of the core The +10% step perturbation in load began 5 s into the run Figure 3 shows the demanded load, the core neutronic power, and the primary loop thermal power delivered to the steam generator Figure 4 presents the reference and simulated average primary coolant temperature as well as the ±0 75 C global controller deadband The first control rod withdrawal signal implemented by the global

controller occurred at 6 s, caused by the combination of errors between the reference and actual average temperature and the power rate error between the turbine and core power The first six control signals were dominated by the power rate error until the neutronic transient is well underway After 12 s, the control signal from the global controller is dominated by the error in the temperature The impact of the supervisory constraints was also apparent From 12 s to 48 s, there were several occasions when the supervisory constraints were violated and the supervisory tier of the controller inserted the control rods For example, at 20 s and again at 24 s, violations of the primary loop thermal power supervisory constraint caused rod insertions as it sought to retard the rate of rise of thermal power The remaining control rod insertion signals resulted from violations of the neutronic power reactivity constraint Of significance is that the supervisory controller kept the neutronic power from exceeding the upper bound of the safety tolerance band (102% power) despite the fact that the global controller was still trying to increase reactor power to bring the average temperature into the deadband zone more rapidly Once the temperature was brought within the 0 75 C dead band at 49 s, rod motion ceased as the reactor settled into a new equilibrium at 100% power The simulation was extended beyond 200 s to ensure that the temperature did in fact return to its reference equilibrium value of 309 0 C It is important to note that none of the local power constraints were violated during this simulation and hence were not shown

This simulation demonstrates the importance of the supervisory level of the digital controller in maintaining control when various global control algorithms are used The supervisory tier maintains both the core neutronic and the primary loop thermal power for large spatially-dependent PWRs within a safe operating envelope despite the fact that the control rods are perhaps being driven by non-optimal global control schemes Moreover, the multi-tiered controller structure allows the control engineer the flexibility of designing plant specific control laws to achieve a desired dynamic response for the primary system average temperature at the global level without challenging the reactor safety systems The supervisory tier ensures that the primary system neutronic and thermal powers remain within a conservative operating region that lies below the bounds of the nuclear safety system trip setpoints

20% to 100% Load Ramp at 5% per Minute

The local control level was evaluated using a ramp increase in load from 20% to 100% power at a rate of 5% per minute This transient was selected because it engendered drastic changes in flux shape as the banks of control rods were moved through the core It is important to bear in mind that the PWR data available to this research was representative of a typical Westinghouse-type 1150 MWe PWR and did not describe an actual facility Accordingly, many of the parameters and safety limits determined by the local tier of the controller are not values that would be found in an actual commercial reactor However, the dynamic PWR behavior is realistic for the data compiled in this research Therefore, the emphasis here is not on the specific values of the local operating parameters and their limits, but on the fact that the dynamic behavior of these three-dimensional parameters can be calculated and monitored in real time during operational transients

All three levels of the controller were activated for this transient The upper tolerance band for the supervisory tier was 102% power The global control level used a rod speed and direction program with a ±0 25 C deadband to calculate control rod velocity as a function of the total equivalent temperature error The following nodal safety limits were imposed on the reactor core minimum DNBR at 3 1, maximum LHGR at 10 0 kW/ft, maximum nuclear flux hot channel factor at 2 5, maximum nuclear enthalpy rise hot channel factor at 1 5, and the axial flux difference limits as per Figure 5

The reactor was initially in a steady-state, xenon-equilibrium condition at 20% power with control rod banks A and B fully withdrawn from the core Banks C and D were initially at heights of 75% and 25% withdrawn, respectively This initial rod configuration was chosen intentionally so that one of the local safety-related parameters would be violated and the logic of the local tier of the controller tested In actual practice, the control rods would be positioned higher in the core to avoid the flux peaking in the lower part of the core as higher power levels are attained

The ramp increase in load began at 5 s and was prematurely halted at 775 s because of repeated violations of the axial flux difference limit at 755 s The local controller halted the increase in neutronic power at 755 s upon the detection of the problem with the AFD However, the demand on the secondary system was allowed to continue rising at the 5% per minute ramp rate Because the digital controller could no longer maintain the appropriate primary system power rise due to the AFD violation, a primary-to-secondary mismatch developed and the transient was halted The specifics of the simulation are shown in Figures 5-9

The simulation can be roughly divided into three segments 0-400 s, 400-755 s, and 755-775 s During the first segment, low magnitude oscillations are present in the power and average temperature (see Figures 6 and 7) These are the result of the initial perturbations of the steam generator which were in turn caused by the change in demand for secondary steam and the corresponding increase in feedwater flow A contributing factor was the lack of strong reactivity feedback effects which would, had it been present, have dampened the oscillation The temperature coefficients of reactivity of the coolant and fuel are relatively small in magnitude when operating at low power Once at 400 s, the power had increased sufficiently to cause the oscillations to be damped out The second phase of the transient ran from 400s to 755 s Nothing abnormal was noted and the global controller's directives were implemented without intervention either by the supervisory constraints or the local control tier

The third phase began at 755 s when the axial flux shape peaked in the bottom of the core in a manner such that the minimum AFD limit for the corresponding power level was violated This is shown in Figure 5 The initial position of the controlling rod banks for this transient was such that, as the rods were withdrawn to achieve the desired power and temperature, the flux peaking in the bottom of the core grew until the limit of -25 8% was breached At the time of the limit being reached, the global controller was signaling for rod withdrawal in order to maintain the average temperature within the allowed deadband The violation occurred at a core power was 82 6% when rod bank C was 91% withdrawn from the core and rod bank D was 41% withdrawn Rod bank D was the primary cause of the flux tilt because it was still 9% below the core midplane, a position too low for the 82.6% power level The local tier of the controller detected the AFD violation and inserted the control rods one step in order to prevent the power from increasing further and possibly creating conditions where DNB might occur From 755 s to 775 s, the global and local control controllers opposed each other, causing step oscillations in neutronic power Each time the local controller inserted the control rods by one step, the power would decrease slightly, bringing the AFD back within the allowed envelope Control would then be returned to the global law because neither the supervisory constraints nor the local limits were being violated The global controller would specify a rod withdrawal signal in an attempt to raise the average temperature to meet the increasing reference temperature The resulting rod motion would cause another violation of the AFD limit, the local controller would again intervene, and the sequence would be repeated This continued until 775 seconds when the secondary pressure and then the primary temperature (Figure 7) began to fall rapidly in order to sustain the demanded load which had intentionally been allowed to continue rising on the specified 5% per minute ramp rate despite the actions of the core controller and the dynamic behavior of the primary system This segment of the simulation is an excellent example of the need for coordinated turbine/generator, steam generator, and reactor core control

Examination of the dynamic behavior of the local safety-related parameters such as DNBR, LHGR, and the hot channel factors showed that no violations occurred of these quantities during the simulated transient. The core minimum DNBR shown in Figure 8 began at 24 3 at 20% power and decreased toward a minimum of 5 0, which occurred during the time of maximum power, 755 s - 775 s

The core maximum LHGR (Figure 9) did not challenge its limit of 10 0 kW/ft during the transient. The LHGR began at 2 2 kW/ft at 20% power and increased to 9 1 kW/ft at the 83% maximum core power level The axial position of the core maximum LHGR followed the withdrawal of the control rods during the transient, reflecting the upward shift in the flux peak as the rods were removed from the core

The dynamic behavior of the nuclear heat flux hot channel factor and the nuclear enthalpy rise hot channel factor were uneventful during the transient. Both parameters moved slightly toward their limits, but did not challenge the local controller setpoints by the time the AFD violation occurred

CONCLUSIONS

A multi-tiered, closed-loop, digital controller designed to manipulate control rods in order to execute PWR operational transients both safely and without violating safety limits has been described and evaluated via simulation The supervisory, global, and local control levels functioned as designed and the controller resulting from their unification will, teamed with coordinated turbine load control and steam generator control, constitute a safe and efficient digital system for the control of PWR operational transients

The supervisory level employs a reactivity constraint and a thermal power constraint that are important in precluding overshoots of either core neutronic or primary loop thermal power during more severe transients such as step changes in load The local control level is an essential component of the overall system with regards to the control of reactors

exhibiting spatially-dependent behavior Even a well-designed global control law can cause violations of local limits if the initial reactor configuration is inappropriate to the conduct of the requested power maneuver It was shown however, that mere intervention by the local controller is not enough There must be a coordinated response that addresses the behavior of the core, steam generator, and turbine Finally, global control laws should be designed with full knowledge of the specific operating characteristics of the plant that is to be controlled The controller structure allows the control engineer flexibility in designing global control laws to meet a specified dynamic response

In summary, the simulations in this paper demonstrate the capability of the multi-tiered controller to safely control the large core of a PWR during operational transients The availability of accurate, real-time analytic models plays an important role in the design of each of the tiers in the controller structure The proposed closed-loop digital controller described in this paper is an important step in realizing automatic plant control by ensuring that the plant component most important in terms of the production of energy, namely the reactor core, can be satisfactorily controlled with digital technology over a wide range of power without challenging safety limits during normal operating transients

ACKNOWLEDGEMENTS

The authors would like to thank Professors Allan F Henry and John E Meyer for their contributions during this project. This research was supported by the U S Department of Energy under Contract No DE-AC02 86-NE37962 A000

REFERENCES

1 B N Aviles, "Digital Control Strategies for Spatially-Dependent Reactor Cores with Thermal-Hydraulic Feedback," Ph D Thesis, Department of Nuclear Engineering, Massachusetts Institute of Technology, Cambridge, MA, February, 1990

2. K.S Smith, "An Analytic Nodal Method for Solving the Two-Group, Multidimensional Static and Transient Neutron Diffusion Equations," N E Thesis, Department of Nuclear Engineering, Massachusetts Institute of Technology, Cambridge, MA, March, 1979

3 P W Kao, "Application of Supernodal Methods to Transient Analysis," Ph D Thesis, Department of Nuclear Engineering, Massachusetts Institute of Technology, Cambridge, MA, August, 1988

4 E L L Cabral, "Three Dimensional Real-Time Thermal-Hydraulic Model and Non-Linear Controller for Large PWR Cores," Ph D Thesis, Department of Nuclear Engineering, Massachusetts Institute of Technology, Cambridge, MA, December, 1988

5 J A Bernard, A F Henry, and D D Lanning, "Application of the 'Reactivity Constraint Approach' to Automatic Reactor Control," Nuclear Science and Engineering, Vol 98 (February 1988), pp 87-95

6 B N Aviles, D D Lanning, and J.A Bernard, "Supervisory Constraints for the Control of Neutronic and Thermal Power in a Pressurized Water Reactor (PWR)," in Proceedings ANS International Topical Meeting on Advances in Mathematics, Computations, and Reactor Physics, Vol 5 (April 1991), pp 24 1 2-1 - 24 1 2-13

7 L S Tong, Principles of Design Improvement for Light Water Reactors, New York Hemisphere Publishing Corp , 1988

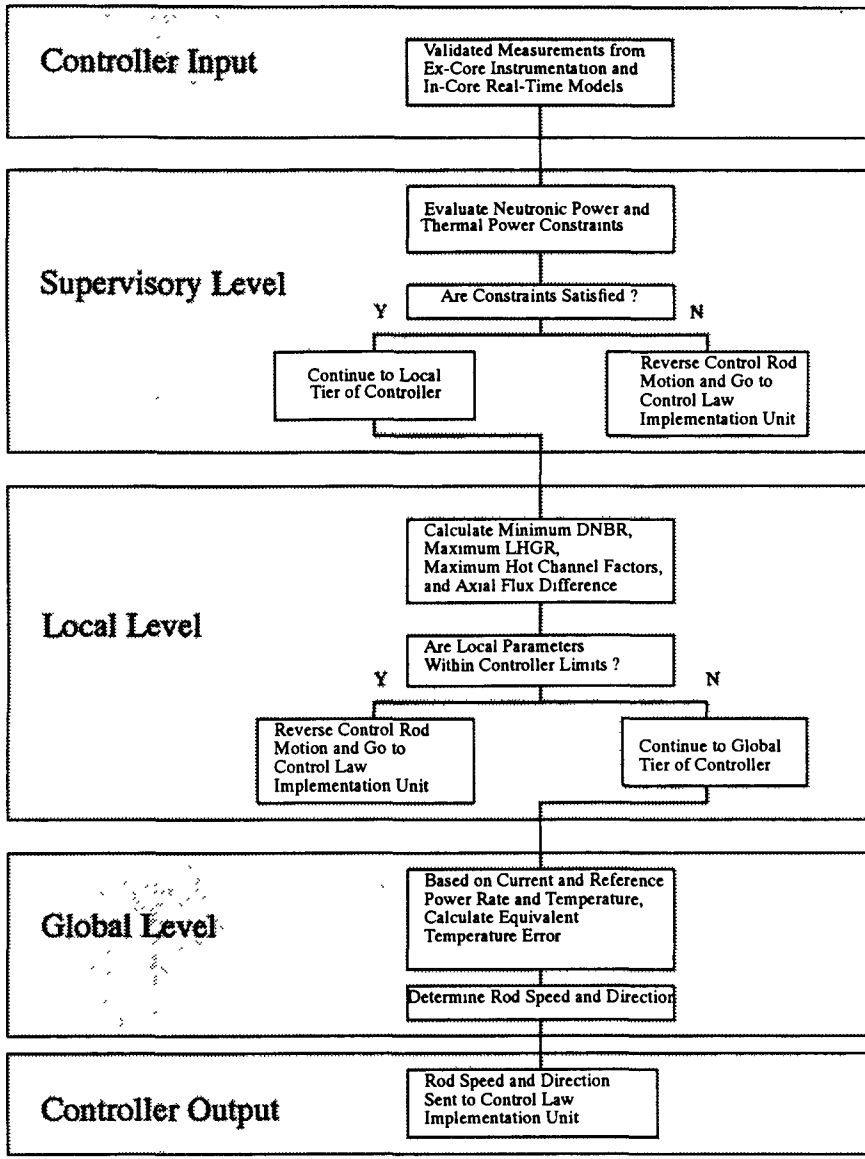

Figure 1. Algorithm for POPSICLE Closed-Loop Digital Controller

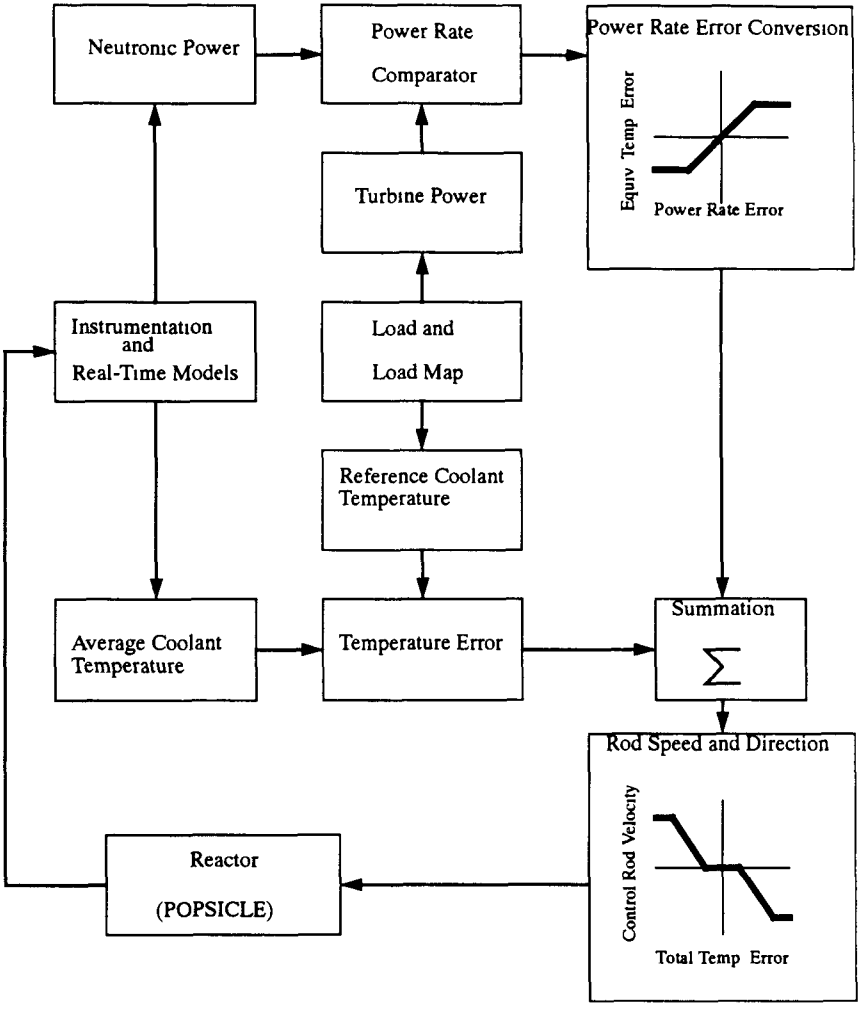

Figure 2 Global Tier of the Proposed Digital Controller

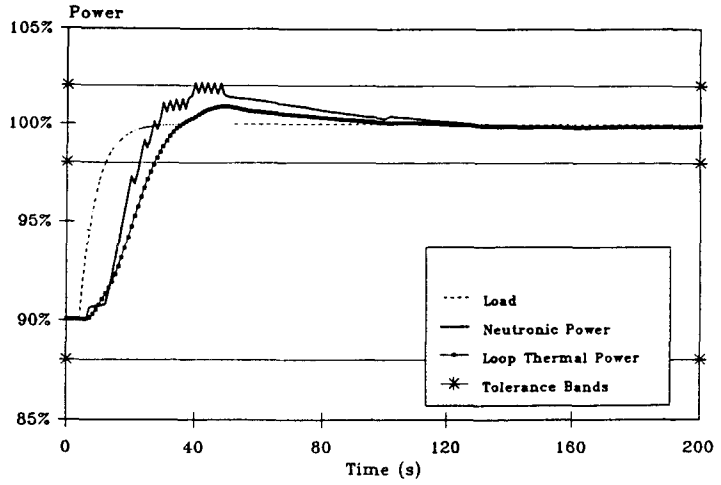

Figure 3. Test of Digital Controller Showing Power Profile Obtained Following a +10% Step Change in Load

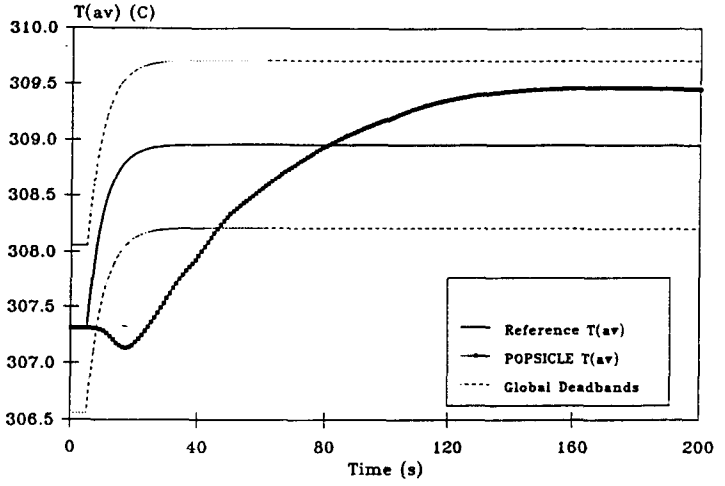

Figure 4. Average Primary Coolant Temperature Dynamic Response for the Transient Shown in Figure 3

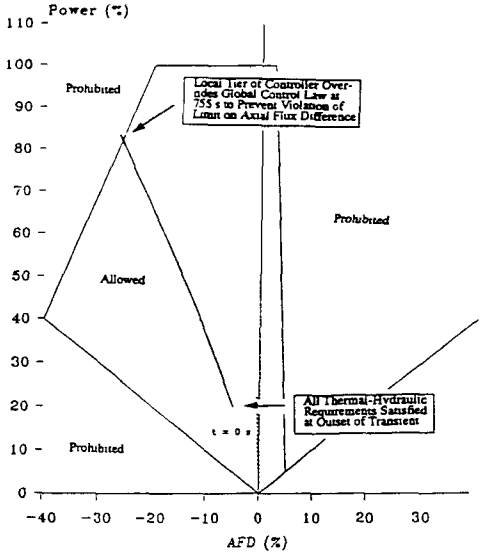

Figure 5. Test of Digital Controller Showing AFD Profile Obtained During a 20% - 100% Ramp Increase in Load

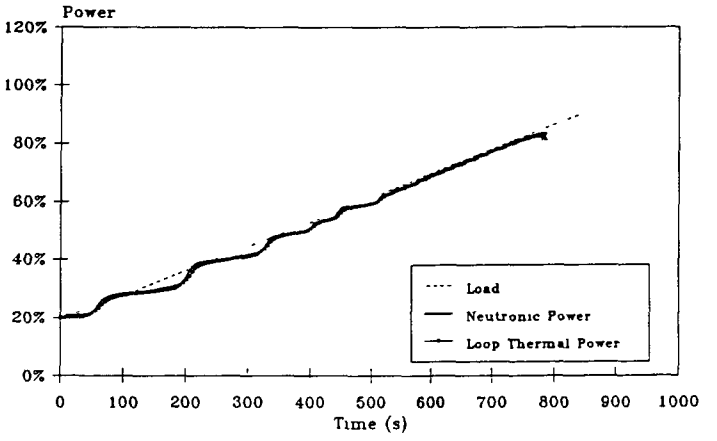

Figure 6. Power Profile for the 20% - 100% Ramp Increase in Load

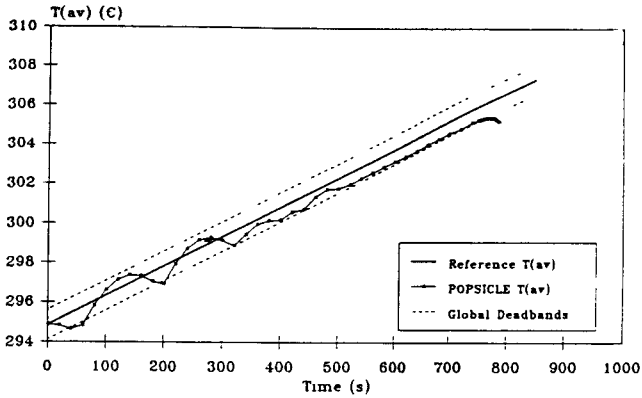

Figure 7. Average Primary Coolant Temperature Response for 20% - 100% Ramp Increase in Load

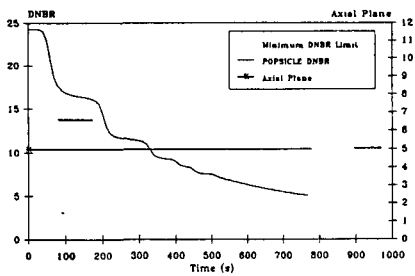

Figure 8. Minimum DNBR Response for 20% - 100% Ramp Increase in Load

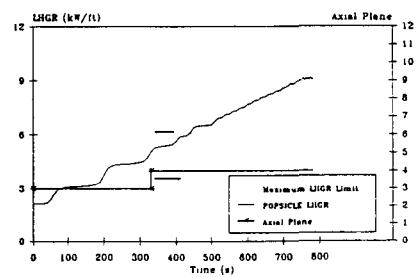

Figure 9. Maximum LHGR Response for 20% - 100% Ramp Increase in Load

ADAPTIVE CONTROL FOR A PWR USING A SELF-TUNING REFERENCE MODEL CONCEPT

G. H. Miley, G. T. Park,* and B. S. Kim*

Dept. of Nuclear Engineering, University of Illinois
103 South Goodwin Avenue, Urbana, IL 61801-2984

*Dept. of Electrical Engineering, Korea University,
Anam-dong, Sungbuk-ku, Seoul, Korea, 136-075

ABSTRACT

Possible applications of an adaptive control method to a pressurized-water reactor (PWR) nuclear power plant are investigated. The self-tuning technique with a reference model concept is employed. This control algorithm is developed by combining the self-tuning controller (STC) with the model reference adaptive control (MRAC). This approach overcomes the difficulties in choosing the appropriate weighting polynomials in the cost function of the self-tuning control.

I. INTRODUCTION

With the appearance of very cheap microprocessors during the last few years, new possibilities for the industrial application of adaptive control systems have opened up. Consequently, adaptive techniques have now become a very attractive approach for system control.

Several problems in nuclear power plants have aspects that seem especially well suited for adaptive control.[1] Examples include plant control systems that are affected by plant "aging" due to gradual changes associated with operational aspects such as residue buildup in ducts and pipes, changes in nuclear core reactivity due to fuel burnup, etc., that gradually degrade performance. On a more rapid time scale, changes in daily load cycles can noticeably affect plant performance and ultimately result in variations in turbine exhaust pressure. Such changes are aggravated by the fact that plant characteristics typically depend on the operating power level. That is, the characteristics at low-level operation can be quite different from those at high-level operation. Finally, power plants are highly complex, nonlinear, time-varying, constrained systems.

Self-tuning control has received increasing attention in recent years to the control of nuclear power plants.[2-5] But in this method it is not obvious how the cost function weighting polynomials should be chosen to ensure specified performance. Another adaptive

approach is the model reference adaptive control (MRAC) method. This adaptive system is proposed to solve a problem in which the specifications are given in terms of a reference model that tells how the process output ideally should respond to the command signal. This scheme was originally developed for the deterministic servo problem.[6] However, Landau found very close connections between STC and MRAC,[7] and proposed a combined MRAC-STC scheme which can behave as a MRAC in a deterministic environment and a STC in a stochastic environment.[8] In this paper this combined scheme which is called the self-tuning controller with the reference model conception is employed to solve the load-following control of a PWR nuclear power plant in the stochastic environments. This model is an extension of one originally developed by Ulens[9] and used by Keyser Van Gauwenberghe[2] for general control system design. In our study, however, a controller is designed based on a simpler, low-order (second-order) model. Instead of estimating the unknown process parameters, the control parameters are "tuned" on line, so that the control input applied to the actual plant is adapted at every sampling instant.

II. THE SYSTEM

The system considered here is a pressurized water reactor (PWR) nuclear power plant. Because we wish to investigate and to control the behavior of the nuclear and thermal systems for load disturbances, the fast dynamic behavior of the turbine and electric generator was not included. It was assumed that a load variation causes a changing steam flow to the turbine. This is illustrated in Figure 1, which shows the representation of the nuclear and thermal parts of the power plant. A mathematical description corresponding to Figure 1 leads to the set of differential equations given in reference 5. The subsequent nomenclature follows that defined in Figure 1 and reference 5.

This process model contains several interesting and important properties: Its dimensionality is still relatively high and the dynamics of the nuclear part contains several nonlinearities; some coefficients given above are not constant, in fact, but vary slowly with the operating point or with time.

III. CONTROL SPECIFICATIONS

The main disturbances are load variations that enter the model as variations of the percent of steam flow p. Such a variation of the steam flow leads to an equivalent variation of the average coolant temperature T_r. Without a closed-loop control, sizable variations in T_r can occur. The resulting variations in the fuel temperature T_f and in the steam temperature T_s are unacceptable because they produce large thermal stresses and can cause damage to the equipment involved. Therefore, we select the reactor coolant temperature T_r as the controlled variable in a load-following control system for use in the PWR power station.

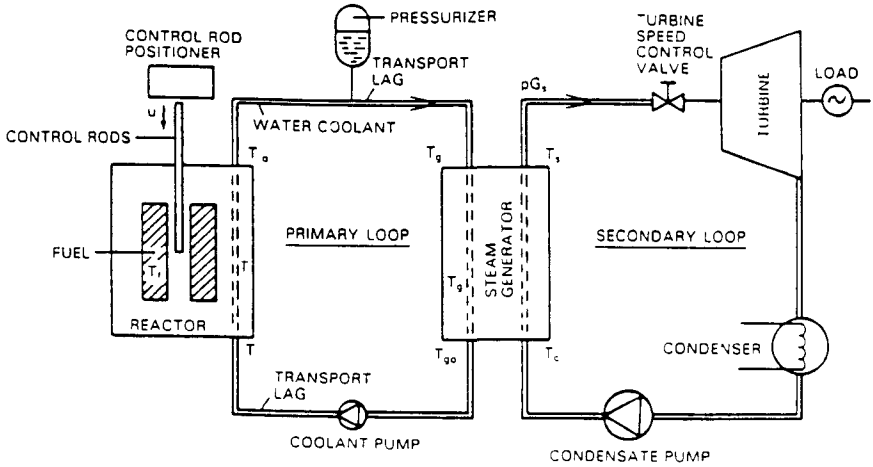

Figure 1. Schematic Diagram of a PWR Nuclear Power Plant.

In practice, however, we must compromise and accept a setpoint T_{rw} that varies slightly with the load. Here we assume that T_{rw} is a linearly increasing function of load.

Besides the load variations, the control system must also contend with noisy disturbances that can occur through a variety of relatively minor influences. These noisy perturbations are not measurable and for that reason require a controller that can deal with stochastic processes.

The appropriate control variable considered in this application is the position of the (neutrons absorbing) control rods, measured as a number of displacement steps. Control rod withdrawal is necessary during a load increase to balance the change in reactivity due to feedback from the fuel and the coolant temperatures. Conversely, control rod insertion is necessary during a load decrease.

The purpose of the control system is to hold the temperature T_r as near as possible to a time-varying reference value T_{rw} despite the disturbances. Thus, the action of the controller is twofold: The output should track a reference signal (servo-control) and disturbances must be eliminated (regulatory control).

IV. CONTROL SYSTEM DESIGN

A general discrete time model of the plant to be controlled is of the form

$$A(q^{-1})y(k) = q^{-d}B(q^{-1})u(k) + q^{-1}\,D\,(q^{-1})v(k) + C(q^{-1})w(k) \qquad (1)$$

where

$$\begin{aligned} A(^{-1}) &= 1 + a_1q^{-1} + \ldots + a_nq^{-n} \\ B(q^{-1}) &= b_o + b_1q^{-1} + \ldots + b_mq^{-m},\ b_o \neq 0 \\ D(q^{-1}) &= d_o + d_1q^{-1} + \ldots + d_sq^{-s},\ d_o \neq 0 \\ C(q^{-1}) &= 1 + c_1q^{-1} + \ldots + c_nq^{-n} \end{aligned} \qquad (2)$$

Here q^{-1} is the backward shift operator; d and l ($d \leq l$) are time delays associated with u and v; y, u and v are output, input and measurable disturbance; and w is a sequence of distributed independent normal $(0, \sigma)$ random variables. It is assumed that the plant is minimum phase and that the plant delays d and l are known.

The design goal for the control system is to regulate the plant such that the plant output will be as close as possible to the output, y_M, of the reference model of the following equation

$$A_M(q^{-1})y_M(k) = q^{-d}B_M(q^{-1})u_M(k) \qquad (3)$$

where A_M is a monic and asymptotically stable polynomial. u_M is a bounded reference input.

The control objective (with both tracking and regulating) can be formulated as follows; find the control u(k) such that the tracking error satisfies;

$$T(q^{-1})(y(k+d) - y_M(k+d)) = R(q^{-1})C(q^{-1})w(k+d) \qquad (4)$$

where $T(q^{-1})$ is a monic and asymptotically stable polynomial which will specify the closed-loop poles. When T = C, the minimum variance tracking and regulation is obtained. Then $R(q^{-1})$ results as:

$$T(q^{-1}) = A(q^{-1})R(q^{-1}) + q^{-d}S(q^{-1}) \qquad (5)$$

which has a unique solution for the polynomials S and R, where

$$\begin{aligned} R(q^{-1}) &= 1 + r_1q^{-1} + \ldots + r_{d-1}q^{-d+1} \\ S(q^{-1}) &= s_o + s_1q^{-1} + \ldots + s_{n-1}q^{-n+1} \end{aligned} \qquad (6)$$

Using Eq. (5) the plant model, Eq. (1), is rewritten as

$$T(q^{-1})y(k+d) = B_r(q^{-1})u(k) + D_r(q^{-1})v(k+d-1) + S(q^{-1})y(k)$$
$$+ R(q^{-1})C(q^{-1})w(k+d) \quad (7)$$

where

$$B_r(q^{-1}) = B(q^{-1})R(q^{-1}) = b_o + q^{-1}B_r^*(q^{-1})$$
$$D_r(q^{-1}) = D(q^{-1})R(q^{-1}) \quad (8)$$

If we choose the control law

$$B_r(q^{-1})u(k) = T(q^{-1})y_M(k+d) - D_r(q^{-1})v(k+d-1) - S(q^{-1})y(k) \quad (9)$$

then, the output of the plant becomes

$$T(q^{-1})y(k+d) = T(q^{-1})y_M(k+d) + R(q^{-1})C(q-1)w(k+d) \quad (10)$$

This accomplishes the control objective. Introducing the notation

$$\phi(k)^T=[u(k)..u(k-m-d+1)\ v(k+d-1..v(k-1-g+1)\ y(k)..y(k-n+1)] \quad (11)$$

$$\theta^T = [b_o\ b_{r1}\ ...brm+d-1\ d_o\ dr1...drg+d-1\ so\ ...\ sn-1] \quad (12)$$

Equation 9 can be expressed in equivalent form as

$$T(q^{-1})y_M(k+d) = \theta^T \phi\ (k) \quad (13)$$

When the plant parameters are unknown, an appropriate adaptation algorithm should be defined such that the control objective in the case of known plant parameters be asymptotically achieved, giving

$$\text{prob}\ (\lim_{k \to \infty} T(q^{-1})[y(k+d)-y_M(k+d)]=R(q^{-1})C(q^{-1})w(k+d)) = 1 \quad (14)$$

The structure remains the same as the case of known parameters, but the fixed parameter vector θ will be replaced by an adjustable parameter vector

$$\hat{\theta}(k)^T=[\hat{b}_o(k)\ \hat{br}_1(k)\ ...\ \hat{d}_o(k)\ ...\ \hat{s}_{n-1}(k)] \quad (15)$$

Then the control law is given by

$$T(q^{-1})y_M(k+d) = \hat{\theta}\ (k)^T\phi(k) \quad (16)$$

In order to guarantee convergence conditions and to improve the transient performance, it is useful to introduce an asymptotically stable filter $1/L(q^{-1})$ yielding

$$z^f(k) = L^{-1}(q^{-1})z(k) \quad (17)$$

The superscript f means that the signal has been filtered through $L(q^{-1})$. When using the filter $L(q^{-1})$, the control can be expressed as follows:

$$u(k) = L(q^{-1})u^f(k) \tag{18}$$

and $u^f(k)$ is computed from

$$T(q^{-1})y_M^f(k+d) = \hat{\theta}(k)^T\phi^f(K) \tag{19}$$

Dugard and Landau[10] proved that by using the following parameters adaptation algorithm (PAA)

$$\hat{\theta}(k) = \hat{\theta}(k^{-1}) + F(k)\phi^f(k-d)e(k) \tag{20}$$

$$F(k+1) = \frac{1}{\lambda_1(k)}\left[F(k) - \frac{F(k)\phi^f(k-d)\phi^f(k-d)^TF(k)}{\lambda_1(k)/\lambda_2(k) + \phi^f(k-d)^TF(k)\phi^f(k-d)}\right] \tag{21}$$

$$e(k) = \frac{H_1(q^{-1})}{H_2(q^{-1})}\,L(q^{-1})[\theta-\hat{\theta}(k)]^T\phi^f(k-d) + \frac{H_1(q^{-1})}{H_2(q^{-1})}\,R(q^{-1})C(q^{-1})w(k) \tag{22}$$

$$F(0) > 0,\ 0<\lambda_1(k) \le 1,\ 0 \le \lambda_2(k) \le 2$$

where $H_1(q^{-1})$, $H_2(q^{-1})$ are asymptotically stable monic polynomials. This PAA will converge if;

$$H(q^{-1}) = \frac{H_1(q^{-1})}{H_2(q^{-1})}\,L(q^{-1}) - \frac{\lambda}{2}, \quad \max_k \lambda_2(k) \le \lambda < 2 \tag{23}$$

is strictly positive real (SPR).

The adaptation error e(k) given by Eq. 22 cannot be used for the implementation since it depends on $\hat{\theta}(k)$. The causal expression for e(k) is given by

$$e(k) = \frac{T(q^{-1})y(k) - \hat{\theta}(k-1)^T\phi^f(k-d) + N(k)}{1 + \phi^f(k-d)^TF(k)\ \phi^f(k-d)} \tag{24}$$

where

$$N(k) = H_1^*(q^{-1})T(q^{-1})y(k) - H_2^*(q^{-1})e(k)$$

$$- H_{1\bullet}^*(q^{-1})[\hat{\theta}(k-1)^T\phi^f(k-d) - \phi^{fT}(k-d)^T F(k)\phi^f(k-d)e(k)]$$

$$H_1(q^{-1}) = 1 + H_1^*(q^{-1}),\quad H_2(q^{-1}) = 1 + H_2^*(q^{-1}),$$

$$H_1(q^{-1})L(q^{-1}) = 1 + H_{1\bullet}^*(q^{-1})$$

Since the poles of the closed-loop will in general depend on the characteristics of the stochastic disturbance, the fixed prefilter $T(q^{-1})$ will no more compensate the closed-loop poles. Therefore the prefilter should be also adapted in order to take in account the drift of the closed-loop poles.[8]

V. APPLICATION TO NUCLEAR POWER PLANT

The nuclear plant results in a strongly nonlinear model. To a good approximation it can be approximated around the equilibrium point (Y_o, U_o, V_o) by a second-order empirical model with unknown variable parameters;

$$A(q^{-1})y(k) = q^{-d}B(q^{-1})u(k) + q^{-1}D(q^{-1})v(k) + C(q^{-1})w(k) \qquad (25)$$

where $y(k) = Y(k) - Y_o$, $u(k) = U(k) - U_o$, $v(k) = V(k) - V_o$ and $w(k)$ is uncorrelated white $N(0,\sigma)$ noise sequence. Here $Y=T_r$, $V=P$ and U is the control rod position. The deviation values are computed with respect to "corresponding reference values" Y_o, U_o, V_o. The unknown polynomials used in the application are defined by

$$A(q^{-1}) = 1 + a_1q^{-1} + a_2q^{-2},\quad B(q^{-1}) = b_o + b_1q^{-1}$$

$$C(q^{-1}) = 1\ , \qquad D(q^{-1}) = d_o + d_1q^{-1} \qquad (26)$$

and d=1, 1=2 due to transport lags with a 3-second sampling period.

The reference mode is defined as:

$$\frac{Y_M(k)}{U_M(k)} = \frac{q^{-d}B_M(q^{-1})}{A_M(q^{-1})} = \frac{q^{-1}(b_{mo} + b_{m1}q^{-1})}{1 + a_{m1}q^{-1} + a_{m2}q^{-2}} \qquad (27)$$

where $U_M(k)$ is the reference value of the average coolant temperature $T_{rw}(k)$. It is a linearly increasing function of load as

$$U_M(k) = 286 + 16.25\ V(k) \qquad (28)$$

and $Y_M(k)$ is the output of the reference model whose deviation is $y_M(k) = Y_M(k) - Y_o$.

A polynomial $T(q^{-1})$ specifying the desired closed-loop poles is chosen as

$$T(q^{-1}) = 1 + t_1 q^{-1} + t_2 q^{-2} \tag{29}$$

Polynomials $R(q^{-1})$ and $S(q^{-1})$ are defined as follows to satisfy Eq. 6.

$$R(q^{-1}) = 1, \; S(q^{-1}) = S_o + s_1 q^{-1} \tag{30}$$

The filtered deviation of the control input $u^f(k)$ is obtained from Eq. 19

$$T(q^{-1}) y_M^f(k+1) = \hat{\theta}(k)^T \theta^f(K) \tag{31}$$

where

$$\hat{\theta}(k)T = [\hat{b}_o(k) \; \hat{b}_1(k) \; \hat{d}_o(k) \; \hat{d}_1(k) \; \hat{s}_o(k) \; \hat{s}_1(k)] \tag{32}$$

$$\phi^f(k)^T = [u^f(k) \; u^f(k-1) \; v^f(k-1) \; v^f(k-2) \; y^f(k) \; y^f(k-1)] \tag{33}$$

$\hat{\theta}(k)$ is estimated by the use of PAA described by Eqs. 20-22. Finally, the control input variable U(k) is calculated from the filtered control input deviation $u^f(k)$:

$$U(k) = U_o + u(k) = U_o + L(q^{-1}) u^f(k) \tag{34}$$

A block diagram of the control system is given in Figure 2.

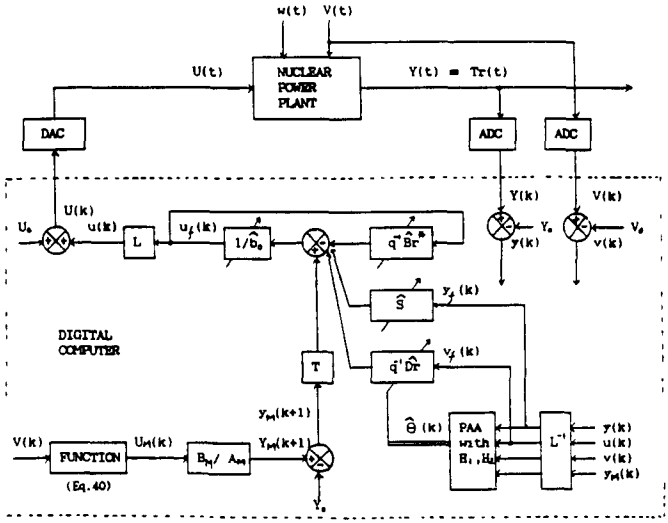

Figure 2. Adaptive control system for a nuclear power plant using self-tuning technique with reference model.

VI. EXAMPLE SIMULATION STUDIES

The nuclear power plant model consists of a large number of linear differential equations, together with some nonlinear effects, two transport lags, and some algebraic equations. It is simulated on a digital computer. The transport lags are simulated by second-order Padé approximations,[11] resulting in a ninth-order model.

The following numerical values are used in the simulation studies:

τ_1 = 11.3 s	τ_2 = 5.58 s
τ_3 = 2.03 s	τ_4 = 80.5 s
τ_5 = 2.08 s	T_1 = 5.0 s
T_2 = 7.0 s	D = 1.078
K_1 = 3.74 °C/s	K_2 = 102.7 °C/s
K_3 = 2.34E-3 Δk/k step^{-1}	ρo = 9.2852E-2 k/k
β = 6.5E-3	Λ = 3.0E-5 s
λ_p = 0.784 s^{-1}	α_f = -2.0E-5 C
α_m = -25.0E-5 C	

The operating condition of the plant is an equilibrium point at a demand power V_o = 80% and a rod position U_o = 135 steps and average coolant temperature Y_o = 299 °C. The reference model is chosen such that the overshoot is within 5%, the rise time is 2s and the DC gain is unity.

The typical demand power(P) for which the control algorithm is tested is shown in Figure 3 together with the desired (T_m) and the uncontrolled real (T_r) coolant temperatures. The controlled temperature together with its desired value and the corresponding rod position are shown in Figure 4 with filters. Other runs without filters show that the control rod goes up and down rapidly during the transient periods due to the perturbations of the estimated parameters and to the incompensation for the drift of the closed-loop poles. However, as shown in Figure 4, much of the rapid oscillatory behavior can be removed simply by the use of filters. This leaves the main control function much the same as achieved without filters, providing a very responsive adaptive load following system.

VII. CONCLUSION

An adaptive control system for a PWR nuclear power plant is developed with the use of a self-tuning technique with the reference model conception which is developed by combining MRAC and STC in order to overcome the difficulty of knowing how to specify the weighting polynomials for the cost function of the generalized self-tuning algorithm. The control system is designed based on the second-order approximated linear model with variable parameters for the complex nuclear plant dynamics.

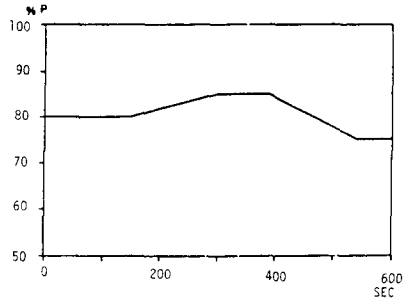

Fig. 3a. Example variation of the demand power (load).

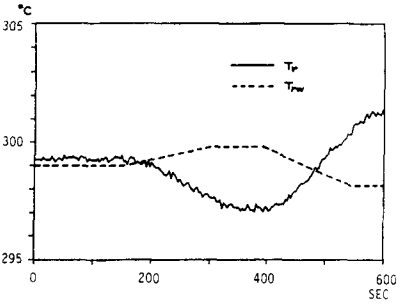

Fig. 3b. Uncontrolled average coolant temperature and setpoint for the load in Fig. 3a.

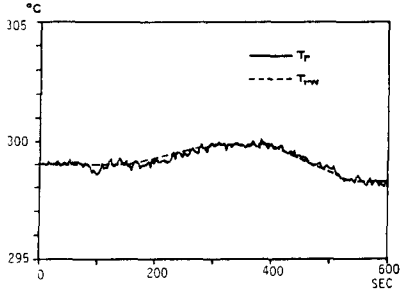

Fig. 4a. Controlled average coolant temperature and setpoint with filters.

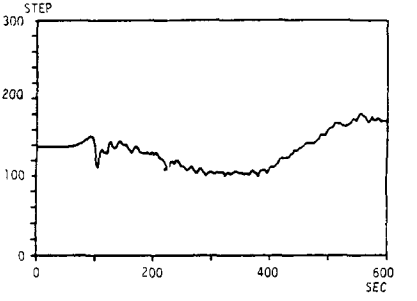

Fig. 4b. Position of control rods corresponding to Fig. 4a.

This study must be viewed as a preliminary investigation of the possible use of this type of adaptive control in a nuclear power plant. The results are quite promising and show that this control system provides good reference following capability.

ACKNOWLEDGEMENT

This work was partially supported by KOSEF grant No. 875-0707-001-2 and NSF Grant INT88-19095.

REFERENCES

1 R. K. Mehra and J. S. Eterno, "Applications of Adaptive Control," edited by K. S. Narendra and R. V. Monopoli, Academic Press, New York, 1980.

2 R. M. C. Keyser and A. R. Van Grauwenberghe, "Self-tuning Load Following Control of a Nuclear Power Plant," Pro. IFAC Symp. South Africa, 227-234, Sept. 15-19, 1980.

3 A. Y. Allidina and F. M. Hughes, "Self-tuning Control of a Nuclear Reactor," IEE Conf. 194, 118-122, 1981.

4 G. T. Park, "Self-tuning Control Application to a Nuclear Power Plant," Int. J. of Control, 43(6), 1823-1840, 1986.

5 G. T. Park and G. H. Miley, "Application of Adaptive Control to a Nuclear Power Plant," Nucl. Sci. and Eng., 94, 145-156, 1986.

6 I. D. Landau, "Adaptive Control, The Model Reference Approach," Dekker, New York, 1979.

7 I. D. Landau, "Adaptive Controllers with Explicit and Implicit Reference Models and Stochastic Self-Tuning Regulators-Equivalence and Duality Aspects," Proc. 17th IEEE-CDC Conference, San Diego, CA, USA.

8 I. D. Landau, "Combining Model Reference Adaptive Controllers and Self-Tuning Regulators," Automatics, 18, No. 1, 77-84, 1982.

9 S. Ulens, "Adatieve Optimale Kontrole van PWR Kernreaktoren," Automatic Control Laboratory, State University of Ghent, Belgium, 1977 (in Dutch).

10 L. Dugard and I. D. Landau, "Recursive Output Error Identification Algorithms Theory and Evaluation," Automatica, 16, 443-462, 1980.

11 K. J. Kurman, "Feedback Control Theory and Design," Elsevier, New York, 1984.

MONITORING NUCLEAR REACTOR SYSTEMS USING NEURAL NETWORKS AND FUZZY LOGIC

A Ikonomopoulos, L H Tsoukalas J A Mullens* R E Uhrig
Department of Nuclear Engineering
The University of Tennessee, Knoxville TN 37996-2300

* Instrumentation and Controls Division
Oak Ridge National Laboratory, Oak Ridge TN 37831-6010

ABSTRACT

A new approach is presented that demonstrates the potential of trained artificial neural networks (ANNs) as generators of membership functions for the purpose of monitoring nuclear reactor systems ANN s provide a complex-to-simple mapping of reactor parameters in a process analogous to that of measurement Through such 'virtual measurements' the value of parameters with operational significance, e g , *control-valve-disk-position valve-line-up* or *performance* can be determined In the methodology presented the output of a virtual measuring device is a set of membership functions which independently represent different states of the system Utilizing a fuzzy logic representation offers the advantage of describing the state of the system in a condensed form developed through linguistic descriptions and convenient for application in monitoring, diagnostics and generally control algorithms The developed methodology is applied to the problem of measuring the disk position of the secondary flow control valve of an experimental reactor using data obtained during a start-up The enhanced noise tolerance of the methodology is clearly demonstrated as well as a method for selecting the actual output The results suggest that it is possible to construct virtual measuring devices through artificial neural networks mapping dynamic time series to a set of membership functions and thus enhance the capability of monitoring systems

INTRODUCTION

Monitoring the performance of equipment and systems in a nuclear facility requires a program for recognizing whether the values of various parameters are within expected, normal off-normal and in general desirable or undesirable ranges The parameters to be monitored are typically specific to a particular system often the outputs of sensors and meters Thus for general plant equipment *voltage current, winding temperature oil* or *water temperature* and *pressure* are monitored For the power supply of a typical motor operated valve, for example one needs to monitor the *voltage, current* and *breaker position*, while monitoring the performance of a steam turbine driven pump requires attention to the indications of *speed, pressure* and *stop valve position* Generally the notions of *performance normal, undesirable* are quantified in technical specifications and operating procedures, in terms of set-points and ranges Yet, in the course of operations they are imputed with meanings that vary not only with the history of a particular system or equipment but also with different operators and the state of the plant as a whole

A *virtual measuring device* is a software-based instrument for the ' measurement of user-specified dynamic variables with operational significance Usually these variables cannot be measured directly, or the failure of a sensor requires that a variable be inferred from other measurements A promising feature of virtual instruments is that their function may be modified by changing their software not hardware Generally *measurement* involves a mapping of complex input patterns to simple output patterns Neural networks can map a complex input pattern of variables to a simplified set of membership functions representing the values of a fuzzy variable[1] They produce membership functions that uniquely and unambiguously represent the values of variables that are fuzzy, such as performance risk, operability and availability

The only fundamental requirements for useful measurements are the *precision* and *reproducibility* of the input-output relation and the functional value of the entire operation of the system doing the measuring The requirement of reproducibility means that the measuring device must be *isolatable* from the system being measured and *resettable* so that the measurements can be repeated an arbitrary number of times to give the same output for the same input pattern Both requirements are met by the artificial neural networks contemplated here

A major problem in the utilization of fuzzy logic for monitoring purposes is the difficulty in generating membership functions[1] In the proposed approach neural networks are used to map a set of time signals representing the state of a nuclear system to a set of membership functions that describe the values of a fuzzy variable, called in this study VALVE_POSITION As can be seen in the general schematic shown in Figure 1, a set of pre-trained neural networks are the receivers of several on-line time-series corresponding to vital nuclear system parameters They filter the noise of the time-series and calculate other system parameters not in the form of time-series but in the form of a membership function Each membership function corresponds to a different value of the monitored variable and has a unique shape.

NEURAL NETWORK - FUZZY LOGIC METHODOLOGY

Fuzzy logic is a convenient tool for describing a system whose behavior can be articulated in fuzzy "IF-THEN" rules[1]. For example, fuzzy rules utilized by fuzzy controllers, describe the relation between state variables and action or control variables, e g.,

IF **flow** is *high* AND **pressure** is *low* THEN **control-valve-position** is *open*.

where, **pressure** is a fuzzy variable describing the state of the system and *high* is one of its fuzzy values, **control-valve-position** is a control variable and *open* is one of its fuzzy values. The above rule is an association between flow, pressure and control-valve-position. Fuzzy logic algorithms have been demonstrated to be reliable and superior in performance to conventional systems[1,2,5]. One of the main issues in the development of these systems, however, is determining the membership functions that represent fuzzy values. In this approach we present a methodology for producing such membership functions via mappings employing neural networks.

The neural networks contemplated in this research are three-layer networks, as illustrated in Figure 2, (input, hidden, output layers). A number of input-output pairs, called examples, are presented to the network and the connection weights are adjusted until the network has "learned" the underlying relationship that the examples represent. This is called supervised learning and the process of weight adjustment is called training. The algorithm for training in the methodology presented is backpropagation with generalized delta rule and momentum term, as supplied by the Plexi software package. The change in weight w_{ji}, due to pattern p, on each connection is proportional to the product of the error signal δ,[6,7] e g.,

$$\Delta_p w_{ji} = \eta \, \delta_{pj} \, o_{pi} \tag{1}$$

where, o_{pi} is the ith component of the actual output pattern, and η is called the "learning rate "

The error signal for output neurons is computed as:

$$\delta_{pj} = (t_{pj} - o_{pj}) \, f_j'(net_{pj}) \tag{2}$$

where, t_{pj} is the jth component of the output produced by the network, and $f_j'(net_{pj})$ is semilinear activation function of the net total output.

The error signal for hidden units - for which there is no specified target - is calculated recursively in terms of those of the units to which it directly connects and the weights of those connections, that is:

$$\delta_{pj} = f_j'(net_{pj}) \sum_k \delta_{pk} w_{kj} \tag{3}$$

A linear threshold function can not be applied in this case, as in the perceptron, because it is discontinuous and its derivative does not exist. Instead we may use the logistic activation function:

$$o_{pj} = \frac{1}{1 + \exp(-\sum_{i} (w_{ji} o_{pi} - \theta_j))} \tag{4}$$

where, θ_j is called "bias." In order to incorporate a term that gives importance to previous weight changes on the current weight change, a "momentum" term is employed:

$$\Delta w_{ji}(t+1) = \eta (\delta_{pj} o_{pi}) + \alpha \Delta w_{ji}(t) \tag{5}$$

where, t is the iteration number, and α is a constant that characterizes the effect of previous weight changes on the current weight change.

In the application through which we examine the presented methodology the input layer of the network consists of five nodes, each one receiving input from a particular time series, i.e., simultaneous values of five variables. The output consists of four (three) nodes corresponding to the peaks of the trapezoidal (triangular) membership function describing the position of the Secondary Flow Control Valve Typically 50 learning cycles will produce a sum of square error of 0.02 when 10 nodes are used in the hidden layer.

After the networks are trained they receive on-line time signals as inputs and produce a set of membership functions as outputs. Generally the outputs will be somewhat different than the membership functions the networks were trained for and moreover one or at most two (if we allow overlap of membership functions) will represent correct values while the rest need to be ignored. It is thus important to identify the correct output. We consider the neural network outputs to be fuzzy numbers and use a *dissemblance index* [2] to estimate the distance between two fuzzy numbers. In this manner we estimate the outputs that are closest to the set of prototype membership functions we trained the network with and select them as the actual output of the monitoring virtual device at any given time.

Suppose, for example, that the network that recognizes the disk position value *closed* has been trained on the output membership function μ_{closed}, and after training it produces an actual output membership function μ^*_{closed} We consider the two membership functions as two fuzzy numbers, call them C and C^*, each with a trapezoidal shape and support on the universe of discourse [0,1]. The support of each function is an interval, i.e.,

$$C = [c_1, c_2,]$$
$$C^* = [c_1^*, c_2^*]$$

We can compute a numerical function $\delta(C, C^*) \in [0,1]$ which is the distance between C and C^*. The α-cuts for the two membership functions are denoted by, C_α, C^*_α, respectively. The *dissemblance index* of the prototype output, C and the actual output, C^*, is defined as:

$$\delta(C, C^*) = \int_{\alpha=0}^{1} \delta(C_\alpha, C^*_\alpha) \, d\alpha \tag{6}$$

When the universe of discourse is [0,1], we can easily derive from Equation 6 a value for the *dissemblance index* in terms of the support of each fuzzy value and the α cuts, $\alpha \in [0,1]$:

$$\delta(C, C^*) = \frac{1}{2} \int_{\alpha=0}^{1} \left(| c_1^{(\alpha)} - c_1^{*(\alpha)} | + | c_2^{(\alpha)} - c_2^{*(\alpha)} | \right) d\alpha \tag{7}$$

The *dissemblance index* is a number ranging from 0 to 1, representing the distance between two fuzzy numbers. If $\delta(C, C^*) \approx 0$ then C and C^* are almost identical, on the other hand, if $\delta(C, C^*) \approx 1$, then C and

C^* are totally different For a virtual gauge with three outputs, i e three trained networks the output with the lowest *dissemblance index* is chosen as the actual output at any given time with two outputs (overlapping membership functions) being given by the pair of values with the two lowest *dissemblance indices*

MODEL DESCRIPTION AND RESULTS

In order to demonstrate the proposed methodology we utilized actual data obtained during a start-up of the High Flux Isotope Reactor (HFIR), three-loop pressurized water reactor operated at the Oak Ridge National Laboratory The parameter which is to be simulated is the position of the Secondary Flow Control Valve This particular valve controls the flow of water in the secondary side of the system and is considered as a vital system component The data used is normalized in the interval 0 1 to 0 9 and sampled every 16 seconds, with a total of 1000 samples available for network training

Five parameters were chosen for describing the Secondary Flow Control Valve position **neutron flux primary flow pressure variation (DP), core inlet temperature core outlet temperature** and **secondary flow** (Figures 3, 4, 5 and 6) All but the last one of the above mentioned time series, contain average values of the corresponding parameters of the three loop system These parameters are selected in order to provide sufficient description of both the primary and secondary sides of HFIR during start-up The time series of these five parameters are used to train three neural networks where each one of them has five nodes at the input layer and four nodes at the output layer (Figure 2) The output is a membership function uniquely labeling a particular position of the Secondary Flow Control Valve

The behavior of the Secondary Flow Control Valve is represented in the space of alternatives (universe of discourse)[1 3] with the fuzzy variable **VALVE_POSITION** which may take three fuzzy values namely, **closed medium_open**, and **open** Each one of these fuzzy values is represented with a membership function, $\mu_{\mathbf{closed}}$, $\mu_{\mathbf{medium\_open}}$, and $\mu_{\mathbf{open}}$ These three membership functions describe the position of the valve at every instant during the start-up period A schematic of the membership functions[3 4] representing the values of the fuzzy variable **VALVE_POSITION**, is shown in Figure 7

The area occupied by every membership function in the universe of discourse depicts the uncertainty associated with that particular class[1] The fuzzy set (or class) **open** in the space of alternatives is characterized by a membership function $\mu_{\mathbf{open}}$ which associates each point in the universe of discourse with the value of $\mu_{\mathbf{open}}$ at this point, representing the grade of membership of that point in the class **open** It is apparent that such a framework provides a natural way of dealing with problems in which the source of imprecision is the absence of sharply defined boundaries of class membership rather than the presence of random variables[1] In the case under consideration the vagueness in the definition of the exact position of the valve disc introduces the fuzziness of the valve position and hence is the reason for the absence of sharply defined criteria. This means that although we deal with a deterministic system, the constraints and the goals set are fuzzy in nature The decision-making process takes place in a fuzzy environment where only the fuzzy goals and the fuzzy constraints can be defined as fuzzy sets (classes) in the space of alternatives The fuzzy decision will be the intersection of the given goals and constraints[2] In our case both goals and constraints are defined by the same set of classes

The membership functions utilized in this particular study have trapezoidal shape or the degenerated (triangular) form of it, which is very useful for computations in the fuzzy control area[2-4] The membership function $\mu_{\mathbf{closed}}$ (Figure 7) is defined by a trapezoid with peak coordinates {(0 09, 0), (0 1, 1), (0 3, 1), (0 5 0)}, where $\mu_{\mathbf{medium\_open}}$ (Figure 7) is represented by the triangle with coordinates {(0 3, 0) (0 5 1) (0 7 0)}, and $\mu_{\mathbf{open}}$ is depicted by the coordinates {(0 5, 0), (0 7 1), (0 9, 1) (0 91 0)} It is obvious from the above geometrical schemes that there is an overlap between the membership functions used The reason for the overlap is the fuzziness of the definition of the different states of the valve position It is characteristic of fuzzy logic to assume, that at a particular moment the valve may be described as **closed** and/or **partially open** Therefore, the uncertainty associated with instrument measurements is reflected on the position of the membership functions in the universe of discourse[2] Henceforth whenever the valve position is between 0 5 and 0 7 it could be characterized as **medium_open** as well as **open** (Figure 7) If the position is above 0 7 then it is definitely **open** This representation offers some unique advantages It maps a set of complicated time series to the universe of discourse of human linguistics, through a neural network which acts as an interpreter of vital information supplied from the nuclear system The information encoded in a time series is in the form of rate of increase/decrease, and

maximum/minimum values attained over a period of time The ANN is trained to represent this kind of 'hidden information in the form of membership functions which can be used by a rule-based diagnostician The shape of the membership function which has been assigned to each valve position is unique and therefore there is a sharp distinction between different states. The membership function provides sufficient information to describe the valve position at a particular time but also to predict the actual valve position in the near future Furthermore, an ANN trained to recognize a specific complicated time pattern will lose much of its ability to deal with noisy input signals since it will tend, for distorted inputs, to produce averaged forms of the desired output, missing therefore vital pieces of information[5]. This handicap can be overcome by the proposed technique which has an output that is a simple membership function[8]

As was pointed out, the position of the valve at a particular time step may be characterized by two membership functions instead of only one. The purpose of the pre-trained neural networks is to calculate both membership functions leaving the task of decision making to the fuzzy controller. Considering therefore the position of the different membership functions in the universe of discourse (Figure 7), the 1000 time steps (input vectors) used as input to the networks should be classified as listed in Table 1. It is apparent from Table 1, that although the neural network responsible for detecting the open position of the valve has to fire all the time steps between 228 and 805, the medium_open neural network is expected to fire also at the time step intervals 228 - 248, 358 - 504, and 612 - 805. This comes as a result of the particular design imposed on the membership functions.

In order to test the ability of each ANN to predict the valve position by calculating the right membership function at any particular time step, different levels of noise were introduced in the input signals. Initially up to 10% noise was introduced to all five input signals and the set of networks was tested with the "noisy" vectors. The appropriate networks fired at the corresponding time steps calculating the coordinates of the peaks of the corresponding membership functions with 98% accuracy. Henceforth there was an excellent prediction of the position of the disc valve during the whole time interval under consideration. Going one step further, 20% noise was introduced to all five input signals and the networks were tested again. The response of the system was the same as in the previous case, but this time the accuracy of the coordinate prediction dropped to 95%. Once again the accuracy of the network response was adequate to define the boundaries of the membership function responsible for firing. It is worthwhile to mention that the effect of noise at the input signals to the system response was expected to be minimum. The reasoning of that statement lays in Figures 3-6 where it is obvious that the initial signals contain a significant amount of noise. Therefore the set of pre-trained networks has already been exposed to noise during the training process. As a result the extra noise added to the input vectors during the testing process tends to distort the information contained in the original signal in a small degree. Certainly the effects of noise would be more pronounced if the original signals were noise free This does not apply in this study, since the data have been obtained from actual reactor operation and not from simulation.

The response of the system during testing may be shown in Figures 8-11 where the results have been summarized for both cases of noise addition. During the first 208 time steps (Figure 8) the neural network responsible for recognizing the closed condition fired throughout the testing interval. For the next 18 time steps (209-227) (Figure 9) both the closed and medium_open networks fired since the condition of the valve could be characterized as closed as well as medium_open. The ambiguity existing in the response of the system is to be resolve by the fuzzy controller. When the data corresponding to time steps 228-805 were tested (Figure 10), the closed network did not fire at all, and this time the medium_open and open networks were active. The prediction of the valve position remained to be open throughout this time interval as well as medium_open at particular time periods. During time steps 228-248, 358-504, and 612-805 the position of the valve disc was predicted as being medium_open, since the valve was not sufficiently open to be classified as strictly open. At the final testing period (806-1000) (Figure 11), the closed network was activated again. During time steps 806-899 the valve position was calculated as both closed and medium_open. This appears plausible since there should be a smooth transition between different states of the valve.

It is obvious from the previous description that the valve position was never calculated as medium_open alone. This is a direct consequence of the artificial separation of the universe of discourse. All points in the interval [0.3, 0.5] in the universe of discourse, are considered as belonging to membership function closed also The rest of the $\mu_{\mathbf{medium\_open}}$ space (0.5, 0.7], is occupied by the $\mu_{\mathbf{open}}$ also. Hence whatever value calculated from the network in the range [0.3, 0.7] is going to be classified not only as medium_open but either open or closed as well. It should be stressed that this particular division of the space of alternatives is widely suggested in the bibliography by different authors[2,5] A more articulate segmentation of the universe of discourse would offer the advantages of more meticulous representation of the state of the valve, but on the other hand it would greatly complicate the

system since a greater number of neural networks would be required Furthermore, characterizations as **almost_open**, **very_closed**, etc , do not seem appropriate in this particular application Membership function modifiers like "almost" and "very" are mostly used in classification problems dealing with more complex categorizations than the one used here[2]

CONCLUSIONS

A methodology for monitoring nuclear reactor systems employing neural networks and fuzzy logic has been developed. It employes the notion of *virtual device*, i e , a software-based instrument for the "measurement" of user-specified dynamic variables with operational significance The function of such devices may be modified by changing their software, not hardware, a promising feature for application-specific monitoring tasks Neural networks are employed to map a complex input pattern of variables to a simplified set of membership functions The produced membership functions uniquely and unambiguously represent the values of variables that are fuzzy, such as performance, risk, operability, and availability

One of the very first points to be made on the basis of the results discussed in the earlier section is the noise tolerance demonstrated by the ANNs. The ability of the neural network to pick up the necessary information from a signal embedded in 20% noise is unique Neural networks have been widely used before[8] in order to reproduce time patterns. Unfortunately a time series is not always helpful for decision making, since it is highly complicated and its representation hardly exact[5] In this study ANNs have been integrated with the representational advantages of fuzzy logic in order to produce fuzzy membership functions.

The representation of the form of the membership functions is sufficient for preserving the necessary information in order to distinguish between different states of the valve. It is apparent that, with the demonstrated methodology, the valve position could be adequately classified as belonging to one (or two adjacent) class(es) as soon as the information "hidden" in the time series is supplied to the neural networks This offer the advantage of predicting the position of the valve for the next few time steps. Introducing membership functions as the output of the ANNs, facilitates automated decision-making by a fuzzy logic diagnostic system that determines the condition of the valve. Furthermore it is not necessary to proceed to full time series analysis in order to infer the valve position, but on the contrary, it is adequate to make a decision after the ANN gives the same response for a number of consecutive time steps[8] The quality of the information provided by the ANN suggests that a fuzzy logic identifier - with a minimum decision making window - would be able to diagnose the exact state of the system

REFERENCES

1. Zadeh, L. A , "Fuzzy Sets," Information and Control, 8, pp 338-353, 1965
2. Kaufmann, A., and Gupta, M.M , Introduction to Fuzzy Arithmetic,Van Nostrand Reinhold, New York, 1991.
3. Zadeh, L.A., "Fuzzy Logic," in IEEE Computer, pp 83-93, April 1988
4. Ragheb, M. and Tsoukalas, L., "Monitoring Performance of Devices Using Coupled Probability-Possibility Method," International Journal of Expert Systems, 1, 1988
5. Tsoukalas, L., Ikonomopoulos, A., Uhrig, R , "Hybrid Expert System - Neural Network Methodology for Transient Identification", Proceedings of the American Power Conference, pp. 1206-1211, Chicago, IL, April, 1991
6. Khanna, T., Foundations of Neural Networks, Addison-Wesley, Publishing Co., Boston, 1990.
7 McClelland, J., Rumelhart, D., Explorations in Parallel Distributed Processing, The MIT Press, Cambridge, 1986.
8. Ikonomopoulos, A., Tsoukalas, L , Uhrig, R , "A Hybrid Neural Network - Fuzzy Logic Approach to Nuclear Power Plant Transient Identification", Proceedings of AI91 Frontiers in Innovative Computing for the Nuclear Industry, pp. 217-226, Jackson, WY, September, 1991.

TABLE 1: TIME STEP CLASSIFICATION

Time Step Number	μ_{closed}	μ_{medium_open}	μ_{open}
001 - 208	*		
209 - 227	*	*	
228 - 248		*	*
249 - 357			*
358 - 504		*	*
505 - 611			*
612 - 805		*	*
806 - 899	*	*	
900 - 1000	*		

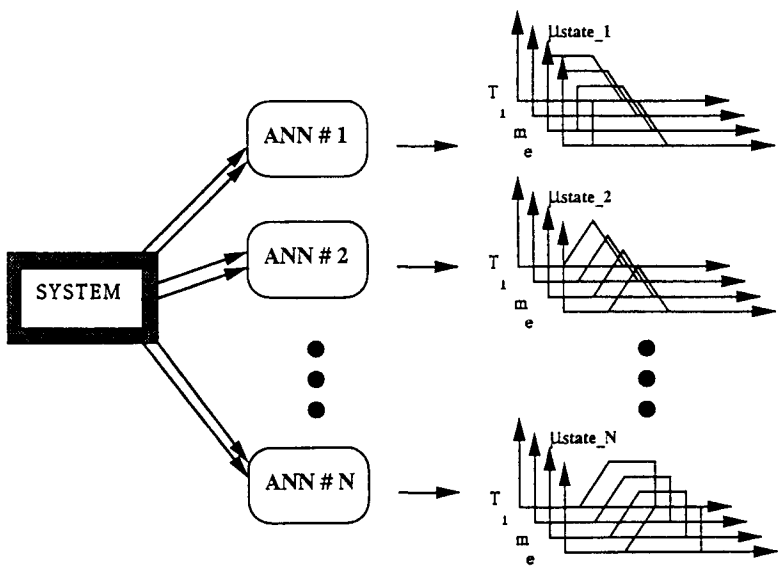

Figure 1 A hybrid neural network - fuzzy logic monitoring system

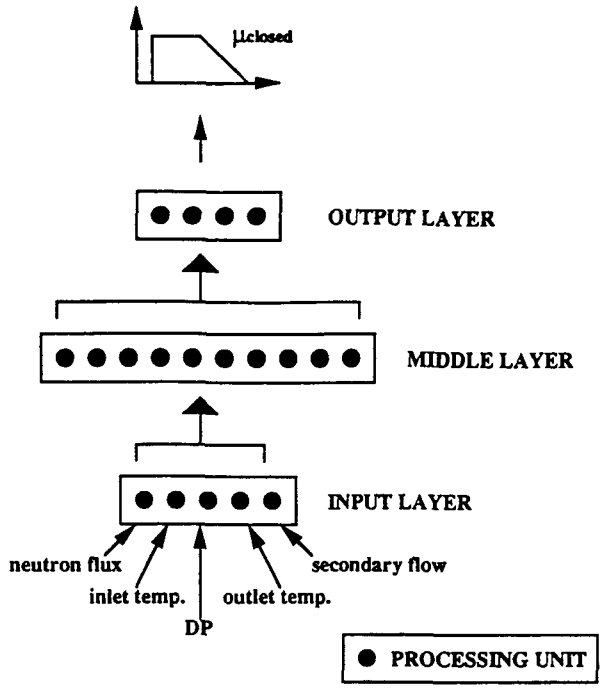

Figure 2. Neural network architecture.

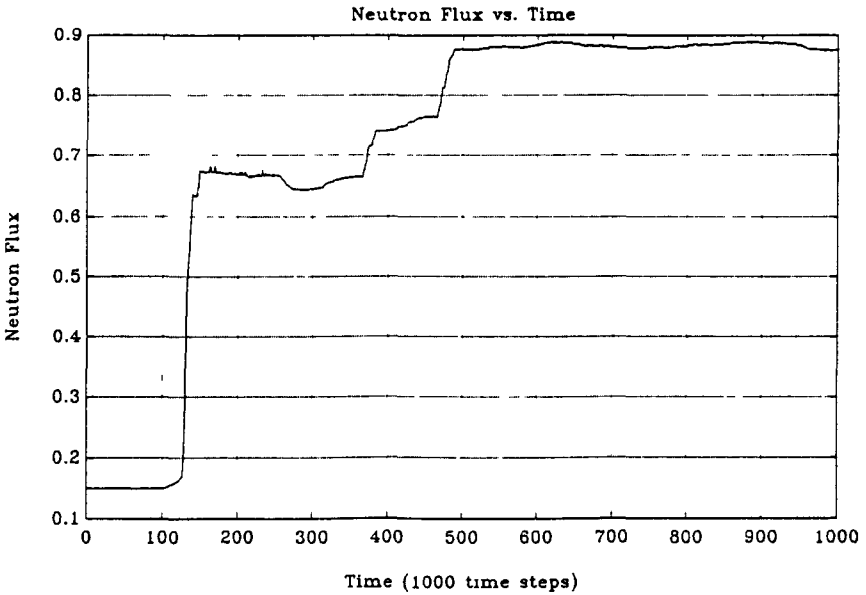

Figure 3. Neutron flux during startup of the reactor (normalized).

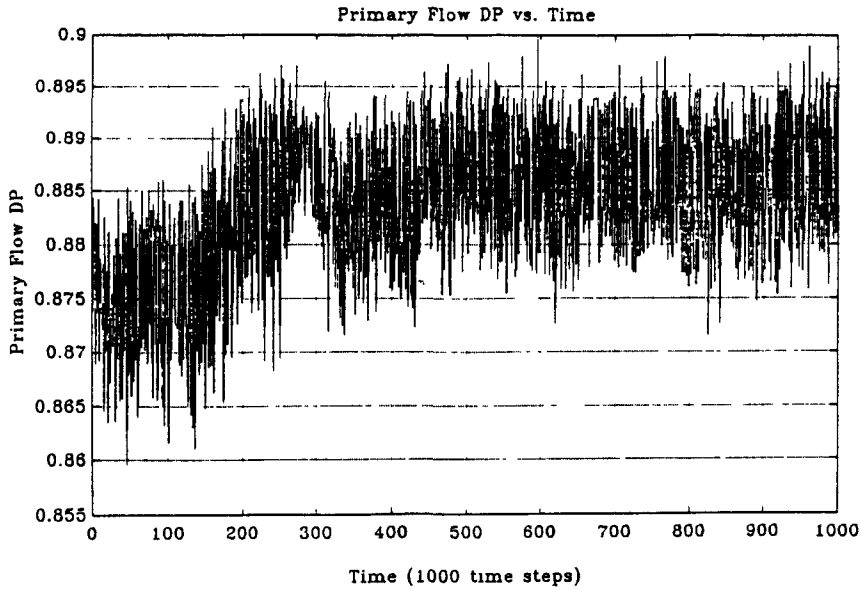

Figure 4. Primary flow ΔP during startup of the reactor (normalized).

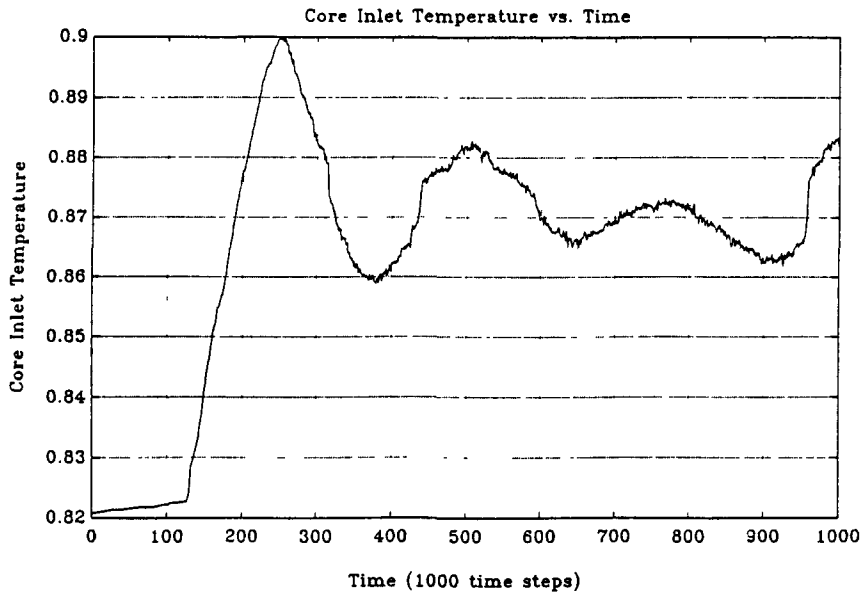

Figure 5. Core inlet temperature during startup of the reactor (normalized).

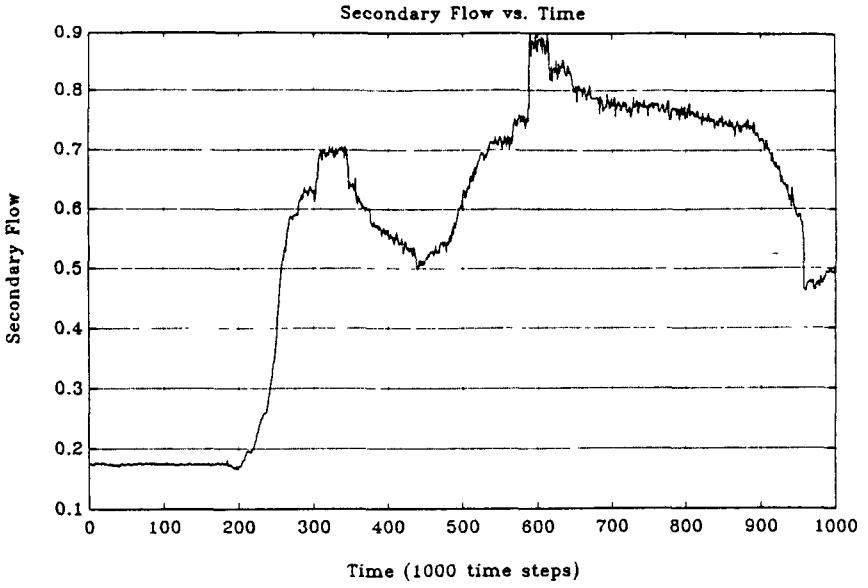

Figure 6. Secondary flow during startup (normalized).

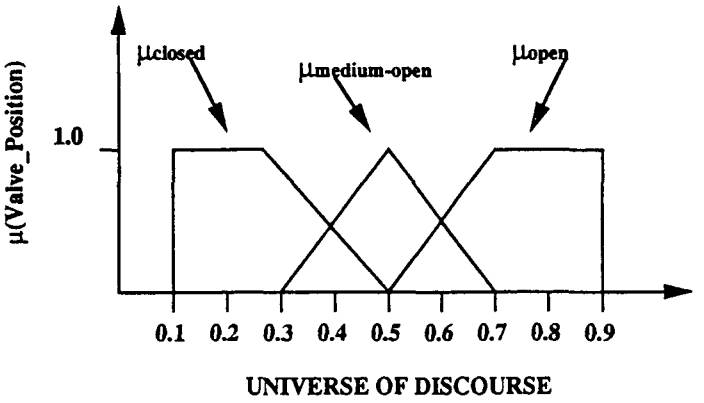

Figure 7. Fuzzy values for the monitored variable VALVE_POSITION.

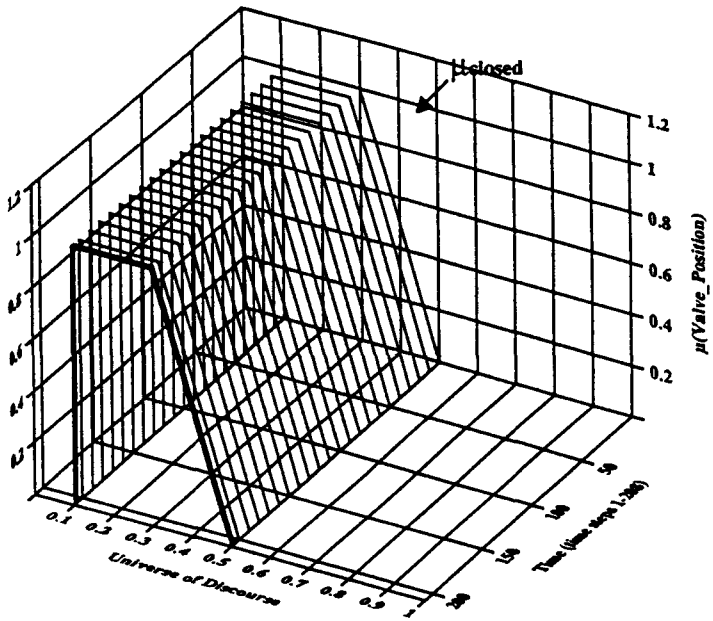

Figure 8. The membership function for the value of VALVE_POSITION during time steps 1-208.

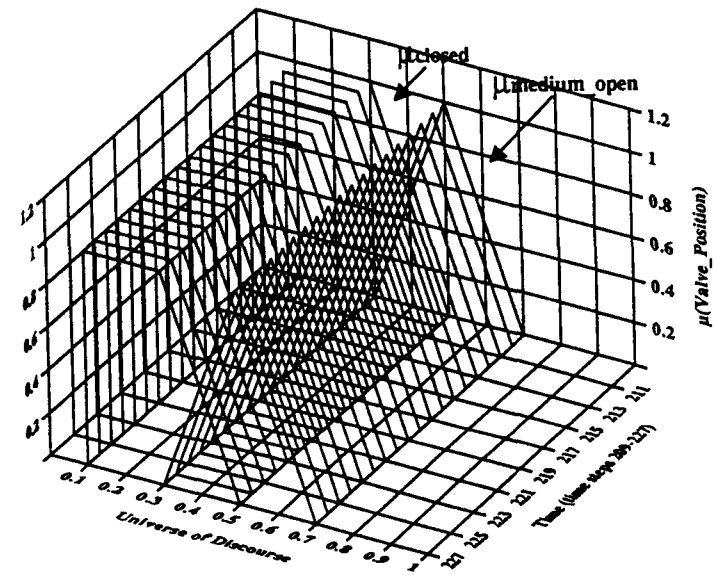

Figure 9. The membership function for the value of VALVE_POSITION during time steps 209-227.

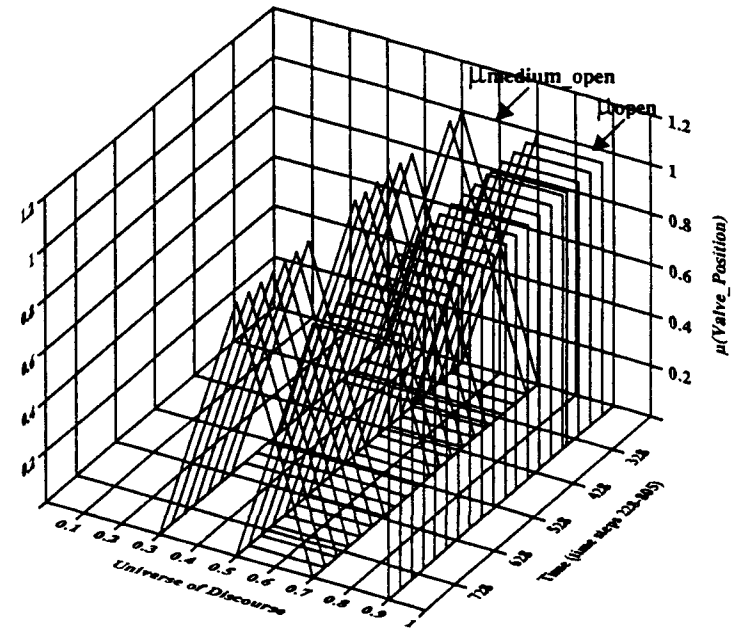

Figure 10. The membership function for the value of VALVE_POSITION during time steps 228-805.

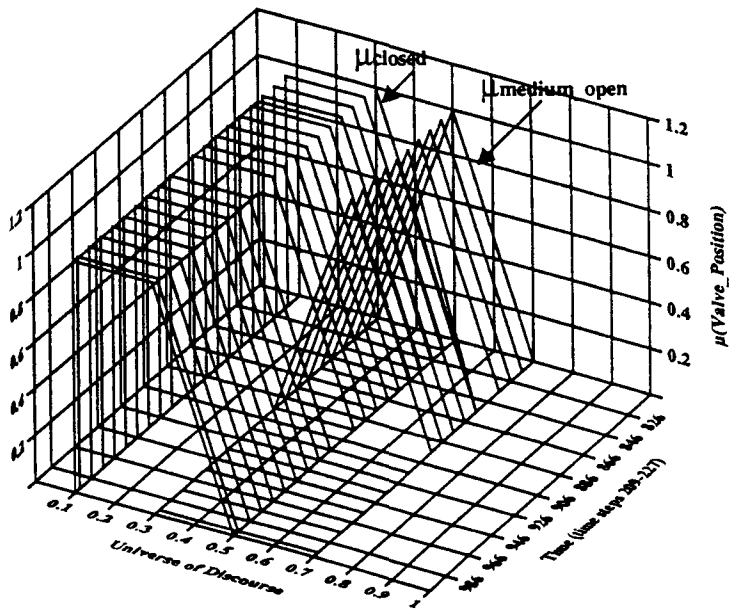

Figure 11. The membership function for the value of VALVE_POSITION during time steps 806-1000.

MODULAR PLANT ANALYSER OF AN ENTIRE POWER PLANT: EXTENT AND VALIDATION

E.K. Puska, M. Hänninen and
J. Ylijoki
Technical Research Centre of Finland
Nuclear Engineering Laboratory
P.O. Box 208
SF-02151, Espoo,Finland

K. Porkholm
Imatran Voima Oy
P.O. Box 112
SF-01601 Vantaa,Finland

ABSTRACT

The present paper concentrates on the description of the contents of the Modular Plant Analyser of the VVER-440 type Loviisa Nuclear Power Plant and on the summary of the validation work that has been performed. The plant analyser is based on the APROS simulation environment. The plant analyser contains quite detailed description of the plant including nuclear and thermal hydraulic modelling of the reactor core, thermal hydraulics of primary and secondary circuits, plant automation system and plant electrical system. An important part of the validation work has been comparison of plant analyser results with plant measurement data. In addition, comparisons of plant analyser results with LOviisa full-scope Training Simulator (LOTS) results and with results of some well-verified codes have been included. Two detailed validation examples discussing the effects of the novel features of the plant analyser thermal hydraulics have been included, too. The paper ends with a short discussion on the applicability of the present plant analyser for other types of plants.

INTRODUCTION

Modular plant analyser of the 465 MWe VVER-440 type Loviisa Nuclear Power Plant has been developed during the years 1988-1991 in a co-operation project of Imatran Voima Oy (IVO) and Technical Research Centre of Finland (VTT). Information on the progress during this effort has been given in some previous reports[1-2]. The extent of this project has been some 25 man years. The Loviisa Plant Analyser (LPA) development has been based on the APROS simulation environment that was produced in an earlier co-operation project during the years 1986-1988. The extent of the APROS-project was some 40 man years. Outline of APROS simulation environment is shown in Figure 1.

Loviisa Plant Analyser can be used either via an alphanumeric

computer terminal or via a graphical workstation. With either means the user can easily construct and/or alter the model of an entire plant using the predefined process components of the system. Process components for nuclear applications include the nuclear reactor model with one- and three-dimensional core alternatives, pressurizer, both horizontal and vertical heat exchangers, turbine section, condenser, tank, several kinds of pumps, pipes and valves, and a large number of automation and electrical system components.

The modular plant analyser has been developed on Alliant FX/40 computer. At present the plant analyser is also available for VAX/VMS computers and for HP-9000/400 and 700 series workstations and DECstation-5000 series workstations.

EXTENT OF PLANT ANALYSER

The components described in the plant analyser in the primary circuit are the nuclear reactor with one- and three-dimensional alternatives, the pressurizer, the six primary loops with horizontal heat exchangers and primary coolant pumps and the core emergency cooling system. On the secondary side of the Loviisa plant there are two turbine units. Thus the secondary circuit model consists of two identical halves each separately described. The components include the high pressure turbines, the intermediate superheaters, the low pressure turbines, the condensers, the low pressure preheaters, the feedwater system and the high pressure preheaters.

The main control systems described in the plant analyser include the plant and power controller, the reactor control, the steam generator level control, the primary circuit pressure control and the pressuriser water level control. Several auxiliary control systems have been included, too.

The plant automation system and plant protection system contain all the essential components. The plant electrical system is described and the plant containment model is also included.

The extent of the present plant analyser model is given in Table 1 in terms of calculational level items comparable to those used in common safety analysis codes. The main components of the primary and secondary circuit with their nodalisation have remained practically constant already for the last 1-2 years. The increase in the extent of the model has taken place mainly in the number of auxiliary systems and in increasing the details of already existing systems.

The plant analyser graphical user interface provides a convenient way of creating a process, starting and controlling the simulation and viewing the simulation results. APROS plant analyser graphical user interface is based on the X Window

System and OSF/Motif and it operates on any VAX/VMS or UNIX computer that has been equipped with suitable interface libraries. In addition to the alphanumeric and graphical user interfaces a process control and display system is available. This operates on a PC and can be connected to APROS via a local area network.

Plant analyser database has been realised using APROS simulation environment database language that provides a means for building the simulated process and controlling of the simulation process. The database contains basic model definition data and system variables. The database is structured in a form which is suitable for vectorisation. The APROS model libraries contain elementary components. The database structure allows also building of more complex structures, such as parametrizable process components and complete subprocesses used in the description of LPA. The entire process to be simulated is also defined via the database commands.

PLANT ANALYSER MODELS

NUCLEAR REACTOR

For nuclear reactor core neutronics modelling there are two alternatives: the one-dimensional model and the three-dimensional model. The one-dimensional model uses two energy groups and six delayed neutron groups. The basic equations are first discretised, then the terms are regrouped and the resulting matrix equation is solved. Calculation of iodine, xenon, samarium and promethium with a user-selected speedup-factor has been included, too. When using the one-dimensional model the core is usually divided into 10 - 30 axial sections. The one-dimensional neutronics model is very fast and it agrees well with the 'real-time' requirement of the plant analyser.

The one-dimensional neutronics model can be combined with a so-called semi-3-dimensional core model, which enables very fast 'three-dimensional' core modelling. The model is primarily ment for demonstration of basic three-dimensional effects. Thus the model uses the results of the one-dimensional core model and user-given core power distribution and subchannel information as input. The number of subchannels defined by the user is typically 20-30. Each subchannel is calculated using the same axial discretisation as in the one-dimensional model. Neutronic and thermal hydraulic analysis for each subchannel is performed in stationary form. Two energy groups and six delayed neutron groups have been used. For each timestep a user-given number of subchannels (typically 1-3) is calculated. In addition, all channels where control rods are moving during the timestep will be calculated. At present the model does not have any feedback to the one-dimensional solution.

The modular plant analyser models include also a true three-dimensional core neutronics model. This uses two energy groups and six delayed neutron groups. The basic equations are first discretised as in the one-dimensional model. The neutron flux equations are then integrated over the node volumes, a few approximations are made and the flux equations are finally solved using Gauss-Seidel iteration process. The delayed neutron groups are obtained as in the one-dimensional model. Iodine, xenon, promethium and samarium calculations are included, too. The Loviisa core has hexagonal geometry. However, the three-dimensional model is also able to describe quadrilateral geometry. In the three-dimensional model the total number of neutronics nodes is about 3600. This results from description of each fuel element at horizontal level as a separate node and from the division of the core in axial direction into ten sections. This model does not, of course, fulfil the real-time requirement. Use of the real three-dimensional model increases the simulation time typically by a factor of 4-10.

THERMAL HYDRAULICS

The thermal hydraulic models available in the modular plant analyser are homogeneous two-phase flow model, separated two-phase flow model with either a 5-equation formulation or true 6-equation formulation, all in one-dimensional form. Three-dimensional homogeneous two-phase flow model is also available. All these models have been obtained by discretisation of the basic equations, linearisation of the nonlinear terms and implicit solution of the resulting equations.

In case of the separate two-phase flow model the user can select either 5-equation or 6-equation alternative. In the 5-equation model the drift flux approach has been applied to describe the different flow velocities of the phases. All flow models include the connnection to the one-dimensional heat conduction model for the solid structure heat flows. Each flow system has its own heat transfer correlation package for the calculation of the heat transfer between the fluid and the heat structures.

Process components like pipes, valves, pumps and heat exchangers can be used with any of the flow models. In the present Loviisa plant analyser the primary circuit including the steam generators is simulated with the 5-equation model and the secondary side with the homogeneous model. The flow models can also be mixed using existing connection components.

The 6-equation model has not yet been used for the simulation of the Loviisa plant, but it has been verified by calculating several separate effect tests. With the aid of tests the interfacial and wall friction correlations as well as interfacial and wall heat transfer correlations have been verified. The experiments calculated so far include the horizontal pipe blow-down experiment or so called Edwards pipe,

the Battelle top-blowdown experiment, Becker's test facility for steady state dryout and Ersec-reflooding test. For the simulation of the reflooding phenomena the heat conduction model has been extended to two dimensions by taking into account the axial heat conduction in the cylindrical coordinate system. For the description of the rewetting front also the moving mesh techniques can be used.

In the final version of the plant analyser the user can select either the 5-equation or the 6-equation two-phase flow model for the primary circuit. The secondary circuit thermal hydraulics will be described with the homogeneous two-phase flow model. Previously also the primary circuit thermal hydraulics was described with the homogeneous two-phase model with the pressurizer described as a tank with separated volumes. The three-dimensional flow model will be used for the downcomer analysis.

AUTOMATION AND ELECTRICAL SYSTEMS

The plant analyser automation system has been constructed using the automation system library of the APROS simulation environment. This contains over 60 components. It enables accurate simulation of most contemporary automation concepts. The plant analyser electrical system has been realised using the APROS electrical components. These enable both modelling of the plant electrical system and grid outside the plant. The process components can be easily connected to the electrical system with a name reference.

CONTAINMENT

The containment model in the plant analyser is based on the common compartment formulation. Heat structures, leakage and sprinkler flows are allowed in any compartment. The compartment atmosphere can contain water droplets. Since the reference plant contains an ice-condenser, a special model for this has been included.

PLANT ANALYSER VALIDATION

Validation efforts of the plant analyser have been performed simultaneously with the plant analyser development. The validation efforts have consisted of three major parts: comparison with the real plant data, comparison with the Loviisa full-scope replica training simulator results and comparison with the results of well-verified computer codes.

The validation efforts have largely concentrated on the validation of the model versus the real plant data. This choice has very practical reasons: since the purpose of the development is a plant analyser of an existing plant it should be tested in conditions where all the essential features of the real plant

including the control systems are described. Most of the actual Loviisa plant measurement data that has been used in the plant analyser validation originates from the plant dynamical tests that were performed during the start-up phase of the Loviisa unit 2 in 1981. The plant data test material contains also two real plant transients. The first case is the feedwater line break that took place at Loviisa plant unit 1 in 1990. The second case is the primary circuit overcooling transient that took place at Loviisa plant unit 2 in 1981.

The major plant analyser validation cases using real plant data have been given in Table 2. The table indicates the success of the plant analyser in each case, and a short comment. The results of all cases have been reported in detail. It has been found out that the plant analyser has been able to describe the behaviour of the plant main parameters well in all cases. However, in a few cases renewed simulation with improved models would be needed for good performance. In this type of validation, proper modelling of the plant control systems and possible operator actions is essential in order to produce results that would be comparable with the plant data.

Comparison of the plant analyser results with the Loviisa Training Simulator (LOTS) has been another important part in the validation. This effort has contained two parts: operational transients and ATWS-events. Some examples of these validation cases with a short comment on the plant analyser performance have been given in Table 3. In general the plant analyser performance has been very satisfactory in these cases, as can be observed from the results indicated in the table. However, in some cases a new simulation with improved models is required.

Validation of the plant analyser using the results of some other well-verified codes has had a much smaller volume than the validation using either the real plant data or the Loviisa Training Simulator results. However, a few such cases have been included. Examples of these have been included in Table 3, too. It can be seen that the plant analyser performance in these cases has been in general quite satisfactory. Some cases need recalculation with improved models, like the separated two-phase flow model. The major part of this type of comparison is still to come. It will include comparison of plant analyser neutronic and thermal hydraulic model results in severe transients with the results of well-verified reactor physics and thermal hydraulics codes.

PLANT ANALYSER VALIDATION EXAMPLES

The two validation examples concentrate on the novel features of the plant analyser thermal hydraulics. In the first case the results of the heterogeneous two-phase flow model using the 5-equation description and the results of the homogeneous two-phase flow model have been compared with real plant data in the case of trip of one primary circuit coolant pump.

The available plant main measurement parameters for this case were the plant neutronics power, the primary circuit pressure and the secondary circuit pressure. Results of the homogeneous two-phase flow model versus data have been presented in Figure 2 and the corresponding results for the two-phase flow model in Figure 3. The figures show that both models are able to predict well the main parameter behaviour in this case. The differences in the predictions of these two models are very small. Further, the results indicate that in this case the homogeneous model would be quite adequate for describing the transient behaviour. The calculation time of the plant analyser with both flow model alternatives in the example was practically the same. The plant analyser is capable in present configuration to real-time calculation using a 0.5 second time-step with Alliant FX/40 (one processor).

In the second case the results of the heterogeneous two-phase flow model using the real six-equation formulation have been discussed with the help of the Battelle top-blowdown experiment (OECD standard problem 6). Figure 4 shows the calculated and measured water levels[3]. It can be seen that the model is able to describe the water level behaviour very well. Figure 5 shows the calculated and measured mass flow at the discharge orifice. The mass flow starts to increase vigorously when the water level in the tank has reached the discharge level. In the calculated result the mass flow starts to increase nearly at the right moment in comparison with the data and the maximum mass flow agrees well with the data. However, the calculated increase in mass flow is somewhat slower than the measured result, which indicates that the model cannot describe the liquid and gas interface as sharply as in reality. The 6-equation two-phase flow model is estimated to be by a factor of two slower than the homogeneous or 5-equation alternatives.

PRESENT AND FUTURE APPLICATIONS

Apart from the validation work the present plant analyser has been used as a help in studying the Loviisa plant systems. In one case the APROS model studies were used when deciding upon the need of pump change in the existing emergency pump system. The simulations indicated that the existing emergency pump system was able to ensure sufficient cooling. Thus the pump change could be avoided. The APROS models have also been used in designing the control system for the new high pressure pre-heaters at the plant. These applications emphasize the importance of complete plant analyser model that has been validated using real plant data.

The components used in the present plant analyser have already been employed successfully in building the plant analyser for VVER-1000 type plant at IVO. This VVER-91 simulation model contains the description of the primary

circuit, the secondary circuit and the main control systems. The extent of this model can be characterised with the following numbers: 235 thermal hydraulic nodes, 289 thermal hydraulic branches, 296 heat structure nodes, 188 heat structure branches, 411 analog signals and 595 binary signals. The model is used at IVO with DECstation-5000/200 workstation.

The most natural expansion of modular plant analyser of the Loviisa plant is, of course, to other VVER-440 type reactors. However, none of these have been performed yet. In these cases the most remarkable differences are expected to be found in the plant automation system description.

Minor pilot-type applications have also been performed with some other PWR-plants. In principle the process components can also produce a BWR-type plant. However, the true validity of the present components in BWR-applications will be measured in context of future projects.

CONCLUSIONS

As a concluding remark it can be pointed out that a modular plant analyser of an existing power plant has been created. The plant analyser is capable of real-time simulation of the plant (with Alliant FX/40, one processor) when one-dimensional core model is used. The plant analyser has been validated quite extensively with existing data. Validation results have been very satisfactory. The physical models and process components created during the Loviisa Plant Analyser development have already been used to some extent in the development of plant analysers for other types of plants.

REFERENCES

1 E.K. Puska et al., Simulation of ATWS Transients with APROS, Proceedings of the International Conference on the Physics of Reactors: Operation, Design and Computation, April 23-27, 1990, Marseille, France, Vol.4, pp. PV.95-PV.105.

2 E.K. Puska and K. Porkholm, Plant Analyser of Loviisa NPP, Proceedings of the International Topical Meeting on Advances in Mathematics, Computations, and Reactor Physics, April 28 - May 2, 1991, Pittsburgh, PA, USA, Vol.3, pp.12.2 4-1...4-12.

3 J. Ylijoki, Calculation of Friction and Interfacial Heat Transfer in a Two-Phase Flow Model, Master's Thesis, Helsinki University of Technology, 1991.

Table 1. Extent of Loviisa Plant Analyser at Calculational Level

Item	Number
Neutronics Nodes (1-D)	10
Neutronics Nodes (3-D)	3600
Thermal Hydraulic Nodes	473
Thermal Hydraulic Branches	562
Heat Structure Nodes	296
Valves	330
Pumps	31
Turbine Sections	18
Analog Signals	778
Binary Signals	2023
Controllers (P, PI)	37

Table 2. Loviisa Plant Analyser Validation using Plant Measurement Data

Case	Behaviour	Comment
Steady State Operation	Good	Main parameters within 2 %
Step Load Test	Good	Main parameters within 5 %
Reactor Trip	Good	Main parameters within 5 %
Feedwater Pump Trip	Good	All main parameters OK.
Primary Coolant Pump Trip	Good	Main parameters within 5 %
Trip of Two Primary Coolant Pumps	Good	All main parameters OK.
Trip of One Turbine	Good	Main parameters within 5 %
Feedwater Line Break	Good	Main parameters within 5 %
Daily Regulation Test	Good	All main parameters OK.
Short-Term Regulation Test	Good	All main parameters OK.
Black-out Test	Fair	All main parameters OK. Performed with incomplete electrical system.
Primary Circuit Overcooling Transient	Fair	All main parameters OK.

Table 3. Loviisa Plant Analyser Validation using Loviisa Training Simulator Data and Code Results

Case	Behaviour	Comment
Control Rod Group Movements	Good	LOTS; All main parameters OK.
Xenon transient	Fair	LOTS; All main parameters OK.
Loss of Feedwater/ATWS	Poor	Code; Most main parameters OK Homogeneous flow model
Turbine Trip/ATWS	Good	LOTS&Code; All main param. OK
Steam Line Break/ATWS	Good	Code; All main parameters OK
Small Break LOCA/ATWS	Good	LOTS&Code; All main param. OK
Opening of Pressurizer Safety Valve/ATWS	Good	LOTS; All main parameters OK
Large Break LOCA/ATWS	Fair	Code; All main parameters OK
Control Rod Withdrawal/ ATWS	Good	LOTS&Code; All main param. OK.

Figure 1. APROS Simulation System.

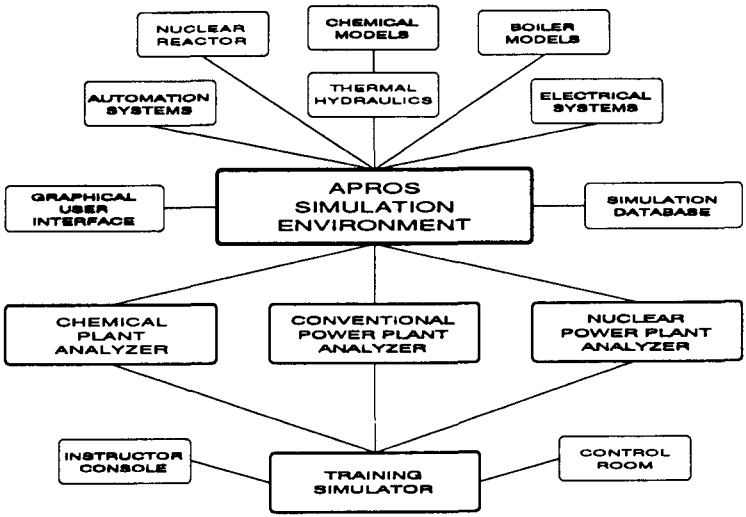

Figure 2. Loviisa Plant Analyser Results with the Homogeneous Thermal Hydraulic Model (curves) for Trip of One Primary Coolant Pump and Corresponding Plant Data (dots).

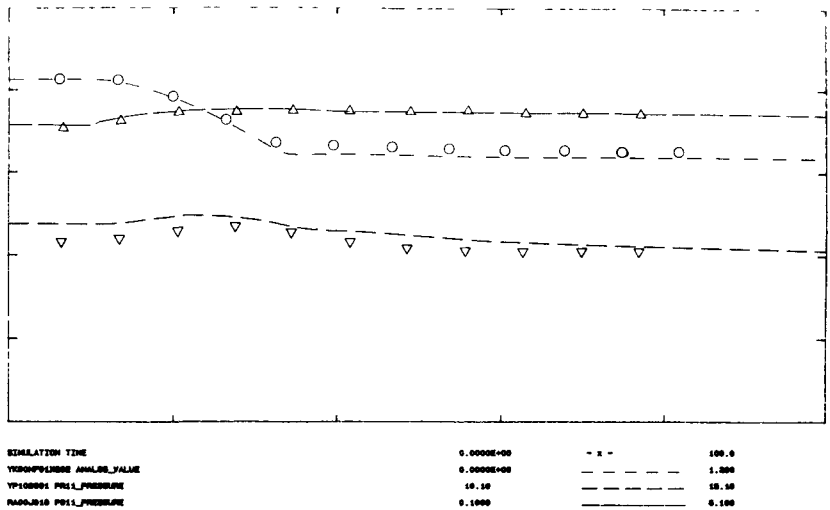

Figure 3. Loviisa Plant Analyser Results with the Five-equation Thermal Hydraulic Model (curves) for Trip of One Primary Coolant Pump and Corresponding Plant Data (dots).

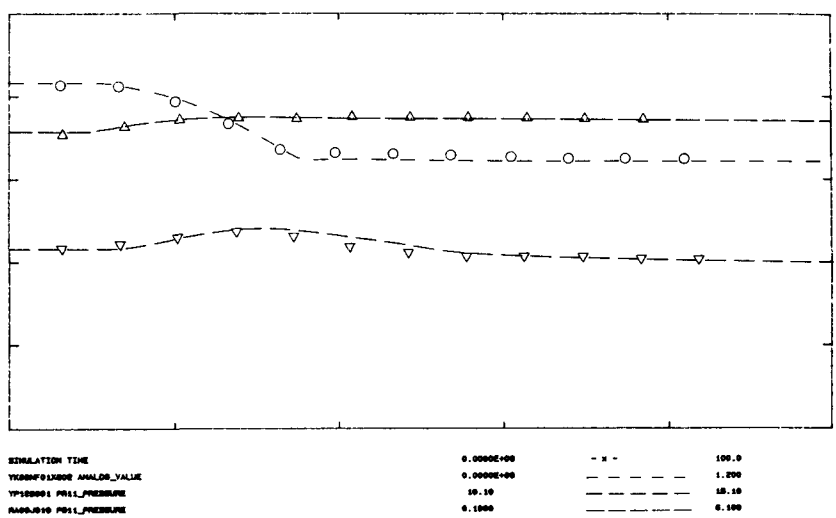

Figure 4. Plant Analyser Six-Equation Thermal Hydraulic Model Results (continuous line) for the OECD Standard Problem 6 and Corresponding Reference Data (broken line). Water Level in the Tank.

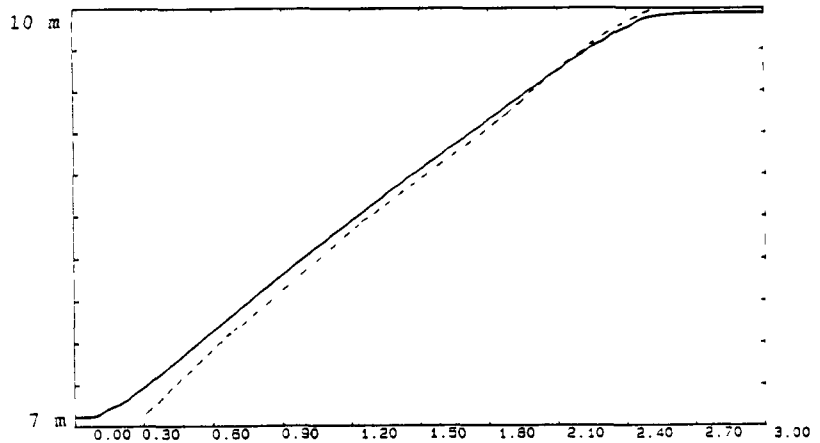

Figure 5. Plant Analyser Six-Equation Thermal Hydraulic Model Results (continuous line) for the OECD Standard Problem 6 and Corresponding Reference Data (broken line). Mass Flow at Discharge Orifice.

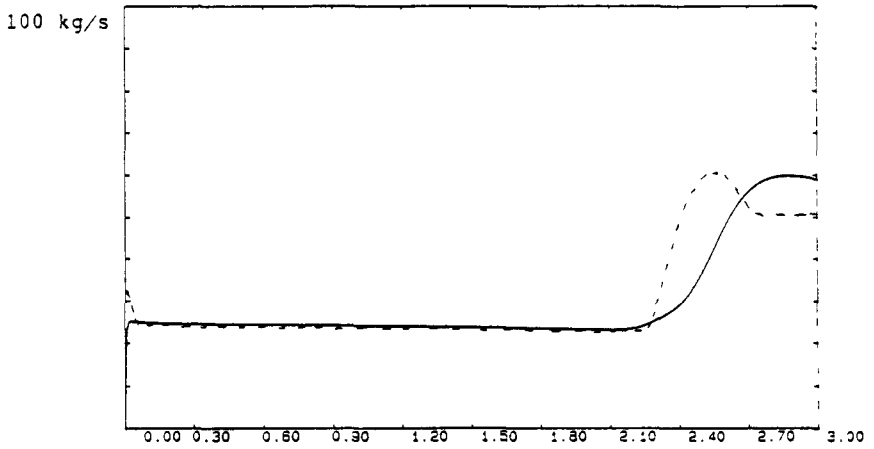

VERIFICATION AND RESULTS OF A REALTIME LUMPED-PARAMETER NUCLEAR-PLANT ANALYZER THAT MODELS A TWO-LOOP, PRESSURIZED WATER REACTOR (U)

*Kim Einar Hammer, Ph D
Westinghouse Savannah River Company
Savannah River Site, MS 773-42A
Aiken, SC 29808
(803)-725-1611

ABSTRACT

A lumped-parameter model of a two-loop, pressurized-water reactor for realtime plant analysis has been developed for a six-megahertz IBM PC-AT The new model, called BADGER, improves upon earlier models by demonstrating two-loop fidelity and an enhanced pressurizer model, it also uses fewer equations to obtain results similar to other models By conserving mass, energy, and momentum, BADGER obtains system pressure, nodal enthalpies, loop-averaged velocities, and volume fraction of the pressurizer It also uses a new algorithm for the primary pressurizer-liquid interface BADGER is stable and accurate up to time-step sizes of 200 msec, requiring 131 msec for each integration step Although BADGER has demonstrated good comparisons with detailed RETRAN analysis of the same plant during symmetric and asymmetric transient scenarios, exceptions clearly demonstrate where the model needs improvements

INTRODUCTION

Traditional methods of thermal hydraulic analysis rely on increasing the number of nodes in a model to resolve unpredicted transient responses In the past, computing engines have limited the number of nodes that could be added This forced modelers to choose their nodalizations conservatively based on engineering judgement. Although new computing engines allow modelers to add more nodes without large capital or time expenditures, the new engines do not eliminate the need for engineering judgement. Becausethe current fiscal environment does not make faster central processing units an option for modelers, developing simple thermal hydraulic models is still an important area of research

*Work performed while Ph D candidate of the Nuclear Engineering and Engineering Physics Department in the College of Engineering at the University of Wisconsin

This paper highlights the University of Wisconsin BADGER model for analysis of pressurized-water reactor, primary coolant systems [1] The project's goal is to develop a state of the art pressurized-water-reactor simulation engine for the best personal computer architecture of the time (a six megahertz IBM PC-AT) This work fills the gap between earlier models by demonstrating the full capability of the architecture BADGER models two loops with momentum equations and adds a better pressurizer model However, the new model would use fewer nodes than previous models The discussion covers the model development including nodalization and equation transformation, results of accuracy and stability testing, and comparison to detailed thermal hydraulic transient analysis The transients demonstrate loss of coolant, loss of heat sink (both symmetric and asymmetric) and asymmetric momentum changes

THE BADGER MODEL

BADGER was developed as a lumped-parameter model of the primary coolant system of a two-loop pressurizer water reactor The Kewaunee Nuclear Power Plant was chosen as the model because of the availability of previous studies [2-4]

BADGER is based on a set of differential/algebraic equations that modeled only the plant parameters used by the control systems or observed by the operator during normal and off normal transients BADGER uses a staggered nodalization of mass and energy conservation equations and the equations of state to obtain differential equations for system pressure, pressurizer volume, and the enthalpy distributions In BADGER, the pressurizer and primary coolant system were chosen for the mass nodes with a moving/mixing boundary The model is built upon two mass conservation equations and four energy conservation equations for the two loops that were modelled. The energy nodes are divided according to the pressurizer as one volume, the two hot legs as another volume, and each cold leg as separate volumes The pressurizer volume expands and contracts within the pressurizer/hot leg combined volumes based on system conditions A new solution algorithm determines whether pressurizer/hot leg mixing or pressurizer volume changes are occurring. The algorithm uses a single set of equations and a single pass solution The mass/energy differential equations were expanded and decoupled in terms of one system pressure, volume-average enthalpies, and the pressurizer-volume fraction using linearized equations of state

A detailed analysis of a single coolant-loop demonstrated that the velocity distribution function was not severely altered during several transients including pump trips, locked pump rotors, and load changes under natural circulation Based on those results, volume-averaged velocity equations were derived for each loop by volume integration of the momentum equation using enthalpy distributions based on the hot and cold enthalpies Loop velocity equations were coupled by sharing frictional pressure losses across the core region

Pressurizer control systems and boundary conditions are included in BADGER The control systems include

- pressurizer heaters
- proportional and continuous-spray valves

- charging and letdown valves
- pressure-relief safety valves

Boundary conditions for the model include
- heat rates
- pump torques
- control-system switches
- safety injection
- steam-generator-tube ruptures

RESULTS

The resulting model uses 13 differential equations to solve the primary coolant system and pressurizer controls One time step required 131 msec of central processing unit time on a six megahertz IBM PC-AT with math coprocessor

Stability of the model was demonstrated using severe step changes in boundary conditions with time steps ranging from 50 msec to 250 msec Then, the stability of solutions with larger time steps were compared to the 50-msec solution The tests included
- 100% core-load rejections with heat sink maintained
- asymmetric 100% steam-generator load rejections with heat source maintained
- single-loop pump trips
- single-loop, locked-pump rotors
- 100 Kg/s steam-generator-tube ruptures
- 100 kg/s struck-open, pressure-operated relief valves

Of the transients considered, the single-loop, locked-rotor test was the most severe (figures 1-4) For all the tests, the unaffected loop had the most severe stability problems Only the loop velocities showed variations, the other system parameters demonstrated little effect due to the perturbation However, the oscillations followed the 50-msec solution and were damped out with time The results of these test showed that BADGER was stable for time steps of 200 msec and less, but was unstable for 250 msec

Six RETRAN transients served as a basis for accuracy and benchmarking The transient included
- reactor/turbine trip (TRIP)
- steam-generator-tube rupture (SGTR)
- struck-open, pressure-operated relief valve (PORV)
- single-loop, reactor-coolant-pump trip (PUMP)
- single-loop, main-steam-line rupture (MSLR)
- steam-generator load reduction (LOAD)

The accuracy of the BADGER model was demonstrated by running six transients using time steps of 50, 100, 150, and 200 msec The differences in time steps were indistinguishable

The model was benchmarked against results of six RETRAN transients designed to test the model under symmetric and asymmetric conditions during losses of mass, energy, or momentum The model performed best during the TRIP, SGTR, PORV, and MSLR transients The MSLR

best demonstrated the accuracy of the model (figures 5 10) [5] However the PUMP and LOAD demonstrated differences between the two models

The PUMP transient demonstrated that the model could not replicate exactly the hot/cold leg enthalpy inversions (figures 11 and 12) The differences are due to two factors First, BADGER has three nodes modeling the two loops, while the RETRAN results clearly demonstrated that the two loops are acting as four independent nodes Second, the single hot leg volume has twice the thermal inertia as the individual RETRAN nodes Both of the factors would be addressed by a four-node primary model BADGER did satisfactorily replicate the RETRAN pressurizer pres sure and level responses (figures 13 and 14)

The LOAD transient demonstrated how the BADGER model could not replicate pressurizer pressure responses (Figure 15) The differences were determined to occur when the pressurizer was undergoing outsurges after insurges Kim demonstrates this to be the fault of the RETRAN nonequilibrium model [6] His work shows that the RETRAN model overestimates pressure losses because of outsurges after insurges when compared to actual pressurizer responses The short comings in the nonequilibrium model were considered during the development of BADGER

CONCLUSIONS

BADGER has demonstrated the state-of-the-art for simplified pressurized water reactor models based on central processing unit limitations The important features of the model include a two-loop model not previously available for the six-megahertz 80286 personal computer, dual coupling of primary system volume changes with surge-line mixing, loop-averaged velocity equations, and detailed pressurizer-control systems Future improvements will include model ling the hot legs as two volumes and a core model with feedback effects

REFERENCES

1 K E Hammer, "Pressurized Water Reactor Lumped Parameter Realtime Simulation Model" Ph D diss , University of Wisconsin. May 1989

2 J J Barry, et al , *Topical Report on the Kewaunee Power Plant Modelling Project*, University of Wisconsin, UWRSR-17 (May 1984)

3 K E Hammer, M H Kim, J Barry, E Coen, M L Corradini, and G A Moses "RETRAN-02, Analysis of a Steam Generator Tube Rupture for the Kewaunee Nuclear Power Plant", *Trans American Nuclear Society* (November 1984)

4 K Hammer, J Olsen, M Corradini, and G Moses, *An Analysis of Selected Operational Transients for the Kewaunee Pressurized Water Reactor*, University of Wisconsin, UWSR-33 (December 1985)

5 J H McFadden *et al* , *RETRAN-02 A Program for Transient Thermal-Hydraulic Analysis of Complex Fluid Systems*, Revision 2, EPRI-NP-1850-CCM, Vol 1-5 (November 1984)

6 S Kim, "An Experimental and Analytical Model of a PWR Pressurizer During Transients Doctoral thesis, Massachusetts Institute of Technology (February 1984)

BIBILOGRAPHY

Delene, J H "A Digital Computer Code for Simulating of Dynamics of Demonstration Size Dual Purpose Desalting Plans using a Pressurized Water Reactor as a Heat Source ORNL TM 4104 September 1973

Hetrick, D L , Girijashankar, P V , and Palusinski, O A "Solution Methods for Simulation of Nuclear Power Systems" Interim Report EPRI-NP 1928, July 1981

Kao, S P "A Multiple-Loop Primary System Model for Pressurized Water Reactor Plant Sensor Validation" Doctoral thesis, Massachusetts Institute of Technology July 1984

Kao, S P "PRISM An Integrated RCS and Steam Generator Simulation Model" Paper presented at the American Nuclear Society Meeting on Math Comp and Reactor Physics Pittsburgh Pennsylvania April 28–May 2, 1991

Motamed, M E "Pressurized Water Reactor Dynamic Simulation Model" Ph D diss , University of California at Los Angeles, 1983

Po, (Pwu) L C "PCTRAN—A personal Computer Transient Analyzer" Paper presented at the American Nuclear Society Topical Meeting on Computer Applications for Nuclear Power Plant Operation and Control Pasco, Washington September 1985

Po, (Pwu) L C ,"TRAN/PWR/BWR—A Fast Running Reactor Transient Code for Small Computers Proceedings of American Nuclear Society 1985 National Heat Transfer Conference pp 151–159 August 1985

Whang, D H , Lee, B H , Chang, S S "Fast Running System Code Development with Analytical Solution Technique and Marching Scheme" Proceedings of the 1985 National Heat Transfer Conference pp 141-150 August 1985

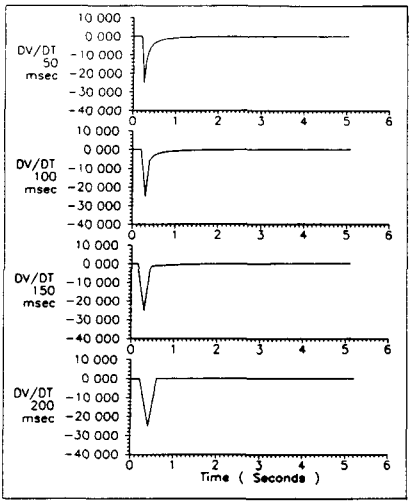

Figure 1. Unlocked loop-velocity derivative during locked-rotor stability tests

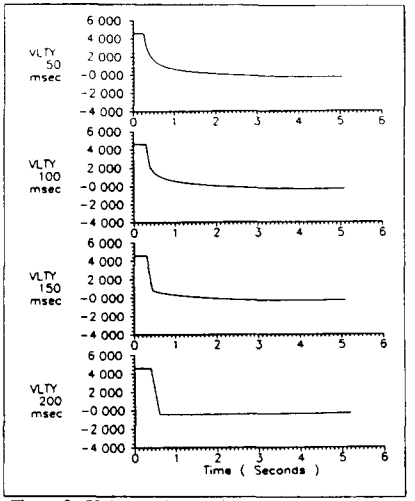

Figure 2. Unlocked loop-velocity responses during locked-rotor stability tests

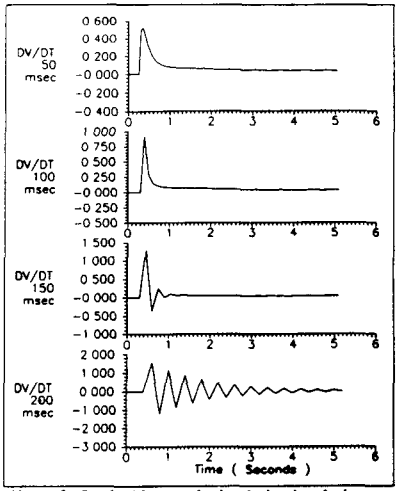

Figure 3. Locked loop-velocity derivative during locked-rotor stability tests

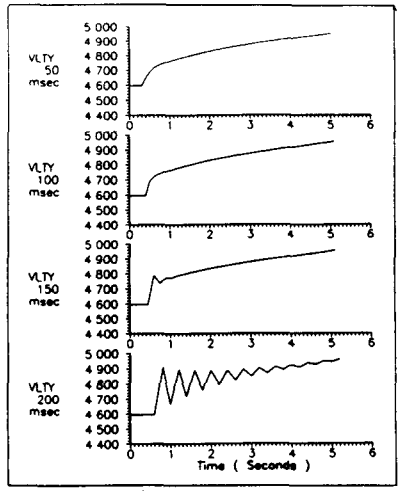

Figure 4. Locked loop-velocity responses during locked-rotor stability tests

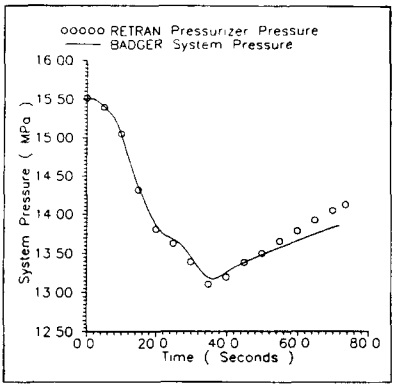

Figure 5. BADGER and RETRAN pressurizer pressure during MSLR transient analysis

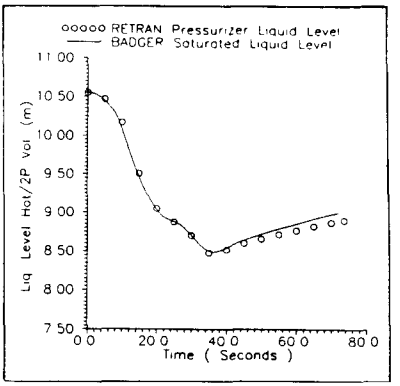

Figure 6. BADGER and RETRAN pressurizer level during MSLR transient analysis

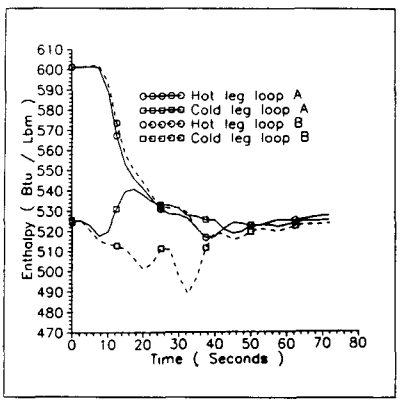

Figure 7. RETRAN enthalpy profile during MSLR transient analysis

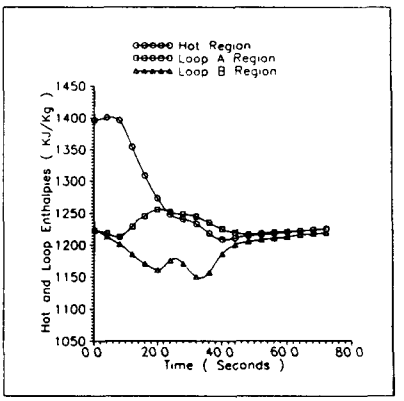

Figure 8. BADGER enthalpy profile during MSLR transient analysis

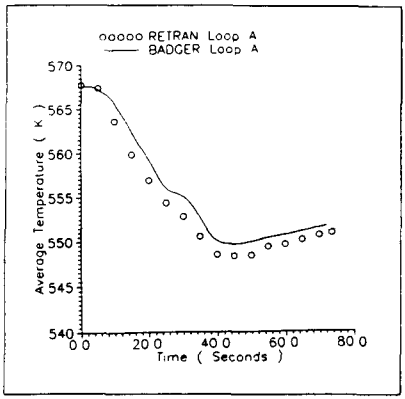

Figure 9. BADGER and RETRAN loop (A) average temperature during MSLR analysis

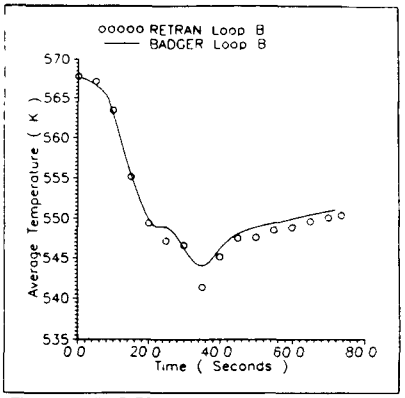

Figure 10. BADGER and RETRAN loop (B) average temperature during MSLR analysis

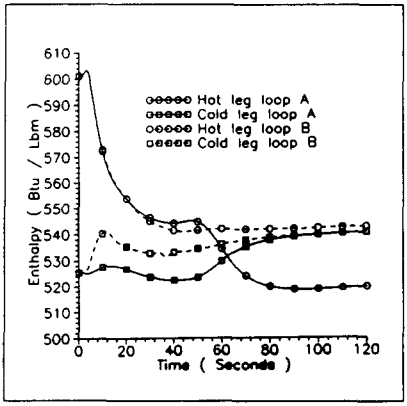

Figure 11. RETRAN enthalpy profile during PUMP (A) transient analysis

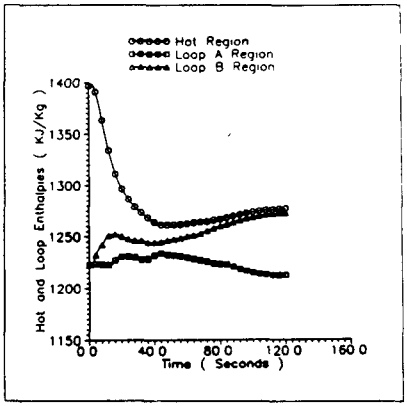

Figure 12. BADGER enthalpy profile during PUMP (A) transient analysis

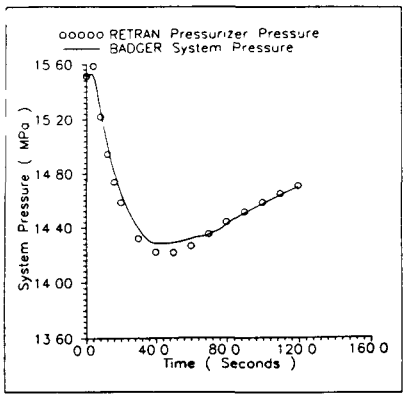

Figure 13. BADGER and RETRAN pressurizer pressure during PUMP (A) transient analysis

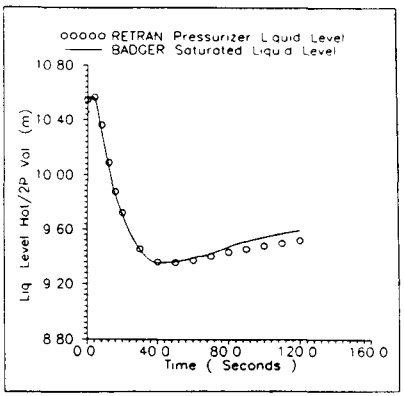

Figure 14. BADGER and RETRAN pressurizer level during PUMP (A) transient analysis

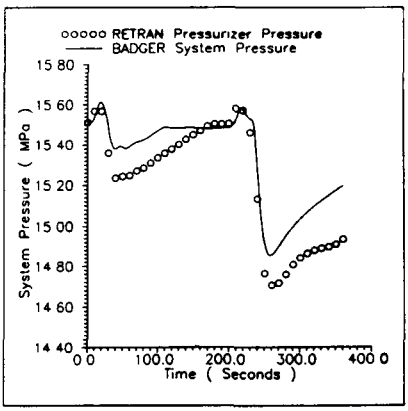

Figure 15. BADGER and RETRAN pressurizer pressure during LOAD transient analysis

HOW DO SPECTRAL INDICES DEPEND ON THE NEUTRON SPECTRUM IN LOW ENRICHED UO_2 - H_2O LATTICES

István VIDOVSZKY

Central Research Institute for Physics
Hungarian Academy of Sciences
H-1525 Budapest 114 P.O.B.49, HUNGARY
Phone 36 1 1699-499, Fax 36 1 1552-530

ABSTRACT

The dependence of selected spectral indices $SI(U^{8c}/Dy)$ and $SI(U^{8c}/U^{5f})$ on the H/U ratio was studied in low enriched UO_2-H_2O lattices. The measurements were carried out on the basis of the parallel irradiation technique, which irradiates activation foils both in a neutron field to be investigated and in a reference field of thermal neutrons. A fuel pellet of UO_2 was used for the measurement of activities caused by the neutron capture of ^{238}U and the fission of ^{235}U. The measurements were carried out at ten different H/U ratios (in the range 67 - 530) to demonstrate the capability of the present method. It was found that the results of the present measurements decrease monotonously with increasing H/U, which fully corresponds to the presumptions. The results of the measrurements are useful to asses the validity of the cell calculations.

INTRODUCTION

To get information about the neutron spectrum in low enriched UO_2-H_2O lattices, one possibility is to introduce parameteres, called spectral indices, which are defined as double ratios·

$$SI\left[\frac{U^{8c}}{Dy}\right] = \frac{\dfrac{A_1^{U8}}{A_1^{Dy}}}{\dfrac{A_r^{U8}}{A_r^{Dy}}}, \quad SI\left[\frac{U^{8c}}{U^{5f}}\right] = \frac{\dfrac{A_1^{U8}}{A_1^{U5}}}{\dfrac{A_r^{U8}}{A_r^{U5}}}, \qquad (1)$$

where A_1^{U8} and A_r^{U8} are the activations of ^{238}U captures in the investigated and in the reference spectra respectively, and A_1^{U5}, A_r^{U5} and A_1^{Dy}, A_r^{Dy} are analogues quantities for ^{235}U fissions and ^{164}Dy captures. The method, based on the irradiation of fuel pellets and dysprosium foils is described in [1]. These measurements have been performed as a part of a research program carried out with the aim of investigating UO_2-H_2O lattices. In this program [2,3] other lattice parameters were studied too. As the main goal of the experimental program was to give a controlled experimental data set for validating computer codes [4], checking the tendencies of the measured parameters as functions of basic lattice parameters was emphasized. In low enriched UO_2 - H_2O lattices the most basic parameter, characterizing the neutron spectrum is the H/U ratio, which is

defined as the ratio of ^{1}H and ^{235}U nuclei So the measured spectral indices were studied as the function of H/U ratio too.

EXPERIMENTAL CONDITIONS

The measurements were performed under the following conditions

- The lattice is hexagonal.
- The lattice pitch is 11.0 ± 0.03, 12.7 ± 0.02 and 15.0 ± 0 05mm respectively.
- The moderator is distilled water.
- The temperature of the core is 21°C, and 130°C respectively.
- The fuel pellets are made of UO_2, and their radius is 3.800±0.025 mm. The density of fuel pellet is dependent on the uranium enrichment. Fuel pellet and fuel rod densities are given in Table 1. The average density of the entire fuel rod is different from each pellet density. The difference can be explained by the presence of air gaps.
- The cladding material is zirconium alloyed with niobium (1 wt%). The outer and inner radii of the cladding tubes are 4.525±0.025 mm and 3.875±0.025 mm, respectively.
- The measurements were carried out in the center of a large core, where an asymptotic neutron spectrum is attained.

The activations A_{1}^{U8}, A_{r}^{U8} etc., defined in Eq.(1) were measured by a semiconductor (*Ge(Li)*) detector. The gamma spectra were evaluated using the computer code RFIT [5]. The procedure of the measurements including data evaluatain is described in [1,2].

RESULTS AND DISCUSSION

The results of the spectral index measurements are given in Tables 2 and 3. The errors given in Tables 2 and 3 are simple σ values calculated from both the errors of counting statistics and applied corrections. Calculated values of the spectral indices are shown in Tables 2 and 3 as well. The caluculations were caried out by the modules of the code system KARATE [6], which has been developed for calculating VVER-1000 reactors.

As it can be seen from Tables 2 and 3, both the given spectral indices decrease with increasing H/U ratio. This tendency, which is illustrated on Figs. 1 and 2, seems to be reasonable, as the increase of H/U leads to the thermalization of the neutron spectrum and consequently to the decrease of the parameters being proportional to the epithermal/thermal flux ratio.

Note, that such important parameters as fuel rod diameter and lattice geometry (all the investigated lattices are hexagonal) have been constant through over the series of experiments. The assumption that parameters like $SI(U^{8c}/Dy)$ or $SI(U^{8c}/U^{5f})$ depend on the H/U ratio and not separately on fuel enrichment, lattice pitch and temperature, is valid for lattices consisting of the same type of fuel rods, e.g. for VVER type lattices.

CONCLUSIONS

The dependence of two spectral indices $SI(U^{8c}/Dy)$ and $SI(U^{8c}/U^{5f})$ on the H/U ratio was measured in low enriched UO_2-H_2O lattices, on the basis of the parallel irradiation technique, which basically irradiates activation detectors both in a neutron field to be investigated and in a reference field of thermal

neutrons. The measurements were carried out at ten different H/U ratios, to demonstrate the capability of the present method. It was found that the results of the present measurements decrease monotonously with increasing H/U, which fully corresponds to the presumptions, so they are useful to asses the validity of the cell calculations. The presented calculational results seem to be in good agreement with the experimental ones.

From the experimental results in lattices of different H/U ratios, it is concluded that the dependence of the spectral indices SI(U^{8c}/Dy) and SI(U^{8c}/U^{5f}) on fuel enrichment, lattice pitch and temperature can be described by their dependence on the H/U ratio. In other words, the neutron spectrum in such lattices can be characterized by the H/U ratio.

REFERENCES

1 Vidovszky, I. J. Nucl.Sci.Technol., 25 (1988) pp.884-888.

2 Bardos, J., Becker, R., Dabrowski,C., Gacsi,L., Gado,J., Jozefowicz,E.T.,Kravchenko,Iu.,Ia., Krinizs,K., Stanolov,A., Szatmary, Z., Turi,L., Vidovszky, I. Final report of TIC, Volume 1, Experimental Investigations of the Physical Poperties of WWER-type Uranium-water Lattices Akademiai Kiado, Budapest, 1985

3 Alvarez, C., Bardos, J., Becker, R., Gacsi,L., Gado,J., Kravchenko,Iu.,Ia., Szatmary,Z., Vidovszky,I.. Final report of TIC, Volume 3, Experimental Investigations of the Physical Properties of WWER-type Uranium - Water Lattices Akademiai Kiado, Budapest 1991

4 Vidovszky, I. Benchmark Data for Light Water Reactors (Based on measurementys, performed in a critical assembly) Advances in Mathematics, Computations and Reactor Physics, Proceedings of the International Topical Meeting, 1991, Pittsburgh, PA, USA, 9.2 3-1

5 Szatmary, Z.: Data Evaluation Problems in Reactor Physics. Theory of the Program RFIT, report, KFKI-1977-43

6 Gado, J., Kereszturi, A., Makai, M., Maroti, L.: The Program System KARATE
IAEA Specialists Meeting on Advanced Calculational Methods for Power Reactors, Cadarache (France) 1990

Table 1

Specification of fuel

Fuel enrichment [a/o ^{235}U]	ρ_{rod} [g/cm^3]	ρ_{pellet} [g/cm^3]
1.6	10.17 ± 0.15	10.33 ± 0.01
3.6	10.28 ± 0.05	10.56 ± 0.03
4.4	10.32 ± 0.10	10.42 ± 0.01

Table 2

The spectral index SI(U^{8c}/Dy)

Lattice pitch [mm]	Fuel enrich-ment [a/o^{235}U]	T [°C]	H/U *	Measured	Calcu-lated
11.0	3.6	130	67.5	7.220 ± 0.090	6.687
11.0	3.6	21	72.1	6.442 ± 0.097	6.231
12.7	4.4	130	102.5	4.720 ± 0.137	4.931
12.7	4.4	21	109.4	4.253 ± 0.128	4.620
12.7	3.6	130	125.8	3.992 ± 0.058	4.264
12.7	3.6	21	134.3	4.017 ± 0.069	4.007
15.0	4.4	21	189.5	3.236 ± 0.102	3.231
15.0	3.6	21	232.5	3.096 ± 0.042	2.870
12.7	1.6	21	305.4	2.544 ± 0.040	2.518
15.0	1.6	21	529.0	2.102 ± 0.050	1.979

* the ratio of ^{1}H to ^{235}U nuclei

Table 3
The spectral index SI(U^{8c}/U^{5f})

Lattice pitch [mm]	Fuel enrich-ment [a/o ^{235}U]	T [°C]	* H/U	Measured	Calcu-lated
11.0	3.6	130	67.5	4.610 ± 0.051	5.086
11.0	3.6	21	72.1	4.415 ± 0.062	4.810
12.7	4.4	130	102.5	3.917 ± 0.112	4.132
12.7	4.4	21	109.4	3.721 ± 0.110	3.901
12.7	3.6	130	125.8	3.480 ± 0.054	3.647
12.7	3.6	21	134.3	3.407 ± 0.054	3.539
15.0	4.4	21	189.5	2.603 ± 0.080	2.913
15.0	3.6	21	232.5	2.420 ± 0.033	2.615
12.7	1.6	21	305.4	2.230 ± 0.042	2.267
15.0	1.6	21	529.0	1.662 ± 0.045	1.850

* the ratio of ^{1}H to ^{235}U nuclei

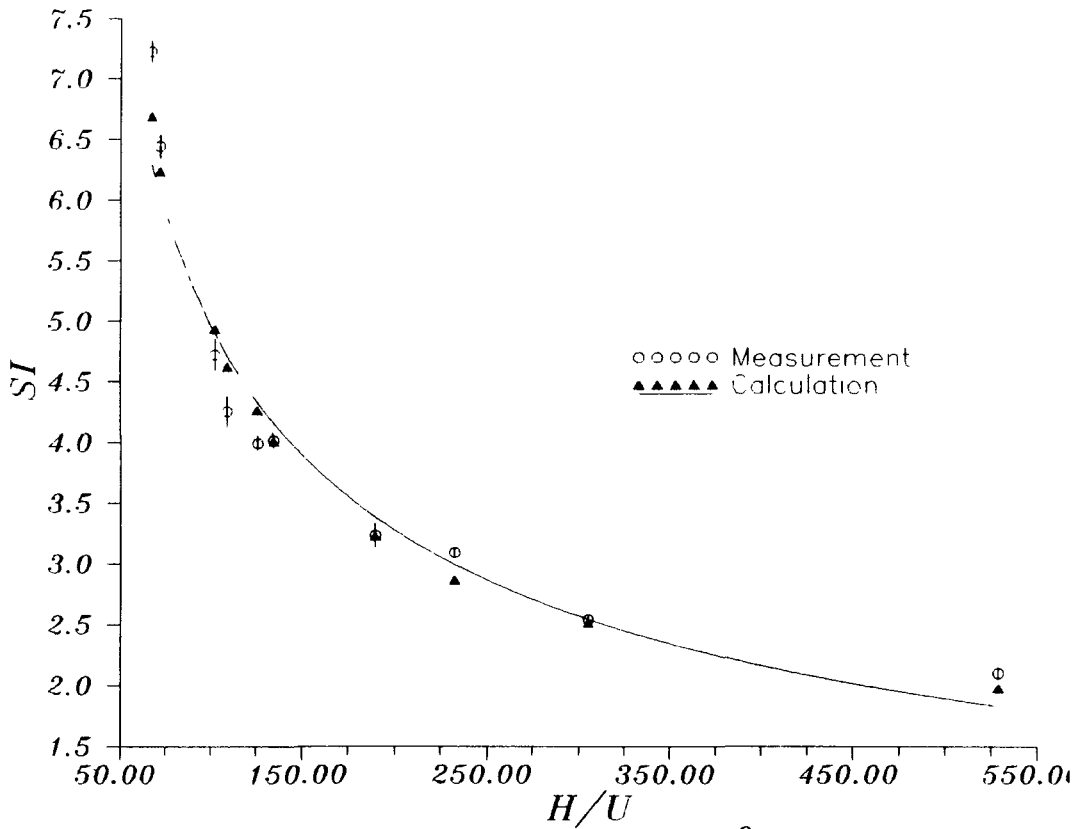

Fig. 1. SI(U^{8c}/Dy)

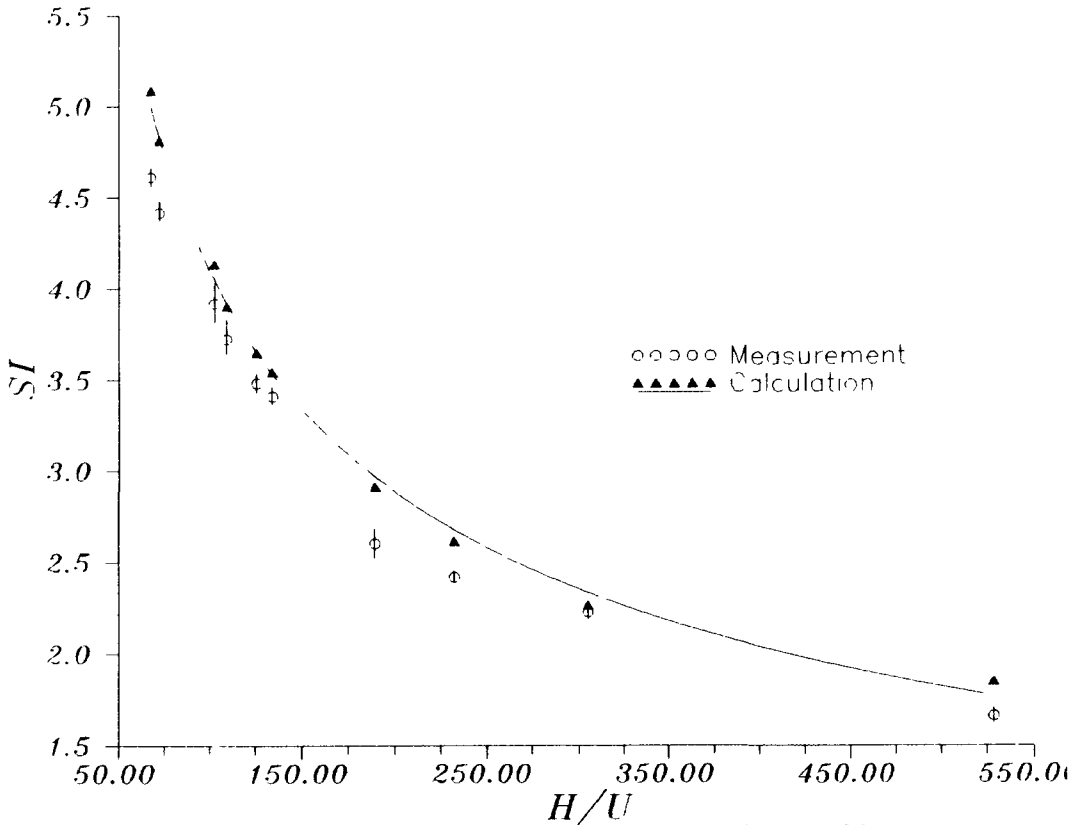

Fig. 2. $SI(U^{8c}/U^{5f})$

AN INTEGRAL EXPERIMENT USING A URANIUM MOCK-UP

V. V. Afanas'iev, A. B. Belevitin, V. L. Romodanov,
Iu. M. Versilov
Moscow Engineering Physics Institute
D. V. Markovsky, G. E. Shatalov
Kurchatov Institute Atomic Energy, Moscow

ABSTRACT

A benchmark experiment using a complex layer system is described. The system includes a uranium neutron breeder and the data obtained by it can be made use of for verification of calculational programs of thermonuclear reactor blankets. Results of the experiment were made use of for verification of "BLANK" program which was based on Monte Carlo method. A good agreement between calculational and experimental results was obtained. Deviation between the values obtained in the medium lithium containing zone of the unit requires further experimentation.

INTRODUCTION

The experiment was made in the framework of a joint program of the Kurchaov Atomic Energy Institute and the Moscow Engineering Physics Institute and was the first in the set of benchmark experiments using complex layer systems. The aim of these experiments is to obtain data necessary to verify calculational programs of nuclear reactors and thermonuclear reactor blankets that use different nuclear cross-sections libraries.

EXPERIMENTAL EQUIPMENT, METHODS OF MEASUREMENTS AND RESULTS OF THE EXPERIMENT

The source of neutrons, the experimental equipment, the methods and the apparatuses that were made use of in the experiment were analogous to those used in the experiments with graphite assemblies. All the experiments were conducted in a plane geometry for the following reasons. The measurements showed that space-energy distributions of neutrons around the target structure of a neutron generator were anisotropic not because of a kinematic character of T(d,n)He reaction but because of the materials its structure is made of. The latter especially influences neutron propagation direction which coincides with the plane of a tritium target. Thus, if a benchmark experiment is made in a spheric geometry, it is necessary to measure functionals of neutron fields at different angles with respect to a beam of accelerated deuterium ions and then to integrate the results obtained. In this case an uncertainty appears in

space-energy distribution of source neutrons which abandons the idea of one-dimensionality of the experimental unit geometry. When measurements are made in a two-dimensional geometry there are no such problems at all or they are of less importance.

The experimental unit, a structure of slab layers of different materials is shown in Fig.1. This structure can be identified with the blanket the surface of which is irradiated by high energy neutrons.

Some nuclear-physical properties of the material of the unit are given in [1](Table.1).

The following values were measured in the experiment:

- nuclear reaction rates of threshold detectors: $^{115}In(n,n')$, $^{204}Pb(n,n')$, $^{64}Zn(n,p)$, $^{27}Al(n,p)$, $^{56}Fe(n,p)$, $^{107}Ag(n,2n)$, $^{63}Cu(n,2n)$, $^{64}Zn(n,2n)$;
- nuclear reaction rates (n,f) in the isotopes: ^{232}Th, ^{237}Np, ^{239}Pu, ^{233}U, ^{235}U;
- nuclear reaction rates (n,γ) and (n,2n) in ^{238}U isotope;
- tritium production rate in lithium 6 end 7 isotopes in lithium containing zone of the system and the reaction rates that modelled them.

All the results obtained are absolute and are normalized to one source neutron and one detector nucleus. The measurements were made in an axial and some radial channels of the experimental unit. Measurement of reaction rates (n,γ) and (n,2n) in ^{238}U were made with the help of a γ-spectrometric method. For tritium production separation on different lithium isotopes measurements were made by detectors with different 6 lithium isotope enrichment.

The errors of nuclear reaction rates were ~5-7%, the errors in measurement of lithium production being ~8%. Neutron spectra in the energy range of neutrons above 0.5 MeV were reconstructed taking into account the nuclear reaction rates that were measured. The error of reconstruction of differential spectra was ~(20-30)%, the error of integral spectra obtained from them being ~5%. This makes it possible to recommend them for comparison with calculational values. Using results of neutron spectra reconstruction it has become possible to obtain the upper group of source neutrons and neutrons scattered into it with ~5% error. It enables us to obtain integral spectra of secondary neutrons and compare them with calculational values. This increases the value of the data obtained from spectral characteristics of neutron fields in integral experiments with 14 MeV neutron source considerably. The neutron spectra reconstructed can be used to model processes having cross-sections of a threshold nature. The same is true of tritium production when an isotope of lithium 7 is irradiated by neutrons Using the reconstructed spectra it was possible to obtain tritium production using this isotope. These results coincided with the results of direct determination of tritium production within experimental errors which enables us to model physical processes and determine effective parameters of threshold detectors with the help of neutron spectrum reconstruction technique. Some results of the experiments are given in Tables 1-5.

A CALCULATIONAL PROGRAM

Comparison of calculational and experimental results was made with the help of "BLANK" program [2], based on Monte Carlo method. All calculations were made in a three-dimensional geometry. In the field of high energy neutrons a modified physical module Fortune-88 was used [3] along with 18 group library of constants on the basis of ENDF-B/IV and ENDL-83 data. Below 0.1 MeV 13 group constants in P_1 approximation were used [4]. Corrections for neutron temperature in a thermal group and mutual influence of resonances were made. As most of the measurements were made inside the experimental assembly material composition of the equipment that was in the experimental room was not taken into consideration.

CONCLUSION

A benchmark experiment in a complex layer system where uranium is used as a neutron breeder is made. Results of the experiment and their error make it possible to verify calculational programs of nuclear reactors and thermonuclear reactor blankets. "BLANK" program was verified according to the results of the experiment. Comparison of calculational and experimental values showed that they were in a satisfactory agreement. Rates of nuclear reactions measured by threshold detectors are in agreement at a 10% level. Calculation of tritium production rate on lithium isotope 7 coincided with the results of the experiment within the experimental error (~8%). Experimental values of tritium production on lithium isotope 6 agree well with calculational ones but disagree for coordinates in the centre of the medium lithium containing zone in the limits of ~20%. This disagreement can't be attributed to errors in the experiment and in the calculation. Additional experiments are required to understand the nature of the disagreement. A scheme for comparison results of benchmark calculational and experimental values is given in Fig. 2.

This scheme allows us to understand the reason of the discrepancy between calculational and experimental results, and to give recommendations on their elimination.

REFERENCES

1 Afanasiev V.V. et. al. Experiment on the hybrid blanket model with uranium multiplier. Proceeding of the XIX-th International Symposium on Nuclear Physics. Gaussing, December 1989, p.34-37.
2 Marin S.V., Markovskij D.V., Shatalov G.E. Preprint IAEh-2382, Moscow 1977.
3 Markovskij D.V., Borisov A.A. Preprint IAEh-4774, Moscow 1989.
4 Shatalov G.E. DENSTY - the code for calculation of macroscopic cross sections, in: Vopr. atomn. Nauki Tekhn., Ser."Physics and Techn. of Nucl. React" 8(21), 1981, P.39-41.(in Russian).

Table 1. Absolute reaction rate distributions in the axial channel of the blanket mock-up, 10^{28} 1/atom/source neutron.

Coordinate mm	$^{115}In(n,n')$	$^{204}Pb(n,n')$	$^{64}Zn(n,p)$	$^{27}Al(n,p)$	$^{56}Fe(n,p)$	$^{63}Cu(n,2n)$	$^{64}Zn(n,2n)$
0	0,76(3)	0,278(10)	0,67(2)	0,252(8)	0,393(14)	1,95(7)	0,621(15)
10	0,88(4)	0,258(9)	0,60(2)	0,212(7)	0,329(13)	1,59(5)	0,474(13)
35	0,86(3)	0,178(6)	0,407(13)	0,126(4)	0,182(6)	0,86(4)	0,259(7)
61	0,58(2)	0,115(4)	0,252(9)	0,076(3)	0,105(4)	0,484(2)	0,142(4)
91	0,387(15)	0,081(3)	0,169(6)	0,052(2)	0,071(3)	0,304(15)	0,092(3)
120	0,264(11)	0,056(2)	0,116(5)	0,0345(10)	0,047(2)	0,192(7)	0,0611(16)
142	0,183(6)	0,047(2)	0,094(4)	0,0265(8)	0,0358(14)	0,141(5)	0,0441(12)
192	0,127(5)	0,029(1)	0,054(2)	0,0169(6)	0,0211(7)	0,082(3)	0,0232(7)
232	0,086(3)	0,0192(7)	0,0356(12)	0,0107(3)	0,0133(15)	0,0511(17)	0,0142(4)
281	0,0486(19)	0,0131(13)	0,0213(7)	0,0064(2)	0,074(3)	0,0284(10)	0,0081(3)
301	0,0374(18)	0,0094(4)	0,0177(6)	0,0051(5)	0,0060(2)	0,0223(9)	0,0063(2)
321	0,0311(16)	0,0080(4)	0,0143(9)	0,0042(1)	0,0049(2)	0,0183(8)	0,00494(15)
340	0,0242(23)	0,0063(3)	0,0116(5)	0,0035(1)	0,0038(2)	0,0130(5)	0,00404(16)
366	0,0175(7)	0,0056(3)	0,0095(5)	0,0028(1)	0,0027(4)	0,0107(10)	0,00306(10)

Table 2

Absolute fission-rate and capture-rate distributions in axial channel of the blanket model, 10^{27} 1/atom/source neutron

Reaction	Distance from the front wall of the mock-up, mm						
	II	I6	24	34	4I	46	60
^{233}U (n,f)	3,79(24)	3,64(24)	3,9I(24)	4,I0(25)	4,07(25)	4,35(25)	4,30(25)
^{235}U (n,f)	I,99(I7)	2,I4(I7)	2,I3(I8)	2,30(I8)	2,42(I8)	2,34(I8)	2,53(I9)
^{238}U (n,γ)	0,I33(5)	0,I44(5)	0,I65(6)	0,I73(6)	0,I83(6)	0,I82(6)	0,337(II)
^{238}U (n,2n)	0,I96(9)	0,I56(9)	0,I56(8)	0,I34(7)	0,I23(7)	0,II9(6)	0,080(6)
^{232}Th (n,f)	0,I55(I2)	0,I45(I2)	0,I36(9)	0,II9(9)	0,086(7)	0,080(7)	0,075(6)
^{237}Np (n,f)	I,56(9)	I,46(8)	I,45(8)	I,I7(7)	I,I4(7)	I,08(6)	0,82(6)
^{238}U (n,f)	0,490(40)	0,458(38)	0,407(34)	0,352(30)	0,283(25)	0,272(25)	0,I94(20)

Table 3

Tritium production rates in axial channel of the blanket model, ^3H/atom/source neutron

Number of zone	Detector coordinate, mm	Isotope	
		Lithium-6, $T_6 \times 10^{27}$	Lithium-7, $T_7 \times 10^{29}$
I	60	1,95 (18)	3,13 (18)
	90	2,62 (16)	2,37 (13)
	105	3,94 (24)	1,99 (11)
	120	7,58 (42)	1,74 (10)
2	141	8,38 (41)	1,35 (8)
	151	4,24 (21)	1,16 (8)
	161	2,49 (13)	1,03 (8)
	171	2,00 (10)	0,88 (6)
	191	1,36 (7)	0,74 (6)
	211	1,06 (7)	0,64 (5)
	231	1,03 (7)	0,54 (4)
	251	1,29 (8)	0,42 (4)
	271	2,25 (13)	0,34 (4)
	281	3,93 (22)	0,31 (9)
3	300	5,07 (27)	0,25 (2)
	310	3,29 (18)	0,23 (2)
	320	2,79 (16)	0,21 (2)
	330	3,40 (19)	0,19 (2)
	340	5,77 (28)	0,17 (2)
	365	7,42 (35)	0,13 (2)

Table 4. Absolute fission rate distributions in the axial channel of the blanket mock-up, 10^{-10} 1/atom/source neutron.

Reaction	Distance from the front wall of the mock-up, mm: 90	105	120	122	125	130	135	139
$^{233}U(n,f)$	0,472 (31)	0,552 (34)	0,950 (62)	1,33 (9)	1,68 (11)	1,79 (12)	1,62 (11)	1,32 (9)
$^{235}U(n,f)$	0,259 (17)	0,319 (22)	0,594 (41)	0,936 (61)	1,23 (8)	1,48 (10)	1,21 (8)	0,941 (62)
$^{239}Pu(n,f)$	0,414 (27)	0,587 (35)	1,21 (8)	1,71 (11)	2,19 (14)	2,69 (17)	2,33 (15)	1,79 (12)
$^{232}Th(n,f)$	0,00499 (32)	-	0,00340 (22)	-	-	-	-	-
$^{237}Np(n,f)$	0,0567 (37)	-	0,0356 (23)	-	-	-	-	-
$^{233}U(n,f)_{Cd}$	0,419 (28)	-	0,523 (34)	-	-	-	-	-
$^{235}U(n,f)_{Cd}$	0,212 (14)	-	0,222 (15)	-	-	-	-	-
$^{239}Pu(n,f)_{Cd}$	0,267 (18)	-	0,305 (21)	-	-	-	-	-

Reaction	141	151	161	191	231	271	281	283
$^{233}U(n,f)$	0,909 (59)	0,606 (42)	0,452 (31)	0,297 (19)	0,214 (14)	0,282 (19)	0,536 (35)	0,719 (47)
$^{235}U(n,f)$	0,605 (42)	0,328 (22)	0,239 (15)	0,156 (11)	0,121 (8)	0,163 (9)	0,283 (19)	0,497 (32)
$^{239}Pu(n,f)$	1,17 (8)	0,688 (45)	0,469 (31)	0,211 (14)	0,138 (8)	0,337 (22)	0,685 (45)	1,03 (7)
$^{232}Th(n,f)$	0,00283 (21)	-	-	0,00159 (18)	0,00104 (7)	-	0,00060 (4)	-
$^{237}Np(n,f)$	0,0264 (18)	-	-	0,0177 (12)	0,0119 (8)	-	0,0072 (5)	-
$^{233}U(n,f)_{Cd}$	0,504 (33)	-	-	0,275 (19)	0,220 (15)	-	0,258 (16)	-
$^{235}U(n,f)_{Cd}$	0,218 (15)	-	-	0,140 (8)	0,119 (7)	-	0,106 (7)	-
$^{239}Pu(n,f)_{Cd}$	0,280 (19)	-	-	0,160 (9)	0,121 (7)	-	0,138 (8)	-

The continuation of Table 4.

Reaction	286	291	296	298	300	310	320	330
$^{233}U(n,f)$	0,771 (51)	0,823 (53)	0,768 (51)	0,706 (46)	0,509 (33)	0,345 (23)	0,300 (21)	0,321 (22)
$^{235}U(n,f)$	0,598 (39)	0,663 (43)	0,544 (35)	0,489 (32)	0,315 (21)	0,173 (11)	0,149 (11)	0,179 (11)
$^{239}Pu(n,f)$	1,20 (8)	1,31 (9)	1,23 (8)	1,05 (7)	0,706 (46)	0,470 (31)	0,421 (27)	0,463 (31)
$^{232}Th(n,f)$	-	-	-	-	0,00047 (3)	-	0,00039 (3)	-
$^{237}Np(n,f)$	-	-	-	-	0,0054 (4)	-	0,0046 (4)	-
$^{233}U(n,f)$	-	-	-	-	0,265 (18)	-	0,230 (15)	-
$^{235}U(n,f)_{Cd}$	-	-	-	-	0,104 (7)	-	0,0948 (61)	-
$^{239}Pu(n,f)_{Cd}$	-	-	-	-	0,129 (7)	-	0,117 (7)	-

Reaction	340	342	345	350	355	359	363	365
$^{233}U(n,f)$	0,547 (36)	0,770 (51)	1,06 (7)	1,22 (8)	1,22 (8)	1,05 (6)	0,869 (56)	0,645 (42)
$^{235}U(n,f)$	0,357 (23)	0,588 (38)	0,849 (55)	0,986 (58)	0,954 (57)	0,855 (54)	0,726 (47)	0,500 (33)
$^{239}Pu(n,f)$	0,806 (52)	1,25 (8)	1,64 (11)	1,81 (12)	1,68 (11)	1,53 (10)	1,35 (9)	0,954 (62)
$^{232}Th(n,f)$	0,000303 (21)	-	-	-	-	-	-	0,000238 (16)
$^{237}Np(n,f)$	0,00381 (25)	-	-	-	-	-	-	0,00297 (19)
$^{233}U(n,f)_{Cd}$	0,221 (15)	-	-	-	-	-	-	0,191 (13)
$^{235}U(n,f)_{Cd}$	0,0814 (57)	-	-	-	-	-	-	0,0523 (34)
$^{239}Pu(n,f)_{Cd}$	0,114 (7)	-	-	-	-	-	-	0,0903 (59)

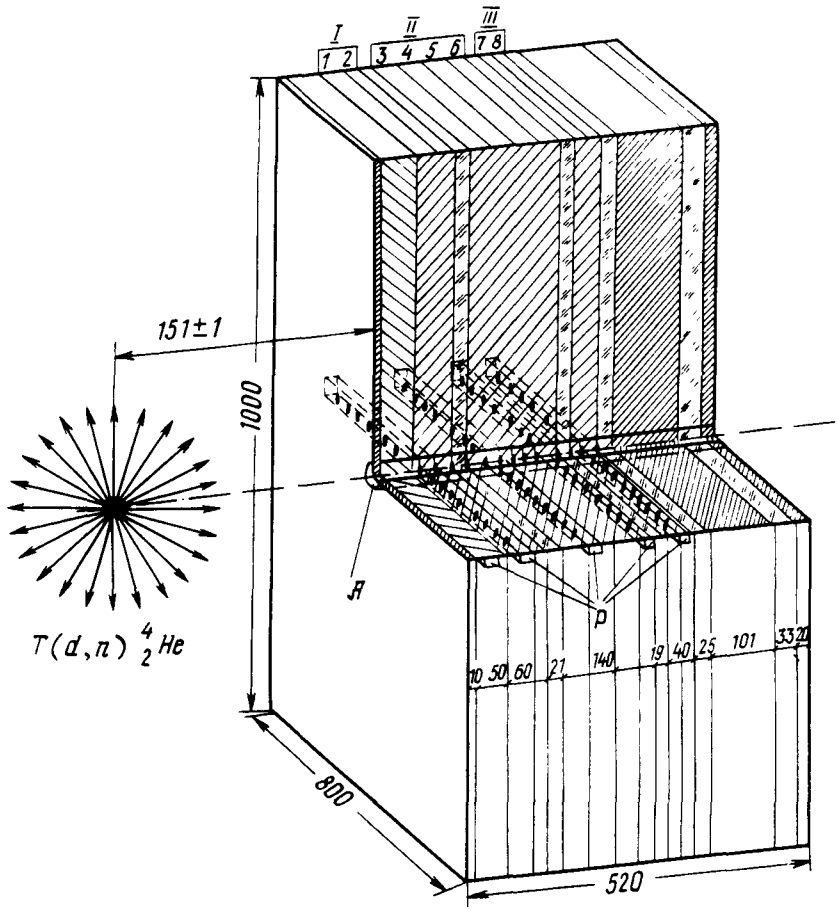

Figure 1. Structural sketch of hybrid blanket mock-up.

Structure of the composition:

- steel 12X18H10T, - metallic uranium, - LiAl-alloy,
- polymetylmetacrylate.

Channels for measurements: A - axial, R - radial, I,II,II - numbers of lithium-containing zones, 1, 2, 3 - numbers of layers.

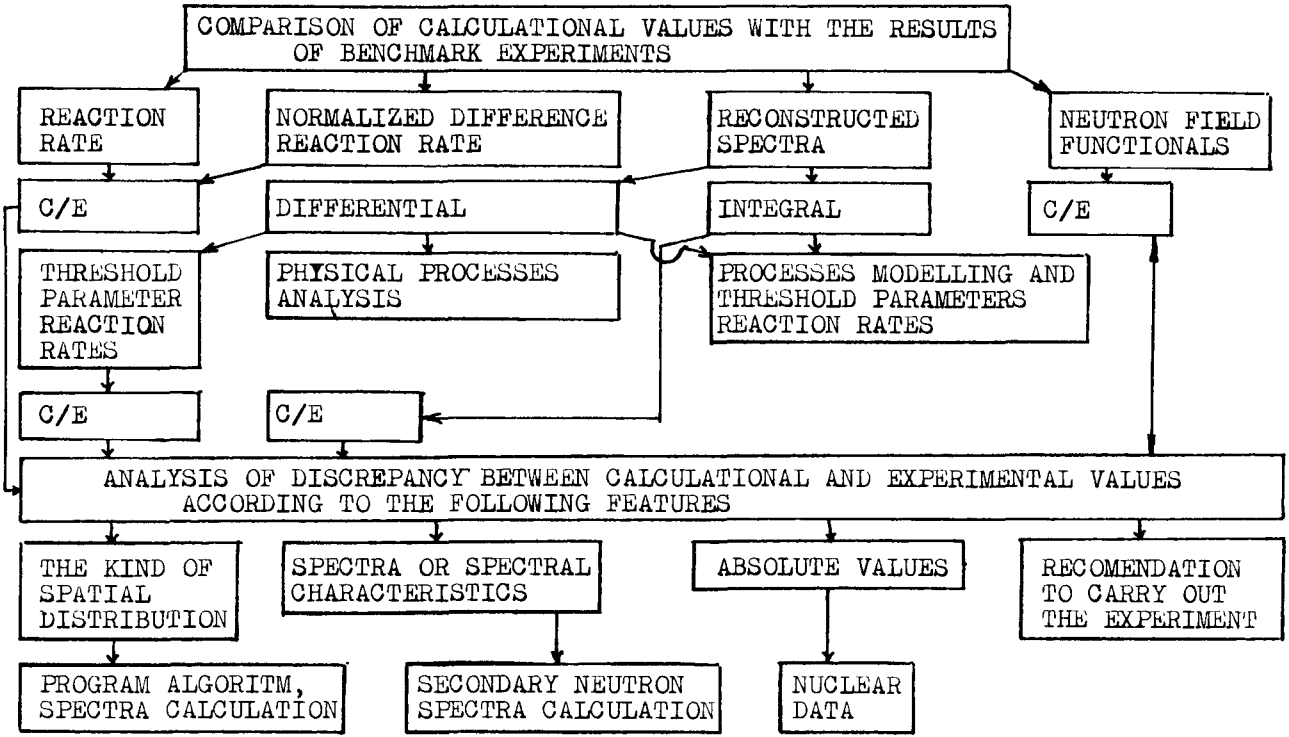

Figure 2. The scheme of comparison of calculational and benchmark experimental results.

AN INTEGRAL EXPERIMENT ON GRAPHITE ASSEMBLIES WITH AN EMPTY CHANNEL

M.I.Andreev, V.V.Afanas'iev, A.B.Belevitin,
V.V.Khromov, V.L.Romodanov, G.V.Tikhomirov, Iu.M.Versilov
Moscow Engineering Physics Institute

ABSTRACT

Results of a benchmark experiment made in graphite assemblies with a homogeneous and an empty channel are discussed. Experimental values are compared with calculational ones with the help of a new technique developed for calculation of heterogeneous systems. The analysis of the results of comparison of calculational and experimental values showed that they agreed well at the level of ~ 10 %. Some discrepancy obtained with ^{64}Zn(n,2n) reaction is likely to be accounted for by exceeding its cross section in files based on ENDF/B-VI data library.

INTRODUCTION

A set of benchmark experiments using models of complex layer systems, the results of which can be made use of for verification of calculational neutron-physical programs of fission and blankets of fusion reactors was carried out in "Neutron Generator" laboratory in the Moscow Engineering Physics Institute. An experiment in graphite assemblies is included into this set because nuclear-physical properties of graphite are studied well enough to consider this experiment as a basic one. As experimental results in graphite assemblies and layer systems are obtained with the help of the same experimental methods and equipment additional possibilities for the investigation of calculational and experimental data in complex systems arise. An experiment in a graphite homogeneous assembly when some very often encountered element of the active zone of a nuclear reactor or a fusion reactor blanket is included into it is the development of a basic experiment in the assembly. This element includes: non-uniformities in the form of some voids that can't be calculated by diffusion equation but are calculated by a higher approximation equation. Thus, an empty channel was included into the graphite assembly, so that results of such an experiment could be made use of for verification of calculational programs of neutron transport along empty cylindrical channels.

EXPERIMENTAL EQUIPMENT, METHODS OF MEASUREMENTS AND RESULTS OF THE EXPERIMENT

The experimental unit was a graphite assembly which consisted of separate blocks in the form of a parallelepiped [1] The unit can make calculations of experimental results both in X-Y and cylindrical geometries, because the assembly configuration allows us to interprete it as a cylinder The diameter of the circumference appears to be equal to 1460 mm, the thickness of the assembly being equal to 500 mm All the measurements were made in an axial direction The empty cylindrical channel, the diameter of which was equal to 44 mm, was in the same direction The graphite assembly was placed on a movable platform and put at a distance of 151 mm from a neutron-generating layer of the target of the neutron generator, that was used as a source of neutrons Neutrons were obtained in $T(d,n)^4He$ reaction, accelerating voltage of deutrons being 150 kV, and the maximum output being equal to $\sim 7 \cdot 10^{10}$ n/s Titanium-tritium targets with the diameter equal to 45 mm on a copper substrate, the thickness of which is equal to 1 mm, were used They were cooled by a water layer 1,5 mm thick, which was placed between the target and the brass wall 0 5 mm thick The absolute measurement of source neutron output was based on a method of α-particles following the reaction of neutron generation, and was made by CAMAC system The error in measurement of neutron output was ~2,7 %

To measure spatial distribution of spectral characteristics of a neutron field the following nuclear reactions were made use of $^{235}U(n,r)$, $^{237}Np(n,f)$, $^{232}Th(n,f)$, $^{115}In(n,n')$, $^{204}Pb(n,n')$, $^{64}Zn(n,p)$, $^{27}Al(n,p)$, $^{56}Fe(n,p)$, $^{106}Ag(n,2n)$, $^{65}Cu(n,2n)$, $^{63}Cu(n,2n)$, $^{64g}Zn(n,2n)$

Activation detectors were in the form of metal disks 18 mm in diameter, their thickness being in the limit of the 0 38-0 95 mm, and were made of materials with 100 % content of a bulk isotope During the experiment light detectors were irradiated in the assemblies simultaneously Their activity was measured using a many channel γ-spectrometric system All the rates of nuclear reactions being measured were absolute and normalized to one neutron source and one nucleus of the detector Reaction rates (n,f) were measured with the help of track solid state detectors Results of the experiment are presented in Fig 1 and Fig 2 They were used for verification of the program based on a new method of calculation of heterogeneous systems [2]

A CALCULATIONAL METHOD

Calculation of the neutron spectrum has been made on the basis of volume-surface balance method, which was used for reactor physics tasks solution In this method considerable modifications were made as far as some peculiarities of the neutron spectra in high energy regions were concerned mainly in calculation of forward directed neutrons in anisotropic scattering In the calculational model the assemblies consist of homogeneous cells in the form of rectangular prisms with a square base A group presentation of neutron energy dependence was used For angular

distribution descriptions directions of a neutron sphere were divided into two hemispheres, forming two angular ranges with different relative neutron source orientations.

In order to correct calculations of neutron anisotropic scattering in the right hemisphere, correction of neutron scattering anisotropy was made by means of different groups and subranges. A library of constants VITAMIN-C of AMPX format was used for these calculations [3]. The results of the experiments were used as benchmark for determination of some calculation parameters. For instance, this may be seen at neutron anisotropy scattering calculation using $^{63}Cu(n,2n)$ reaction rates. A number of members of scattering function expansion was determined in terms of Legendre polynomials according to the table.

Table

$^{63}Cu(n,2n)$ Deviations of calculatinal and experimental values of reaction rates from the numbers of members in scattering function distribution.

The number of member scattering function	1	2	3	4
Deviation of calculational and experimental values, %	66	42	20	5

It was decided, that the number of members equal to four gave deviation within experimental errors. Thus further increase of the number of members is of noise.

COMPARISON OF CALCULATIONAL AND EXPERIMENTAL RESULTS

Spatial ratio distributions of relative and absolute values of calculational and experimental rates of nuclear reactions -C/E were obtained. Calculations were made with the help of different libraries of nuclear constants. As a considerable part of detector activity is determined by source neutrons then it should be excluded from the total activity to obtain data on the secondary neutron spectrum.The principal part of neutron field detectors has threshold dependence of cross-section on neutron energy. Thus, to obtain data on spectral characteristics of the secondary neutron spectrum, differences of various detector reaction rates normalized to the reaction rates of the same detectors were used used. The reaction rates were measured at the distance equal to 151 mm from the neutron source when the unit was not available. Such a technique makes it possible to practically exclude contribution of source neutrons to detector activity, and to make comparison of calculational and experimental reaction rates for different energy regions of neutron spectra. Influence of an empty channel on the transport of different energy neutrons was obtained with the help of "k" quantity, equal to the ratio of the reaction rates measured in the assembly with an empty channel to the reaction rates measured in the assembly . Some results of comparison of calculational and experimental values are given in Figures 3-5 .

CONCLUSION

Results of comparison of calculational and experimental values showed, that they coincided in the limit of ~ (5-10)%. A considerable, up to 25 % discrepancy between calculational and experimental values of the reaction rate of $^{64}Zn(n,2n)$, having 13,7 MeV energy threshold in the neutron spectrum available in the experimental unit was found. The analysis of the cause of this discrepancy showed, that the value of the calculational cross-section in the 14-15 MeV energy range was in the limit of 202 to 224 mb, while the value obtained in this experiment was (169±10) mb. When the value was measured and evaluate using data obtained by other workers [4], the value of this reaction cross-section was found to be 175 and 162.2 mb respectively. This enables us to suggest that the discrepancy of experimental and calculatinal data is likely to be accounted for by a higher value of $^{64}Zn(n,2n)$ reaction cross-section in files based on ENDF/B-VI library. It is shown, that results of the experiment can be used as benchmark to find number members of indicatriss of neutron scattering with the aim of showing its anisotropy adequately. The technique of applying reaction rate differences, normalized to reaction rates of these very detectors measured, when the assembly was not available, showed that one could carry out comparison of calculational and experimental characteristics of secondary neutron spectra without taking into account the contribution made by source neutrons to detector activation. The latter favours verification of programs and makes the data obtained by the detectors used in the experiment more reliable.The analysis of the process of verification of calculational programs shows that though there is no possibility to define the cause of discrepancy between calculational and experimental values directly, still there is a way to define it taking into account the behavior of a set of spatial relative and absolute distributions of C/E values.

REFERENCES

1 V.V.Afanasiev et. al. Experimental and Calculational Provision of Neutron Field Functional Investigation of Fusion Reactors Blankets. Proceeding of the XIX-th International Symposium on Nuclear Physics. Gaussig, December 1989 , p.19-22.

2 V.V.Khromov, E.F.Krjuchkov, G.V.Tikhomirov Solving the Transport Equation in Three-Dimensional Heterogeneous Systems. International Conference on the Physics of Reactors: Physor-90, Marcille-France, April 26-29, 1990, V.3, p.62.

3 R.W.Rousinn et. al. VITAMIN-C. The CTR Processed Multigroup Cross Se c tion Library for Neutronics Studies, ORNL-RSIC-37,1980.

4 Annals of Nuclear Energy. 1987, Vol.14, p.494

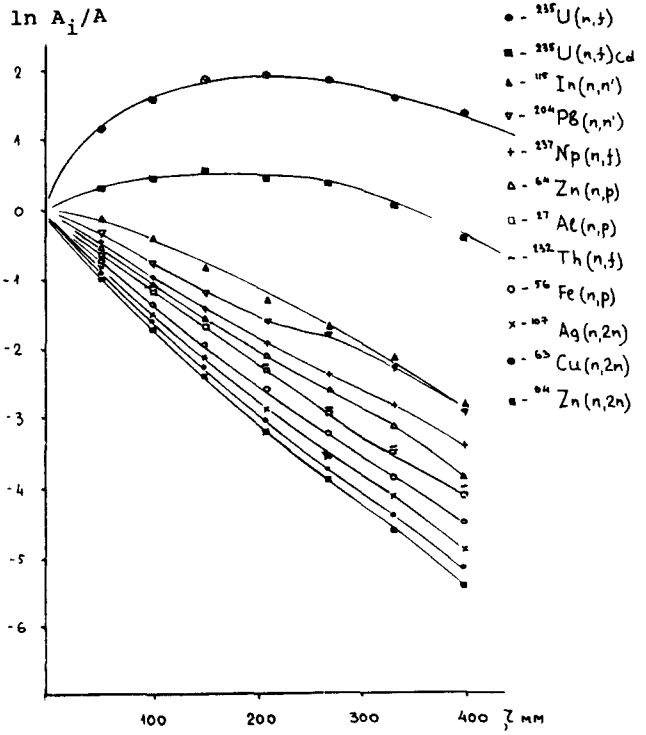

Figure 1. Experimental results of reaction rate measurements in the graphite assembly;
A- reaction rate on the front of surface blanket mock-up,
A_i-reaction rate in the coordinate „ r " inside the assembly.

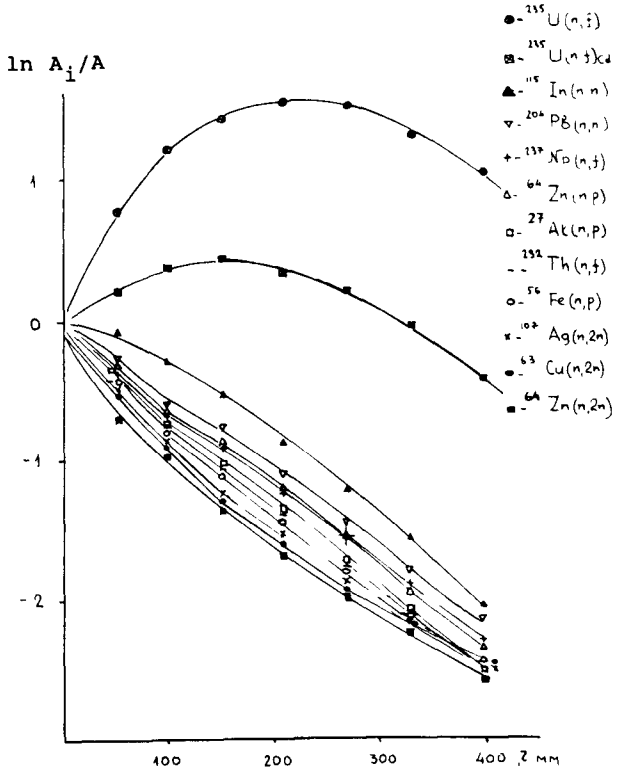

Figure 2. Experimental results of reaction rate measurements in the graphite assembly with empty channel
A -reaction rate on the front of surface blanket mock-up,
A_i -reaction rate in the coordinate „ r inside the assembly.

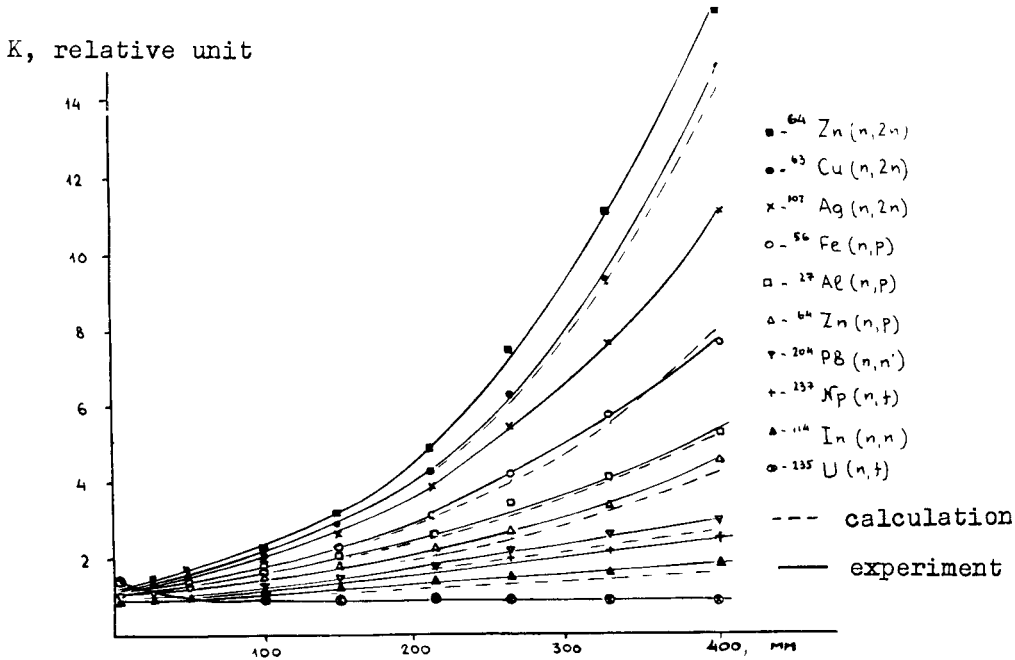

Figure 3. Spatial dependence of reaction rate relations in the graphite assembly with an empty channel on the measured ones in the graphite assembly

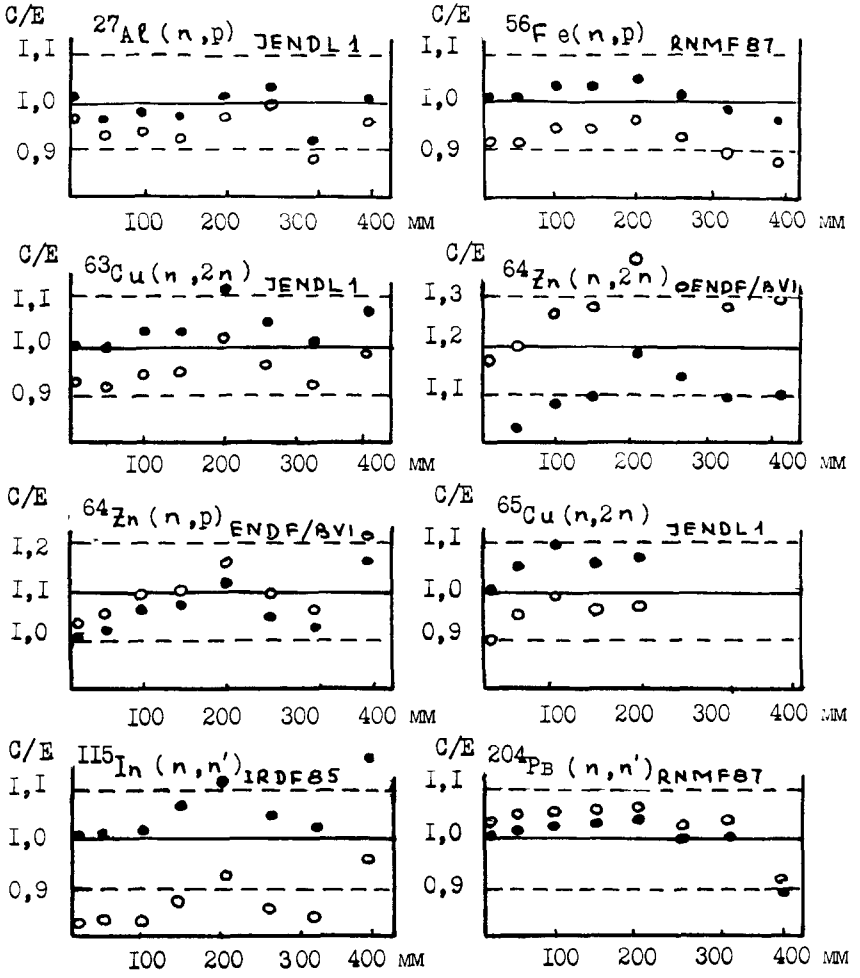

Figure 4.Comparison of calculational and experimental results in the graphite assembly.

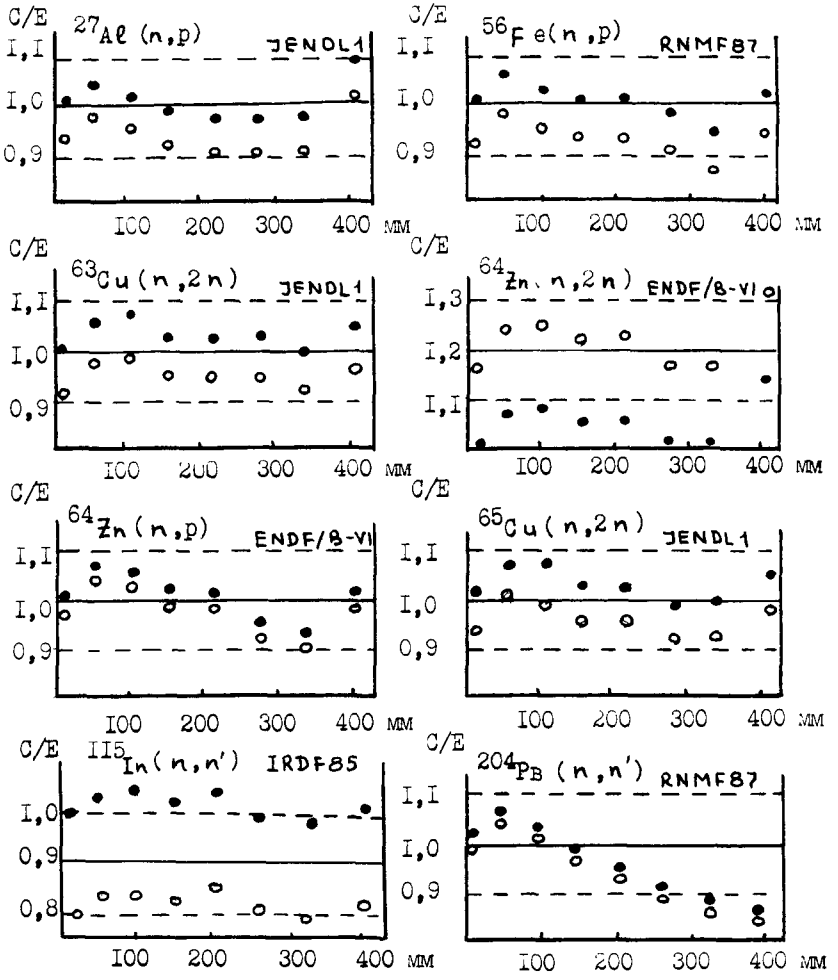

Figure 5.Comparison of calculational and experimental results in the graphite assembly with an empty channel.

CALCULATION OF CRITICAL EXPERIMENT PARAMETERS FOR THE HIGH FLUX ISOTOPE REACTOR

R T Primm, III
Oak Ridge National Laboratory
Oak Ridge, Tennessee 37831-6363
(615)574-0566

ABSTRACT

Six critical experiments were performed shortly before the initial ascension to power of the High Flux Isotope Reactor (HFIR) Critical configurations were determined at various control rod positions by varying the soluble boron content in the light water coolant Calculated k-effective was 2% high at beginning-of-life (BOL) typical conditions, but was 1 0 at end-of-life (EOL) typical conditions Axially averaged power distributions for a given radial location were frequently within experimental error At specific r,z locations with the core, the calculated power densities were significantly different from the experimentally derived values A reassessment of the foil activation data seems desirable

INTRODUCTION

The HFIR is a beryllium reflected, light-water cooled, high-enriched uranium fueled reactor The fuel elements consist of two concentric rings having a fueled height of 50 8 cm, an outer radius of 21 cm and an inner radius of 7 1 cm The rings are composed of 1 27 mm thick, Al clad plates bent into the shape of an involute of a circle A uniform, 1 27 mm thick water gap exists between plates The initial approach to critical was in 1965

As a part of establishing the operating limits for the HFIR, a set of six critical experiments were performed shortly before the initial ascension to full power The HFIR reactor physics report (Ref 1) includes a description of the experiments with the following statement of objectives "These experiments, referred to as the HFIRCE-4 experiments, were performed to (1) investigate small differences (between previous criticals) and the HFIR overall core assemblies, (2) obtain more detailed power-distribution data, (3) calibrate the control rods, and (4) investigate more thoroughly the question of reproducibility"

All experiments were critical Variation in control rod height for the six experiments was achieved by the addition of soluble boron to the light water coolant All but one of the experiments had a simulated water target in the central island of the reactor The final experiment had a target believed at the time to accurately approximate the neutron absorption in the planned Pu-242 target rods

The local power densities were determined through activation of uranium foils The foils were counted in a gamma ionization chamber with a counting accuracy of + 1% "Performance of multiple irradiations indicated that the accuracy of the relative power distribution was about 5% (97% of the points agree within +-5%)" (Ref 1) Power distribution data for a 1 cm (radial) by 2 cm (axial) grid are provided in Ref 1 for each critical experiment The power distributions are interpolations between or extrapolations from the locations with activated foils Some foils were circular with a surface area of 0 5 cm**2, others rectangular with a length of 6 35 cm and a width of 0 16 cm

CROSS SECTION PROCESSING

Before physics parameters can be calculated, nuclear data must be processed into a usable format A description of the nuclear data source and the computer programs used to process the data follows The processing models are described to a sufficient degree so as to allow for recreation of the few group library should that be necessary Finally, a discussion is given of the few group library which is the end product of the cross section processing procedure

NUCLEAR DATA LIBRARY

The starting point for nuclear data preparation is the 39 group ANSL-V General Purpose Neutron library (Ref 2) All of the data extracted from this library for use in the HFIR calculations were derived from data from the Evaluated Nuclear Data File/B - Version V (ENDF/B-V Ref 3) The procedure by which ENDF/B-V data were collapsed to the 39 group structure is described in Ref 2

The 39 group library is in what is termed "AMPX master format" This means that each nuclide in the library must be processed further to obtain correct cross section values for the unresolved and resolved resonance regions for that nuclide A description of the AMPX master format is contained in Ref 2

COMPUTER PROGRAMS USED TO PROCESS NUCLEAR DATA

All programs described in this section are modules of the AMPX system (Ref 4) However better documentation of the programs and required input can be found in Ref 5

The first program executed is the AJAX module The sole purpose of this step is to extract only those nuclides from the library which are to be used in modeling the HFIR reactor A new AMPX master library is created which will be used in subsequent steps By creating a small subset of the original 39 group library some computational time is saved in succeeding steps

The second program executed is the BONAMI module The purpose of this step is to generate correct cross section values for the unresolved resonance energy range (see Ref 5) The algorithm to accomplish this task is simple First, the infinitely dilute values of the various reactions are computed for each nuclide Then "Bondarenko factors" are determined by calculating each nuclide's cross section as a function of "background" cross section and generating the ratio of that value to the infinitely dilute value By generating cross sections corresponding to several background cross section values and for several temperatures, a table can be constructed and interpolation used to determine intermediate values

The BONAMI step and the two succeeding steps require some identification of a "unit cell" This unit cell geometry is input directly into the BONAMI and XSDRNPM (described subsequently) steps and indirectly into the NITAWL (described next) step

For a conventional power reactor, a unit fuel cell is defined as a single fuel pin and its surrounding water channel The analogy for HFIR would be to select a single involute plate and its associated water channel However this assumption would be incorrect due to the small size of the HFIR core

In a power reactor, the external dimensions of the reactor core are very large compared to the diameter of a fuel pin (several hundred times larger) But for the HFIR, the thickness of the fuel region of the annular core is only about 140 mm The escape probability for a neutron born in the HFIR is much, much greater than for one born in a power reactor core Indeed, the purpose of the HFIR is to leak neutrons to the central region where they may be absorbed in target rods

The neutron spectra in the core is dominated by the thermal neutrons returning from the beryllium reflector It is noted in Ref 1 that the homogenization of fuel, clad and coolant is acceptable since the thermal flux depression from coolant centerline to fuel centerline is only 6 8% Consequently, for the HFIR, the "unit cell" is the entire reactor

For the BONAMI step, a cylindrical, four zone problem was created The inner zone was a homogenized HFIR target Surrounding this region was a representative fuel region with only trace amounts of fission products Adjacent to the fuel was a control region The outermost region was beryllium

The target region actinide composition is shown in Table 1 Table 1 is based on data for Transuranium Facility campaign 65 (January, 1986) supplied by C W Alexander ORNL

Table 1 HFIR Target Rod Initial Composition

Nuclide	Grams	Unit Cell Atom Density (atoms per barn*cm)
Pu238	0 00111	2 23946e-8
Pu239	0 00060	1 20546e-8
Pu240	0 21320	4 26554e-6
Pu241	0 00002	3 98485e-10
Pu242	0 00057	1 13099e 8
Am241	0 0459	9 14522e 7
Am243	0 1463	2 89092e-6
Cm244	4 5730	8 99933e-5
Cm245	0 0656	1 28569e-6
Cm246	3 1523	6 15306e-5
Cm247	0 0889	1 72823e-6
Cm248	0 5507	1 06626e-5
Cf252	0 000015	1 85818e-10

The pellets in the target rods are 0 632 cm in diameter and are assumed to be clad with 0 24 cm thick Al-6061 The pins are located on a triangular pitch of 1 689 cm Appropriate atom densities

for the constituents of water and Al-6061 were included with the smeared actinide atom densities in the BONAMI model

One other input to the BONAMI model is the Dancoff (rod shadow) factor Continuing the argument made previously, since the whole core is the unit cell, the Dancoff factor must be calculated for the whole core In most instances, the Dancoff factor for a one lump object is 0 0 However the annular geometry for the HFIR means that there is some probability that a neutron entering the central target region will pass through and cause a fission on the "other side" of the annulus

The CSAS1 module of the SCALE system (Ref 5) was used to determine the Dancoff factor of an annulus having the same homogenized fuel region atom densities as the HFIR but with water in the central target region The calculated Dancoff factor was 0 001774 and this value was input to the BONAMI program Note that this exceptionally low value indicates that the annulus acts as if it were a single lump

The third step in cross section processing is to execute the NITAWL module to properly process the resolved resonance energy region for those nuclides which have resolved resonances With the exception of the uranium isotopes, all actinides are assumed to be present in "infinitely dilute" quantities Likewise certain alloying agents in Al-6061 which have resolved resonance data are assumed to have infinitely dilute concentrations The uranium isotopic ratios are assumed to be typical values from those reported in Ref 1 The NITAWL model is based on the Nordheim integral treatment for a homogeneous annulus

It is in the NITAWL step that the temperature of the nuclide is used to select appropriate scattering data and correctly doppler broaden the cross section resonances All of the target actinides and all of the fuel nuclides and fission products are assumed to have a temperature of 430 degrees Kelvin The water coolant, structural materials and beryllium reflector are all assumed to have a temperature of 343 degrees Kelvin Note that the master cross-section library contains nuclear data only at certain temperatures The NITAWL code selects data at a temperature closest to that entered by the user No interpolation is performed

The final step in the cross section processing procedure is to execute the XSDRNPM program XSDRNPM is a one-dimensional, discrete ordinates solution to the Boltzman transport equation The model input to XSDRNPM is the same as that shown in Table A.6 of Ref 1 except for two changes

The central target zone was modified to be three zones with smeared atom densities corresponding to the current target configuration The innermost zone corresponded to the hydraulic irradiation tube The second zone represented the 15 curium target rods The third zone represented the 16 irradiation positions (assumed to be Al tubes)

The second change was to split the control rod zone into two regions This allowed for representation of both the europium "black" and the tantalum "grey" regions in the same model A k-effective calculation was performed with XSDRNPM using a buckling factor corresponding to the geometric height of the fueled region of the core (50 8 cm + extrapolation distance) The calculated value was 1 0691

Forcing the calculated k-effective value to be 1 00 would have required a buckling height less than the physical height However, the buckling factor for the thermal group is negative flux peaking outside the core For the epithermal and fast groups, it is likely to be close to the geometric

buckling Since the better procedure of having group dependent buckling is not available in XSDRNPM, the buckling height was set to the geometric height

The 39 group cross section set was collapsed to a 7 group set with the energy boundaries shown in Table 2 The selection of these boundaries is based on parametric studies performed as a part of the design of the Advanced Neutron Source reactor (Ref 6)

Table 2 Group Structure for 7-Group Cross Section Library

Group Number	Upper Energy Boundary
1	20 0 MeV
2	100 keV
3	100 eV
4	0 625 eV
5	0 33 eV
6	0 162 eV
7	0 0300 eV
	0 00001 eV

In order to calculate temperature coefficients of reactivity, it is necessary to have cross-section data at elevated temperatures Specifically, hydrogen datasets are needed at multiple temperatures The same calculational sequence was used for the generation of elevated temperature datasets Alternate temperature values were specified in the BONAMI and NITAWL datasets and the group collapse performed using the existing XSDRNPM dataset

REACTOR ANALYSIS

The BOLD-VENTURE system for nuclear reactor analysis was used to determine k-effectives, fluxes, and power distributions (Ref 7) The VENTURE diffusion theory module of the system had, as input, an R - Z model created with 17 annular fuel zones, target, reflector and control blade regions The input to the VENTURE system was based on data provided in Figs A.8 through A.10 and Table A.6 of Ref 1 This section will present those parts of the input dataset which differed from the description given in Ref 1

FUEL REGION

Deviating from the description in Ref 1, the fuel element sideplates were explicitly represented in the VENTURE model Also, the atom densities for the constituents of the fuel zones were based on Al-6061 rather than pure Al. Both the Al filler and fuel plate clad were assumed to be Al-6061 The atom densities for the boron and uranium isotopes were calculated from Figs A.9 and A.10 (schematic drawings of the inner and outer fuel plates respectively) and compared to values given in Table A.6 of Ref 1 Agreement was excellent (usually within 1%) The total quantity of U-235 as tallied from the input was found to be 9 46 Kg The value quoted in Ref 1 is 9 40 Kg

The radial mesh in the VENTURE model was the same as that noted in Table A.6 of Ref 1 The axial mesh varied according to the critical experiment being modeled, the control blade position varying according to coolant boron loading for a given critical experiment

CONTROL BLADES

In Ref 1, the outer element sideplate and inner control blade and water gap between these structures were all homogenized into one region In the VENTURE model these structures were represented separately However, for the control blade, the Al clad was homogenized with the control poison material

The "black" control material reported in Table A.6 of Ref 1 is boron The actual control blades used in the HFIRCE-4 experiments had europium in this region The VENTURE model contains atom densities corresponding to the europium oxide - tantalum - Al design (still the current HFIR configuration) The dimensions and content of the control blade were supplied by R W Hobbs, Research Reactors Division

Initial calculations of experiments with the control rod fully inserted yielded unusually low values of calculated k-effective The nuclear data for the control region was examined and the diffusion coefficient for the europium region was modified via a procedure described in Appendix A. All calculated k-effective values reported here are for models incorporating the modified europium diffusion coefficient

RESULTS OF CALCULATIONS

The calculated values of k-effective are shown in Table 3 The best agreement between calculation and experiment is seen in the "cleanest" core configuration (blades out) At this point, agreement is -0 3% The worst case is with control blades fully inserted and a water target agreement being 2 2%

Table 3 Calculated k-effectives for HFIR Critical Experiments

Expt No	Control Blade Position (cm)	Boron Conc in Coolant (g per L)	Target Material	k-effective
4 1	44 45	0 0	water	1 0219
4 2	49 28	0 527	water	9872
4 3	54 09	0 910	water	9872
4 4	61 72	1 25	water	9890
4 5	67 31 (out)	1 35	water	9967
4 6	42 16	0 0	sim Pu	1 0206

The source of the discrepancy at beginning-of-life typical conditions (2%) is unknown By comparison of cases 4 1 and 4 6, it would appear that the source of the discrepancy is independent of target material The calculational bias changes sign as the control blade is withdrawn and then approaches 1 0 Based on the assumption that the 67 31 cm rod position represents end-of-life, there should be no bias applied to actual reactor calculations when attempting to determine cycle length for a given reactor configuration

The effect on k-effective of varying the number of mesh points in the fuel is shown in Table 4 For all cases examined, there is a slight increase in calculated k-effective (0 002 to 0 004) as the number of mesh points in the fuel is increased However, the previously identified discrepancies remain largely unchanged

Table 4 Effect of Mesh Point Spacing on Calculated K-effectives

	Mesh Points in Fuel		
Expt No	R	Z	K-effective
4 1	19	30	1 022
4 1	68	78	1 026
4 2	19	34	0 987
4 2	68	63	0 989
4 5	19	30	0 997
4 5	68	78	1 000
4 6	19	30	1 021
4 6	68	86	1 024

HFIR procedures stipulate that any change/addition to the irradiation positions must be certified to cause no more than a 5% increase in local power density at any given position in the reactor Frequently this certification is made by comparison to previously performed experiments For new materials or designs, certification must rely on computations

Comparisons of calculated and experimentally derived local power densities for each of the six critical experiments are given in Figs 1 and 2 The description of the experiments, the measurement procedure, some of the experimental data, and all of the experimentally derived local power densities are contained in Ref 1

As the control blades are withdrawn (Expts 4 1 - 4 5), the power densities in the inner element change from being generally overpredicted to being underpredicted Likewise, as the blades (located outside the outer element) are withdrawn, the power densities at the outside edge of the outer element are overpredicted and those at the inside edge are underpredicted

For convenience, the locations and values of the maximum point power densities are contained in Table 5 Also shown there are the locations and values of the greatest percentage difference by which the experimentally measured local power density exceeds the calculated value The former is important because of safety considerations related to the "hot spot" power density The latter is important for determining maximum bias factors which could be applied to calculations to insure conservatism regarding thermal-hydraulic limits

The impact on calculated power distribution of increasing the number of mesh points was studied for experiment 4.6, the fine mesh calculation exhibits poorer agreement with experiment The fine mesh calculation appears to yield a more strongly buckled flux distribution than experimental measurements yield.

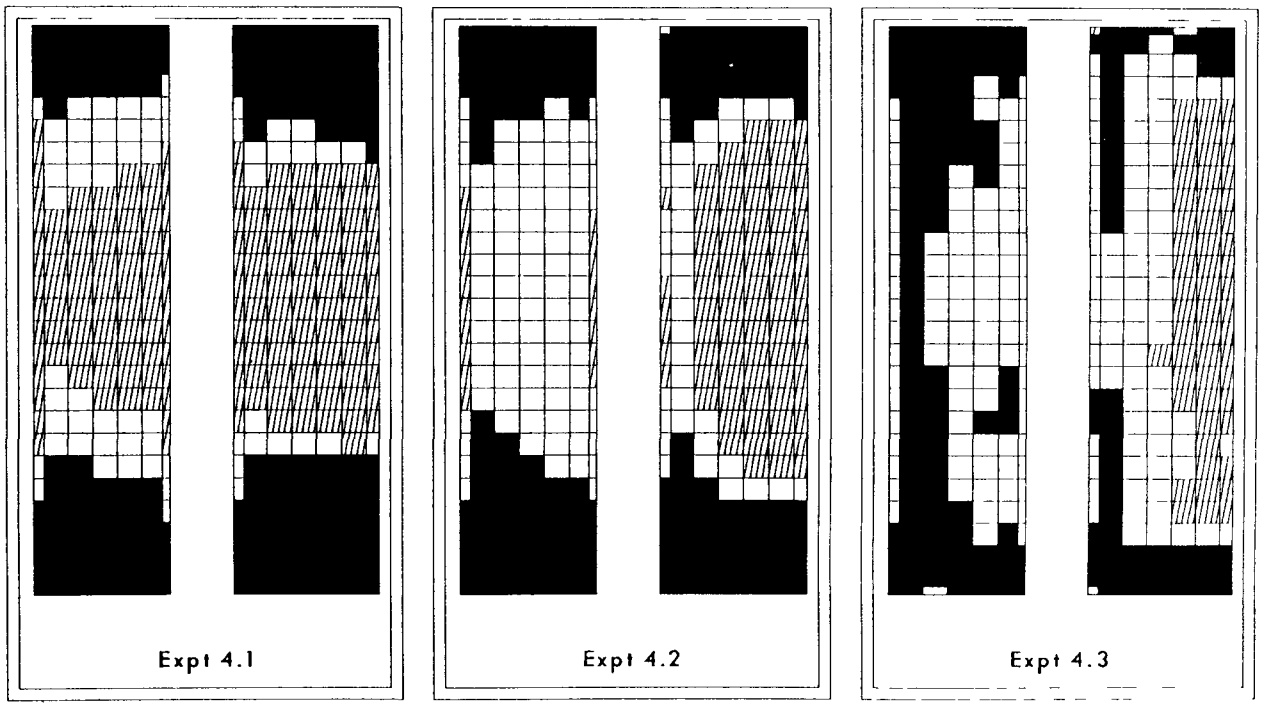

Fig. 1 Comparisons of calulated and measured power densities for HFIR critical experiments; inner element at left, outer at right; light shade = undercalculate by more than 5%, dark shade = overcalculate by more than 5%.

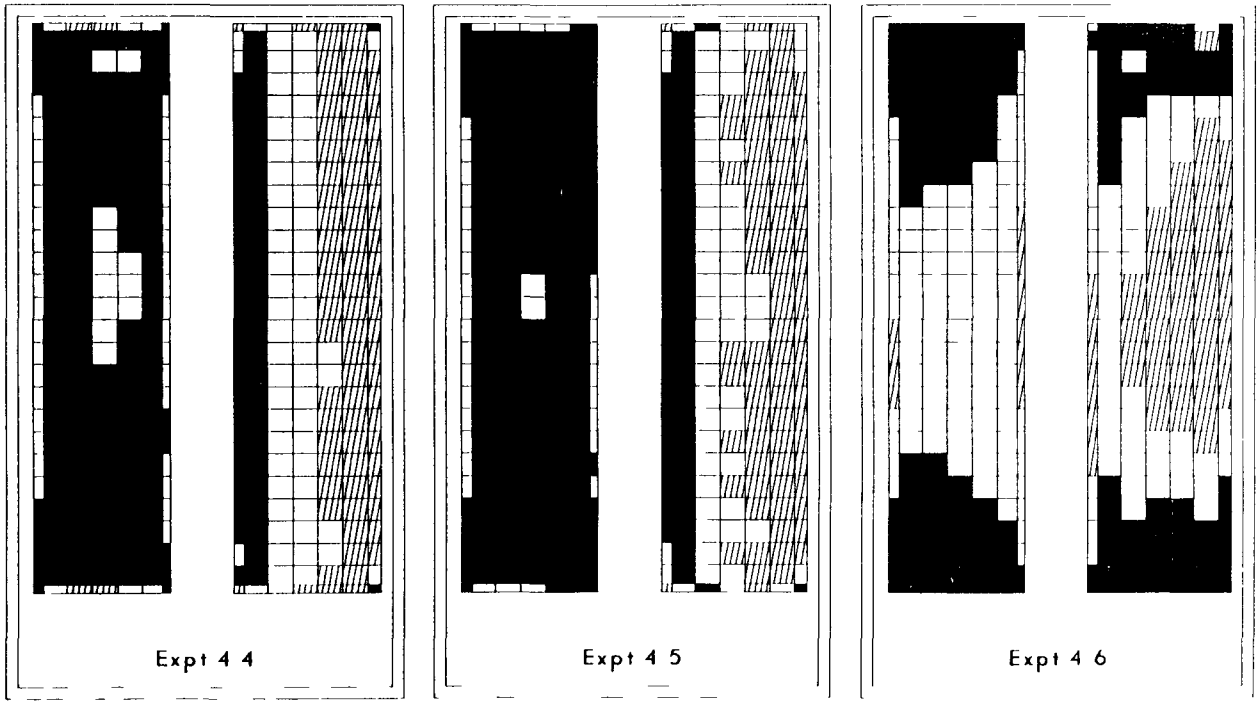

Fig. 2 Additional comparisons of calulated and measured power densities for HFIR critical experiments; inner element at left, outer at right, light shade = undercalculate by more than 5%, dark shade = overcalculate by more than 5%

Table 5 Peak Power Locations for Critical Experiments

	Max. Relative Power Density			Max. % Expt Over Calc		
		Location (cm)			Location (cm)	
Expt No	Value	Radial	Axial	Value	Radial	Axial
4 1	2 38	17 00	25 40	34 69	21 00	2 00
4 2	1 64	7 14	0 00	29 29	21 00	4 00
4 3	1 62	7 14	0 00	22 66	20 00	16 00
4 4	1 56	7 14	0 00	19 04	21 00	18 00
4 5	1 50	7 14	0 00	17 66	21 00	8 00
4 6	2 11	10 00	25 40	30 50	21 00	4 00

For calculation of margin to incipient boiling, the key parameter of interest is the quantity of energy deposited in the water coolant as it flows downward through the core Consequently, it is desirable to accurately estimate the quantity of heat generated along any axial pathway inside the core Table 6 provides a comparison of experimentally measured and calculated axially averaged relative power densities for each of the six critical experiments In almost all cases the level of agreement is within the experimental uncertainty (5%)

The accuracy of calculated local power densities for these critical experiments is summarized in a slightly different manner in Table 7 The second column in the table contains the calculation-to-experiment (c/e) ratio for the point in the core at which the percentage by which the experimental value exceeds the calculated value is largest That is, the point at which the computational method would most underpredict the power on a percentage basis The third and fourth columns provide data for the hottest axial coolant path in the core The third column shows the axially averaged c/e ratio The fourth column shows c/e ratios for the point in the hottest axial path at which the computational method would most underpredict the power on a percentage basis

The variation in the max. local c/e ratio for whole core casts some doubt on the ability to accurately determine the worth of a perturbation A reassessment of the manner in which the irradiated foil data were transformed to power density maps seems desirable since no details of the procedure are contained in Ref 1 A significant impact on experiment/ calculation agreement could occur depending on the procedure used to count the foil activity Since the length of these foils is greater than the mesh spacing for which the experimentally derived data is reported, the manner in which the foils were analyzed (cut into pieces or measured whole) must be known to correctly interpret the values reported in Ref 1

Table 6 Comparison of Experimental and Calculated Axially Averaged Relative Power Densities
100*(Expt.-Calc)/Expt

Radius (cm)	Experiment Number					
	4 1	4 2	4 3	4 4	4 5	4 6
7 14	4 56	66	- 25	-4 31	-5 09	2 88
8 0	-4 80	-9 06	-10 14	-15 82	-15 70	9 37
9 0	-2 48	-6 29	-7 49	-10 73	-12 38	6 70
10 0	- 26	-3 58	-4 18	-6 11	-8 05	6 00
11 0	91	-2 39	-3 82	-6 12	7 80	4 72
12 0	55	-4 07	-5 25	-9 35	-10 79	3 30
12 6	5 70	- 61	- 34	-5 16	7 02	2 58
15 15	3 32	- 63	-3 77	-8 09	-7 28	3 03
16 0	-3 59	-6 15	-6 52	-8 54	-8 54	4 91
17 0	- 51	- 38	13	07	40	93
18 0	- 76	2 41	2 22	3 19	4 30	2 20
19 0	-1 64	4 75	5 40	6 78	6 06	6 23
20 0	-1 58	9 67	11 19	12 27	11 93	14 16
21 0	-6 76	10 42	9 41	14 67	14 70	14 17

Table 7 Local Power Density Ratios for HFIR Critical Experiments

Control Blade Position (cm)	Calculation-to-Experiment Ratio		
	Max. Local for Whole Core	"Hot Streak" Axial Ave	"Hot Streak" Max. Local
42 16	0 695	1 029	0 944
44 45	0 653	0 954	0 838
49 28	0 707	0 993	0 910
54 09	0 773	1 002	0 966
61 72	0 810	1 043	0 991
67 31 (out)	0 823	0 853	0 823

While the worst position for the whole core has a c/e ratio much lower than desired (experimental error +-5%), the axially averaged values for the hot streak are acceptable in all but one case However, the 67 31 cm case is the only critical configuration in which the "hot streak" lies along the outside edge of the outer fuel element This region lies at the point of transition between a weakly absorbing region (Be, Al, water) and a strongly absorbing region (highly enriched uranium) The assumptions underlying diffusion theory would be least applicable at that point in the model

The ability to accurately calculate axially averaged power densities is important because the temperature at the exit of the "hot streak" determines the margin to incipient boiling and therefore the maximum steady-state overpower limit These calculations indicate that reactor physics calculation input to the thermal-hydraulic computer codes should yield accurate (within experimental uncertainties) "hot streak" exit temperatures for all except the "rods full out" position At that configuration, a bias of 15% should be applied

CONCLUSIONS

HFIR specific, few group neutron and coupled neutron-gamma libraries have been prepared These are based on data from ENDF/B-V and beginning-of-life (BOL) conditions The neutron library includes actinide data for curium target rods In previous calculations reported in 1971, only simulated Pu-242 target data were utilized.

Six critical experiments, collectively designated HFIR critical experiment 4, were analyzed Calculated k-effective was 2% high at BOL-typical conditions but was 1 0 at end-of-life-typical conditions These results indicated that if exposure related parameters can be estimated accurately, an accurate estimate of cycle length should be attainable

Through studies of the critical experiments, it was determined that a special blackness treatment was required in order to obtain correct diffusion coefficients for the europium regions of the control blades Nevertheless, the variance in k-effective as a function of control blade position indicated that reviews of the exact positions of the control blades and the exact boron concentrations in the coolant were needed

The local power density distributions were calculated for each of the critical experiments The axially averaged values at a given radius were frequently within experimental error However at individual points, the calculated local power densities were significantly different from the experimentally derived values (several times greater than experimental uncertainty) A reassessment of the foil activation data seems desirable

One potential use of diffusion calculations is in the certification of reactor experiments It is required that a given experiment will not change any local power density by more than 5% The critical experiment calculations indicate that only certain experiments could be certified using diffusion theory

If the reactivity worth of the experiment is small (control blade movement less than a centimeter), then unperturbed and perturbed distributions could be compared to determine percentage difference However, if the pre- and post-experiment-insertion control blade positions are significantly different, then the differences in the power distributions among the critical experiments indicates that an effect due to the experiment would not be quantifiable This is due to differences in calculation/experiment agreement for a given physical position among the critical experiments usually exceeding 5% Again, a reassessment of foil activation data could modify this conclusion

REFERENCES

1 R D Cheverton and T M Sims, "HFIR Core Nuclear Design," ORNL-4621 (July 1971)

2 W E Ford, III, et al , "ANSL-V ENDF/B-V Based Multigroup Cross section Libraries for Advanced Neutron Source (ANS) Reactor Studies," ORNL-6618 (September 1990)

3 R Kinsey, ed "ENDF/B Summary Documentation," BNL-NCS 17541 (ENDF 201) 3rd ed Brookhaven National Laboratory (1979)

4 N M Greene, et al , "AMPX A Modular Code System for Generating Coupled Multigroup Neutron Gamma Libraries from ENDF/B," ORNL-TM-3706 (March 1976)

5 "SCALE A Modular Code System for Performing Standardized Computer Analyses for Licensing Evaluation, Vols 1-3," NUREG/CR-0200, U S Nuclear Regulatory Commission (originally issued July 1980, reissued January 1982, Rev 1 issued July 1982, Rev 2 issued June 1983, Rev 3 issued December 1984)

6 R T Primm, III, "Accuracy of Calculated Power Distribution Using Few Group Cross-Section Sets," Trans Am Nucl Soc , Vol 61 (June 1990)

7 D R Vondy, T B Fowler, and G W Cunningham, III, "The Bold Venture Computation System for Nuclear Reactor Core Analysis, Version III," ORNL-5711 (June 1981)

8 A. F Henry, Nuclear Reactor Analysis, The MIT Press, pp 433-454 (1975)

APPENDIX A

Equivalent Diffusion Theory Coefficients Derived From Transport Theory Calculations

Initial calculations of the six critical experiments showed that those in which the control blades were fully or nearly fully withdrawn yielded k-effectives close to 1.0. However, those in which the control blades were inserted yielded k-effectives which were low (0.9). After verifying the model input regarding control blade position and boron content in the coolant, it was suspected that the diffusion coefficients as generated by the computational procedure were in error. A procedure by A. F. Henry (Ref. 8) for dealing with bladed control rods was employed to derive new diffusion coefficients.

Henry states, "for the one dimensional case, we use the fact that parameters which preserve all the integrated reaction rates within all subregions V_i must necessarily preserve the net leakage rate out of each V_i.... In slab geometry (or in this case, annular geometry in which the height >> thickness of the annulus) this extra restriction implies that, if we know from more accurate calculations (in this case discrete ordinates calculations from XSDRNPM) the column vector $J(r_i)$ of group currents at the point x_i separating a zone of thickness Δ_{i-1} from its neighbor of thickness Δ_i, we want the equivalent diffusion-theory parameters for these zones to be such that solution of the group diffusion equations containing the effective constants will reproduce the $J(r_i)$. If we also require that the column vector of group fluxes $\Phi(r_i)$ at all the interfaces match those values known from more accurate calculations (again, discrete ordinates calculations using XSDRNPM), a systematic procedure for finding the equivalent parameters emerges."

"We consider first the one-group case with the material inside Δ_i homogeneous but not of a nature such that diffusion theory should be valid." In this case, a control blade with no annular or axial (height >> thickness) variation. If equivalent constants $\overline{v\sum_f}$, $\overline{\sum_a}$, and $\overline{D}$ can be found for this case, they will be such that within Δ_i the one-group P_1 equations are

$$\frac{d}{dr}J(r) + \overline{\sum_a}\Phi(r) = \overline{v\sum_f}\Phi(r),$$

$$\frac{d}{dr}\Phi(r) + \frac{1}{\overline{D}}J(r) = 0.$$

Note that for this problem $\overline{v\sum_f} = 0$. Also note, that the above equations are applicable to the multigroup solution if we assume that there is no scattering between groups. Given the seven-group energy structure and the fact that the control blades are composed of europium (atomic number = 63) this is a good assumption.

In matrix form these become:

$$\frac{d}{dr}\begin{bmatrix}\Phi\\ J\end{bmatrix} = -\begin{bmatrix}0 & \frac{1}{\overline{D}}\\ \overline{\Sigma}_a & 0\end{bmatrix}\begin{bmatrix}\Phi\\ J\end{bmatrix}, \tag{1}$$

and, with the definitions:

$$[u(r)] \equiv \begin{bmatrix}\Phi(r)\\ J(r)\end{bmatrix}, \qquad [N] \equiv \begin{bmatrix}0 & \frac{1}{\overline{D}}\\ \overline{\Sigma}_a & 0\end{bmatrix}$$

(1) becomes

$$\frac{d}{dr}[u(r)] + [N][u(r)] = 0\,. \tag{2}$$

The solution to this equation is given in Ref. 8 and is shown to be

$$\begin{bmatrix}\Phi(r_{i+1})\\ J(r_{i+1})\end{bmatrix} = \begin{bmatrix}\cosh\kappa\Delta & -(\overline{D}\kappa)^{-1}\sinh\kappa\Delta\\ -\overline{D}\sinh\kappa\Delta & \cosh\kappa\Delta\end{bmatrix}\begin{bmatrix}\Phi(r_i)\\ J(r_i)\end{bmatrix}.$$

where the subscripts i, i+1 represent intervals in the problem and $\kappa^2 = \dfrac{\overline{\Sigma}_a - \overline{\nu\Sigma}_f}{\overline{D}} = \dfrac{\overline{\Sigma}_a}{\overline{D}}$.

Defining blackness coefficients α and β by

$$\alpha \equiv \frac{J(r_i) - J(r_{i+1})}{\Phi(r_i) + \Phi(r_{i+1})}, \qquad \beta \equiv \frac{J(r_i) + J(r_{i+1})}{\Phi(r_i) - \Phi(r_{i+1})},$$

it can be shown that

$$\sinh\kappa\Delta = \sqrt{(\cosh^2\kappa\Delta - 1)} = \frac{2\sqrt{(2\beta)}}{\beta - 2}$$

and

$$\overline{D} = \frac{1}{\kappa}\sqrt{(\alpha\beta)}$$

For the calculations described in this document, multigroup flux and current values for mesh points on the front and rear faces of the control blade were used to define α and β. The group diffusion coefficients were then determined directly.

The VENTURE neutronics module has an input option whereby two constants, a and b, can be entered and the value of the diffusion coefficients, for a given zone, as calculated from the cross-section data library are modified according to the formula

$$\text{new diffusion coefficient} = a\ (\text{old diffusion coefficient}) + b$$

The diffusion coefficients for the europium region of the control rod were compared to the "old" values derived from the data library and could be linearly correlated with a correlation coefficient R^2, equal to 0 998 The value of a was determined to be 0 01937 and the value of b was determined to be 0 001665

USE OF THE APOLLO2 TRANSPORT CODE

FOR PWR ASSEMBLY STUDIES

D. BELHAFFAF, M. COSTE, R. LENAIN, G. MATHONNIERE, R SANCHEZ,
Z. STANKOVSKI and I ZMIJAREVIC

Commissariat à l'Energie Atomique
Département de Mécanique et Technologie
Service d'Etudes de Réacteurs et de Mathématiques Appliquées
Centre d'Etudes de Saclay

ABSTRACT

This paper presents some validation and application aspects of the APOLLO2 , user oriented, modular code for multigroup transport assembly calculation which is developped at the French Commissariat à l'Energie Atomique. The main points approached in this paper are : the two dimensional collision probability convergence, critical leakage calculation schemes, self shielding spatial discretization, and the equivalence procedure

INTRODUCTION

APOLLO2[1,2] is the successor of the spectrum transport code APOLLO[3,4] which has been used for almost two decades as the main computational tool for neutronic analysis in the French PWR program. APOLLO2 is a fully modular code in which each module corresponds to a specific task: access to the library, creation of isotopes, geometry definition, self shielding calculation, computation of multigroup collision probabilities, flux calculations, etc... Modules communicate exclusively by "objects" containing structured data, these objects are identified by user's given names. In this way the user can use the macrolanguage to define its own chain of calculations. So APOLLO2 can be used in order to obtain a best estimate calculation which validates APOLLO2 industrial simplified schemes.

The framework of the APOLLO2 applications presented here is the PWR assembly calculations The main points analyzed are:

- convergence analysis of assembly calculations by two dimensional collision probabilities method
- critical leakage calculation schemes
- sensitivities of the fuel depletion effects to the self shielding model and to the numerical approximations used
- calculation schemes based on equivalence between heterogeneous (collision probability) and homogeneous cell (collision probabilities or discrete ordinates).

COLLISION PROBABILITIES

The assemblies can be calculated by many options. A flat-flux approximation, together with isotropic scattering and either a uniform double P0 (UP0) or a uniform double P1 (UP1) or a linear angular flux approximation on the surfaces (LP0) is used to compute collision, escape and transmission probabilities. Multicell methods (based on cell cylinderization) and direct methods[5,6] (direct integration in the entire assembly) are available for uniform and non uniform rectangular meshes, for rectangular cells containing concentric pins and angular sectors.

We present the multicell and 2D exact method results for MOX zoned and uranium rodded assemblies (figures 1 and 2).

2D EXACT

The 2D direct collision probability method uses a double numerical integration over ρ (line) and ϕ (angle). The integration mesh consists of sets of parallel neutron trajectories with different orientations.

It is obvious that the accuracy of the calculation depends on the one of the numeric integration formula defined by the parameters $\Delta\rho$ and $\Delta\phi$ ($\Delta\rho$ and $\Delta\phi$ represents respectively the interval between 2 discrete values of ρ and ϕ). The convergence with the angular parameter $\Delta\phi$ has the same behaviour for the two assemblies : rodded uranium and zoned MOX.

Figure 1 shows the reactivity changes due to the different options and integration parameters.

We note that the ρ convergence depends strongly on the ϕ value. For $\Delta\rho$=0.1 and $\Delta\phi = \Pi/48$ we obtain a change in reactivity of about 450 pcm between the calculation without sector discretization and the calulation with sector discretization (figure 1).

MULTICELL

UP0 option

- For the rodded assembly, the discrepancies with the converged 2D exact calculation reach 400 pcm (figure 1) on k_∞ and 8% on the flux at the assembly corner (figure 2).

UP1 option

- For the rodded assembly, the discrepancies with the converged 2D exact calculation reach 100 pcm (figure 1) on k_∞ and 1% on the flux at the assembly corner (figure 2).

SOME APOLLO2 SELF-SHIELDING SCHEMES

GENERALITIES

The models[7,8,9] used in APOLLO2 for the computation of the self shielding cross sections account for space and energy resonance interference between resonant isotopes located in a heterogeneous geometry or in an homogeneous medium. The two available models are the PIC model and the more sophisticated Background Matrix Formalism[9](BMF).

The self shieding calculation is based on a double equivalence:

- Homogenization: for each self-shielding region, an equivalent homogeneous medium is determined, preserving the resonance integral calculated with an approximate slowing down model for the resonant scattering (narrow, wide or intermediary resonance : NR, WR, IR) and a given moderator source. Homogenization can be performed on each group or for a macrogroup encompassing several groups. The reaction rates for each group are then interpolated from homogeneous reaction-rate tabulations.
- Multigroup equivalence: selfshielded multigroup cross sections are calculated by preserving actual reactions rates on each group.

ASSEMBLY GEOMETRY

Thanks to the modular structure of the code, self shielding calculation can be performed in a simplified or altogether different geometry. We present some typical self shielding geometry for the computation of a PWR assembly. The self-shielding can be processed with any other approximation or geometry than the one used for the flux calculation. In the "self-shielding" column (table below) the modelization to perform the Pij's calculations used in the self-shielding process is denoted as follows:

"39"	all fuel cells are different (39 selfshielded cross-section sets)
"12"	fuel cells are grouped in 12 classes (12 selfshielded cross-section sets)
"<ass>"	all fuel cells are grouped in a single class Each assembly cell has the same selfshielded cross-sections in the flux calculation step.
"1"	the selfshielding calculation is not performed in the assembly geometry but in a geometry representing a single cell. Each assembly cell has the same selfshielded cross-sections in the flux calculation step.

Table below gives the infinite multiplication factor (k_∞) and the computation time for all these cases. The APOLLO2 code permits the user to define his own modelization in a very large range of precision and calculation time.

cell number (flux)	Pij	time (flux)	self shielding Pic NR	time (self .shielding)	Δ Kinf (pcm)
45	2Dxy	549	39 2Dxy	930	0
45	2Dxy	532	12 UPO	28	-78
45	2Dxy	527	<ass> 2Dxy	856	-5
45	UP1	360	39 UPO	311	39
45	UP1	355	12 UPO	28	44
45	UP1	343	<ass>UPO	274	-37
45	UP1	343	"1" UPO	1	142
12	UP1	19	<ass>UPO	28	44
45	UPO	90	39 UPO	315	-8
45	UPO	68	12 UPO	28	-4
45	UPO	65	<ass>UPO	266	10
12	UPO	14	"1" UPO	1	
12	UPO	14	<ass>UPO	28	8
45	ROTH	70	39 UPO	308	18
45	ROTH	52	12 UPO	28	22
45	ROTH	50	<ass>UPO	266	12
12	ROTH	10	"1" UPO	1	
12	ROTH	10	<ass>UPO	28	33

reactivity discrepancies and computation time (arbitrary units)

CELL GEOMETRY

In order to show the effect of the fuel discretization on the reactivity we calculate a fuel cell (moderator,clad,fuel) in infinite medium. The pellet is divided into equivolumetric rings,where each ring defines a self shielding zone.

Figure 3-a shows the dependance of the calculated k_∞ versus the fuel spatial discretization with the PIC and BMF models. The chosen parameter is the number of self shielding zones, this parameter varies from 1 to 48. The discrepancy between 1 zone calculation k_∞ and the asymptotic k_∞ value is 500 pcm. We note that the difference between PIC and BMF is lower than 145 pcm.

FUEL DEPLETION

APOLLO2 can calculate the time variation of the isotopic concentrations in any number of media within a geometric domain, containing burnable isotopes (figures 3-b,c). A depletion calculation consists in a serie of depletion steps. The depletion modelization in the fuel depends strongly on the uranium self shielding option and particularly on the spatial discretization.In our application the self shielding calculation is performed at the beginning of life with the PIC NR approximation. Figures (3-c,d) illustrate the sensibility of the ^{239}Pu isotope evolution with the number of self shielded rings. The one-ring selfshielded calculation overestimates the plutonium concentration by about: 3% at 32 GWj/t and more than 4% at 60 GWj/t

EQUIVALENCE

In order to calculate two-dimensional structures larger than an assembly, one of the approach can be the homogenization of each cell (consisting of a fuel pin, clad and moderator) in each of the assemblies calculated separately on a fine spatial mesh.

The homogenization is done by a reaction rate preserving equivalence procedure[10] wich can be performed between two types of transport calculations used in the code

The calculations are performed on two configurations of a 17x17 pins PWR assembly, one with 24 inserted absorption rods containing AIC and one with 25 water holes. The heterogeneous problem is solved with a multicell option (rectangular,uniform double P1 scattering) where all the cells have a different flux.

The equivalence procedure is applied with collision probability methods (multicell and 2D) and Sn methods (finite differences and nodal approximation). Each cell is homogenized in order to obtain the equivalent cross sections on the defined output energy mesh (2 to 99 groups).

We show that the equivalence procedure must be used for both types of assembly. The higher is the energy group number the larger is the discrepancy between homogeneous and heterogeneous calculations without equivalence (following table).

	energy group number	Sn d f dif	Sn n nodal	2D	UP1	UP0
rodded	2	-3948	-3139	-2567		-2250
	8	-5561	-4276	-3459		
	20	-5989	-4552	-3694		
	37	6107	-4630	-2757		
	99	-6304	-4732	-3836	-3478	-3263
unrodded	2	100	85	65		57
	8	39	28	32		
	20	29	21	28		
	37	8	3	16		
	99	5	-1	14	17	20

reactivity discrepancy between homogeneous and heterogeneous assembly calculations without equivalence(pcm)

The equivalence procedure has to compensate the differences between operators: homogenization, transport equation resolution (P_{ij} 2D multicell, Sn finite differences: Sn d and nodal: Sn n) and the spatial convergence of the homogeneous operator.

We can see for the water hole, AIC rod and and fuel cells the coupling between energy and space problems. For example at the 6.7 ev (^{238}U resonance, group 48) the equivalence factor reaches its highest value in all the cells (figures 4-a,b,c).

For a 5x5 cell lattice motif with water hole and B4C rod, we present the spatial dependance of 2 group equivalence factors in the cases of homogeneous P_{ij} and Sn calculations.

The heterogeneous reference calculation is an UP1 multicell approximation, the asymptotic value of the equivalence factor is reached for a size mesh equal to one ninth of a cell, its value is closer to one in the case of the homogeneous P_{ij} (figures 5-a,b,c).

LEAKAGE CALCULATION SCHEMES

The modularity of the APOLLO2 code allows us to perform different iteration strategies in order to compute critical buckling and leakage coefficient.

VOLUMETRIC LEAKAGE MODEL

The homogenization with volumetric leakage, begins with collision, escape and transmission probability calculations for the assembly in infinite medium with zero leakage then two kinds of iterative procedures can be performed (figure 6-a).

- first option:
  - → - homogenized medium, fundamental critical leakage calculations in homogeneous infinite medium -> D B^2
  - - introduction of the leakage as an artificial equivalent absorption uniformly distributed throughout the assembly
  - - computation of the heterogenous multigroup flux with this leakage
- second option:
  - - initialization : homogenized medium, critical leakage calculations in homogeneous infinite medium -> D B^2
  - → - introduction of the leakage as an artificial equivalent absorption uniformly distributed throughout the assembly
  - - computation of the heterogenous multigroup flux with this leakage
  - - use of a perturbative formula for critical B^2

SURFACE LEAKAGE MODEL

Retaining the fundamental mode hypothesis in order to simulate the assembly environment, the basic idea of this model[11] is to modelize leakage by a term of incoming current on the outer surfaces. This model needs the calculation of collision, escape, and transmission probabilities corresponding to vacuum boundary conditions; the isotropicaly reflected Pij's are only used in the initialization step (zero leakage initial flux calculation). Then the critical leakage calculation scheme consists on two kinds of iterative procedures (figure 6-b):

- first option:
  - → - homogenized medium, fundamental critical leakage calculations in homogeneous infinite medium -> D B^2
  - - incoming angular flux computation with the fundamental leakage rate
  - - calculation of the heterogeneous flux with the Pij corresponding to albedo=0 and imposed incoming angular flux on outer boundaries
- second option:
  - - initialization : homogenized medium, critical leakage calculations in homogeneous infinite medium -> D B^2
  - → - incoming angular flux computation with the fundamental leakage rate
  - - calculation of the heterogeneous flux with the Pij corresponding to albedo=0 and imposed incoming angular flux on outer boundaries
  - - use of a perturbative formula for critical B^2

CALCULATION EXAMPLES

As an example we give the comparison between the two leakage calculation methods applied to the 17x17 PWR assemblies with uranium and mixed oxyde fuel with and without absorbing rods. Collision probabilities were computed with the multicell option UP0. The effect on rods efficiency depends slightly on the boron concentration (figure 7).The surface leakage model introduces always a greater power or flux gradient inside the assembly (figure 8). For the rodded assemblies the surface leakage model is well adapted but for unrodded assemblies the leakage model gives a very different fine structure without significant reactivity effect.

CONCLUSION

APOLLO2 code's validation is under progress and we present some important aspects, to take into account for building any future calculational scheme using new potentialities developped into APOLLO2.

REFERENCES

1 R Sanchez, J Mondot, Z Stankovski, A Cossic, I Zmijarevic, "APOLLO-II A User Oriented, Portable, Modular Code for Multigroup Transport Assembly Calculations", Nucl Sci Eng., 100, 352 (1988)

2 M Coste, R Sanchez, Z Stankovski, C Van der Gucht and I Zmijarevic, "APOLLO-II ASSEMBLY SPECTRUM CODE NEW FEATURES", Advances in Mathematics, Computations and Reactor Physics, International Topical Meeting, Pittsburg, May, 1991

3 A Kavenoky, R Sanchez, "The Apollo assembly spectrum code", ANS International Topical Meeting on Advances in Reactor Physics, Mathematics and Computations, Paris, April 27-30, 1987

4 A KAVENOKY, "APOLLO A General Code for Transport, Slowing-Down and Thermalization Calculations in Heterogeneous Media, "Proc. Natl. Topl. Mtg. Mathematical Models and computational Techniques for Analysis of Nuclear Systems, Ann Arbor, Michigan, April 19-11, 1973

5 R Sanchez, Nucl. Sci. Eng., 92, 247 (1986)

6 A Kavenoky, M Lam-Hime and Z Stankovski, "Improvement of the Integral Transport Theory Method", Proc. Topical Mtg on Computational Methods in Nucl. Eng. ANS, Williamsburg II 7-55 (1979)

7 R Sanchez, M Coste, Z. Stankovski, C Van der Gucht, "Models for Multigroup Selfshielded cross sections calculations in the code APOLLO-II", PHYSOR, Marseille, France, April 23-27, 1990

8 R Sanchez and J Mondot, "A Model for Calculating Multigroup Self-Shielded Cross Sections for a Mixture of Resonance Absorbers in Heterogeneous Media", Proc. Mtg. Advances in Reactor Physics and Radiation Protection and Shielding, Chicago, Illinois, September 17-19 (1984)

9 M Coste, H. Tellier, C Brienne and C Van Der Gucht, "Heavy Nucleus Resonance Absorptions in Heterogeneous Lattices", this meeting

10 A Hebert and A Kavenoky, "Development of the SPH Homogenization Method", ANS/ENS International Topical Meeting on Advances in Mathematical Methods for the Solution of Nuclear Engineering Problems, Munich, April 1981

11 A Hebert and P Benoist, "Application of the SPH Method to the Homogeneous Diffusion Procedure" 12th Int. Top. Mtg. Advances in Reactor Physics, Mathematics and Computations, Paris, France, April 27-30, 1987

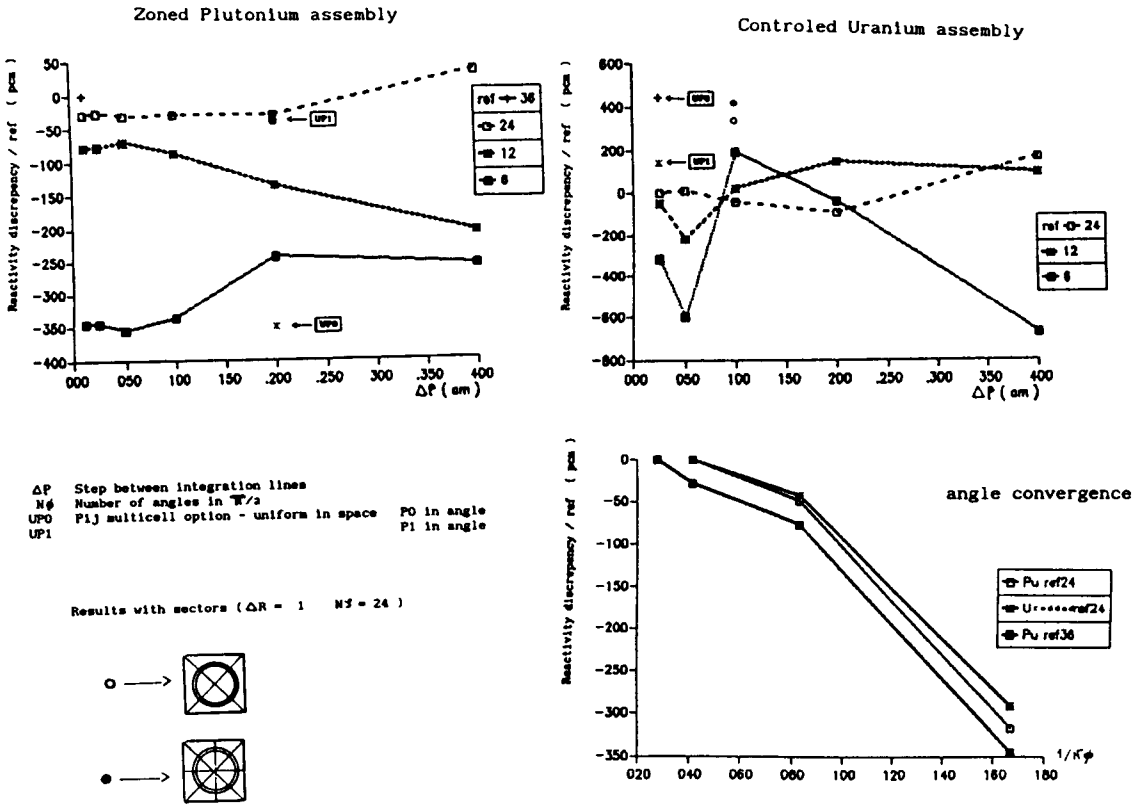

figure 1 reactivity dependance on collision probability options

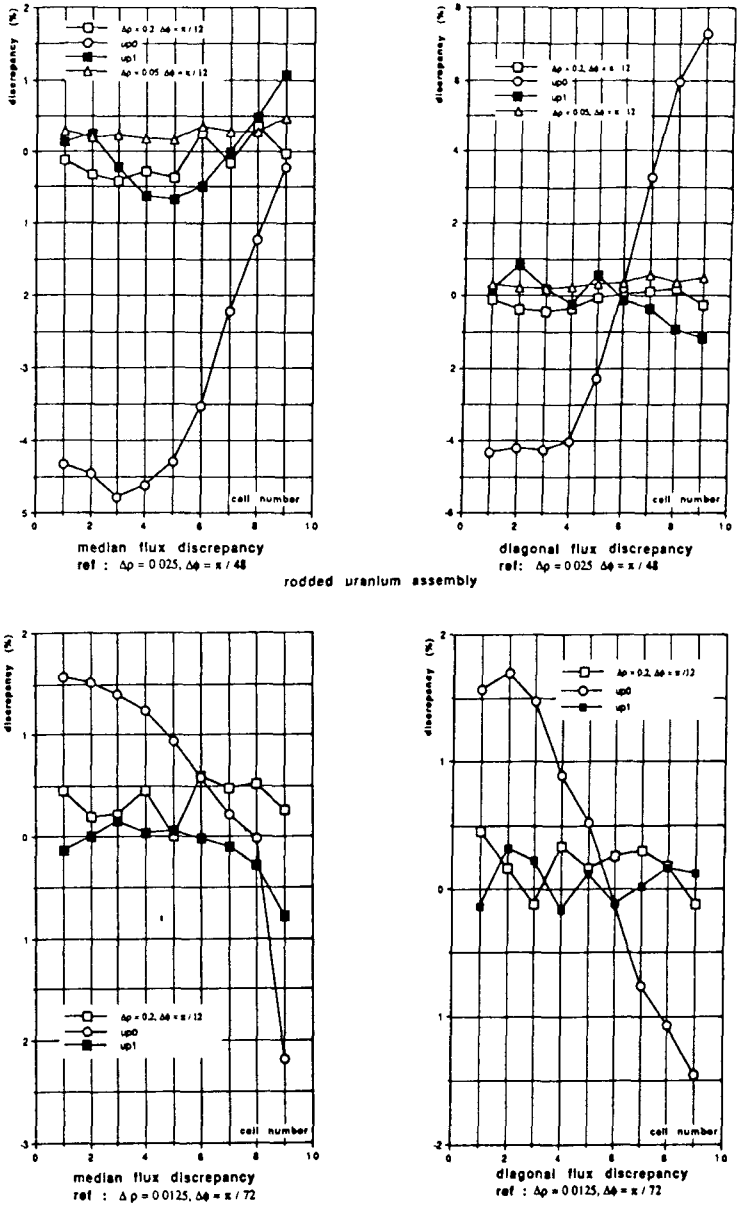

figure 2 : one group flux discrepancies on the assembly diagonal and median

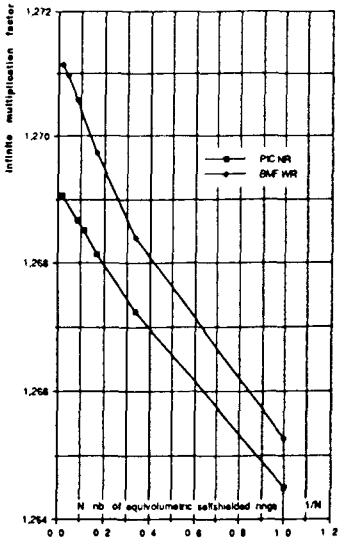

-a: Kinf versus the number of selfshielded rings

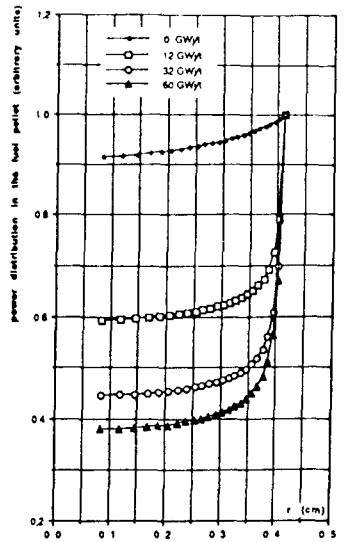

-b: radial power distribution in the fuel pellet

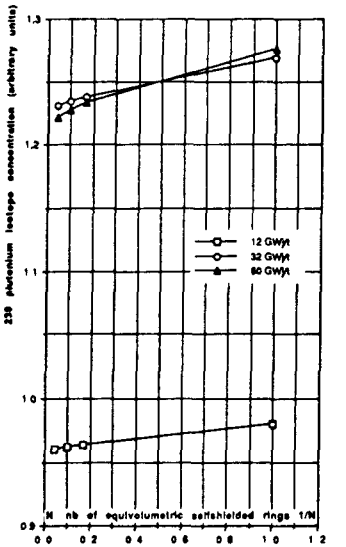

-c: 239 plutonium concentration versus the number of selfshielded rings

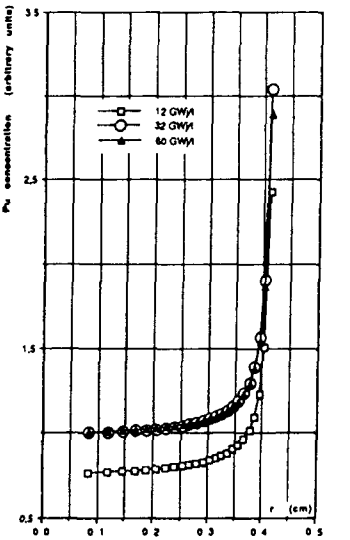

-d: radial distribution of the Pu 239 concentration

figure 3 : sensibility to the selfshielded zone number

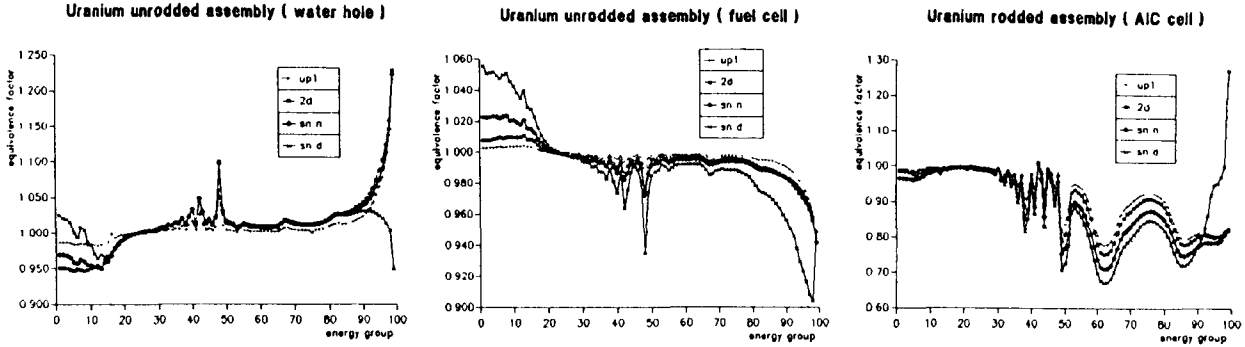

figure 4 : 99 group equivalence factors

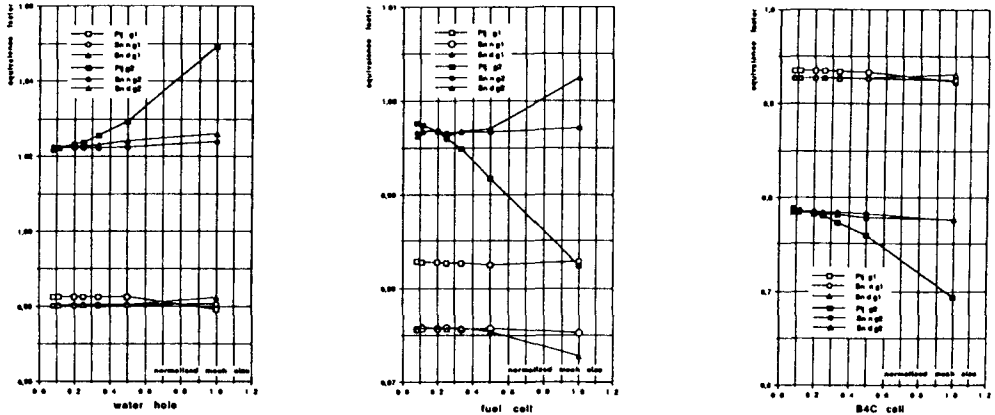

figure 5 : 2 group equivalence factors, spatial convergence

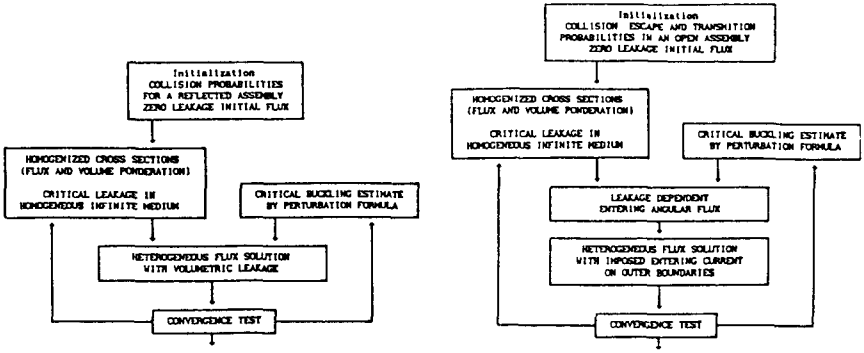

a) - Volumetric leakage model

b) - Surface leakage model

figure 6 Iteration schemes for leakage coefficient and critical buckling search

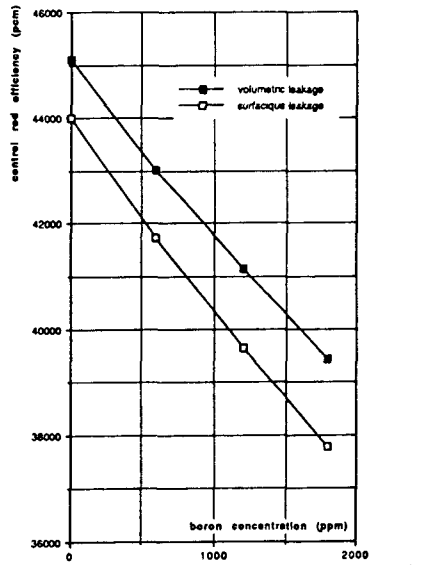

AIC control rod efficiency versus boron concentration

figure 7

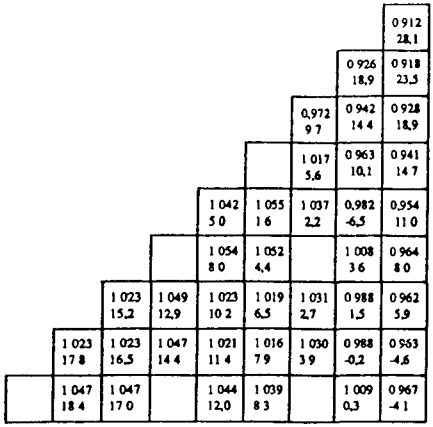

							0 912 28 1
						0 926 18,9	0 918 23,5
					0,972 9 7	0 942 14 4	0 928 18,9
					1 017 5,6	0 963 10,1	0 941 14 7
				1 042 5 0	1 055 1 6	1 037 2,2	0,982 -6,5	0,954 11 0
			1 054 8 0	1 052 4,4		1 008 3 6	0,964 8 0
		1 023 15,2	1 049 12,9	1 023 10 2	1 019 6,5	1 031 2,7	0 988 1,5	0,962 5,9
	1 023 17 8	1 023 16,5	1 047 14 4	1 021 11 4	1 016 7 9	1 030 3 9	0 988 -0,2	0,963 -4,6
	1 047 18 4	1 047 17 0		1 044 12,0	1 039 8 3		1 009 0,3	0,967 -4 1

unrodded U assembly	volumetric	surface
Kinf	1 26812	1 26895
B²	0 004580	0 004598

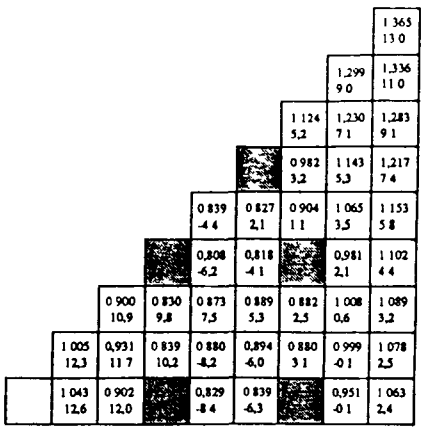

							1 365 13 0
						1,299 9 0	1,336 11 0
					1 124 5,2	1,230 7 1	1,283 9 1
					0 982 3,2	1 143 5,3	1,217 7 4
				0 839 -4 4	0 827 2,1	0 904 1 1	1 065 3,5	1 153 5 8
			0,808 -6,2	0,818 -4 1		0,981 2,1	1 102 4 4
		0 900 10,9	0 830 9,8	0 873 7,5	0 889 5,3	0 882 2,5	1 008 0,6	1 089 3,2
	1 005 12,3	0,931 11 7	0 839 10,2	0 880 -8,2	0,894 -6,0	0 880 3 1	0 999 -0 1	1 078 2,5
	1 043 12,6	0 902 12,0		0,829 -8 4	0 839 -6,3		0,951 -0 1	1 063 2,4

rodded U assembly	volumetric	surface
Kinf	0 82473	0 83552
B²	0 003282	0 003073

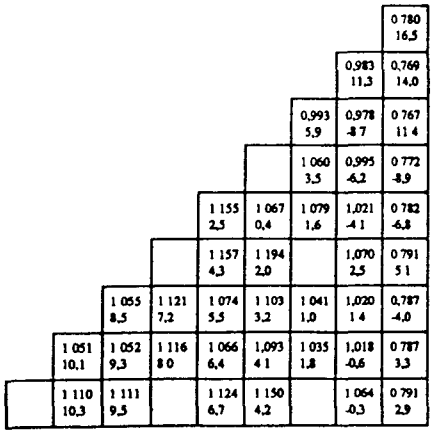

							0 780 16,5
						0,983 11,3	0,769 14,0
					0,993 5,9	0,978 -8 7	0 767 11 4
					1 060 3,5	0,995 -6,2	0 772 -8,9
				1 155 2,5	1 067 0,4	1 079 1,6	1,021 -4 1	0 782 -6,8
			1 157 4,3	1 194 2,0		1,070 2,5	0 791 5 1
		1 055 8,5	1 121 7,2	1 074 5,5	1 103 3,2	1 041 1,0	1,020 1 4	0,787 -4,0
	1 051 10,1	1 052 9,3	1 116 8 0	1 066 6,4	1,093 4 1	1 035 1,8	1,018 -0,6	0 787 3,3
	1 110 10,3	1 111 9,5		1 124 6,7	1 150 4,2		1 064 -0,3	0 791 2,9

unrodded Pu assembly	volumetric	surface
Kinf	1 13283	1 13440
B²	0 002438	0 002468

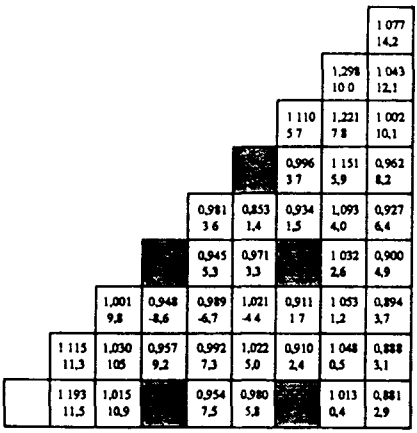

							1 077 14,2
						1,298 10 0	1 043 12,1
					1 110 5 7	1,221 7 8	1 002 10,1
					0,996 3 7	1 151 5,9	0,962 8,2
				0,981 3 6	0,853 1,4	0,934 1,5	1,093 4,0	0,927 6,4
			0,945 5,3	0,971 3,3		1 032 2,6	0,900 4,9
		1,001 9,8	0,948 -8,6	0,989 -6,7	1,021 -4 4	0,911 1 7	1 053 1,2	0,894 3,7
	1 115 11,3	1,030 10 5	0,957 9,2	0,992 7,3	1,022 5,0	0,910 2,4	1 048 0,5	0,888 3,1
	1 193 11,5	1,015 10,9		0,954 7,5	0,980 5,8		1 013 0,4	0,881 2,9

rodded Pu assembly	volumetric	surface
Kinf	0 85216	0 85741
B²	-0 002816	0 002713

figure 8 - pin power distribution with volumetric leakage
- discrepancy between volumetric (a) and surface (b) leakage b/a-1 (%)

NAUTILE : AN INTELLIGENT FRONT-END FOR CORE COMPUTATION SYSTEM

P. Girieud, O. Loussouarn
M. Roshd, A. Vallée

FRAMATOME, TOUR FIAT, Cedex 16,
92084 PARIS LA DEFENSE

ABSTRACT

The new nuclear design system developed by FRAMATOME provides an extensive range of neutronic methodologies capable of analysing current and future PWR fuel and core designs. This system is highly modular allowing the engineer a complete choice of degree of sophistication and precision he wants to apply to his design problems.
To give the designer a full control and convivial utilisation of these modules, the system NAUTILE has been developed.

NAUTILE is an integrated software system applying some of the most up-to-date data processing, information management, knowledge engineering, and graphic interfaces and visualisation techniques. It provides an intelligent guidance and supervises the planning, preparation and execution of all analysis tasks.

INTRODUCTION

The nuclear design system, called SCIENCE, has been under intensive development at FRAMATOME for the last four years. The objectives are :

- to provide an advanced highly versatile, system of neutronic codes capable of modeling current and future PWR fuel and cores in almost any degree of sophistication required;

- to make available to the designer some of the most modern data processing, information management techniques which would create a user environment with a high degree of conviviality, quality assurance and engineering time saving.

THE NUCLEAR DESIGN SYSTEM

Efforts have been focused on extending neutronic methodologies in order to cover all possible design problems. This has resulted in a highly modular system that includes numerous calculational methods · diffusion theory in finite differences, finite elements or nodal forms , transport theory is represented by modules based on discreet ordinates or collision probability techniques, and eventually a Monte-Carlo module will be added to the system.

The 3-D physical models can be either in X-Y-Z, RZθ or, in some cases, hexagonal geometries.

Full description of these modules is given a paper presented at this meeting. (Ref 1)

MODULARITY OF THE SYSTEM

Due to the high modularity of the system the designer does not face a hardwired code unwieldy and impossible to alter without internal intervention by the developer.
Here the user can choose the degree of sophistication adapted to his problem, he can even try several combinations of modules, before finally "softwiring" the system by a procedure which then becomes the recommended design method The system is an adaptable tool in the hands of the nuclear designer.

This is made possible by the fact that each module has been programmed to perform a well defined task. The required input is in the form of a set of structured data objects which would lead, after transformation by a module, to another set of objects. The transmission of information between modules during execution is via these objects, and thus the modules can either stand alone or be in any number of possible combinations.

The language used for developing this system is called ESOPE. This is a superset of FORTRAN 77; it has in addition to the latter a small number of instructions permitting the creation and manipulation of data objects. It is to be stressed here that the programme, after preprocessing, results in pure FORTRAN instructions which can then be compiled and executed in the usual manner.

During the execution of the modules various objects are deposited in computer memory for other modules to use. Since some of these objects will not be used by the rest of the job or will be used

at a much later phase of the calculation, a memory manager called GEMAT, keeps track of all objects and retires to mass storage any objects that are either idle or of low priority

This memory space optimization is very useful for large cases

The modularity of the system has also made it easy to create a new control language, called GIBIANE, which is used for "softwiring" a set of modules in a simple and efficient way. The instruction to activate any module is reduced to giving, in very simple syntax, its name, the names of the objects required by it to do its tasks, and finally the name of objects desired as result.

These instructions can be conditional or can be included in a loop giving rise to very interesting calculational schemes without having to go back to the developer with different specifications each time a new idea is to be tried by the designer.

When the job being processed is terminated a number of selected objects could be saved in order to be used for graphical visualisation, further analysis or for restarts at later dates. These objects are saved on a file with well defined structure such that any object or part of can be accessed by utility programs developed for this purpose. These files, called databanks, become the information carriers outside the modules.

A part of these databanks consisting of small objects are saved in a relational database while the databanks themselves are sent to a central mass storage.

INFORMATION MANAGEMENT

As mentioned earlier information is transmitted between modules via objects during execution and via databanks after execution But this is not the only information the designer has to worry about. He has to create new databanks or update old ones using basic engineering data (assembly or core geometry, compositions ... etc). This is traditionally stored on a special set of files. The results of design calculations are saved and catalogued on other files. The utility programs for interrogating one set might be different from the ones used for the other set. The user has also to know the procedures used for his analysis, and keep track of them separately. The choice of a particular procedure among possibly hundreds, or finding whether any results exist from a previous analysis of a similar problem might be very time consuming.

It would also be reckless to give the analyst more possibilities by increasing the range of methodologies at his disposal allowing him to create more sophisticated models and procedures generating, perhaps, a large amount of data (by the powerful new workstations or supercomputers) without giving him the tools to facilitate his job and control the flow of information in his system

USER ENVIRONMENT SOFTWARE

It is becoming abundantly clear that in an industry where analysis results have to be of the highest accuracy and reliability, an environment have to be created to permit the engineer an easy, reliable and rapid access to the different modules, the basic engineering data the calculation procedures or any other information he might require for his analysis.

Some of the criteria for designing such environment software are listed here :

1. Increasing flexibility of the nuclear design system without sacrificing quality assurance.

2. Defining and structuring data in such a way that its transmission and processing could be done with the same tools, created for this purpose, regardless of its origin whether it be of calculational, experimental or engineering nature.

3. Ensuring portability of the software on most machine types.

4. Providing an integrated intelligent interface which would act as a guide and a help in organizing, preparing and executing the calculations needed by the analyst This has led to adopting some of the well established techniques used in knowledge engineering.

The flow of information between the different components of NAUTILE system is shown in Fig.1

Functionally the system goes through three different stages :

1. Planning of the analysis strategy

2. Assembling and preparing the particular modules and their input data objects.

3. Executing the calculation and handling the resulting objects.

1. PLANNING THE ANALYSIS STRATEGY

The engineer would first, through a dialogue with PILOTE, specify his design problem and his objectives.
He naturally first would like to know whether similar analysis had been done in the past.

A request from PILOTE to the relational data base SINDBAD would be able to supply an answer. This is possible because SINDBAD stores summaries of the most important results of previous analyses. If these results do not fully satisfy the problem at hand further dialogue with PILOTE would now help to determine the methodology to use, which is normally embodied into a procedure. The latter consists of a set of verified rules defining the steps, modules and conditions required for design analysis. A procedure could be simple such as running a particular module to get given results, or could be complex, e.g. a complete accident or transient analysis; in which case different modules of various geometry models and physical conditions might be needed.

Information on these procedures forms a knowledge base through which PILOTE can search using its inference engine and backward chaining.

Pilote is implemented in SPIRAL, a logical programming language based on PROLOG with added object-oriented features.

2. ASSEMBLING AND PREPARING THE COMPUTATION TASKS

Having chosen the procedure to apply to the specified problem as described above, the job, however, is not yet ready for execution as each module would require its own particular input data objects. This functionality is accomplished by MAX (see fig.1)

MAX is also programmed in SPIRAL and has its own knowledge base containing information on the different modules, their functions, options, limitations and their input and output data objects.

A convivial dialogue with MAX would lead to specification of data required.

The designer would have to give directly as few data as possible but he is asked by the system to specify the type of fuel, core and irradiation cycle. Pertinent information is then fetched directly from the data base by MAX.

Having assembled all the necessary components, MAX then generates automaticaly a set of GIBIANE instructions The procedure is now instanciated and ready for execution under the control of CONGRE

3. EXECUTION OF THE COMPUTATION TASKS

CONGRE dispatches the job to the CRAY computer for execution but remains active waiting for the return of some predesignated objects at predetermined interruption points in the sequence of modules execution.

Quick diagnostic would determine whether execution is still on course and results are reasonable. This is hoped to eliminate most of the costly divergent cases. The development of an automatic intelligent diagnostic module might be beneficial for almost all cases.

When the job is satisfactorily completed, the databanks produced are sent to the central mass storage after having extracted a summary of the most important results to be included in the SINDBAD database.

Databanks could also be requested by ECUME for further post-processing and graphic visualisation. In addition ECUME allows the engineer to prepare and publish documents or reports that would include tables or graphics.

SUMMARY

FRAMATOME has developed a new nuclear design system with vastly improved neutronic methodologies for treating PWR design problems.

NAUTILE, the user environment software has introduced a large degree of conviviality without sacrificing rigour in analysis or quality assurance. It is implemented using up-to-date techniques in data processing, information management, knowledge engineering and graphic visualisation.

NAUTILE allows an easy, reliable and rapid access to any information item required by the nuclear design system. It also acts as an intelligent guide and a supervisor during all stages of analysis planning, preparation and execution.

REFERENCES

1. A. Vallée, et al, "SCIENCE : a new Reactor Physics Codes Package Approach"
ANS 1992 Topical Meeting on Advances in Reactor Physics, March 8-11, 1992.

Figure 1: User Environment Software

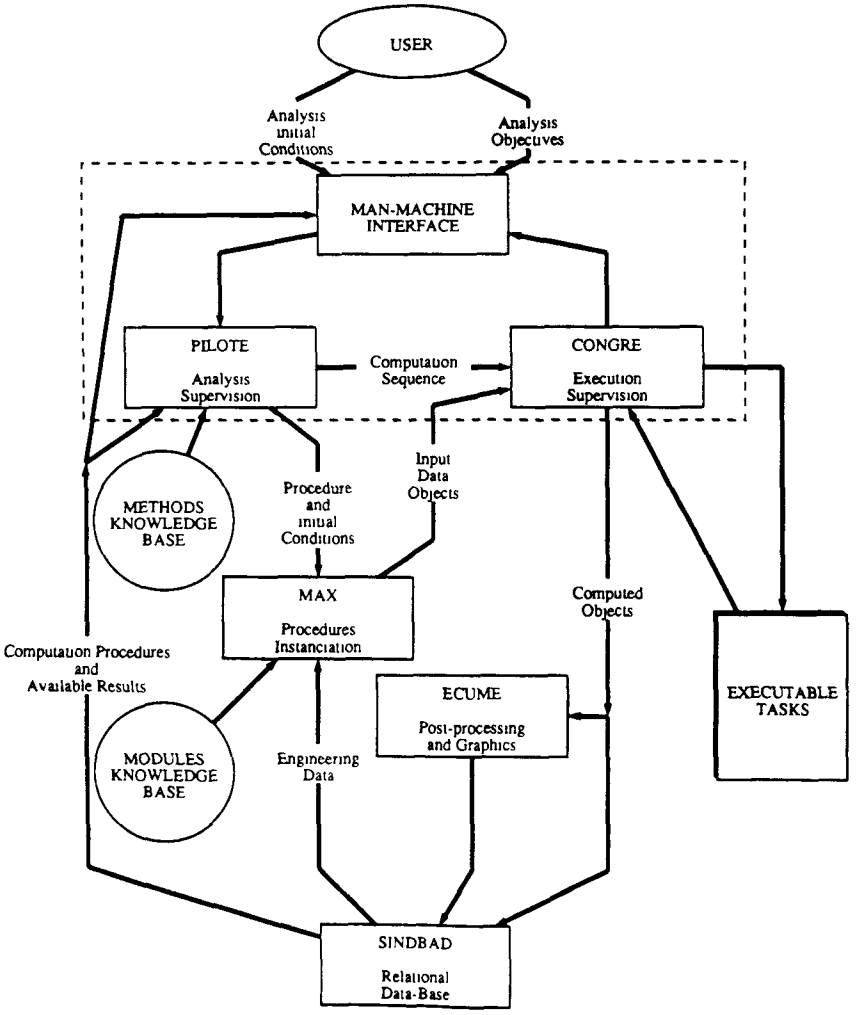

APOLLO-II CODE UTILIZATION FOR PROJECT CALCULATIONS

G.B BRUNA*, P L CORNILUS*, M. GROSSHANS*, M NOBILE**,
M L.VERGAIN*

** CEA,DMT/SERMA - CEN SACLAY,
detached to FRAMATOME
* FRAMATOME, TOUR FIAT, Cedex 16,
92084 PARIS LA DEFENSE

ABSTRACT

APOLLO II is a second-generation, fully modular, general purpose multigroup transport code It has been developed by the Commissariat à l'Energie Atomique, (CEA) in the 80's, and integrated, recently, by FRAMATOME into its new project computational chain, SCIENCE.

After presenting an outline of its most important computational options, we provide, in this paper, some examples of APOLLO-II applications to PWR project studies, as well as an outline of several recommanded computational procedures.

INTRODUCTION

APOLLO-II (Ref.1), a multigroup transport code developed by the French Commissariat à l'Energie Atomique (CEA) and fully documented in a wide set of previous papers (Refs. 2,3), has been included as an up-stream module, in the frame of the FRAMATOME's new project computational chain, SCIENCE (Ref.4), a schematic view of which can be seen in Figure 1.

APOLLO-II is a user oriented, fully modular system, each of its 50 modules, has been conceived to assume an elementary computational function, e.g., input reading, library access, generation of isotope data sets, description of geometry, self-shielding and flux computations, exploitation of results and editing

All modules communicate with each other via data structures called "objects"

A macrolanguage, GIBIANE, deals with the transmission and transformation of the objects through the modules of the system. This allows any user to define his own computational pattern.

The large flexibility of the system, which is really of use as far as fundamental analysis and parametrical studies are concerned, would seem somewhat impractical for standard project applications

In order to avoid confusion and inconsistencies, related to this choice, a big effort was made in FRAMATOME with the aim of defining and validating suitable computational schemes, well adapted to any particular project circumstance A quite complete set of standard procedures was thus defined, and an expert system, MAX (Ref 5), has been conceived in order to help users to construct them in a fully automated way.

The validation of these procedures was made via computation-measurement comparisons, and, when the experimental information was either missing or incomplete, via computational benchmarking

In this paper, after presenting the APOLLO II main physical and computational features, we provide several examples, chosen in a quite large set, of the accuracy of the system results in project applications

APOLLO-II MAIN FEATURES

Since main physical and computational features of APOLLO II have been described widely in the above-mentioned literature, only the most project-oriented options of the code will be discussed here

- LIBRARY the standard APOLLO-II library contains approximatively 400 isotopes Generated by the THEMIS-NJOY system, (Ref 6), it is based on the standard APOLLO I library, (Ref 7), up-dated to JEF-1, (Ref 8)
The 99 group library supports any degree of cross-sections anisotropy

- SELF-SHIELDING the computation of the self-shielded cross-sections in APOLLO-II accounts for space and energy resonance overlapping among isotopes, in heterogeneous media
The overlapping is computed either via a simple isotope iterative scheme, or by mixture dependent probability tables

- FLUX COMPUTATIONS APOLLO-II offers the user a wide set of flux computational otions, including

integral transport, (collision probability method),
discrete ordinates, (SN)

FLUXES can be computed (for the usual 1D (slab) and three 2D geometries, (X,Y), (R,Z), and hexagonal) on the basis of

- exact collision probabilities, (quoted as exact CP),
- multicell formalism, with an anisotropic description of the angular flux at interfaces,
- multicell formalism, with an isotropic description of the interface flux

When a 2D collision probability computation is performed via an exact direct method, subdivision of pins into subregions and angular discretisation of the flux in sectors are allowed.

The bulk of its SN modules allow APOLLO-II to compute heterogeneous flux using the discrete ordinate solution of the integro-differential transport equation, taking into account highly anisotropic scattering by the Pn formalism.

- DEPLETION : APOLLO-II computes the variation in time of the densities of isotopes in any number of media, subdividing the depletion interval into a series of steps, each beginning with the estimation of new densities on the basis of a reaction-rate extrapolation. This stage, called the predictor stage, makes use of a fourth order Runge-Kutta method.

One can choose a local or global depletion variable and the process convergence is automatically verified.

- LEAKAGE · the original APOLLO-I method based on the calculation of homogenized diffusion coefficient and B^2 has been generalized in APOLLO-II ; it treats mutually interacting sub-systems and computes a diffusion coefficient per assembly, which can be used in subsequent diffusion calculations.

- OUTPUT · beside flux collapsing and homogenization, the APOLLO-II system can perform equivalence processes, in which the cross-sections are adjusted in order to preserve the reaction rates of any reference calculation.
Suitable output routines have been conceived in order to couple the code to down-stream modules of the SCIENCE chain, mainly the 3D nodal and 2D discrete options of the SMART system.

A simple zero-dimension, 2 group, analytical perturbation formula was also developed ; it allows splitting differences of reactivity into elementary components, mainly those related to isotopes and cross-sections (Ref. 9).
This formula is very practical when validation of computational procedures against a reference and comparative analysis are to be made.

APPLICATIONS

High APOLLO-II computational performance can be really of use in a very large range of project cases.

In the following, we present some examples of APOLLO-II calculations, performed in the framework of FRAMATOME project studies and chain validation.

A first example of APOLLO-II use can be found in the series of core, cluster and assembly calculations we made for analyzing the very heterogeneous CAMELEON (Ref. 10) and EPICURE (Ref. 12) integral experiments.

A wide set of configurations, including black and gray absorbers, gadolinium pins in presence of water holes, pyrex and gadolinium poisoned clusters, UO2-MOX arrays, have been studied, both in homogeneous and heterogeneous descriptions. Easy and low cost APOLLO-II computations were made possible by the heterogeneous to homogeneous equivalence process, which preserves the heterogenous reaction rate values on homogenized regions

Several multicell options, in which the elementary cells are coupled via an interface current technique, were used in assembly configuration both with isotropic and anisotropic expansions at the boundaries, to generate suitable two group cross-sections for diffusion calculations.

All the results have been compared to reference transport calculations and to experimental results using a core scale factor technique (Ref. 11)

APOLLO-II computes also fuel and non fuel depletion, multiregion and multimixture, using a predictor-corrector technique, as presented before

The gadolinium depletion procedure includes (Ref. 13) :

- a 4 concentric region depletion model,

- an individual self-shielding of main Gd isotopes,

- a full description of depletion chains.

The results of the analysis of the GEDEON experiment testify to the accuracy of the APOLLO-II computations.

APOLLO-II was also used to search for a reference cross-section generation scheme for annular fuel pins . the impact of radial self-shielding and temperature distribution in the pellet have been investigated broadly in a parametrical way, as a function of the hole diameter for different computational options

PRESENTATION OF SOME RESULTS

CAMELEON

Most CAMELEON (Figure 2) analysis performed with APOLLO-I code has been broadly presented and discussed in two previous works (Refs. 10 and 11).

In the framework of APOLLO-II validation, several of these studies have been reconducted and confirm the previous results. In this paper, we only summarize the most important conclusions.

The purpose of CAMELEON studies was to establish a suitable validation basis for computational procedures of the SCIENCE chain, on the ground of a quite large set of experimental cluster configurations.

The results broadly confirmed the reliability of the exact CP transport option as a reference for the equivalence process aimed at the generation of diffusion data, and the deshomogenization in nodal calculations (Figures 3 and 4)

Moreover, the reliability of the whole diffusion cross-section generation process in the SCIENCE chain has been demonstrated, (Figures 5 and 6).

EPICURE

The EPICURE program, launched in 1987, is now in progress in the EOLE facility at the CEA Center of Cadarache.

According to a tripartite agreement (EDF,CEA and FRAMATOME), the program should support the test and validation of MOX (Mixed Oxyde) fuel project computational procedures. In order to meet this quite ambitious goal, a series of different configurations, simulating MOX and UO2 patterns, have been considered. Until now, only one configuration has been fully analyzed (Ref. 12) , we present here part of a large scale analysis we made at FRAMATOME on the so called UMZONE layout (Figure 7).

In order to allow the analysis of the very physically meaningful MOX-UO2 transition zone, the whole study has been based on a cluster description of the central core zone including the MOX three zone central assembly and a three cell thick UO2 surrounding region.

According to the complexity of the problem, two kinds of collision probability methods were selected . either an exact direct method (exact CP) or a multicell approximation with an isotropic description of the angular flux at cell interface.

The comparisons between calculation and experiment make use of heterogeneous and homogeneous computational schemes :

. A subdivision of cells into subregions through radial and angular discretisation (Figure 8) and exact CP calculations allow an accurate estimation of fluxes in the cluster, mainly for MOX-UO2 assembly interface cells which present a strong variation of the spectrum and neutron flux.

. The multicell approximation was used for self-shielding calculations, 2 group diffusion data generation and 99 group heterogeneous-homogeneous transport equivalence process in order to generate equivalent homogeneous cell data.

. Using these equivalent data, a homogeneous procedure allows the calculation of the "core scale factors" which simulate the core effects in the experiment computation comparison. These pointwise correction factors are estimated directly by comparing the power distributions calculated in the full core and in the cluster ; both descriptions used homogeneous cells, with exact CP computations.

Figure 9 shows, in a synoptic way, the (C-M) deviation of the point-power distribution, through the central MOX assembly-wise zone, the interface and UO2 surrounding zone. The results have been respectively obtained from an exact CP heterogeneous solution and homogeneous scheme transport calculations.

The uncertainty due to experimental techniques based on particular gamma ray peak scanning, may be up to $\pm$ 5 % at 2 σ (Ref. 14) so that the confidence level of the comparisons between measurement and calculation actually depends on this quite large experimental uncertainty.

However, the figure 9 shows the possibility of an improvement of heterogeneous results mainly at the transition zone.

In addition, 2D discrete centered mesh diffusion xy calculations have been run with 2 macrogroup cross-sections issued from multicell calculations as in project procedure (Figure 10).

It can be seen that an overall good agreement is found.

GEDEON

The GEDEON experiment has been carried out in the MELUSINE facility at the CEA Center of Grenoble. Two phases were scheduled ; we present here some preliminary results of phase I.

The experiment has provided a suitable experimental data set for the definition and validation of project computational procedures for gadolinium burnable poisons. The main items in the experiment were burn-up aspects, the steady state validation being achieved via CAMELEON experiment analysis, as seen before.

In order to reach a sufficient burn-up of the four gadolinium poisoned pins loaded in the central test region of the facility, a particular MELUSINE configuration was designed (Figure 11), with a feeding driver external zone.

The depletion of the system was calculated with the APOLLO-II code, in an infinite medium assembly approximation ; we previously verified that this representation was satisfactory for poisoned pin burn-up simulation. The computed isotopical densities have been compared, for different computational options, to the experimental results.

Figure 12 shows very satisfactory results in the case of our reference computational procedure. Figure 13 gives some complementary informations about gadolinium depletion, particularly the discrepancy of the one zone - Gadolinium pin depletion results.

ANNULAR PELLET

Usual project calculations are performed with only one computation region in the pellet. This method does not take into account the spatial energy interference for resonant isotopes.

In order to evaluate the impact of this approximation for a standard UO2 cell, we subdivided the fuel pin into ten equivolumetric regions and an accurate self-shielding calculation (Ref. 1) was performed with an improved PIC model, a narrow resonance aproximation and a groupwise homogenization.

We found that the one region calculation underestimates the U238 absorption by about 200 pcm. Figure 14 shows the U238 absorption rate per region For the accurate (10 points in the pellet) and the simplified (1 point in the pellet) computations, the depletion was performed up to a burnup of 60 GWd/t. At this stage, the simplified computation overestimates the average Plutonium production (especially Pu239) by about 2.9 %. Figure 14 also presents the spatial distribution of Pu239 concentration in the pellet at 60 GWd/t.

Figure 15 shows the average Pu239 concentration at 30 GWd/t and 60 GWd/t for both simplified and accurate calculations

This approach was performed in order to search for a specific computational procedure for pins containing an annular pellet APOLLO II performance has then been very useful allowing a broad analysis of most annular pellet physical features

Further studies of the cross-sectional sensitivity to

- the computation of a radially dependent self-shielding,
- a multiregion description of the pellet in burn-up calculation,
- a radial temperature profile description

are in progress

CONCLUSION

We present in this paper an overview of the most important APOLLO-II computational options and provide several examples of its use in a project context at FRAMATOME

Thanks to its flexibility and its very wide choice of computational options, APOLLO-II can be used for the development of new computational methods and the analysis of new and advanced reactor models and components

On the basis of this preliminary but quite large experience APOLLO-II shows up being a very accurate and well adapted up-stream module for the newly developed SCIENCE project computational chain

REFERENCES

1/ M. COSTE, R. SANCHEZ, Z. STANKOVSKI, C. VAN DER GUCHT, and I ZMIJAREVIC, "APOLLO-II Assembly Spectrum Code : New Features", in Proceedings of the International Topical Meeting on Advances in Mathematics, Computations and Reactor Physics, PITTSBURGH, April 28 - May 2, 1991 ;

2/ R. SANCHEZ, J. MONDOT, Z. STANKOVSKI, A. COSSIC, I. ZMIJAREVIC, "APOLLO-II : A user Oriented, Portable, Modular Code for Multigroup Transport Assembly Calculations", in Proceedings of the ANS International Topical Meeting on Advances in Reactor Physics, Mathematics and Computation, PARIS, April 27-30, 1987 ;

3/ R. SANCHEZ, M. COSTE, Z. STANKOVSKI, "Models for Multigroup Self-shielded Cross Sections Calculations in the Code APOLLO-II", in Proceedings of the Physor'90 Meeting, MARSEILLE, April 23-27, 1990 ;

4/ A. VALLEE, G. FRANCILLON, J. PELET, "SCIENCE, a new Reactor Physics Code Package Approach" to be presented at this Meeting ;

5/ O. LOUSSOUARN, A. BOIVINEAU, C. FERRARIS, "MAX : An Expert System for Running the Modular Transport Code APOLLO-II", in Proceedings of the Physor'90 Meeting, MARSEILLE, April 23-27, 1990 ;

6/ C.M. DIOP, D CHAIGNE, G. DEJONGHE, J. GONNORD, J.M. DE VILLENEUVE, "THEMIS . Système de Traitement des Sections Efficaces. Présentation, Manuel d'Utilisation", DEMT/88/280 SERMA/LEPP/881022 ,

7/ A. KAVENOKY, R. SANCHEZ, "The APOLLO Assembly Spectrum Code", in Proceedings of the ANS International topical Meeting on Advances in Reactor Physics, Mathematics and Computation, PARIS, April 27-30, 1987 ;

8/ J.L. ROWLANDS and N. TUBBS, "The Joint Evaluated File : A New Nuclear Data Library for Reactor Calculations", in Nuclear Data for Basic and Applied Science, Vol. 2, (1985) ;

9/ J. PORTA, J.Y. DORIATH, A. MOURGUES, M. NOBILE, A. VALLEE and G.B. BRUNA, Nucl. Sci Eng. 95, 266-281, (1987) ;

10/ G.B. BRUNA, M. NOBILE, A. VALLEE "Transport and Diffusion Infinite Medium Assembly Calculations of Pin Power Distribution", in Proceedings of the ANS Topical Meeting on Advances in Mathematics, Computations and Reactor Physics, PITTSBURGH, April 28, May 2, 1991.

11/ G.B. BRUNA, J.P. CHAUVIN, M. NOBILE, G. PALMIOTTI, C. VAN FRANK, M.L. VERGAIN, "Search for a Transport Method for the Calculation of the PWR Control and Safety Clusters", in Proc. of Physor'90 Meeting, MARSEILLE, April 23-27, 1990.

12/ J. MONDOT, J.C. GAUTHIER, P CHAUCHEPRAT, J.P. CHAUVIN, C. GARZENNE, J.L. LEFEBVRE, "EPICURE : An Experimental Program devoted to the Validation of the Calculational Schemes for Plutonium Recycling in PWRs" in Proceedings of the Physor'90 Meeting, MARSEILLE, April 23-27, 1990.

13/ P. CHAUCHEPRAT, "Qualification du calcul des poisons consommables au gadolinium dans les réacteurs à eau", Thesis Orsay, April 21, 1988.

14/ J.P. CHAUVIN, G. GRANGET, M. MARTINI, J. MONDOT, J.C. LEFEVRE, A. VALLEE, "Validation of the Experimental Methods used in the EPICURE Programme and their Associated Uncertainties" to be presented at this meeting.

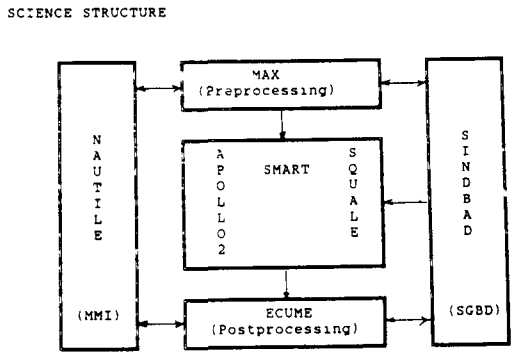

FIGURE 1 SCIENCE project Computational chain Structure

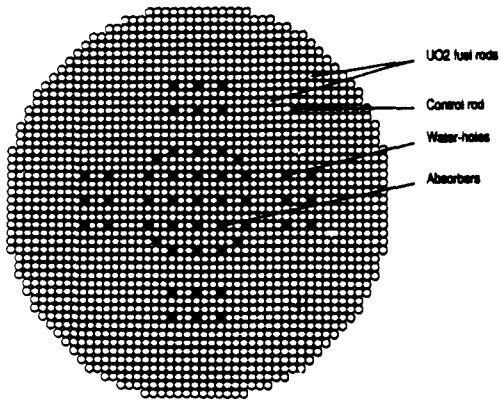

FIGURE 2 : CAMELEON - Radial cross-section of the core

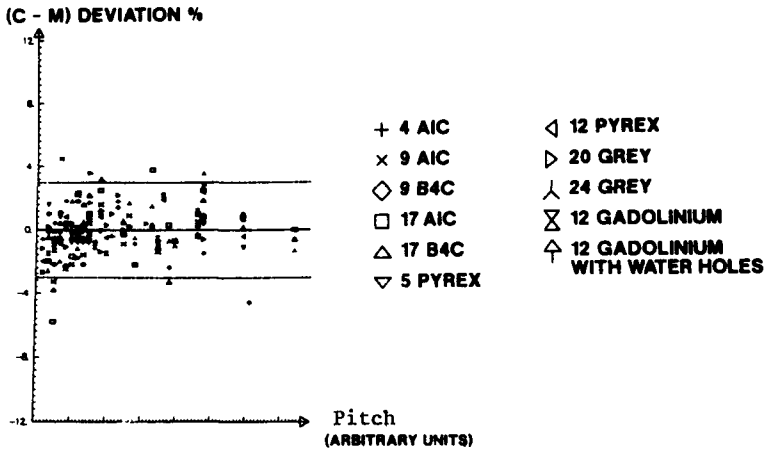

FIGURE 3 : CAMELEON - 2D exact CP calculation-experiment comparisons

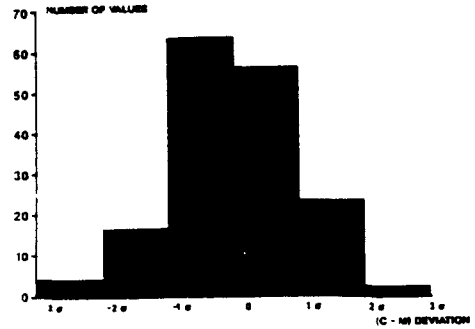

FIGURE 4 : CAMELEON - Overall results histogram (2D exact CP calculation)

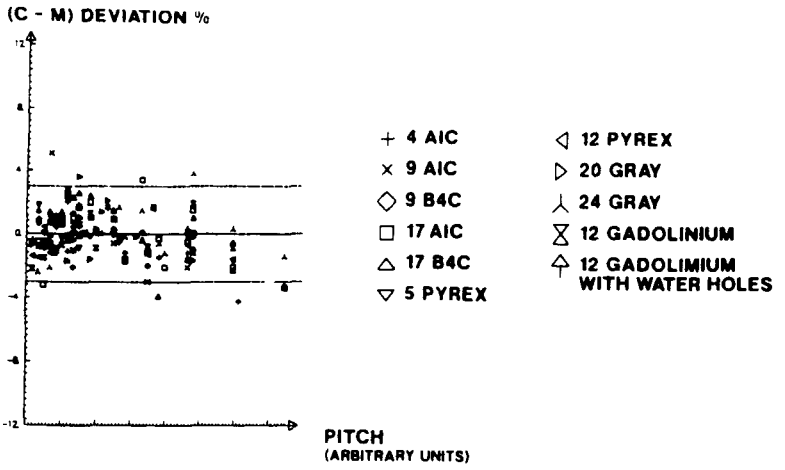

FIGURE 5 : CAMELEON - Diffusion calculation-experiment comparisons

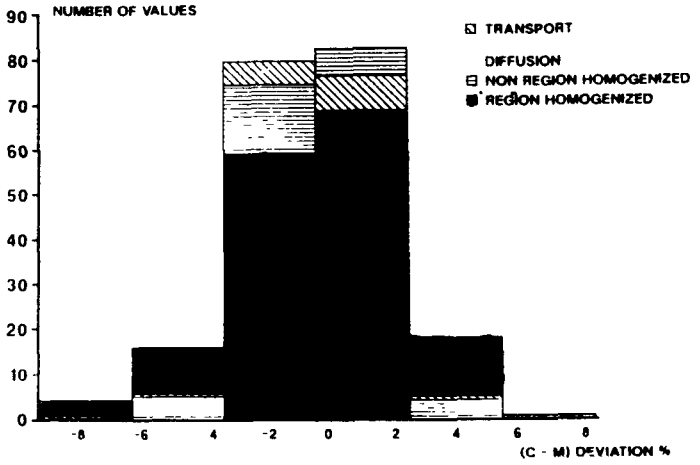

FIGURE 6 : CAMELEON - Overall results histogram

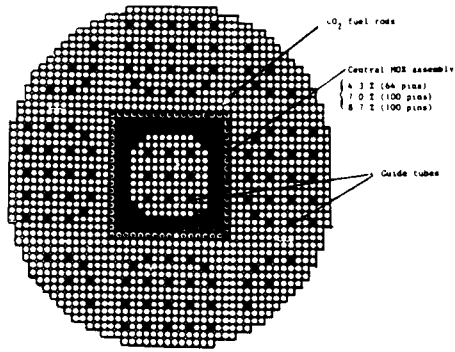

FIGURE 7 : EPICURE - Radial cross-section

of the UMZONE layout

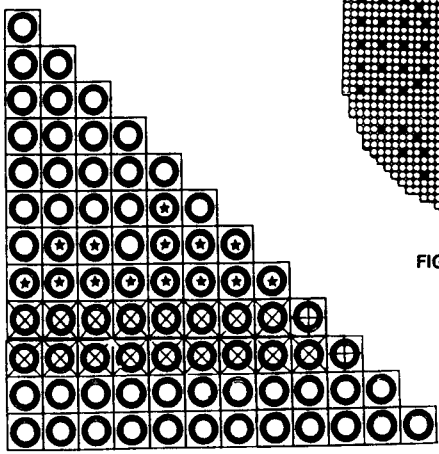

FIGURE 8 : EPICURE -

Heterogeneous cluster 2D transport calculation geometry

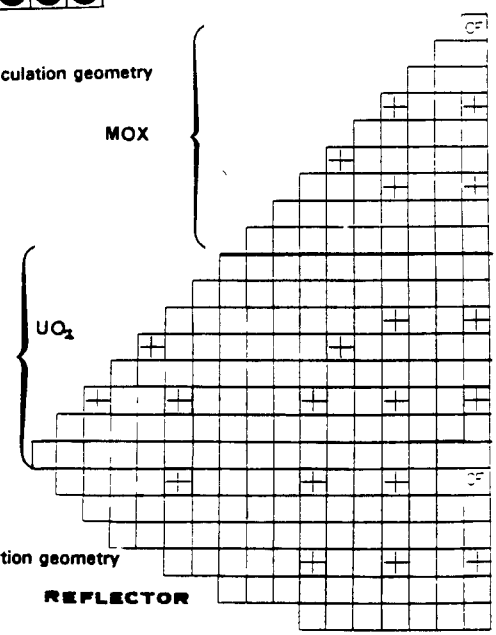

FIGURE 8bis : EPICURE -

Homogeneous core 2D transport calculation geometry

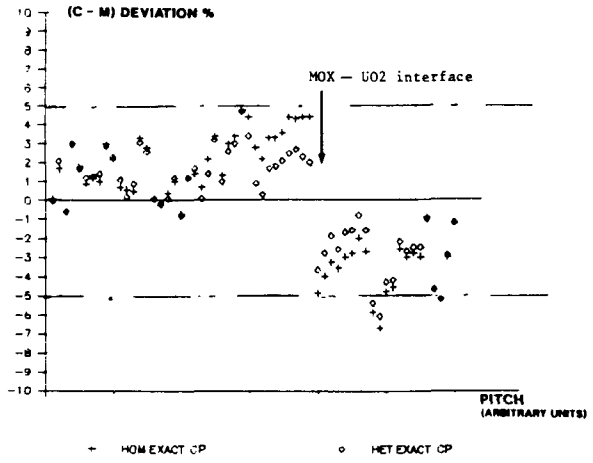

FIGURE 9 : EPICURE - Exact CP computation-experiment comparisons ((C - M) %)

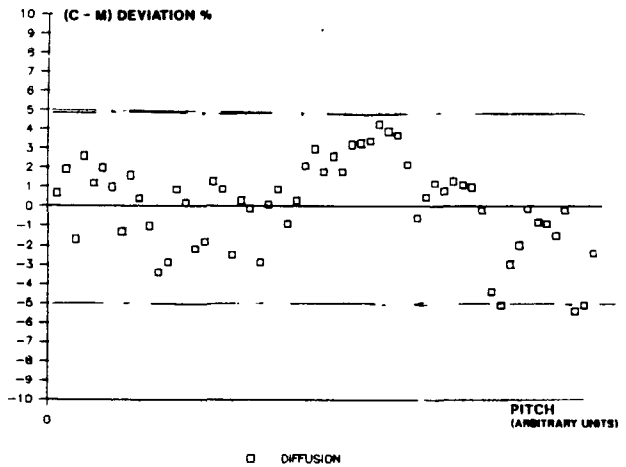

FIGURE 10 : EPICURE - Diffusion computation-experiment comparisons ((C - M) %)

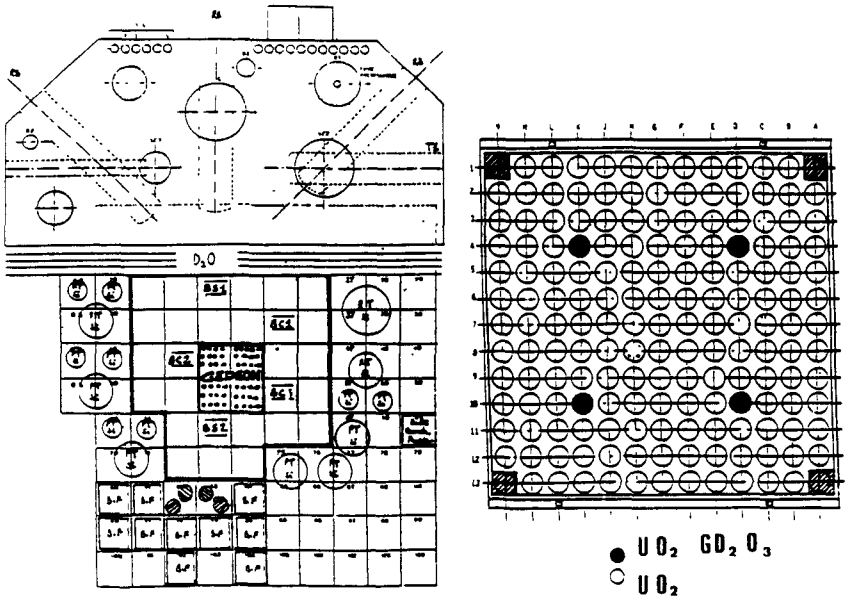

FIGURE 11 : GEDEON - Radial cross-section of Melusine core and the central test assembly

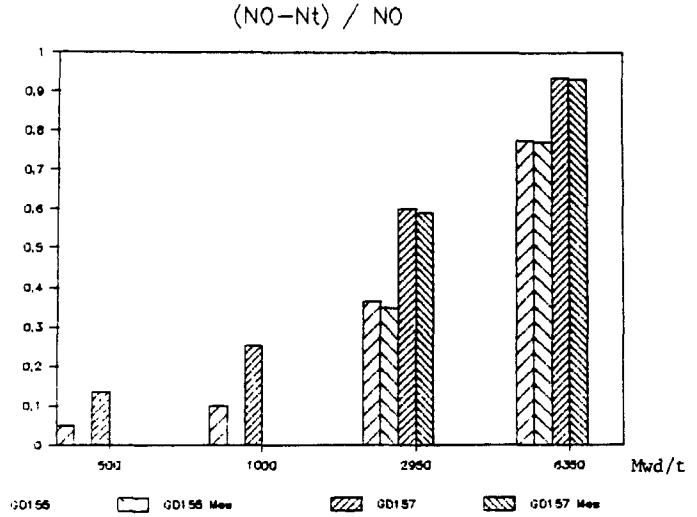

FIGURE 12 : GEDEON I - Gadolinium depletion calculation-experiment comparison

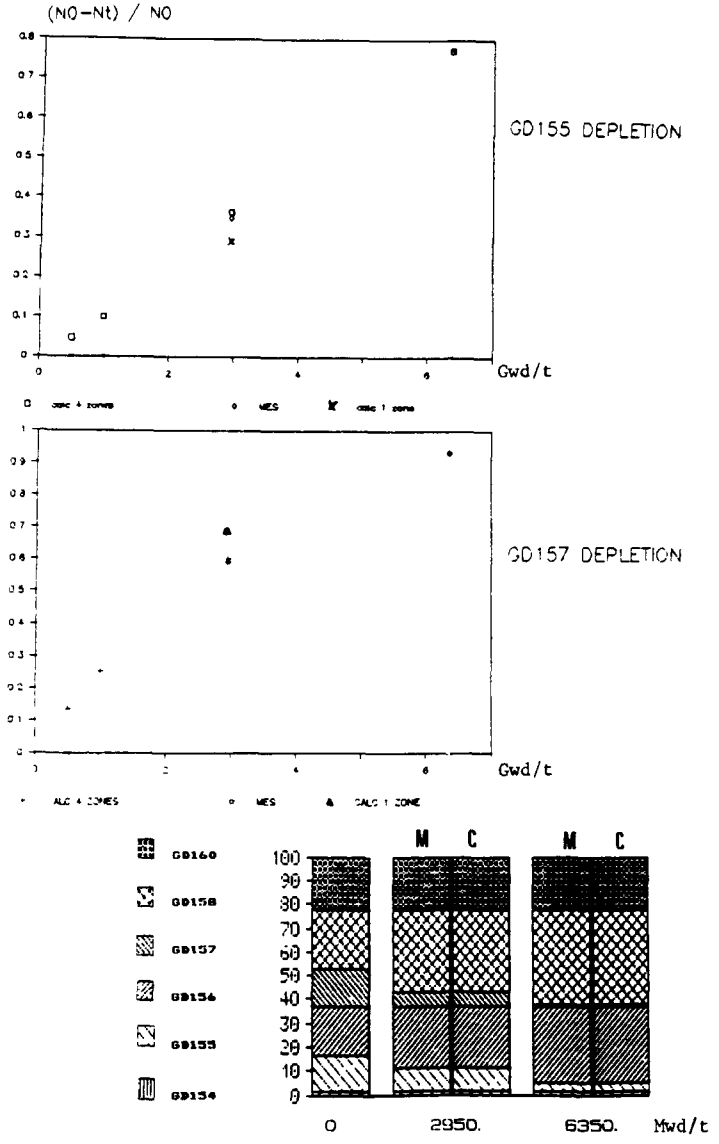

FIGURE 13 : GEDEON I - Gd155 and Gd157 depletion calculation-experiment comparisons (1 and 4 zones) Gd isotopic contribution calculation-experiment comparisons (4 zones)

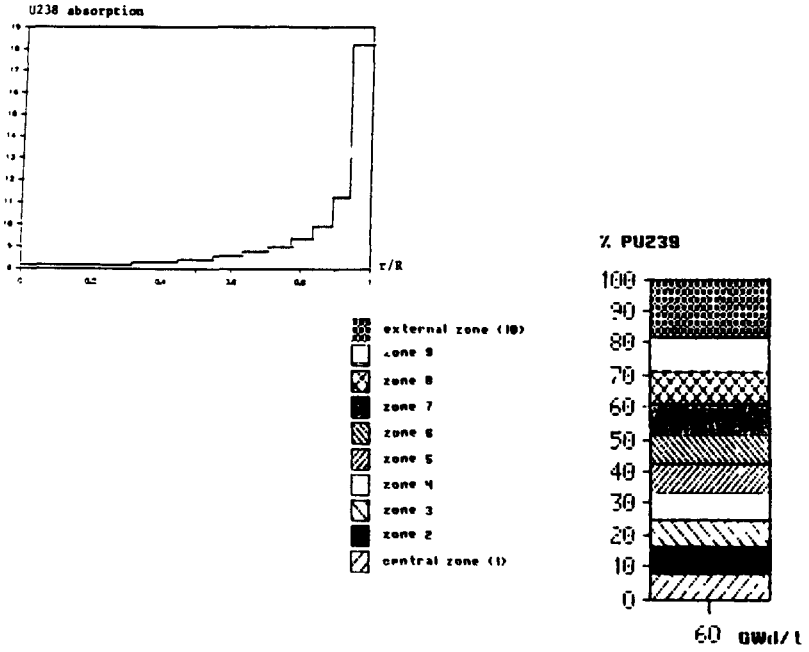

FIGURE 14 : U238 absorption rate distribution inside the pellet and PU239 concentration at 60 Gwd/t (10 zone computation)

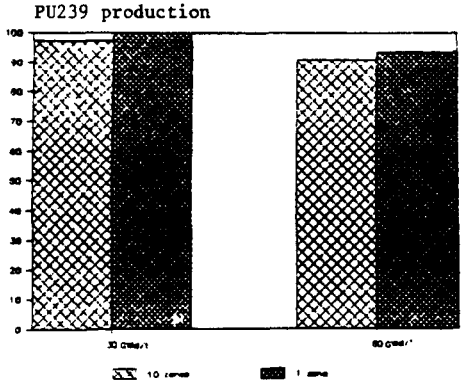

FIGURE 15 : PU239 production comparison between one and ten zone pellet computations

SCIENCE : a new Reactor Physics Codes Package approach

By A.Vallee, G.Francillon, J.Pelet
FRAMATOME Tour Fiat-Cedex 16
92084 Paris la Defense FRANCE

GENERAL OVERVIEW

Nuclear analysis and design in FRAMATOME present various features. First this is due to the wide spectrum of subjects to be treated, and secondly, to the large number of engineers involved in the process (more than 100). Among them, we can mention Reload Analyses of about 45 plants every year, new releases of Safety Reports of operating plants, PSAR and FSAR for plants under construction, design analyses for future plants and predesign studies for various concepts of core and fuel assemblies (High Conversion LWR, Highly Moderated Reactors, new fuel assemblies, burnable poisons and control rods,...).

All these reasons imply a very specific organization of the Reactor Physics Computer Codes. Consequently, FRAMATOME has developped a new Neutronic Codes Package, called ***SCIENCE*** , short for Système de Calcul Integre pour les Etudes Neutroniques des Chaudieres a Eau, (i.e. Integrated Calculation System for Neutronic Analyses of Water Reactors).

The program for ***SCIENCE***, which represents more than 1 million instructions, was launched in 1988, and is close to completion.

It includes advanced transport and nodal codes, Knowledge and Data Management Systems, a friendly Man Machine Interface, all of them fully integrated in a consistant package.

Five major aims have been retained as bases for ***SCIENCE*** : flexibility, productivity, quality, versatility and portability.

FLEXIBILITY

Flexibility implies the whole set of the Nuclear Analyses is subdivided into separate components, which can be organized in different ways, according to specific targets. So, each element has to be as general as possible, and when a change is needed, only few elements have to be modified. It must be clear that a fully generic approach is completly theoretical and unachievable, but the structure of SCIENCE is designed to be easily adaptatable by the following ways :

. there is a distinct separation between what is relevant to the calculation process (codes) to the methodology (knowledge) and to the data (core fuel assemblies, ...),

. each of these 3 groups is structured, and the basic level is the module for the codes the task for the methodology, and the object for the data,

. all basic elements are part of a Data Base Management System (SINDBAD) through which the user (or super-users) can store and manage all the informations related to the codes input and output, code configurations, and knowledge basis,

. Expert-Systems and Planification Processes help the engineers and physicists generating correct calculation schemes.

PRODUCTIVITY

Productivity means reducing the cost in man-power of Nuclear Analyses , transferring actions previously realized by hand into computerized processes.

This goal is achieved through a man/machine interface, and some specific tools for pre and post-processing :

. the man/machine interface (NAUTILE), based on an Expert-System. This interface proposes to the User some selected menues, covering a classical set of studies, and a specific gate for new kind of analyses. The Expert-System helps the user to organize his studies (planification), and, depending on the goal, can automate part or all of the calculation runs.

. the pre-processing codes (MAX), of use mostly when analyses are specific, and a procedural approach is impossible. The preprocessors are also based on an Expert-System approach. In a last step, they translate the user needs into codes input.

. the post-processing codes (ECUME), which allows the user to treat the results of codes by mathematical tools (flexible algorithms defined by the user, statistics). Finally, tables, graphs can be generated and included in reports.

This approach is strenghtened by the computers organization on an open network. Mostly, the scientific calculations are performed with the FRAMATOME supercomputer (CRAY-YMP), Expert-Systems are run on Workstation (SUN and HP), and the DBMS on specific servers (SUN and CDC). The link is assumed by an ETHERNET network.

QUALITY

The quality of such a large code package as ***SCIENCE*** is very dependant on the development process (project management, quality assurance, tests). Our purpose is not to detail this part but to describe performances we can reach through the physical models which have been implemented, and to point out their accuracy through results of qualification.

Using ***SCIENCE***, engineers can handle a large spectrum of physical models, some being developped by FRAMATOME, others in cooperation with close partners (Commissariat a l'Energie Atomique, B&W Fuel Company).

SCIENCE includes APOLLO-2 system (/1/,/2/,/4/) developped by CEA, and then adapted and qualified by FRAMATOME to its specific needs. APOLLO-2 is a transport code (collision probabilities and SN),allowing treatment of various geometries. Core calculations can be performed by an Advanced Nodal Model, NEMO, developped with BWFC Finite Elements modules (transport and diffusion) coming from the CEA system CRONOS, and Finite Differences (1D or fine mesh 2D) modules. All these modules are consistant, allowing an easy change from one model to another, and are included in a core calculation subsystem, called SMART

The package is under qualification mostly from FRAMATOME builtplants and critical experiments or specific tests performed in CEA facilities. Both include evidently Uranium fuel in a large range of enrichments, but also MOX fuel, burnable poisons (glass Gadolinia) control rods ... A specific subsystem (SQUALE) has been developped for automating all the tasks relevant to the qualification

VERSATILITY

Some models are of use for standard analyses; among them, the most important ones are :

- 2D transport multicells for self-shielding, and fine energy calculations (99 groups),

- 2D transport (few energy groups) for exact geometry fuel assembly or color set treatments,

- a 3D ,homogeneous, advanced nodal model with microscopic depletion for core calculation,

- a pin power reconstruction module from the 3D nodal model,

- 2D pin per pin finite-difference model.

These models are included in the APOLLO-2 and NEMO codes which will be detailed later.

Other models, such as these allowing transport core computations are used as reference to define methodology for new products

PORTABILITY

As told before, the FRAMATOME computing network is heterogeneous (superconputer, servers, workstations); all the computers are operated with UNIX or UNIX-like OS. Softwares are systematically tested on different machines in order to check their portability.

Basic languages are current standards :

. the FORTRAN-77 for physics codes.

. the 'C" language for data processing,

But, in a large development such as this one higher level languages are also needed. In order to ensure portability, translators or library functions are written in C or FORTRAN and are included in the codes package. The most important are :

. ESOPE, from CEA /1/, allowing the use of structured data in FORTRAN-77

. GIBIANE, from CEA /1/, allowing the linkage between modules to create a specific code,

. SPIRAL /3/, which is a PROLOG language, with Oriented Object approach, and graphic connections, of use for Expert-Systems.

SCIENCE STRUCTURE

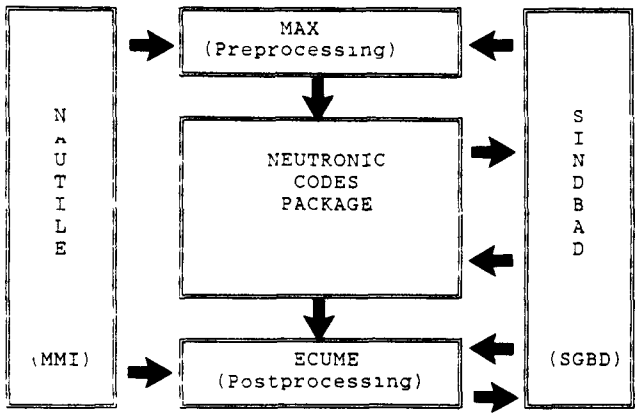

The figure herewith shows the general organization of *SCIENCE*. Details on the peripherical parts (NAUTILE, SINDBAD, MAX, ECUME) are provided in reference /5/, to be presented at this meeting

In this paper, we shall emphasize only on the central part of the system : the neutronic codes package, and describe mostly the models of use in standard calculations.

APOLLO-2

APOLLO-2 features and performances have been described in a large number of papers (/1/,/2/,/4/). Besides the basic development, FRAMATOME has introduced adaptations to make it an industrial core design and analysis tool :

. ***Developping modules allowing a fine treatment of temperatures in the fuel rods and fuel assembly,***

FRAMATOME took advantage of APOLLO-2 modular structure to easily combine basic CEA flux computation and self-shielding modules with temperature computation modules developped in FRAMATOME. This allows reference iterative calculations giving coherent flux and temperature radial distributions in the fuel pellet. Therefore, the effective temperature model (i.e. the search for a homogeneous temperature in the pellet that gives the same reaction rates as those calculated with an exact radial temperature distribution) can be easily obtained.

. *Implementing the interface modules with the nodal code NEMO,*

Various input values of NEMO (such as average discontinuity factors, reduced depletion chains ..) are not included in the standard outputs of CEA APOLLO-2. The modules performing the computation of these values were developed in FRAMATOME and then became parts of general GIBIANE procedures which assured the whole generation of homogenized data for a given assembly (see further- NEMO).

. *Integrating FRAMATOME "neutronic analysis toolkit",*

Formerly developped codes, which proved very useful to physicists in FRAMATOME (performing either synthetic outputs or perturbative analysis of transport code results or feedback effects analysis), were re-written and became mere modules of APOLLO-2. Thereby, APOLLO-2 could easily meet FRAMATOME users' particuliar requirements.

. *Organizing the data to interface with SINDBAD,*

Every user of the APOLLO-2 system manipulates procedures which read and write results from and to SCIENCE DataBase. Just like basic APOLLO-2 modules manipulate GIBIANE objects, SCIENCE procedures produce after execution greater data structures that are composed of a set of GIBIANE objects (of which localisation is managed by DBMS) and a summary (containing essential results, procedure inputs, execution status which are parts of the DataBase). This unique and mandatory structure allows easy managing of the DataBase by SINDBAD. That is why generic tools that create summaries and select objects to be stored in the DataBase were needed by FRAMATOME.

More generally, APOLLO-2 fully open and modular structure allowed to interface it with several up-stream and down-stream modules and to build, this way, an efficient industrial tool.

NEMO

General overview

NEMO (Nodal Expansion Method Optimized) is a two-group 3 dimensional diffusion code which has been developped jointly by B&W Fuel Company and FRAMATOME. It allows the treatment of square assembly cores with various geometry description (full core, quarter of core, 1/8th core, ...) and with a variable axial

reshing. The nodal engine coupled with an isotopic depletion calculation and pin power reconstruction ensure that NEMO can be used as a reference tool for core design calculations.

Methodology

Any nodal design scheme can be split into 3 steps.

- Cross sections homogenization
- Nodal calculation
- Pin power reconstruction

These three steps are strongly coupled, and any homogenization choice (from clusters or assembly calculations) imposes the type of nodal calculation and the pin power reconstruction methodology.
The NEMO methodology is based on a single assembly homogenization.

1) The homogenization. The Cross sections Data bases

In the NEMO code, it is assured that all the nodal cross sections (microscopic macroscopic and discontinuity factors) are functions of 6 independent parameters : Burnup, boron concentration, Xenon concentration, moderator specific volume, fuel temperature, and a spectral parameter.
During the homogenization phase, a set of tables storing the cross section dependency as a function of the 6 parameters is calculated. A direct interpolation in these tables, according to each node conditions, is performed, providing local cross sections. A predefined table structure with an efficient interpolation algorithm ensures that the feedback calculation is optimized (cost/accuracy).
The assembly calculations are performed with a transport code which automatically generates the base depletions and the restart cases to create the tables needed by NEMO.

2) The nodal code NEMO

The nodal engine of NEMO is based on a nodal expansion method.

The system of nodal equations is composed of :

- the nodal balance linking the surface currents and the average fluxes.

- The transverse 1 D equations which allow the evaluation of surface currents at each node interface as a function of the two neighbouring node fluxes. The resolution of these equations rests on the selection of the 1D flux expansion functions. The fast flux is composed of a fourth order polynomial, and the thermal flux can be either composed of

a fourth order polynomial or composed of polynomial and hyperbolic functions (to take into account the fast spectrum variations that can occur at interfaces).

As a result 20 coefficients (10 per group) have to be determined to get the 10 interface fluxes currents They are obtained through a system of 20 equations, which are :

For a node n and a group g

- The conservation of the average nodal flux
- The application of the weighted residual method with order 0, 1, and 2
- The heterogeneous surface flux continuity (using homogeneous flux and discontinuity factors)
- The surface current continuity

To make the nodal system efficient NEMO ensures two important points

A) The homogeneous cross sections take into account the depletion gradient inside the node

B) The transverse 1D equations are integrated with the accurate quadratic transverse leakage model.

The nodal engine is coupled with a microscopic depletion model, which allows more than 30 isotopes.

3) The pinpower reconstruction

NEMO also calculates the pin power reconstruction. The method is based on the hypothesis that the pin by pin power can be written as :

P(x,y) = P hom (x,y) *SA form function*

where P hom is the intranodal power distribution, and *SA form function* is a single assembly form function taking into account the state of the node.
P hom (x,y) is evaluated as follows :

$$P_{nom}(x,y) = k\Sigma_{f1}(x,y)\phi_1(x,y) + k\Sigma_{f2}(x,y)\phi_2(x,y)$$

where $^{k}\Sigma_{pg}(x,y)$ and $\phi_g(x,y)$ are the intranodal cross section and flux distributions.

$k\Sigma_{pg}(x, y)$ is a biquadratic function evaluated from the average surface values of $k\Sigma_{pg}$ and corrected by a surface spectral effect. The surface spectral effect accounts for the cross sections changes that occur at the surface of dismilar assemblies as they are depleted.

$\phi_g(x, y)$ is assumed to be in the form

$$\phi_1(x,y) = \sum_{i,j=0}^{4} a_{ij} x^i y^j$$

$$\phi_2(x,y) = C_{oo}\,\phi_1(x,y) + \sum_{\substack{i,j=0 \\ i=j\neq 0}}^{4} C_{ij} F_i(x) F_j(y)$$

with $F_0(u) = 1$ $F_1(u) = \sinh(ku)$ $F_2(u) = \cosh(ku)$

$F3(u) = \sinh(2ku)$ $F4(u) = \cosh(2ku)$ and

$$k = h\sqrt{\frac{\Sigma a_2}{D_2}}$$

CONCLUSIONS

SCIENCE is a codes package, developped with the purpose to be at the top of the state of the art both in industrial neutronic tools, and in man-machine interface. Its development is now close to completion, and the experience is too short to allow general conclusions. The first returns from the users show an interest having, in the same system, capacities for reference and standard calculations : most of the users performed at the begining reference calculations they were unable to do before to check the valadity of previous ones, or ongoing analyses realized with current tools. The use of graphics to introduce data on reactor, core, fuel assemblies and fuel rods, and moreover, all the man machine interface implemented on work station has been very appreciated.

The full qualification is scheduled for the end of '93, because on such a large system, a long period is needed to adjust the codes and optimize the process after return of experiment.

____000____

REFERENCES

/1/ "APOLLO-2 assembly spectrum code : new features" by M.Coste, R.Sanchez et al. (Proceeding of the ANS Topical Meeting, Pittsburgh, April/May 1991).

/2/ "A user Oriented Portable, Modular Code for Multigroup Transport Assembly Calculations" by R.Sanchez, J.Mondot et al. (Proceeding of ANS Topical Meeting, Paris, April 1987).

/3/ "An Expert-System for localisation of containment leakage during an accident in a PWR" by J.M.Martinez et al. (Proceeding of the ANS Topical Meeting, Pittsburgh, April/May 1991).

/4/ "APOLLO-2 Code Utilization for Project Calculations" by G.B.Bruna et al. (ANS Topical Meeting, Charleston, March 1992).

/5/ "NAUTILE : an Intelligent Front-End for core computation system" by P.Girieud and al. (ANS Topical Meeting, Charleston, March 1992).

EIGENVALUE ANALYSIS USING A FULL CORE MONTE CARLO METHOD (U)*

by

K. C. Okafor and J. F. Zino

Westinghouse Savannah River Company
Savannah River Site
Aiken, South Carolina 29808

ABSTRACT

A versatile three-dimensional, full-core model of the Savannah River Site (SRS) production reactors is developed using the Los Alamos Monte Carlo code MCNP The lattice model is based on the "tilted-hex" unit, which encloses a control cluster at the origin, and six surrounding assembly positions that can contain different assembly types. This model represents in detail all components in the core with little or no geometric or physical approximations that are common to most reactor physics models.

Application of the model in the analysis of eigenvalues for the initial critical control rod positions for previous K-reactor cycles at SRS show that the acceptability band in the prediction of initial critical control rod positions for future cycles can be reduced by a factor of five.

*The information in this article was developed during the course of work under Contract No. DE-AC09-89SR18035 with the U.S. Department of Energy.

M9106022i

INTRODUCTION

For many years, most of the deterministic codes developed for reactor physics analysis at the Savannah River Site (SRS) have been benchmarked using experimental and operational data However, in many cases, it was difficult to make valid comparisons because of the inherent difficulties in using computer codes to model experimental or operational conditions Examples of such conditions are the effects of depletion, fission product poisoning, temperature effects, and control rod positions Furthermore, the differences between the codes and the operational data are compounded by the various geometric and analytical approximations commonly associated with deterministic codes (e g , one-dimensional, two-dimensional, infinite medium, homogenization, and multigroup cross-section treatment) These differences in some cases have been significant[1] and it cannot be determined whether the discrepancies are a result of the differences in the models or the limitations of the deterministic codes

As a result, applications of these codes for critical analysis require qualification from other independent computer codes (i e Monte Carlo codes) to determine the range of their validity This is especially true of applications which have a direct impact on reactor safety and reactor operations Because of this need for independent assessment, the Monte Carlo technique can be beneficial, provided that the physical domain of the analyzed system can be transformed into an equivalent mathematical (or geometric) domain. Since the Monte Carlo method simulates individual particle tracks through a given system, it can provide a very accurate probabilistic transport solution Also, many Monte Carlo codes have the advantage of using a continuous cross section energy treatment as opposed to a multigroup approach These reasons give the Monte Carlo method its greatest advantage over the deterministic methods

One such Monte Carlo code is the Los Alamos-developed General Code for Neutron and Photon Transport (referred to as MCNP)[2], which is used worldwide for reactor physics and criticality applications A three-dimensional, full core model of the SRS reactors is described in this document. This description will start with the two-dimensional, axially uniform, and infinite model This model is based on the "tilted-hex" lattice[3] The unit of this lattice is a hexagonal prism with seven assembly positions. These units fill the entire reactor tank space

Production Reactor Description

The Savannah River Site (SRS) reactors are low temperature and pressure, material production reactors that are moderated and cooled by heavy water (D_2O) The reactors are operated by the Westinghouse Savannah River Company for the U.S. Department of Energy (DOE) The basic SRS reactor lattice consists of a hexagonal array of six assemblies surrounding a central control housing. Each assembly consists of four concentric tubes—two fuel tubes and two target tubes. The spaces between the fuel and target tubes act as coolant channels where D_2O is circulated. The entire assembly (fuel, target, and coolant) is housed inside an aluminum sleeve which penetrates the reactor tank. The tank is filled with D_2O moderator.

Reactor Model Description

The repeated structures capability of MCNP is used to create a full core, three-dimensional, geometric model of the SRS reactors The primary tool used in the description of the full core model is the fill array matrix specification, which is one of the tools of the repeated structures

capability of MCNP This tool makes the filling of elements in a lattice structure possible The fill specification can by applied in two different ways, either as a single integer designating that the lattice is filled with the same object, or as an array of integers designating the various objects (filling cells) that can fill the various elements (filled cells) of a lattice

Closely associated with the fill specification is the universe specification The universe is defined by the integer on the fill specification on a cell card In the case of a lattice (array), these integers define the universes that fill the elements of the lattice In other words, any filled cell card will show a fill specification A filling cell card of the filled cell will show an integer on the universe specification that is the same as the integer on the fill specification on the filled cell card

The fill array matrix which describes the tilted–hex (gang) model is defined in Figure 1 This fill array is a 15 by 15 - element square matrix that designates the universes that fill the various lattice positions in the reactor tank The lattice unit is a tilted hexagonal prism that en closes a maximum of seven assemblies The hexagonal prism is tilted on the x-y plane 10 898° in order to form a repeating lattice structure that completely fills the volume of the reactor tank The reactor core is radially divided into four segments—gangs I-III, and the buckled zone (Fig ure 2) The array elements with the same integer (universe) belong to the same gang, except ele ments with different control cluster arrangements due to the sparjets in gang I, the safety rod po sitions in gang III, and the non-existent control positions in the buckle zone

Lattice Structure

The central control cluster (the 0,0,0 element) in gang I (Figure 3) corresponds to fill array matrix element $a_{8\,8}$, where a is an integer that corresponds to the universe number The remain ing matrix elements in the central row (row 8) correspond to the hexagonal prisms in the central row in Figure 3. The elements in the matrix above the central row ($a_{8,j}$) correspond to the rows below the central row in Figure 3. The elements below the central row of the matrix correspond to the rows above the central row in Figure 3 This lattice structure allows communication with one control cluster at a time The elements in the matrix that have integers that cannot be lo cated in Figure 3 are non-existent hexagonal prisms that may be beyond the radial bounds of the reactor tank Figure 4 shows the complete hexagonal lattice structure filled with six assembly positions, one central control position, and all associated interstitial safety rod positions

RESULTS/DISCUSSION

In order to validate the above model, past operating data from the SRS reactors are used as an experimental benchmark. This data is the observed initial critical eigenvalues of the K–series reactor cores

The MCNP model is set up to duplicate the startup conditions of the reactor cycles—i e fresh fuel, no fission products, and ambient temperature (300 K) Also, full-and partial length control rod positions throughout the core are specified to match the observed initial critical con figurations

The MCNP calculations were run on a Los Alamos National Laboratory Cray through the Integrated Computing Network (ICN) Due to the size of the reactor system, nonconvergence of

the source may be expected if there are not enough starting source particles per cycle or enough total particle histories Scoping studies determined that 10,000 source particles per cycle for 100 cycles (i e , 1 million particle histories) were adequate for each case Also, the first 30 cycles were skipped for tallying purposes

Subsequent to the first calculation (i e , K–4 cycle), a source tape (SRCTP) was generated and used as the starting source distribution for the remaining cases

Table I shows the initial critical eigenvalues predicted by the model for four previous K reactor cycles It can be observed from the table that

(a) The calculated eigenvalues are essentially the same for all four cases despite the different control rod configurations and charge material contents

(b) There exists a consistent bias of 0 019 Δk in the calculated eigenvalues

Due to the large discrepancy between the observed critical eigenvalues (i e K_{eff}=1 0) and the calculated eigenvalues, an investigation into the possible cause(s) of the 1 9%Δk bias was performed By varying the fuel and target material contents independently within the accepted measurement uncertainties for a representative case, it was observed that a significant change to the calculated eigenvalue can occur Table II shows the variation of the initial critical eigenvalue as a function of the modified material contents for the K-5 cycle The combined effect of these uncertainties can account for the 1 9%Δk bias in the observed initial critical eigenvalues

Also, the consistency in the calculated eigenvalues indicates that there could be a systematic bias in the determination of material contents for all four cases As a result, predictions of initial critical control rod positions for future reactor startups can be made with improved accuracy

Acknowledgement

The information contained in this article was developed during the course of work done under contract NO DE-AC09-89SR18035 with the U S Department of Energy

References

1 Revolinski, S M , *Notes on Mark 22 Reactivity Anomolies,* OPS–RTS–900180, October 1990

2 Briemeister, J F (Ed), *MCNP–A General Monte Carlo Code for Neutron and Photon Transport,* Version 3 b , LA–7396, September 1986

3 Okafor, K C , *Finite Lattice Modeling With MCNP,* WSRC–TR–91–163, April 1991

M9106022i

Table I

Initial Critical Predictions with MCNP

Cycle	Eigenvalue	Critical Rod Position*
K–4	0.9821 ± 0.0012	3.27
K–5	0.9817 ± 0.0010	3.46
K–6	0.9816 ± 0.0010	3.45
K–13	0.9809 ± 0.0011	3.10

* Number of full control rods inserted in each cluster

Table II

Eigenvalue Variation with Material Contents

(K–5 cycle as base case)

Nominal	+3% IF*	+7% OF	–3% IT	–10% OT
0.9817	0.9871	0.9970	0.9843	0.9993

*IF -- Inner Fuel Tube ^{235}U contents

OF -- Outer Fuel Tube ^{235}U contents

IT -- Inner Target Tube ^{6}Li contents

OT -- Outer Target Tube ^{6}Li contents

55	55	55	55	55	55	55	55	55	55	55	55	55	55	55
55	55	55	55	55	55	55	55	55	52	53	54	55	55	55
55	55	55	55	55	55	55	51	28	29	30	13	31	55	55
55	55	55	55	55	50	27	12	12	10	10	12	13	32	55
55	55	55	55	49	26	10	08	08	08	08	10	14	33	55
55	55	55	48	26	10	08	06	01	07	08	10	14	34	55
55	55	55	25	10	08	01	01	01	01	08	10	15	55	55
55	55	47	11	08	05	01	01	01	02	08	09	35	55	55
55	46	24	10	08	04	01	03	08	10	17	36	55	55	55
55	45	23	11	08	08	08	08	10	18	37	55	55	55	55
55	44	22	11	10	10	10	09	19	38	55	55	55	55	55
55	55	43	21	20	20	19	39	55	55	55	55	55	55	55
55	55	55	42	41	40	55	55	55	55	55	55	55	55	55
55	55	55	55	55	55	55	55	55	55	55	55	55	55	55

Figure 1. Fill Array Matrix

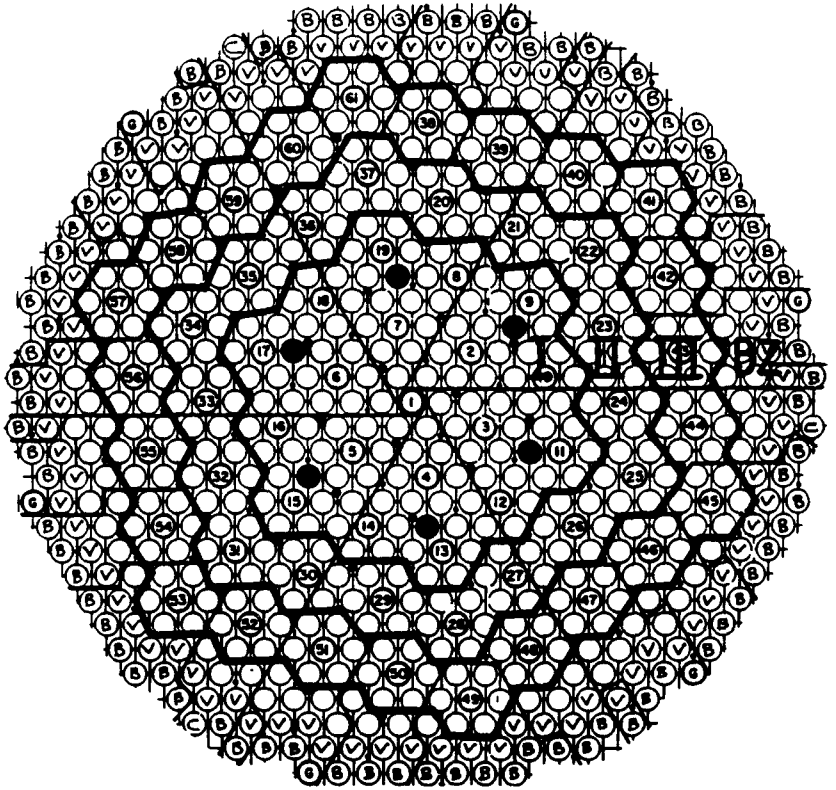

Figure 2. Reactor Core Gang Description

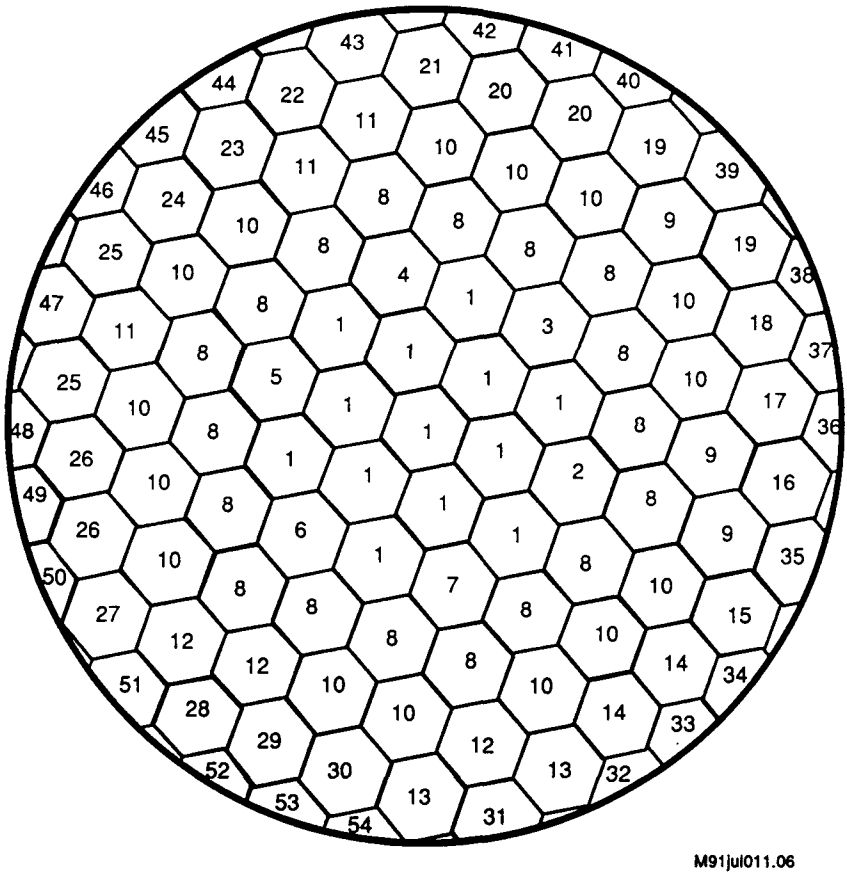

M91jul011.06

Figure 3. Assignment of Universes in Lattice

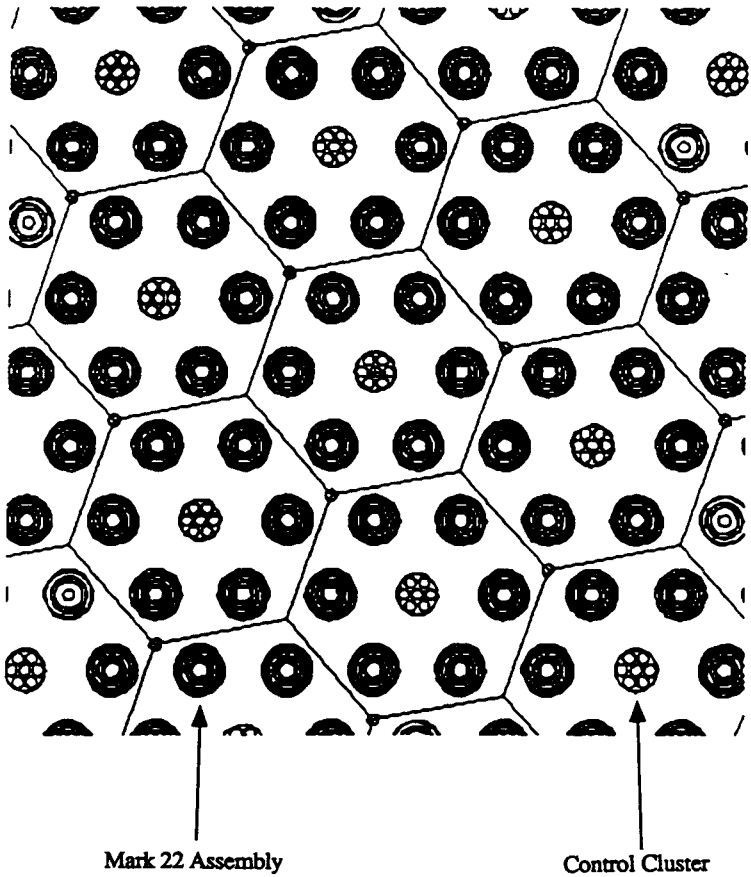

Figure 4. MCNP Model of SRS Reactor Core

REACTOR CORE GEOMETRIC MODELING WITH MCNP (U)*

by

K C Okafor and J F Zino

Westinghouse Savannah River Company
Savannah River Laboratory
Aiken, South Carolina 29808

ABSTRACT

The repeated structures and lattice capabilities of the Los Alamos-developed Monte Carlo transport code MCNP are used to develop the full-core and three-dimensional geometric models of three different reactor types These capabilities can be used for reactor physics and safety analysis applications The models represent the evolutionary process in the application of the code for geometric modeling of small research reactor lattices, large hexagonal production reactor lattices, and the nested Pressurized Water Reactor lattices

* The information contained in this article was developed during the course of work done under Contract No DE-AC09-89SR18035 with the U S Department of Energy

M9106023i

INTRODUCTION

Traditionally, neutron transport analyses of reactor cores have been limited by the ability of the calculational method to represent the physical domain of the system being analyzed These limitations are usually due to restrictions in the geometric modeling capability of most transport codes As a result, the modeling represents approximations of the physical system Examples of these approximations are infinite representations, one– and two–dimensional approximations, and homogenization of transport media

Recently, the geometric modeling capabilities of some transport codes have been enhanced to provide the ability to represent three–dimensional objects (or systems) An example of this is the Los Alamos–developed Monte Carlo Code for Neutron and Photon Transport (referred to as MCNP) [1] The code has three–dimensional geometry representation, repeated structure and lattice capability, coupled neutron–photon transport, and continuous energy treatment with up–to–date cross–section data

The repeated structures capability will be applied in this paper to describe the geometric modeling of three different reactor cores a university research reactor, a material production reactor, and a commercial pressurized water reactor (PWR)

These reactor types were chosen to show the evolutionary process in the application of the Monte Carlo methods, particularly MCNP The research reactor will show the use of discrete objects (fuel plates) in the modeling of small reactor lattices The production reactor will utilize the fill array option of the repeated structures capability of MCNP to model a large, hexagonal lattice The commercial PWR will show a further extension of the fill array option in the model ing of an array inside another array (i e , the fuel pin array inside the fuel assembly array)

Repeated Structures Modeling

There are several features in MCNP which make it possible to describe geometric systems which may contain many identical (or similar) components arranged in a specific pattern (like a reactor) These features include the *universe* concept, *cell translation*, the *fill specification*, and the *like* option These features are briefly described below

Universe	Any cell or cells (filling cells) which fill another cell (filled cell) Designated with $u=a_i$, where a_i is an integer
Cell translation	Any cell or cells can be spatially translated to other points in the system Designated with *trcl=(x y z)*, where *x*, *y*, and *z* are the coordinates of the new location where the cell or cells are translated.
Fill specification	Defines the universe that fills a particular cell or lattice It can be either a single integer (designating that the cell is filled with a particular universe), or an array of integers (designating that the cell is filled with a lattice)
Like option	Used to duplicate a cell or group of cells at different locations in the system Designated with *m like n but* , where *m* and *n* are cell designators

M9106023i

Reactor Modeling Examples

Research Reactor Description

The first example to be discussed is the Georgia Tech Research Reactor (GTRR) model created for the analysis of the He–3 reactor fast shutdown system experiment The GTRR is a heavy water (D_2O) moderated and cooled research reactor The GTRR is composed of a 1 82m diameter reactor vessel that contains 19 fuel assembly positions arranged on a 15 24cm triangular pitch [2] Each fuel assembly contains 16 uranium–aluminum alloy plates spaced 0 396cm apart with coolant channels located in–between

MCNP Model

The fundamental cell of the GTRR core is a single fuel plate This is the simplest repeat able geometry in the core Therefore, the geometric modeling begins with defining a fuel plate Figure 1 shows a schematic of a fuel plate It is composed of a slab of fuel alloy surrounded on all sides by aluminum cladding The cell defining the fuel slab is created through the intersection of four planes defining the edges of the fuel meat and is enclosed in a rectangular shell of cladding The cells of the fuel plate are defined in the x–y plane as infinite rectangular plates which will be bounded as a universe in a finite assembly housing

The cells of the fuel plate are duplicated and translated to 16 different x–coordinate locations in order to create the fuel region of a single fuel assembly The complement operator (#) is used to define the remaining regions of space between the fuel plates as D_2O coolant

After creating an entire assembly in this manner, the TRCL command is again used to repeat and translate the fuel assembly to 17 different x–y lattice positions in the core

A shim safety blade was created by intersecting six planar surfaces in free space to create a hexahedra (solid rectangle) two surfaces normal to the x–axis, two normal to the y–axis, and two normal to the z–axis The cells defining the shim safety blades are repeated, translated, and rotated to four positions above the core as shown in Figure 2

Other components in the core include vertical and horizontal irradiation ports, and a cadmium regulating rod These components are similarly defined and translated to their respective locations in the core Figure 2 shows a cross section view of the MCNP geometric model of the GTRR It shows the 17 fuel assemblies, the four shim safety blades, and the vertical ports It also shows a blowup of a single fuel assembly revealing the individual fuel plates

The full–core MCNP model of the GTRR describes approximately 1000 discrete regions of three–dimensional space However, due to the nested nature of the geometry description in the MCNP input file, only 75 card images are required to completely describe the model

Production Reactor Description

The Savannah River Site (SRS) reactors are low temperature and pressure material production reactors moderated and cooled by heavy water The reactors are operated by the Westinghouse Savannah River Company for the U S Department of Energy (DOE) The basic SRS reactor lattice consists of a hexagonal array of six assemblies surrounding a central control

housing Each assembly consists of four concentric tubes — two fuel tubes and two target tubes The spaces between the fuel and target tubes act as coolant channels where D_2O is circulated The entire assembly (fuel, target, and coolant) is housed inside an aluminum sleeve that penetrates the reactor tank The tank is filled with D_2O moderator

MCNP Model

The lattice unit of the SRS reactor cores is obtained through the following steps [3]

(1) Choose any control cluster or an assembly (toward the periphery) occupying a similar position

(2) Draw lines through the center, joining all adjacent control clusters or assemblies occupying such positions in all possible directions (six directions)

(3) Bisect these lines at points half–way between any two control clusters

(4) The six bisecting lines will form the arms of a tilted hexagon, which is a repeating unit–cell This unit–cell, when translated in all directions, will form a hexagonal lattice (Figure 3)

(5) This super cell hexagonal unit encloses a maximum of 10 elements For example, the hexagon containing control cluster one has one control element six fuel assemblies and three safety rod positions

The various components in the reactor core, which are located in different lattice elements are described with the fill array matrix The matrix is a representation of the fill array specification that designates the different universes that can exist in a lattice Figure 4 shows the MCNP geometric model of the SRS reactor core [4]

PWR Reactor Description

Figure 5 shows an octant of a generic pressurized water reactor [5] It is made up of a square lattice Each lattice element constitutes a fuel assembly which contains a 15 by 15 square array of pin locations (204 fuel and 21 non–fuel locations) There are three enrichment types for the fuel pins, and different combinations of burnable poison and control rod locations

MCNP Model

The core of the PWR is made up of two array lattices an assembly (or primary) array and a pin (or secondary) array The repeated structures capability of MCNP is first used to create a hexahedral lattice making up the fuel assembly positions, with its associated primary fill array matrix Second, another hexahedral lattice is created in each of the assembly positions in the primary fill array forming the pin lattice, also with its associated fill array matrix The pin lattice is then filled with the various components of the fuel assembly (i e , fuel pins, burnable poison rods, and control rods) to make up the assemblies that constitute the entire reactor core Figure 6 shows the MCNP geometric model of a typical PWR fuel assembly

Using this technique, a full core three–dimensional model of a typical PWR (having over 200,000 discrete regions of space) can be described with approximately 300 input card images

M9106023t

References

1 J Briesmeister, Ed , *MCNP – A General Monte Carlo Code for Neutron and Photon Transport, Version 3A*, LA–7396–M, Rev 2, Los Alamos National Laboratory (1986)

2 Graham, W W III and Walker, D M , *Safety Analysis Report for the 5 Mw Georgia Tech Research Reactor*, GT–NE–7 (December 1967)

3 Okafor, K C , *Finite Lattice Modeling with MCNP*, WSRC–TR–91–163 April 1991

4 Okafor, K C and Zino, J F , *Eigenvalue Analysis Using a Full Core Monte Carlo Method* ANS Topical Meeting on Advances in Reactor Physics, March 1992

5 Henry, A F and Honeck, H C , *The Physics of Water Reactors*, lecture notes, July 1989

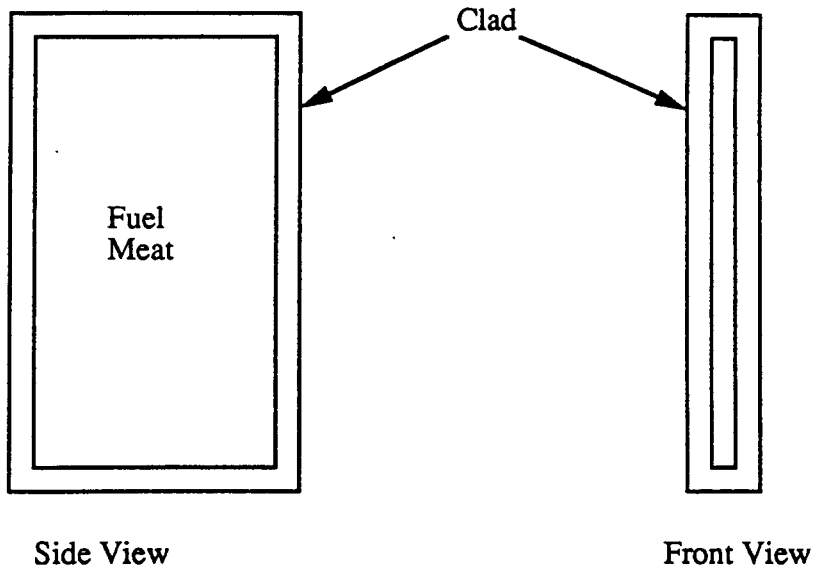

Figure 1. Fuel Plate Schematic

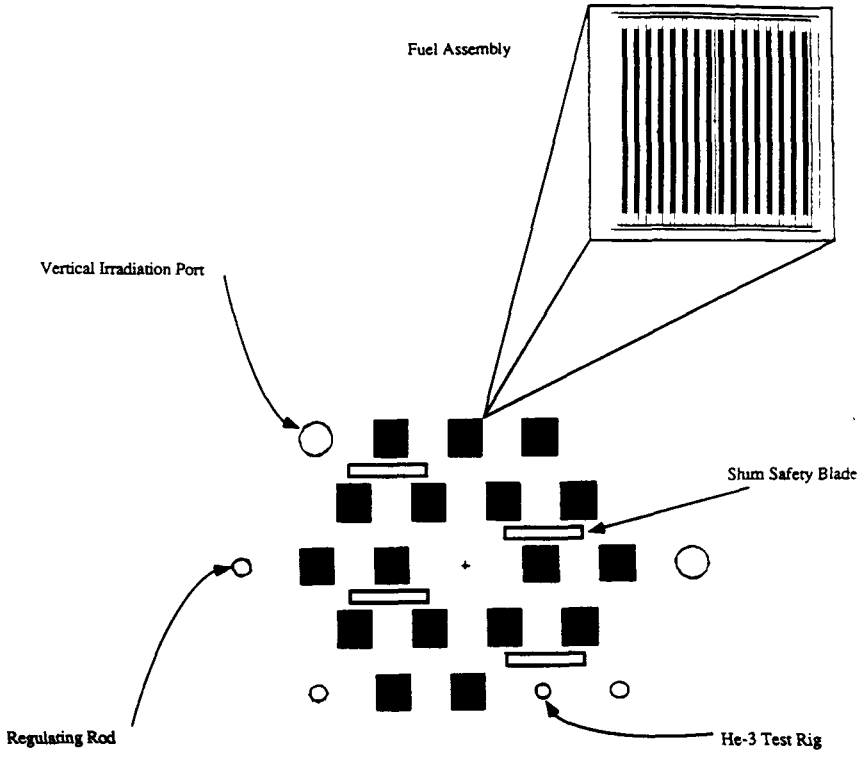

Figure 2. MCNP Model of GTRR Core

M9106023

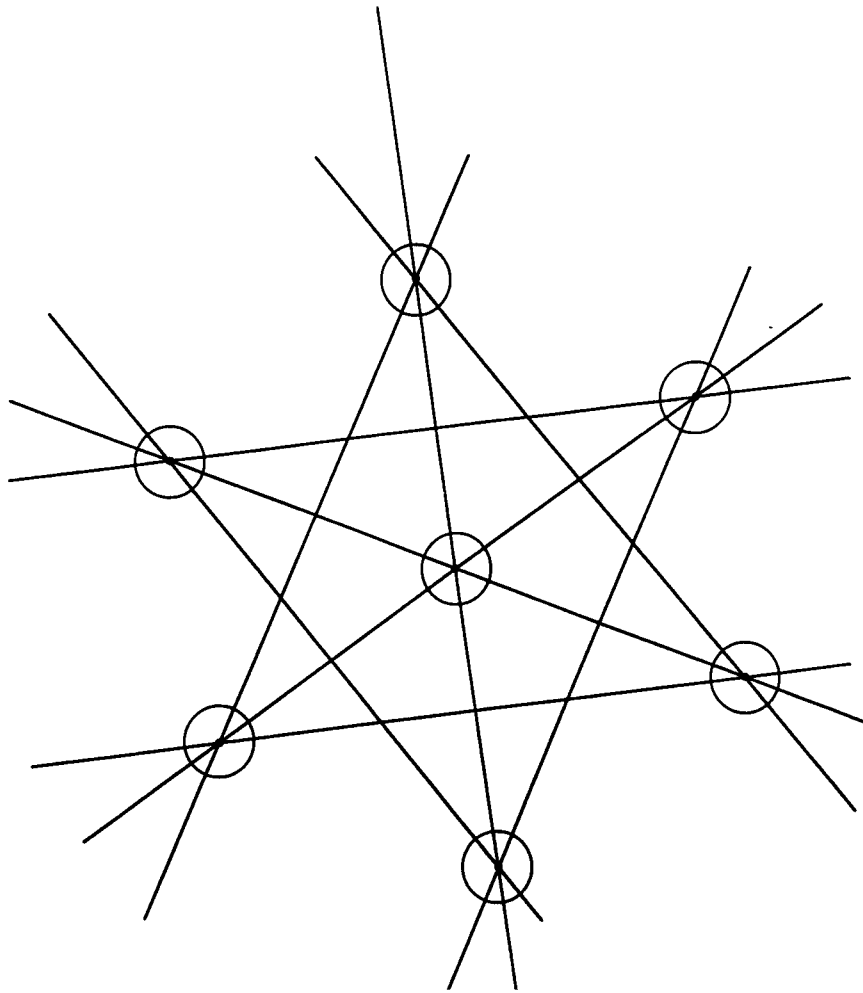

Figure 3. Tilted–Hex Lattice Unit

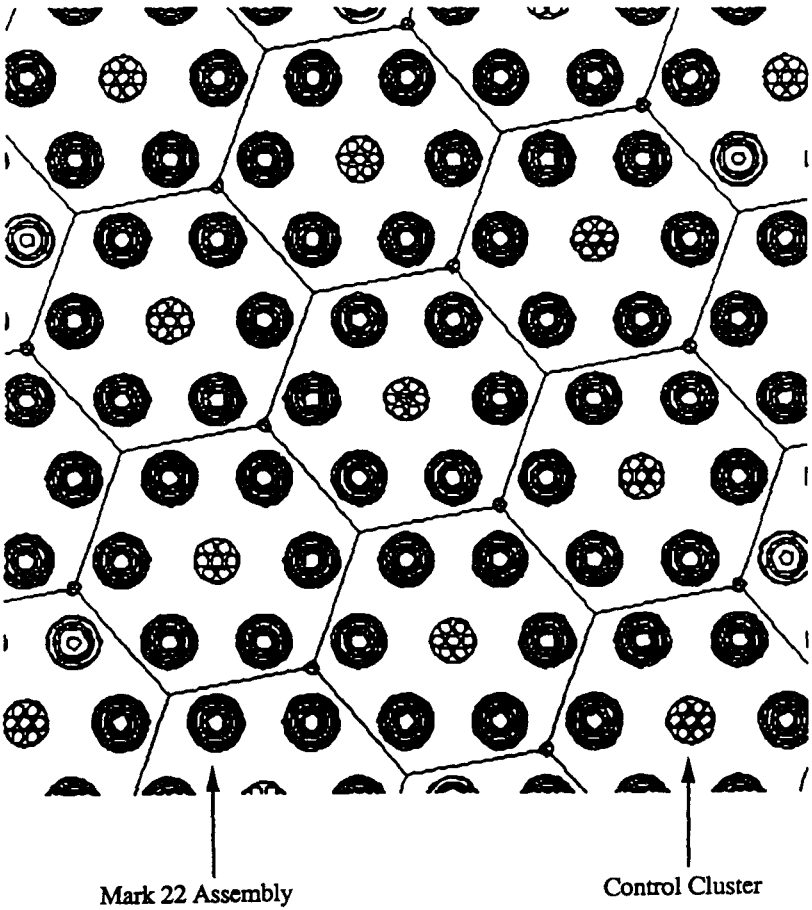

Figure 4. MCNP Model of SRS Reactor Core

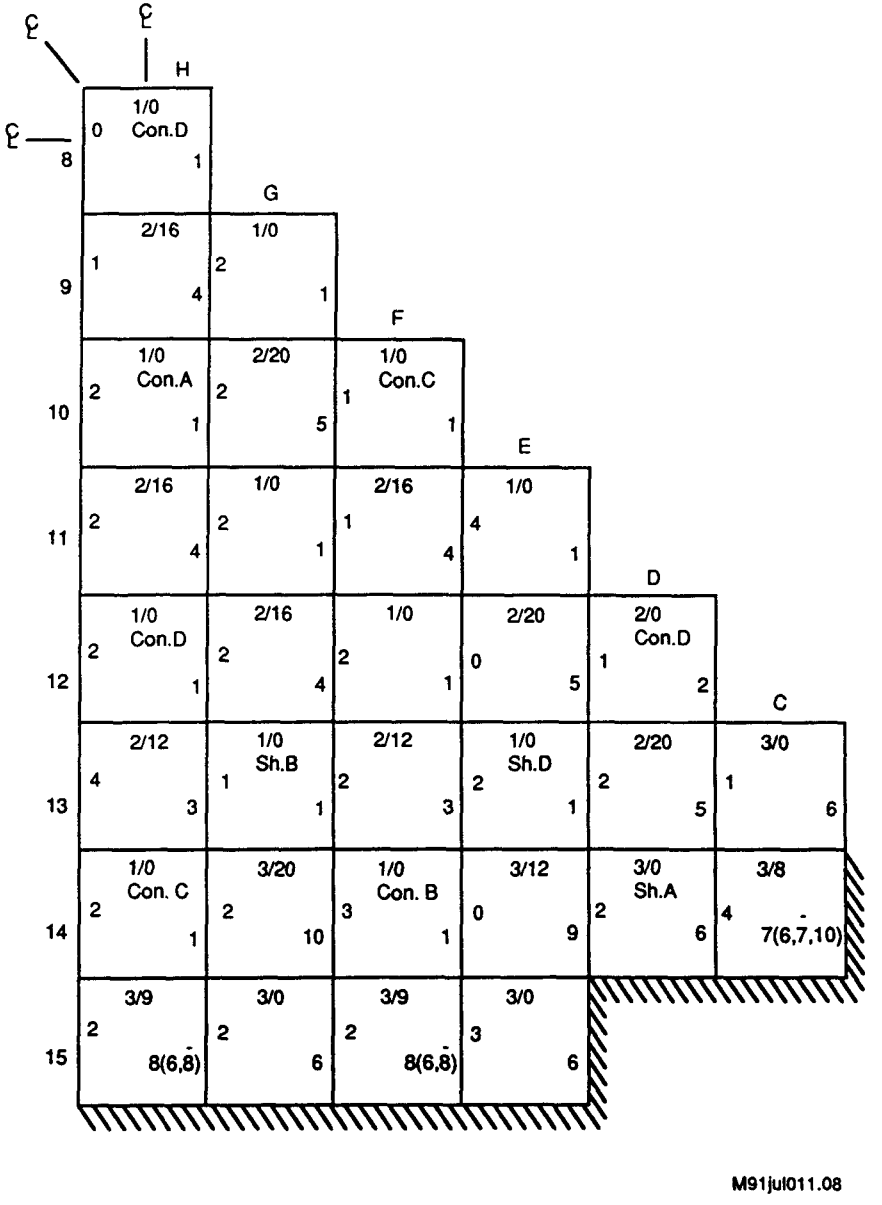

Figure 5. Pressurized Water Reactor Octant

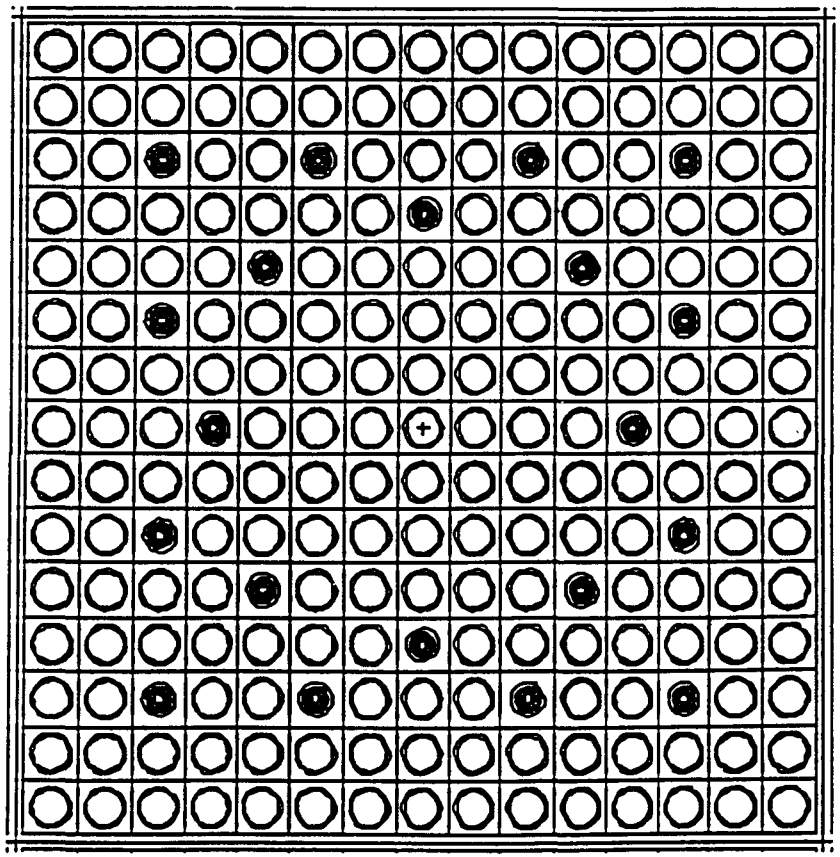

= Fuel Rod

= Burnable Poison Rod

Figure 6. MCNP Model of PWR Fuel Assembly

"LOCAL" EXPONENTIAL TRANSFORM METHODS FOR THE MONTE CARLO SIMULATION OF MULTIGROUP TRANSPORT PROBLEMS

Kasem N Abotel, Edward W Larsen, and William R Martin
Department of Nuclear Engineering
University of Michigan
Ann Arbor, Michigan 48109 USA

ABSTRACT

The "Local" Exponential Transform variance reduction method, which has recently been developed for the Monte Carlo simultation of one-group general geometry transport problems[1], is here generalized to multigroup transport problems This method is a practical approximation to a zero-variance method in which a detailed adjoint transport solution must be known The essence of the approximation is to replace the adjoint transport solution by its diffusion approximation, which is obtained numerically (deterministically) Within each cell, exponential approximations to the continuous adjoint transport solution are formulated using the numerical diffusion solution This yields an approximation to the zero-variance method which, within each spatial cell, closely resembles the conventional exponential transform However, all of the "local" biasing parameters, which depend on the spatial cell and energy group, are uniquely determined by the discretized adjoint diffusion calculation We develop two versions of this method, one with angular biasing and one without Numerical comparisons show that both methods are efficient for multigroup problems and have a significantly better figure of merit than conventional Splitting with Russian Roulette

I. INTRODUCTION

Variance reduction methods are essential for lowering the running times of many Monte Carlo transport calculations Several such methods are widely used, among them Splitting with Russian Roulette, the Weight Window, and the Exponential Transform[1-8] However, each of these methods requires the user to choose one or more "biasing" parameters, and the optimal values of these parameters depend on the problem to be solved, a good choice often depends on experience and luck or a lengthy process of trial-and-error In an effort to develop efficient Monte Carlo variance reduction methods in which the computer itself determines the biasing parameters, we have recently formulated a new "local" exponential transform method for one group transport problems[1] Our numerical results have shown that this one-group method outperforms other widely-known variance

reduction methods, often by a very wide margin. In this paper we describe and give numerical results for two generalizations of this method (one with angular biasing, and one without) to multigroup transport problems

The derivation of the Local Exponential Transform method consists of three steps

1. A zero-variance method is formulated in which all source particles are guaranteed to score with exactly the same weight This method is impractical because it requires detailed knowledge of the solution of an adjoint transport problem
2. A diffusion approximation to the adjoint transport problem is formulated and solved numerically
3. Within each spatial cell, the spatial variation of each adjoint transport group flux is approximated by an exponential function, with group-dependent amplitudes and decay constants (the biasing parameters) determined by the numerical diffusion solution In this way, the zero-variance method is approximated and made practical. If the approximation to the adjoint transport solution is taken to be isotropic, one obtains a method with no angular biasing If the approximation has angular dependence, one obtains a method with angular biasing

The remainder of this paper is organized as follows In Sec II we formulate a zero-variance method for multigroup slab geometry transport problems Using this result, we develop the Local Exponential Transform method without angular biasing in Sec III In Sec IV we define "local" (in space and energy) biasing parameters λ^*_{gJ} that are needed in Sec III In Sec V we develop a Local Exponential Transform method with angular biasing In Sec VI we give numerical results, comparing the two new Local Exponential Transform methods with Splitting and Russian Roulette We conclude, in Sec VII, with a brief discussion

II. A ZERO-VARIANCE METHOD

To keep the presentation as simple as possible, we shall consider a planar geometry multigroup transport problem with isotropic scattering

$$\mu\frac{\partial\psi_g}{\partial x}(x,\mu)+\sigma_{t,g}\psi_g(x,\mu)=\sum_{g'=1}^{G}\frac{\sigma_{s,g'\to g}}{2}\int_{-1}^{1}\psi_{g'}(x,\mu')d\mu' \ ,$$

$$0<x<X \ , \ -1\le\mu\le 1 \ , \ 1\le g\le G \ , \tag{1a}$$

$$\psi_g(0,\mu)=\frac{\delta(\mu-\mu_{inc})}{\mu_{inc}}\delta_{g,\bar{g}} \ , \ 0<\mu\le 1 \ , \ 1\le g\le G \ , \tag{1b}$$

$$\psi_g(X,\mu)=0 \ , \ -1\le\mu<0 \ , \ 1\le g\le G \tag{1c}$$

This problem is driven by an incident monoenergetic ($g=\bar{g}$), monodirectional ($\mu=\mu_{inc}$) beam on the left boundary We wish to compute the transmitted current in (possibly another) group $\hat{g}$

$$J_{\hat{g}}(X)=\int_0^1\mu'\psi_{\hat{g}}(X,\mu')d\mu' \tag{2}$$

To solve this problem, let us consider the adjoint transport problem

$$-\mu\frac{\partial\psi_g^*}{\partial x}(x,\mu)+\sigma_{t,g}\psi_g^*(x,\mu)=\sum_{g'=1}^{G}\frac{\sigma_{s,g\to g'}}{2}\int_{-1}^{1}\psi_{g'}^*(x,\mu')d\mu' \ ,$$

$$0<x<X \ , \ -1\le\mu\le 1 \ , \ 1\le g\le G \ , \tag{3a}$$

$$\psi_g^*(0,\mu)=0 \ , \ -1\le\mu<0 \ , \ 1\le g\le G \ , \tag{3b}$$

$$\psi_g^*(X,\mu)=\delta_{g,\hat{g}} \ , \ 0<\mu\le 1 \ , \ 1\le g\le G \ . \tag{3c}$$

It is easy to verify that

$$\int_0^1\mu'\psi_{\hat{g}}(X,\mu')d\mu'=\psi_{\hat{g}}^*(0,\mu_{inc}) \ . \tag{4}$$

Therefore, if we know the solution of problem (3), we can immediately obtain the solution of problem (1), (2)

Using problem (3), we will now construct a zero variance Monte Carlo method for problem (1) Let us define $\zeta_g(x,\mu)$ by

$$\psi_g(x,\mu)=\frac{\zeta_g(x,\mu)}{\psi_g^*(x,\mu)} \ . \tag{5}$$

Using Eq (5) to eliminate ψ_g from Eqs. (1), we obtain the following problem for ζ_g.

$$\mu\frac{\partial\zeta_g}{\partial x}(x,\mu)+\tilde{\sigma}_{t,g}\zeta_g(x,\mu)=\sum_{g'=1}^{G}\frac{1}{2}\int_{-1}^{1}\tilde{\sigma}_{s,g'\to g}(x,\mu',\mu)\zeta_{g'}(x,\mu')d\mu' \ ,$$

$$0<x<X \ , \ -1\le\mu\le 1 \ , \ 1\le g\le G \ , \tag{6a}$$

$$\zeta_g(0,\mu)=\frac{\delta(\mu-\mu_{inc})}{\mu_{inc}}\delta_{g,\hat{g}}\psi_g^*(0,\mu) \ , \ 0<\mu\le 1 \ , \ 1\le g\le G \ , \tag{6b}$$

$$\zeta_g(X,\mu)=0 \ , \ -1\le\mu<0 \ , \ 1\le g\le G \ . \tag{6c}$$

Here $\tilde{\sigma}_{t,g}$ and $\tilde{\sigma}_{s,g'\to g}$ are "effective" cross sections, defined by

$$\tilde{\sigma}_{t,g}(x,\mu)=\sigma_{t,g}-\mu\frac{\partial}{\partial x}\ln\psi_g^*(x,\mu) \ , \tag{7a}$$

$$\tilde{\sigma}_{s,g'\to g}(x,\mu',\mu)=\sigma_{s,g'\to g}\frac{\psi_g^*(x,\mu)}{\psi_{g'}^*(x,\mu')} \ . \tag{7b}$$

Eqs (5)-(7) hold for any functions $\psi_g^*(x,\mu)$. However, because we have chosen the functions ψ_g^* to satisfy Eqs (3a), it is easily seen that the "effective" cross sections satisfy

$$\frac{1}{2}\sum_{g=1}^{G}\int_{-1}^{1}\tilde{\sigma}_{s,g'\to g}(x,\mu',\mu)d\mu=\tilde{\sigma}_{t,g'}(x,\mu') \ . \tag{8}$$

Therefore, Eq. (6a) is "conservative"; it describes a scattering process in which particles are neither gained nor lost. Moreover, Eqs. (3a) and (7a) yield

$$\tilde{\sigma}_{t,g}(x,\mu)=\frac{\sum_{g'=1}^{G}\sigma_{s,g\to g'}\int_{-1}^{1}\psi_{g'}^*(x,\mu')d\mu'}{2\psi_g^*(x,\mu)} \tag{9}$$

This and Eqs (3b), (3c) imply

$$\lim_{x\to 0^+} \tilde{\sigma}_{t,g}(x,\mu) = +\infty \ , \quad -1 \le \mu < 0 \ , \quad 1 \le g \le G \ , \tag{10a}$$

$$\lim_{x\to X^-} \tilde{\sigma}_{t,g}(x,\mu) = +\infty \ , \quad 0 < \mu \le 1 \ , \quad 1 \le g \le \hat{g}-1 \ , \quad \hat{g}+1 \le g \le G \ , \tag{10b}$$

$$\lim_{x\to X^-} \tilde{\sigma}_{t,\hat{g}}(x,\mu) < +\infty \ , \quad 0 < \mu \le 1 \tag{10c}$$

Thus, in the transport process described by Eqs (6) and (7), particles are never gained or lost in collisions [Eq (8)], and all particles eventually escape the system through the right boundary in group $\hat{g}$ [Eqs (10)] By Eqs (3c) and (5), the transmitted current is the desired result, namely

$$\sum_{g=1}^{G} \int_0^1 \mu\zeta_g(X,\mu)\,d\mu = \sum_{g=1}^{G} \int_0^1 \mu\psi_g(X,\mu)\delta_{g,\hat{g}}\,d\mu = \int_0^1 \mu\psi_{\hat{g}}(X,\mu)\,d\mu \tag{11}$$

It follows that analog Monte Carlo applied to problem (6), (7) is a Monte Carlo method for solving the original transport problem (1) with zero variance [This method has also been discussed by Williams[9]] In the remainder of this paper we demonstrate the following. *if a sufficiently simple but accurate approximation to ψ_g^* is used in Eqs (6) and (7), one obtains a Monte Carlo method with a high figure of merit Moreover, if the accuracy of the approximation is improved without significantly increasing the complexity of the resulting method, the figure of merit will increase*

III. THE LOCAL EXPONENTIAL TRANSFORM WITHOUT ANGULAR BIASING

The zero-variance method described in Sec II is impractical because to implement it, one must have complete knowledge of $\psi_g^*(x,\mu)$ The Local Exponential Transform method is an approximation to this zero variance method, obtained by "replacing" $\psi_g^*(x,\mu)$ by its diffusion approximation, which is solved numerically (and relatively cheaply)

The diffusion approximation to problem (3) is given by:

$$-\frac{d}{dx}\frac{1}{3\sigma_{t,g}}\frac{d}{dx}\phi_g^*(x) + \sigma_{t,g}\phi_g^*(x) = \sum_{g'=1}^{G} \sigma_{s,g\to g'}\phi_{g'}^*(x) \ , \quad 0 < x < X \ , \quad 1 \le g \le G \ , \tag{12a}$$

$$\phi_g^*(0) - \frac{2}{3\sigma_{t,g}}\frac{d\phi_g^*}{dx}(0) = 0 \ , \quad 1 \le g \le G \ , \tag{12b}$$

$$\phi_g^*(X) + \frac{2}{3\sigma_{t,g}}\frac{d\phi_g^*}{dx}(X) = 2\delta_{g,\hat{g}} \ , \quad 1 \le g \le G \tag{12c}$$

We impose a spatial grid $0 = x_{1/2} < x_{3/2} < \quad < x_{J+1/2} = X$ and solve this problem numerically, using the conventional three point cell-edge discretization. The resulting cell-edge adjoint scalar fluxes, $\phi_{g,j+1/2}^*$ $(1 \le g \le G, 0 \le j \le J)$ are positive Using this solution, we approximate $\psi_g^*(x,\mu)$ by an isotropic exponential function in each spatial cell:

$$\psi_g^*(x,\mu) \cong \frac{1}{2}\phi_{g,j}^* \left[\alpha_{g,j}^* e^{\rho_{g,j}^*(x-x_j)}\right] \ , \quad x_{j-1/2} < x < x_{j+1/2} \ , \quad -1 \le \mu \le 1 \tag{13}$$

Here

$$\phi^*_{g,j} = \frac{1}{2}(\phi^*_{g,j+1/2} + \phi^*_{g,j-1/2}) \tag{14a}$$

is the numerical cell-average group flux,

$$\rho^*_{g,j} = \frac{1}{h_j} \ln\left(\frac{\phi^*_{g,j+1/2}}{\phi^*_{g,j-1/2}}\right) \tag{14b}$$

is the numerical logarithmic derivative of the group flux,

$$\alpha^*_{g,j} = \left[\frac{2}{\rho^*_{g,j} h_j} \sinh\frac{\rho^*_{g,j} h_j}{2}\right]^{-1} \tag{14c}$$

is the normalization factor that makes the bracketed term in Eq. (13) a "shape function" (it has the mean value of unity in the j-th cell), and

$$x_j = \frac{1}{2}(x_{j+1/2} + x_{j-1/2}) \quad , \quad h_j = x_{j+1/2} - x_{j-1/2} \quad . \tag{14d}$$

For reasons discussed in the following section, we replace $\rho^*_{g,j}$ in Eq. (13) by $\lambda^*_{g,j}$, defined by

$$\lambda^*_{g,j} = \begin{cases} \rho^*_{g,j}\sqrt{\frac{\sigma_{t,g}+\sigma_{s,g\to g}}{3\sigma_{t,g}}} & if \quad |\rho^*_{g,j}| < \sqrt{3\sigma_{t,g}(\sigma_{t,g}-\sigma_{s,g\to g})} \quad , \\ \frac{\rho^*_{g,j}}{|\rho^*_{g,j}|}\sqrt{(\sigma_{t,g}-\sigma_{s,g\to g})(\sigma_{t,g}+\sigma_{s,g\to g})} & if \quad |\rho^*_{g,j}| \geq \sqrt{3\sigma_{t,g}(\sigma_{t,g}-\sigma_{s,g\to g})} \quad . \end{cases} \tag{15}$$

Then, we define $\eta_g(x,\mu)$ in the j-th spatial cell by:

$$\psi_g(x,\mu) = \frac{\eta_g(x,\mu)}{\frac{1}{2}\phi^*_{g,j}\left[\alpha^*_{g,j} e^{\lambda^*_{g,j}(x-x_j)}\right]} \quad , \quad x_{j-1/2} < x < x_{j+1/2} \quad . \tag{16}$$

Here, η_g is an approximation to ζ_g defined in Eq. (5). Introducing Eq. (16) into Eqs. (1), we obtain the following problem for $\eta_g(x,\mu)$:

$$\mu\frac{\partial\eta_g}{\partial x}(x,\mu) + \left[\sigma_{t,g,j} - \mu\lambda^*_{g,j}\right]\eta_g(x,\mu)$$

$$= \sum_{g'=1}^{G}\frac{1}{2}\int_{-1}^{1}\left[\sigma_{s,g'\to g}\left(\frac{\phi^*_{g,j}\alpha^*_{g,j}}{\phi^*_{g',j}\alpha^*_{g',j}}\right)e^{(\rho^*_{g,j}-\rho^*_{g',j})(x-x_j)}\right]\eta_{g'}(x,\mu)\,d\mu' \quad ,$$

$$x_{j-1/2} < x < x_{j+1/2} \quad , \quad 1 \leq j \leq J \quad , \quad -1 \leq \mu \leq 1 \quad , \quad 1 \leq g \leq G \quad , \tag{17a}$$

$$\eta_g(0,\mu) = \frac{\delta(\mu-\mu_{inc})}{\mu_{inc}}\delta_{g,\bar{g}}\left(\frac{1}{2}\phi^*_{g,1}\right)\left[\alpha^*_{g,j}e^{-\rho^*_{g,1}h_1/2}\right] \quad , \quad 0 < \mu \leq 1 \quad , \quad 1 \leq g \leq G \quad , \tag{17b}$$

$$\eta_g(X,\mu) = 0 \quad , \quad -1 \leq \mu < 0 \quad , \quad 1 \leq g \leq G \quad . \tag{17c}$$

The Local Exponential Transform Monte Carlo method solves problem (17), utilizing variable weights and survival biasing because there may be absorption collisions in the modified game. This method approximates the zero-variance analog Monte Carlo solution of problem (6). Because the approximation to $\psi^*_{g,j}$ in Eqs. (13) and (16) is isotropic, the approximate method has no angular biasing.

Problem (17) has the following interpretation within each spatial cell, we have introduced an exponential transform [Eq (16)] with "local" space and group-dependent "amplitudes" $[\phi^*_{g,j}]$ and "logarithmic derivatives" $[\lambda^*_{g,j}]$ that are fully determined by the numerical diffusion solution These amplitudes and logarithmic derivative parameters collectively bias the Monte Carlo process in space and energy (but not angle) Within each cell, the effective total cross section [in brackets on the left side of Eq (17a)] is independent of x, as in the conventional exponential transform, but the effective group-transfer scattering cross sections [in brackets on the right side of Eq (17a)] are continuously space-dependent Therefore, if a particle undergoes a collision at two different points x and x' within the j-th cell, the probabilities of its scattering to other groups will generally differ However, the effective total and group-transfer cross sections can change discontinuously at cell edges

IV. DEFINITION OF λ^*_{gJ}

In deriving the Local Exponential Transform without angular biasing, we have replaced the logarithmic derivative $\rho^*_{g\,j}$ by $\lambda^*_{g\,j}$ [defined in Eq (15)] The formula (15) specifies two definitions of $\lambda^*_{g\,j}$, one for "small" $\rho^*_{g,j}$ satisfying $|\rho^*_{g,j}| \leq \sqrt{3\sigma_{t,g}(\sigma_{t,g} - \sigma_{s,g\to g})}$, and one for "large" $\rho^*_{g\,j}$ satisfying $|\rho^*_{g\,j}| \geq \sqrt{3\sigma_{t,g}(\sigma_{t,g} - \sigma_{s\,g\to g})}$ To motivate these definitions, suppose that for the one-group homogeneous-medium transport problem

$$\mu\frac{\partial\psi}{\partial x}(x,\mu) + \sigma_t\psi(x,\mu) = \frac{\sigma_s}{2}\int_{-1}^{1}\psi(x,\mu')d\mu' \quad , \quad 0 < x < X, \quad -1 \leq \mu \leq 1 \quad , \tag{18a}$$

$$\psi(0,\mu) = 1 \quad , \quad 0 < \mu \leq 1 \quad , \tag{18b}$$

$$\psi(X,\mu) = 0 \quad , \quad -1 \leq \mu < 1 \quad , \tag{18c}$$

we wish to compute the transmitted current

$$J(X) = \int_0^1 \mu\psi(X,\mu)d\mu \tag{18d}$$

We numerically solved this problem using Monte Carlo with the conventional exponential transform

$$\psi(x,\mu) = e^{-\lambda^* x}\zeta(x,\mu) \tag{19}$$

for numerous values of λ^*, σ_t, σ_s and X On the basis of these calculations, we found that the optimal value of the biasing parameter λ^* is nearly insensitive to X and is well-approximated by

$$\lambda^*_{opt} \approx \sqrt{(\sigma_t + \sigma_s)\sigma_a} = \sqrt{\sigma_t^2 - \sigma_s^2} \tag{20}$$

For $\lambda^* < \lambda^*_{opt}$ the exponential transform underbiases, and for $\lambda^* > \lambda^*_{opt}$ it overbiases

We wish to relate the formula (20) for λ^*_{opt} to the solution of the adjoint diffusion problem

$$-\frac{d}{dx}\frac{1}{3\sigma_t}\frac{d}{dx}\phi^*(x) + \sigma_a\phi^* = 0 \quad , \quad 0 < x < X, \tag{21a}$$

$$\phi^*(0) - \frac{2}{3\sigma_t}\frac{d\phi^*}{dx}(0) = 0 \ , \ \phi^*(X) + \frac{2}{3\sigma_t}\frac{d\phi^*}{dx}(X) = 2 \ . \tag{21b}$$

Away from the boundaries, the solution of this problem satisfies

$$\phi^*(x) \approx A^* e^{\sqrt{3\sigma_t\sigma_a}x} \ , \tag{22}$$

where A^* is a constant. Therefore,

$$\sqrt{\frac{\sigma_t+\sigma_s}{3\sigma_t}}\frac{d}{dx}\ln\phi^*(x) \approx \sqrt{\frac{\sigma_t+\sigma_s}{3\sigma_t}}\sqrt{3\sigma_t\sigma_a} = \sqrt{(\sigma_t+\sigma_s)\sigma_a} \approx \lambda_{opt} \ . \tag{23}$$

This suggests [see Eq (14b)] that we define a "local" value of λ^* by

$$\lambda_j^* = \sqrt{\frac{\sigma_t+\sigma_s}{3\sigma_t}}\rho_j^* \ , \ x_{j-1/2} < x < x_{j+1/2} \ . \tag{24}$$

In practice, we use

$$\lambda_j^* = \begin{cases} \sqrt{\frac{\sigma_t+\sigma_s}{3\sigma_t}}\rho_j^* & \text{if } \sqrt{\frac{\sigma_t+\sigma_s}{3\sigma_t}}\rho_j^* < \sqrt{\sigma_t^2-\sigma_s^2} \ , \\ \sqrt{\sigma_t^2-\sigma_s^2} & \text{if } \sqrt{\frac{\sigma_t+\sigma_s}{3\sigma_t}}\rho_j^* \geq \sqrt{\sigma_t^2-\sigma_s^2} \ . \end{cases} \tag{25}$$

This formula uses Eq. (24) for "small" ρ_j^* and prevents overbiasing for "large" ρ_j^*. We have found that it works quite well in one and multigroup problems. The reasons why it is necessary to replace $\rho_{g,j}^*$ by $\lambda_{g,j}^*$ are:

1. The diffusion solution, even for ideal problems having purely exponential solutions, has a different exponential decay rate (i.e., logarithmic derivative) than the transport solution.
2. The zero variance method biases all of the variables, whereas the method discussed above does not bias the angular variable. Therefore, adjustments should be made to the biasing parameter to compensate for the neglect of angular biasing.

In the next section, we derive a Local Exponential Transform method that includes angular biasing. We do this in a way that makes it unnecessary to modify "small" values of ρ_j^*. This procedure avoids the use of Eq. (20), which is obtained from experiment rather than theory. It also leads to a more efficient method, because including angular dependence in the approximation to the adjoint transport solution yields a more accurate approximation, hence a method that is closer in performance to the zero-variance method.

V. THE LOCAL EXPONENTIAL TRANSFORM WITH ANGULAR BIASING

Now let us consider the "asymptotic" diffusion approximation to the adjoint problem (3):

$$-\frac{d}{dx}D_g\frac{d}{dx}\phi_g^*(x) + \sigma_{t,g}\phi_g^*(x) = \sum_{g'=1}^{G}\sigma_{s,g\to g'}\phi_{g'}^*(x) \ , \ 0 < x < X \ , \ 1 \leq g \leq G \ , \tag{26a}$$

$$\phi_g^*(0) - 2D_g \frac{d\phi_g^*}{dx}(0) = 0 \quad , \quad 1 \le g \le G \quad , \tag{26b}$$

$$\phi_g^*(X) + 2D_g \frac{d\phi_g^*}{dx}(X) = 2\delta_{g,\hat{g}} \quad , \quad 1 \le g \le G \tag{26c}$$

Here, we take

$$D_g = (\sigma_{t,g} - \sigma_{s,g\to g}) \left(\frac{\nu_{0,g}}{\sigma_{t,g}} \right)^2 \quad , \tag{27}$$

where $\nu_{0,g}$ is the "discrete" transport eigenvalue for the g-th group, defined by the dispersion law

$$1 = \frac{c_g \nu_{0,g}}{2} \int_{-1}^{1} \frac{d\mu}{\nu_{0,g} - \mu} \quad , \quad c_g = \frac{\sigma_{s,g\to g}}{\sigma_{t,g}} \tag{28}$$

Problem (26) has the following property: for a one-group problem having a purely exponentially growing solution, $\phi_g^*(x)$ has the same exponential growth as $\psi_g^*(x,\mu)$, namely $\exp(\sigma_{t,g}x/\nu_{0,g})$

As outlined in Sec. III, we solve problem (26) numerically Then, using this solution, we approximate $\psi_g^*(x,\mu)$ by the following function of x and μ in each spatial cell:

$$\psi_g^*(x,\mu) \cong \frac{1}{2}\phi_{g,j}^* \left[\beta_{g,j}^* \left(\frac{\sigma_{t,g,j}}{\sigma_{t,g,j} - \rho_{g,j}^* \mu} \right) e^{\rho_{g,j}^*(x - x_j)} \right] \quad , \quad x_{j-1/2} < x < x_{j+1/2} \quad , \quad -1 \le \mu \le 1 \tag{29}$$

Here

$$\beta_{g,j}^* = \left[\frac{2}{\rho_{g,j}^* h_j} \left(\sinh \frac{\rho_{g,j}^* h_j}{2} \right) \frac{\sigma_{t,g,j}}{2\rho_{g,j}^*} \left(\ln \frac{\sigma_{t,g,j} + \rho_{g,j}^*}{\sigma_{t,g,j} - \rho_{g,j}^*} \right) \right]^{-1} \tag{30}$$

is the normalization factor that makes the bracketed term in Eq. (29) a shape function (it has the mean value of unity in the j-th cell). The motivation for the particular angular dependence in Eq (29) is that for one-group problems, Eq. (29) satisfies the adjoint transport equation if

$$\rho^* = \frac{\sigma_t}{\nu_0} \quad , \tag{31a}$$

where ν_0 is defined by Eq (28). However, the exponentially-growing adjoint diffusion solution for Eq (26a) satisfies

$$\frac{d}{dx} \ln \phi^*(x) = \frac{\sigma_t}{\nu_0} \quad . \tag{31b}$$

Therefore, a reasonable "local" definition of ρ^* is:

$$\rho_j^* = \frac{\ln \phi_{j+1/2}^* - \ln \phi_{j-1/2}^*}{h_j} \tag{31c}$$

This formula agrees with Eq. (14c), which we explicitly use in Eqs (29) and (30)

We now define $\xi_g(x,\mu)$ in the j-th spatial cell by

$$\psi_g(x,\mu) = \frac{\xi_g(x,\mu)}{\frac{1}{2}\phi_{g,j}^* \left[\beta_{g,j}^* \left(\frac{\sigma_{t,g,j}}{\sigma_{t,g,j} - \rho_{g,j}^* \mu} \right) e^{\rho_{g,j}^*(x - x_j)} \right]} \tag{32}$$

Here, ξ_g is an approximation to ζ_g defined in Eq. (5). Introducing Eq. (32) into Eqs. (1), we obtain the following problem for $\xi_g(x,\mu)$:

$$\mu\frac{\partial\xi_g}{\partial x}(x,\mu)+\left[\sigma_{t,g,j}-\mu\rho^*_{g,j}\right]\xi_g(x,\mu)$$

$$=\sum_{g'=1}^{G}\frac{1}{2}\int_{-1}^{1}\left[\sigma_{s\,g'\to g}\left(\frac{\phi^*_{g,j}\beta^*_{g,j}}{\phi^*_{g',j}\beta^*_{g',j}}\right)\left(\frac{1-\mu'\rho^*_{g',j}/\sigma_{t,g',j}}{1-\mu\rho^*_{g,j}/\sigma_{t,g\,j}}\right)e^{(\rho^*_{g\,j}-\rho^*_{g',j})(x-x_j)}\right]\xi_{g'}(x,\mu)\,d\mu'\ ,$$

$$x_{j-1/2}<x<x_{j+1/2}\ ,\quad 1\le j\le J\ ,\quad -1\le\mu\le 1\ ,\quad 1\le g\le G\ , \tag{33a}$$

$$\xi_g(0,\mu)=\frac{\delta(\mu-\mu_{inc})}{\mu_{inc}}\delta_{g,\bar{g}}\left(\frac{1}{2}\phi^*_{g,1}\right)\left[\beta^*_{g,j}\frac{\sigma_{t,g,1}}{\sigma_{t\,g,1}-\rho^*_{g,1}\mu}e^{-\rho^*_{g\,1}h_1/2}\right]\ ,\quad 0<\mu\le 1\ ,\quad 1\le g\le G\ , \tag{33b}$$

$$\xi_g(X,\mu)=0\ ,\quad -1\le\mu\le 0\ ,\quad 1\le g\le G \tag{33c}$$

The Local Exponential Transform Monte Carlo method with angular biasing solves problem (33), utilizing variable weights and survival biasing because there may be absorption collisions in the modified game This method approximates the zero-variance analog Monte Carlo solution of problem (6) and generalizes a space-angle biasing method proposed earlier by Dwivedi[5] Because the angle-dependent approximation (29) to ψ^*_g is generally more accurate than the isotropic approximation (13), it is tempting to speculate that the Monte Carlo method resulting from Eq (29) will generally be more efficient (closer in performance to the zero-variance method) than the Monte Carlo method based on Eq (13) In the next section, we present numerical results that confirm this reasoning

VI. NUMERICAL RESULTS

In this section, we present numerical results obtained by using Monte Carlo with three variance reduction methods the two Local Exponential Transform methods described earlier in this paper, and Splitting with Russian Roulette In the Splitting with Russian Roulette calculations we used the Weight Window as it is implemented in MCNP[7], with the adjoint diffusion solution of problem (12) as the importance function for determining the splitting ratios For example, we took the splitting ratio across the splitting plane at $x_{j+1/2}$ to be $\min(\phi^*_{g,j+1}/\phi^*_{g,j},\theta)$, where θ is an experimentally determined number for each problem Also, in the Local Exponential Transform calculations we used a local weight cutoff We tested the Weight Window with the Local Exponential transform methods but found that the extra storage and computation required by the splitting does not produce a sufficiently lower variance, for the problems we have run, the Local Exponential Transform methods yield better figures of merit without the Weight Window

1 Planar Geometry Problems

We first consider five two-group planar geometry problems For each of these five problems, $\sigma_{t\,1}=\sigma_{t\,2}=1$ cm^{-1} and $\sigma_{s,2\to 1}=0$ (downscattering only), scattering is isotropic, an isotropic group 1 flux is incident on the left boundary $x=0$, all other incident fluxes are zero, and we wish to compute the group 2 current at the right boundary $X=15$ cm Problems 1 through 4 are for a homogeneous 15 cm thick slab, while problem 5 is for a heterogeneous slab consisting of three subregions, each 5 cm thick. The cross sections for these problems are given in Table 1 In

Problem 1, both groups are weakly absorbing, in Problem 2, both groups are strongly absorbing, in Problem 3, the first group is weakly absorbing and the second group is strongly absorbing, and in Problem 4 the first group is strongly absorbing and the second group is weakly absorbing The three regions in Problem 5, from left to right, consist of 5 cm subregions of the materials in problem 1, 2, and 1 respectively To calculate the adjoint diffusion solutions for these problems, we divided each problem into 15 cells with $\Delta x = 1$ cm

For Problems 1-5 we list in Table 2 the Benefit factors B (defined as the conventional figure-of-merit[7] divided by the figure-of-merit for Monte Carlo with survival biasing only) for the Local Exponential Transform methods and Splitting with Russian Roulette

2 X,Y-Geometry Problems

We have defined the Local Exponential transform method earlier in this paper for planar geometry problems, but it can easily be extended to problems in general geometry Although space limitations prevent us from presenting the details of this extension here, we shall present results from five two-group x,y-geometry problems

For each of these five problems, $\sigma_{t,1} = \sigma_{t,2} = 1$ cm^{-1} and $\sigma_{s,2\to1} = 0$ (downscattering only), scattering is isotropic, the system is a square defined by $(0 < x < 16, 0 < y < 16)$, a uniform source exists for group 1 in the square subregion $(3 < x < 4, 3 < y < 4)$, and we wish to compute the group 2 detector response for the square subregion $(14 < x < 16, 10 < y < 12)$ Problems 6 through 9 are for a homogeneous 16 cm × 16 cm rectangle, while problem 10 is for a heterogeneous rectangule consisting of the three subregions $(0 < x < 4, 0 < y < 16), (4 < x < 12, 0 < y < 16)$, and $(12 < x < 16, 0 < y < 16)$ The cross sections for these problems are given in Table 3 To calculate the adjoint diffusion solutions for these problems, we divided the system into 8 × 8 cells with $\Delta x = \Delta y = 2$ cm For these problems the Benefit Factors B for the Local Exponential Transform and Splitting with Russian Roulette methods are listed in Table 4

In each of the above problems, the Local Exponential Transform method with angular biasing outperforms the Local Exponential transform without angular biasing (particularly for highly scattering problems), which in turn outperforms Splitting with Russian Roulette We also note that the Local Exponential Transform methods require significantly less static computer storage than Splitting with Russian Roulette because they do not require the storage of any daughter particles that would arise from splitting

VII. DISCUSSION

We have derived two new Local Exponential Transform variance reduction methods for the Monte Carlo simulation of multigroup neutron transport problems One of these methods has angular biasing, the other does not These methods generalize (and are a minor variation of) the one-group method presented in reference 1 They are obtained by replacing an adjoint transport solution by a diffusion approximation in a zero-variance Monte Carlo method As expected, the angle-dependent approximation (which is more accurate than the isotropic approximation) yields a better approximation to the zero variance method, hence is more efficient Both methods are

simple to implement and can be interpreted as an exponential transform that is "local" in both space and energy An essential feature of these methods is that all of the "local" biasing parameters are determined automatically in terms of the adjoint diffusion solution This eliminates the trial-and-error process of selecting the biasing parameters for conventional variance reduction methods

We have previously shown the success of the "Local" one-group method for one- and two-dimensional geometry problems, and in this paper our numerical results show the success of our methods in multigroup problems For all of the multigroup transport problems that we have run, the new methods are easier to use, more efficient, and require less computer storage than Splitting with Russian Roulette

ACKNOWLEDGMENTS

This work was partially supported by the National Science Foundation grant EET-8721680

REFERENCES

1 K N Abotel, E W Larsen, and W R Martin, "A 'Local' Exponential Transform Method for Monte Carlo Transport Calculations," Proc ANS Conference, *Advances in Mathematics, Computation, and Reactor Physics*, April 29 - May 2, 1991, Pittsburgh, Vol 5, Sec 23 1, pp 1-2 through 1-12 (1991)

2 F H Clark, "The Exponential Transform Method as an Important Sampling Device," ORNL-RSIC-14, Oak Ridge National Laboratory (Jan 1966)

3 J Spanier and E Gelbard, **Monte Carlo Principles and Neutron Transport Problems**, Addison-Wesley, Reading, Mass (1969)

4 L L Carter and E E Cashwell, **Particle-Transport Simulation with the Monte Carlo Method**, ERDA Critical Review Series, TID-26607 (1975) (Available from the National Technical Information Service, U S Department of Commerce, Springfield, VA 22161)

5 S R Dwivedi, "A New Importance Biasing Scheme for Deep-Penetration Monte Carlo," *Ann Nucl Energy* **9**, 359 (1982)

6 E E Lewis and W F Miller, Jr , **Computational Methods of Neutron Transport**, Wiley-Interscience, New York (1984)

7 J D Briesmeister (Editor), "MCNP - A General Monte Carlo Code for Neutron and Photon Transport," Version 3A, LA-7396-M, Rev 2, Manual, Los Alamos National Laboratory (Sept 1986)

8 I Lux and L Koblinger, **Monte Carlo Particle Transport Methods: Neutron and Photon Calculations**, CRC Press, Boca Raton (1991)

9 M L Williams, "Generalized Contributon Response Theory," *Nucl Sci Eng* **108**, 355 (1991)

Table 1 Configuration for Problems 1-5 (Two Group Planar Geometry)(σ in cm^{-1})

	Region (cm)	$\sigma_{s\,1\to1}$	$\sigma_{s\,1\to2}$	$\sigma_{a\,1}$	$\sigma_{t,1}$	$\sigma_{s\,2\to2}$	$\sigma_{s\,2\to1}$	$\sigma_{a\,2}$	$\sigma_{t\,2}$
1	$0 < x < 15$	0 90	0 08	0 02	1 00	0 90	0 00	0 10	1 00
2	$0 < x < 15$	0 10	0 10	0 80	1 00	0 10	0 00	0 90	1 00
3	$0 < x < 15$	0 90	0 08	0 02	1 00	0 10	0 00	0 90	1 00
4	$0 < x < 15$	0 10	0 10	0 80	1 00	0 90	0 00	0 10	1 00
5	$0 < x < 5$	0 90	0 08	0 02	1 00	0 90	0 00	0 10	1 00
	$5 < x < 10$	0 10	0 10	0 80	1 00	0 10	0 00	0 90	1 00
	$10 < x < 15$	0 90	0 08	0 02	1 00	0 90	0 00	0 10	1 00

Table 2 Benefit Factors (B) for Problems 1-5 (Two Group Planar Geometry)

	Problem Description	Local Exponential Transform		Splitting with Russian Roulette
		No Angular Bias	With Angular Bias	
1	$c_1 = c_2 = 0\,9$	8 7	132 5	5 5
2	$c_1 = c_2 = 0\,1$	14366 3	34579 1	1190 5
3	$c_1 = 0\,9$ $c_2 = 0\,1$	123 03	250 1	59 9
4	$c_1 = 0\,1$, $c_2 = 0\,9$	19 79	801 4	13 2
5	heterogeneous	306 57	1020 9	57 4

Table 3 Configuration for Problems 6-10 (Two Group X,Y-Geometry) (σ in cm^{-1})

	Region (cm)	$\sigma_{s\,1\to1}$	$\sigma_{s,1\to2}$	$\sigma_{a\,1}$	$\sigma_{t,1}$	$\sigma_{s,2\to2}$	$\sigma_{s\,2\to1}$	$\sigma_{a\,2}$	$\sigma_{t\,2}$
6	$0 < x < 16$ $0 < y < 16$	0 90	0 08	0 02	1 00	0 90	0 00	0 10	1 00
7	$0 < x < 16$, $0 < y < 16$	0 10	0 10	0 80	1 00	0 10	0 00	0 90	1 00
8	$0 < x < 16$, $0 < y < 16$	0 90	0 08	0 02	1 00	0 10	0 00	0 90	1 00
9	$0 < x < 16$, $0 < y < 16$	0 10	0 10	0 80	1 00	0 90	0 00	0 10	1 00
10	$0 < x < 4$, $0 < y < 16$	0 90	0 08	0 02	1 00	0 90	0 00	0 10	1 00
	$4 < x < 12$ $0 < y < 16$	0 10	0 10	0 80	1 00	0 10	0 00	0 90	1 00
	$12 < x < 16$, $0 < y < 16$	0 90	0 08	0 02	1 00	0 90	0 00	0 10	1 00

Table 4 Benefit Factors (B) for Problems 6-10 (Two Group X,Y-Geometry)

	Problem Description	Local Exponential Transform		Splitting with Russian Roulette
		No Angular Bias	With Angular Bias	
6	$c_1 = c_2 = 0\,9$	6 4	79 0	3 7
7	$c_1 = c_2 = 0\,1$	1160 3	5286 2	490 5
8	$c_1 = 0\,9$, $c_2 = 0\,1$	45 7	135 7	7 9
9	$c_1 = 0\,1$, $c_2 = 0\,9$	12 2	193 6	3 5
10	heterogeneous	131 6	410 2	25 0

LOSS OF FUEL ACCIDENT ANALYSIS WITH MCNP (U)*

by

K. C. Okafor and J. F. Zino

Westinghouse Savannah River Company
Savannah River Laboratory
Aiken, South Carolina 29808

ABSTRACT

A full–core, detailed MCNP model of the Savannah River Site (SRS) reactors has been developed and applied in the analyses of a postulated Loss of Fuel Accident (LOFA). The analyses serve as a benchmark for the integral transport and diffusion theory codes GLASS/GRIMHX, which are specifically tailored to the SRS reactors. The GLASS–hex MCNP model duplicates the hexagonal lattice geometry of these deterministic codes commonly used for analyses of the SRS reactors.

LOFA is an accident scenario in which the fuel melts toward the center of the reactor core, and the melted fuel particles are subsequently transported in the coolant through a region of high netron importance. Results show that the GLASS/GRIMHX calculations of the net reactivity changes are conservative throughout the duration of the transient.

* The information contained in this article was developed during the course of work done under Contract No. DE–AC09–89SR18035 with the U.S. Department of Energy.

INTRODUCTION

The Loss of Fuel Accident (LOFA) is a postulated accident scenario involving the melting of fuel towards the center of the reactor core in a region of high neutron importance Due to the downward flow of coolant in the fuel assemblies, the melted fuel particles are transported to the bottom of the reactor tank, and become entrained in the moderator in the surrounding space These particles are then transported upward with moderator flow and out of the reactor core As a result of the upward flow of the debris through the reactor core, a net reactivity change is expected This change is a required parameter needed to set reactor operating limits

The objectives of this work are to quantify the reactivity changes over the period of such a transient (five seconds) with a full-core model using the General Monte Carlo Code for Neutron and Photon Transport (referred to as MCNP) [1] These calculations will serve as a benchmark for the GLASS/GRIMHX (Integral transport and diffusion theory) codes being used in this applica tion

Reactor Description

The Savannah River Site (SRS) reactors are low temperature and pressure material produc tion reactors that are moderated and cooled by heavy water (D_2O) The reactors are operated by the Westinghouse Savannah River Company for the U S Department of Energy (DOE) The basic SRS reactor lattice consists of a hexagonal array of six assemblies surrounding a central control housing Each assembly consists of four concentric tubes—two fuel tubes and two target tubes The spaces between the fuel and target tubes act as coolant channels where D_2O is circu lated The entire assembly (fuel, target, and coolant) is housed inside an aluminum sleeve which penetrates the reactor tank The tank is filled with D_2O moderator

Accident Description

For the LOFA scenario it was assumed that

(1) Both fuel tubes of the Mark 22 assembly adjacent to the center septifoil housing are allowed to melt while the target tubes, cladding, and Universal Sleeve Housing (USH) remain intact. Figure 1 shows the melting sequence of the fuel as a function of time

(2) The melted fuel regions are replaced by steam

(3) A fraction of the melted debris flows out with the coolant and the remainder becomes entrained in the moderator space surrounding several adjacent assemblies The fraction of debris which becomes entrained in the moderator is defined as a percentage by the particle separation efficiency

(4) The affected area of the core is confined in one triangular section that has the central control position at its apex (Figure 2)

Both the radial and axial distributions of the debris in the moderator space are obtained through a series of two-dimensional finite element calculations performed at each time step of the transient Figure 3 shows the axial segmentation of the moderator space surrounding an assembly

Model Description

The lattice structure capability of MCNP is used to develop a suitable geometric full–core model of the SRS reactors that is based on the GLASS/GRIMHX hexagonal unit. This lattice unit, which is called the GLASS–Hex unit,[2] is an upright (in the x–y plane) hexagonal prism that encloses an assembly position at its origin with D_2O filling the remaining space in the unit. Starting from the origin of the reactor tank, GLASS–Hex units fill the tank space in all directions.

Figure 4 outlines a cross–sectional view showing the GLASS–Hex lattice, with the universes (a universe is a unique integer associated with all cells that fill another cell) filling the elemental lattice positions. Figure 5 shows the fill array matrix. The fill array used for this reactor model is a 33x33 element square matrix that designates the universes that fill the various lattice positions in the reactor tank.

For the LOFA analysis, the affected area of the core is assumed to be limited to the shaded region in Figure 2. This region is divided into rows and isolated from the rest of the core by universes. Figure 6 shows the universe description of the debris triangle. The corresponding moderator space in each of these universes is axially segmented into 16 regions to account for the variation in the debris concentration.

RESULTS/DISCUSSION

Two cases were run: (1) uniform debris concentration[3] in the moderator space, and (2) varied axial debris concentrations in the moderator space. The first case was a scoping study using a simplified version of the accident to determine the applicability of the diffusion theory code for this type of analysis. The second case modeled the actual transient in question.

The conditions of the core before the fuel melt and the onset of the Loss of Fuel Accident transient was assumed to be cold (20°C) and clean (no fission products). All calculations were done on the Los Alamos National Laboratory (LANL) Cray via the Integrated Computer Network (ICN). Each calculation ran approximately 1 million particle histories (10,000 source particles per batch for 100 batches) requiring about 900 CPU minutes each.

Figures 7 and 8 show the plots of the net reactivity versus concentration and time, respectively. It can be observed from both figures that:

(a) The MCNP and GLASS/GRIMHX curves show very good agreement in both cases. In Figure 7, the agreement becomes better with increasing concentration in the moderator. Figure 8 shows a maximum reactivity at t=3 seconds for both MCNP and GLASS/GRIMHX. Also, Figure 8 shows a smoother curve for GLASS/GRIMHX than MCNP, which may be a consequence of the averaging effect in the homogenization process associated with the diffusion theory calculation.

(b) The GLASS/GRIMHX values of the net reactivity worth in Figure 7 are conservative, but GLASS/GRIMHX seems to overpredict the reactivity worth, relative to MCNP, with time in Figure 8. This overprediction may be a result of the explicit nature of the represented debris in MCNP as opposed to an averaged representation, smeared over the height of the moderator space in GLASS/GRIMHX.

References

1 Breismeister, J F (Ed), MCNP – *A General Monte Carlo Code for Neutron and Photon Transport*, LA–7396, September 1986

2 Okafor, K C , *Finite Lattice Modeling with MCNP*, WSRC–TR–91–163, April 1991

3 Okafor, K. C and Zino, J F , *Scoping Studies for the Loss of Fuel Accident*, SCS–RPG–910025, January 30, 1991

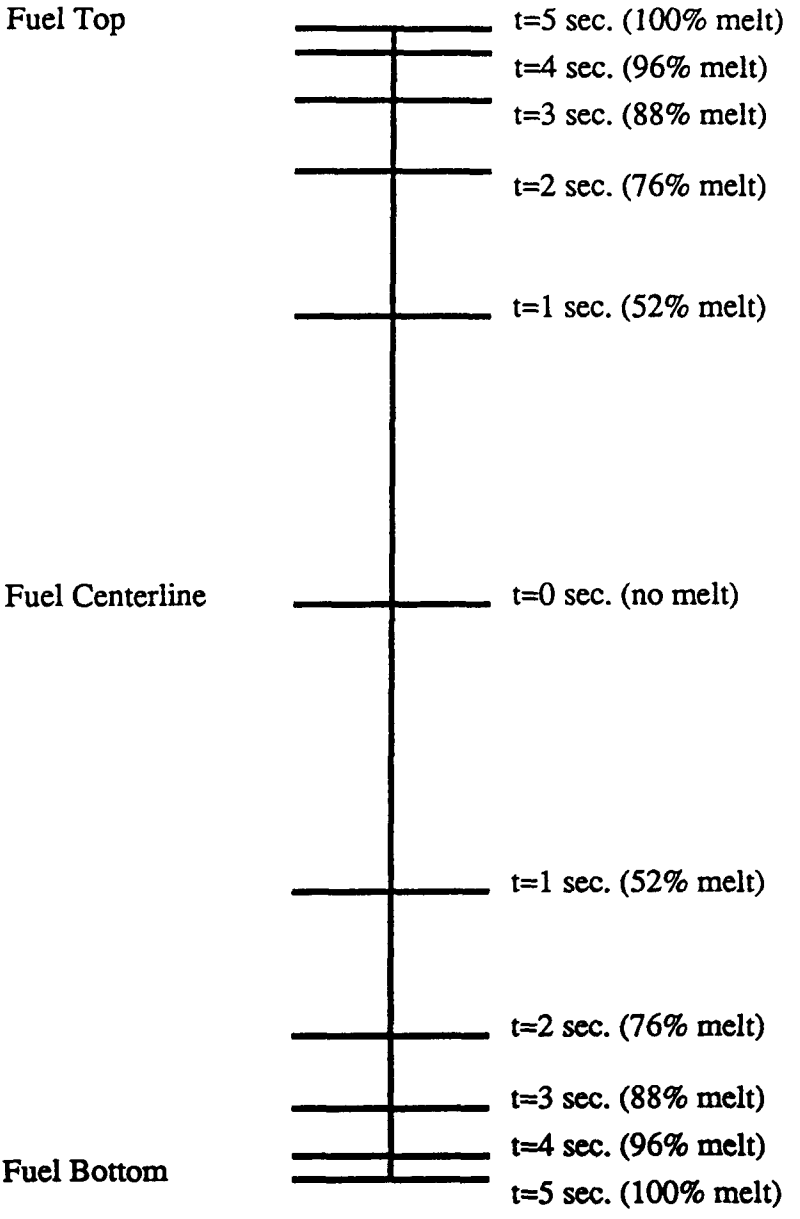

Figure 1. Centerline Fuel Melting Transient

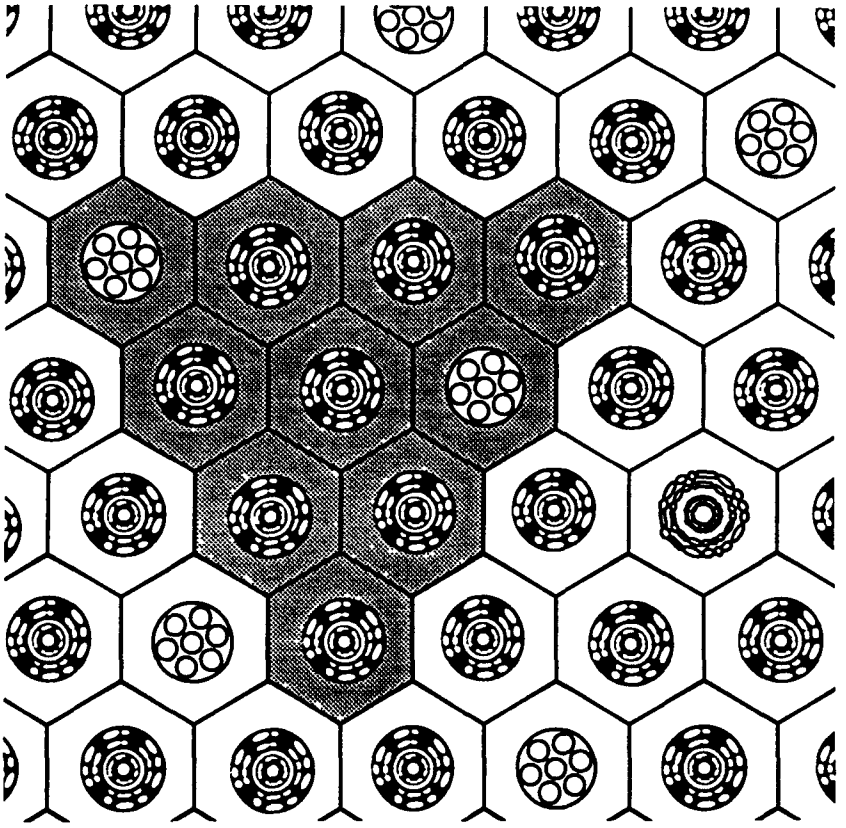

M91jul011.01

Figure 2. Radial Spread of Debris

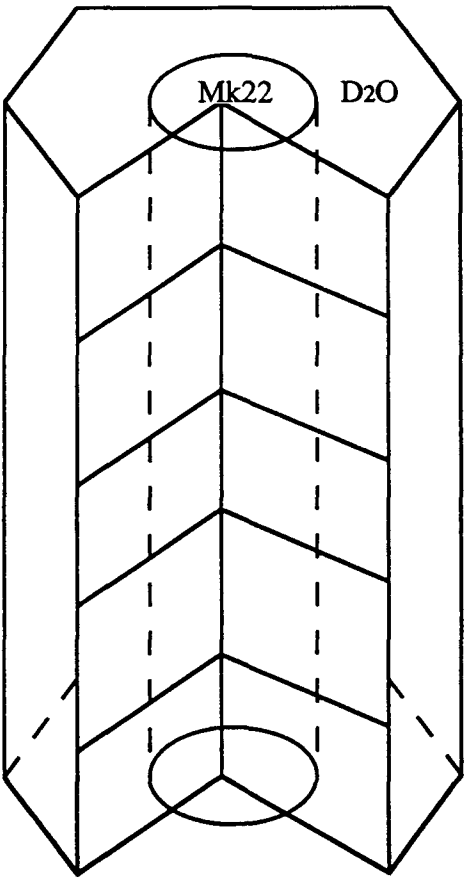

Figure 3. Axial Segmentation of Single Moderator Space

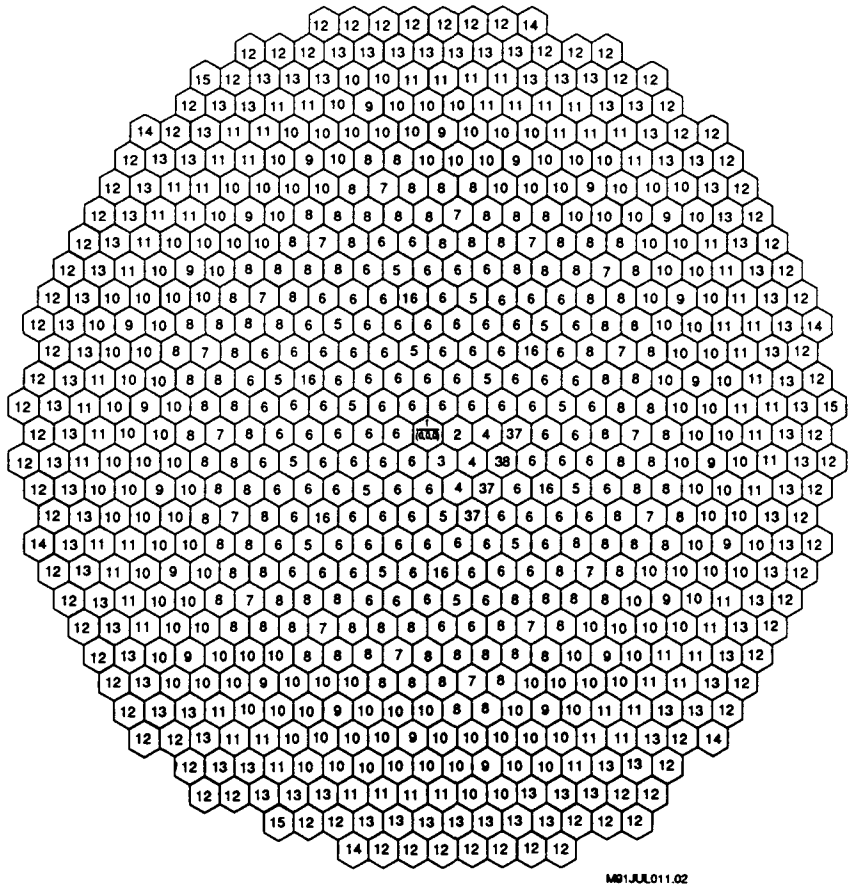

Figure 4. Cross–Sectional View of GLASS–Hex Lattice

30 30 30 30 30 30 30 30 30 30 30 30 30 30 30 30 30 30 30 30 30 30 30 30 30 30 30 30 30 30 30 30
30 30 30 30 30 30 30 30 30 30 30 30 30 30 30 30 30 30 30 30 14 12 12 12 12 12 12 12 30 30 30 30 30
30 30 30 30 30 30 30 30 30 30 30 30 30 30 30 30 30 15 12 12 13 13 13 13 13 13 13 12 12 12 30 30 30
30 30 30 30 30 30 30 30 30 30 30 30 30 30 30 30 12 12 13 13 13 11 11 11 11 10 10 13 13 13 12 12 30 30
30 30 30 30 30 30 30 30 30 30 30 30 30 30 30 12 13 13 11 10 10 10 10 10 10 09 10 10 11 13 13 12 30 30
30 30 30 30 30 30 30 30 30 30 30 30 12 12 13 11 11 10 10 10 10 09 10 10 10 10 10 11 11 13 12 14 30
30 30 30 30 30 30 30 30 30 30 30 12 13 13 11 10 10 10 09 10 10 10 08 08 10 09 10 11 11 13 13 12 30
30 30 30 30 30 30 30 30 30 30 12 13 10 10 10 09 10 10 10 08 08 08 07 08 10 10 10 10 11 11 13 12 30
30 30 30 30 30 30 30 30 30 12 13 10 09 10 10 10 08 08 08 07 08 08 08 08 08 10 09 10 11 11 13 12 30
30 30 30 30 30 30 30 30 12 13 11 10 10 08 08 08 07 08 08 08 06 06 08 07 08 10 10 10 10 11 13 12 30
30 30 30 30 30 30 12 13 11 10 10 08 07 08 08 06 16 06 06 06 05 37 06 06 06 06 08 07 08 10 10 13 12 30
30 30 30 30 30 12 13 11 10 09 10 08 08 06 06 06 05 06 06 04 37 06 16 05 06 08 08 10 10 11 13 12 30 30
30 30 30 30 14 13 11 11 10 10 08 08 06 05 06 06 06 06 06 06 05 06 08 08 08 08 10 09 10 13 12 30
30 30 30 30 30 12 13 10 10 10 08 07 08 06 16 06 06 06 05 06 06 06 06 08 08 08 08 10 09 10 13 12 30
30 30 30 30 30 12 13 10 10 09 10 08 08 06 06 06 05 06 06 06 03 04 38 06 06 06 08 08 10 09 10 11 13 12 30 30
30 30 30 30 12 13 11 10 10 08 07 08 06 06 06 06 06 01 02 04 37 06 06 08 07 08 10 10 11 13 12 30 30 30
30 30 12 13 11 10 09 10 08 08 06 06 06 05 06 06 06 06 06 06 05 06 08 08 10 10 11 11 13 15 30 30 30
30 30 12 13 11 10 10 08 08 06 05 16 06 06 06 06 06 05 06 06 06 08 08 10 09 10 11 13 12 30 30 30 30
30 30 12 13 10 10 08 07 08 06 06 06 06 06 05 06 06 06 16 06 08 07 08 10 10 11 13 12 30 30 30 30 30
30 12 13 10 09 10 08 08 08 08 06 05 06 06 06 06 06 06 05 06 08 08 10 10 11 11 13 14 30 30 30 30 30
30 12 13 10 10 10 10 08 07 08 06 06 06 16 06 05 06 06 06 08 08 10 09 10 11 13 12 30 30 30 30 30 30
30 12 13 11 10 09 10 08 08 08 08 06 05 06 06 06 08 08 08 07 08 10 10 11 13 12 30 30 30 30 30 30 30
30 12 13 11 10 10 10 10 08 07 08 06 06 08 08 08 07 08 08 08 10 10 11 13 12 30 30 30 30 30 30 30 30
30 12 13 11 11 10 09 10 08 08 08 08 08 07 08 08 08 10 10 10 09 10 13 12 30 30 30 30 30 30 30 30 30
30 12 13 11 11 10 10 10 10 08 07 08 08 08 10 10 10 09 10 10 10 13 12 30 30 30 30 30 30 30 30 30 30
30 12 13 13 11 11 10 09 10 08 08 10 10 10 09 10 10 10 11 13 13 12 30 30 30 30 30 30 30 30 30 30 30
30 14 12 13 11 11 10 10 10 10 10 09 10 10 10 11 11 11 13 12 12 30 30 30 30 30 30 30 30 30 30 30 30
30 30 12 13 13 11 11 10 09 10 10 10 11 11 11 11 13 13 12 30 30 30 30 30 30 30 30 30 30 30 30 30 30
30 30 15 12 13 13 13 10 10 11 11 11 11 13 13 13 12 12 30 30 30 30 30 30 30 30 30 30 30 30 30 30 30
30 30 30 12 12 12 13 13 13 13 13 13 13 12 12 12 30 30 30 30 30 30 30 30 30 30 30 30 30 30 30 30 30
30 30 30 30 30 12 12 12 12 12 12 12 14 30 30 30 30 30 30 30 30 30 30 30 30 30 30 30 30 30 30 30 30
30 30 30 30 30 30 30 30 30 30 30 30 30 30 30 30 30 30 30 30 30 30 30 30 30 30 30 30 30 30 30 30 30

Figure 5. Fill Array Matrix

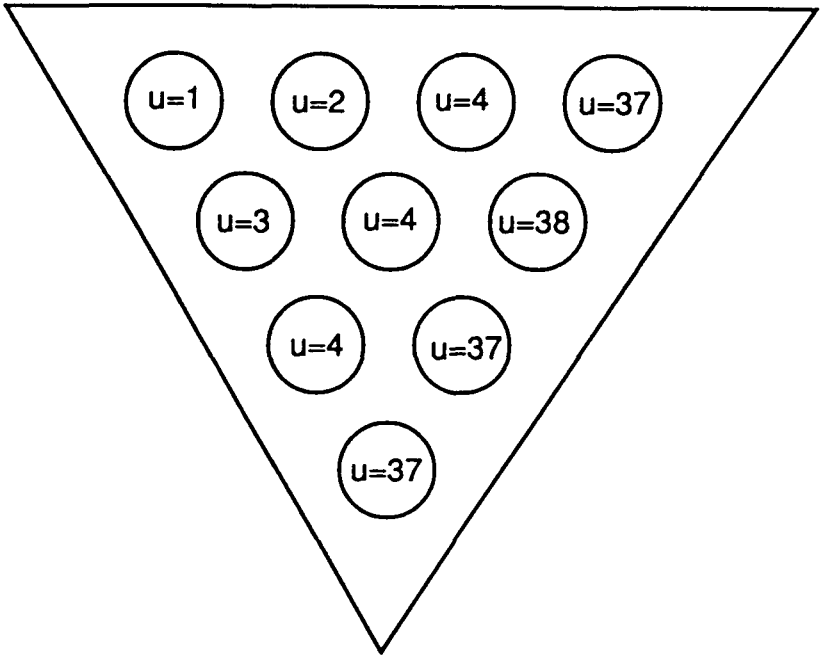

M91jul011.03

Figure 6. Universe Description of Debris Triangle

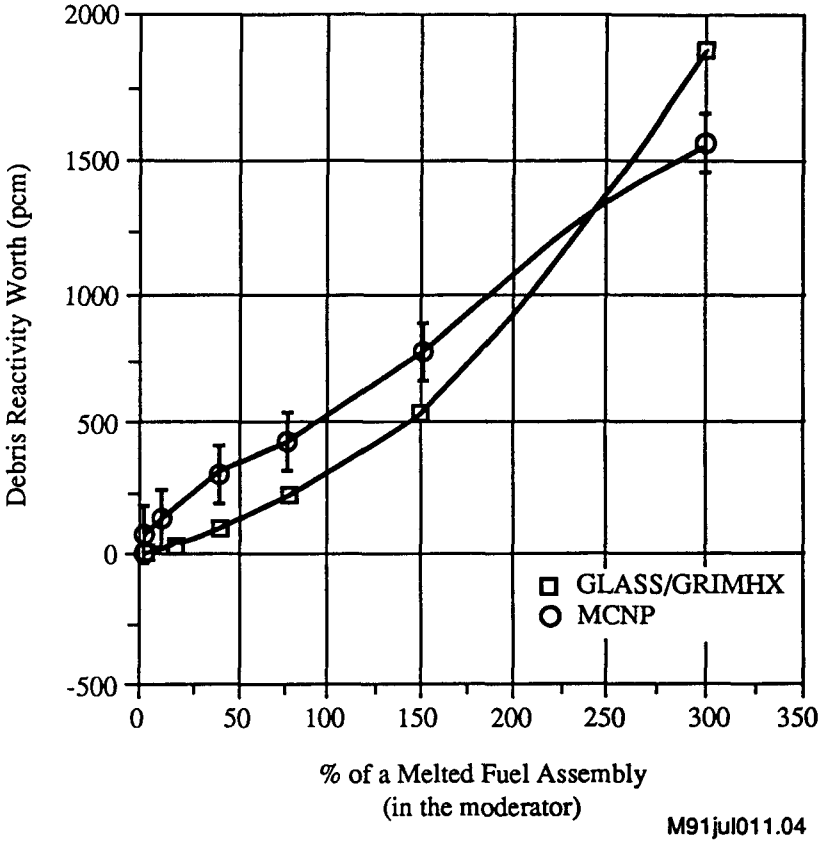

Figure 7. Uniform Debris Reactivity Worth

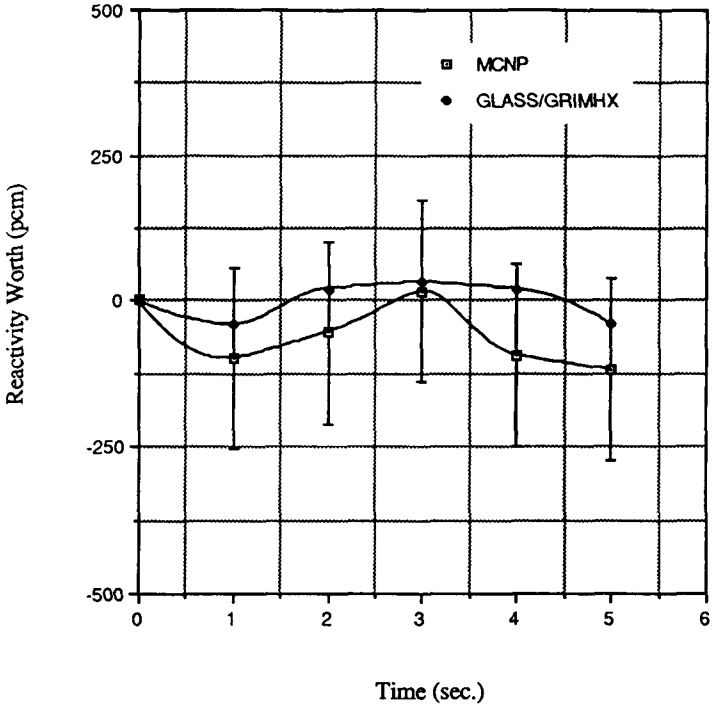

Figure 8. Reactivity Worth vs. Time (50% Particle Separation Efficiency)

AN INVESTIGATION OF AXIAL XENON STABILITY IN VVER-1000 REACTOR DESIGNS

P.K. Doshi, Commercial Nuclear Fuel Division, Westinghouse Electric Corporation, P.O. Box 355, Pittsburgh, PA 15230-0355

R. W. Miller, Commercial Nuclear Fuel Division, Westinghouse Electric Corporation, P.O. Box 355, Pittsburgh, PA 15230-0355

Abstract

It has been reported[1] that nuclear plants of the VVER-1000 design have experienced frequent xenon oscillation control problems. In most PWRs, xenon oscillations are largely a problem in the axial direction. Radially, PWRs tend to be very stable relative to xenon oscillation. Axial Xenon oscillations as a minimum cause operational problems requiring frequent operator intervention to control the oscillation and increased duty on the various control mechanisms (Control rod and soluble boron systems). This paper investigates simple methods available to improve the control of these axial xenon distributions. It is shown that well proven techniques currently in use by Western PWRs work equally as well in the VVER-1000

Introduction

It has been reported[1] that nuclear plants of the VVER-1000 design have experienced frequent xenon oscillation control problems. In most PWRs, xenon oscillations are largely a problem in the axial direction. Radially, PWRs tend to be very stable relative to xenon oscillation. Axial Xenon oscillations as a minimum cause operational problems requiring frequent operator intervention to control the oscillation and increased duty on the various control mechanisms (Control rod and soluble boron systems). In more severe cases, these oscillations can cause power reductions (or plant trips) due to high core peaking factors, thereby reducing overall plant capacity factors. In the worst case, uncontrolled xenon oscillations can lead to fuel damage from either pellet clad interaction (PCI), DNB failure, or fuel centerline melting if the plant does not have adequate safety system protection for tripping the plant on high local core peaking factors resulting from highly skewed axial power distributions.

Investigation Of The Problem

Xe-135 is generated in the core directly from fission and by the decay of Iodine-135 (Half life ~6.7 hr). Less than 1% of U-235 fissions result directly in a Xenon-135 atom while ~6% of fissions results in an Iodine-135 atom. Therefore, the the spatial xenon distribution at a given time is a reflection of what the spatial flux is at that time (small) and what the spatial flux has been over the previous day (~4 half lives of Iodine) (large). Because of this delayed effect of flux on the xenon distribution, any change in the flux amplitude or shape can initiate a transient in the amplitude and shape of the xenon distribution. Because of the large thermal absorption cross section (10^6 barns), any change in the xenon distribution will have a significant impact on the core power distribution.

From a basic core design viewpoint it is not obvious why VVER-1000 design reactors should be significantly different from typical western reactors in terms of xenon characteristics. Table 1 compares global VVER-1000 core parameters to those of typical Westinghouse design 3 and 4 loop cores.

In addition, global core reactivity parameters such as moderator temperature coefficients, boron worths, and power defect are comparable to western designs. Therefore, one would not expect the behavior of the axial xenon distribution to be significantly different either. In fact, Reference 2 indicates that the axial stability index of the VVER-1000 designs is indeed similar to western designs. (The decay of an axial xenon oscillation can be characterised by an exponential decay, e^{bt}, where b is the stability index. b can be determinde from the oscillation period and the change in amplitude between successive periods.)

If the axial xenon distribution is no more unstable than in western plants, what is the cause of the xenon oscillation problems? Reference 3 indicates that the control rod worths of the VVER-1000 designs are somewhat lower than is typical of Westinghouse designed core. In addition, there is very little overlap of the individual control banks. In would therefore appear that the control rod worth and overlap were optimized to minimize the effect of the control rods on the axial power distribution and therefore reducing the possibility of the rods initializing a xenon oscillation. However, once an oscillation begins, this control rod system is very ineffective at controlling the oscillation.

Finally, as indicated in Reference 3, a power distribution control strategy that controls the core axial power distribution skewing as indicated by the parameter axial offset (AO) is only now being developed. (AO is a measure of axial power distribution skewing and is defined as

$$AO = \frac{P^{TOP} - P^{BOT}}{P^{TOP} + P^{BOT}}$$

where P^{TOP} and P^{BOT} are the average power produced in the top half and bottom half of the core respectively. There AO is positive for top skew axial power distributions and negative for bottom skewed distributions. The magnitude of AO is an indication of the degree of skewing.)

To examine the controlability of the current design, we first set up a one dimensional core model representative of the VVER-1000 design. Although the VVER-1000 hexagonal lattice core is significantly different from the square lattice used in Western designs, in a one-dimensional axial sense there is very little difference from Western designs. A typical reload cycle one-dimensional core model was adjusted to reflect the different core thermal power by a simple adjustment to enthalpy rise and temeperatures. Adjusts to the feedback models were used to normalize the model to VVER-1000 axial power distributions and reactivity coefficents. This model was then used to evaluate core behavior during typical power change maneuvers that result in non-equilibrium xenon conditions. Figure 1 shows the how the lack of a power distribution control strategy combined with the low worth control banks influence power distribution control. Figure 1 shows a typical daily load follow cycle for three days where core power is reduced to 50% power during the night. Shown in the figure are core power level, control rod insertion, axial offset, the core axial peaking factor and a measure of the core axial xenon distribution called Delta-xenon (ΔXe). Delta xenon is defined as the difference in the average xenon concentration in the top half of the core minus the average in the bottom half of the core, e.g.

$$\Delta XE = Xe^{TOP} - Xe^{BOT}$$

Thus ΔXe is positive when the axial xenon distribution is skewed toward the top of the core and is negative when the axial xenon distribution is skewed toward the bottom. As in AO, the magnitude indicates the degree of skewing.

As can be seen in Figure 1, the power change combined with control rod motion set off a large axial xenon oscillation as indicated by large changes in the value (both magnitude and sign) of ΔXe, resulting in large swings in the core axial offset. It should be observed that during a xenon transient, AO and ΔXe are always "out of phase", that is when power is top skewed, xenon is bottom skew and visa versa. Also note that large absolute values of AO (and ΔXe) result in large axial peaking factors. In this example, the xenon transient resulted in axial peaking factors in excess of 2.0 even when the core was near full power. While high axial peaking factors are acceptable if the corresponding radial peaking factors are low, current fuel designs and loading pattern concepts would not typically allow axial peaking factors at full power greater than about 1.3 - 1.4. Therefore it is unlikely that this operation would be acceptable in actual plant operation. Operating procedures, power distribution Technical Specifications, and core control and protection system setpoints would need to be in place to prevent this type of operation.

Investigation Of Solutions

An investigation of possible improvements to this design was made. First, an attempt was made to simply use the Westinghouse developed concept of Constant Axial Offset Control (CAOC)(5). Basically, CAOC requires that the core average AO be maintained within an allowed band around a target value of AO. The "Target AO" is defined as the natural AO of the reactor core when it is operated at the full power, equilibrium xenon, all control rods essentially withdrawn condition. Since the axial power distribution is under the control of the plant operator and the plant control systems, CAOC effectively controls overall core peaking factors and limits the amount of axial xenon skewing which in turn limits the consequences of postulated accidents. (The radial component of the core power distibution is determined by the fuel loading pattern and the radial placement of the control rods. The radial power distribution is extremely stable to radial xenon oscillations and is rather insensitive to power level and control rod motion. The effects of power changes, rod motion and fuel burnup are easily determined during the core design process.)

Figure 2 shows the results of the same load follow maneuver using the CAOC procedure with a bandwidth of 5%. The CAOC concept alone worked well during the first day of the power maneuver. However, as the xenon oscillation was continued to be driven by the power changes, the control rods lost the ability to control the AO within the prescribed band. This is not due to a shortfall in the CAOC concept but is due to the control rod system lacking the basic ability to control the AO in the "intuitive" sense. That is, when the rods are inserted, the AO should get more negative and when the rods are withdrawn the AO should get more positive. The AO behavior as a function of control rod insertion for the VVER-1000 reactor is shown in Figure 3. For an operator to control the AO effectively requires a nearly monotonic relationship between AO and control rod insertion (at least for the range of insertion that can be expected during routine power maneuvers.)

Given that the control rods are ineffective in controlling axial xenon oscillations once they begin, one alternative is to attempt to not allow any oscillations to start. An example of this type of operation is shown in Figure 4. In this case the AO is controlled within a very tight (1%) band about the target. In this case, the control rods were about to control the power distribution very near the target and no axial xenon oscillation was initiated. This is observable by noticing that with AO controlled close to the target value, ΔXe is always very near the equilibrium value. In addition, notice that the axial peaking factors are now very low relative to the previous cases. However, there are operational difficulties with this type of operation. To control the axial offset, the control rods must move from the position required from a pure reactivity balance point of view. The reactivity change associated with this control rod motion must be compensated by another reactivity change mechanism. The only other effective mechanism for other than very minor reactivity changes in many plants is a change in boron concentration in the reactor coolant. This means that the any changes in reactor conditions that could cause an axial xenon oscillation to begin must be made in a time frame during which the boron concentration can be changed by the necessary amount. In the very smooth operation modeled here this is not difficult, but there would be little capability to respond to unexpected changes, such as a step change in power demand.

To insure the capability to respond to rapid demands on the system, a wider CAOC band is required. In order to maintain AO within this band, a nearly monotonic relation between AO and rod insertion is needed.

To make this improvement in the controlability of the reactor, control rod overlap was set to be more typical of current Westinghouse plants[4]. Figure 5 shows the same three days of load follow operation using these changes. As can be seen, Figure 5 indicates that these changes

result in very stable core xenon behavior with little deviation of the core axial power distribution from it's equilibrium value of AO with correspondingly low axial peaking factors. In addition to reducing the potential for large axial xenon oscillations and providing the ability to control an oscillation should one begin, this provides other benefits. One noticeable benefit is that the control rods are less deeply inserted into the core (Compare Figure 5 to Figure 1). This can led to significant benefits in safety analysis, most notably in the rod ejection accident. Because some of the reactivity change requirements are handled by the boron system rather than the control rods, there tends to be less inserted reactivity associated with the control rod insertion. This is true even though Bank 9 is inserted into the core earlier. Since Bank 10 is much less inserted, the total worth is the same or in most cases reduce. There is therefore no loss in shutdown margin and since the xenon skewing is reduced the results of the steamline break accident would also be expected to improve.

Conclusion

In conclusion, there is no indication that xenon oscillations are an inherent problem in the VVER-1000 core design. Simple changes to the control rod system coupled with a sound power distribution control strategy that has been proven to be an effective but simple procedure to follow eliminate xenon control problems. Further, a protection system that uses AO as an input to the trip signal to reduce the power level at which the plant trips as the absolute value of AO becomes large will assure more safe plant operation in the case that a large xenon oscillation does occur.

The changes described in this paper can be implemented in a very cost effective manner. There are no equipment changes needed, existing control rods can be used. Only software changes (control rod overlap, AO band limits) and associated Technical Specifications and procedure changes are required. Basic core monitoring only requires the use of two section EXCORE detectors to monitor AO, although significant benefits can be obtained through the use of continuous three-dimensional core monitoring, using the VVER-1000 fixed incore detectors in conjunction with state of the art software such as the BEACON system[6]. Additional benefits can be obtained by using multiple banks of control rods moving independently. Such a design is the Westinghouse MSHIM[7] system designed for the AP600. The use of an MSHIM system would eliminate the need for boron concentration changes during load following type maneuvers and at the same time automate the control of the axial power distribution.

References:

1) Nucleonics Week, Vol. 32, No. 27, July 4, 1991

2) Kurchatov Institute Of Atomic Energy, "Nekotoryye Voprosy Kontsepii Aes S Reaktornoy Ustanovkoy VVER-1000", June 5-9, 1989

3) J. Svarny, et al., "Safety Aspects Of VVER Reactor Core Design and Skoda Computational System", Advances in Mathematics, Computations, and Reactor Physics, International Topical Meeting, April 28 -May 2, 1991

4) D. Rombouts, et. al., "Simple Modifications Improve Operational Flexibility", Nuclear Engineering International, October, 1988

5) T. Morita, et. al., "Load-Follow Demonstrations Employing Constant Axial Offset Power-Distribution Control Procedures", Nuclear Technology, Vol. 31, October, 1976

6) C.L. Beard, et. al., "Core Power Distribution Methodology in the BEACON PWR Core Monitoring System", 1988 International Reactor Physics Conference, Jackson Hole, Wyoming, USA.

7) T. Morita & W.R. Carlson, "MSHIM Load Follow Operation In The Westinghouse AP600 Plant Design", Topical Meeting: The Next Generation of Nuclear Power Plants - A Status Report, ANS 1991 Winter Meeting, November 10-14, 1991

Table 1
Comparison Of Basic Core Parameters

	Westinghouse		VVER-1000
Thermal Power	2775	3411	3000
Number Of Loops	3	4	4
Number Of Assemblies	157	193	163
Core Equivalent Diamter (m)	3.04	3.37	3.24
Core Active Fuel Height (m)	3.66	3.66	3.53
Core Volume (m^3)	26.6	32.6	29.1
Core Unranium Loading (MTU)	67-72	82-88	74.3
Core Power Density (kw/l)	105	105	103
Core Specific Power (kw/kg)	38-41	38-41	40
Core delta T, °C	36	36	30.3

FIGURE 1
VVER-1000
LOAD CHANGE WITH NO AXIAL POWER DISTRIBUTION CONTROL AND CURRENT CONTROL ROD SYSTEM

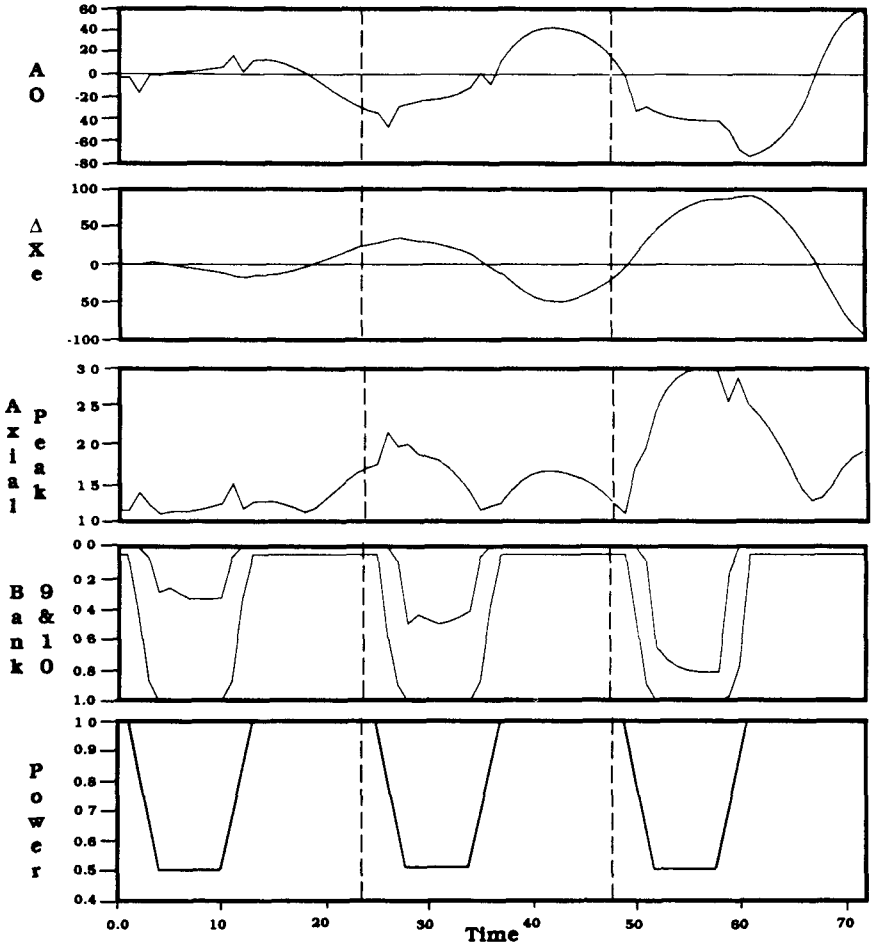

FIGURE 2
VVER-1000
LOAD CHANGE WITH ±5% POWER DISTRIBUTION CONTROL AND CURRENT CONTROL ROD SYSTEM

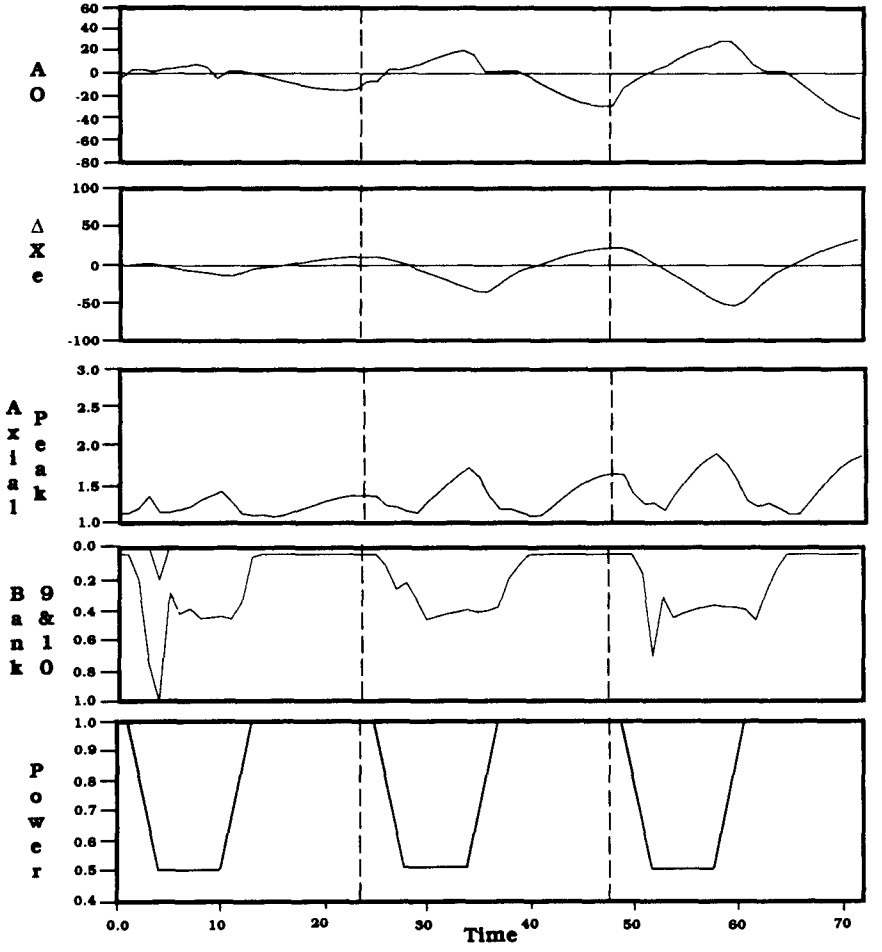

FIGURE 3
VVER-1000
AXIAL OFFSET AS A FUNCTION OF CONTROL ROD INSERTION
CURRENT CONTROL ROD SYSTEM

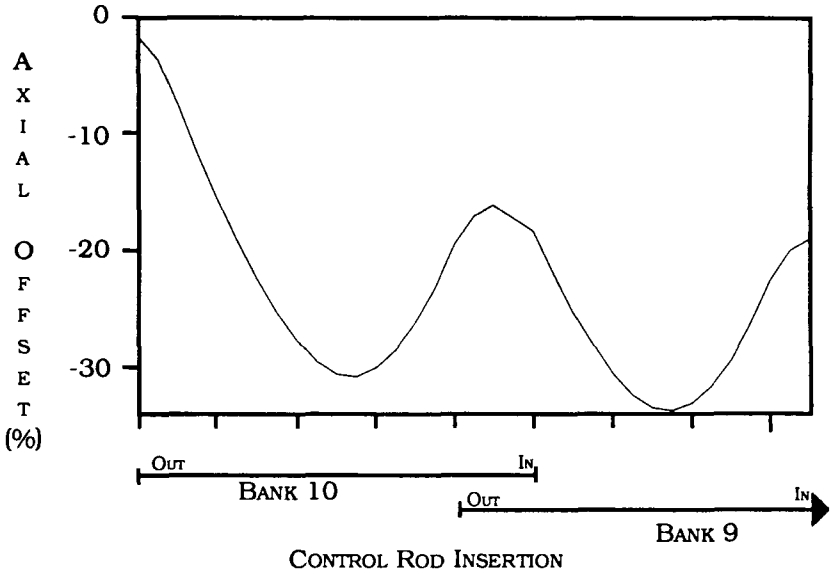

FIGURE 4
VVER-1000
LOAD CHANGE WITH ±1% POWER DISTRIBUTION CONTROL AND CURRENT CONTROL ROD SYSTEM

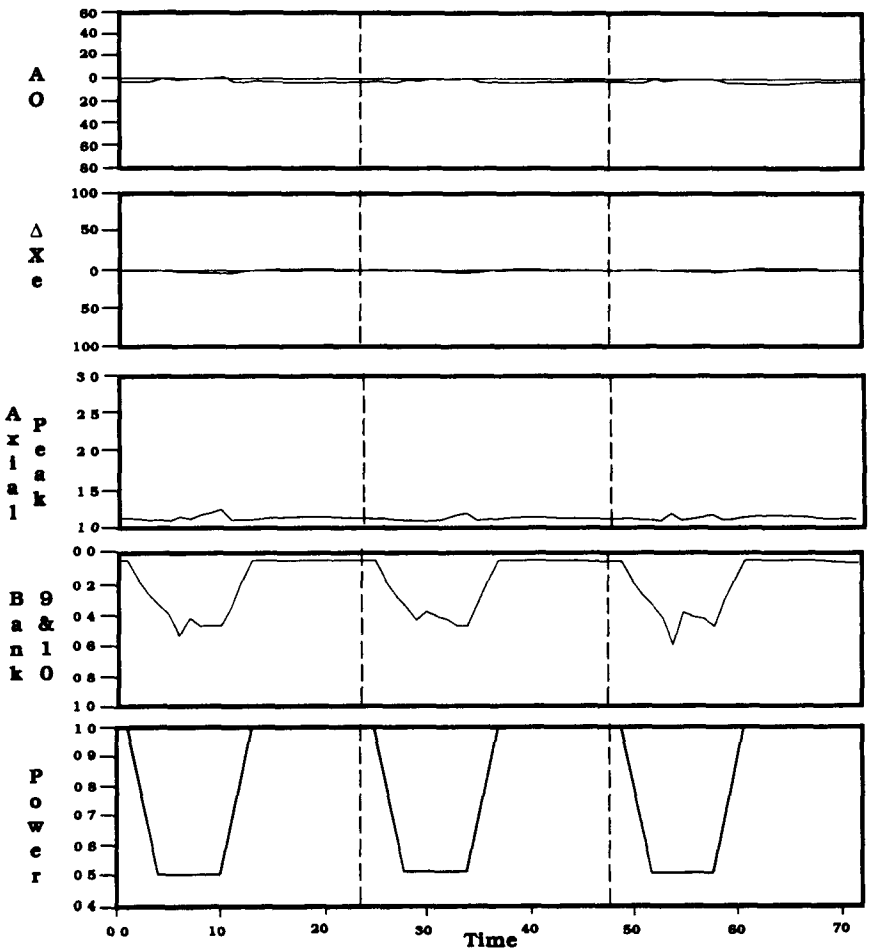

FIGURE 5
VVER-1000
LOAD CHANGE WITH ±5% POWER DISTRIBUTION CONTROL AND IMPROVED CONTROL ROD OVERLAP

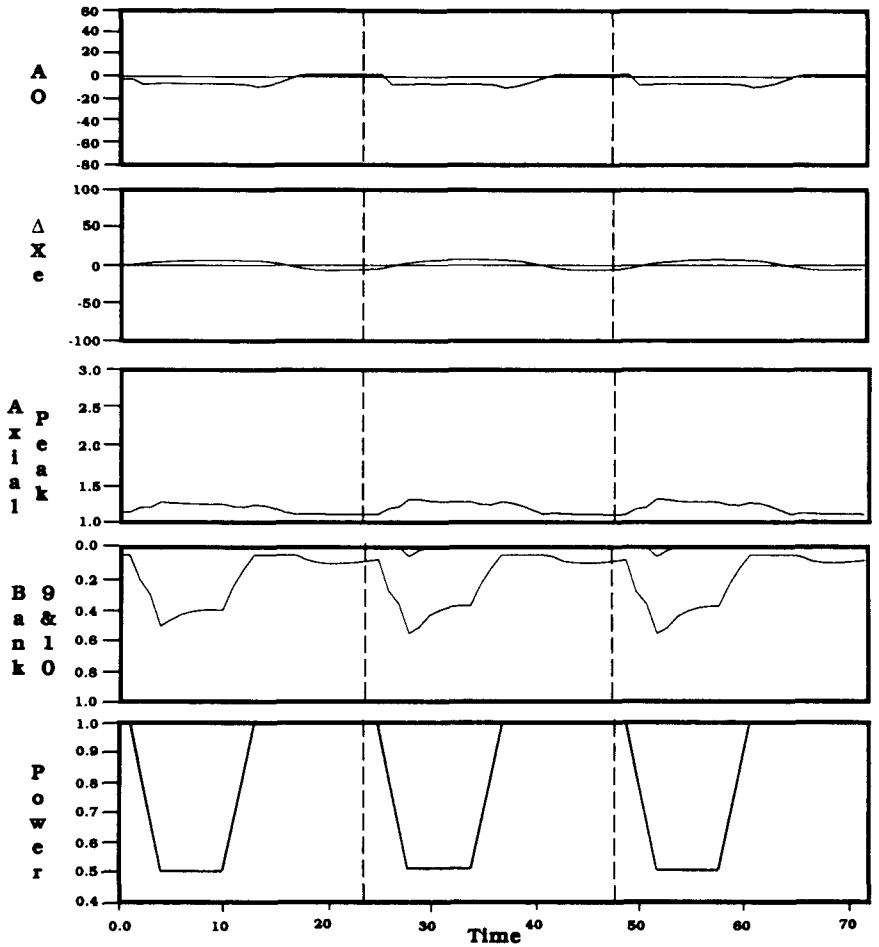

THERMOFLUID–NEUTRONIC STABILITY OF THE ROTATING, FLUIDIZED BED, SPACE–POWER REACTOR

C C Lee,[1] O C Jones, M Becker[2]

Rensselaer Polytechnic Institute
Department of Nuclear Engineering and Engineering Physics
Troy, New York 12180–3590 U S A

ABSTRACT

A rotating fluidized bed nuclear reactor has the potential of being an attractive option for very high power space power and propulsion systems Research has already examined fuel bed expansion due to variations in state variables propellant flow rate and rotational speed as well as questions of thermal stress This paper describes the results of a coupled thermofluid–neutronic analysis where perturbations in fuel bed height caused by maneuvering changes in operating conditions alter power levels due to varying absorption of neutrons which would otherwise leak from the system, mainly through the nozzle The analysis utilized view factors coupled with Fermi–age and diffusion theories coupled with the void propagation equation in the fluidized fuel bed to determine the linearized transfer function for the mutual feedback between the flow and power It was found that power fluctuations were larger by 100 db or more than those expected in a packed bed However, no power excursions were found since the transfer function always had less than unity gain Margins to unity gain in some cases were sufficiently small that the approximations in this quasi–2–dimensional model may not be sufficiently accurate to preclude significant excursions

INTRODUCTION

The increasing activity in space will eventually reach the stage where nuclear reactor systems must be developed for applications to space craft propulsion and prime space platform power Appropriate design concepts of nuclear reactors will require high power density capability, perhaps in the multi–megawatt or gigawatt power range, along with other limits that are usually related to thermal behavior The rotating fluidized bed reactor (RBR) has been suggested as an attractive option among the various candidate nuclear reactor systems

A rotating fluidized bed reactor concept was first described by Hatch et al , in the mid 1960's,[1] and subsequently studied by Botts et al [2] and by Jones [3] Small spheroidal fuel particles increase the fuel surface to volume ratio by factors of 10–100 or more over commercial reactors so higher power densities can be achieved without decreasing thermal margins in the core The gas coolant/propellant enters radially through a rotating porous drum in which the fuel particles are contained (refer to Figure 1) The fuel bed core is designed to expand inward freely due to the drag forces induced by the propellant flow, but are stabilized below the fuel carryover limit by the high centrifugal forces in the rotating drum After passing through the fuel bed into the center of the core's cavity region, the gas propellant exits axially through a nozzle

Such an RBR is expected to have frequent perturbations of gas coolant/propellant flow for maneuvering purposes These may result in power level transients due to the inherent coupling between thermofluids and neutronics It is common knowledge that in conventional nuclear reactors, the thermal responses of fuel and coolant following an operational perturbation generally give favorable negative effects to reactivity changes of the power level[4] But, in an RBR, besides having these effects as in conventional reactors, a flow perturbation yields a positive feedback parameter in the power level transients which is caused by the expansion behavior of the fuel bed and resultant absorption of neutrons which would otherwise leak out the exhaust nozzle The purpose of this paper is to describe the results of an analysis of these effects

1 Currently at Korean Advanced Energy Research Institute, P O Box 7 Daeduk–Danji, Daejon

2 Currently at University of Miami, Coral Gables, Florida

Figure 1 Schematic of the Rotating Fluidized Bed Reactor-Based Space Propulsion System

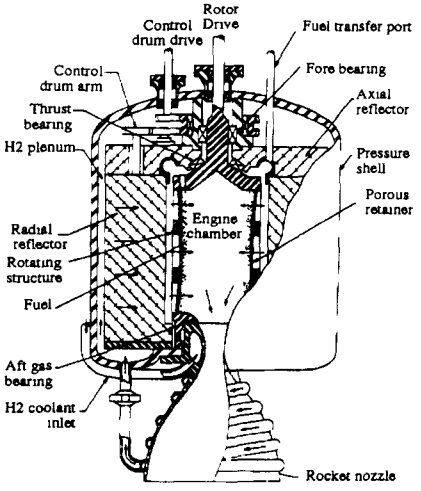

Figure 2 Geometry Chosen to Analyze RBR Behavior

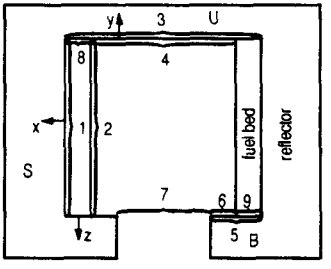

Figure 3 Feedback Scheme Chosen to Analyze RBR Behavior

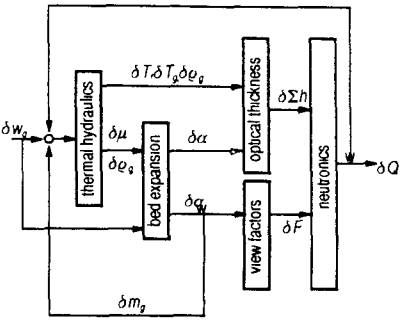

Figure 4 Possible Geometries for two Fuel Particulates for the RBR

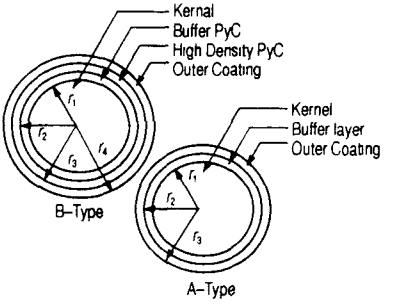

GENERAL FEEDBACK SCHEME

The thermofluid–neutronic coupling is analyzed using linearized closed–loop feedback methods The major new effect not heretofore considered in reactor analysis is the change in neutron absorption due to variations in fuel bed thickness and resultant changes in neutron leakage out the exhaust nozzle These effects are described through the optical thickness of the fuel bed itself a void propagation equation which couples flow behavior to transient fuel bed behavior and view factors which describe how the various surfaces communicate visually A diagram of the geometry used is shown in Fig 2 and the overall feedback scheme in Fig 3 where the view factors F_j describe the visual communication between surfaces i and j Both the case where the reactor has insufficient propellant flow rate to levitate the fuel particles (packed bed) and the fluidized bed case where the fuel bed expands inward due to drag from the coolant flow are considered The reader is directed to the Ph D thesis by Lee[5] for the details of the lengthy analysis summarized herein

Particulate Fuel. The advantages of the RBR are realized in part due to the size and configuration of the fuel particles where the surface–to–volume ratio is maximized by making the size of each particle as small as practical As shown in Fig 4 two possible configurations are given[6,7] which involve uranium carbide coated with zirconium carbide with possible layers of low and high density carbon between (Table 1)

Packed Bed. If a flow perturbation does not alter an initially packed bed geometry with fixed depth h the view factors of neutron leakage will not vary, and only the perturbation of optical thickness Σh will cause the power level transients Assuming an increase of propellant flow rate the subsequent decrease of the fuel and gas temperature causes an increase of neutron absorption cross–section Σ with a resultant increase in optical thickness The substantial growth of optical thickness causes a power level increase, which increases the gas and fuel temperature and sets up a potential for either oscillations or self regulation

Table 1 Assumed matrix configuration of the RBR Fuel

Type	Matrix #	Component	Radius μm	Density g/cc
A–Type	1	UC	236	10 0
	2	ZrC	246	1 0
	3	ZrC	250	2 0
B–Type	1	UC_2	250	10 7
	2	Low density C	340	1 09
	3	High density C	380	1 9
	4	ZrC	425	6 7

Feedback Parameters. The following parameters are considered in the analysis

(1) Optical Thickness Referring to the general feedback scheme shown in Fig 3, a perturbation of optical thickness can be linearized with respect to the perturbations of thermofluid parameters as

$$\delta\Sigma h = \left(\frac{\partial\Sigma h}{\partial\alpha}\right)_o \delta\alpha + \left(\frac{\partial\Sigma h}{\partial p_g}\right)_o \delta p_g + \left(\frac{\partial\Sigma h}{\partial T_g}\right)_o \delta T_g + \sum_i \left(\frac{\partial\Sigma h}{\partial T_{fi}}\right)_o \delta T_{fi} \tag{1}$$

where a perturbed parameter is represented by δ and the subscript o denotes the equilibrium state, Σh is the optical thickness of the fuel bed, α is the bed void fraction p_g and T_g are gas pressure and temperature, and T_{fi} is the average temperature of fuel zone–i

(2) View Factors Considering that the bed depth is a function of the gas volume fraction the perturbed view factors of thermal neutrons are

$$\delta F_{ij} = \left(\frac{\partial F_{ij}}{\partial\alpha}\right)_o \delta\alpha \tag{2}$$

(3) Gas Volume Fraction A disturbance of the gas volume fraction occurs only in a fluidized state ($\delta\alpha \neq 0$) In such a case, the perturbed gas volume fraction is determined by the parametric changes of gas density, ρ_g and viscosity, μ, and by the dynamic behavior of the bed expansion which is directly related to the perturbation of the gas flow rate itself, δw_g The void perturbation is then given by

$$\delta\alpha = \begin{cases} 0 & \alpha \le \alpha_p \\ \left(\frac{\partial\alpha}{\partial p_g}\right)_o \delta p_g + \left(\frac{\partial\alpha}{\partial\mu}\right)_o \delta\mu + G_\alpha \delta w_g & \alpha > \alpha_p \end{cases} \tag{3}$$

where G_α represents a mathematical evaluation describing the dynamic behavior of bed expansion based on an adiabatic incompressible flow, and α_p is the void fraction for the fuel in the packed–bed state The effects of gas compressibility and gas temperature on void fraction is accounted for by the evaluation of $\delta\rho_g$ and $\delta\mu$

(4) Gas Viscosity and Density The dependency of viscosity on pressure is ignored [8] The perturbed viscosity and gas density are then

$$\delta\mu = \left(\frac{d\mu}{dT_g}\right)_o \delta T_g \tag{4}$$

$$\delta\varrho_g = \left(\frac{d\varrho_g}{dT_g}\right)_o \delta T_g + \left(\frac{d\varrho_g}{dp}\right)_o \delta p \tag{5}$$

(5) Fuel and Gas Temperature Change in absorption of neutrons in the gas due to gas temperature changes are neglected and only the changes in fuel absorption with temperature are considered in the optical thickness Eq (1) However the gas temperature behaves as an important factor for the determination of the disturbed thermal neutron view factor because the view factor is strongly dependent on the gas volume fraction as described above

NEUTRONIC MODEL

As shown in Fig 1, an RBR has reflector/moderator zones surrounding the fuel bed radially and axially except for the nozzle opening Thus fast neutrons born in the fuel bed become thermal by slowing down in the reflector zones before moving back into the fuel to be absorbed causing fission During this neutron cycle, it is inevitable that some thermal and fast neutrons leak our the exhaust nozzle

In general, Fermi–age theory is known to be appropriate for describing the slowing down of fast neutrons in a heavy moderator such as beryllium [9] the suggested moderator for an RBR Slowing down by the fuel bed is neglected After fast neutrons are thermalized in the reflector zone, they diffuse through the reflector before reentering the fuel bed Thermal neutron diffusion in the reflector zone is generally described by diffusion theory However diffusion theory cannot be used in the fuel bed because of the strong absorption of thermal neutrons in this region This particular combination of reflector and fuel bed can be effectively overcome by using blackness theory in matching two such differently–characterized substances [10][11] In this combination, the fuel bed is considered a pure absorber for thermal neutrons because the scattering–to–absorption ratio of thermal neutrons is negligibly small

Throughout the neutronic modeling, neutron loss from the exhaust port is accounted for by applying surface–to–surface view factors to boundary or matching conditions This view factor concept is physically the same as the one used in radiative heat transfer [12] For mathematical convenience, a one–dimensional slab geometry is assumed in modeling the neutron field The reflector is divided into three zones side, upper and bottom (Fig 2) The coordinate systems x, y and z are assigned to each of three reflector zones specified by the letters S U and B The origin of the coordinate systems is the interface of reflector and fuel bed In Fig 2 the numbers from 1 to 9 indicate the index of each surface of the reflectors, fuel bed and exhaust nozzle

Slowing Down Density. For the beryllium moderator, the ratio of slowing down time to diffusion time is small of the order of 10^{-2} (c f Refs 9,14) Therefore to simplify the system dynamics it can be assumed that the fast neutrons rapidly become quasi–static as compared with the diffusion of the thermal neutron [10,15] Then, in each reflector zone Fermi–age theory is described by

$$\frac{d^2}{dx^2} q_\eta(x,t,\tau) = -\frac{d}{d\tau} q_\eta(x,t,\tau) \tag{6}$$

where q is a slowing down density, t is time, τ is the Fermi–age, and η represents S, U or B

In general, the reflector of an RBR is designed to be more than twice as thick as the neutron migration length Therefore as a boundary condition, it is assumed that the slowing down density vanishes at the extreme position of the reflector from the core This yields

$$\lim_{\xi\to\infty} q_\eta(\xi,t,\tau) = 0 \tag{7}$$

where ξ is a generalized coordinate representing x, y, or z A fuel bed is mostly transparent for fast neutron because the absorption or scattering processes of fast neutrons are negligible Thus the slowing down of fast neutrons is assumed to start at the interface of the reflector and the fuel bed with no local fast neutron source in the reflector Then, the slowing down densities at zero age ($t = 0$) vanish except at the boundaries of $x = 0$, $y = 0$ and $z = 0$

Because the total neutrons at zero age must equal the fast neutron source another boundary condition is

$$\lim_{\tau \to 0} \int_0^{\infty} q_\eta(x, t, \tau) d\xi = K_\eta \frac{S(t)}{2} \tag{8}$$

where $K_S = (1 + F_{11})$, $K_U = (A_1/A_3)F_{13}$, and $L_B = (A_1/A_5)F_{15}$ Recall that F_{ij} is a diffuse view factor of surface i to surface j and A_i is the area of surface i $S(t)$ is a planer source strength of fission neutrons Examining Eq (8) the right-hand-side terms indicate the number of fission neutrons per unit area injected into each reflector zone When each term is multiplied by the associated surface areas A_1 A_3 and A_5 the summation of the three resultant terms yields the total number of fission neutrons produced in the fuel bed $[A_1 S(t)]$ minus fission neutrons leaked through the exhaust port $[A_1 S(t)F_{17}]$ The summation of the view factors F_{11}, F_{13} F_{15} and F_{17} is unity

Thermal Neutron Flux. The diffusion process of thermal neutrons in three reflector zones is described by the following diffusion equation

$$\frac{1}{v}\frac{\partial}{\partial t}\Phi_\eta(\xi, t) = D\frac{\partial^2}{\partial \xi^2}\Phi_\eta + \Sigma_{aS}\Phi_\eta + q_\eta(\xi, t, \tau) \tag{9}$$

where v is the fission production multiplier and ϕ_η is the neutron flux in zone-η The macroscopic absorption cross-sections of the upper and bottom reflector, Σ_{aU} and Σ_{aB}, are substantially the same as for pure beryllium but poisoning by the control drums is included in the side reflector Σ_{aS}

As in the slowing down density, a boundary condition for the perturbed diffusion equation can be set by assuming that the thermal neutron flux vanishes at the extreme position of the reflector from the fuel bed This yields

$$\lim_{\xi \to \infty} \Phi_\eta(\xi, t) = 0 \tag{10}$$

At the interface of reflector and fuel bed the neutron net currents of the reflectors must match continuously with those of the fuel bed If J_S, J_U and J_B represent the neutron net currents at the three interfaces determined from blackness theory then

$$\lim_{\xi \to 0} D\frac{\partial}{\partial \xi}\Phi_\eta = -J_\eta(0, t) \tag{11}$$

Matching Condition by Blackness Theory. The application of blackness coefficients in specifying the matching conditions at the interface of highly absorbing and scattering medium is an accurate mathematical approach and makes solving such a two region problem quite simple [8] In this model, diffusion theory is used for an approximate solution in the reflector region as described in the previous subsection, and the blackness coefficients obtained by an accurate approach in the fuel bed region are employed as matching parameters at the given interface

Assuming that the neutron current intensity leaving the fuel bed reflector or core cavity is uniform over the emitting surface, the neutron intensity from one reflector surface to another can easily be evaluated by using the view factor concept as

$$at \quad x = 0, \quad -A_1 J_S = A_1 J_S - A_1 J_S F_{11} T_{1,0}(\Sigma D_c) - (A_4 J_U F_{42} + A_6 J_B F_{62}) T_{1,0}(\Sigma h) \tag{12}$$

$$at \quad y = 0, \quad -A_4 J_U = A_4 J_U - A_1 J_S F_{13} \frac{A_4}{A_3} T_{1,0}(\Sigma h) - A_6 J_B F_{64} \tag{13}$$

$$at \quad z = 0, \quad -A_1 J_B = A_1 J_B - A_1 J_S F_{15} \frac{A_6}{A_5} T_{1,0}(\Sigma h) - A_4 J_U F_{46} \tag{14}$$

where, $T_{1,0}$ is the transmission coefficient (defined by an exponential integral function of order 3), and D_c is the core diameter In this evaluation, the thermal neutrons injected from the surfaces of A_6 and A_6 to the fuel bed are assumed to be absorbed fully in the fuel bed without any transmission In other words, the thermal neutrons of $A_6 J_U$ and $A_6 J_B$ cannot contribute to the neutron currents on other reflector surfaces

Also, if η is defined as the ratio of fission neutrons produced to thermal neutrons absorbed in the fuel bed, the neutron source strength S is determined by the absorption rate of thermal neutrons multiplied by η yielding

$$S = -\eta \begin{Bmatrix} J_S F_{11}[1 - T_{1,0}(\Sigma D_c)] + J_U W_{81} + J_B W_{91} + [J_S \\ (1 - F_{11}) + J_U W_{42} + J_B W_{62}][1 - T_{1,0}(\Sigma h)] \end{Bmatrix} \quad (15)$$

Transient Response of Power Level. The perturbed expressions of field equations and boundary conditions given by Eqs (6) to (15) are derived by linearization where any parameter $\xi(t) = \xi^o + \delta\xi(t)$ yielding the perturbed power level [14] Note that, among the various view factors, the fast neutrons (F_{11}, F_{13} and F_{15}) are not disturbed by a flow perturbation because such factors do not depend on fuel bed depth Furthermore in a heterogeneous reactor like an RBR the neutron constants like Fermi–age thermal neutron velocity and reflector macroscopic absorption cross–section are almost invariable for thermal disturbances

By taking Laplace transforms with respect to time and solving the perturbed field equations for the given boundary and matching conditions the perturbed power level, δQ, in terms of the perturbations of optical thickness and gas volume fraction is

$$\frac{\tilde{\delta Q}}{Q^o} = G_h \tilde{\delta\Sigma h} + G_F \tilde{\delta\alpha} \quad (16)$$

where G_h represents the transfer function due to an input perturbation of optical thickness Σh, and G_F represents the transfer function due to a perturbation of view factor caused by a perturbation of gas volume fraction

Criticality Equation for the Equilibrium Core. The diffusion equations and the boundary conditions describing the equilibrium core are similar to those for the transient core except that the neutron flux is independent of the time variable Therefore the mathematical procedure to get the thermal neutron flux distributions in the steady state core is identical to the one used for the transient core where the dependency of neutron flux on time is expressed by the Laplace transform

By inserting J_S^o, J_U^o, and J_B^o obtained from Fermi–age and the diffusion equations into Eq (15) and eliminating S^o in both sides of the resultant equation, a complicated transcendental expression representing the critical condition of the equilibrium core is derived as

$$f(F_{ij}, \Sigma h, \Sigma_{aS}, \Sigma_U, \Sigma_{aB}) = 1 \quad (17)$$

As shown in Fig 1, the power level of an RBR is controlled by rotating the control drums located in the side reflector Thus, the reactor criticality is adjusted by changing the macroscopic absorption cross–section of the side reflector (Σ_{aS}) Therefore, the macroscopic absorption cross–section of the reflector, by which reactor criticality is achieved for the given operational conditions, should be obtained through numerical iterations of Eq (17) until k_{eff} of unity is achieved

BED EXPANSION BEHAVIOR

In an RBR, the inside of the fuel bed is designed to be free to expand inward due to the induced drag force of gas propellant However the fuel particles are held stable inside the rotating fnt cylinder by the high centrifugal forces inside the core, without any *elutnation* or carryover Such high rotational g–fields accommodate a large flow rate of gas coolant/propellant thereby providing excellent heat transfer for the particles

Considering a gas–solid system like the RBR, in which both drag force and g–field are imposed on the fuel particles a radial gas flow through the fuel bed gives rise to a fixed bed at low flow rate the particles remain fixed relative to the fnt cylinder wall If gas flow is increased above the minimum required to fluidize the fuel bed, the particles become freely supported in the gas fluid, and the average distance between the particles becomes greater This bed expansion is herein expressed through the drift–flux approach by which the gas volume fraction of an equilibrium bed is predicted This method was first described by Wallis,[13] and has been applied to the RBR system by Jones [3,16]

Gas Volume Fraction in the Equilibrium Bed. The drift–flux is defined as the velocity of a component relative to a surface moving at the volumetric–average velocity In this dispersed–flow model attention is focused on the relative motion rather than on the motion of the individual phases This model is considered to be particularly useful if the relative motion is determined by a few key kinematic parameters and is independent of the flow rate of each phase

In an RBR, wall friction cannot be a factor in determining the drift flux because the fuel bed has no wall in the direction of relative motion between the fuel particle and the gas propellant Also, since the fuel bed behaves like a mostly dense body and the gas core acts as a potential vortex, it is assumed that the fuel bed rotates as a rigid body Thus the gas flow anywhere within the bed is radially inward[3 17 18,19] and the relative motion between the rotating frit cylinder and the fuel bed has no influence on the bed expansion behavior

The local gas volume fraction in the equilibrium bed can be obtained by using the following relation deduced from the drift–flux model [3]

$$\alpha = \begin{cases} \left(\dfrac{j_g}{v_\infty}\right)^{1/n} & \text{for } j_g > j_{gm} \\ \alpha_p & \text{for } j_g \le j_{gm} \end{cases} \tag{18}$$

with j_g the volume flux of the gas, j_{gm} the drift flux, and the key parameters to be determined are the terminal velocity v_∞ and the expansion exponent n The terminal Reynolds number is explicitly expressed as a function of the Archimedes number[3] as

$$\mathrm{Re}_\infty = \begin{cases} \dfrac{Ar}{18}\left[1 + 0.0487\left(\dfrac{4}{3}Ar\right)^{0.452}\right]^{-1} & Ar < 3.227\times10^5 \\ 1.74\sqrt{Ar} & Ar \ge 3.227\times10^5 \end{cases} \tag{19}$$

where for fuel particles of size δ_d in a gravity field g, $Ar = g\rho\Delta\rho\delta_d^3/\mu^2$ In this case $\Delta\rho$ is the fuel–fluid density difference For the expansion exponent, a simple relation which is generally applicable in the whole range of terminal Reynolds numbers was developed by Jones and Shin[20] as

$$n = 5.65\left[1 - \frac{1}{2}\tanh\left(\frac{\mathrm{Re}_\infty}{90}\right)^{0.4}\right] \tag{20}$$

The gas superficial velocity is given by $j_g = w_g/2\pi rH\rho_g$, where w_g is the flow rate, r is the radial position in the core H is the length of the fuel bved Note that if nothing else changes, j_g increases as r decreases In addition, the terminal velocity and expansion exponent decrease with r, because the Archimedes number decreases with local effective gravity Therefore, Eq (18) shows that the local gas volume fraction increases through the bed from the frit cylinder to the core when fluidize

Transient Response of Gas Volume Fraction Referring to Eq (3), G_α represents a general expression for the transient response of the gas volume fraction based on the incompressible and adiabatic flow This kinematic behavior is evaluated by using the void propagation equation derived from the continuity of the gas phase in a gas–solid system [21]

If a cylindrical geometry is used to account for the strong dependency of gas volume on radial position, the perturbed void propagation is derived in the absence of compressibility and dependency of gas density or temperature as

$$\frac{\partial\delta\alpha}{\partial t} + C_k^2\frac{\partial\delta\alpha}{\partial r} + \left(\frac{\partial\alpha}{\partial r}\right)\delta C_k + \frac{\delta j_{gs}}{r} = 0 \tag{21}$$

where j_{gs} is the drift–flux and C_k is generally called the kinematic wave velocity defined as

$$C_k = j + \frac{\partial j_{gs}}{\partial\alpha} \tag{22}$$

Eq (21) is solved numerically due to the complicacy of the parameters Considering that, at the interface of the frit cylinder and fuel bed $r=R_c$, a fluctuation of void fraction originates only from a perturbation of gas flow, a boundary condition of Eq (21) is set as

$$(\delta\alpha)_{r=R_c} = \left(\frac{\partial\alpha}{\partial W_g}\right)_{\alpha|_{R=R_c}}\delta w_g \tag{23}$$

Thermal Response of the Fuel Bed

Through physical modeling for the thermal transient responses of the fuel bed following a flow perturbation as is usuall in neutron kinetic problems the thermal transport parameters such as the heat transfer coefficient thermal conductivity and specific heat capacity are assumed to be invariable for a gas flow perturbation in order to simplify the mathematical expression Note that the center temperature of the fuel particle is generally only 20–30 K above the coolant temperature This is due to the small size of the particles (500 μm) and the high heat transfer coefficient (approximately 3000 kW/m^2–K) The Biot number for the fuel particles however was generally in the vicinity of 7 or more indicating that the internal temperature gradients could not be ignored Therefore fuel particles were separated into four volume zones (Fig 4) to account more realistically for the thermal transient effects

From these models and assumptions the transient response of the volume–averaged fuel temperature and the gas coolant bulk temperature are derived in terms of the perturbed gas flow rate and power level These are Laplace transformed with respect to the time where the Ω's are influence coefficients in terms of the transformed variables to obtain

$$\bar{\delta}T_{fi} = \Omega_i^w \bar{\delta}w_g + \Omega_i^q \bar{\delta}Q \quad \text{for} \quad i = 1, 2, 3, 4 \tag{24}$$

$$\bar{\delta}T_g = \Omega_g^w \bar{\delta}w_g + \Omega_g^q \bar{\delta}Q \tag{25}$$

Transfer Function Power level transients are evaluated as a function of flow perturbations Therefore as is customary in linear feedback schemes,[14,22] the system transfer function is defined by the ratio of the Laplace transform of an output power level to the Laplace transform of an input propellant flow rate If the input and output are normalized by their initial values in the equilibrium state the transfer function in terms of s, the transformed time variable, is given by

$$T(s) = \frac{\bar{\delta}Q/Q^o}{\bar{\delta}w_g/w_g^o} \tag{26}$$

Then by combining the solutions obtained through neutronic and thermofluid modeling, i e Eq (1) (3) (4) (5) (16) (24) and (25) a linearized system transfer function defined by Eq (26) can be obtained which yields

$$T(s) = \frac{w_g^o(G_h\Lambda_h^w + G_F\Lambda_c^w)}{1 - Q^o(G_h\Lambda_h^q + G_F\Lambda_c^q)} \tag{27}$$

where

$$\Lambda_h^w = \left(\frac{\partial\Sigma h}{\partial\alpha}\right)_o \Lambda_c^q + A_h^o\Omega_g^w + \sum_i \left(\frac{\partial\Sigma h}{\partial T_{fi}}\right)_o \Omega_i^w, \tag{28}$$

$$\Lambda_h^q = \left(\frac{\partial\Sigma h}{\partial\alpha}\right)_o \Lambda_c^q + A_h^o\Omega_g^q + \sum_i \left(\frac{\partial\Sigma h}{\partial T_{fi}}\right)_o \Omega_i^q, \tag{29}$$

$$\Lambda_c^w = \begin{cases} 0 & \alpha \le \alpha_p \\ A_c^o\Omega_g^w + G_\alpha & \alpha > \alpha_p \end{cases} \tag{30}$$

$$\Lambda_c^q = \begin{cases} 0 & \alpha \le \alpha_p \\ A_c^o\Omega_g^q & \alpha > \alpha_p \end{cases} \tag{31}$$

$$A_h^o = \left(\frac{\partial\Sigma h}{\partial p_g}\right)_o \left(\frac{\partial p_g}{\partial T_g}\right)_o + \left(\frac{\partial\Sigma h}{\partial T_g}\right)_o, \tag{32}$$

Table 2 Rotating bed reactor point design parameters

Quantity	CASE 1	CASE 2	CASE 3
Thermal Power, GW	0 25	1 0	5 0
Core Radius, cm	15	25	40
Core Length, cm	15	50	80
Fuel Diameter μm	500	500	500
Propellant/Coolant	Hydrogen	Hydrogen	Hydrogen
Flow Rate kg/s	5 7	22 8	114
Inlet Temperature, K	300	300	300
Cavity Temperature K	3000	3000	3000
Cavity Pressure, bar	100	100	100
Packed Bed Depth, cm	3 0	2 5	4 0
Fuel Loading, kg	21 1	103	400

$$A_2^o = \left(\frac{\partial \alpha}{\partial \rho_g}\right)_o \left(\frac{\partial \rho_g}{\partial T_g}\right)_o + \left(\frac{\partial \alpha}{\partial \mu}\right)_o \left(\frac{\partial \mu}{\partial T_g}\right)_o \tag{33}$$

In this evaluation, the effects of gas pressure perturbation on power level is neglected because, in a fluidized state the pressure drop across the fuel bed is almost independent of a gas flow rate Even in the packed state, the pressure drop is in general just a few bars compared with the cavity pressure of about 100 bars Therefore for a flow perturbation the fluctuation of gas pressure is negligible in the fuel bed

RESULTS AND DISCUSSION

In Table 2 three typical point designs of the RBR are compared CASE 1 – small size CASE 2 – intermediate size and CASE 3 – large size For each of the point design cases, thermal neutron loss rate through the exhaust port changes with the bed expansion because the fuel bed is a strong absorber for thermal neutrons In the case of fast neutrons, leakage is almost independent of the bed depth because the fuel bed is a weak absorber of fast neutrons Due to this fact, reactor criticality is affected mostly by the thermal neutron end–path leakage and by the bed expansion

In an RBR, the reactor power or the reactor criticality is regulated by providing variable poisoning of the radial (side) reflector with material which is highly absorbant of thermal neutrons In effect this adjusts the macroscopic absorption cross–section of the reflector to achieve reactor criticality for given core conditions Figure 5 shows the *critical* macroscopic absorption cross–section of the side reflector as a function of gas volume fraction, indirectly indicating the effects of thermal neutron end–path leakage on reactor power level This portrayal has been obtained from an iterative solution of Eq (17)

As the gas volume fraction increases and the fuel bed expands, more thermal neutrons are captured by the fuel, especially those returning from the end (upper) reflector, and the leakage is reduced This is more clearly shown in Fig 5d where the variation in critical absorption cross section in the radial reflector is much larger due to increases in fuel bed void fraction From these results, it can be expected that, when a propellant flow perturbation causes a bed height fluctuation, the resultant amplitude of power level transient would be high in CASE 1 as compared with the other two cases

Note that the view factors between the bottom of the fuel bed and the exhaust nozzle were 30% larger for the small core (CASE 1) than for the larger cores Furthermore the view factor between the blind end of the cylindrical core and the opposite nozzle, end was 300% larger in the smaller reactor geometry This also suggests that perturbations in fuel bed thickness would be much more important in the former than the latter cases

The transient power responses to a propellant flow perturbation have been investigated along with the fluidization regimes of the fuel bed by analyzing the system transfer function in the frequency domain Figure 6 shows for each case the amplitude plane of the system transfer function defined by Eq (39) Here the gas volume fraction of the initial equilibrium bed is 0 35 for the packed state and 0 495 for the fluidized state As seen in this figure, the fluidized bed has much higher responses of amplitude, 100 db or more, than the packed bed In addition, it was found that the phase angle between packed and fluidized cases was approximately 180 degrees at low frequencies

Figure 5 Comparison of Macroscopic absorption cross-section of the side reflector required for criticality for the three point design cases (a – c) three different nozzle-to-core diameter ratios Y Solid line Y=0 3 long dash Y=0 45 short dash Y=0 6 (d) Y=0 45 long dash=CASE 1 solid=CASE 2 short dash=CASE 3

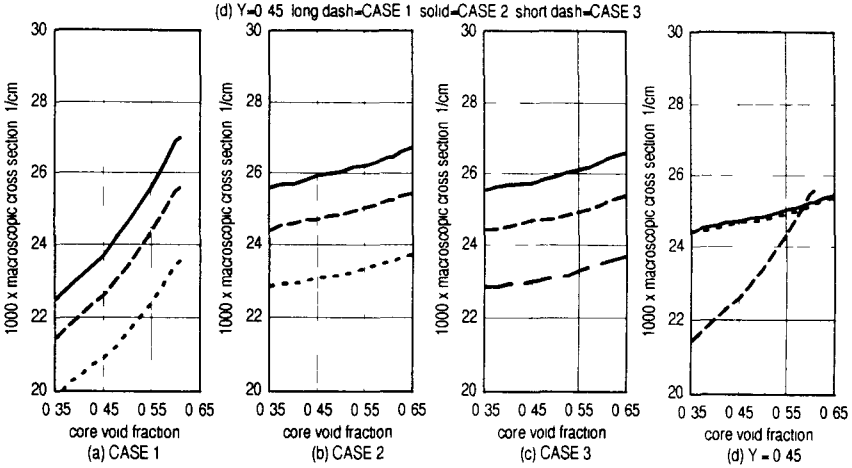

Figure 6 Comparison of power-to-flow transfer function amplitude response for the three point design cases for both packed and fluidized bed states Solid fluidized bed core with average void fraction of 0 495 dashed packed bed core

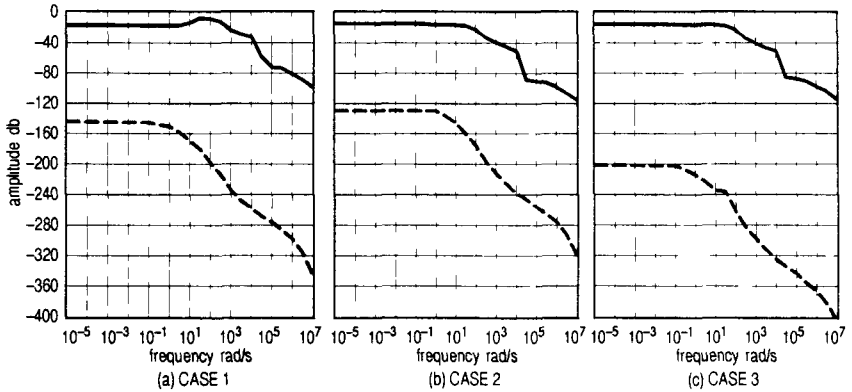

For each of the three reference cases such big differences of amplitudes are due to the fact that the responses of the fluidized bed depend not only on the parametric disturbance of the optical thickness but also on the view factors while the packed bed is independent of the latter In other words the loss rate of thermal neutrons through the exhaust port fluctuates with the fuel bed height and consequently it affects the power level of the fluidized bed but not the packed fuel bed

Examining Figure 6 the first break frequency appears above approximately 0 1 rad/s and is due to neutronic effects alone For the packed bed the roll off is monotonic at approximately 20 db/decade For the fluidized state the amplitude for the small reactor (CASE 1) increases slightly near 10 rad/s due to in-phase feedback between flow rate and power level and then decreases Breaks at higher frequencies are

Figure 7 Comparison of the three point design cases in packed-bed state Y=0 45

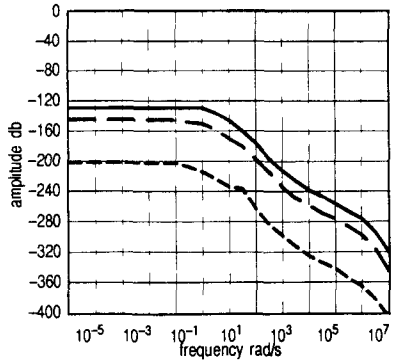

Figure 8 Comparison of the there point design cases in fluidized-bed state Y=0 45

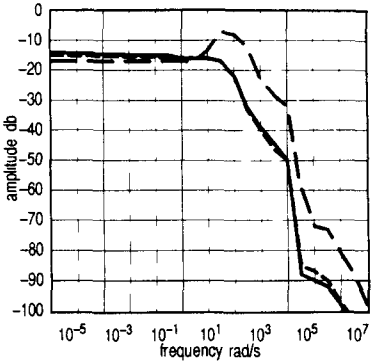

due to the effects of the different fuel zones and of the coolant The coolant thermal behavior appears to be dominant above the frequency of about 10^6 rad/s In the fluidized bed the sharp roll off near 10^4 rad/s represents the out-of-phase effects of bed height fluctuation on power level

For the packed bed the amplitudes versus frequency of the three referenced RBRs are compared in Figure 7 The nozzle-to-core diameter ratio in all three cases was taken as 0 45 As seen in this figure the amplitude for CASE 2 is larger than that of the other two cases This trend shows that the response varies inversely with the optical thickness of the fuel bed Physically it can be inferred that in a thin bed the thermal neutron absorption rate is easily affected by a flow perturbation but such fluctuation is small in a thick bed because the thick bed absorbs most of the thermal neutrons injected Therefore in a packed bed the thinner the optical thickness the higher the amplitude of power level transients resulting from a flow perturbation

Figure 8 presents similar comparisons for the fluidized bed again for nozzle-to-core diameter ratio of 0 45 The average gas volume fraction of each case is 0 495 at constant flow As mentioned before the neutronic break frequency appears at about 0 1 rad/s whereas the thermofluid responses begin to be dominant above a frequency of 10^2 rad/s In other words the thermofluid responses would be less coupled with the neutronic responses above this frequency where the effects of bed height fluctuation on power level appear to be coupled on a one-to-one basis If comparisons of the amplitudes are made in this frequency range the CASE 1 reactor has the largest amplitude responses while the other two cases follow almost the same trends yielding lower amplitudes than CASE 1

CONCLUSIONS

The thermofluid-neutronic coupling and stability of the rotating fluidized bed reactor has been presented It has been shown that the rotating fluidized bed reactor is more neutronically active to flow perturbations by orders of magnitude than the reactor with a fixed-thickness core but is still apparently stable This activity can be explained by the combined effects of the variations in both optical thickness and view factors due to perturbed fuel bed thickness The variations in optical thickness change the overall fraction of thermal neutrons absorbed by the fuel Changes in the view factors cause changes in leakage fraction of thermalized neutrons returning from the reflector/moderator regions

The packed bed amplitude response of the power-to-flow transfer function for the three point design cases examined all were below -120 db and rolled off at 20 db/decade for frequencies above 0 1 rad/s The fluidized bed response amplitudes started near -15 db and for the small reactor design examined increased to -7 db at about 100 rad/s before rolling off to approximately -100 db at frequencies near 10^6 rad/s The other cases rolled off monotonically after approximately 10 rad/s Specific conclusions include

(1) A propellant flow perturbation in an initial equilibrium-state RBR causes a power level transient by disturbing the bed optical thickness and the thermal neutron end-path leakage rate

- In a packed bed, only the optical thickness is of any consequence for the determination of power level and therefore the amplitude responses are generally small the thinner the optical thickness, the higher the response amplitude
- In a fluidized bed, bed height fluctuations significantly affect the thermal neutron end-path leakage rate resulting in a higher power level response amplitude, 100 db or more, than in the packed bed

(2) Examining the amplitude versus frequency a propellant flow perturbation may not result in a power excursion from the standpoint of the inherent feedback between thermofluids and neutronics as developed in this paper However the margin to gains greater than unity becomes so small, order of -7 db in some instances, that power excursion cannot be ruled out on the basis of this quasi-two-dimensional analysis

ACKNOWLEDGEMENTS

This research was sponsored by the Air Force Office of Scientific Research Air Force Systems Command USAF under contract No AFOSR-83-0261 The United States Government is authorized to reproduce and distribute reprints for governmental purposes notwithstanding any copyright notation hereon

REFERENCES

1 Hatch, L P , Regan, W H , and Powell, J R , "Fluidized Bed for Rocket Propulsion ' **Nucleonics, 18** 12 102-103 1960

2 Botts, T , Powell J , and Makowitz, H , "A Compact High-Performance Electrical Power Source Based upon the Rotating Bed Nuclear Reactor," BNL-27460, January, 1980

3 Jones, O C , Jr , "Thermal Design Concepts for the Rotating Fluidized Bed Reactor," **Nuclear Science and Engineering, 87** 13-27 1984

4 Lewins, J , **Nucleam Reactor Kinetics and Control**, Pregamon Press, New York, 1978

5 Lee C C , **Thermal Hydraulic and Neutronic Interaction in the Rotating Fluidized Bed Reactor** Ph D Thesis Rensselaer Polytechnic Institute, Troy, New York, May, 1986

6 Gulden, T D , and Watson, J F , "High-Temperature Fuels for Advanced Nuclear Systems, ' GA-A16908 October 1982

7 Kaae, J L , 'Private communication," October, 1983

8 White, F M **Viscous Fluid Flow**, McGraw-Hill New York, 1974

9 Lamarsh, J R , **Introduction to Nuclear Reactor Theory**, Addison-Wesley Publishing Company Inc Massachusetts 1966

10 McNeil, H , and Becker, M , 'The Interaction of Neutronics and Acoustics in a Gaseous Core Nuclear Rocket **Nuclear Science and Engineering, 42**, 220-229, 1970

11 Maynard, C W , "Blackness Theory for Slabs," in **Naval Reactors Handbook**, A Radkowsky, Ed , U S Atomic Energy Commission Washington, D C , 1964

12 Rohsenow, W M , and Hartnett, J P **Handbook of Heat Transfer** Section 15, McGraw-Hill New York 1973

13 Wallis, G B , "A Simplified One-Dimensional REpresentation of Two-Component Vertical Flow and its Application to Batch Sedimentation " **Sym. Proc. Interaction Between Fluid and Particles**, 9-12 Inst Chem Engrs , London, 1962

14 "Reactor Physics Constants," ANL-5800, 2nd ed , Section 3 USAEC, 1963

15 Podney, W N , and Smith, H P , Jr , 'Prompt-Neutron Kinetics of a Spherical-Cavity Reactor ' **Nuclear Science and Engineering, 29**, 373-380, 1967

16 Jones, O C , Jr , "Calculation of Fuel Bed Expansion for the Rotative Fluidized Bed Reactor," **Trans. Ans., 14** 458-459 1982

17 Botts, T E , Horn, F L Jones, O C , Jr , Luzareth, O W Ludewig, H Powell, J R , and Usher J L The Rotating and Fixed Bed Reactor Concepts," AFRPL TR-83-023, November, 1983

18 Lindauer, G C , Tichler, P , and Hatch, L P , 'Experimental Studies on High Gravity Rotating Fluidized Beds BNL-50013 September 1966

19 Kroger, D G , "Flow Characteristics in Packed and Fluidized Rotating Bed," **Power Technology, 24** 9-18 1977

20 Jones, O C , Jr , and Shin, T S , "The Expansion of Gas-Solid Fluidized Bed Reactor," Proceedings **1st Symposium in Space Nuclear Power**, December, 1983

21 Zuber, N , and Staub, F W , "An Analytical Investigation of the Transient Response of the Volumetric Concentration in a Boiling Forced-Flow System," **Nuclear Science and Engineering, 30**, 268-278, 1967

22 Weaver, L E , **System Analysis of Nuclear Reactor Dynamics** Rowman and Little Field Inc New York, 1963

DEVELOPMENT OF HFIR SUBCRITICALITY MONITORING METHODS

Richard B. Rothrock
Oak Ridge National Laboratory
Oak Ridge, Tennessee 37831

ABSTRACT

Use of subcritical source multiplication measurements during refueling has been investigated as a possible replacement for out-of-reactor subcriticality measurements formerly made on fresh HFIR fuel elements at the ORNL Critical Experiment Facility. These measurements have been used in the past for preparation of estimated critical rod positions, and as a partial verification, prior to reactor startup, that the requirements for operational shutdown margin would be met. Results of subcritical count rate data collection during recent HFIR refuelings and supporting calculations are described, illustrating the intended measurement method and its expected uncertainty. These results are compared to historical uses of the out-of-reactor core measurements and their accuracy requirements, and a planned in-reactor test is described which will establish the sensitivity of the method and calibrate it for future routine use during HFIR refueling.

INTRODUCTION

The High Flux Isotope Reactor (HFIR), located at the Oak Ridge National Laboratory (ORNL) at Oak Ridge, TN, provides unique experimental capabilities for neutron beam research, production of transplutonium isotopes in a central flux trap region, and irradiation of experimental materials in the beryllium reflector. The HFIR core consists of two concentric fueled annuli, and is designed to promote high neutron leakage into the central flux trap region where a high thermal flux is desired for isotope production. Four different nuclear core designs were developed and fabricated for HFIR initial operation and its preceding critical experiments, varying in fuel loading and distribution, burnable poison, or both, in an effort to optimize the core flux, power peaking, and endurance. In order to interrelate nuclear measurements made with these various cores, and to monitor the potentially large variations in core reactivity which could result from commercial fabrication of HFIR fuel within the allowable manufacturing tolerances, a method was devised to measure the reactivity of each fresh HFIR core in the water immersed and reflected condition before loading it into the reactor. Since the fuel is normally only slightly subcritical under these conditions (typically $2 to $3), the measurement was done in the ORNL Critical Experiment Facility ("CEF") which also supported a variety of other experimental programs during the HFIR design and early operating period. Because the preoperational core reactivity measurement could identify cores with abnormally high or low reactivity which might indicate manufacturing process deviations, provide an input for the calculation of expected critical rod position, and ensure that the core reactivity was within the range leading to acceptable shutdown margins prior to reactor startup, this measurement was continued and has now been performed on over 300 fresh cores prior to their installation into the HFIR.

The CEF was shut down in 1986, along with other research reactors at ORNL, for a review of the facility, operations, and management; and upgrading as necessary to meet current standards. At the time of its shutdown, there were 25 fuels remaining in inventory whose reactivity had been previously measured, and the HFIR fuel monitoring program was the only experimental activity still carried out in the CEF although portions of the building were used for other purposes.

In view of the successful experience in commercial fabrication of HFIR fuel during the 25 years since HFIR startup, the extensive inspections performed on the fuel to ensure conformance to specifications, and the cost in time and resources to upgrade the CEF to meet current standards, it was decided to explore other approaches to HFIR fuel monitoring which do not require the use of a Class B reactor in preference to upgrading and restarting the CEF solely for this purpose. The following sections of this paper describe the role of preoperational fuel reactivity measurements in HFIR operations and safety; the unique features of the HFIR core and reactor nuclear design which affect the capability for in-reactor measurements; and the approach developed, and results obtained to date, for fuel monitoring by source multiplication techniques during HFIR refueling.

ROLE OF PREOPERATIONAL FUEL MONITORING

A survey of the uses (real or potential) of the fuel reactivity measurements showed that they were involved by reference in key documents, by custom, or by direct use of the results, in the following areas relating to HFIR operations and safety:

1. Assurance of criticality safety during fuel handling in the HFIR pools and fuel loading into the reactor;

2. Preparation of Estimated Critical Position (ECP) calculations for each HFIR startup with a fresh fuel; and

3. Assurance, prior to startup, that the fuel element itself had no reactivity anomalies sufficient to encroach on the operational shutdown margin required to handle design basis reactivity accidents.

In regard to the first issue, a review of shutdown margin measurements performed on the HFIR critical experiments by pulsed neutron methods[1] showed that the shutdown margin at refueling conditions was adequate to accommodate the maximum possible reactivity anomaly which could be caused by undetected fuel manufacturing defects (a complete absence of burnable poison from the inner fuel annulus), combined with a metal to water ratio and total fuel loading simultaneously at the worst extremes of their tolerance bands. Furthermore, the HFIR fresh cores are manufactured in two pieces, an inner and outer annulus, which are each subcritical individually under water. Since these two fuel annuli are handled separately during refueling and are not assembled until they are installed in the reactor, it was concluded that a measurement of the subcriticality of the assembled fuel under water prior to refueling was not essential to the criticality safety of the fuel handling process.

To find an alternate method for ECP calculation without reliance on reactivity measurements on individual fresh cores, the as-built fuel data packages prepared by the fuel supplier were reviewed for parameters which could be used to estimate core reactivity. These data include results of extensive inspections on the cores, including fuel distribution measurements of each fuel plate by X ray methods, individual coolant channel thickness profiles, and records of the fuel and burnable

poison loadings. From these results, the total fuel and boron loading and the average coolant channel thickness were selected as representative of the major influences on core reactivity, and measured reactivities for several cores were correlated with these as-built parameters by multiple regression analysis. The results of this exercise showed that the measured reactivity could be predicted within a standard error of about 20 cents (compared with an estimated uncertainty in the CEF measurement of 10 cents), with a maximum deviation for the sample of 60 cents. For comparison, the allowable deviation between estimated and achieved start of cycle critical rod position is equivalent to about $1.5 in reactivity, so the increased uncertainty associated with using as-built fuel data in lieu of measured core reactivity for preparation of the ECP should not have a large impact on the probability of a missed ECP.

To address the third issue, the verification of adequate shutdown margin for operational reactivity accidents prior to initiating startup, a risk evaluation was made focusing on the incremental impact of the preoperational core reactivity measurement on reduction of accident risk or consequences. Since the net reactor shutdown margin (including the effects of the control rods, target and experiments as well as the fuel) is verified by checking the control rod position as soon as criticality is reached on the initial startup, a prior measurement of the core reactivity alone is somewhat redundant, and therefore likely to have only a small impact on total risk. This conclusion was verified by the quantitative risk study, which showed the safety impact of the preoperational fuel reactivity measurement to be very small. Nevertheless, it was considered a useful practice to obtain some direct experimental confirmation of the core reactivity for both safety and operational reasons (e.g., as an aid in diagnosing causes of a missed ECP in case of an "outlier" fuel element). For these purposes it was judged that an increased uncertainty would be acceptable, and the possibility of inferring subcriticality from the normal count rate data available during a HFIR refueling was therefore examined carefully as a possible cost effective alternative to resumption of CEF operation.

PRINCIPAL HFIR DESIGN FEATURES

The important features of the HFIR nuclear design are illustrated in Figure 1. A fresh core, comprised of an inner and outer fuel annulus, is installed for each operating cycle (of about 21 days' duration). Operational reactivity control and rapid scram shutdown are provided by two control cylinders located in the annulus between the fuel and reflector, as shown in the Figure. During refueling, the "black" sections of the control cylinders (europium loaded segments of 22 inch length) are fully inserted, overlapping the 20 inch fuel length on each end. The inner control cylinder, or shim-regulating cylinder, consists of four 90-degree segments welded together which move as a unit. This cylinder is withdrawn downwards to start up. The outer control cylinder is also composed of four 90-degree segments, or shim-safety plates, which operate independently. The shim safety plates are withdrawn upwards for startup, and are spring loaded for rapid insertion on a scram. The two control cylinders also have 5-inch tantalum "gray" follower segments at the ends of the europium plates, and are withdrawn in opposing directions and operated at power in a symmetrical fashion to maintain axial power balance. For a typical HFIR cycle, the rods are withdrawn at startup sufficiently that the europium segments are inserted about three inches into the fuel region, and a "window" of about four inches exists between the ends of the tantalum follower sections at the core midplane. At the end of a cycle, the europium and tantalum sections are withdrawn to approximately the ends of the fuel plates.

Low-level neutron monitoring is provided by three wide-range counting channels (WRCC), which utilize movable fission chambers mounted in thimbles extending to about 12 inches below the bottom of the fuel. The chambers are fully inserted at shutdown, and are automatically withdrawn

at higher power levels to avoid saturation of the counting channels. During refueling activities the principal source is due to neutron production in the reflector from photon sources which exceed the beryllium photoneutron threshold of about 1.69 MEV. Chief among these is Eu-156, which is produced in the control cylinders. Because the two cylinders are withdrawn in opposite directions and only a few inches of their tips are inserted in the core at power, the activity is concentrated near the rod tips. These highly activated regions are located at the top and bottom of the core at refueling conditions for the inner control cylinder and the outer cylinder (or safety plates), respectively. Because the inner and outer control rods are replaced at different times and are also sometimes stored for intervals that are long compared to the Eu-156 half life (15 days), the axial distribution of the neutron source at refueling conditions is complex and varies widely. Other unique features of the HFIR nuclear design are more fully described in reference 1.

APPLICATION OF SOURCE MULTIPLICATION TECHNIQUES TO HFIR REFUELING

FUEL MONITORING METHODS

For the two-piece HFIR core, subcritical count rates can be recorded at three distinct stages of the refueling process: (1) background count rate, prior to fuel loading; (2) the partially loaded count rate after the outer fuel annulus is loaded; and (3) the fully loaded count rate, after the inner annulus is loaded. Ratios of these count rates are desired, in order to cancel variations in detector efficiency or source strength which may occur from cycle to cycle; and due to difficulty in obtaining an accurate measurement of the low background count rate, the ratios which involve the background level directly (i.e., other than as a background correction) are less likely to yield a practical method. These considerations led to selecting the ratio of count rates of the fully loaded and partially loaded core configurations for possible use as an indicator of shutdown margin in the refueling condition.

For reasons described earlier, the normal refueling source due to activated europium control cylinders has substantial axial variations from cycle to cycle. Since the relative activity of the two control cylinders varies with time, both the absolute count rates due to the activated europium and their ratios will also change in response to this changing source, masking the effects of changes in the core multiplication which it is desired to detect. To avoid this difficulty, additional refueling sources have been built, in the form of antimony source rods, and activated in the HFIR reflector to provide photoneutrons from the decay of Sb-124. Since the axial distribution of the antimony activity remains constant, ratios of count rates due to these sources are affected only by changes in the core multiplication, and should therefore be useful as an indicator of net multiplication in the refueling state.

The count rates during refueling may vary from a few counts per minute with a weak source and no fuel loaded, to a few hundred counts per second, with a strong source and a fully loaded core. Accurate counting data are difficult to obtain at the lower count rates, due to sporadic electrical interference which occurs in some of the counting channels. Consequently, refueling count rates were monitored for several reactor cycles to determine the feasibility of measuring count rates accurately during refueling, and to establish the repeatability of key count rate ratios, before proceeding with plans for a demonstration and calibration test of the fuel monitoring method.

The present data collection method utilizes three single board multichannel scalers (model "MCS-II" manufactured by Tennelec/Nucleus, Inc.) installed in a personal computer host. The scalers operate in a multitasking environment, allowing simultaneous data collection from all three HFIR WRCC. For each core and source configuration of interest, several data records (each containing

from 1024 to 8192 channels of data) are collected and stored for each WRCC. To assist in identifying and eliminating interference, the channel dwell times are adjusted for an average of about one count per channel It has been found that the interference typically consists of bursts of pulses resulting in the collection of many counts in a few channels of the multichannel scaler data records By viewing these data records on the monitor, affected portions of the data record can often be identified visually and marked for rejection of noisy data during subsequent data processing Isolated noise spikes can also be identified and rejected by adjusting an acceptance threshold during data processing One or both of these noise rejection methods is applied to the raw data, if necessary, by a computer program which also prepares a data histogram, computes the average count rate and its uncertainty, and performs a chi-squared test for Poisson statistics. This approach has proven satisfactory so far, as shown by the fact that count rate ratios derived from noisy channels after processing for noise elimination, are approximately equal to those derived from noise-free counting channels.

Subcritical count rate data characterizing the HFIR refueling process was initially collected with only the normal activated europium control plate sources, and once the antimony refueling sources were available, additional count rate data were obtained with and without the sources installed. The results of these measurements are described in the following section

RESULTS OF REFUELING DATA COLLECTION

As discussed previously, the arrangement of the HFIR control elements results in photoneutron sources concentrated at the top or bottom of the core in the refueling state, due to Eu-156 activity in the control cylinder or safety plates, respectively These differing source distributions result in axial tilts of the core fission rate distribution towards or away from the fission chambers located below the core, and consequently have a strong effect on the apparent core multiplication inferred from count rate measurements during refueling This effect is most pronounced with only the outer fuel loaded (and a low core multiplication factor), and decreases with the loading of the inner fuel element as the fission distribution more nearly approaches the symmetric fundamental shape These effects lead to substantial variations in the measured multiplication ratios due to changes in photoneutron sources caused by normal control rod irradiation and replacement activities. Typical results are presented in Table 1 There were only minor variations in reactivity of the fresh fuel elements installed during these refuelings, hence the variations in the results are believed due principally to the changing source distributions.

When the data from Table 1 are classified according to the source distribution (i e , location of the dominant Eu-156 activity), as shown in the second column of the table, they show good consistency within each group However, the wide range of results would mask the effects of typical core reactivity perturbations which it is desired to detect, unless the variations in control element source distribution can be accurately determined and accounted for in the interpretation of the results Since HFIR control rod management typically results in complex irradiation histories, and the calculation of higher order europium activations in the HFIR control rods is not very precise, it was considered more practical to employ a separate refueling source with a fixed axial shape For this purpose, four antimony sources were fabricated and activated for use in the HFIR

Antimony refueling sources were installed in the HFIR reflector for activation near the end of Cycle 297, and have now been used in refueling count rate measurements for four cycles Results of these measurements are summarized in Table 2. The count rates due to the antimony sources alone are obtained by measuring the count rates with the refueling sources in and out of the reflector, and subtracting these two measurements. With the possible exception of the first use of

the sources in Cycle 298, when they were only partially activated and the measurement precision was consequently poor, the remaining measurements appear consistent and the results for all counting channels for all of the latter three measurements have a standard deviation of 2% to 3% of their mean, consistent with the results obtained previously with the natural control plate sources when those data are separated according to source distribution.

RESULTS OF SUPPORTING CALCULATIONS

The changes in subcritical multiplication during HFIR refueling were calculated for comparison with measurements, in order to ensure that all important effects were understood and to validate a model which could be used to calculate the effects of small parameter variations which may contribute to the uncertainty in future measurements. The "DORT" two-dimensional transport computer code[2] was used, with a basic HFIR model originally developed by the ORNL Engineering Physics and Mathematics Division for use in updating the HFIR safety analyses Calculations were made in the subcritical source multiplication mode, and fission chamber count rates were represented by U-235 fission activations calculated at the locations of the fully-inserted fission chambers

The ratio of count rates with all fuel loaded to the count rate with only the outer fuel element loaded was calculated as 3 9, using an axial source distribution equal to the measured axial thermal flux distribution in the HFIR reflector, where the antimony sources were activated For comparison, measurements with the antimony sources (excluding the measurements for Cycle 298, which had lower count rate precision due to the relatively weak source) yield an average value of 4 17, or about 7% higher than the calculated value. This bias is approximately consistent with other experimental comparisons, which indicate that the model undercalculates the core eigenvalue in the rods-in state. To verify that differences in this ratio which had been observed with the europium control plate source were due to changes in its axial distribution, additional cases were calculated with sources peaked near the top and bottom of the core, and qualitative agreement was obtained with the trends of the measurements, as shown in Table 1 A more precise comparison is not possible due to lack of definitive information on the axial distribution of the europium activity within the control plates The expected sensitivity of the source multiplication measurement to variations in core reactivity was also calculated, yielding a predicted increase of 5 to 6% in core fission rate (or counting channel reading) per $1 increase in core reactivity Since the count rate ratios measured to date have a repeatability of around 2% to 3% (for constant source distribution), the inherent uncertainty in this measurement method should be around $0.5. This uncertainty will probably be increased somewhat, if applied exclusively to the core reactivity, to allow for other factors which may affect the shutdown count rates such as depletion of the control plates, nevertheless, the accuracy is expected to be satisfactory for practical use in verifying the HFIR shutdown margin prior to startup

VERIFICATION TEST OF SOURCE MULTIPLICATION METHOD

A verification test of the source multiplication method for fresh fuel monitoring was performed in the HFIR during the pre-Cycle 302 refueling outage. The test involved the use of three specially built experimental flux trap inserts — aluminum cans containing plastic cylinders with different sizes of central holes — to alter the core reactivity through the mechanism of the flux trap region void worth Because of the positive void coefficient in this region, this effect was carefully studied experimentally during the HFIR design and startup testing in order to validate safety analyses of hypothetical reactivity accidents which could be caused by rapid entry of voids into the flux trap region through the target coolant passages while critical. These earlier experimental results had been obtained using special plastic cans which were inserted into the flux trap containing varying water and

void fractions. Although the original plastic flux trap inserts are no longer available, the results from the measurements were used to design a new set of aluminum-canned plastic cylinders which were expected to yield reactivity increases up to about $4, compared to the normal refueling condition (water-filled flux trap). This use of special experimental components to induce reactivity changes of a few dollars was necessary because the fresh HFIR cores remaining in inventory are too similar in reactivity to provide, by themselves, an accurately measurable change in subcritical count rates. The test method and preliminary results from analysis of one of the three WRCC fission chamber subcritical count rate data are summarized below. More complete results will be included in the oral presentation, following evaluation of the remainder of the experimental data.

The three aluminum-canned plastic cylinders were designed so that one (solid) cylinder had a slightly higher hydrogen atom density than the water which it displaced, while the other two had central holes intended to produce reactivity changes of about +$2 and +$4 compared to a water-filled flux trap. After the inner and outer fuel elements were loaded and the normal subcritical count rate data was collected, each of the three experimental flux trap inserts was installed in turn, and count rates were measured with and without the antimony sources present. Although it was desired to measure the effect of changes in core multiplication alone on WRCC count rates, the central holes in the flux trap inserts also affect the detector efficiency by allowing increased neutron transmission through the holes to the fission chambers below the core. Therefore, corrections were included for this effect, based on calculations using the computer codes and models described previously.

Following the subcritical WRCC count rate measurement, the reactor was brought critical at low power with each of the three experimental flux trap inserts installed, and the critical rod positions were measured in order to determine more accurately the reactivity differences between the three flux trap inserts. The preliminary results of these measurements, based on original control rod calibration data and partial processing of subcritical count rate data from one of the three WRCC channels, are shown in Table III.

The ratio of subcritical count rates, adjusted for detector efficiency, are in very good agreement with the fundamental mode multiplication changes which would be predicted from the measured reactivity differences, given an initial subcritical reactivity (with the solid plastic cylinder insert) of about -$14. Due to the high density plastic used, this cylinder has somewhat more hydrogen than the water it displaces and was, therefore, expected to reduce the core reactivity from that of the normal refueling state. While this could not be directly measured, due to safety restrictions on operation of the reactor with a water-filled flux trap, evaluation of the WRCC count rate data indicates a subcriticality of about -$13 for the normal refueling state during this experiment. This conclusion is consistent with pulsed neutron measurements performed in the HFIR critical experiments to measure the shutdown margins with various flux trap contents.

These preliminary results show that changes in subcritical count rates measured by the HFIR WRCC fission chambers in response to variations in core reactivity will be sufficient to permit detection of core reactivity deviations on the order of $1 or less. This sensitivity is adequate to verify HFIR shutdown margin requirements prior to startup, and should permit use of the in-reactor source multiplication measurement in lieu of a fuel reactivity measurement in a special ex-reactor facility.

REFERENCES

1. R. D. Cheverton and T. M. Sims: "HFIR Core Nuclear Design," ORNL-4621, Oak Ridge National Laboratory, July, 1971.

2. "DORT, Two-Dimensional Discrete Ordinates Transport Code," Code Package CCC-484, Radiation Shielding Information Center.

Table 1. Refueling Monitoring Results with Control Plate Source

HFIR Cycle	Source Distribution[a]	Measured Multiplication Ratios[b] Channel 1	Channel 2	Channel 3	Average
290	Bottom	2.49	NA[c]	NA	2.49
291	Bottom	2.47	2.48	2.45	2.47
292	Bottom	2.47	2.33	2.39	2.40
293	Top	8.8	7.5	8.9	8.4
294	Bottom	2.44	2.57	2.54	2.52
295	Bottom	2.51	2.51	2.59	2.54
296	Top	8.1	8.3	8.0	8.1
297	Equal	3.13	3.26	3.37	3.25
298	Equal	3.12	2.94	3.15	3.07
299	Equal	2.89	3.20	2.94	3.01

[a]Bottom, Top: Source dominated by Eu-156 activity at bottom or top of core. Equal: EU-156 sources at bottom and top of core and approximately equal.

[b]Multiplication Ratio: Ratio of background-corrected count rate with both (innter and outer) fuel elements loaded to count rate with only outer fuel element loaded.

[c]NA: Data not available.

Table 2. Refueling Monitoring Results Using Antimony Sources

	Measured Multiplication Ratios[a]			
HFIR Cycle	Channel 1	Channel 2	Channel 3	Average
298[b]	4 33	4 53	4 43	4 43
299	4 23	4 14	4 10	4 16
300	4 07	4 02	4 18	4 09
301	N/A	4 36	4 25	4 30

[a]Ratio of count rate due to antimony sources with full core installed to count rate with outer fuel element only installed, for individual wide range counting channels

[b]Uncertainty in results for Cycle 298 approximately 5%, due to lower counting precision with weaker refueling sources, other cycles have approximately 2% precision in ratios

Table 3 Preliminary Results of Verification Test

Experimental Plastic Insert	Subcritical Count Rate Ratio	Relative Multiplication[a]	Incremental Reactivity
Solid Cylinder	1 0	1 0	0
Small Central Hole	1 28	1 22	$2 5
Large Central Hole	1 74	1 55	$5 2

[a]Adjusted for changes in detector efficiency

Figure 1 HFIR Core Arrangement

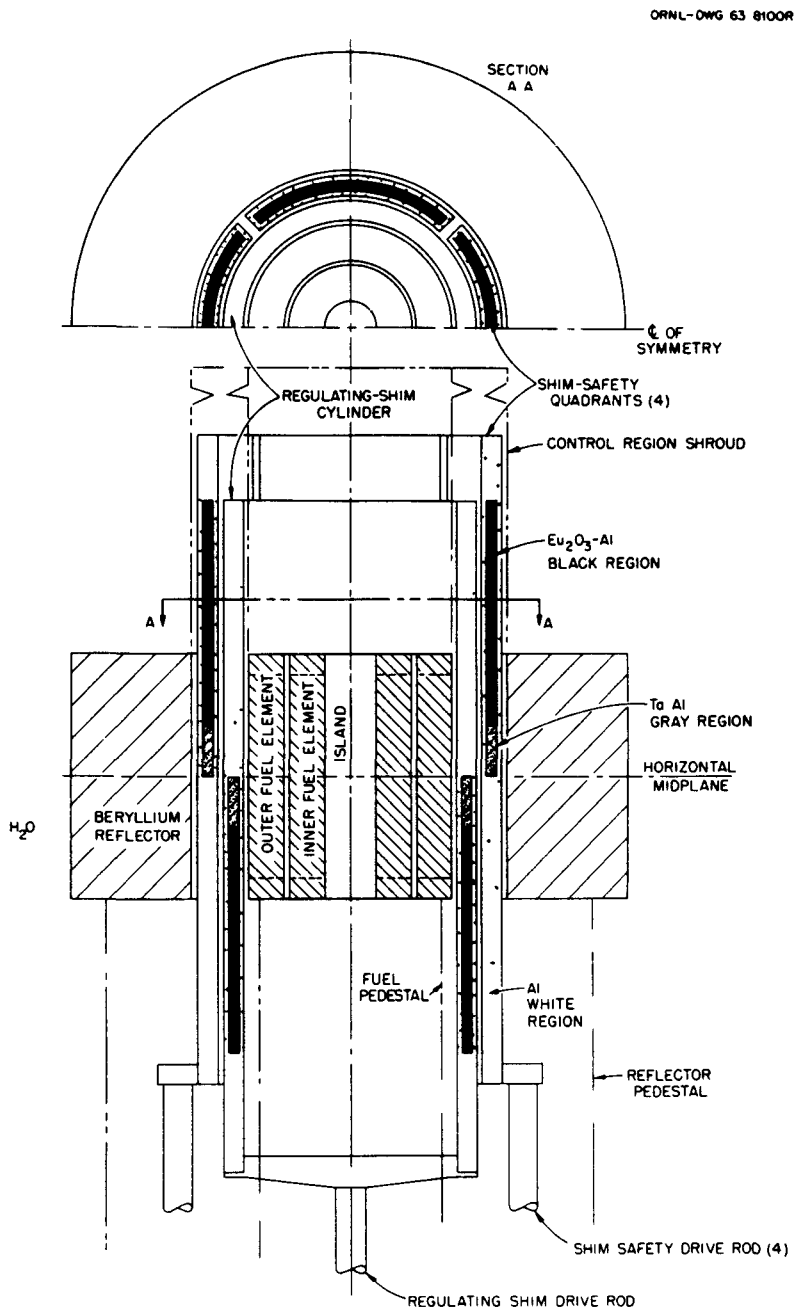

MULTYBARRIERS PROTECTION AND THE HIGH-SAFETY REACTOR GENERAL DEMANDS

V.S.Paranyushkin and V.N.Petrov
Atomic Centre of
Moscow Engineering Physics Institute,
Kashirskoe shosse,31, Moscow, 115409, USSR
fax: (095)-324-21-11

ABSTRACT

The approach to the quantification of the nuclear reactor safety barriers efficiency allowing to elaborate technical strategy to rise safety of the nuclear installations is presented.

On the base of performed comparative analysis of safety barriers efficiency and its priority is found that the high-safety reactor must to have most-effective first barriers (fuel matrix, fuel cladding).

Suggestion of the high-safety reactor conception is executed on the base of equal risk convention under normal reactor operation and emergency conditions.

Preliminary estimations of high-safety reactor variety criteria is made with suggestion conception.

INTRODUCTION

The principle of multybarrier protection is used both in Soviet National Safety Rules (for example, in "General Safety Demands" - ОПБ-88) and in international safety documents[1]. For each reactor barriers quantity and quality conditions are proved in the design documentation were are taken into account many reasons: type and power of reactor, fuel type, specific energy of fuel, operating conditions and so on. As a rule, arrived limit in that is guaranteeing of the safe radiation dose limits and the discharge radioactive effluence concentrations on the site margin.

In this work, the principle of multybarrier protection is used for construction on the object "nuclear reactor" of the system for the safety analisys and the safety barriers quntification. The environment for this system is humanity, which must be able to have influence on the system variable

and parameters. Here we will take into account the only reactor harm source - the radiactivity accumulation in the core.

SYSTEM CONSTRUCTION

DEFINITION OF THE SYSTEM VARIABLES

To study of safety barriers efficiency and its priority we will be show on a core accidents as a realizing of probable transients from normal operating to hard damage with consequence barriers destruction.

If to define a damage measure (transit) of barrier number j for initial event k as :

$u(j,k) = 0$ - for the intact barrier and

$u(j,k) = 1$ - for the full destroy barrier,

and if $p(k)$ - probability of event k then total effective transit of j's barrier can be estimated as

$$U(j,L) = \sum_{k=1}^{L} u(j,k)p(k), \qquad (1)$$

were L - set of initial events taken into account.

The confirmation of such form for Eq.(1) are following considerations:
if the set of initial events is made in the order of the increasing of safety barrier transits then for any barrier the sequence $u(j,k)$ is nonreducing function of k with range from $u(j,1)=0$ to $u(j,L)\leqslant 1$. In that order for "good" reactor the value $p(k)$ is the reducing function with $p(L)\approx 0$ for hardest event with the order number L. Thus the curve of u and p multiplication start at zero, have a maximum and after that decrease to zero with increasing of k. Consequently, sum $U(j,L)$ have a limit with increasing of L (i.e. $U(j,\infty)=U_{j,eq}$) and his estimate may be obtained by extrapolation of $U(j,L)$.

DEFINITION OF THE SYSTEM PARAMETERS

Moreover we define the measure of the accident evolution $A(j)$ as a quantity harm characteristic of complite damage of j's and preceedings barriers (it may be, for example, public dose, contaminated area and so on). For this define

$$A(1) < A(2) < A(3)... \qquad (2)$$

and the total effective accident measure of reactor (with count of Eq.(1)) is defined as

$$A_{eff} = A(1)U(1)+\ldots+A(J)\cdot\prod_{j=1}^{J} U(J,L) \qquad (3)$$

where J - count of the safety barriers.
If to write Eq.(3) for four barriers, as example, in form

$$A_{eff} = [A(1)+[A(2)+[A(3)+A(4)U(4,L)]U(3,L)]U(2,L)U(1,L) \qquad (4)$$

then general demands for barriers can be viewed from the condition of minimazing of A_{eff}:

1. For barriers next after first:

$$\begin{aligned} &\text{it's necessary} \quad U(J,L) \leqslant A(J-1)/A(J), \text{ and} \\ &\text{it's sufficiently } U(J,L) \simeq 0.1\cdot A(J-1)/A(J). \end{aligned} \qquad (5)$$

2. If the safety barriers transits is not followed to this, then must be make provisions for an accident localizing systems of the required efficiency.

3. The safety barriers priority is defined by the order of the accident sequence thus first barriers have a large weight in the reactor safety.

DEFINITION OF
THE ENVIRONMENT DEMANDS

To obtain the quantity requirements for barriers transits, we used the high safety reactor definition as a reactor wich give the equal harm risk under normal operation and at the emergency conditions.

This definition is consequence from following considerations:
In normal operation conditions the risk given by the operating reactor to public has acceptable level. Following to UNSCEAR conception of the "dose-effect" linear dependence[2] we must to consider the harm risk by addable value, i.e:

$$R(sum) = R(norm.operation)+R(accidents) \qquad (6)$$

were for hazard value R we use the ordinary expression:

$$R(i) = Y(i)P(i)Ps(i) \qquad (7)$$

were $Y(i)$ - i's event real loss;
$P(i)$ - i's event probability;
$Ps(i)$ - social-psyhological factor for the count of a public treatment to event i.

There we must to make remark, that a real (impartial) hazard is estimated by Eq.(7) with $Ps=1$ and a partial risk assesments being made by public are estimated with $Ps\neq1$ (often

$Ps(accidents) \gg 1$).

From Eq.(6) it should be infered that for the insurance $R(sum) \propto R(norm.operation)$ it's necessary $R(accident) \ll R(norm.operation)$ (or $R(accident) \propto R(norm.operation)$ as a minimal requirement).

In terms of Eq.(3) it means that the sum of accident items must not be greate then sum of items not leading to safety limits exceedigs, i.e.

$$A(J)U(J,L) = A(J)U(J,norm.oper.) + A(J)U(J,accid.) \propto$$
$$\propto A(J)U(J,norm.oper.)$$

consequently,

$$U(J,accid.) \leqslant U(J,norm.oper.) \qquad (8)$$

This requirement to system variables and parameters we will count as key definition of the hight safety reactor.

CERTAIN DEMO APPLICATION

Preliminary estimations of high-safety reactor variety criteria may be made with suggestion conception if define safety barrier transit value as a ratio of the radioactivity at the barrier outside to the inside activity.

CORE DAMAGE

Thus, for the first barrier (fuel matrix and cladding) of the lot of nuclear reactors $U(1,norm.operation) \propto 10^{-7}...10^{-5}$. Consequently, supposing the normal operation probability near to one (i.e. $p(norm.operation) \propto 1$) we must to limit the value of product $u(1,hard\ damage)p(hard\ damage)$ in the sum like Eq.(1) by the quantity is not far from $U(1,norm.operation)$. It seems to us, the value $u(1,hard\ damage)$ may be estimated as not so far to 0.1, therefore the total probability of the core hard damages must not be greate then $10^{-8}...10^{-6}$.

If to consider the reactor operation time near 50 years then performing safety analysis for the high safety reactor variety one may not to take into account initial events with probability less then 10^{-8} events on reactor per year leading to hard accidents (like core melting).

CONFINMENT DAMAGE

For the last safety barrier (confinment or continment) quantity estimates now we will use the 7-levels international emergency score of IAEA[3] (INES), with approximetly logarifmic

scale.

In term of our work this score may be regarded as discret resolving form for the parametr A_{eff} (Eq.3).

The level 7 in this scale correspond to the full destroy of the reactor confinment at emergency conditions, level 5 is approximetly corresponding to intact confinment under the full destroy of the preceeding barriers, and level 4 is approximetly corresponding to intact barrier before confainment. If to take into consideration it then:
- from Eq.5 - $U(conf.) \simeq 10^{-3}$ or release rate about 1% per day (if deposition rate constant for fission products about 10^{-4} 1/s)
- connection between the damage weight and the damage probability is followed from Eq.8 :

$$p(k) \leqslant U(conf.)/u(conf.,k),$$

thus for initial event following to release rate 100% per day probability must be less than 10^{-2} and so on.

COMMON REMARK

This estimates may will be more severe in case of *Ps*-factor count (Eq.(7)). As example we make mention of the interrogatory rezults quoted in UNSCEAR Report'85 and which are informing that public is exaggerating the NPP hazard more then 100 times.

REFERENCES

1. Basic Safety Principles for Nuclear Power Plant. Safety Series No 75 INSAG-3, IAEA, Vienna, 1988.
2. RADIATION: Doses,Effect,Risks. UNEP, 1985.
3. A.M.Bukrinsky, V.F.Fedulov, " International Scale of NPP Accident Harm Assesment", *Atomic Energy*, v.70, No.1, 1991.

ANALYSIS OF THE NP-MHTGR CONCEPT A COMPARISON OF REACTOR PHYSICS METHODS

Denise B Pelowitz, Joseph L Sapir, and Janet E Wing*
NPR Safety Project Office
Los Alamos National Laboratory
Los Alamos, New Mexico 87545

ABSTRACT

Using the MCNP and ONEDANT analysis codes, we investigated basic neutronic characteristics of the NP-MHTGR preconceptual design Exploratory steady-state analyses of k_{eff}, neutron reaction rates, and temperature reactivity coefficients were conducted to check the ability of our reactor physics methods to adequately model the highly heterogeneous NP-MHTGR reactor Results of unit-fuel-cell analyses indicate that a three-region ONEDANT model adequately approximates the unit-fuel-cell lattice geometry However, core-block analyses indicate that approximating an hexagonal heterogeneous block by a one-dimensional annular target cell can introduce significant calculational error Investigating the core-block temperature coefficient of reactivity, we found that all components of the coefficient are negative and the delayed component contributes ≈85% of the total temperature effect Investigation of the full reactor temperature coefficient in the NP-MHTGR determined that all contributions from the active core are negative, with prompt effects again contributing ≈15% of the total core coefficient. Temperature-coefficient contributions from each of the reflector regions appear to be positive, but exhibit a significantly smaller magnitude than the negative contributions from the core These positive contributions apparently are caused by reduced carbon and boron absorptions at the higher reflector temperatures From a safety perspective, a conclusion as to the adequacy of the temperature coefficient cannot be drawn from its magnitude alone, but must be based on specific transient or accident analyses which incorporate all feedback effects Calculational differences between MCNP and ONEDANT were as high as ≈1 2% for the reactor criticality eigenvalue and on the order of 20% for the core temperature coefficient.

INTRODUCTION

In 1989, the Los Alamos National Laboratory formed a dedicated New Production Reactors Safety Project Office (NPR/SPO) to fulfill its commitment to support independent safety reviews for the Department of Energy's Office of New Production Reactors (DOE/NP) One of the reactor concepts being considered for development is the New Production Modular High Temperature Gas-Cooled Reactor (NP-MHTGR)

Accurate reactor physics characteristics are essential to understanding both the normal operation and the transient and accident response of the NP-MHTGR Key characteristics important to safety include temperature coefficients of reactivity, material and control-poison worths, and

---

* Reactor Design & Analysis Group, Los Alamos National Laboratory

detailed power distributions for both fission power and gamma heating The reactor analyses must be both in-depth and comprehensive because the variation of those characteristics important to safety must be understood as a function of location, control-element position, temperature, time (since a given perturbation), fuel, target, and poison depletion, and buildup and depletion of fission and target products

From January through September of 1990, we investigated basic neutronic characteristics of the NP-MHTGR preconceptual design developed for the New Production Reactor (NPR) program Although additional information on the evolving nuclear design became available in FY 1990, the analysis models were not updated to reflect the conceptual NP-MHTGR design because the reactor design was still being refined Also, the work reported here is directed more toward applying our physics calculational methods to the NP-MHTGR and understanding what causes certain reactivity changes, and less toward determining the absolute magnitude of such changes The reasons for reactivity changes are not expected to be dependent on the fine details of the reactor design Exploratory analyses were conducted to check the ability of our reactor physics methods to adequately model the highly heterogeneous NP-MHTGR reactor design Before performing off-normal and transient analyses, we must develop confidence that our codes can accurately simulate the steady-state condition

To better understand the behavior of, and interactions among, the reactor components, both Monte Carlo and discrete ordinates methods were utilized Increasing in complexity from the unit fuel cell to the detailed full reactor design, we evaluated neutronic attributes of the NP-MHTGR Parameters calculated during this effort included the criticality eigenvalue, k_{eff}, neutron reaction rates, and temperature reactivity coefficients The calculations reported here support the technical basis for application of existing Los Alamos neutronic codes (specifically, the three-dimensional Monte Carlo code, MCNP[1], and the one-dimensional discrete ordinates code, ONEDANT[2]) to NP-MHTGR safety-related analyses More in-depth analyses will be introduced as the NP-MHTGR design matures during the preliminary design phase of the NPR project.

The heterogeneous configuration of the thermal-spectrum NP-MHTGR design poses an analysis challenge to traditional reactor physics methodologies Neither MCNP nor ONEDANT alone provides the capability to characterize the core interactions with a high level of confidence Preparation of appropriately homogenized multigroup cross sections for use by ONEDANT that match true reaction rates is difficult and requires several simplifying assumptions for this thermal-spectrum, highly-heterogeneous array of absorber, fuel, and moderator MCNP, on the other hand, uses continuous-energy cross sections that need no adjustment and can model the heterogeneity with little or no homogenization necessary However, because of its statistical nature, MCNP cannot efficiently and cost-effectively characterize phenomena that produce small perturbations in k_{eff} and/or reaction rates Some of these phenomena, such as temperature coefficients of reactivity, determine the neutronic behavior of the reactor and are important to performance of a safety review Therefore, we chose to exploit the advantages of the two methods by using them in parallel and comparing the results

NP-MHTGR PRECONCEPTUAL DESIGN DESCRIPTION

The reactor core of the NP-MHTGR preconceptual design (Fig 1) uses hexagonal fuel elements, or core blocks, stacked in ten-block columns to form the active core annulus Of the 660 fuel elements in the core, 540 are standard elements (Fig 1b) and 120 are reserve shutdown elements (Fig 1a) Standard fuel elements contain a pattern of fuel and coolant holes in a graphite matrix interrupted by one central element-handling hole and two target channels The handling hole extends down about one-third of the block height Reserve shutdown fuel elements have, in addition to the handling and target holes, a channel for reserve shutdown control material This

channel replaces 28 of the 138 fuel holes and 13 of the 70 coolant holes present in a standard element.

Fuel compacts are stacked within each core-block fuel hole. Each cylindrical compact, which measures 1.029 cm (0.405 in) diametrically and approximately 4.1 cm (1.6 in) axially in the preconceptual design, is a mixture of TRISO-coated fuel particles and graphite shim material bonded by a carbonaceous matrix. The fuel kernels are dense microspheres of UCO composed of highly-enriched (93.15%) uranium.

Every fuel element and 60 of the outer reflector elements (six reflector columns) (Fig. 1f) contain two channels that hold target assemblies. Target assemblies are annular compacts of tritium-producing material contained within inner and outer graphite sleeves. Using a process resembling the fuel compact formation, the target compacts are fabricated from TRISO-coated lithium aluminate particles bonded with a carbonaceous binder.

Columns of hexagonal graphite reflector elements surround the active core and reside in the central region created by the core annulus (Fig. 1e). These graphite elements have the same size, shape, and handling-hole positions as the core blocks. The side reflector includes two rows of hexagonal reflector columns. Twenty-four columns of the side reflector and six of the central reflector have control rod channels (Fig. 1c and 1d). As already mentioned, six side-reflector columns contain target elements. Permanent side reflectors (Fig. 1g) extend radially from the outer surfaces of the side-reflector elements to the inside surface of the core lateral restraint to form a right circular cylindrical reactor configuration.

No radial or axial material zoning is specified for the preconceptual design. All fuel positions contain the same loading of fissile material with the same enrichment, and all target positions contain the same loading of target material. For simplicity of analysis, the handling holes have been replaced by solid graphite. Because ONEDANT is a one-dimensional analysis tool, and for the sake of comparison, no axial features beyond the active core region are represented in either the MCNP or the ONEDANT models. Thus no axial dependence exists in our current reactor models.

REACTOR PHYSICS ANALYSIS METHODOLOGY

Two codes, NJOY[3] and TRANSX[4] process the basic cross-section data from the ENDF[5] evaluated nuclear data file into formats required by our two reactivity calculational techniques, Monte Carlo and S_n transport. (We are currently using ENDF/B-V, but are in the process of preparing cross sections based on the recently evaluated B-VI data file.) NJOY produces either pointwise or multigroup cross sections. The pointwise cross sections are used directly by the Monte Carlo code, the multigroup cross sections are further processed by TRANSX into a format compatible with the S_n codes. The resultant multigroup cross sections include resonance self-shielding, Doppler broadening, transfer matrices, and thermalization effects, including upscattering, for free and bound scatterers. In addition, TRANSX allows group collapsing and cell flux weighting to obtain spatial disadvantage factors.

Monte Carlo neutron-transport methods randomly sample numerous neutron histories to determine the average behavior of the particles. Because Monte Carlo is a statistical process, an uncertainty is associated with each result. The general-purpose Monte Carlo transport code used in the NP-MHTGR analyses is the three-dimensional code, MCNP. This coupled neutron-photon code features time dependence and uses continuous-energy cross sections. For important scattering substances, including graphite, thermal scattering $S(\alpha,\beta)$ cross sections that account for the effects of chemical binding and crystalline structure are available. MCNP can calculate eigenvalues for multiplying systems and allows very detailed and accurate geometrical representation of complicated reactor configurations.

S_n transport-theory codes numerically solve the multigroup form of the Boltzmann transport equation using the discrete ordinates approximation to treat the angular flux dependency The specific code selected for these analyses is the one-dimensional ONEDANT code Our thermal-reactor calculations use a 69-group cross-section set that includes 40 thermal groups, 20 upscattering groups, and a thermal cut-off at 2 1 eV

Each of the calculational techniques, Monte Carlo and S_n transport, possesses particular advantages that are emphasized in our neutronic analyses Because of its detailed geometrical capabilities and the associated ability to calculate localized flux distributions, Monte Carlo provides the best estimate of k_{eff} and control rod worths Similarly, off-design and accident configurations are calculated with MCNP

On the other hand, S_n codes can calculate to tight convergence criteria, benefit from the availability of appropriate cross sections, and are particularly suited for depletion calculations Therefore, discrete ordinates transport codes are used to estimate relatively small reactivity changes such as temperature effects and material worths Additionally, S_n codes include convenient and flexible edit routines that provide space- and energy-dependent characteristics such as flux spectra, power distributions, and reaction rates

For ONEDANT calculations of the unit fuel cell and core block, an S_4 angular quadrature order with P_1 scattering (incorporating the Bell-Hansen-Sandmeier transport correction) was specified The reactor calculations used an S_4/P_0 approximation Cross sections for the discrete ordinates analyses were developed from the 69-group MATXS7EX library using TRANSX, version S11 These cross sections incorporated crystalline scattering laws for graphite

Two versions of MCNP were used to calculate the results discussed in this report The first, denoted MCNP 3B5, did not include the repeated structures capability but was the public version at Los Alamos National Laboratory (LANL) when the analyses were performed The second, version 4 0, does incorporate the repeated structures feature and is the current public version Consequently, calculations that utilized the repeated structures capability were computed using MCNP version 4 0, otherwise, version 3B5 was the selected analysis tool The 300 K continuous-energy cross sections chosen for the MCNP analyses were those designated by LANL's Radiation Transport Group (X-6) as the "best" available evaluations For the temperature coefficient studies, we used ^{235}U and ^{238}U cross sections that had been processed at 300 and 900 K Graphite $S(\alpha,\beta)$ cross sections were available at 300 and 800 K

RESULTS

A discussion of our results appears in the following sections and is presented in the same order as that in which the calculations were completed We began the reactor physics analysis of the NP-MHTGR design by evaluating the basic active-core element, the unit fuel cell After checking the accuracy of our unit-cell modeling assumptions, we investigated the standard fuel element, or core block Finally, neutronic attributes of the detailed full reactor design were calculated All calculational models were based upon preconceptual design details provided by the designers

NP-MHTGR UNIT FUEL CELL DESCRIPTION AND ANALYSES

The unit fuel cell represents an infinite array of an unperturbed fuel and coolant-channel lattice that exists in the standard fuel block The unit fuel cell of the preconceptual NP-MHTGR design comprises one fuel compact, the equivalent of one-half coolant channel, and graphite matrix material In the provided design information, no gap was specified between the fuel compact and the core-block graphite This omission is not expected to affect the results or conclusions of our

analyses Several models of this unit cell were constructed and analyzed at 300 K to 1) compare results of MCNP and ONEDANT calculational models that are geometrically and compositionally identical, 2) quantify the effect of homogenization approximations introduced by modeling procedures, and 3) provide homogenized cross sections for the ONEDANT full-reactor calculations The results include k_{eff}, reaction rates for ^{235}U and ^{238}U fission, neutron production, and neutron capture The reaction rates (normalized per neutron born) were computed for each of three energy ranges fast (≥ 9 118 keV), intermediate (between 9 118 keV and 1 5 eV), and slow (< 1 5 eV)

For the unit-cell MCNP eigenvalue calculations, the one-sigma relative error is less than 0 15% Additionally, the one-sigma relative error of the reaction-rate tallies is consistently less than 1% with the exception of the ^{238}U resonance region, within this region, occasionally the statistical error is slightly greater than 4%

First, to compare reaction-rate and criticality values calculated by ONEDANT and by MCNP, two cylindrical models were developed Within each, all material was conserved The outer radial boundary condition for these cylindrical unit-fuel-cell models is reflective for the MCNP calculations and 'white' for those analyzed by ONEDANT The white boundary condition returns the outgoing flux across a boundary isotropically such that the net flux across that boundary is zero For MCNP, reflective axial boundaries also were specified to simulate unit cells of infinite height

The first model consists of a single homogeneous region in which the fuel, graphite, and coolant regions are all mixed For this homogeneous case, k_{eff} values calculated by ONEDANT and MCNP agree very well, differing by only 0 0015 Δk_{eff} Also, reaction-rate tallies calculated by the two methods for this single-region model are within 1% of each other

The second cylindrical model comprises three regions and is the most realistic representation of the unit fuel cell that ONEDANT is able to compute The inner region represents the fuel compact, the middle a full-density graphite annulus surrounding the fuel, and the outer a mixture of coolant and remaining graphite For this more complicated model, MCNP yields an eigenvalue approximately 0 005 Δk_{eff} (0 26%) greater than ONEDANT, about 2 5 times the quoted MCNP error

For the three-region unit-fuel-cell model, small differences in the reaction rates calculated by ONEDANT and MCNP are evident Because statistical uncertainties are intrinsic to the Monte Carlo method, ascertaining the cause of these minor variations is difficult MCNP predicts fewer resonance captures in the uranium isotopes than does ONEDANT The difference between the two methods is about 5% for the ^{238}U captures in this intermediate neutron-energy range For the other reaction-rate tallies, the values calculated by ONEDANT and by MCNP are consistently within about 3% of one another

The cylindrical unit-fuel-cell geometry required by ONEDANT is an approximation to the actual triangular lattice that exists in the NP-MHTGR fuel block To investigate the accuracy of this approximation, an "exact" unit-fuel-cell configuration was modeled with reflective boundaries using MCNP The MCNP criticality values of the triangular and cylindrical unit-cell models are not statistically different Therefore, for eigenvalue calculations, the cylindrical approximation of the unit fuel cell appears to be a good representation of the actual heterogeneous geometry

Examination of the reaction-rate results for this exact model indicates slightly more activity in the intermediate energy range and slightly less in both the fast and slow regimes for the discretized MCNP model than for the MCNP three-region homogeneous version Because of MCNP's statistical nature, the magnitude of this difference is uncertain Reaction rates calculated using "the best', ONEDANT and MCNP unit-fuel-cell representations are generally within 3% of one another

From these results we conclude that the ONEDANT three region analysis model adequately approximates the unit-fuel-cell configuration

The neutron energy spectrum of the NP-MHTGR unit fuel cell, in which 77% of the fissions are caused by neutrons with energies less than 1 5 eV, is quite thermal However, in these simplistic NP-MHTGR unit-fuel-cell models, the absorptive effect of lithium targets is not yet included The addition of target material will cause the neutron spectrum to shift Because the fuel is highly enriched (93 15% ^{235}U), only small quantities of ^{238}U are present in the fuel Consequently, very little activity is associated with the ^{238}U, which accounts for fewer than 2% of the total absorptions and essentially no fissions Thus, ^{238}U Doppler contributions to the negative reactivity temperature coefficient are minimal Additionally, as evidenced by the ONEDANT results of the unit-fuel-cell analyses, parasitic capture by isotopes of elements other than uranium account for fewer than 2% of the total absorptions

NP-MHTGR CORE BLOCK DESCRIPTION AND ANALYSES AT 300 K

To extend the applicability of our NP-MHTGR physics analyses, we next evaluated a standard core block The core block, or fuel element, comprises fuel compacts, target compacts, and coolant channels in a hexagonal graphite matrix Three different models of the core block were developed and analyzed As before, MCNP and ONEDANT were the analysis tools

For modeling simplicity, the detailed MCNP model of the NP-MHTGR core block treated the handling hole as solid graphite, however, each fuel compact, coolant hole, and lithium target was explicitly depicted. The calculated MCNP value of k_{eff} at 300 K for this heterogeneous core-block with a reflective outer boundary condition is 1 1302±0 16% The MCNP relative error of uranium and ^{6}Li reaction-rate tallies for the fast, intermediate, and slow energy ranges is consistently less than 1 0% with the exception of the ^{238}U resonance region where the statistical error occasionally approaches 5%

By using the repeated structures capability, MCNP can calculate the criticality of an infinite periodic arrangement of these blocks The resulting k_{eff} for this more realistic periodic configuration of core blocks is 1 1316±0 21% or within 0 14% Δk_{eff} of the value for a single block with reflective boundary conditions Since the two eigenvalues are within one sigma of each other, we conclude that the reflective boundary condition is a reasonable approximation to the periodic fuel-element lattice

Because the core blocks are geometrically complex, we evaluated the validity of a second, simpler, MCNP calculational model This hexagonal prism block model retains the explicit target configurations and a thin graphite buffer region outside of each target Except for a thin full-density graphite region at the periphery of the block, the remaining block constituents, namely fuel compacts, coolant holes, and graphite matrix have been homogenized Masses of all components are conserved Homogenization of the fuel compacts, coolant channels, and graphite matrix increased the computed k_{eff} value to 1 1644±0 26%, or 0 0342 Δk_{eff} a rather significant amount Evidently, simplification of the core block by homogenizing the fuel compacts, coolant holes, and graphite matrix induces a significant bias on k_{eff}

Although MCNP has very powerful geometric capabilities, there are several important safety parameters such as temperature coefficients and fuel burnup effects that are not well-suited for MCNP analysis These characteristics require the use of deterministic transport- or diffusion-theory codes Because of the heterogeneous nature of this reactor configuration, the best approach would be to use a supercell code to accurately calculate the flux and energy spectra in the basic lattice geometry and produce appropriate homogenized cross sections for a global calculation Los Alamos is presently developing such a supercell code

As an interim approach, we investigated the use of the one-dimensional ONEDANT code to produce these cross sections Applying this approach, we approximated the core block by a central target element surrounded by equivalent annular regions of graphite and fuel-graphite mixtures to represent the material in one-half of an actual core block. This simplified half-block model, called a target cell,' represents our third core-block model

Of the ten annular regions which describe the target cell model, the inner seven explicitly model a single NP-MHTGR target element including the associated gaps exactly as was done in the previous MCNP core-block models The eighth region is a full-density graphite annulus between the target element and the fuel-pin lattice Region 9 represents the fuel-pin lattice, a mixture of fuel compacts, graphite matrix, and coolant holes associated with one target element Finally, region 10, the outermost region, represents the remaining graphite at the edge of the block that is not incorporated in the fuel lattice region Materials and areas that constitute one half of a core block have been conserved in the target-cell model A reflective boundary condition was specified for the outer radial surface of the MCNP model, a white boundary condition was chosen for the ONEDANT model

Two target cells were calculated The first, which incorporates a homogeneous mixture of fuel, graphite, and coolant in region 9, was calculated by both MCNP and ONEDANT for comparison purposes The second ONEDANT target cell used cross sections in region 9 that were derived from flux-weighting an equivalent unit fuel cell thereby accounting for resonance and spatial self-shielding in the fuel compacts Results of this calculation represent our best ONEDANT approximation of the fully heterogeneous core block that was calculated by MCNP

With 80% of the fissions in the core block caused by slow neutrons, the neutron energy spectrum in the block is slightly softer than that calculated for the unit fuel cell (77%) Approximately 96 5% of all neutrons produced in the fuel element are absorbed in either ^{235}U or ^{6}Li The ^{238}U accounts for fewer than 1% of the total absorptions and essentially no fissions Parasitic capture by isotopes other than uranium or lithium account for approximately 2 5% of the total absorptions

Comparison of the MCNP calculations for the homogenized core block and the target cell indicates that approximating a hexagonal homogeneous block by an annular target cell is rather good, with the calculated difference being 0 0037 Δk_{eff} a value within a one and one-half sigma confidence interval The ONEDANT target cell with homogeneous fuel has a predicted k_{eff} that is 0 005 Δk_{eff} less than the corresponding MCNP calculation, an amount consistent with the differences previously calculated for unit fuel cells However, whereas MCNP predicts a heterogeneity effect of -0 0342±0 0035 Δk_{eff}, the corresponding ONEDANT prediction is only -0 0085 Δk_{eff}

To investigate this rather large discrepancy, two MCNP models were constructed to more closely represent the ONEDANT target-cell calculations In one model, the unit fuel cells were homogenized In the other, the unit fuel cells surrounding the target were constructed to match the geometry used to prepare self-shielded cross sections for the ONEDANT calculations Comparison of the two MCNP models, one homogeneous and one heterogeneous, yields an estimated heterogeneity effect of -0 0065±0 0031 Δk_{eff} This value agrees relatively well with the ONEDANT estimate This investigation illustrates the limitation of representing these complicated geometries with a one-dimensional model

NP-MHTGR CORE BLOCK TEMPERATURE-COEFFICIENT ANALYSES

The temperature coefficient of reactivity is an important safety parameter because it contributes greatly to the reactor response during transient and accident conditions Temperature changes in

reactor materials affect the neutron balance and, hence, the reactor k_{eff} The primary temperature effect in the NP-MHTGR is the hardening of the thermal-neutron spectrum with increasing moderator temperature The harder spectrum changes the relative absorptions between the lithium and uranium isotopes, and, in a finite reactor, allows more neutrons to leak from the core A second temperature effect is the Doppler broadening of the neutron resonance-absorption cross sections In HTGR reactors that contain low-enriched fuel or fertile materials, increased neutron captures associated with Doppler broadening in the ^{238}U or ^{232}Th resonances can cause significant negative temperature coefficients This effect is greatly diminished in the highly-enriched fuel used in the NP-MHTGR Thirdly, thermal expansion causes a general reduction in the densities of reactor materials, resulting in greater neutron leakage, and a corresponding reactivity loss

To begin the temperature coefficient investigation for the NP-MHTGR, we calculated with ONEDANT the effect of temperature on k_{eff} for the target cell These calculations considered only temperature-dependent cross section changes, and did not include density changes, which affect neutron mean free path length and later, in full reactor calculations, neutron leakage The TRANSX code was used to generate cross sections at temperatures of 300, 600, 800, 900, and 1200 K These cross sections incorporated crystalline scattering laws for graphite as well as Doppler broadening for resonance absorbers

Reactor temperature coefficients are generally classified as prompt or delayed, depending on their time response to power/cooling perturbations In the NP-MHTGR the temperature coefficient associated with the fuel compacts, which includes both Doppler effects in the uranium kernels and scattering effects in the pyrocarbon fuel-particle coatings and the graphite compact matrix, is regarded as prompt On the other hand, temperature coefficients associated with the graphite block matrix and target elements are considered to be delayed because of the time delay associated with heat transfer from the fuel compacts to these regions

ONEDANT-calculated k_{eff} changes in the target cell as a function of temperature indicate that all components of the coefficient are negative and that the delayed component contributes ≈85% of the total temperature effect The total k_{eff} change from ambient (300 K) to operating conditions (900 K) is 2 8% Δk_{eff} and the total isothermal temperature coefficient from 900 to 1200 K (potential transient conditions) is $-2\ 7 \times 10^{-5}\ \Delta k_{eff}/C$

As previously mentioned, the temperature-induced reactivity change in the infinite target-cell calculation is caused primarily by the competition between uranium and lithium reactions as the neutron spectrum hardens The decrease in ^{235}U fissions (which determines the decrease in k_{eff}) is essentially balanced by (or actually caused by) the increase in ^{6}Li captures The effects can be broken down into a homogeneous component caused by relative changes in the ^{6}Li capture and ^{235}U fission cross sections as a function of energy (temperature), and a heterogeneous component caused by lumping of the target material and consequent self-shielding of the ^{6}Li

To further explain this phenomenon, the relative ^{6}Li capture cross section and ^{235}U fission cross section, normalized to unity at ≈300 K versus neutron temperature were examined The ^{6}Li capture cross section decreases less rapidly with temperature than the uranium fission cross section, causing the lithium to be a relatively more effective absorber in the harder neutron spectrum To further quantify this effect, we examined the ratio of the ^{6}Li capture to ^{235}U fission cross sections normalized to unity at 300 K and we observed that the relative ^{6}Li effectiveness increases by ≈16% between 300 and 1200 K

At higher temperatures the mean free path of neutrons in the fueled portion of the block increases, thereby allowing more neutrons to reach the lithium target where they are captured (a heterogeneity effect) We performed MCNP and ONEDANT calculations to quantify the relative contribution of these homogeneous and heterogeneous effects For these calculations, the k_{eff}

change from 300 to 1200 K was calculated for the target cell and for a homogeneous version of that cell Both methods showed that the heterogeneous lumping effect predominated, accounting for ≈70% of the calculated k_{eff} change

Because of the uncertainties inherent in the Monte Carlo method, MCNP is not usually suitable for temperature coefficient calculations which often require the determination of small differences in k_{eff} However, the temperature range of the NP MHTGR is sufficiently large that statistically significant ambient-to-operating k_{eff} changes may be determined with reasonable computer running times We, therefore, attempted to use MCNP to determine the temperature effects between 300 and 800 K in an infinite array of heterogeneous core blocks As in the ONEDANT computations, these calculations considered only temperature-dependent cross-section changes and did not include density changes

The results of the MCNP calculations, including the one-sigma uncertainties, indicate that although the prompt k_{eff} change calculated with MCNP was 12% higher than the corresponding ONEDANT result, the relative error in the MCNP value is quite high and its confidence is therefore low The MCNP-calculated delayed effect caused by the matrix and target-graphite constituents is approximately 20% less than the corresponding ONEDANT result with a one-sigma uncertainty of 17% These calculations show that MCNP may be used to calculate an average temperature coefficient in the NP-MHTGR for temperature differences of 500 C or greater However, average coefficients over such a broad temperature difference are not suitable for transient or accident analyses

NP-MHTGR REACTOR ANALYSES

Proceeding to the next step in our investigations, we created both ONEDANT and MCNP models of the finite preconceptual NP MHTGR design As was assumed previously, temperature coefficient calculations for the reactor considered only temperature-dependent cross-section changes and did not include density changes

MCNP and ONEDANT reactor models were used to calculate neutronic characteristics of the finite reactor The control rods are not included in either model Using the repeated-structures capability, the detailed 360° MCNP model of the reactor was developed In this explicit model, internal and external graphite reflector blocks are defined, fully-explicit core blocks appear in their correct relative positions, reserve shutdown holes and control-rod channels are incorporated, and a permanent reflector region surrounds the outer reflector blocks

To prepare the ONEDANT model, we homogenized various reactor regions into cylinders while conserving cross-sectional areas and material masses First, the standard-fuel-block regions were homogenized by flux and volume weighting the target-cell configuration described previously This homogenization process conserves reaction rates in the target-cell model The target-cell flux distribution was then used a second time to homogenize the reserve shutdown and reflector target blocks All other ONEDANT regions were homogenized by a simple volume weighting procedure Axial leakage was approximated by specifying a buckling height in the one-dimensional ONEDANT calculation The core is defined as the standard-fuel and reserve-shutdown blocks, the inner reflector consists of the inner graphite and inner control-rod blocks, and the outer reflector consists of the reflector-target, outer control-rod, and side-reflector blocks as well as the permanent side reflector region

Representing the highly heterogeneous NP-MHTGR by the ONEDANT (r-z) analysis model required several approximations These approximations include 1) use of one-dimensional, cylindrical target cells to obtain homogeneous cross sections, 2) not accounting for flux variations caused by changing boundary conditions in the homogenization process, and 3) removal of

azimuthal variations by representing a hexagonal configuration as concentric cylinders Nevertheless, by comparing the ONEDANT calculations to more rigorous MCNP calculations, we can better understand and quantify the effects of these approximations as we develop more rigorous methods

A series of ONEDANT calculations was performed to evaluate the reactor temperature coefficients In addition to k_{eff}, ONEDANT provides detailed edits and neutron balances that can be used to discern the causes of calculated reactivity changes The following four problems were calculated

Problem #1 - All material at 300 K
Problem #2 - Change core (fuel-bearing blocks) to 1200 K
Problem #3 - Change inner reflector in problem #2 to 1200 K
Problem #4 - Change outer reflector in problem #3 to 1200 K

As evidenced by the problem definitions above, we chose a value of 1200 K for the elevated temperature in the ONEDANT calculations This value was chosen to enhance the temperature effects, and consequently make it easier to discern changes in the neutron balance that explain these effects

In general, radial leakage from the core is rather significant, especially in the outward direction (≈11% of neutrons born), while axial leakage does not play an important role Additionally, most of the neutrons leaking from the core are absorbed in either boron-equivalent impurities or carbon in the reflector regions, with relatively few neutrons actually leaking from the system Whereas the boron-equivalent impurities have an insignificant effect in the core, they are significant absorbers in the thermalizing reflectors where there is no competition from uranium or ^6Li In analyzing the leakage effects, recall that temperature-dependent material density changes have not yet been included

A significant reactivity loss occurs when the core is heated to 1200 K while the reflectors remain at 300 K This loss is primarily caused by increased ^6Li absorptions in the core, as explained in the previous section Recall that raising the temperature from 300 to 1200 K of an infinite array of standard fuel blocks (in which no leakage occurs) causes a reactivity loss of -0 036 Δk_{eff} In the finite reactor, increased radial leakage at the higher moderator temperature produces an additional reactivity loss resulting in a total Δk_{eff} of -0 043

Elevating the temperature first of the inner and then of the outer reflector both cause a positive differential in k_{eff} (a small, but positive temperature coefficient) Although this phenomenon has been previously reported, the underlying causes have not, to our knowledge, been discussed in the literature The causes may be deduced by examining the neutron balance of the reactor at each condition At the higher reflector temperatures the carbon and boron-equivalent absorptions are reduced Consequently, more neutrons are available to reenter the core where some fraction of them produce additional fissions in the uranium This effect appears to be especially sensitive in the inner reflector where all extra neutrons not absorbed must reenter the core (since axial leakage is negligible), whereas, in the outer reflector, a significant number of these extra neutrons leak from the outer radial boundary

The ONEDANT results can be compared to corresponding MCNP calculations The fully explicit 300 K MCNP calculation yielded a k_{eff} of 0 9920 ± 0 021% or 0 0115 Δk_{eff} higher than the comparable ONEDANT result (As the design has evolved from the preconceptual design phase, changes have been incorporated to provide adequate excess reactivity In the future we will evaluate the effectiveness of these changes) To cover the expected operating range, the hot MCNP calculations were run at 800 K, therefore the MCNP values are not directly comparable with the 1200 K ONEDANT calculations However, the value of $\Delta k_{eff}/C$ (the average temperature

coefficient for the range) for the two methods can be compared if we assume the effect is approximately linear These average temperature coefficients are listed in Table 1

Because of the relatively small reactivity changes and associated large statistical uncertainties, MCNP values for the reflector effects are suspect Nevertheless, agreement between the two methods is good for both the core and inner reflector For the outer reflector MCNP predicts a much smaller effect (not statistically different than zero) than does ONEDANT

CONCLUSIONS

We applied two of our reactor-physics transport codes, MCNP and ONEDANT, to calculate the preconceptual design NP-MHTGR Thus far we have emphasized the determination of k_{eff} and the changes in k_{eff} associated with temperature increases in the core and reflectors Using the repeated structures capability in MCNP we generated a very detailed geometrical model that explicitly represented the fuel compacts, target element, coolant holes, reserve shutdown holes, and control rod channels For this reactor model, calculation of each k_{eff} value with an associated one-sigma uncertainty of ≈0 21% required tracking of approximately 170,000 neutron histories and consumed 600 minutes (10 hr) of CRAY-YMP computer time This level of uncertainty is adequate for most determinations of safety-related physics parameters These MCNP calculations allowed the determination of temperature coefficients with a 17% uncertainty for temperature changes of 500 C Longer running times would reduce the uncertainty level Therefore, we conclude that MCNP may be used to calculate values of selective average total temperature coefficients for temperature changes of 500 C or more

The ONEDANT calculations required geometrical approximations to calculate the complicated NP-MHTGR geometry Incorporating these approximations in both cell and full-reactor calculations resulted in k_{eff} differences of 1 2% to 1 7% and core temperature-coefficient differences of ≈20% compared to MCNP As our modeling becomes more precise, we hope to reduce these differences

As one result of this investigation, we determined the general magnitude of temperature coefficients in the NP-MHTGR All contributions from the active core are negative The prompt component from uranium Doppler and fuel-compact graphite contributes approximately 15% of the total core coefficient, which includes delayed effects from the core-block graphite matrix and target elements Temperature coefficients in the reflector (a further, significantly more-delayed effect) appear to be positive, but exhibit a smaller magnitude than those in the core Additional calculations are necessary to quantify this phenomenon more accurately

REFERENCES

1 J F Briesmeister, editor, MCNP-A General Monte Carlo Code for Neutron and Photon Transport, Version 3A,' Los Alamos National Laboratory report LA-7396-M, Rev 2 (September 1986)

2 R D O'Dell, F W Brinkley, and D R Marr, 'A User s Manual for ONEDANT A Code Package for One-Dimensional, Diffusion-Accelerated, Neutral-Particle Transport, Los Alamos National Laboratory report LA-9184-M (February 1982)

3 R E MacFarlane, R D Barrett, D W Muir, and R M Boicourt, 'The NJOY Nuclear Data Processing System User's Manual," Los Alamos Scientific Laboratory report LA-7584-M (December 1978)

4 R. E. MacFarlane, "TRANSX-CTR: A Code for Interfacing MATXS Cross-Section Libraries to Nuclear Transport Codes for Fusion Systems Analysis," Los Alamos National Laboratory report LA-9863-MX (February 1984).

5 R. Kinsey (Comp.), "ENDF-201: ENDF/B Summary Documentation," Brookhaven National Laboratory report BNL-NCS-17541 (ENDF-201), 3rd Edition ENDF/B-V (1979).

Table 1. NP-MHTGR Average Temperature Coefficient
Δk_{eff} (x 10^{-5})/C

Component	ONEDANT	MCNP
Hot Core	-4.81	-5.10 ± 11%
Hot Inner Reflector	+0.97	+1.24 ± 47%
Hot Outer Reflector	+1.26	+0.24 ± 242%

Figure 1. Plan view schematic of the NP-MHTGR core.

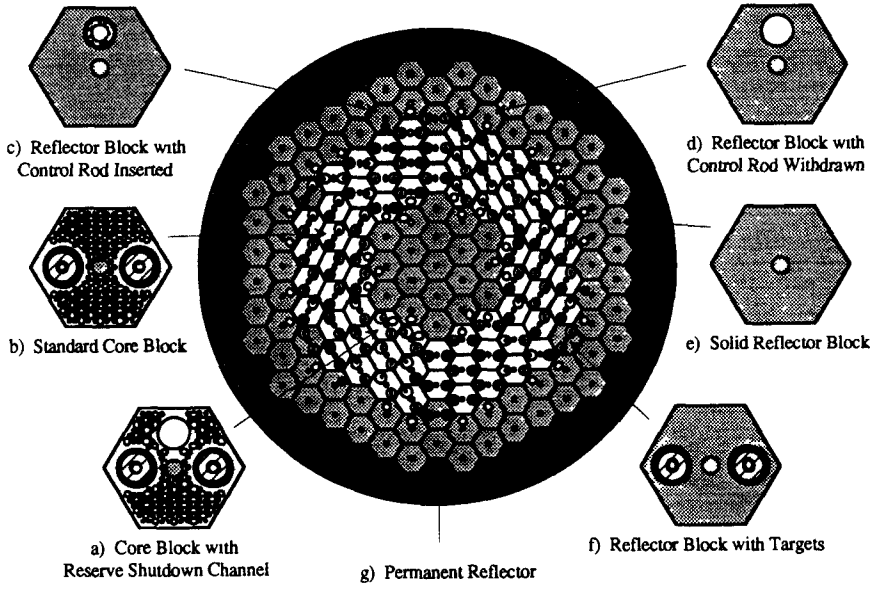

HEAVY NUCLEUS RESONANCE ABSORPTION IN HETEROGENEOUS LATTICES

M. COSTE, H. TELLIER, C. BRIENNE-RAEPSAET and C. VAN DER GUCHT
Service d'Etudes de Réacteurs et de Mathématiques Appliquées
Centre d'Etudes Nucléaires de SACLAY
91191 GIF SUR YVETTE CEDEX - France

ABSTRACT

To compute easily the neutron reaction rates in the resonance energy range, the reactor physicists use the self-shielding formalism and the effective cross-section concept. Usually, for these calculations, an equivalence process is used, in such a way that the absorption rate is correctly computed for the whole fuel pin. This procedure does not allow to preserve the spatial absorption rate distribution inside the pin. It is an important handicap if we want to reproduce the plutonium distribution in a spent fuel. To avoid this inconvenience, new improvements of the self-shielding formalism have been recently introduced in the new assembly calculation code of the French Atomic Energy Commission, APOLLO 2. With this improved formalism, it is now possible to represent the spatial and energetic dependence of the heavy nucleus absorption inside the fuel pin and to use a fine energy dependent equivalence process. As it does not exist clean experimental results for the spatial and energetic dependence of the absorption, we used reference calculations to qualify the self-shielding formalism. For the strongly self-shielded nuclei of interest in reactor physics, U238, Pu240 and Th232, the agreement between the self-shielding calculation and the reference ones is fairly good for the spatial and energetic dependence of the absorption rate.

INTRODUCTION

The computation of the heavy nucleus resonance absorption in a heterogeneous lattice is one of the hardest works in reactor physics. Generally, the computer codes, which are used in every day core calculations, solve the Boltzmann equation in the multigroup approximation. The number of energy groups is around one hundred. Because of the resonant structure, it is not possible to represent finely the cross section behaviour with so few energy points. Thus, the reactor physicists use effective cross sections which take into account the heterogeneity of the lattice and the fine structure of the neutron flux which is induced by the resonances. These cross sections which allow to obtain the right reaction rate with a coarse energy mesh are generated through self-shielding formalisms. Formerly, in all the reactor core calculations, an averaged self-shielding in the whole fuel assembly was used. This simplified assumption had important consequences in the case of several types of fuel in the same assembly and, in particular, it was not possible to reproduce correctly the plutonium distribution inside a fuel pin. New improvements and a generalization of the

self-shielding formalism have been recently performed. They are introduced in the new assembly calculation code APOLLO 2[1] With this new formalism, it is now possible to use several self-shielding regions and to represent the spatial dependence of the heavy nucleus absorption inside a fuel rod. It is also possible to have a fine energy dependent equivalence process. In the following sections we propose to describe briefly the new self-shielding formalism and to qualify its new possibilities which constitute an important improvement for the reactor physicists. As it does not exist clean experimental results of the spatial and energetic dependence of the heavy nucleus absorption rate inside a fuel pin, we have qualified the self-shielding calculation against very detailed computations which can be considered as reference ones. The suitable energy range for the self-shielding is the one of the resonances. It is mainly governed by the slowing-down process. Consequently we have used as a reference a slowing-down calculation in the multigroup approximation with a very fine energy mesh and a Monte Carlo calculation with a pointwise representation of the neutron cross sections. Thereafter we will present examples of the comparisons obtained in the cases of the strongly self-shielded nuclei of interest for reactor physics, Uranium 238, Thorium 232 and Plutonium 240.

NEW SELF-SHIELDING FORMALISM

The self-shielding calculation[2] is a problem which depends both on space and energy. The spatial domain is divided into several self-shielding regions grouping media where resonant mixtures are the same. For each self-shielding region and each group of the resonance energy range, self-shielded cross sections are calculated by preserving the geometry-dependent reaction rates. Since the actual flux is unknown, the reaction rates are obtained in an equivalent homogeneous medium which preserves the resonance integral calculated with an approximate slowing-down model for the resonant nucleus. Homogeneous reaction rates are calculated by a fine multigroup code[3,4]. In order to use one parameter tabulations, we simplify the setting in which the equivalence is performed by considering a slowing-down problem with given moderator sources. In this way we represent all the non resonant cross sections by a single background cross section. So, an equivalent homogeneous medium, characterized by a background cross section, will be found for each self-shielding region and each group of the resonance energy range. The energy dependence of this equivalence process allows to fit the approximate slowing-down model to the treated resonance. We use three approximate slowing-down models: the narrow resonance one (NR), the wide resonance one (WR) and an intermediate one (IR), where the flux is a linear combination of the NR and WR fluxes. The choice of the approximate slowing-down model is effected by comparing the Doppler broadened width of each resonance to the average gain of lethargy per collision. The space dependence of the equivalence process allows to get several self-shielded isotopes for one heavy nucleus and then, for instance, to represent the spatial dependence of the heavy nucleus reaction rates inside a fuel rod.

An important new improvement of the code is that it can take exactly into account spatial interferences between resonant mixtures when all the self-shielding regions have the same isotopic vector[5]. It is the background matrix method.

We briefly describe this new improvement which allows to obtain the space dependent resonance integral for each self-shielding region.

With the assumption of a slowing-down problem in the resonance energy domain with given moderator sources, and in the framework of flat-flux collision probabilities, with isotropic scattering, the flux is given by

$$\Sigma V \vec{\phi} = P V (R_0 \vec{\phi} + \vec{S_1}) \tag{1}$$

where $\vec{\phi} = (\phi_i)$ is the flux on each calculational region i, $\vec{S_1}$ is the moderator source, P the collision matrix, and Σ, V, R_0 are diagonal matrices which represent, respectively, the total cross sections, the volumes and the resonant slowing-down operators in each region i.

By grouping calculational regions i, in which resonant mixtures are the same, into a self-shielding region α, and by using an average weighting flux ϕ_α on region α, the fluxes are given by:

$$\vec{\phi_0} = C\, r_0 \vec{\phi_0} + \vec{S} \tag{2}$$

$\vec{\phi_0}$ is the flux on each self-shielding region α, r_0 is the average microscopic slowing-down operator. S and C are given by the following formulas:

$$S_\alpha = \frac{\sum_{i\in\alpha}\sum_{j} P_{ij} V_j S_{1j}}{\sum_{i\in\alpha} \Sigma_i V_i}, \quad C_{\alpha\beta} = \frac{\sum_{i\in\alpha}\sum_{j\in\beta} P_{ij} V_j N_{0j}}{\sum_{i\in\alpha} \Sigma_i V_i} \tag{3}$$

The background matrix formalism is based on the fact that the matrix C can be diagonalized when all the resonant mixtures are similar. Then a base of eigenvectors $\vec{\psi}_\beta$ can be found for C:

$$C\ \vec{\psi_\beta} = \lambda_\beta \vec{\psi_\beta}, \tag{4}$$

By using a slowing-down model for resonant scattering, equation (2) becomes:

NR approximation: $$\vec{\phi_0} = C\, \sigma_p \vec{\phi^{as}} + \vec{S} \tag{5}$$

WR approximation: $$\vec{\phi_0} = C\, \sigma_s \vec{\phi_0} + \vec{S} \tag{6}$$

where σ_p is the potential cross section, and σ_s the scattering cross section.

By decomposing vectors on the eigenvector base,

$$\vec{\phi_0} = \sum_\beta \gamma_\beta \vec{\psi_\beta}, \qquad \vec{S} = \sum_\beta \nu_\beta \vec{\psi_\beta}, \qquad \vec{\phi_0^{as}} = \sum_\beta \mu_\beta \vec{\psi_\beta}, \tag{7}$$

and by setting:

$$\sigma_{e,\beta} = \frac{1}{\lambda_\beta} - \sigma, \qquad \gamma_\beta = \frac{\nu_\beta}{1 - \sigma\,\lambda_\beta}, \tag{8}$$

where σ is the total resonant cross section and σ_a the absorption resonant cross section, we obtain a system of independent equations:

$$\text{NR approximation} \quad \varphi_\beta = \frac{\sigma_p\,\mu_\beta + \gamma_\beta\,\sigma_{e,\beta}}{\sigma_{e,\beta} + \sigma} \tag{9}$$

$$\text{WR approximation} \quad \varphi_\beta = \frac{\gamma_\beta\,\sigma_{e,\beta}}{\sigma_{e,\beta} + \sigma_a} \tag{10}$$

Then the resonance integrals are obtained from:

$$\tau^G_{a,\alpha} = \sum_\beta \int_G \sigma_a(u)\,\varphi_\beta(u)\,\psi^\alpha_\beta(u)\,du \tag{11}$$

These quantities allow us to determine the background cross sections and then the self shielded cross sections. The reactions taken into account are the absorption, the scattering and the production.

VALIDATION PROCEDURE

To qualify the reactor physics computations, people generally use experimental results which are obtained in clean critical facilities. The geometry of these experiments must be very simple in such a way that they can be computed without geometrical and numerical approximations. Unfortunately such clean experimental results do not exist in the case of self-shielding validation. For example we can obtain some information about the spatial dependence of the absorption rate of Uranium 238 inside a fuel pin, by measuring the spatial distribution of the Plutonium 239 in a spent fuel. But the interpretation of such measurements is too much dependent on the calculation scheme approximations. That is why we have chosen to compare the self-shielding calculations, to very detailed and accurate computations which can be considered as reference ones. Two different types of reference calculations were used.

In thermal neutron reactors, the self-shielding effect mainly occurs in the low energy resonance range, below a few keV. It is an energy range essentially governed by the slowing-down process. Consequently the first type of calculation was a slowing-down one. The calculations were performed with the SECOL code[6] which solves the slowing-down equation in an heterogeneous geometry and a multigroup approximation. To obtain a very fine description of the cross sections, about ten thousand groups were used. The second kind of reference calculation is a Monte Carlo calculation with a pointwise representation of the cross sections. This second set of calculations was performed with the TRIPOLI Code[7]. To make the comparison between the results of the three kinds of calculations, it is necessary to have strictly the same neutron library for the codes. That is

why, starting from the ENDF/B5 file we have generated, with the same approximation and accuracy, the input libraries for the three codes. The compatibility of the multigroup and the pointwise cross sections has been carefully checked. The infinite dilution and self-shielded libraries of APOLLO 2 were generated with the 99 or 172 neutron energy group mesh The calculation sheme is displayed on figure 1

The first qualification computations were realized in the case of the simple geometry of a light water reactor cell with three regions: the fuel, the clad and the moderator. The spatial discretization of this cell must satisfy two criteria: the total absorption in the whole pin must not be dependent on the number of calculation points and the distribution of the absorption inside the pin must be well represented. The total number of points is also limited by the numerical problems which can happen in the computation of the background matrix eigenvectors. Preliminary calculations showed that ten areas of equal volume in the fuel and two in the moderator constitute a good compromise. In order to avoid, in a first step, mutual interferences between the resonances of several nuclei in the fuel, only one resonant isotope has been introduced in the fuel pin. For the same reason the material of the clad has been chosen without resonance in the energy range of interest. We adopted an aluminium clad. The fuel was dioxide and the concentration of heavy isotope is the one of Uranium 238 in a light water reactor fuel. For these calculations the temperature was constant inside the fuel.

RESULTS AND ANALYSIS

The qualification consists in a source calculation. We emit a 3 keV neutron with a flat distribution in the moderator and determine for one neutron slown-down below 1.51 keV the absorption rate of the heavy nucleus between 1.51 keV and the thermal cut-off (about 3 eV). The energy groups between 3 and 1.51 keV are needed to eliminate the effect of the transcients which are not exactly the same in the three codes SECOL, TRIPOLI and APOLLO 2. The same procedure was applied to the three kinds of fuel $^{238}UO_2$, $^{232}ThO_2$ and $^{240}PuO_2$. The results are given in table I in which we can find, for the whole energy range and the whole pin, the total absorption rate in 10^{-5} unit of the heavy nucleus which has been obtained in the Monte Carlo calculation and the differences between the slowing-down or the self-shielding calculation and the Monte Carlo one. The error bar is the one sigma confidence interval of the Monte Carlo calculation.

Table I

Nucleus	Monte Carlo	Slowing-down	Self-shielding
Uranium 238	20 229	+ 20 ± 75	- 101 ± 75
Thorium 232	11 712	- 135 ± 85	- 100 ± 85
Plutonium 240	19 471	- 155 ± 110	- 86 ± 110

The self-shielding calculations are performed with the background matrix formalism, the equivalence is done with the NR approximation above 50 eV and the WR approximation below 50 eV. Taking into account of the confidence interval of the Monte Carlo calculation, the agreement between the three computations is very satisfactory in the case of the total absorption rate. The comparisons of the radial distributions of the absorption rate obtained in Monte Carlo and slowing-down calculations and in Monte Carlo and self-shielding calculations are displayed on figures 2

and 3 for the Uranium 238 case. The hachures represent the confidence interval of the TRIPOLI calculations. The agreement is satisfactory for the slowing-down calculation (SECOL computation) but in the case of the self-shielding calculation (APOLLO 2 computation), it exists a compensation between the center of the pin where the absorption rate seems too low and the areas near the periphery where it is a little too high. It seems that these discrepancies can be attributed to the 36.7 eV and 102 5 eV resonances as it can be seen in figures 4 and 5 which display the energy dependence of the absorption rate for the central area and the area number 9 which is close to the periphery. The abscissa is the group number of the broad energy mesh of the APOLLO 2 library (99 or 172 groups) These two resonances are characterized by a reduced neutron width much higher than the average reduced neutron width of the resolved resonances. Table II gives the numerical values of these parameters and also the ones of the 69.2 eV resonance of Thorium 232 and of the 66.2 eV resonance of the Plutonium 240. These two last resonances present the same property, a high reduced neutron width. The consequences are also the same. For these resonances we observed an over-prediction of the absorption rate in the periphery and an underprediction in the center of the pin. As an example, figures 6 and 7 give the comparison of the energy dependence of the heavy nucleus absorption rate in the peripheral area for the Thorium 232 and Plutonium 240 calculations.

Table II

Nucleus	Energy (eV)	Γ_n^o (meV)
U238	36.7	5.58
	102.5	6.9
	Resolved resonances	2.51
Th 232	69.2	5.24
	Resolved resonances	1.41
Pu 240	66.2	6.6
	Resolved resonances	1.26

The strange behaviour of such resonances gave us the idea of two improvements. First, in a usual self-shielding calculation, the equivalence process is only done for the absorption and the background cross section is assumed to be the same for the absorption and for the scattering. We propose to use separate background cross sections. The removal cross section from a group g towards a group g' is factorized into two components, the initial energy group scattering cross section and the transfer probability matrix

$$\Sigma_{g\to g'} = \Sigma_s(g) \cdot P_{g\to g'}$$

and only $\Sigma_s(g)$ was initially self-shielded. The second improvement consists in the self-shielding of the transfer probability matrix.

Modifications of the formalism and library format have been introduced in the APOLLO 2 code to take into account these two improvements. The use of two separate equivalences for absorption and scattering slightly modifies the scattering rate but does not change the absorption rate. On the other hand, the self-shielding of the removal cross sections, for the

slowing-down energy range and for these three nuclei does not seem to modify consequently the absorption rates (about 20.10^{-5}) but that effect could be more important with a lower water density (accidental boiling).

CONCLUSION

For the even-even actinides, we observe a good agreement between the calculation of the absorption rate (in the resolved resonance energy range and above the thermal cut off) by the Monte Carlo or fine mesh slowing-down methods and the self-shielding formalism. We are now more confident in this latter technics for reactor core calculations. In addition, with the new possibilities we are able to obtain a good spatial description of the absorption rate inside a fuel pin, and thus to perform more accurate computation of the Plutonium content in a spent fuel. The self-shielding of the removal cross sections seems to have a slight impact in the energy range below a few keV in the case of normal operating conditions of the water moderated reactor, when the slowing-down by the water is predominant. When it is not the case, very tight lattices or accidental conditions, the self-shielding of the removal cross sections could be more important. The study of these topics is under investigation.

ACKNOWLEDGEMENTS

The authors are indebted to Pr. P. Reuss and Dr. P. Ribon for their advices and to Mrs. J. Vanuxeem and Mr. A. Constans for their help to process the nuclear data and the neutron libraries.

REFERENCES

1. R. Sanchez, J. Mondot, Z. Stankovski, A. Cossic, I. Zmijarevic, "APOLLO-II: A User Oriented, Portable, Modular Code for Multigroup Transport Assembly Calculations", ANS International Topical Meeting on Advances in Reactor Physics, Mathematics and Computations, Paris, Vol. III, 1563 (1987).

2. R. Sanchez, M. Coste, Z. Stankovski, C. Van der Gucht, "Models for Multigroup Self-shielded cross sections calculations in the code APOLLO-II", PHYSOR, Marseille, France, Vol. III, P II, 149 (1990).

3. M. Grandotto-Biettoli, "AUTOSECOL: un calcul automatique de l'autoprotection des résonances des isotopes lourds", Note CEA-N-1961, (1976).

4. R.E. Mac Farlane, D.W. Muir and R.M. Boiscourt: The NJOY Nuclear Data System, L.A. 9303M (1982).

5. P. Reuss, "A Generalization of the Livolant-Jeanpierre Theory for Resonance Absorption Calculation", Nucl. Sci. Eng., 92, 261 (1986).

6. A. Livolant and F. Jeanpierre, "Autoprotection des Résonances dans les Réacteurs Nucléaires", Note CEA-R-4533, Commissariat à l'Energie Atomique (1974).

7. J.C. Nimal et al.: "TRIPOLI: Energy dependent three dimensional Monte Carlo Programm". ORNL-OLS-80-110 (1980).

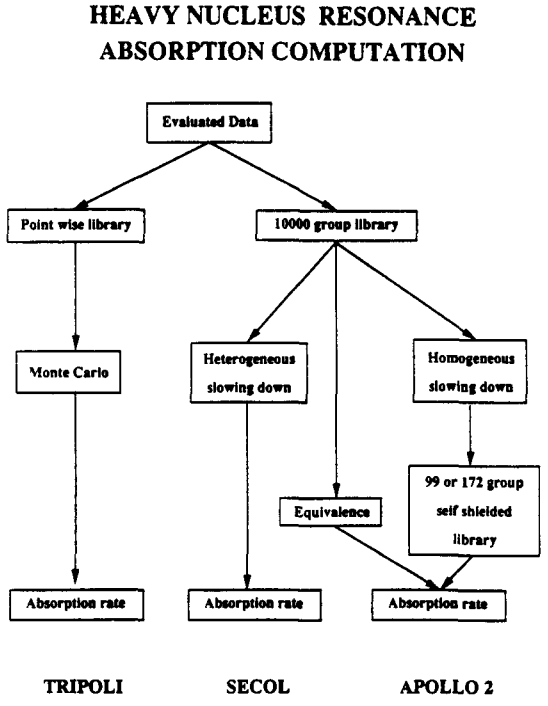

Figure 1

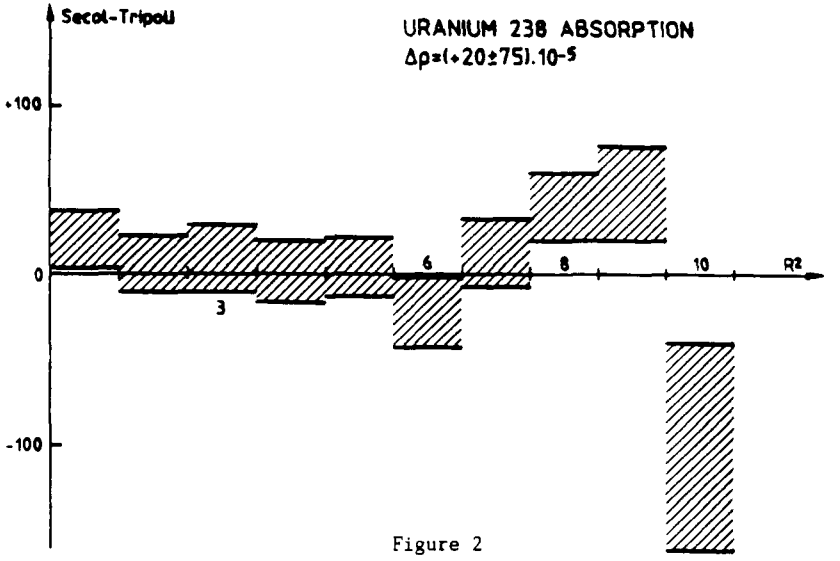

Figure 2

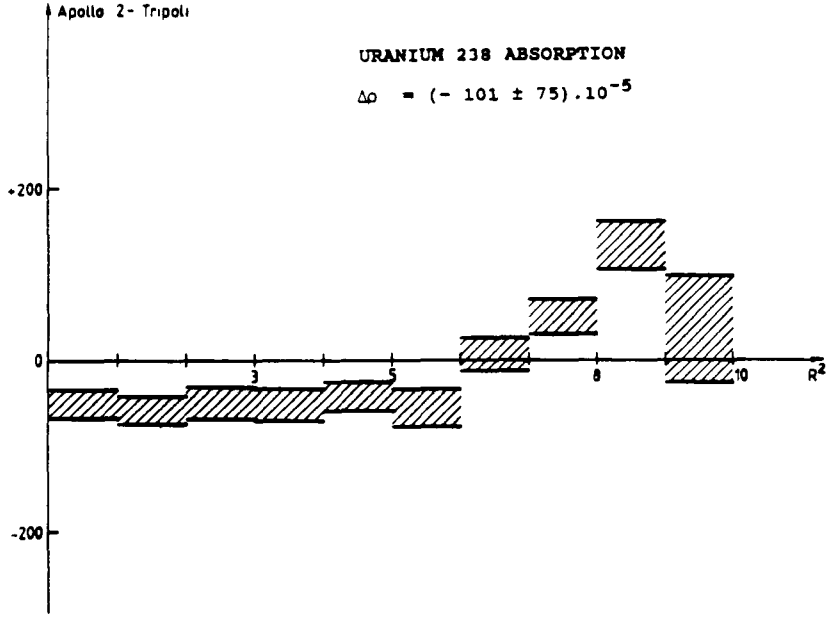

Figure 3

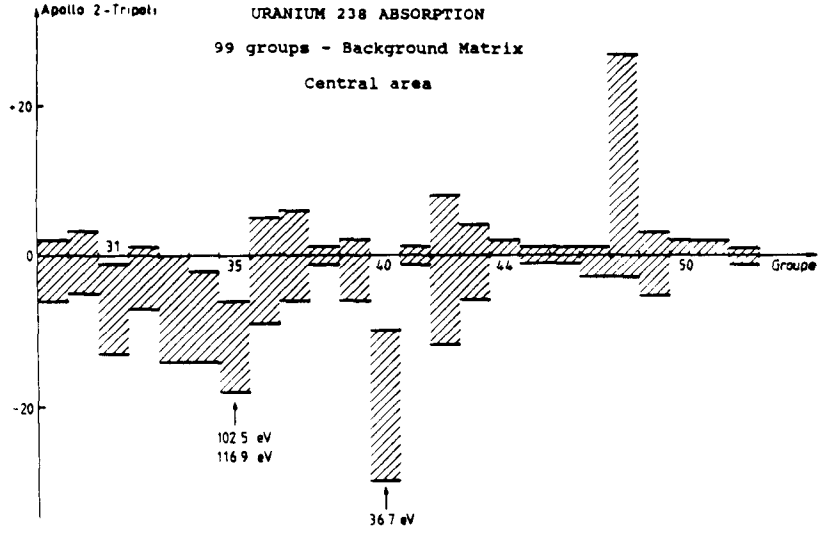

Figure 4

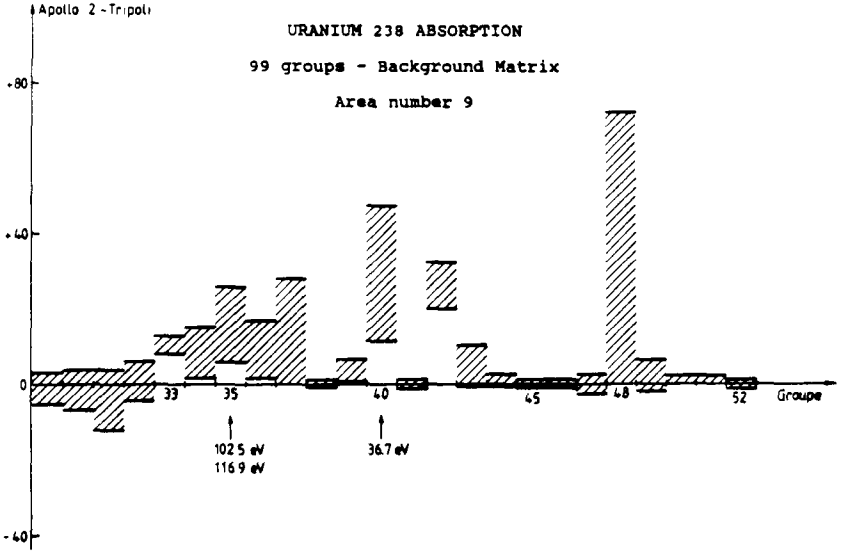

Figure 5

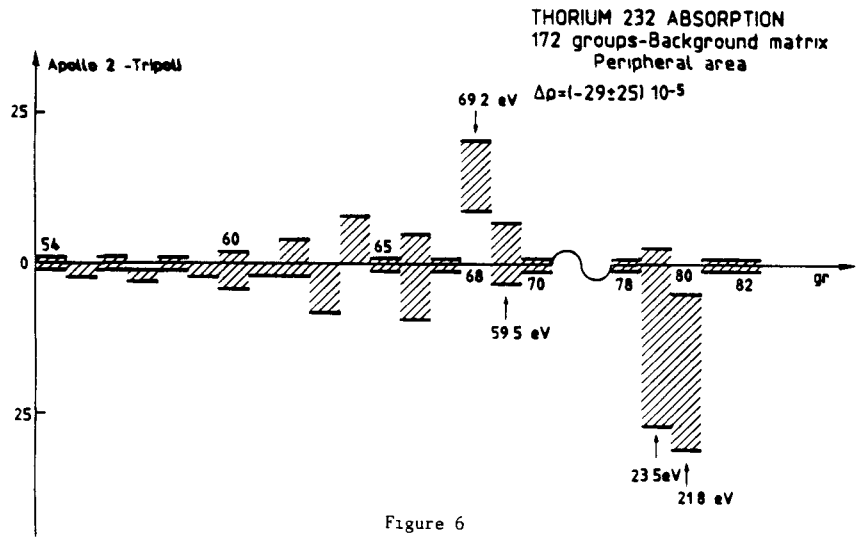

Figure 6

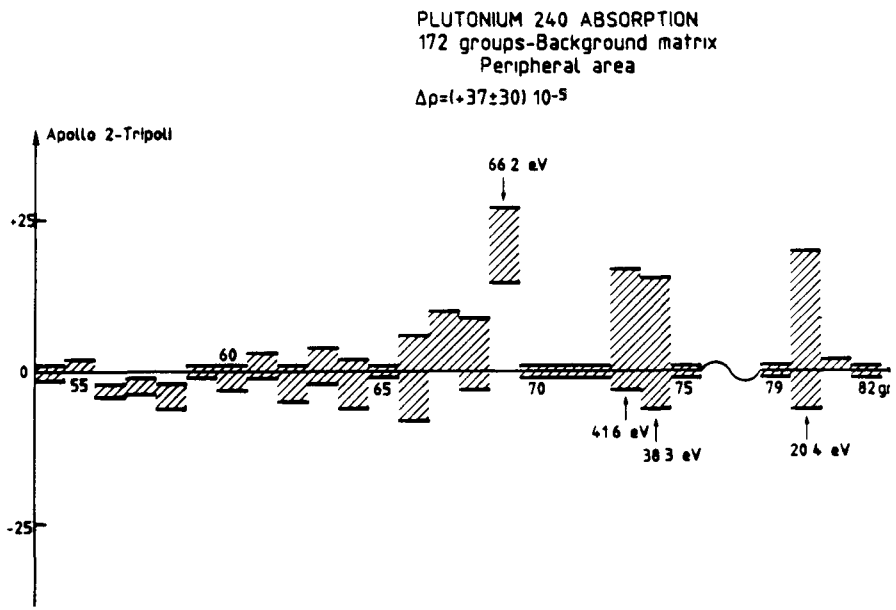

Figure 7

VALIDATION OF THE EXPERIMENTAL METHODS USED IN THE EPICURE PROGRAMME AND THEIR ASSOCIATED UNCERTAINTIES

J P CHAUVIN*, G GRANGET*, M MARTINI*, J MONDOT*
J C. LEFEBVRE**, A VALLEE***

* CEA/DRP/SPRC - CEN/CADARACHE 13108 - SAINT PAUL LEZ DURANCE Cedex
** EDF/SEPTEN - 12-14, Av Dutrievoz 69628 - VILLEURBANNE Cedex
*** FRAMATOME, TOUR FIAT, Cedex 16, 92084 - PARIS LA DEFENSE

ASTRACT

The Epicure programme, planned since 1987 within the framework of a collaboration between CEA, EDF and FRAMATOME, is devoted to the validation of the calculational schemes for plutonium recycling in PWRs

This experiment, performed in the EOLE critical facility at the Nuclear Center of Cadarache, is overall based in the measurements of power distributions in the core by the use of fission chambers, fission detectors and γ integral measurements of the irradiated pins

The validation of calculation procedures is meaningful only if the uncertainties on measured parameters are small compared with the calculation ones, so this paper trays to fix and to validate the uncertainties on fission rate distributions by

- the analysis of the experimental techniques,
- the irradiations of fuel pins in a reference neutron flux,
- the comparison of calculated and measured results in simple experiments of substitution between U and Pu pins

Experimental results seem to confirm that uncertainties on fission rate distributions are always less than ± 5 % (at 2 σ), as foreseen for the most pessimistic configurations in presence of Mox assemblies

I - INTRODUCTION

The Epicure programme, planned since 1987 within the framework of a collaboration between CEA, EDF and FRAMATOME, is devoted to the validation of the calculational schemes for plutonium recycling in PWRs[1-2]

This experiment, performed in the Eole critical facility at the Nuclear Centre of Cadarache, is based on measurements of the following physical parameters

the pin by pin power distribution,
control rod effectiveness,
cynetic and reactivity coefficients,
reactivity loss per cycle

Experiments have already been made in two different kinds of assembly, the main results, concerning radial and axial fission rate distributions, are discussed in this paper

II - THE GENERAL OBJECTIVES OF THE EPICURE PROGRAM

A common agreement exists among the French partners about the uncertainties on calculations used at present for UO_2 fuelled cores These uncertainties have been established on the basis of a large validation of the calculation methods by the measurement results obtained either in power stations or in experimental facilities

Concerning Mox fuel, the data available are less numerous and often derive from experiments not at all representative of neutronic conditions characteristic of the mixed cores, that we are at present considering

Moreover calculation methods for PWRs with Pu recycling are affected by supplementary difficulties due to the following reasons in particular

the heterogeneous structure of the MOX assembly (which includes three zones with different enrichments) and of the core at the interface between the two kind of fuels where strong variations of neutron flux and spectrum occur,

a poor knowledge of cross section data for the transuranium elements which are more important in a Mox assembly than in uranium irradiated fuel

Of course, the reduction of the uncertainties deriving from these considerations will be based on the comparison between calculated results and measurements performed in power stations , but this is not sufficient because a lot of parameters are not measured and others are obtained by indirect ways Moreover the establishment of a discrepancy between prediction and measurement does not permit the identification and no correction of the failures of calculation procedure, unless some particular results, obtained by experiments in critical facilities, could be considered as basis reference values

Therefore the aim of the EPICURE program is to bring validation tools on

- parameters not directly measurable on power stations,
- or on basic points which will permit us to correct possible failures of calculation procedure and at the same time to optimize the utilisation of experimental results coming from power reactors

In every case this validation is possible and meaningful, only if the uncertainties on measured parameters are small compared with calculation ones

Therefore this paper trays to determine and to validate the uncertainties on fission rate distributions by means of

- the analysis of the experimental techniques and their comparison in deriving axial and radial buckling,
  the irradiations of fuel pins in a reference position (the thermal column of the Harmonie reactor),
- the comparison between calculated and measured results obtained, in very simple experiments, by substituting in a uranium homogeneous medium a central pin by an equivalent Pu one

III - FISSION RATE DISTRIBUTION

III.1 - Measurement techniques

Fission rates in a reactor can be obtained directly by using fission chambers and/or indirectly by means of activation technics based on the detection of gamma-ray emitted from the totality or from a well established fission product.

Both these techniques were utilized in particular :

- integral gamma measurements of irradiated fuel pins in their central part and of U235, U238, Pu239 foils irradiated inside the fuel pins,
- for the same pins and foils measurements of the gamma ray peaks emitted from four fission products : table 1 lists those gamma rays, their energies and their half-life,
- U235, U238, Pu239, Np237 fission chambers inserted in a Zr guide tube at different radial positions.

All measurement positions were carefully chosen to get the maximum of information (in particular in transition zones) and to allow a verification of neutron flux symmetry.

III.2 - Experimental uncertainties

Experiments have been made in two different cores :

- a uranium core, with different water to fuel volume ratios, to study fundamental neutronic effects (in particular K^{∞} by buckling measurements), radial and axial fission rate distributions,
- a uranium core, with a Mox assembly located in the centre of the UO_2 zone to measure the pin by pin power distribution in the Mox (1/8 of assembly) and in the surrounding UO_2 pins.

The experimental technics used for determination of the core power distribution, the absolute core power, the axial and radial buckling and fast neutron flux were very similar for the two experiments, but uncertainties in the two cases are different of about a factor 2.

III.2.1 - Uncertainties in the UO_2 reference core (fig. 1)

Relative integral measurements are the basis of the pin-to-pin power determination, so that the largest source of uncertainty on gamma-ray counts in that arising from counting statistics. Experimental measurements normally have uncertainties due to counting statistics better than 1 % : this value is including the uncertainties due to background subtraction and decay correction, evaluated by counting a "reference" pin, contemporaneously and for the same time, in another counting system.

The global uncertainty, obtained by a quadratic combination of elementary uncertainties, is given in table 2 and it is about ± 1 % at 1 σ.

III.2.2 - Uncertainties in the Mox-UO_2 core

In this case a Mox assembly has been placed at the center of the UO_2 core (fig. 2) with the main purpose of measuring the pin by pin power distribution in the 3 zone Mox assembly and in the adjacent UO_2 zone. When power maps have to be correlated among these zones with different fuels or fuel enrichments, the gamma counts cannot be considered as proportional to the fission rates with an unique factor.

Then the technique of counting particular gamma ray peaks must be used and the experimental uncertainty must account, in addition to statistical errors, for relative selfshielded cross sections, composition of fissile isotopes in the pins and for yields of the examined fission products.

Table 3 shows the list of the thermal neutron yields for U235, Pu239 and Pu241 issued from JEF2[3] for the fission products utilized in this work.

The total estimated uncertainty, obtained as a quadratic combination of the elementary ones (see table 2) is of about ± 2.5 % at 1 σ.

IV - UNCERTAINTY VALIDATION

As a general principle there is no doubt about the uncertainties obtained, when relative power distributions are measured inside an homogeneous core : the technique is very simple either one utilizes U235 fission chambers, thin fissile foils (with the same diameter as the pin) located inside the fuel and/or integral gamma scanning on the irradiated pins.

In fact in this case (and for all the announced technics) the counting rates are proportional to the fissions or the power of the zone under examination. Therefore the comparison of the axial and radial fission rate distributions obtained with the different technics is enough to confirm the uncertainties.

The measurements on particular γ ray peaks present several problems concerning experimental technique and basic nuclear data :

- the determination of the net peak area for each kind of fuel in the presence of background which is different in intensity and in energetic distribution,
- the evaluation or the measurement of the yields for the used fission product,
- the calculation of the self-shielded fission cross sections, which determine not only the absolute number of fissions in the fuel, but their distributions inside the pins with a different γ attenuation between the production and the detection point.

A global verification of the announced uncertainties can be realized by a comparison between calculations and measurements in substitution experiments : a Pu pin (with different enrichments) replaces an U equivalent one in the central part of a homogeneous medium.

In this case interface perturbations, generally present in calculations of Mox assemblies, are minimized and the differences between the fission rates calculated and measured in U and Pu pins (with regard to similar experiments in a homogeneous medium) must depend only on experimental uncertainties.

IV.1 - Buckling measurements

Buckling determination, used to check the neutron balance calculations, is based on fission rate measurements which were performed by using the usual techniques : fission chambers, fissile foils and integral gamma scanning of irradiated fuel pins.

The mean value found during this measurement campaign, together with the critical mass, and the power distributions, confirms the precedent results obtained in 1989 on a similar configuration[1]. The comparison (table 4) shows the validity of the experimental method and the lack of systematic

errors due in particular to fuel rearrangement in the core. Therefore only counting statistics can be considered as the largest source of uncertainty, when relative fission rate distributions are measured.

IV.2 - Irradiations in a reference thermal flux

By successive irradiations in the graphite column of the Harmonie reactor, where the neutron flux is well thermalised (see table 5), we have validated step by step the measurement technic, based in the counting of particular gamma ray peaks.

a) Irradiations of thin U foils with different U235 enrichment are made to validate the determination of the net counting rate of the peak of interest after the overlapping peaks (due to other fission-product gamma rays) are subtracted.

The results, presented in table 7 for the peak of the La^{140}, show a satisfactory agreement : the largest difference is about 4 %, and on average, the discrepancies on the ratios between U235 nuclides and measured activities are within the range of the foreseen uncertainties.

b) Simultaneous irradiations of U and Pu foils to validate, together with the first point, thermal cross-sections and yields.

c) Irradiations of several pairs of U and Pu pins to confirm the totality of measurement uncertainties.

The mean value of the ratio between Pu and U experimental and calculated activities :

$$\frac{\text{Pu (counts)}}{\text{U (counts)}} \Big/ \frac{\sum_i \text{Ni ri Yi}}{(N\,\sigma\,Y)U^5} = Pu^9,\ Pu^{41},\ U^5 \qquad (1)$$

is equal to 0.96 which is just inside foreseen uncertainties and therefore confirms the validity of the measurement procedure.

IV.3 - Substitution measurements

A parametric approach has been followed during these substitution measurements : in fact different Pu pins with enrichment ranging from 4.3 % to 11 % were loaded in the centre of the U core. The power distribution was measured pins by pins in the whole of the central part of the core by the usual technics (see fig. 3).

The analysis of the experimental results has been performed using :

- the Apollo[4-5] cell-code to provide self-shielded multigroup cross sections and to homogenize the different cells,
- the Bistro[6] Sn transport code for two dimensions XY core calculations.

The comparison between the calculated and measured reaction rates, seems to show a good agreement between those results inside the announced uncertainties.

So this analysis seems to confirm the validity of the measurement technic.

V CONCLUSIONS

The Epicure program, restarted in July 90 after the replacement of the control board of Eole, is planned to last for 3 years

Reduction of uncertainties in the main parameters related to safety and operation in a Mox core will be a logical consequence of the analysis of this experiment, in particular for power distribution In fact the results, we obtained during the measurement campaign reported in this paper, have shown that the experimental methods used are not only well suited to simulate measurements in a standard PWR, but also that associated uncertainties are always lower than ± 5 % (at 2 σ), as evaluated, on the basis of a quadratic combination of elementary uncertainties related to each measurable parameter, in a Mox assembly

Therefore they can be considered suitable for the validation of calculation methods

REFERENCES

1 J Mondot, J P Chauvin, P Chaucheprat, A Vallee, J C Lefebvre
Epicure an Experimental Programme devoted to the validation of the calculational schemes for Plutonium Recycling in PWRs in proc of Physor (Vol 1 VI-53) - Marseille (France) - April 1990

2 J Mondot & al
Private communication

3 Nordborg C - Conference Julich - 13-17 May 1991

4 A Kavenoky, "APOLLO A General Code for Transport, Slowing-Down and Thermalization Calculations in Heterogeneous Media" Proc Natl Topl Mtg Mathematical Models and Computational Techniques for Analysis of Nuclear Systems, Ann Arbor, Michigan, April 9-11, 1973

5 R Sanchez and J Mondot "APOLLO II A user Oriented Portable, Modular Code for Multigroup Transport Assembly Calculations" Nucl Sci Eng - 100, 352-362 (1988)

6 G Palmiotti & al , "Optimized two Dimension Sn transport (BISTRO)", Proc International topical meeting on advances in reactor physics, mathematics and computation, April 1987 PARIS, Vol 2 p 615

Table 1. Characteristics of gamma-ray utilised for fission rate distribution

Isotope	Half-life (d)	Gamma-ray energy (KeV)
La 140	12.746	1596.17
Zr 95	64.06	756.74 - 724.23
Ru 103	39.276	497.08
Sr 92	0.1129	1380.0

Table 2. Uncertainties on fission-rate measurements (1 σ) uncertainties

	Uncertainties		Observations
Integral measurements	pin linear mass	< 1 %	used for pins of the same fuel
	counting statistic*	< 1 %	
	Total	between 1 % and 1.4 %	
Single peak measurements	pin linear mass	< 1 %	used for pins of different fuels
	counting statistic*	< 1 %	
	background (overlapping peaks)	1 %	
	ratio of fission product yields	1.5 %	
	cross section self shielding	1 %	
	Total	2.5 %	

* Comprehensive of positionning errors in the core or in the counting system.

Table 3. Fission yields for thermal neutrons[3]

	Sr 92	Ba 140	Zr 95	Ru 103
U 235	5.851	6.214	6.490	3.104
Pu 239	2.999	5.261	4.917	6.895
Pu 241	2.264	5.807	3.967	6.780

Table 4. Buckling measurements : reproducibility using different experimental techniques

Technique	ΔB^2 (%)*
Integral gamma measurements	
N° 1	0.0 ± 1.5
N° 2	0.0 ± 1.5
N° 3	0.0 ± 1.5
Fission chambers	
U 235	+ 0.2 ± 2.1
U 238	- 0.4 ± 2.1
Pu 239	- 0.1 ± 2.1
Np 237	+ 0.3 ± 2.1
U 235 foils	+ 0.4 ± 1.2

* ΔB^2 represents the difference between each measured value and the mean value obtained by averaging all measurements.

Table 5. Cadmium ratio* values measured in the thermal column of Harmonie

U 235 (n,f)	2260
U 238 (n,γ)	63
Pu 239 (n,f)	3530
Au 197 (n,γ)	326

μm thick

* standard Cd box 1 mm thick

Table 6. Thermal cross sections utilized in the analysis of the experiments (barns)

	Infinite dilution	in the U pin	in the Mox pin
U 235 (n,f)	568.7	264.4	222.3
Pu 239 (n,f)	789.5	-	328.3
Pu 241 (n,f)	1057.6	-	430.3

Table 7. A relative comparison of fission foil activities for La 140 gamma-ray

Measurement number	U 235 nuclide ratio	Measured activity ratio	Mean difference for the same type of foil
1	2.019	2.010	0.5 %
2	4.50	4.31	4 %
3	2.23	2.15	2 %
4	2.23	2.23	
5	4.67	4.52	
6	4.67	4.70	0.2 %
7	4.67	4.77	

Fig. 1

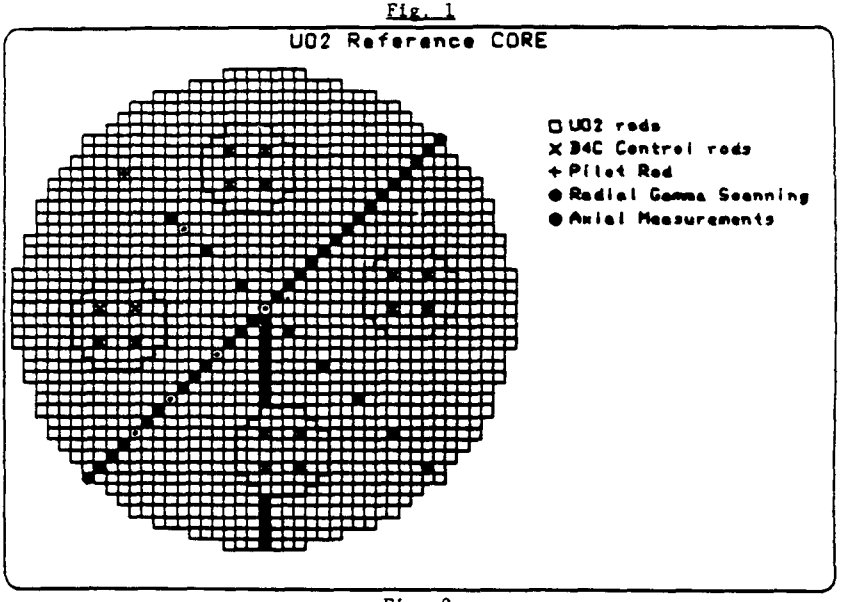
UO2 Reference CORE
UO2 rods
B4C Control rods
Pilot Rod
Radial Gamma Scanning
Axial Measurements

Fig. 2

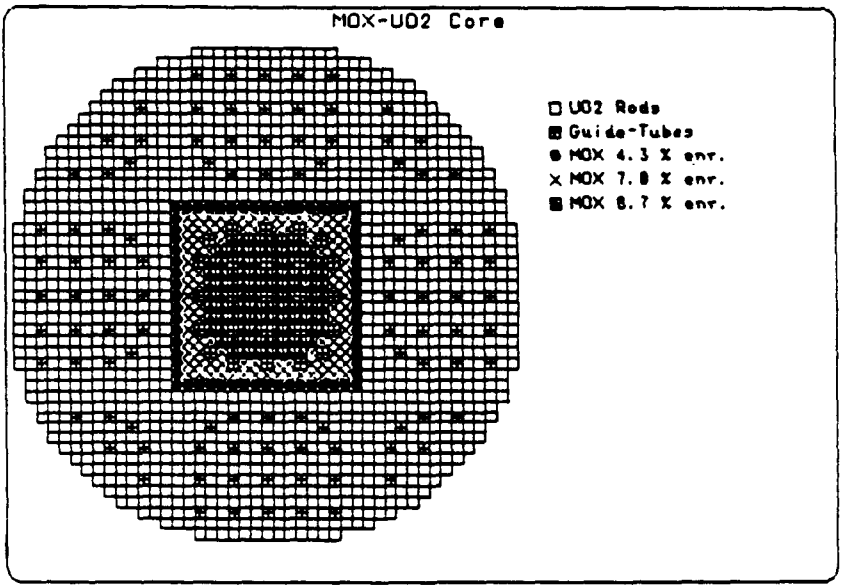
MOX-UO2 Core
UO2 Rods
Guide-Tubes
MOX 4.3 % enr.
MOX 7.0 % enr.
MOX 8.7 % enr.

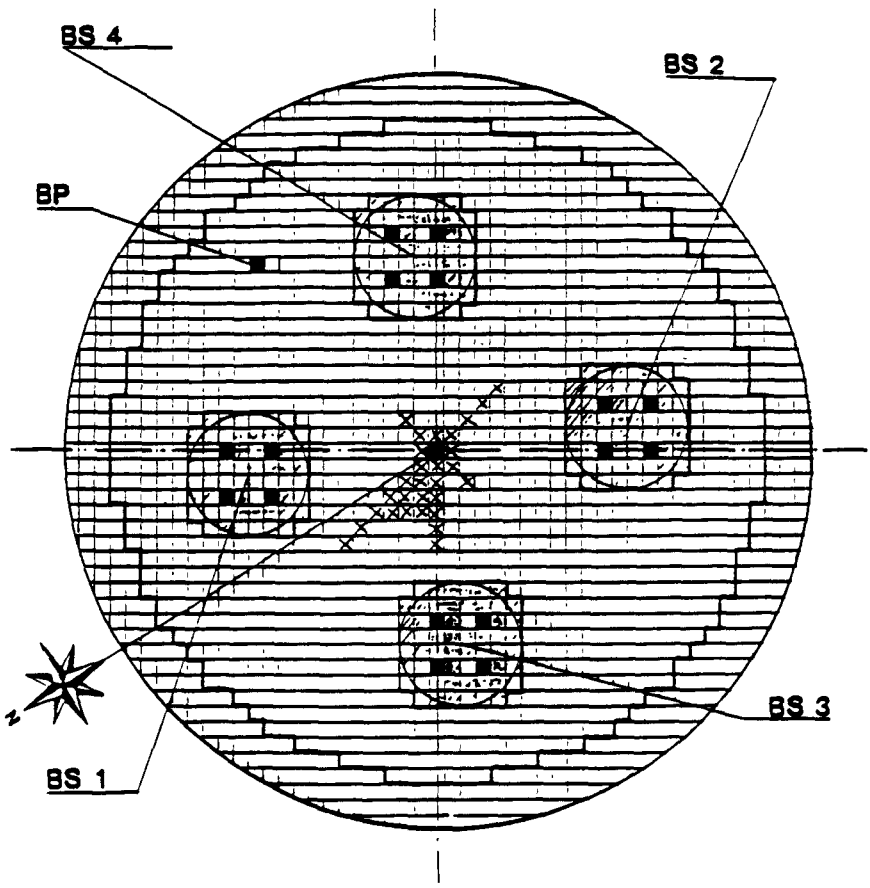

Fig. 3. Measurements positions for central Mox substitution experiment

VALIDATION OF BASIC NUCLEAR DATA FOR HCLWR USING ZERO POWER CRITICAL EXPERIMENTS

S. CATHALAU

Commissariat a l'Energie Atomique
Centre d'études nucléaires de Cadarache
Service de Physique des Réacteurs et du Cycle
Département d'Etude des Réacteurs.
13108 St-Paul-lez-Durance-FRANCE

ABSTRACT

During the past few years, a major effort has been made in France to obtain experimental validation of neutronic parameters of undermoderated lattices fuelled with mixed oxide, for which the fundamental neutronic parameters are not so well-known as those concerning uranium oxide lattices. In order to reduce the uncertainties, an extensive experimental program has been undertaken, associated with some adaptations of the cell codes. This paper presents the first qualification of the new library based on the European Data File JEF-2 using "benchmark" experimental results obtained in the ERASME experiments and compared with the CEA-86 library results.

INTRODUCTION

Since 1984, an extensive experimental program has been devoted to the validation of the High Conversion Light Water Reactor ('**HCLWR**') concept in order to reduce the uncertainties in calculations of the fundamental parameters. In 1982, our sensitivity studies indicated very big uncertainties in calculated fundamental parameters (+/- 5000 pcm on Keff, +/- 10 % on conversion factor and +/- 40 pcm/% of void on global voidage coefficient for example).

The French experimental program comprises 3 types of experiments designed to validate HCLWR calculational methods : the ERASME[1-3] experiments which were devoted to the measurement most of the fundamental neutronic parameters of HCLWRs which could be obtained in the zero power critical facility EOLE at Cadarache ; the MORGANE[4-6] experiments which have been carried out in the zero power pool reactor MINERVE at Cadarache in order to measure the total fission-product capture effect by oscillation

techniques ; the **ICARE**[7] experiments centered in the MELUSINE power reactor at Grenoble for measuring the capture cross-sections of the major heavy nuclides and of some fission-products.

At the same time, some of improvements have been made to the cell codes : a new self-shielding calculation method for resonance overlapping, treatment of the self-shielding and Doppler broadening effects of the "thermal" resonances of 240Pu and 242Pu respectively at 1.06 eV and 2.68 eV, a new cross-section library involving new evaluations and a method for triangular pitch geometry collision probability calculations. Furthermore, a new cross-section library based on the JEF-2 nuclear data base[8] is still under development : the experimental results obtained from the validation program are very useful for its qualification.

This paper presents the results obtained from these experiments which are suitable for the validation of the basic nuclear data. In particular, we propose experimental results carried out in the ERASME experiments as benchmark exercises for the cell codes APOLLO-1[9] and APOLLO-2[10] with the associated nuclear data library "CEA-86" and the new library based on the European nuclear data file JEF-2.

THE ERASME EXPERIMENTS

These comprised 3 phases devoted to the measurement of the main fundamental parameters (Keff, conversion factor, spectral indices, absorber worths,...) and specific characteristics concerning reactor design and safety (voidage coefficient, clusters, power maps, boron efficiency,...), over all the moderation ratio range involved in HCLWR design (Vm/Vf=0.5, 0.9 and 2.1).

The two tighter lattices (ERASME/S and ERASME/R with moderation ratios respectively Vmod/Vfuel=0.5 and 0.9) comprising 1500 and 1200 mixed oxide fuel rods (11% total Pu) with stainless steel cladding were centered inside a PWR driver core built with 3.5 % enriched UO2 fuel pins and having a size which was adapted to obtain the criticality of the core. In order to improve the spectrum adaptation, a buffer zone comprising 550 UO2 rods in tight pitch stainless-steel clad, was located between the test zone and the driver core (Fig 1). The tight lattices were placed in a water-tight vessel of aluminium and stainless-steel (in order to measure the global voidage effect).

In order to carry out very accurate measurements (to obtain +/- 0.3 % in $\delta k/k$ consistent with the HCLWR design requirements), the design of each zone of the core has been optimized (radius of the test zones, thickness of

the adaptation zone and the water-tight vessel, same fuel height in order to limit the 3D effects).

The test zone for the largest pitch experiment (ERASME/L with a moderation ratio of 2.1) was in two forms : a square array of 800 rods with no soluble boron in the first study, and 1560 UPuO2 rods with 1550 ppm of soluble boron in the second phase (fig. 2). These experiments have been carried out in order to have a third validation point concerning undermoderated lattice calculations and to constitute a first point of Pu recycling experimental validation.

The measurements carried out in the ERASME experiments were concerned :

* Determination of the buckling through reaction rate distributions,

* Conversion factor through the measurement of the spectrum index $\sigma_c^{238}U/\sigma_f^{235}U$,

* Fission rates of the major heavy isotopes (^{235}U, ^{238}U, ^{239}Pu, ^{240}Pu, ^{241}Pu and ^{242}Pu),

* Absorber worths and cluster configurations (natural and enriched B4C, Ag-In-Cd alloy, natural hafnium, guide-tubes, depleted fertile UO2 rods).

CALCULATIONAL SCHEME

CELL CODE

In order to improve the accuracy of calculations for HCLWR, the APOLLO-1 transport code was developed in both nuclear data and calculational method fields :

* A 99 group library was produced in 1986 and implemented in APOLLO. This "CEA-86" cross-section set was based on recent data files (ENDF/BV, JEF 1). In the same way, a new cross-section library is now being developed and implemented in APOLLO-1 and APOLLO-2, based on the JEF-2 data file.

* New routines have been developed in APOLLO-1 (Hexagonal cell collision probability calculations, a more accurate model for treating resonance interference between nuclides, and a new procedure in order to improve resonance self-shielding and Doppler calculations in the "thermal" neutron range specifically for 240Pu and 242Pu).

The new cell code APOLLO-2 is a user-oriented, portable modular code for multigroup transport assembly calculations using collision probability or Sn methods.

It uses sophisticated software for data structuring, using dynamic memory management and a user macrolanguage. Several specific developments have been devoted to the self-shielding calculation method and especially to heterogeneous/homogeneous equivalence (1 Bell factor per group for example).

These codes are essentially used to qualify the fundamental parameters and to homogenize and to collapse the cross-sections used in the core calculations.

CORE CALCULATION CODE

Core calculations have been performed by using the BISTRO code[11] which solves the transport equation using the Sn approximation, and was previously devoted to fast breeder core calculations : a new module for up-scattering treatment has been implemented in the code in order to perform light water core calculations.

Some perturbation modules included in this code allowed us to perform sensitivity coefficient calculations[12] and representativity factors were calcultated for each core and each fundamental parameter in order to qualify the new cross-section library.

Core calculations have been made by using the following scheme : cell calculations by APOLLO-1 (CEA-86 procedure) in order to homogenize and collapse to 47 groups using a transport-transport equivalence for heterogeneities (guide-tubes, absorbers, etc...), followed by BISTRO whole core calculation.

BENCHMARKING PURPOSE

Preliminary measurements showed that the fundamental mode was established over a large tight lattice zone. Our experimental techniques allowed us to obtain the fundamental parameters (Keff, conversion ratio, spectrum indices and absorber worths) with an accuracy consistent with the requirements for basic nuclear data qualification.

CALCULATIONS

Table 1 presents our cell calculations of Keff obtained with the libraries CEA-86 (APOLLO-1 and APOLLO-2) and JEF-2 (APOLLO-1). These results show the good agreement between the calculations performed with the APOLLO-1 and APOLLO-2 cell codes with the CEA-86 procedure and the experimental values. The JEF-2 library gives more accurate Keff values at about 150 pcm lower than those CEA-86. Furthermore, the slope seems to be lower and the results are more centered. However, these results are preliminary and must be analysed in more

detail, especially including the sensitivity coefficient calculations performed with the BISTRO code (examples are given fig. 3 to 5). Furthermore, an extensive study is being actually devoted to the overlapping resonance and self-shielding effects, and the down-scattering model in order to understand the same trends observed with the "adjusted" CEA-86 library and the new JEF-2 library.

Table 2 presents the experiment/calculational discrepancies concerning the conversion factor and the spectral indices. The spectral index $\sigma f9Pu/\sigma f5U$ results indicate an overestimation of the 239Pu fission resonance integral in the CEA-86 library (JEF-1 nuclear data processed with the Reich & Moore formalism) and more accurate results with the new JEF-2 library. The calculated spectral index $\sigma f238U/\sigma f235U$ is in agreement with the measurements but the positive C/E discrepancy observed with the JEF-2 library in each case, seems to indicate that the 238U capture rate is too high that is not consistent with the trend observed on Keff calculations (table 2 and the figure 6 which presents $\sigma f238U/\sigma f235U$ sensitivity coefficient profiles to 238U capture). Table 2 also shows that the 240Pu and 241Pu fission cross-sections seem to be too high in the high energy range, 242Pu fission cross-section is too low.

Table 3 presents the results obtained for the absorber worths (normalized to 1.00 for natural B4C) using the new hexagonal pitch collision probability calculational method in APOLLO-1. These results show that the nuclear data for absorbers in the "CEA-86" library are satisfactory for HCLWR control rod calculations. The JEF-2 results do not show any significant variation in the C/E discrepancies.

The BISTRO code allowed us to qualify the absolute absorber worth in the core ERASME/L. The results are summarized in table 4 : the calculation gives results in very good agreement with the experiment for natural and enriched B4C. Nevertheless, AIC worth seems to be overestimated (as presented in table 3) : this could result from an underestimation of Ag nuclide self-shielding and resonance overlapping with those of 238U. In order to qualify directly the absorber cross-sections and the collision probability calculational methods, we have defined benchmark experimental values using the following formula :

$$p_{ben} = p_{exp} \cdot \frac{\phi_1^{APOLLO}}{\phi_1^{BISTRO}} \qquad (1)$$

Where :

p_{ben} : "Normalized" fission rate for benchmarking validation.

P^{exp} : Experimental fission rate.

^{BISTRO} : Fast flux calculated by the BISTRO code.

^{APOLLO} : Fast flux calculated by the APOLLO code.

This formula assumes accurate spatial calculations with the BISTRO code and a good fast spectrum obtained by APOLLO (An experimental validation of this formula is actually carried out in the EPICURE experiment[13,14] by measuring the fast flux with depleted uranium foils inserted directly in the fuel). Figures 7 and 8 present the C/E discrepancies concerning fission rate distributions around the central enriched and natural B4C rod in the ERASME/L experiment using the formula 1. The APOLLO calculated values (with CEA-86 and JEF-2 libraries) are in good agreement with the experimental results (JEF-2 values seem to be better than CEA-86 values). Figure 9 presents an example of fission rate distribution calculated values (BISTRO) for enriched B4C compared with the experimental values. The observed C/E discrepancies are included in the experimental uncertainties (2 = +/- 2.5 %).

CONCLUSIONS

The ERASME studies give the HCLWR fundamental parameters with low experimental uncertainties which allow us to validate basic nuclear data in undermoderated neutron spectra. In particular, the APOLLO-1 and APOLLO-2 calculations using the CEA-86 library and associated procedures do not show any significant experimental/calculational discrepancies. Keff is calculated with an averaged uncertainty of about + 350 +/- 400 pcm, and the mean calculated spectral indices are consistent with the experimental uncertainties.

For the preliminary JEF-2 evaluation, our calculations give more accurate results on Keff, and the slope in function of the moderation ratio is lower than these observed with CEA-86 library. An overestimation of the 238U capture resonance integral by about 1 or 2 % is also observed. These preliminary results and especially the different trends, must be confirmed and especially analysed by sensitivity coefficient calculations.

The results concerning the absorber worths did not show great discrepancies between the JEF-2 cross-sections and experimental values. A normalization method for experimental fission rates has been studied in order to validate directly by using "multicell" approximation calculations : no experimental/calculational discrepancies have been found and after the experimental validation of the normalization formula, a large

experimental data base will be at our disposal to qualify the new absorber JEF-2 cross-sections.

REFERENCES

1 A. SANTAMARINA, L. MARTIN-DEIDIER, S. CATHALAU et Al., "ERASME : An Extensive Experiment for LWHCR Design Qualification" Top. Meet. on Reactor Physics - Saratoga Springs Sept 1986.

2 A. SANTAMARINA, S. CATHALAU, L. MARTIN-DEIDIER et Al., "Undermoderated PWR Neutronic Qualification Through the ERASME Experiments" Top. Meet. on Advances in Reactor Physics, Mathematics and Computation. Paris (France) 1987.

3 J.P. CHAUVIN , G. PALMIOTTI "ERASME : An Experimental Program to Validate the Fundamental Neutronic Parameters in LWHCR Spectrum Experiment and Sensitivity Coefficient". Top. Meet. on Reactor Physics. Marseille (France) April 1990

4 J. MONDOT ,P. CHAUCHEPRAT et Al. "MORGANE/S : Fission-Product Capture Measurements in a HCLWR Tight Lattice". Top. Meet. on Reactor Physics - Jackson Hole (USA) Sept 1988

5 P. CHAUCHEPRAT and J. MONDOT, "Synthesis of the Experimental Validation of Global Fission-Product Capture for PWR's and Advanced Reactors," Top. Meet. on Reactor Physics - Marseille (France) April 1990

6 J. MONDOT, J.P. CHAUVIN and J.P. WEST "Validation of Fission Product Capture Cross-Sections by the Analysis of Thermal and Epithermal Integral Experiments," Int. Conf. on Nuclear Data for Science and Technology. Julich (Germany) May 1991.

7 P. CHAUCHEPRAT, L. MARTIN-DEIDIER, J.M. GOMIT. "ICARE Experiments for the Qualification of Capture Cross-Sections in the Neutron Spectrum of Undermoderated Reactors." Int. Conf. on Nuclear Data for Science and Technology. Mito (Japan) June 1988.

8 K. NORDBORG , NEA-DATABANK - Saclay. Personnal communication.

9 A. KAVENOKY, "APOLLO : a General Code for Transport, Slowing-Down and Thermalization Calculations in Heterogeneous Media," Top. Meet. on Mathematics and Computation Techniques for Analysis of Nuclear Systems. Ann Arbor (Michigan) April 1973.

10 R. SANCHEZ, J. MONDOT et Al., "APOLLO-II : A User-Oriented, Portable, Modular Code for Multigroup Transport Assembly Calculations." Nucl. Sci. & Ing.,100 (1988).

11 G. PALMIOTTI, J.M. RIEUNIER, et Al.,"Optimized Two Dimension Sn Transport (BISTRO)". Top. Meet. on Reactor Physics. Paris (France) April 1987

12 J.P. CHAUVIN and G. PALMIOTTI, "ERASME :An Experimental Programme to Validate The Fundamental Neutronic Parameters in LWHCR Specturm Experiment and Sensitivity Coefficient" Top. Meet. on Reactor Physics. Marseille (France) April 1990

13 J. MONDOT, J.C. GAUTHIER, et Al., "EPICURE : An Experimental Programme Devoted to the Validation of the Calculational Schemes for Plutonium Recycling".Top. Meet. on Reactor Physics. Marseille (France) April 1990

14 J.P. CHAUVIN, G. GRANGET, M. MARTINI et Al., "Validation of the Experimental Methods used in the EPICURE Programme and Their Associated Uncertainties". To be Published at this Conference.

Table 1. Keff Calculations

K eff (C-E)/E	ERASME/S MR=0.5 0 ppm	ERASME/R MR=0.9 0 ppm	ERASME/L MR=2.1 0 ppm	ERASME/L MR=2.1 1650 ppm
AP1 a	+ 740	+ 280	+ 130	+ 100
AP1 b	+ 570	+ 290	+ 50	+ 160
AP2 a	+ 720	+ 300	- 220	+ 180
σexp *	560	540	280	300

* 2 s.d. experimental uncertainties.
a : CEA-86 library.
b : JEF-2 library.

Table 2. Spectral indices interpretation.
(C-E/E in %)

S. Index	ERASME/S	ERASME/R	ERASME/L
σf238U	+ 0.4 (a)	+ 0.9	+ 1.8
-------	5.0 (c)	5.0	4.0
σf235U	+ 3.6 (b)	+ 5.0	+ 5.0
σf239Pu	+ 3.9	+ 1.8	- 1.3
-------	4.0	4.0	4.0
σf235U	+ 2.0	+ 0.6	- 1.6
σf240Pu	- 3.9	- 8.1	- 9.1
-------	8.0	8.0	7.0
σf239Pu	+ 7.5	+ 4.1	+ 2.8
σf241Pu	- 0.6	- 3.4	- 2.7
-------	6.0	6.0	5.5
σf239Pu	+ 5.9	+ 2.2	+ 2.0
σf242Pu	- 9.4	- 2.3	+ 0.5
-------	10.0	10.0	10.0
σf239Pu	- 4.7	+ 3.6	+ 5.5
σc238U	+ 3.4	+ 2.3	Not
-------	4.6	4.2	
σf235U	+ 5.8	+ 4.4	Measured

(a) : CEA-86 library.
(b) : JEF-2 library.
(c) : 2σ experimental uncertainty.

Table 3. Absorber worth interpretation (CEA-86 library)

Absorber	ERASME/S		ERASME/R		ERASME/L	
	Exp	Cal	Exp	Cal	Exp	Cal
Enr. B4C	/	/	-1.79	-1.70	-1.54	-1.53
Nat. B4C	-1.00	-1.00	-1.00	-1.00	-1.00	-1.00
Nat. Hf	-0.68	-0.70	-0.69	-0.70	-0.75	-0.74
Ag-In-Cd	-0.63	-0.64	-0.65	-0.67	-0.70	-0.73
Dep. UO2	-0.07	-0.07	-0.04	-0.05	-0.06	-0.06
Guide-Tube	+0.10	+0.09	+0.12	+0.11	+0.03	+0.03

Table 4. Absorber worth (ERASME/L Core calculations)
CEA86-Exp in pcm.

Absorber	Diffusion	Trans. P0	Trans. P1
Enr. B4C	- 83 %- 35 a	+ 0 %- 35	- 3 %- 35
Nat. B4C	- 40 %- 40	+ 10 %- 40	+ 14 %- 40
Ag-In-Cd	- 57 %- 40	- 29 %- 40	- 49 %- 40

a : 2σ experimental uncertainty

Figure 1 : Radial Cross-Section
of ERASME/S & R Experiments

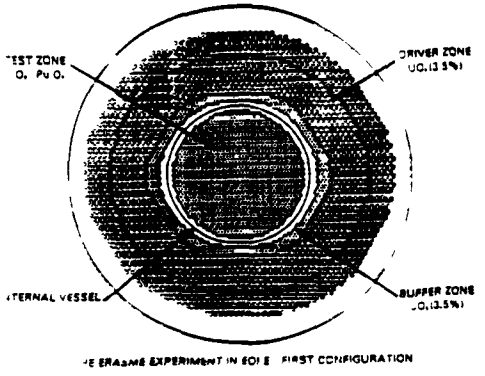

E ERASME EXPERIMENT IN EOLE FIRST CONFIGURATION

Figure 2 : Radial Cross-Section
of ERASME/L Experiment.

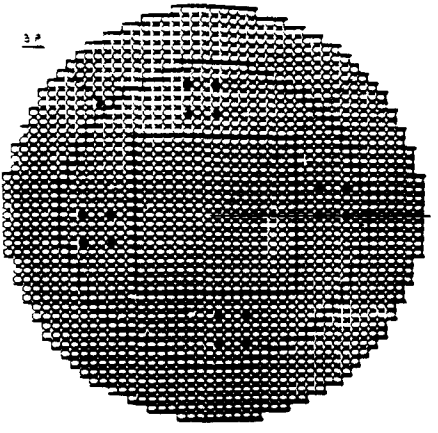

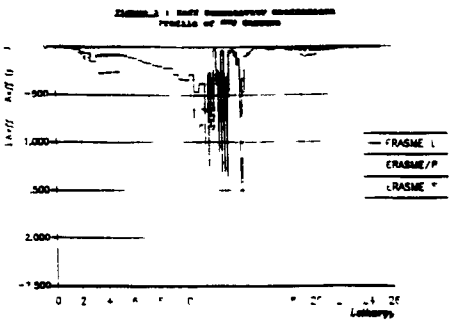
ERASME L
ERASME/P
ERASME

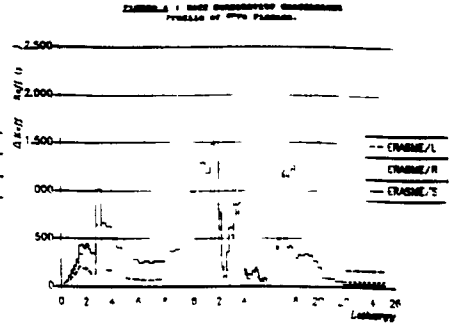
ERASME/L
ERASME/R
ERASME/S

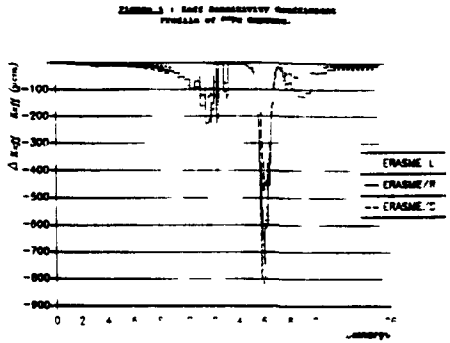
ERASME L
ERASME/R

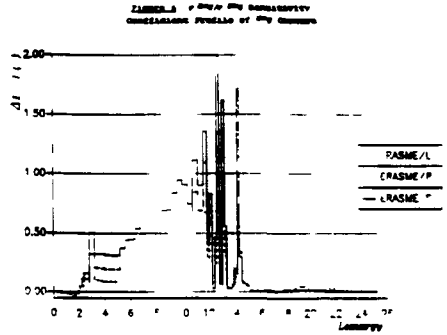
ERASME/L
ERASME/P

		+ 1
		1 4
	1 1	
	1 1	
	+ 0 4	
	+ 0 4	
	- 0.2 (a)	+ 0.3
	+ 0.0 (b)	+ 0.3
	+ 0 4	+ 1 0 + 0 1
	+ 0.2	+ 0 9 + 0 1

(a) CEA-86 library

(b) JEF-2 library

		+ 0.5
		+ 0.5
	+ 0 6	
	+ 0 6	
	+ 0 8	
	+ 0 8	
	+ 0.3 (a)	- 2.3
	+ 0.2 (b)	- 2.3
	- 0.2	+ 0 3 + 0 4
	- 0.1	+ 0.3 + 0 4

(a) CEA-86 library

(b) JEF-2 library

			+ 0 1
			+ 0.2
		- 0.6	
		- 0 4	
	0 0		
	+ 0 3		
	- 1 5 (a)	0 0	
	- 2.0 (b)	+ 0 4	
	- 1 1	+ 1 4	+ 0.2
	- 2.8	+ 2.0	+ 0 8

(a) Transport P1/S8

(b) Diffusion

RE-EVALUATION OF SAVANNAH RIVER REACTOR TRANSIENT REACTIVITY COEFFICIENT TESTS: THE EFFECT OF DELAYED NEUTRON CONSTANTS AND SPATIAL VARIATIONS

by

T W T Burnett
Westinghouse Electric Corporation
Pittsburgh, Pennsylvania
and
W E Graves
Westinghouse Savannah River Company
Aiken, South Carolina

ABSTRACT

Transient reactivity tests conducted in one of the Savannah River production reactors in 1962 have been re-evaluated A significantly lower (more negative) coolant temperature coefficient is now ascribed to that test, -1 pcm/Deg-C vs the previously obtained +2 pcm/Deg-C The change from the previous value is because of revisions to delayed neutron constants and accounting for spatial effects The new value is in reasonable agreement with the currently calculated value of -2 pcm/Deg-C, considering measurement and calculational uncertainties Therefore, we conclude that the current analytic models for physics and transient analysis are fully consistent with the 1962 test observation, and that there is no basis for assigning a calculational bias or increasing uncertainty allowances

INTRODUCTION

In 1962, transient reactivity tests were conducted in one of the Savannah River Production reactors containing a uniform lattice tritium producing charge In these tests, special "delta-k rods' were used to introduce a small, rapid reactivity perturbation (about 30 pcm in 75 milliseconds) The change in measured flux was used to infer a set of reactivity coefficients At the lowest reactor exposure, a +2 pcm/Deg-C prompt feedback coefficient (from the coolant channel), when combined with the point kinetics and thermal kinetics models in use at the time, gave the closest fit to the observed flux response in the first few seconds after the reactivity perturbation Because of the design of the SRS reactors, isothermal coefficients are neither meaningful nor easy to measure, so this 1962 test has been considered to be the only reactor measurement of the prompt reactivity coefficient in a tritium producing reactor

As part of establishing the reactor physics and safety analysis methodology in 1989-90 for reactor restart, Westinghouse Savannah River Company committed to revisit this 1962 test with current calculational methods used for physics and for transient analysis, for the purpose of justifying the uncertainty assigned to current calculations of reactivity coefficients

Current physics methods calculated an effective prompt coefficient at low exposure of -2 3 pcm/Deg-C (fuel, coolant, and target were computed as 0 0, -2 2, and -0 1 pcm/Deg-C, respectively), with a uncertainty in the range of 1 to 1 5 pcm/Deg-C The discrepancy of 4 pcm/Deg-C from the 1962 observation required investigation and explanation

DISCUSSION

We must emphasize that the 1962 tests did NOT measure reactivity coefficients The test measured the transient response to a reactivity perturbation of unknown magnitude Reactivity coefficients can be inferred from the test results, based on analytic models for the transient response and spatial effects Errors in these models -- as well as errors in the test measurements -- would cause error in the inferred coefficient.

Our re-evaluation of the 1962 test data found the best fit for a prompt coefficient of -1 3 pcm/Deg-C, or about 1 pcm/Deg-C more positive than the current calculated coefficient. The current prompt coefficient inferred from the test data is 3 pcm/Deg-C more negative than historic inferred values The more negative value is caused by·

- Revised delayed neutron constants[1] Estimated delayed neutron parameters have shifted considerably in the last two decades In particular, the shortest delayed neutron group fraction has increased four-fold, compared to the Keepin data[2] used in the earlier analysis, affecting the very short-term response to a step reactivity change This has little effect on safety analysis, but has a marked effect on estimating the feedback effects from a reactivity step of unknown magnitude The change in delayed neutron constants alone decreases (makes more negative) the inferred prompt coefficient by 2 pcm/Deg-C.

- Spatial effects Prior evaluations of the 1962 tests assumed that the detector response was proportional to core power. That's not strictly true The delta-k perturbation was near the center of the core, changing the relation between detector and core average power by about 0 7% That's a far bigger effect than it appears For example, where the detector reported a 4 3% increase, the core average power probably increased 4 3% plus 0 7%, or 5 0% -- at least a 15% larger change than previously considered This effect decreases the inferred prompt coefficient by about 1 pcm/Deg-C

  The change in the shape was found to be accurately fit by the equation, Tilt(t) = A*[1-B*F(t)], where A is the steady state tilt (1 007 in this case), B is the fraction delayed (098 in this case), and F(t) is the delayed neutron relaxation function, or Sum{ Beta(i) * Exp[-Lambda(i)*t]} / Sum{ Beta(i) }

- Improved transient models Current transient models permit explicit modeling of each tube in the fuel assembly, and also a more accurate representation of flow patterns in the moderator tank Because the fuel temperature changes both more and faster than does the coolant temperature, explicit modeling of fuel temperature feedback has been found necessary In this particular instance, however, these improvements had no effect The calculated fuel coefficient is zero for the 1962 core at beginning of cycle, and the calculated target coefficient is very small (-0 1 pcm/Deg-C) Also, attention is limited to the first few seconds, when potential error in the moderator flow patterns will have little influence

Both the size of the reactivity insertion, dk, and the feedback effects are unknowns that must be inferred from the test observations The current inferred results, compared to the 1962 inferences, are tabulated below for the size of the reactivity insertion and the prompt coefficients

Exposure (MWD)	dk, pcm		Prompt Coef, pcm/Deg C	
	Prior	Present	Prior	Present
14,000	28 5	36 8	+1 7	1 3
91,000	28 5	35 7	+0 5	2 4
199,000	32 5	39 7	2 0	5 0

Figure 1 shows the measured detector response, and the calculated response for the old and "new" evaluations The "old" evaluation included the old delayed neutron constants, had no spatial correction, and was fit with a dk of 28 0 pcm and a prompt coefficient of +1 6 pcm/Deg-C The 'new' evaluation included current delayed neutron constants[1], the spatial correction to core average power, and was fit with a dk of 36 8 pcm and a prompt coefficient of 1 27 Deg C The curves labeled "reactivity" are the total reactivity as a function of time that are consistent with the two power curves shown The difference in the shape of the reactivity curve is quite pronounced in the first two seconds

UNCERTAINTIES

Measurement uncertainties include (a) scatter in data points, (b) uncertainty in timing and shape of reactivity insertion, (c) uncertainty in initial test conditions, and (d) uncertainty in detector location The error due to those four components is estimated (at the 95% confidence level) to be in the range of 0 5 to 1 pcm/Deg-C

Uncertainties in delayed neutron constants are still significant despite advancements over the years In addition to basic uncertainties, the shape of neutron flux within the first few seconds may not be adequately described by the conventional six collapsed groups The uncertainties tend to increase for the shorter-lived precursors, which are important within the first few seconds Uncertainties in delayed neutron constants, as they would affect the shape of the flux response curve in the first few seconds are considered to contribute an uncertainty of perhaps 1 pcm/Deg-C to inferred temperature coefficients

In both of the areas just discussed, the effective uncertainties would have been smaller if measurements had been made at zero power as well as at power In that case, much of these uncertainties would have cancelled in comparing the cases If future measurements of this sort are made, this will certainly be done

Calculated temperature coefficients use a lattice physics code with associated cross section libraries Uncertainties in the calculation and cross sections, combined with uncertainties in material contents in the charge, are expected to be in the range 1-1 5 pcm/Deg C

The total of the above contributors to uncertainty appears to be in the neighborhood of 2 pcm/Deg-C Since the difference between the current inferred and calculated prompt temperature coefficients is only about 1 pcm/Deg-C, (comparable to the uncertainty allowance in the calculated coefficient alone), the discrepancy does not appear to be significant

CONCLUSIONS

We conclude that the current analytic models - the combination of physics and transient methodology - are fully consistent with the 1962 test observations, and that there is no basis for assigning a calculational bias or increasing uncertainty allowances.

ACKNOWLEDGEMENT

The information contained in this article was developed during the course of work done under Contract No. DE-AC09-89SR18035 with the U.S. Department of Energy.

REFERENCES

1. M.C. Brady and T. R. England, Delayed Neutron Data and Group Parameters for 43 Fissioning Systems, Nuclear Science and Engineering 103, 129-149 (1989).

2. G.R. Keepin, Physics of Nuclear Kinetics, Addison-Wesley Publishing Company, Reading, Massachusetts (1956).

FIGURE 1:

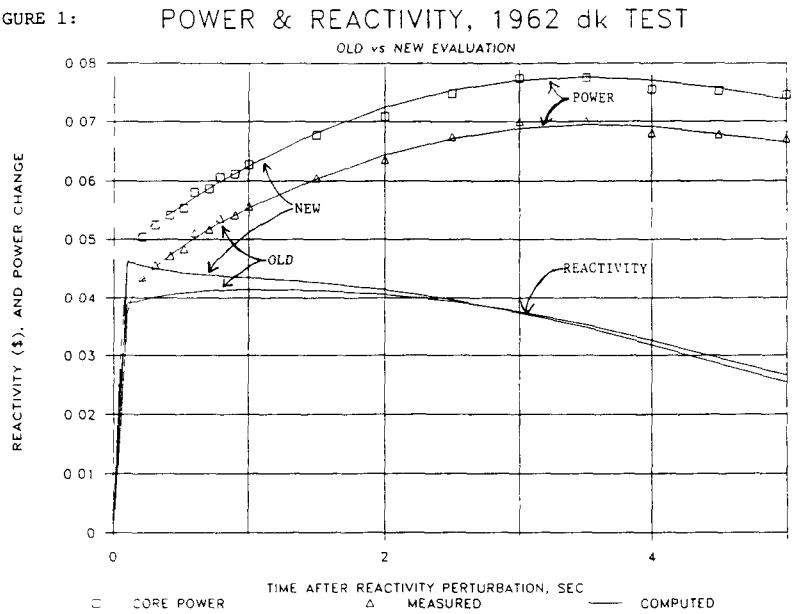

PROMPT NEUTRON LIFETIME IN A STRONGLY HETEROGENEOUS LATTICE

E. F. Trumble, N. P. Baumann & W. E. Graves
Westinghouse Savannah River Company
Savannah River Laboratory
Aiken, SC 29808

ABSTRACT

The prompt neutron lifetime is an important input parameter to the solution of the point reactor kinetics equations. In the past, many methods of determining the prompt neutron lifetime included the assumption that the thermal neutron lifetime was a good approximation to the prompt neutron lifetime. It has been found that strong heterogeneities within a lattice cause the calculation of the thermal neutron lifetime to significantly overpredict the prompt neutron lifetime. Therefore, a new method for the calculation of the prompt neutron lifetime is presented. This new method, the Alpha Search Method (ASM), is based on the time eigenvalue and does not suffer from the overprediction of the neutron lifetime as approximated by the thermal neutron lifetime. The causes of this overprediction, as well as comparisons of lifetimes computed by the ASM and other methods will be presented.

INTRODUCTION

The prompt neutron lifetime (ℓ_p) is an important input parameter to the solution of the point reactor kinetics equations. It is defined as the average time between a prompt neutron emission and its subsequent capture. The thermal neutron lifetime (ℓ) is a measure of the average time a neutron spends at thermal energies before being captured. For a thermal reactor, the majority of the time between a neutron's birth and it's capture is spent at thermal energies. Over the years, several methods have been developed to calculate the prompt neutron lifetime, or approximations to it. Many of these approximations, such as the thermal Inverse Velocity method, rely on "conventional wisdom" which dictates that for thermal reactors, the lifetime is dominated by thermal neutrons, and consequently little error accrues from the use of the thermal neutron lifetime as an approximation to the prompt lifetime. This is not necessarily true in strongly heterogeneous lattices such as those used at the Savannah River Site (SRS).

Explicit calculations of the prompt neutron lifetime have shown that calculation of the thermal neutron lifetime can result in the overprediction of the prompt lifetime by as much as 15% in a typical SRS lattice.

Therefore, a new method for calculating the prompt neutron lifetime has been developed. The Alpha Search Method (ASM) utilizes the results of an alpha (time eigenvalue) search performed by the GLASS lattice physics code to compute the full spectrum lifetime. This method has been found not to succumb to the same overprediction as the methods using the thermal neutron lifetime.

The Inverse Velocity method and the problems associated with its use in strongly heterogeneous lattices as well as the formulation of the new ASM will be presented. The Eigenvalue method has been chosen as a further comparison method to the two mentioned above, and results of these three methods for several different media will be shown and discussed.

DISCUSSION

INVERSE VELOCITY

Historically, the Inverse Velocity method has been used at SRS for the calculation of the neutron lifetimes. Based on the assumption that the thermal neutron lifetime is a good approximation of the prompt neutron lifetime, the following procedure was used to calculate the thermal lifetime.

Typically, GLASS is run and standard two-group macroscopic cross sections, such as the average thermal absorption cross section ($\overline{\Sigma_{a2}}$), are edited. A utility code, AVEVEL, evaluates the energy and space averaged inverse velocities ($\overline{1/v}$) over specified multigroup intervals. If the interval coincides with the thermal group in GLASS, then the Inverse Velocity method predicts the thermal neutron lifetime from the formula: [1]

$$\ell = \frac{\overline{1/v}}{\overline{\Sigma_{a2}}\left(1 + L^2B^2\right)} .$$

The term $(1+L^2B^2)$ accounts for leakage from the lattice. It was expected that the thermal neutron lifetime calculated by this method would be close to the prompt lifetime in SRS lattices because:

1) most reactions are thermal
2) for $1/v$ absorbers, lifetime is independent of neutron energy
3) in a highly enriched tritium producing charge, U-235 and Li-6 closely approximate $1/v$ absorbers.

Calculations for several different reactor media however, show that this method of determining the thermal neutron lifetime overpredicts the prompt lifetime value by as much as 15%.

The strong heterogeneities found in SRS lattices have been shown to cause the overprediction of the thermal neutron lifetime and consequently the prompt neutron lifetime. The overprediction was determined to arise from the heterogeneity of the lattice with absorbers concentrated in a fuel assembly at the center of the cell. The reason can be seen from the schematic cross section dependence shown in Figure 1. For a homogeneous lattice, the cross section of a $1/v$ absorber is a straight line when plotted against the logarithm of the neutron energy. This behavior is also true in a heterogeneous lattice if the intracell flux profile is independent of neutron energy. In typical SRS lattices, the epithermal neutron flux is relatively flat across the cell. The thermal flux however is depressed in the fuel assembly and the fast flux is peaked. Application of advantage factors (ratios of flux in components to the cell average flux) by energy gives the effective functional cross section shape shown. Thus, the effective cell-averaged cross section for a $1/v$ absorber in a heterogeneous lattice does not have a $1/v$ energy dependence. This effect makes the cell averaged lifetime for thermal neutrons significantly longer than for epithermal and fast neutrons and hence is an overestimation of the full spectrum lifetime. Therefore, a method to calculate lifetime which does not include this assumption is needed. The Alpha Search Method is one such method.

ALPHA SEARCH METHOD

A new formulation for the neutron lifetime, based on the time eigenvalue, has been developed which does not incorporate the assumption that the prompt neutron lifetime can be modeled by the thermal neutron lifetime. This method - the Alpha Search Method (ASM) - uses the alpha search (time eigenvalue) option in GLASS to calculate the lifetime. The alpha search option in GLASS is an iterative procedure using an effective absorption cross section of [1]

$$\Sigma_a(eff) = \Sigma_a - \frac{\alpha}{v}$$

in a perturbation analysis. A search is performed to compute the value of α (the stable asymptotic period) which achieves a desired k'. Given a guess of α and an initial k, GLASS uses the following formula to calculate the change in α ($\delta\alpha$) required to produce a desired k'.

$$\delta\alpha = \left(\frac{k' - k}{k}\right)\left(\frac{v\Sigma_a}{1 + L^2B^2}\right)$$

The relationship between this GLASS calculated time eigenvalue and the neutron lifetime can be seen if the time dependent diffusion equation is studied

$$\frac{\partial n}{\partial t} = D\nabla^2\Phi - \Sigma_a\Phi + \upsilon\Sigma_f\Phi$$

Using the relationship that

$$\Phi = nv, \text{ therefore } \frac{\partial n}{\partial t} = \frac{1}{v}\frac{\partial \Phi}{\partial t}$$

this equation becomes

$$\frac{1}{v}\frac{\partial \Phi}{\partial t} = D\nabla^2\Phi - \Sigma_a\Phi + \upsilon\Sigma_f\Phi$$

A basic premise is that the flux can be separated in space and time The flux therefore can be represented as [2]

$$\Phi(r,t) = \Psi(r)T(t)$$

substituting this relationship into the diffusion equation and dividing by

$$\Psi(r)T(t)$$

yields

$$\frac{1}{T}\frac{dT}{dt} = v\left[\frac{D\nabla^2\Psi}{\Psi} + \left(\upsilon\Sigma_f - \Sigma_a\right)\right] = -\alpha$$

Thus the original partial differential equation becomes the two following ordinary differential equations

$$\frac{dT}{dt} = -\alpha T$$

and

$$vD\nabla^2\Psi + v\upsilon\Sigma_f\Psi - v\Sigma_a\Psi = -\alpha\Psi$$

The second of which can be rearranged to

$$vD\nabla^2\Psi + \left(v\upsilon\Sigma_f - v\Sigma_a + \alpha\right)\Psi = 0 .$$

The solution to the first equation is of the form

$$T(t) = T(0)e^{-\alpha t}$$

Since the lattice is assumed to be in a near critical state, the following approximation can be used in the second equation.

$$\nabla^2\Psi = -B^2\Psi$$

After substitution of this relationship into the modified second differential equation and division by the flux is performed the equation becomes

$$\alpha = vDB^2 - v\upsilon\Sigma_f + v\Sigma_a .$$

Using the definition

$$L^2 = \frac{D}{\Sigma_a} ,$$

the time eigenvalue can be written as

$$\alpha = v\Sigma_a\left(1 + L^2B^2\right)\left(1 - \frac{\upsilon\Sigma_f/\Sigma_a}{1 + L^2B^2}\right).$$

It is from this equation for alpha that the formulation for the lifetime can be determined. If k is defined to be [3]

$$k = \frac{\upsilon\Sigma_f/\Sigma_a}{1 + L^2B^2} ,$$

then by substituting this expression for k and using the definition of finite lattice neutron lifetime given earlier, the equation for alpha can be rewritten as

$$\alpha = \frac{(1-k)}{\ell_p}$$

which can be rearranged to solve for ℓ_p to give

$$\ell_p = \frac{(1-k)}{\alpha}$$

where k is the eigenvalue with $\alpha = 0.0$.

Thus, from a single GLASS calculation with a k search (with α equal to zero) and an α search (with k equal to one), the inputs are determined to calculate ℓ_p. Since this method does not involve the thermal neutron lifetime, it is not influenced by the effects of the heterogeneities in the lattice. This method is much simpler than that employed in the thermal Inverse Velocity method, and will be shown to be more accurate. In order to provide a measure of the accuracy of the Alpha Search Method, results from an independent calculation of the lifetime will be compared.

EIGENVALUE METHOD

As an independent check of the Alpha Search method's accuracy, calculations were performed using the "Eigenvalue Method". [4,5] This method works by adding an artificial 1/v absorber (with a 1 barn cross section at 2200 m/sec) to each group and each region of the lattice. Keff values with and without this absorber are then used in the formula

$$\ell_p = \frac{\Delta k/k}{\Sigma_a * v} ,$$

which for this artificial 1/v absorber corresponds to

$$\ell_p = \frac{\Delta k/k}{N * 2.2E5}$$

where N is the number density of 1/v absorber in atm/b-cm.

RESULTS

Tables 1 and 2 show the results of calculations of the neutron lifetime by several different methods: the Inverse Velocity method(AVEVEL), the Eigenvalue method, and the Alpha Search method. As can be seen, the thermal Inverse Velocity method predicts up to a 15% longer lifetime than that calculated by the other methods. Calculations were performed to determine the reason for the discrepancy. These calculations were performed on a homogeneous lattice, a two region cell of U-235/Li-6 and D2O, and an explicit representation of the

tritium producing charge with control (Mark 22 geometry). The results from these calculations make several points apparent:

1) The thermal neutron lifetime calculated by the Inverse Velocity method for a homogeneous mix of U-235, Li-6 and D2O shows much closer agreement with that from the Alpha Search method than the same comparison for a heterogeneous lattice. It was also noted that as the amount of heterogeneity was increased, the relative error between the Alpha Search method and the thermal Inverse Velocity method increased.

2) By using the Inverse Velocity method for the neutron lifetime, but collapsing to a single "Few-group" over the entire multigroup structure, one can get very close agreement with the Alpha Search method.

Cases were run for the homogeneous lattice by all three methods: Inverse Velocity (AVEVEL), Alpha Search, and Eigenvalue. Table 1 shows excellent agreement between the average Inverse Velocity method (using one group) and the Alpha Search method. It can also be seen that as the amount of $1/v$ absorber is decreased, the lifetime as calculated by the Eigenvalue method approaches the value given by the Alpha Search method.

The formulation of the Eigenvalue method is analytically independent of the magnitude of the $1/v$ added. Since lifetimes by the Eigenvalue method tend toward those from the Alpha Search method as the added $1/v$ absorber tends toward zero, it appears that the Alpha Search method is equivalent to extrapolating the Eigenvalue method to zero perturbation. Unfortunately, it cannot be demonstrated that the Eigenvalue method asymptotically approaches the Alpha Search method due to a lack of significant digits in the GLASS calculations of Δk as the concentration of $1/v$ absorber gets smaller.

Similar calculations were performed for a two region cell and for the explicit tritium producing assembly (Mark 22 geometry). Table 2 shows the results. Once again there is good agreement between the Alpha Search method and the Inverse Velocity method (using 1 group). The Eigenvalue method continues to trend towards the lifetime calculated by the ASM as the concentration of $1/v$ decreases. The reason for the discrepancy between the ASM results and the apparent asymptotic value from the Eigenvalue calculations lies in the method in which GLASS treats the multigroup spatial distributions in the two cases. In the ASM, these spatial distributions are calculated only for the initial k (eigenvalue) search with alpha equal to zero; the same shape is assumed for the alpha search. In the Eigenvalue method, the spatial distributions are computed separately for the reference condition and for the added $1/v$. It can be seen that the overprediction of the neutron lifetime is most pronounced in the Mark 22 geometry case. The Inverse Velocity method for the thermal lifetime overpredicted this case (which had the largest amount of heterogeneity) by 15%.

CONCLUSIONS

Due to heterogeneous effects, the thermal Inverse Velocity method historically used at the Savannah River Site for the determination of prompt neutron lifetimes is inadequate. This method overpredicts the correct value of the prompt neutron lifetime by as much as 15%. In order to correct this deficiency a new method, the Alpha Search method which incorporates the alpha search option in GLASS, has been developed and tested. This method gives close agreement with values obtained by applying the Inverse Velocity method over the entire spectrum, but is much simpler to perform. The Alpha Search method compares favorably with the Eigenvalue method, is considerably easier to implement, and is not dependent on the amount of $1/v$ absorber that is added to the lattice. For these reasons the Alpha Search method is now the recommended procedure for evaluating neutron lifetimes in SRS lattices.

It should be noted that a precise value for the prompt neutron lifetime is essential only when calculations are performed near prompt critical. Since this is seldom the case, changes to the neutron lifetime as calculated by the Alpha Search method are not expected to impact the results of previous calculations. Sensitivity analysis has been performed on the point kinetics equations used in safety analysis to verify this result.

REFERENCES

[1] H. C. Honeck. *Joshua Users Manual.*, DPSTM-500, Vol IV, p F.2.12, Savannah River Site, Aiken, SC 29808 (1970).

[2] J. L. Meem. *Two Group Reactor Theory.*, p 128, Gordon and Breach, London (1964).

[3] J. J. Duderstadt and L. J. Hamilton. *Nuclear Reactor Analysis.*, p 204, John Wiley & Sons, New York (1976).

[4] G. R. Keepin. *Physics of Nuclear Reactor Kinetics.*, p 346, Addison-Wesley, Reading, Mass. (1965).

[5] R. Avery, *et al.*, *Proceedings of Second Geneva Conference*, p 151 (1958).

Table 1. Lifetimes in Homogeneous Media

Method	absorber (atm/b-cm)	lifetime (x10-6 sec)	percent difference
Alpha Search	0	51.90	-
AVEVEL (1 group)	0	51.90	0.0
Eigenvalue	1.0E-3	51.34	-1.1
Eigenvalue	5.0E-4	51.62	-0.5

Table 2. Lifetimes in Heterogeneous Media

Method	absorber (atm/b-cm)	lifetime (x10-6 sec)	percent difference
Two region cell			
Alpha Search	0	50.2	0.0
AVEVEL (1 group)	0	50.0	-0.4
AVEVEL (2 group) [a]	0	52.3	4.1
Eigenvalue	1.0E-3	49.4	-1.6
Eigenvalue	5.0E-4	49.8	-0.8
Eigenvalue	1.0E-4	50.1	-0.2
Mark 22			
Alpha Search	0	127	0.0
AVEVEL (1 group)	0	125	-1.6
AVEVEL (2 group) [a]	0	146	15.0
Eigenvalue	1.0E-3	119	-6.3
Eigenvalue	5.0E-4	121	-4.7
Eigenvalue	1.0E-4	123	-3.1

[a] Using thermal group only

Figure 1. Effect of Heterogeneity on a 1/v Absorber

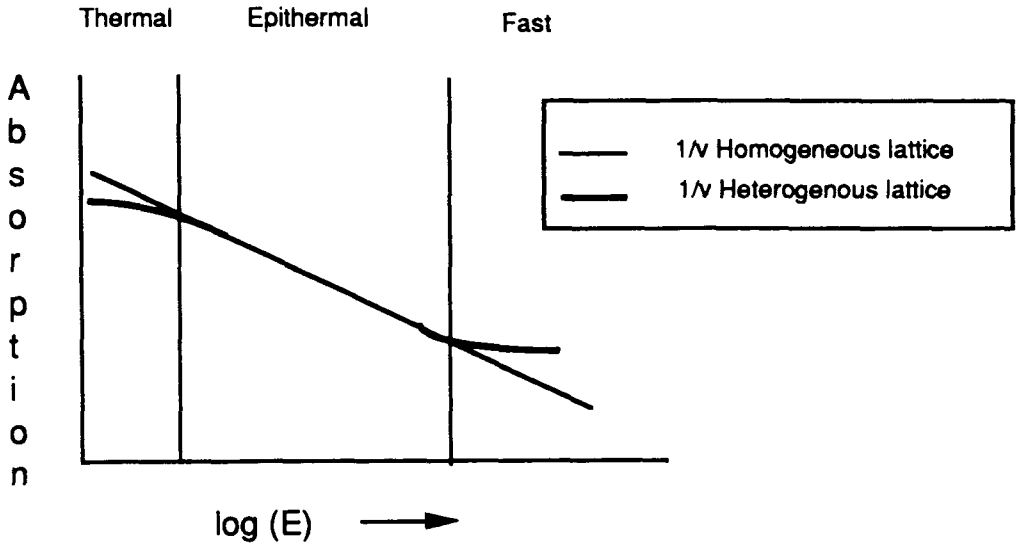

SPATIAL KINETICS ANALYSIS OF THE LOSS OF CONTROL-ROD COOLING ACCIDENT FOR THE SAVANNAH RIVER K-REACTOR

B R Bardini,* R G Steinke, J W Durkee, Jr., and R D Mosteller
Nuclear Technology and Engineering Division
Los Alamos National Laboratory
Los Alamos, NM 87545

and

D Y Chung
Office of Engineering and Operations Support
U S Department of Energy
Washington, DC 20545

ABSTRACT

A postulated loss of control-rod cooling (LCRC) accident for the Savannah River K-Reactor is analyzed using the advanced neutronics nodal code NEM and the TRAC system thermal-hydraulics code NEM has a transient capability and provides linkage to the TRAC thermal-hydraulics model This analysis demonstrates that there is a significant margin of safety for the LCRC accident at the anticipated restart power level for the K-Reactor This study also constitutes the first application of a transient three-dimensional nodal neutronics code to an event included in Chapter 15 of the Safety Analysis Report for the K-Reactor

INTRODUCTION

Los Alamos National Laboratory (LANL), as a contractor to the U S Department of Energy, currently is performing independent safety evaluations of the K-Reactor at the Savannah River Site prior to its restart One aspect of this review concerns the appropriate restart power level for that reactor

Although it is not currently the most limiting accident with respect to the restart power level for the K-Reactor, the analysis of the loss of control-rod cooling (LCRC) accident performed

*Current affiliation Westinghouse-Bettis Atomic Power Laboratory, West Mifflin, PA

by Westinghouse Savannah River Company (WSRC) does restrict the restart power level to approximately one-third of its historical full power WSRC analyzes this transient with a point-kinetics model for the K-Reactor core. In order to demonstrate conservatism, that model necessarily includes extreme (and sometimes contradictory) assumptions.[1,2] Since the LCRC accident has the potential for limiting the operating power of the reactor, a spatial kinetics analysis of the event has been performed at LANL based upon the same general scenario assumed by WSRC A spatial kinetics model can eliminate some of the contradictory assumptions employed in the point-kinetics analysis while still maintaining demonstrated conservatism.

The three-dimensional neutronics calculations were performed with the NEM code,[3] an advanced nodal code based on the nodal expansion method.[4] LANL currently is in the process of incorporating NEM into the TRAC system thermal-hydraulics code.[5] This analysis constitutes the first application of a transient three-dimensional nodal neutronics code to an event included in Chapter 15 of the Safety Analysis Report (SAR) for the K-Reactor.

The cross sections employed in this analysis were provided by WSRC[6] and are the same as those used in the steady-state three-dimensional neutronics calculations that generated input for WSRC's point-kinetics model [2] These cross sections do not account for thermal-hydraulic feedback. The reactivity behavior of the core therefore is independent of both the core power level and the coolant temperature Consequently, the LANL analysis of this event consists of two distinct phases: first, a nodal kinetics calculation with no thermal-hydraulic feedback was performed with the NEM module, and then a TRAC thermal-hydraulic analysis was performed for the hot channel based upon the time-dependent power distribution predicted by NEM

DESCRIPTION OF THE LCRC ACCIDENT

The control rods in the K-Reactor are used to maintain core criticality and to produce the desired power shape. Each control-rod cluster is contained inside an individual septifoil channel that has a source of cooling water independent of that for the fuel-assembly channels Consequently, the coolant flow to a septifoil could be lost without affecting the coolant flow to fuel assemblies or to other septifoils. In the case of a mis-seated septifoil, a partial loss of coolant flow occurs. Depending upon the flow reduction and the heating rate of the control rods inside the mis-seated septifoil, those control rods eventually could melt and drop below the bottom of the core, thereby adding positive reactivity to the core

The positive reactivity added by the melting of the control rods causes the neutron flux (and hence the reactor power) to rise very rapidly from its steady-state level. The higher flux level is detected by an ex-core high-flux monitor, which sends a scram signal to the safety rods The power excursion is terminated by the insertion of the safety rods

CONSERVATIVE ASPECTS OF THE ANALYSIS

The LANL analysis of the LCRC accident follows the conservative scenario specified in Chapter 15 of the K-Reactor SAR except in those instances where a three-dimensional kinetics model allows specific assumptions to be removed Conservative assumptions about the initial power distribution, the position and melting of the control rods, detection of the flux increase, neutronic characteristics, and behavior of the safety rods all have been retained An acceptance criterion somewhat more stringent than that used by WSRC has been applied to the coolant effluent temperature from the highest power assembly, however

It is assumed for the purposes of this analysis that the K-reactor power distribution initially is at those limits of permissible operation that produce the largest reactivity insertion upon the simultaneous melting of the control rods inside a single septifoil In particular, it is assumed that the septifoil in which the melting occurs contains one part-length and two full-length control rods in order to maximize the reactivity insertion It also is assumed that the initial power distribution prior to melting is such that the highest-power fuel assembly is adjacent to the septifoil in which the melting occurs It is assumed further that the axial power distribution in the assemblies near the mis-seated septifoil is such that all of the part-length rod and the central two-thirds of the full-length rods melt simultaneously and drop instantaneously out of the active core, producing a step increase in reactivity and thereby a prompt jump in reactor power

The high-flux monitor is designed to send a scram signal when the flux level reaches 106% of the initial steady-state power level To account for uncertainties and to assure a conservative analysis, it was assumed that the scram signal was not sent until the flux had reached 115% of that level In addition, a conservative response time for the detector was assumed

A number of conservative assumptions have been made about the neutronic characteristics of the reactor core, as well Delayed-neutron data[7] are consistent with those from ENDF/B-VI, except that the delayed-neutron fraction has been reduced by 5% to produce a larger power increase In addition, it is assumed that all the energy in the reactor is produced promptly (i e , with no decay heat), which overestimates the initial power increase produced by the reactivity insertion Finally, the omission of thermal-hydraulic feedback from the cross sections is a conservative assumption, since the net temperature coefficient of reactivity remains negative throughout the accident.

Three substantially conservative assumptions about the safety rods are incorporated into the analysis First, the reactivity worth of the safety rods has been reduced to a value that is two standard deviations less than the best-estimate value[8] Second, a worst-case single failure of the negative pulse circuit in the scram system is assumed to delay the insertion of the safety rods by 0 3 seconds Finally, 3 of the 66 safety rods are assumed not to respond to the scram signal, and another 6 are assumed to insert so slowly that they have no significant reactivity impact on the course of the transient. The NEM calculations reported herein use the same reactivity worth for the safety rods as does the WSRC model However, separate NEM calculations were run for scenarios where all 66 safety rods insert and where only 57 of them insert In the latter case, the failed and slowly-inserting safety rods are assumed to be the nine rods closest to the septifoil with the melted control rods in order to produce a worst-case result

LANL has chosen to apply a more conservative acceptance criterion to the limiting condition of the accident than did WSRC That limiting condition is the effluent coolant temperature for the highest-power assembly Both LANL and WSRC subtract a penalty of two standard deviations (7 1C) from the best-estimate FI temperature limit to account for possible biases and uncertainties in its value In addition, however, LANL requires that temperature to remain below the flow-instability (FI) temperature limit by three standard deviations in the accuracy of its thermocouple measurement (3 84C) In contrast, WSRC requires that it remain below the limit by two standard deviations plus a bias (2 9C)

NEUTRONIC ANALYSIS

The NEM model in hexagonal geometry was derived from the nodal option in an early version of the DIF3D code[9] that did not itself have a transient capability Several full-core steady-state calculations were performed with DIF3D and NEM prior to the analysis of the LCRC accident These steady-state calculations provide assurance that the basic DIF3D neutronic model has been implemented correctly in NEM In addition, they demonstrate the level of consistency between NEM and GRIMHX,[10] the three-dimensional core code that WSRC used to generate neutronics input for the point kinetics analysis

STEADY-STATE ANALYSIS

The spatial representation for the NEM core model assigns a separate hexagonal column to each fuel-assembly or control-assembly cell and then, within the active portion of the K-Reactor core, divides each column into 15 axial nodes The same spatial representation is employed for the DIF3D core model GRIMHX is a coarse-mesh, finite-difference, diffusion-theory code, and the WSRC analysis used a mesh structure such that each spatial mesh point corresponds to one node in the NEM representation

Steady-state NEM and DIF3D calculations were performed for various combinations of melted or unmelted control rods and inserted or uninserted safety rods Results from these calculations, which are summarized in Table 1, provide the reactivity worth of the melted control rods as well as the worth of the inserted safety rods In order to account for uncertainties and to assure a conservative analysis, the cross sections of the septifoil with melted control rods were adjusted artificially to increase the reactivity worth of the melted control rods Steady-state results for cases with this adjustment also are given in Table 1

The steady-state eigenvalues and hot-assembly power-peaking factors from NEM and DIF3D are in excellent agreement, as would be expected Both NEM and DIF3D compute a reactivity worth of 178 pcm (00178 $\Delta\rho$) for the melted control rods before the cross-section adjustment and a worth of 210 pcm afterwards The steady-state GRIMHX calculations[2] with and without melted control rods produced eigenvalues of 1 0047 and 1 0067, respectively, with corresponding hot-assembly power-peaking factors of 1 13 and 1 76 Consequently, relative to GRIMHX, NEM and DIF3D predict eigenvalues that are slightly more than 400 pcm higher, a reactivity worth for the melted control rods that is slightly lower (178 pcm versus 189 pcm), and power-peaking factors for the hottest assembly that are approximately 5% higher It should be noted that these

differences occur even though exactly the same cross sections were used in the calculations with all three codes The principal cause of these differences is believed to be approximations inherent in coarse-mesh finite-difference diffusion-theory calculations

TRANSIENT ANALYSIS

As was noted earlier, the NEM cross sections for the septifoil with the melted control rods were adjusted artificially to increase the reactivity worth of the melted rods The resulting cross sections produce a reactivity worth of 210 pcm, which is the same worth assumed by WSRC in their point-kinetics analysis The NEM calculation was initialized to a steady-state condition with unadjusted cross sections prior to melting The analysis subsequent to control-rod melting employed the adjusted cross sections

Two transient NEM calculations were performed, one with 66 safety rods inserting and the other with only 57 safety rods inserting These calculations were performed with uniform time steps of 0 02 seconds, based on a sensitivity study that demonstrated the adequacy of such time steps

Since NEM currently does not have the capability to monitor the behavior of ex-core detectors, the high-flux scram signal and the initial motion of the safety rods were assumed to occur at the same times as in the WSRC analysis

The results for the average core power and for the power in the hottest assembly from the two NEM transient calculations are shown in Figures 1 and 2, respectively The power initially rises as a prompt jump and then increases nearly linearly until the safety rods reach the active core The second stage of the rise in power actually is exponential, but the period is so long relative to the length of the accident that the rise appears to be linear These figures demonstrate that the time of insertion of the safety rods (which are assumed to reach the top of the active core 1 168 seconds after the control rods melt) is the critical factor in limiting the power rise and therefore the severity of the transient The omission of the nine clustered safety rods affects the magnitude of the power peak only slightly

THERMAL-HYDRAULIC ANALYSIS

The time-dependent axial power profiles for the hottest assembly from the NEM transient calculations were used as input to a detailed fuel-assembly model[11] for evaluation with the TRAC code Each of the coolant channels in the assembly was modeled hydraulically by a pipe component, and each of the annular elements of the fuel assembly was modeled thermally by a heat-structure component Constant-pressure boundary conditions were obtained from an existing steady-state TRAC solution for the full K-Reactor plant in its current configuration

The inlet coolant temperature for the K-Reactor exhibits seasonal variations, and the limiting power level must be adjusted to account for those variations TRAC cases were analyzed for inlet temperatures of 40 0C, 26 4C, and 13 3C Based on the WSRC analysis,[12] these inlet

temperatures correspond, respectively, to the maximum, average, and minimum expected seasonal variations and to power limits of 30 4%, 36 0%, and 41 7% of historical full power

The safety objective for this particular accident is to prevent FI conditions that can lead to voiding in the coolant channels of a fuel assembly WSRC has established the assembly effluent temperature limit as its criterion for satisfying this objective An alternative criterion is a Stanton number based on the Saha-Zuber correlation,[12] with some allowance for conservatism When an allowance of 30% is applied, a value of 0 00455 is obtained for the maximum acceptable Stanton number

The results from the six TRAC calculations are given in Table 2 The results show considerable margin to both the FI limit and the Stanton-number limit They are in marked contrast to the results obtained by WSRC with their point-kinetics model, which show very little margin to the FI limit (approximately 0 5C) This difference is made even more striking by the fact that NEM predicts a power-peaking factor for the hottest assembly that is approximately 5% higher than that used in the WSRC analysis The cases where only 57 safety rods insert are only slightly more limiting than the corresponding cases where all 66 safety rods insert.

Additional TRAC calculations were run to determine the limiting steady-state power level for the LCRC accident for the K-Reactor The temperature at the core inlet needed to be adjusted for each transient, since it increases slightly as the reactor power increases The results, which are summarized in Table 3, demonstrate that the K-Reactor power level could be increased by approximately 5% of historical power while preserving a margin of 0 5C to the FI limit

SUMMARY AND CONCLUSIONS

This conservative analysis of the LCRC accident has shown that sizeable margins to safety limits exist at all three power levels identified by WSRC In fact, these results indicate that acceptable margins both to the FI limit and to the maximum Stanton number are possible at power levels that are higher than those identified by WSRC by approximately 5% of historical full power

These results demonstrate the benefit of applying a spatial kinetics model to the analysis of transients for the K-Reactor, even when a very conservative scenario is assumed Based on comparisons with results from nodal DIF3D calculations, they also demonstrate the accuracy of the NEM module for K-Reactor calculations

ACKNOWLEDGMENT

This research at LANL was performed under the auspices of U S Department of Energy under contract W-7405-ENG-36

REFERENCES

1 K-Reactor Safety Analysis Report, Chapter 15, Amendment 2, SRL-USA-910279 (Draft), Westinghouse Savannah River Company, September 14, 1991

2 Robert L Frost, E Fitz Trumble, and Pete J Vescovi, "Physics Analysis of the Loss of Control Rod Cooling Accident," WSRC-TR-91-034, Savannah River Laboratory, April 1991

3 Bernard Ronald Bandini, "A Three-Dimensional Transient Neutronics Routine for the TRAC-PF1 Reactor Thermal Hydraulic Computer Code," Ph D Thesis, The Pennsylvania State University, May 1990

4 H Finneman, *et al*, "Interface Current Techniques for Multidimensional Reactor Calculations," *Atomkernenergie*, **30**, 123 (1977)

5 "TRAC-PF1 An Advanced Best-Estimate Computer Code for PWR LOCA Analysis, Volume 1 Methods, Models, User Information, and Programming Details," LA-7279-MS, Los Alamos National Laboratory (1984)

6 Robert L Frost, Westinghouse Savannah River Company, personal communication (June, 1991)

7 M C Brady and T R England, "Delayed Neutron Data and Group Parameters for 43 Fissioning Systems," *Nucl Sci Eng*, **103**, 129-149, October 1989

8 P B Parks, W E Graves, and N H Kuehn, "Estimates of the Safety Rod Timing, Worth and Post-Power Peaking in Mark 22 Charges," DPST-88-865, Savannah River Laboratory, January 1989

9 R D Lawrence, "The DIF3D Nodal Neutronics Option for Two- and Three-Dimensional Diffusion Theory Calculations in Hexagonal Geometry," ANL-83-1, Argonne National Laboratory, March 1983

10 H L Dodds, Jr, H C Honeck, and D E Hostetler, "Coarse-Mesh Method for Two-Dimensional Mixed-Lattice Diffusion Theory Calculations," *Trans Am Nucl Soc*, **21**, 223 (1975)

11 S Rodriguez and M Morgan, 'Best-Estimate Mark 22 Power Limits Based on Onset of Flow-Instability Criteria During Large-Break LOCAs,' LA-CP-90-439, Los Alamos National Laboratory, November 1990

12 P Saha and N Zuber, "Point of Net Vapor Generation and Vapor Void Fraction in Subcooled Boiling," *Proceedings of the Fifth International Heat Conference*, Vol 4, September 1974

Table 1. Results from Steady-State NEM and DIF3D Calculations

Control Rods Melted	Safety Rods Inserted	k_{eff} NEM	k_{eff} DIF3D	Hot Assembly Power-Peaking Factor NEM	Hot Assembly Power-Peaking Factor DIF3D
No	0	1.00891	1.00893	1.19	1.19
Yes	0	1.01073	1.01075	1.84	1.84
No	57	0.99209	0.99211	2.32	2.32
No	66	0.98625	0.98627	1.17	1.18
Yes[a]	0	1.01105	1.01107	1.98	1.98
Yes[a]	57	0.99770	0.99770	3.63	3.65
Yes[a]	66	0.98824	0.98826	1.93	1.96

[a]Cross sections of control cell with melted control rods have been altered for these cases to increase the reactivity worth of the melted control rods

Table 2. Thermal-Hydraulic Results for the Hottest Assembly in the LCRC Accident

Inlet Temperature (C)	Number of Safety Rods Inserting	Core Power (Percent of Historical Full Power)	Assembly Maximum Effluent Temperature (C)	Assembly Margin to FI Limit (C)	Conservative Maximum Stanton Number
40.0	57	30.4	84.2	8.9	0.0009545
40.0	66	30.4	83.9	9.2	0.0009477
26.4	57	36.0	79.0	8.7	0.0010339
26.4	66	36.0	78.7	8.9	0.0010285
13.3	57	41.7	74.8	7.7	0.0011225
13.3	66	41.7	74.6	7.9	0.0011173

Table 3 Power Limits for the LCRC Accident

Inlet Temperature (C)	Number of Safety Rods Inserting	Core Power (Percent of Historical Full Power)	Assembly Maximum Effluent Temperature (C)	Assembly Margin to FI Limit (C)	Conservative Maximum Stanton Number
41 7	57	35 5	93 3	0 5	0 0012488
27 7	57	41 1	87 8	0 5	0 0013080
14 2	57	46 2	82 4	0 5	0 0013580

Figure 1 Normalized Core Power during the LCRC Accident.

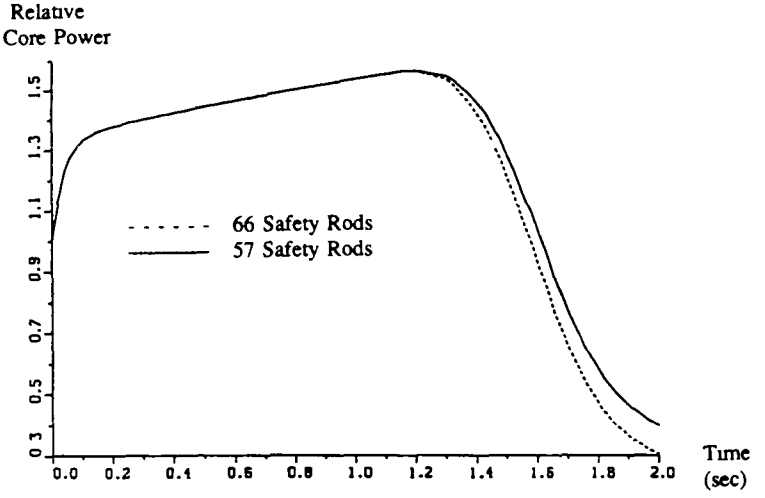

Figure 2 Normalized Power in the Hottest Assembly during the LCRC Accident.

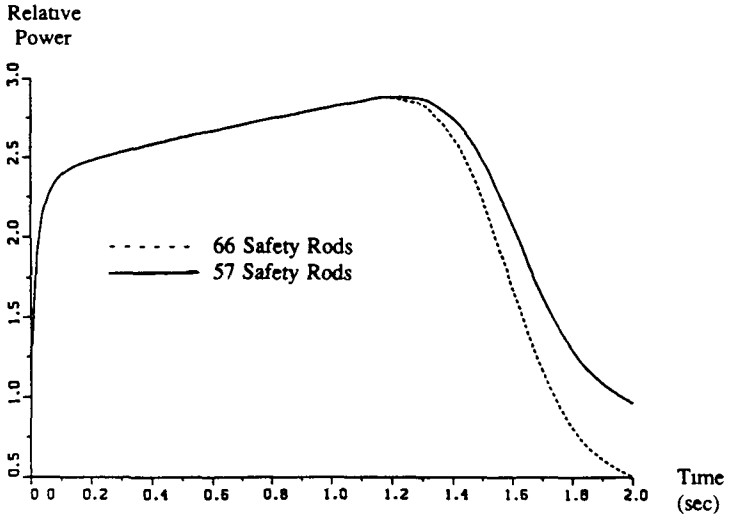

METHODS USED IN THE SPACE-TIME REACTOR KINETICS CODE TANK FOR SIMULATING POSTULATED TRANSIENT SCENARIOS IN THE MAPLE-X10 REACTOR

R.J. ELLIS

AECL Research
Whiteshell Laboratories
Pinawa, Manitoba, CANADA ROE 1LO
(204) 753-2311

ABSTRACT

The purpose of this paper is to present the methodology used in the two-dimensional reactor kinetics code TANK (Transient Analysis with Neutron Kinetics) to simulate reactor behaviour in postulated accidents in the light-water-cooled and -moderated heavy-water-reflected MAPLE-X10 Reactor The method of solution of the two-group neutron diffusion equations and the scheme of modelling the numerous reactivity feedback mechanisms by incremental cross-section changes are discussed The results of two sample transient simulations are presented to illustrate some of the simulation techniques used in TANK The postulated scenarios are loss-of-regulation accidents (LORAs) from low power with and without coolant heat removal and with an initially high concentration of ^{135}Xe

INTRODUCTION TO TANK

TANK[1,2] is a two-dimensional (2-D) space-time reactor kinetics computer code created for simulating reactivity transients in the MAPLE[3] class of research reactors (e.g., MAPLE-X10) being developed by AECL Research. In TANK, reactor neutronics are solved in two neutron-energy groups: fast neutrons, with kinetic energy $\geq$0.625 eV, and thermal neutrons, with kinetic energy <0.625 eV.

In TANK, reactors are modelled on a 2-D hexagonal mesh lattice and allowances are made for effects in the third (i.e., axial) dimension. In addition to the reactor neutronics, TANK simulates the thermalhydraulics conditions in the reactor core. A heat transfer package used by the AECL Research thermalhydraulics code CATHENA[4] is currently linked to TANK to provide heat transfer coefficients and coolant characteristics at each time step for each fuelled assembly in the reactor lattice

TANK can be used to simulate a wide range of postulated transient scenarios, including coolant flow perturbations, symmetric reactivity insertions, and asymmetric reactivity insertions (e g., single absorber rod withdrawals), which lead to flux-tilt situations. The code has been validated[2] for step reactivity-insertion transients by benchmarking against SPERT-1B (24/32) reactor transient experiments.

Reactivity feedback effects are modelled in TANK simulations by changes in the two-group cross sections representing the various hexagonal cells of the TANK model. This method is discussed below.

DESCRIPTION OF MAPLE-X10

The MAPLE-X10 Reactor is light-water-cooled and -moderated, but heavy-water-reflected. It will operate at a steady-state power level of 10 MW and is to be cooled by forced circulation. Figure 1 is a schematic of the MAPLE-X10 Reactor showing the major features of the concept.

The core is situated near the bottom of a deep light-water-filled pool. The MAPLE-X10 Reactor core is fuelled with the metallic dispersion fuel U_3Si-Al. The 19-site MAPLE-X10 initial core consists of ten 36-element driver fuel assemblies with aluminum-clad fuel elements; six 18-element fuel assemblies (control and shutdown rod sites); and three 12-element dummy fuel assemblies with steel or aluminum elements replacing fuel.

The forced cooling of the reactor core is accomplished by a total flow of light-water coolant from the pump equal to about 290 kg/s. Of this, 90% enters an inlet plenum beneath the core and is forced through the core. The remaining 10% is bypass flow, which mixes with the reactor pool water. During the standard operation of the reactor, the primary coolant pump draws water in through suction line ports located above the core. The water entering the suction lines is a mixture of the hot coolant water that has passed through the core and pool water that comes down the chimney (the main purpose of the bypass flow), which is open to the pool. Coolant from the core does not go up through the top of the chimney during normal operation. The reactor coolant inlet temperature is 35C in the core inlet plenum and increases to about 44C at the core outlet. A heat exchanger maintains the core inlet coolant temperature of 35C by removing nominally 10 MW of heat.

TANK SIMULATION METHODS

Figure 2 depicts the hexagonal lattice map used in TANK to represent the MAPLE-X10 Reactor. The core sites are closely modelled by hexagons while other components of the reactor, such as irradiation sites, are approximately represented by hexagonal cells. The TANK model for MAPLE-X10 has a total of 649 hexagonal cells arranged in 31 rows. The neutronics of the entire reactor are determined based on the influence of each cell on the overall flux solutions.

Each of the 649 hexagonal lattice cells is characterized by a set of nine kinetics parameters obtained using the multigroup transport code WIMS-AECL.[5,6] The nine kinetics parameters are:

(a) average fast neutron velocity, v_1,
(b) average thermal neutron velocity, v_2,
(c) macroscopic fast neutron absorption cross section, Σ_a^1,
(d) macroscopic thermal neutron absorption cross section, Σ_a^2,
(e) macroscopic fast neutron fission production cross section, $\nu_1\Sigma_f^1$,
(f) macroscopic thermal neutron fission production cross section, $\nu_2\Sigma_f^2$,
(g) macroscopic fast-to-thermal neutron removal cross section, Σ_r^1,
(h) fast neutron diffusion coefficient, D_1, and
(i) thermal neutron diffusion coefficient, D_2.

The kinetics parameters are determined for a range of fuel and coolant conditions for models describing appropriate lattice cells. From this information, parameterized equations are developed for the kinetics parameters as functions of fuel temperature, moderator temperature, coolant temperature and coolant density, void bubble fraction and ^{135}Xe concentration. These equations constitute part of the input data to TANK for the MAPLE-X10 model.

Routines in TANK calculate the temperatures of fuel, cladding, and coolant on a site-by-site basis. Prior knowledge from calculations with the three-dimensional neutron diffusion code 3DDT[7] for the axial power density and neutron flux distributions for the fuel assemblies are used in the calcualtion of the peak fuel centreline and cladding wall temperatures. Importance weighting functions based on the square of axial distribution of neutron flux levels are used to determine effective fuel and water temperatures for each fuel assembly. The temperature component of the macroscopic cross sections is determined by solving the above-mentioned parameterized equations at the effective water and fuel temperatures. The temperature of the coolant entering the core is updated to reflect the coolant circulation time, the heat exchanger system, and the power histories of the reactor core fuel assemblies.

Axial flux-squared-weighted, cell-average fuel and water temperatures were used in the calculation of the kinetics parameters. Axial flux-squared weighting of appropriate cross sections accounts for the effects of control and shutdown absorber rod positions.

The methods for modelling reactivity feedback effects in TANK simulations are as follows: The values for neutron cross sections and neutron diffusion coefficients are calculated at each simulation time step using the parameterized equations. The ongoing flux solutions from the diffusion equations then represent the transient neutronic behaviour.

The improved quasistatic approximation method with its flux-factorization technique[8] is used in TANK for calculating neutron flux levels. Each neutron flux level considered is the product of a time-dependent amplitude function and a position-dependent (but weakly time-dependent) shape function. The flux factorization approach used in TANK is represented by $\phi(r,t)=\psi(t,t)N(t)$ where ϕ is the space-time neutron flux, ψ is the primarily space-dependent shape function and N is the time-dependent amplitude function.

The kinetics calculations in TANK account for delayed neutrons in addition to the prompt fission neutrons. Six delayed-neutron precursor groups are considered in the neutronics solution in TANK. The time-dependent densities of the delayed-neutron precursor groups have an important role in the behaviour of the inverse reactor period and hence the transient behaviour of the reactor. The six delayed-neutron precursor group decay constants and fractions were determined for the MAPLE-X10 fuel composition and power distribution using the recent delayed-neutron data of Brady and England.[9]

The instantaneous inverse reactor period, $\alpha(t)$, is determined from the following equation:

$$\alpha(t) = \frac{\rho - \beta}{\Lambda} + \frac{\Sigma \lambda_i \eta_i}{N} ,$$

where ρ is the reactivity, β is the total delayed-neutron precursor fraction, Λ is the prompt neutron generation time, N is the relative amplitude (power),

λ_i are the delayed-neutron-group decay constants, η_i are normalized concentrations of the delayed-neutron precursor groups. The variables ρ, Λ, and η_i are integral quantities determined in TANK from appropriate inner products of the matrices representing the transient kinetics equations listed below. The two-neutron-energy-group reactor kinetics equations and the delayed-neutron precursor equations form the following set of differential equations for the fast and thermal neutron flux levels:

$$\frac{1}{v_1}\frac{\partial\phi_1}{\partial t} = \nabla\cdot D_1\nabla\phi_1 - \{\Sigma_a^1 + \Sigma_r^1 + D_1B_z^2\}\phi_1 + (1-\beta)\{\nu_1\Sigma_f^1\phi_1 + \nu_2\Sigma_f^2\phi_2\} + \sum_{i=1}^{6}\lambda_i C_i$$

$$\frac{1}{v_2}\frac{\partial\phi_2}{\partial t} = \nabla\cdot D_2\nabla\phi_2 - \{\Sigma_a^2 + D_2B_z^2\}\phi_2 + \Sigma_r^1\phi_1$$

$$\frac{\partial C_i}{\partial t} = \beta_i\{\nu_1\Sigma_f^1\phi_1 + \nu_2\Sigma_f^2\phi_2\} - \lambda_i C_i,$$

where B_z^2 is the axial buckling - its use in these equations simulates axial neutron leakage. The other variables are as defined earlier. The spatial and time dependence of the variables ϕ_1, ϕ_2, and C_i is implied, but not indicated (for clarity), in the equations. As mentioned above, these equations can be written in matrix form. The steady-state neutron flux levels are determined by solving the above equations when the left-hand sides are equal to zero. At the same time, adjoint neutron flux levels are determined by solving the adjoint matrix operation. These adjoint flux values are used in the inner product calculations for the integral quantities.

For the decay-heat contributions to assembly powers, 23 decay-heat groups based on the 1978 American Nuclear Society (ANS) Standard[10] are considered for each fissionable nuclide. The behaviour and level of decay heat is modelled in TANK on a site-by-site basis, depending on the power history of each fuel assembly. The time-dependent decay-heat fraction is determined for each fuel assembly during the transient simulation.

The build-up and 2-D spatial distribution of the fission-product-poison ^{135}Xe and its effect on macroscopic neutron cross sections are considered for each fuel assembly. The concentration levels of ^{135}Xe and ^{135}I in each fuel assembly are updated during a transient simulation as the power densities and flux levels change.

SAMPLE TRANSIENT SIMULATIONS USING TANK

In this section, two postulated loss-of-regulation accident scenarios from low power levels in the MAPLE-X10 Reactor are analyzed and discussed to illustrate the methods used in TANK. A number of observations are made about the behaviour of the MAPLE-X10 Reactor.

The first transient scenario involved a slow loss-of-regulation accident (LORA) in which the three Hf control absorber rods withdraw at a speed that initially inserts reactivity at a rate of 0.05 mk/s. This postulated scenario

is representative of the types of cases involved in the safety assessment for the MAPLE-X10 Reactor. The reactor power level was initially 1 kW, and the water temperature 20C. This scenario also assumed that the level of ^{135}Xe was higher than its 10 MW operation equilibrium value, but that the level of ^{135}I was much lower. This corresponds to the situation in which the reactor is brought back up to power after a poison-out period. At the start of the transient, the level of ^{135}Xe was at 150% of its equilibrium 10 MW operation value. Once the transient begins, the control absorber rods withdraw until the power level exceeded 12 MW. In this scenario, the control absorber rods are released when the power level exceeds 12 MW but are assumed to freeze in place, prevented from falling back into the core. The burnout of excess ^{135}Xe continues to add reactivity at a slow rate.

Figure 3 summarizes the results of the transient simulation using TANK The simulation was carried out to 800 s. The maximum anticipated operator intervention delay time used in MAPLE-X10 transient simulations is 900 s. The reactivity curve peaked at 3.5 mk at about 80 s, at which point the negative reactivity feedback effects exceeded the reactivity inserted. The power level at this time was 1.6 MW. Once the power level exceeded 12 MW, the control absorber rods were assumed frozen in place. The power peaked initially at 16 MW at about 110 s. The small oscillations in power after this point were caused by the circulation of coolant with a period of nearly 16 s; the small "steps" seen in the reactivity curve were associated with the ingress of cooled water (with its positive reactivity effect) into the fuel assemblies. In Figure 3, the amount of reactivity inserted by the burnout of excess ^{135}Xe is shown. This reactivity addition was dependent on, and approximately proportional to, the reactor power level. By 800 s, just over 7 mk had been added in this manner. This excess reactivity was almost completely compensated by the negative reactivity effect of heated water. However, the small amount of reactivity that was not overcome caused the reactor power to rise at a steady gradual rate.

Figure 4 shows plots of several temperatures in the MAPLE-X10 Reactor All the temperature plots begin at 20C, the initial reactor temperature. The peak fuel centreline temperature (at the hottest axial plane) is shown for a fuel element of an 18-element shutdown fuel assembly (see Figure 1). The fuel temperature responded quickly to the transient reactor power level. The first peak in the fuel temperature reached 192C. The subsequent peaks corresponded to the power peaks (see Figure 3) and the gradual rise in the fuel temperature was caused by the steady increases in the power level and coolant temperature. The water entering the pumps was a mixture of coolant that has passed through the core (90%) and bypass flow from the pool (10%). The temperature of the pump inlet water rose from 20 to 35C in 120 s. In this transient scenario, once the pump water has reached this temperature, the heat exchanger was assumed to start removing heat (to a maximum rate of 10 MW) from the water to maintain it at 35C. The coolant circulation time delayed the ingress of the cooled water into the inlet plenum. This effect was seen in the time-wise displacement of the inlet plenum coolant temperature curve The temperature of the coolant entering the pumps exceeded 72C at 440 s. This is the temperature for the MAPLE-X10 coolant pumping system at which pump cavitation would commence degrading the coolant mass flow This added complication was not modelled in the simulations presented in this paper. The average pool water temperature slowly rose to about 28C from 20C by 800 s through mixing with the warm bypass flow water.

Figure 5 summarizes the results of the TANK simulation for the second transient scenario mentioned above. This case is the same as the one discussed with Figures 3 and 4 except that no heat was assumed removed from the coolant by the heat exchanger. The power peaked (16 MW) at the same time (110 s) as in the scenario with the heat exchanger on, but there are no subsequent sharp power peaks, because the coolant inlet temperature (see Figure 6) was increasing smoothly. The coolant temperature rose quickly and caused (in conjunction with the increased fuel temperature) the net reactivity to drop to -0.8 mk by 180 s. The burnout of excess ^{135}Xe added reactivity (3.2 mk by 800 s) at a reduced rate from that seen in Figure 3 because the power level was lower. The added xenon burnout reactivity still caused the power level to rise from its dip at 4.3 MW at 270 s to 5.7 MW by 800 s.

Figure 6 shows that the fuel centreline temperature rises (as in Figure 5, for the first scenario) to a peak of 192C at 110 s, but then dropped as the power level subsided. This temperature and the inlet plenum coolant temperature then increased as the power level rose. The pump inlet water temperature quickly rose to about 60C as no heat was removed by the heat exchanger. The inlet plenum coolant temperature was again delayed by the 15.5 s coolant circulation time. The coolant inlet plenum temperature increased to 71C by 800 s and the pump inlet water temperature reached 71.5C at this time, just below the onset of pump cavitation. The pool temperature reached 28.2C by 800 s, slightly cooler than in Figure 4.

Figure 7 provides a comparison of the simulations of the two transient scenarios. The dashed curves correspond to the second scenario in which no heat exchanger operation was modelled. The solid curves represent the first scenario where heat exchanger heat removal up to 10 MW was modelled once the pump inlet water temperature reached 35C. The power level and net reactivity curves from the simulation of the first scenario have a lot of structure because of the reactivity effects of the rapidly changing coolant temperature (see Figure 4). The curves for the second scenario are much smoother. The undershoot/overshoot behaviour of the net reactivity curve is typical of transients in which coolant temperature and density reactivity effects play a major role.

SUMMARY

This paper describes the reactor kinetics and combined thermalhydraulics methods and models used in TANK to simulate transient scenarios. The differential neutron diffusion equations solved for the two-group neutron flux levels are presented and the scheme developed for modelling various reactivity feedback mechanisms in TANK is discussed. Spatial ^{135}Xe build-up and spatial decay-heat considerations have recently been added to TANK, allowing for more realism in transient simulations.

Two postulated loss-of-regulation accident scenarios from low power levels in the MAPLE-X10 Reactor are analyzed and discussed to illustrate the capabilities of TANK in simulating transient behaviour in nuclear reactors. A number of observations are made about the behaviour of the MAPLE-X10 Reactor. The MAPLE-X10 Reactor has negative reactivity feedback effects associated with fuel temperature rise and overall water temperature rise.

CONCLUSIONS

The methodology employed in TANK permits the detailed simulation of postulated accident scenarios in the MAPLE-X10 Reactor. Neutronic effects and thermalhydraulic behaviour are equally important and it is necessary to consider the coupled effects. Preliminary analyses were completed for sample transient simulations involving a postulated loss-of-regulation accident in MAPLE-X10, starting from low power, but with a relatively high concentration level of ^{135}Xe and a low concentration level of ^{135}I. This situation is qualitatively similar to the start-up of the reactor after a poison-out period.

If the coolant pumping system is operating, but the heat exchanger is left idle, the coolant will heat up fairly quickly. This would cause the reactor power level to drop because of the negative reactivity effect of the rise in water temperature. The burnout of the excess ^{135}Xe, with the Hf control and shutdown absorber rods frozen, adds reactivity to the reactor at a rate, in the short term, that is roughly proportional to the power level. This reactivity is compensated by a general increase in reactor fuel and coolant temperatures.

The consequences of these postulated accidents are minimal within the short-term, 800-s duration of the simulations. The scenario in which the heat exchanger was operating reached a higher power level and higher temperatures. The temperature of the coolant entering the pumps exceeded the point at which pump cavitation would commence degrading the coolant mass flow. This added complication was not modelled in the simulations presented.

Thus, it would be advisable to delay the operation of the heat exchanger heat removal system until it is apparent that the reactor is behaving properly. In the unlikely event of a LORA, the freedom for the coolant to heat up quickly will act to mitigate the transient excursion.

REFERENCES

1 R.J. ELLIS, "Transient Analyses of Postulated Reactivity-Insertion Accidents in the MAPLE-X10 Reactor Using the Reactor Kinetics Code TANK," in Proceedings of the American Nuclear Society International Topical Meeting on Safety, Status, and Future of Non-Commercial Reactors and Irradiation Facilities, Boise, ID, U.S.A., 1990 September 30 - October 4, SAFOR90-112 (1990).

2 R.J. ELLIS, "The Reactor Kinetics Code TANK: A Validation Against Selected SPERT-1B Experiments," in Proceedings of the IAEA/CRNL International Symposium on Research Reactor Safety, Operations and Modifications, Chalk River, ON, 1989 October 23-27, IAEA-SM-310/103 (1989).

3 R.F. LIDSTONE, A.G. LEE, and G.E. GILLESPIE, "MAPLE Facilities for National Nuclear Programs," Atomic Energy of Canada Limited Report, AECL-9976 (1989).

4 D.J. RICHARDS, B.N. HANNA, N. HOBSON, and K.H. ARDRON, "ATHENA: A Two-Fluid Code for CANDU LOCA Analysis," in Proceedings of the Third International Topical Meeting on Reactor Thermalhydraulics, Newport, RI, U.S.A., 1985 October 15-18, pp. 7.E-1 - 7.E-14 (1986). Note: This code has since been renamed CATHENA.

5 J.R. ASKEW, F.J. FAYERS, and P.B. KEMSHELL, "A General Description of the Lattice Code WIMS," J. Brit. Nucl. Energy Soc., Vol. 5, No. 4, p. 564 (1966).

6 J.V. DONNELLY, "WIMS-CRNL - A User's Manual for the Chalk River Version of WIMS," Atomic Energy of Canada Limited Report, AECL-8955 (1986).

7 J.C. VIGIL, "3DDT, a Three-Dimensional Multigroup Diffusion-Burnup Program," Los Alamos Scientific Laboratory Report, LA-4396, (1970).

8 K.O. OTT and D.A. MENELEY, "Accuracy of the Quasistatic Treatment of Spatial Reactor Kinetics", Nucl. Sci. Eng., Vol. 36, p. 402 (1969).

9 M.C. BRADY and T.R. ENGLAND, "Delayed Neutron Data and Group Parameters for 43 Fissioning Systems", Nucl. Sci. Eng., Vol.103, pp. 109-149 (1989).

10 V.E. SCHROCK, "A Revised ANS Standard of Decay Heat from Fission Products," Nucl. Tech. Vol. 46, p. 323 (1979).

FIGURE 1: Schematic of MAPLE-X10 Reactor.

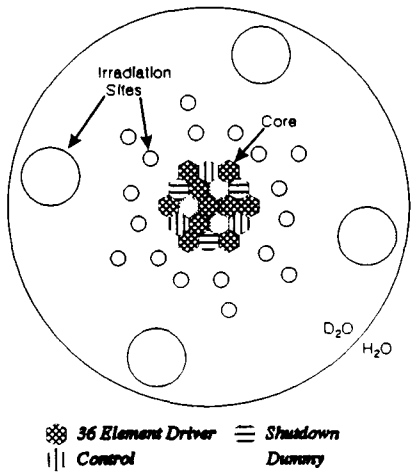

FIGURE 2: TANK Model of MAPLE-X10 Reactor.

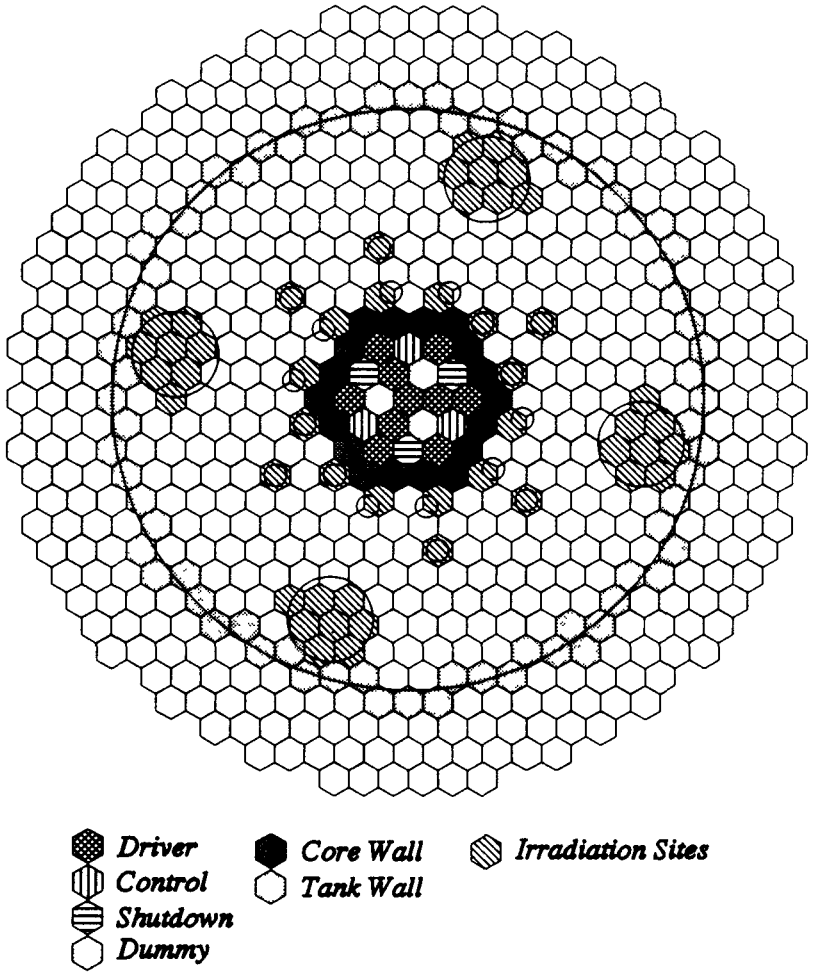

FIGURE 3: Postulated loss-of-regulation accident simulated with TANK. Transient is initiated from a low power level and a high concentration of ^{135}Xe. Heat removal rate was 10 MW once the water temperature exceeded 35C.

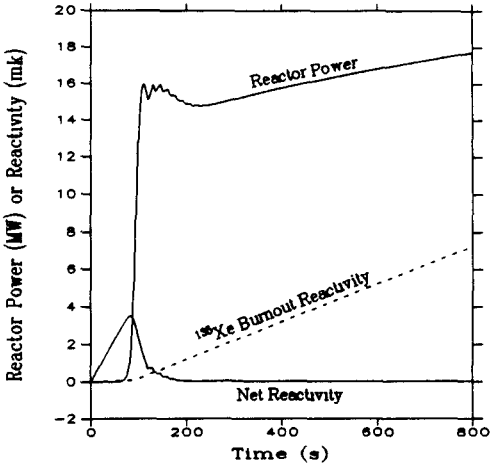

FIGURE 4: Some transient water and fuel temperatures calculated in the TANK simulation.

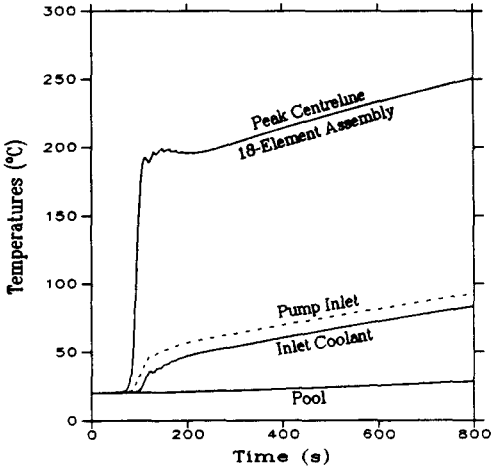

FIGURE 5: Postulated loss-of-regulation accident simulated with TANK. Transient was initiated from a low power level and a high concentration of ^{135}Xe. In this scenario there was no assumed heat removal from the coolant.

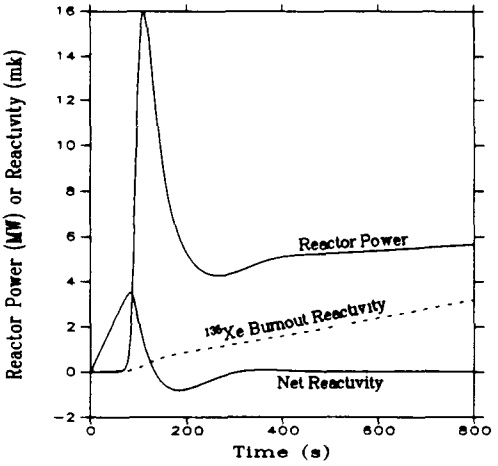

FIGURE 6: Some transient water and fuel temperatures calculated in the TANK simulation. There was no heat removal from the coolant.

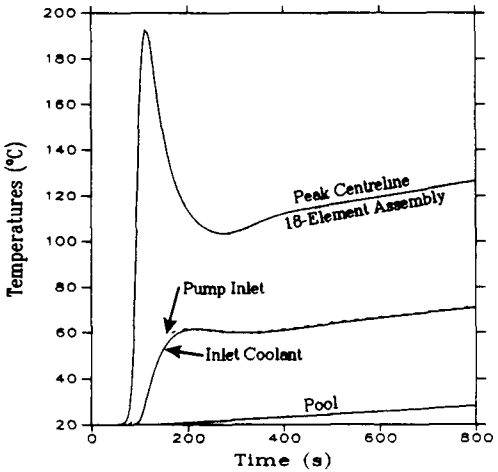

FIGURE 7: Comparison of the transient reactor power and reactivity, as simulated with TANK, with and without coolant heat removal.

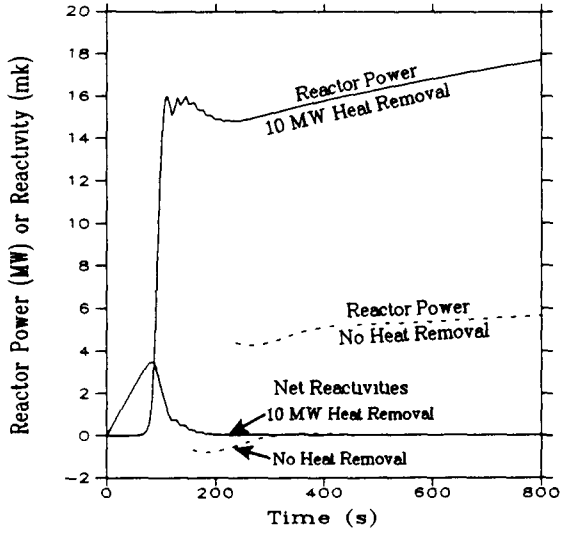

A Lyapunov Function–Free Method for Stability Domains of Nonlinear Reactors

Chae Yong Yang and Nam Zin Cho

Korea Advanced Institute of Science and Technology
Department of Nuclear Engineering
P.O. Box 150 Cheongryang, Seoul, Korea

ABSTRACT

A constructive method for estimating asymptotic stability domains of nonlinear reactor models is developed. The method is based on expansion of a positive definite function instead of a Lyapunov function and thus it is easy to come up with a starting region. The method starts with the region given by a specific positive definite function and provides a sequence of regions that eventually converges to the exact stability domain. From a large starting region, the entire stability region is estimated effectively after sufficient iterations. It is particularly useful for reactor systems that are stiff. The method is applied to several nonlinear reactor models known in the literature and the results are compared.

INTRODUCTION

The stability of nonlinear systems depends on the magnitude of initial perturbations of the variables from equilibrium, unlike linear systems which do not depend on these perturbations. The system which is linearly stable may not be globally stable. That is, if the system is stable but not stable in the large, the system may run away for greater perturbations than the critical perturbation. Thus, one of our interests is to determine the largest region of initial perturbations for which the system is stable.

In this study we characterize the stability of nonlinear reactor systems using bifurcation theory and develop a constructive method to estimate the entire stability domain of the steady–state operating point. We propose a new method to determine the entire stability region that is applicable to general nonlinear systems and that is particularly useful for stiff systems. The new method for estimating the stability regions is based on the stability definitions of Lyapunov itself. The method requires only a positive definite function instead of a Lyapunov function to come up with a starting region. Thus, the determination of a starting region is easy. From the starting region, the entire stability region is estimated after sufficient iterations by using an expansion scheme.

STABILITY OF NONLINEAR SYSTEMS

We consider a dynamics system governed by the nonlinear differential equation of the form

$$\frac{dx}{dt} = f(x, \mu), \quad x \in R^n, \tag{1}$$

where $x = x(t) \in R^n$ is a vector valued function of dependent variables and μ is a parameter vector that determines the design or operating condition of the system. It is of our interest to examine dynamics of the nonlinear system around equilibrium solutions.

Consider that the system Eq. (1) has the equilibrium solution x_e at the origin 0, of which stability is to be treated. The definitions of stability are given by Lyapunov as follows[1] (See Fig. 1).

Definition 1

The equilibrium solution x_e is stable if there is an $r \leq R$ such that if

$$\|x(t_0)\| < S(r)$$

then

$$\|x(t)\| < S(R)$$

for all $t > t_0$ and any R.

Definition 2

The equilibrium solution x_e is asymptotically stable if it is stable and $x(t)$ tends to x_e as time increases indefinitely.

We define a scalar energy function $V(x)$ said to be positive definite with the following properties:

(a) $V(x)$ is continuous together with its first partial derivatives in a certain open region Ω around x_e

(b) $V(x_e) = 0$

(c) $V(x) > 0$ in Ω except x_e

If in addition $\dot{V} \leq 0$ in Ω, V is called a Lyapunov function.

Theorem 1: Stability theorem (LaSalle and Lefschetz[1])

If there exists a Lyapunov function $V(x)$ in some neighborhood Ω of x_e, then the equilibrium solution x_e is stable.

Theorem 2 Asymptotic stability theorem (LaSalle and Lefschetz[1])

If there exists a positive definite $V(x)$ with $\dot{V} < 0$ in some neighborhood Ω of x_e, then the equilibrium solution x_e is asymptotically stable

AN EXPANSION METHOD FOR FINDING STABILITY DOMAINS

The existence of a Lyapunov function implies stability of the system in a particular region The problem is that a particular Lyapunov function is a strong sufficient condition for stability but that it is not to provide necessary conditions We do not guarantee that the entire stability domain is discovered in this manner, which is what one wants in practice In other words, there exists no method for finding a suitable Lyapunov function $V(x)$ offering the entire stability domain

To find a Lyapunov function giving the entire stability region requires insight and is artistry The local Lyapunov function obtained from the Lyapunov equation generally provides far smaller domain than the entire stability region, because the Lyapunov equation is obtained for infinitesimal perturbations around an equilibrium solution

Chiang and Thorp[2] proposed a method that can estimate the entire stability regions, based on expansion of a Lyapunov function However, some nonlinear systems may require long computing times to obtain the accurate stability region using this method In particular, for stiff systems in which fast and slowly varying variables coexist some variables within the stability region consume long times to intersect the given starting boundary Furthermore, in higher order systems it is very difficult to determine the level values of the Lyapunov function, in particular, the critical level value We provide in the following a theorem to overcome these problems First we define $\Phi(x_0, t) \quad R \rightarrow R^n$ as a trajectory defined by $x(t)$, the solution of the system after t from an initial point $x(0) = x_0$, and we need a definition and a lemma

Definition 3[3]

A point p is said to be in the ω–limit set (positive limiting set) of x if corresponding to each $\epsilon > 0$ and $T > 0$, there is a $t > T$ with the property that $\|\Phi(x, t) - p\| < \epsilon$

One of the fundamental properties of the ω–limit set is as follows If $\Phi(x, t)$ is bounded for $t \geq 0$, then its ω–limit set is nonempty

Lemma 1

For a nonlinear system for which an equilibrium point ($x_e = 0$) is asymptotically stable, consider the asymptotic stability region S of the equilibrium point and its boundary ∂S Let D be a set consisting of ω–limit sets (not including x_e itself) of any point in the state space of Eq (1) Let K_2 be a compact set containing no other equilibrium points and no

points in D Then, (i) there exists inside K_2 a set S_∞ that contains S and that every trajectory $\Phi(x,-t)$ starting in S_∞ approaches ∂S as t increases, and (ii) every trajectory starting from a subset of S_∞ that is outside S eventually leaves S_∞

Proof The lemma follows trivially from the definitions of the sets S, S_∞, D, and K_2 (see Fig 2)

Theorem 3

Consider a nonlinear system for which an equilibrium point ($x_e = 0$) is asymptotically stable and a positive definite function $W(x)$ $R^n \to R$ for the equilibrium point Let K_2 be a compact set containing no other equilibrium points and no points in D as in Lemma 1 Then, there exists a $\xi > 0$ such that for the connected set $S_{W_0}(\xi) = \{x \in R^n \;\; W(x) < \xi \text{ and } x \in K_2\}$, the t–expanded region $S_{W_t}(\xi) = \{x \in R^n \;\; W_t(x) = W(\Phi(x,t)) < \xi\}$ converges to the stability region as t increases

Proof From Lemma 1, the boundary ∂S_∞ is outside the stability boundary ∂S of interest but it is inside K_2 We can choose a positive ξ so that $S_{W_0}(\xi)$ is in S_∞, since we know from Lemma 1 that S_∞ is nonempty and $W(x)$ is a positive definite function Note that the t–expanded region $S_{W_t}(\xi)$ consists of all starting points x of which trajectories at t, $\Phi(x,t)$, enter in the region $S_{W_0}(\xi)$ Consider a general case that $S_{W_0}(\xi)$ consists of a subset of S and a set outside S First, consider all points that are outside S and in $S_{W_0}(\xi)$ (unstable subset in the starting region) From Lemma 1, the trajectories from these starting points leave $S_{W_0}(\xi)$ after some finite time and eventually leave S_∞ Furthermore $\Phi(x,-t)$ eventually approaches ∂S as t increases Hence, in expanding $W_t(x) = W(\Phi(x,t)) < \xi$ with t, this subset approaches the stability boundary ∂S as t increases Next, consider all points in S There exists some finite time t_1 such that the trajectory starting from this subset enters in $S_{W_0}(\xi) \cap S$ at t_1 In fact, $\Phi(x,t)$ with these starting points approach the equilibrium point x_e due to the properties of asymptotic stability Some of the points that start from S may leave $S_{W_0}(\xi) \cap S$ for a while but will enter again in $S_W(\xi) \cap S$ after some finite time Therefore, the t–expanded region $W_t(x) = W(\Phi(x,t)) < \xi$ eventually converges to S as t increases Fig 2 shows that the expanded regions eventually disappear at an unstable subset and expand at a stable subset □

Remarks A point to note in application of the theorem is how to choose the level value ξ, largest as possible, so that $S_{W_0}(\xi)$ is still within S_∞ For many systems, S_∞ is a large set around S Reactor dynamics systems generally have a trivial solution corresponding to the zero power state and a nonzero solution corresponding to the operating power state (some feedback systems can have several nonzero solutions) For most of these reactor systems

S_∞ is easily determined. That is, the positive domain of the state space (inside K_2), which is physically meaningful, usually becomes S_∞.

We can estimate the entire stability region by a procedure based on Theorem 3. Note that the starting function $W(x)$ need not be a Lyapunov function in contrast to that of the method of Chiang and Thorp[2]. We require a positive definite function as the starting function. Generally it is very easy to obtain a positive definite function for the system, because the positive definite function can be found independently of the dynamical system. The procedure yields a sequence of positive definite functions, which is used to estimate the interim regions through the following scheme:

$$\begin{aligned} &W(x) < \xi, \\ &W_1(x) = W\big(\Phi(x;t_1)\big) < \xi, \\ &W_2(x) = W\big(\Phi(x;t_2)\big) < \xi, \\ &\quad\vdots \\ &W_i(x) = W\big(\Phi(x;t_i)\big) < \xi. \end{aligned} \tag{2}$$

Eq. (2) can be rewritten using $t_i = i \cdot d$ as

$$\begin{aligned} &W(x) < \xi, \\ &W_1(x) = W\big(\Phi(x;d)\big) < \xi, \\ &W_2(x) = W_1\big(\Phi(x;d)\big) < \xi, \\ &\quad\vdots \\ &W_i(x) = W_{i-1}\big(\Phi(x;d)\big) < \xi. \end{aligned} \tag{3}$$

A suitable numerical scheme is used for following the trajectory $\Phi(x;t)$. We emphasize that the interim region after i time steps, $W_i(x) < \xi$, is estimated not by solving the differential equation and finding all trajectories up to $t = t_i$, but by solving the algebraic equation $W_i(x) = \xi$. A point to note is that we cannot guarantee whether each of the resulting interim regions is in the entire stability region. Hence, we find the stability region only after sufficient expansions. However, this is not a severe problem because, if we choose a suitable value of ξ, the interim regions converge very quickly.

In particular, in dealing with stiff systems, the cause of problem is that the starting stability region obtained from the usual method is far smaller than the exact stability region and thus the trajectory starting from the initial points around the boundary of the exact stability region takes too much time to arrive on the starting stability boundary. In many

cases, we can choose ξ easily Hence, we can estimate the exact stability region effectively by using a starting region that is relatively large (choosing large ξ) based on Theorem 3

The procedure is as follows

(1) Find a positive definite function $W(x)$

(2) Choose a suitable level value ξ of the positive definite function $W(x)$

(3) Construct a new positive definite function by expansion of the present positive definite function

(4) Determine the interim region from the new positive definite function using the ξ from Step (2)

(5) Repeat Steps (3) and (4) until the estimated region converges

In general, it is difficult to find roots of the ith expanded equation $W_i(x) = \xi$ such as Eqs (2) and (3) directly We can find their roots from a given function $W(x)$ of a known mathematical form An efficient implementation of Newton–Raphson method for finding roots of the ith expanded function is described in Ref 4

APPLICATIONS TO REACTOR MODELS

One–Temperature Feedback Model

Consider the effective–lifetime model with a one–region temperature coefficient and a power–coefficient, as formulated by Devooght and Smets[5]

$$\begin{aligned} \frac{dn}{dt} &= \frac{\rho}{l} n, \\ \frac{dT}{dt} &= Kn - \gamma T, \\ \rho &= \rho_0 - \alpha T - \kappa n, \end{aligned} \tag{4}$$

where κ is the power coefficient, α is the temperature coefficient, γ is the reciprocal time constant of heat loss, and ρ_0 is the external reactivity Steady–state solutions (n_s, T_s) of this system are a zero solution $(0,0)$ and a nonzero solution $(n_0, T_0) = (\frac{\gamma\rho_0}{\alpha K + \gamma\kappa}, \frac{K\rho_0}{\alpha K + \gamma\kappa})$

For $\rho_0 > 0$, the zero solution corresponds to a zero power state that is unstable for infinitesimal disturbances (linearly unstable) and the nonzero solution (n_0, T_0) corresponds to an operating power state that may or may not be stable for infinitesimal disturbances (linearly stable or not, respectively) depending upon the parameter $\mu = \frac{\rho_0}{l}$ It is of our interest to see how the operating state of the reactor responds to large disturbances

Choosing the parameters $K = 50$, $\frac{\alpha}{l} = 1$, $\frac{\kappa}{l} = -1$, and $\gamma = 10$, the steady-state solution diagram and linear stability of each solution are shown in Fig 3 as a function of the parameter μ Running the BIFOR2 code[6], we obtain that $\mu_{cr} = 40$ is a Hopf bifurcation point and stable limit cycles exist at μ slightly larger than μ_{cr}

Let $x = n - n_0$ and $y = T - T_0$, then the system Eq (4) is transformed into the following form

$$\frac{dx}{dt} = \frac{-\kappa x - \alpha y}{l}(x + n_0),$$
$$\frac{dy}{dt} = Kx - \gamma y \tag{5}$$

The zero power state is also transformed into $(-n_0, -T_0)$ and the operating power state is transformed into $(0,0)$

Devooght and Smets[5] used four methods to determine the nonlinear stability region of the operating power state $(0,0)$ topological method, Lyapunov's second method, Aizermann's method, and Rosen's method As a result, applications of Lyapunov's second method yielded the largest domain of stability than other methods Each of the stability regions estimated by four methods is still very small compared with the entire stability domain Hence, we want to find the entire stability region by applying the method described in this paper

The Lyapunov function used by Devooght and Smets may be written as

$$V(x,y) = x - n_0 \log\left(\frac{x}{n_0} + 1\right) + \frac{[\alpha y - \gamma l \log(\frac{x}{n_0} + 1)]^2}{2l(\alpha K + \gamma\kappa)} \tag{6}$$

The region of nonlinear asymptotic stability is determined by plotting the curve $V = V_{\max}$ that is just tangent to $\frac{dV}{dt} = 0$

We will find the stability region in the case of $\mu = 6$ $V_{\max}$ turns out to be 26 05 [7] First, let us use Chiang and Thorp's method given in Ref 2 $V_{\max}$ is the critical level value η defined in this method We determine the stability region by starting with the given Lyapunov function Eq (6) By repeating the procedure of the expansion scheme of the Lyapunov function with the critical level value $\eta = 26\ 05$, we obtain a sequence of stability regions of the operating point $(0,0)$, as shown in Fig 4

The stability region of the operating state is not a closed set but an open set in phase space That is, the stability domain expands continually as the number of expansions of the Lyapunov function increases

Let us now estimate the stability region by using the new method described in this paper that starts from a positive definite function The sequence of regions expanded from $W(x,y) = V(x,y)$ in Eq (6), which is a positive definite function, is sketched in Fig 5 We used an arbitrary choice $\xi = 100$ The unstable subset of the starting region given as $S_V(\xi)$ disappears after a few expansions because its dynamics evolves very quickly With a comparable number of expansions, the stability regions identified by the new method are much wider than those identified by the method of Chiang and Thorp

Xenon–Feedback Model

Chernick, Lellouche, and Wollman[8] considered the space-independent kinetics equations to investigate dynamics of a reactor with xenon and temperature effects They showed the boundedness of the solution for a reactor with negative prompt flux coefficient, which is a stable limit cycle around the equilibrium solution Recently, Rizwan-uddin[9] presented results obtained using the BIFDD code for this simple reactor model of space-independent xenon oscillations He showed that, depending on the value of ρ_0, subcritical or supercritical Hopf bifurcation occurs and hence there exist unstable or stable limit cycle solutions at various operating points in $\gamma - \rho_0$ parameter space

The space-independent kinetics equations they used are as follows

$$\begin{aligned} l\frac{d\phi}{dt} &= (\rho_0 - \frac{\sigma_x X}{c\Sigma_f} - \gamma\phi)\phi, \\ \frac{dX}{dt} &= y_x\Sigma_f\phi - \lambda_x X + \lambda_i I - \sigma_x X\phi, \\ \frac{dI}{dt} &= y_i\Sigma_f\phi - \lambda_i I, \end{aligned} \tag{7}$$

where X and I are the Xe^{135} and I^{135} concentrations, respectively, γ is the overall flux coefficient, and ρ_0 is the external reactivity at a steady-state point Steady-state solutions (ϕ_s, X_s, I_s) are $(0,0,0)$ and (ϕ_0, X_0, I_0)

When the parameters are given as $\sigma_x = 3 \times 10^{-18} cm^2$, $y_i = 6\,4 \times 10^{-2}$, $y_x = 0$, $\lambda_x = 2\,09 \times 10^{-5}/sec$, $\lambda_i = 2\,87 \times 10^{-5}/sec$, $l = 0\,1 sec$, $\Sigma_f = 0\,05 cm^{-1}$, $c = 1\,5$, and $\gamma = 0\,03 \times 10^{-14}$, a bifurcation diagram in $\gamma - \rho_0$ parameter space is given in Ref 9 Using the BIFOR2 code, we find three Hopf bifurcation points, of which one leads to supercritical bifurcation (stable limit cycle) and the other two lead to subcritical bifurcations (unstable limit cycles) as the value of ρ_0 increases The solution diagram is shown in Fig 6

Let $x = \phi - \phi_0$, $y = X - X_0$, and $z = I - I_0$, then the system becomes

$$\begin{aligned} \frac{dx}{dt} &= -\frac{\gamma}{l}x^2 - \frac{\gamma\phi_0}{l}x - \frac{\sigma_x}{lc\Sigma_f}xy - \frac{\sigma_x\phi_0}{lc\Sigma_f}y, \\ \frac{dy}{dt} &= (y_x\Sigma_f - \sigma_x X_0)x - (\lambda_x + \sigma_x\phi_0)y + \lambda_i z, \\ \frac{dz}{dt} &= y_i\Sigma_f x - \lambda_i z, \end{aligned} \tag{8}$$

and the corresponding steady-state solutions (x_s, y_s, z_s) become $(-\phi_0, -X_0, -I_0)$ and $(0,0,0)$

Since the xenon feedback model Eq (8) is a stiff system, it is very time consuming to determine the entire stability region by using Chiang and Thorp's method, which is not practical in current computation This is overcome by increasing the time step using

an implicit scheme and by expanding the starting positive definite function using the new method.

Following the procedure of the new method given in this paper, we can effectively find the stability boundary of xenon oscillation of the equilibrium point $(0,0,0)$. Choosing a specific positive definite function $W(x,y,z) = 100x^2 + 10y^2 + z^2$ and a level value $\xi = 1 \times 10^{24}$, we obtain the stability region converged at about 7,000 expansions (using fully implicit scheme). The stability region cut by the $I = 0$ plane for $\rho_0 = 5.7 \times 10^{-4}$ is shown in Fig. 7.

CONCLUSIONS

We have developed a constructive method for estimating asymptotic stability domains of nonlinear reactor models: a new method that is based on expansion of any positive definite function instead of a Lyapunov function. This new method allows us to estimate the exact stability domain more easily even for stiff systems, compared to the existing methods that require knowledge of the Lyapunov function.

We applied these methods to several reactor models reported in the literature. The results show that the methods in this paper, in particular, the new expansion method provides estimates of the exact stability domains much more effectively, while the existing methods identify only small subsets, if at all, of the entire stability domains.

REFERENCES

1. J. P. LaSalle and S. Lefschetz, *Stability by Liapunov's Direct Method with Applications*, Academic Press, New York, 1961.
2. H. D. Chiang and J. S. Thorp, "Stability Regions of Nonlinear Dynamical Systems: A Constructive Methodology," IEEE Trans. Automat. Contr., **34**, 1229, 1989.
3. J. P. LaSalle, "Some Extensions of Liapunov's Second Method," in J. K. Aggarwal and M. Vidyasagar, *Nonlinear Systems: Stability Analysis*, Dowden, Hutchinson & Ross, Inc., 1977.
4. C. Y. Yang, *Nonlinear Stability Analysis of Nuclear Reactors under Reactivity Feedbacks*, Korea Advanced Institute of Science and Technology, PhD Thesis (in preparation).
5. J. Devooght and H. B. Smets, "Determination of Stability Domains in Point Reactor Dynamics," Nucl. Sci. Eng., **32**, 82, 1967.
6. B. D. Hassard, N. D. Kazarinoff, and Y.-H. Wan, *Theory and Applications of Hopf Bifurcation*, London Mathematical Society Lecture Note Series 41, Cambridge Univ. Press, 1981
7. D. L. Hetrick, *Dynamics of Nuclear Reactors*, The University of Chicago Press, Chicago, 1971.
8. J. Chernick, G. Lellouche, and W. Wollman, "The Effect of Temperature on Xenon Instability," Nucl. Sci. Eng., **10**, 120, 1961.
9. Rizwan-uddin, "Space-Independent Xenon Oscillations Revisited," Tran. Am. Nucl. Soc., **60**, 343, 1989.

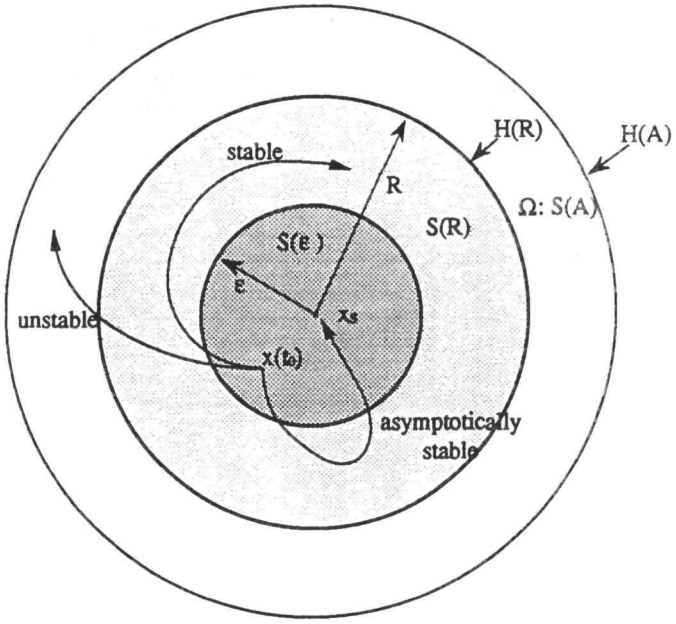

Figure 1. Definitions of stability: LaSalle and Lefschetz (1961)

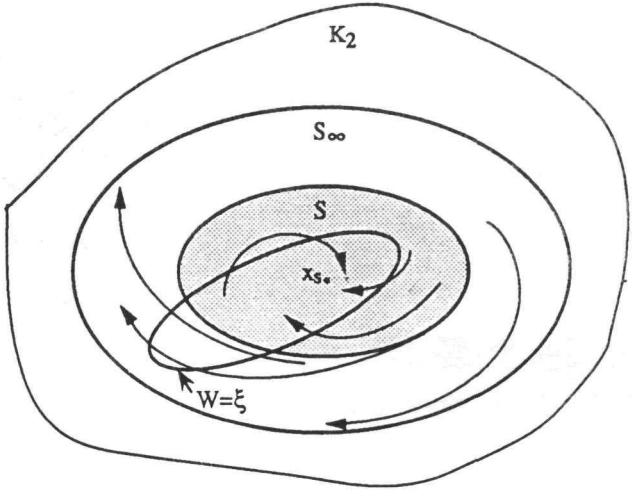

Figure 2. Time trajectories around the stability region S

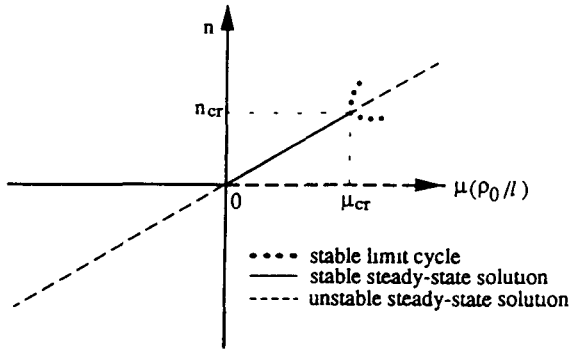

Figure 3. Solution diagram: $(\mu_{cr}, n_{cr}) = (40,10)$

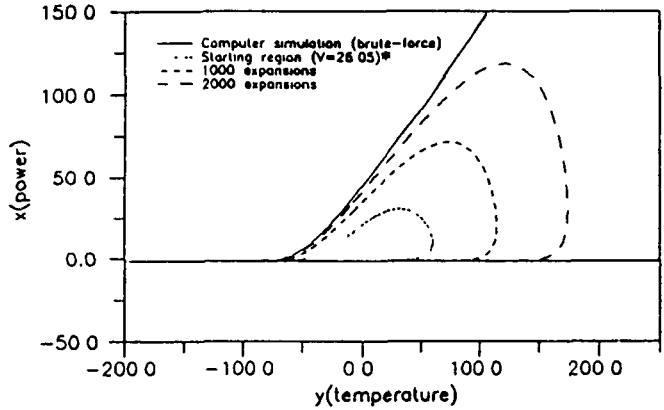

Figure 4. Stability regions at each expansion
: Chiang and Thorp's method (d=0.001)
(* Stability region found by Devooght and Smets using the Lyapunov function)

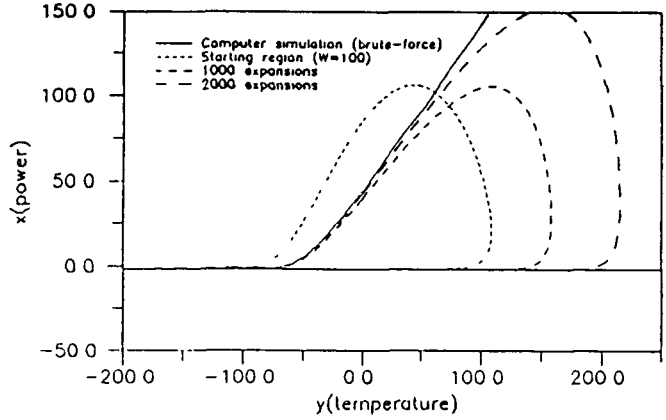

Figure 5. Interim regions at each expansion: new method (d=0.001)

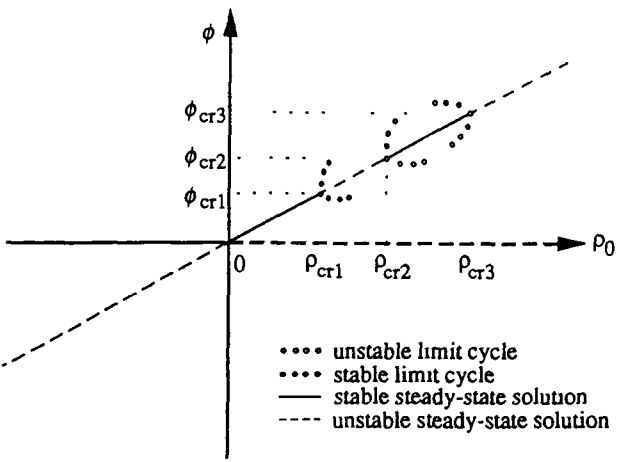

Figure 6. Solution diagram : (ρ_{cr1}, ϕ_{cr1})=(6.616e-6,1.029e9)
(ρ_{cr2}, ϕ_{cr2})=(5.520e-4,7.019e10)
(ρ_{cr3}, ϕ_{cr3})=(5.095e-3,8.890e11)

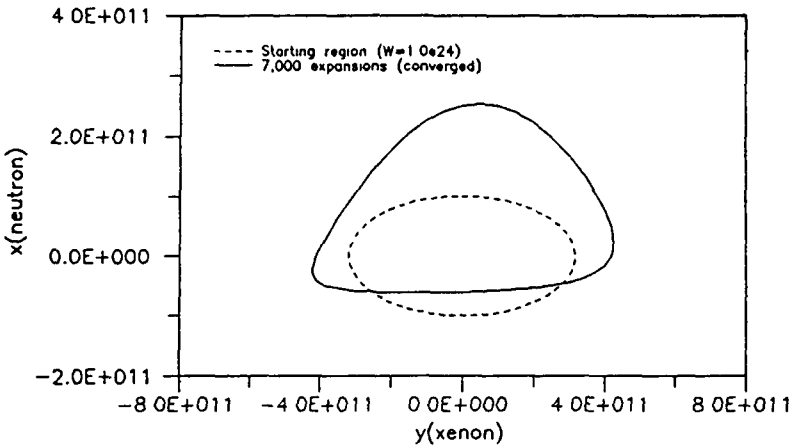

Figure 7. Stability region using new method (d=1000.0)
: cutaway view by the z(iodine) = 0 plane

A Variable Timestep Generalized Runge-Kutta Method for the Numerical Integration of the Space-Time Diffusion Equations

B N. Aviles, T M. Sutton, and D J Kelly, III

Knolls Atomic Power Laboratory
P O Box 1072
Schenectady, NY 12301-1072

ABSTRACT

A generalized Runge-Kutta method has been employed in the numerical integration of the stiff space-time diffusion equations The method is fourth-order accurate, using an embedded third-order solution to arrive at an estimate of the truncation error for automatic timestep control The efficiency of the Runge-Kutta method is enhanced by a block factorization technique that exploits the sparse structure of the matrix system resulting from the space and energy discretized form of the time-dependent neutron diffusion equations Preliminary numerical evaluation using a one-dimensional finite difference code shows the sparse matrix implementation of the generalized Runge-Kutta method to be highly accurate and efficient when compared to an optimized iterative theta method

INTRODUCTION

Several time differencing methods have been developed for the solution of the space-time diffusion equations Examples include the theta method[1,3], the improved quasi-static method[4,5], the stiffness confinement method[6], and the exponential transform method[7] Recently, an implicit generalized Runge-Kutta (GRK) method developed by Kaps and Rentrop[8,9] has been applied successfully to the solution of the point kinetics equations[10] The Kaps-Rentrop GRK method has been shown to be more accurate and efficient than other time differencing techniques for point kinetics transients due to its higher order and systematic variable timestep algorithm[11] This paper describes a sparse matrix implementation of the Kaps-Rentrop GRK method that is suitable for space-time diffusion applications

KAPS-RENTROP GENERALIZED RUNGE-KUTTA FORMULAS

We begin with the following initial value problem

$$y'(x) = f(y(x)) \tag{1}$$

where

$y(x)$ = vector of N dependent variables,

$y'(x)$ = vector of $y(x)$ derivatives with respect to x, and

$y(x_0) = y_0$

To advance the system solution from x_0 to $x_0 + h$, the Kaps-Rentrop GRK method[8-9] forms the following general solution

$$y(x_0 + h) = y_0 + \sum_{i=1}^{s} c_i k_i \tag{2}$$

where

h = step size,

s = number of stages,

c_i = fixed expansion constants, and

k_i = vector of expansion coefficients

The k_i vectors are found by solving a system of N linear equations for s different right hand sides[8]

$$\left[I - \gamma h f'(y_0)\right] k_i = hf\left(y_0 + \sum_{j=1}^{i-1} \alpha_{ij} k_j\right) + hf'(y_0) \sum_{j=1}^{i-1} \gamma_{ij} k_j \text{, for } i = 1, \quad ,s \tag{3}$$

where

I = identity matrix,

$\gamma, \gamma_{ij}, \alpha_{ij}$ = problem independent fixed constants,

$f(\ )$ = explicit function evaluation, and

$f'(y_0)$ = N x N Jacobi matrix of partial derivatives, $\left.\frac{\partial f}{\partial y}\right|_{y_0}$

The Kaps-Rentrop scheme employs a Runge-Kutta-Fehlberg method[12] to obtain an embedded estimate for $y(x_0 + h)$ This is accomplished by computing a lower order estimate, $\hat{y}(x_0 + h)$, using different expansion constants, $\hat{c}_i$, for $i = 1, \quad ,\hat{s}$, where $\hat{s} < s$, but the k_i expansion coefficients remain the same The smallest values allowing an embedded solution are $\hat{s} = 3$ and $s = 4$, resulting in a fourth-order method[8]

Expanding Eq (3) for $s = 4$ yields the four linear equation systems to be solved for the k_i vectors[9]

$$(i) \qquad [I - \gamma h f'(y_0)]\, k_1 = hf(y_0)$$

$$(ii) \qquad [I - \gamma h f'(y_0)]\, (k_2 + \frac{\gamma_{21}}{\gamma} k_1) = hf(y_0 + \alpha_{21} k_1) + \frac{\gamma_{21}}{\gamma} k_1$$

$$(iii) \qquad [I - \gamma h f'(y_0)]\, (k_3 + \frac{\gamma_{31}}{\gamma} k_1 + \frac{\gamma_{32}}{\gamma} k_2) = hf(y_0 + \alpha_{31} k_1 + \alpha_{32} k_2) + \frac{\gamma_{31}}{\gamma} k_1 + \frac{\gamma_{32}}{\gamma} k_2 \tag{4}$$

$$(iv) \qquad [I - \gamma h f'(y_0)]\, (k_4 + \frac{\gamma_{41}}{\gamma} k_1 + \frac{\gamma_{42}}{\gamma} k_2 + \frac{\gamma_{43}}{\gamma} k_3)$$

$$= hf(y_0 + \alpha_{41} k_1 + \alpha_{42} k_2 + \alpha_{43} k_3) + \frac{\gamma_{41}}{\gamma} k_1 + \frac{\gamma_{42}}{\gamma} k_2 + \frac{\gamma_{43}}{\gamma} k_3$$

Each integration step requires one L-U decomposition of the matrix $[I - \gamma h f'(y_0)]$ followed by four back-substitution steps to determine the four k_i vectors

The fixed expansion constants, γ, γ_{ij}, and α_{ij}, result from solving the "equations of condition" associated with the Runge-Kutta method Kaps and Rentrop provide two sets of constants and their associated regions of stability[8] The

set chosen for this study, denoted as GRK4T, is $A(89.3°)$ stable for the fourth-order method and has been shown to perform better than other constant sets in numerical tests[8]. The constants are listed in Table 1.

AUTOMATIC STEPSIZE CONTROL

The Kaps-Rentrop method exploits the availability of both third and fourth order estimates of $y(x_0 + h)$ to control step size automatically[8]. If we denote

$$y_{4th} = y(x_0 + h) = y_0 + \sum_{i=1}^{4} c_i k_i \tag{5}$$

and

$$y_{3rd} = \hat{y}(x_0 + h) = y_0 + \sum_{i=1}^{3} \hat{c}_i k_i$$

then the exact solution, y_{exact}, can then be expressed as

$$y_{exact} = y_{4th} + h^5 g_{5th} + \quad = y_{3rd} + h^4 g_{4th} + \tag{6}$$

where g_{5th} and g_{4th} represent higher order terms. Thus, the maximum scaled truncation error for the step is

$$Err = max\left|\frac{y_{4th} - y_{3rd}}{y_{scal}}\right| = max\left|\frac{h^4 g_{4th} + }{y_{scal}}\right|, \tag{7}$$

where y_{scal} is an appropriate scaling vector. For a successful integration step, we require the maximum scaled truncation error to be smaller than a specified error tolerance, ε

$$Err < \varepsilon \tag{8}$$

In order for the next timestep, h_{next}, to be successful, we also require

$$\left(\frac{max\left|h_{next}^4 g_{4th,next}\right|}{y_{scal}}\right) < \varepsilon \tag{9}$$

If we assume $g_{4th,next} = g_{4th}$, an estimate of h_{next} can be made

$$h_{next} < h\left(\frac{\varepsilon}{Err}\right)^{1/4} \tag{10}$$

Finally, to reduce the number of steps that are rejected and to prevent a zig-zag behavior in successful step sizes, a safety factor of 0.9 is included in the determination of h_{next}, and h_{next} is bounded

$$h_{next} < 0.9\ h\left(\frac{\varepsilon}{Err}\right)^{1/4}, \qquad 0.5h < h_{next} < 1.5h \tag{11}$$

APPLICATION OF THE KAPS-RENTROP METHOD TO THE TIME-DEPENDENT DIFFUSION EQUATIONS

The next two sections describe the implementation of the Kaps-Rentrop method for space-time diffusion theory applications. The few-group, time-dependent diffusion equations without group skipping are written as

$$\frac{1}{v_g}\frac{\partial \Phi_g}{\partial t} = D_g \nabla^2 \Phi_g - \Sigma_g \Phi_g + \Sigma_{g-1 \to g} \Phi_{g-1} + (1-\bar{\beta})\chi_g^p \sum_{\bar{g}} \frac{\nu}{k_{eff}} \Sigma_{f\bar{g}} \Phi_{\bar{g}} + \chi_g^d \sum_l \lambda_l C_l$$

$$\text{for } g = 1, \quad , G \tag{12}$$

and

$$\frac{\partial C_l}{\partial t} = \bar{\beta}_l \sum_{\bar{g}} \frac{\nu}{k_{eff}} \Sigma_{f\bar{g}} \Phi_{\bar{g}} - \lambda_l C_l$$

$$\text{for } l = 1, \quad , L$$

where the spatial indexing has been suppressed for simplicity. In matrix form, Eqs. (12) become

$$\frac{dy}{dt} = [F]y \tag{13}$$

where

$$y = col\left[\vec{\Phi}_1, \vec{\Phi}_2, \quad , \vec{\Phi}_G, \vec{C}_1, \vec{C}_2, \quad , \vec{C}_L\right],$$

$$\vec{\Phi}_g = col\left[\Phi_g^1, \Phi_g^2, \quad , \Phi_g^M\right],$$

$$\vec{C}_l = col\left[C_l^1, C_l^2, \quad , C_l^M\right],$$

M = total number of nodes,

G = number of flux energy groups,

L = number of delayed neutron precursor groups, and

$[F]$ = coefficient matrix arising from the time dependent diffusion equations.

Figure 1 presents the generic structure of the $[F]$ matrix for a three-dimensional, two flux energy group and six delayed neutron precursor group problem. It is important to note that the difference in the matrix structure for one-, two-, or three-dimensional geometries is manifested in the G three-, five-, or seven-stripe diagonal flux blocks.

The Kaps-Rentrop Jacobi matrix, $[I - \gamma h f'(y_0)]$, retains the structure of the $[F]$ coefficient matrix. Therefore, each timestep requires one L-U decomposition of a matrix with the structure of Figure 1, followed by four back-substitutions to obtain the four k_i expansion coefficient vectors. It is obvious that, for a large number of nodes, an L-U decomposition of the full matrix becomes prohibitive. Iterative solution methods are not thought practical in this situation for two reasons. First, four complete iterative solutions must be performed each timestep to obtain the four k_i vectors. Second, the k_i vectors can be numerically very close to zero for mild transients and are identically zero for a null (extended steady state) transient. Iterating on near-zero values leads to slow convergence behavior for standard iterative procedures. Therefore, a direct matrix solution procedure tailored to the sparse matrix structure of Figure 1 has been developed and is described next.

SPARSE MATRIX L-U DECOMPOSITION ALGORITHM

The structure of the Jacobi Matrix (Figure 1) lends itself easily to a block factorization L-U decomposition technique. The sparse structure is of a doubly-bordered block diagonal form[13]. This section describes an efficient block factorization technique, referred to in reference 13 as "one-way dissection," that can be used to solve a system having a

doubly-bordered block diagonal form This method reduces the solution computational time when compared to a standard L-U decomposition of the full matrix system Also, storage reduction techniques that reduce the amount of required memory have been implemented

We begin by breaking the Jacobi matrix into blocks denoted by $[A_{ij}]$ in Figure 2 Because the structures of the $[A_{12}]$, $[A_{21}]$, and $[A_{22}]$ matrices are known, they can be stored in vector rather than matrix form

1) The diagonal matrix $[A_{22}]$ $(M\ \ L \times M\ \ L)$ is stored in a vector of length $M\ \ L$

2) The matrix $[A_{12}]$ $(M\ \ G \times M\ \ L)$ is stored by row in a vector of length $M\ \ G\ \ L$

3) The matrix $[A_{21}]$ $(M\ \ L \times M\ \ G)$ is stored by column in a vector of length $M\ \ G\ \ L$

Currently, storage of the $[A_{11}]$ matrix remains full $(M\ \ G \times M\ \ G)$, although its sparse structure can also be exploited to reduce storage

Given the matrix system with multiple right hand sides, $[A]k_i = b_i$, the one-way dissection proceeds as follows

1) Decompose the system matrix, $[A]$, into blocks as described above Note that the constant vector and the unknown vector will each be split into two pieces, b_{1i}, b_{2i}, k_{1i}, and k_{2i}, respectively

2) Compute $[D_{11}] = [A_{11}] - [A_{12}][A_{22}]^{-1}[A_{21}]$ (14)

Note that this operation can be performed efficiently because inverting the $[A_{22}]$ matrix is trivial and the product operations involve only vector multiplication The $[D_{11}]$ matrix retains the structure of the original $[A_{11}]$ block

3) Perform an L-U decomposition on the $[D_{11}]$ matrix Currently, an L-U decomposition is performed on the full $[D_{11}]$ matrix For large problems or many neutron energy groups, the sparse structure of this matrix must also be exploited with an appropriate decomposition technique

For each of the four k_i vectors and associated constant vectors, b_i, from the Kaps-Rentrop equations (Eq 5)

4) Compute $q_{2i} = [A_{22}]^{-1} b_{2i}$ (15)

5) Solve $[D_{11}]q_{1i} = b_{1i} - [A_{12}]q_{2i}$ for q_{1i} by back substitution (16)

6) Then $k_{1i} = q_{1i}$ and $k_{2i} = q_{2i} - [A_{22}]^{-1}[A_{21}]k_{1i}$ (17)

In summary, for each Kaps-Rentrop integration step, steps (1) through (3) must be performed once to arrive at the L-U form of the $[D_{11}]$ matrix Steps (4) through (6) must then be performed four times to compute the k_i vectors The most CPU intensive step of the sparse matrix algorithm is the L U decomposition in step (3)

METHOD EVALUATION USING A ONE-DIMENSIONAL FINITE-DIFFERENCE CODE

The sparse matrix block factorization implementation of the Kaps-Rentrop method (denoted as K-R Sparse) was evaluated using a one-dimensional finite-difference code The K-R Sparse algorithm was compared to the Kaps-Rentrop method with an L-U decomposition performed on the full Kaps-Rentrop Jacobi matrix (hereafter referred to as K-R Full) The K-R Sparse algorithm was also compared to an optimized Theta method employing a block succes-

sive over-relaxation (block-SOR) technique[14] The Theta method was optimized for the one-dimensional finite-difference code by (1) using an explicit solution method for the (1-D) tridiagonal flux blocks[15], (2) computing an optimum over-relaxation parameter from the spectral radius of the Jacobi iteration matrix, (3) choosing the implicit method ($\theta = 1$) for both fluxes and precursors and (4) employing a step-doubling technique for error control and automatic timestep selection[15]

Several transient comparisons were made for a one-dimensional geometry based on the ANL benchmark problem BSS-6[16] The geometry and group constant data are presented in Figure 3 and Table 2, respectively All transients were initiated from a tightly converged solution obtained using the finite-difference option of the KAPL Nodal Expansion Method code, NODEX[17] All reported CPU times are for a single processor on a CRAY YMP/8

Transient 1 Ramp Reactivity Increase

The first transient involved a 1% linear decrease of Region 1 thermal absorption cross section in 1 0 second (ANL BSS-6-A2)[16] Each model consisted of 120 nodes The initial timestep size was 1 0E-3 seconds and the relative truncation error tolerance, ε, was chosen to be 1 0E-2 for both the Kaps-Rentrop and Theta method to ensure accurate solutions Table 3 summarizes the results and Figure 4 is a plot of power versus time From Table 3, it can be seen that both the Kaps-Rentrop and Theta method are very accurate (error in total power at t=4 seconds is less than 0 4%), but the K-R Sparse method required fewer timesteps due to its higher order accuracy and required significantly less CPU time than did the Theta method The effects of the block factorization technique and the improved vector storage can be seen in the K-R Sparse versus K-R Full results The two implementations of the Kaps-Rentrop method produce identical results, but the sparse matrix implementation executes the transient in 1/40th of the CPU time and requires 1/25th of the storage

Transient 2 Sinusoidal Reactivity Perturbation

The second transient was a sinusoidal reactivity perturbation due to a sinusoidal variation of Region 1 thermal absorption cross section by 1% with a period of 1 0 second continuously for four seconds Node size, error tolerance, and initial timestep size remained the same as in Transient 1 Table 4 and Figure 5 present the results of this simulation Both the Kaps-Rentrop and Theta method exhibit similar accuracy, forced by the truncation error tolerance requirements The results of this transient highlight the benefit of the fourth-order Runge-Kutta method over the first-order Theta method The Kaps-Rentrop method required only 92 timesteps and 8 8 seconds to complete the transient, whereas the Theta method required 2 7 times as many steps and over forty times more CPU time

EXTENSION OF KAPS-RENTROP METHOD TO OTHER PROBLEM SIZES

The results presented in this paper involve a one-dimensional geometry with 120 nodes A question arises as to how well the Kaps-Rentrop method performs for larger problems For the 1-D finite difference cases, a parametric study was performed comparing CPU time per timestep versus problem size for the Kaps-Rentrop method and optimized 1-D Theta method Because both Kaps-Rentrop methods use a direct L-U decomposition, the CPU time per timestep scales roughly as N^3, where $N = M \ (G+L)$ for K-R Full, and $N = M \ G$ for K-R Sparse The iterative block-SOR Theta method scales approximately linearly with N, where $N = M \ (G+L)$ Therefore, at some problem size (roughly 600 nodes for the sinusoid problem), the K-R Sparse algorithm requires more CPU time per timestep than does the Theta method However, recall that Kaps-Rentrop took three times fewer steps to complete the transient, indicating that the K-R Sparse method would still require less total CPU time for a 960 node problem

For three-dimensional geometries, the Kaps-Rentrop CPU time per timestep curve would remain basically the same because we are performing an L-U decomposition on the full $[D_{11}]$ flux matrix ($M \ G \times M \ G$) The Theta method will necessarily become more expensive because the flux blocks will lose the desirable tridiagonal structure Therefore, the CPU time per timestep comparison would favor the Kaps-Rentrop Sparse method for 3-D geometries For very large three-dimensional problems, a more efficient L-U decomposition algorithm exploiting the structure of the $[D_{11}]$ matrix must be employed

CONCLUSIONS

This paper has described a variable timestep Generalized Runge-Kutta method suitable for time-dependent diffusion theory applications The basic method, timestep control, and sparse matrix implementation are derived from sound

mathematical theory. The method utilizes a direct matrix solution algorithm, therefore its CPU time per timestep behavior is invariant to the type of transient and depends only on the problem size The sparse matrix implementation of the Kaps-Rentrop GRK method is fourth-order accurate and very efficient for the range of 1-D test problems investigated. The Kaps-Rentrop sparse matrix method took consistently fewer timesteps and less CPU time when compared to an optimized 1-D Theta method.

ACKNOWLEDGEMENTS

The authors would like to thank Dr. M.R. Mendelson and Dr. R.G. Gamino for their suggestions during this research

REFERENCES

1. A.V. Vota, N.J Curlee, and A.F. Henry, "WIGL3 - A Program for the Steady-State and Transient Solution of the One-Dimensional, Two-Group, Space Time Diffusion Equations Accounting for Temperature, Xenon, and Control Feedback," WAPD-TM-788, February 1969.

2. K.S. Smith, "An Analytic Nodal Method for Solving the Two-Group, Multidimensional Static and Transient Neutron Diffusion Equations," S M. and N.E. Thesis, Massachusetts Institute of Technology, Cambridge, MA, March 1979.

3 T.A. Taiwo and H.S. Khalil, "The DIF3D Nodal Kinetics Capability in Hex-Z Geometry -- Formulation and Preliminary Tests," Proc. Adv. in Math., Comp , and Reactor Phys , Vol 5, 23 2 2-1, Pittsburgh, PA, April 28 - May 2 1991

4. P.W. Kao, "Application of Supernodal Methods to Transient Analysis," Ph.D. Thesis, Massachusetts Institute of Technology Department of Nuclear Engineering, Cambridge, MA, August 1988.

5. H. Sano, Y Ishii, J. Koyama, and Y. Bessho, "Three-Dimensional, Multi-Group Nuclear Reactor Kinetic Program Based on a Vectorized Nodal Expansion Method," Proc. Adv. in Math , Comp., and Reactor Phys , Vol. 5, 30.2 5-1, Pittsburgh, PA, April 28 - May 2 1991.

6 Y.A. Chao and P. Huang, "Theory and Performance of the Fast-Running Multi-Dimensional PWR Kinetic Code, SPNOVA-K," Proc. ANS Int. Reac. Phys Conf., IV-153, Jackson Hole, WY, September 18-22, 1988.

7. P K. Hutt and M.P. Knight, "The Development of a Transient Neutron Flux Solution in the PANTHER Code," Trans. Amer. Nucl. Soc., Vol. 61, p. 348, Nashville, TN, June 1990.

8. P. Kaps and P. Rentrop, "Generalized Runge-Kutta Methods of Order Four with Stepsize Control for Stiff Ordinary Differential Equations," Numerische Mathematik, Vol. 33, pp. 55-68, 1979.

9. W.H. Press and S.A. Teukolsky, "Integrating Stiff Ordinary Differential Equations," Computers in Physics, May/ June 1989, pp. 88-91.

10. J. Sanchez, "On the Numerical Solution of the Point Reactor Kinetics Equations by Generalized Runge-Kutta Methods," Nucl. Sci. and Eng., Vol. 103, pp. 94-99, 1989.

11. D.J. Kelly and D.R. Harris, "Comparison of Variable Timestep Differencing Methods Applied to the Point Reactor Kinetic Equations," to be published in Trans. Amer. Nucl. Soc , Vol. 64, San Francisco, CA, Nov. 1991.

12. J. Stoer and R. Bulirsch, Introduction to Numerical Analysis, Springer-Verlag, New York, 1980

13. I.S. Duff, A.M. Erisman and J.K. Reid, Direct Methods for Sparse Matrices, Oxford University Press, New YOrk, 1986.

14. J.R. Westlake, A Handbook of Numerical Matrix Inversion and Solution of Linear Equations, John Wiley and Sons, New York, 1968.

15. W.H. Press, B.P. Flannery, S.A. Teukolsky and W.T. Vetterling, Numerical Recipes: The Art of Scientific Computing, Cambridge University Press, New York, 1986.

16. National Energy Software Center, Benchmark Problem Book, ANL-7416-Supplement 3, December 1985.

17. T M. Sutton, "NODEX: A High Order NEM-Based Multigroup Nodal Code," Proc. Adv. Nucl. Eng. Comp. and Rad. Shield., Sante Fe, NM, April 1989.

TABLE 1. GRK4T Expansion Constants (reference 8)

γ = 0 231	γ_{21} = 0 270629667752
γ_{31} = 0 311254483294	γ_{32} = 0 852445628482E-2
γ_{41} = 0 282816832044	γ_{42} = 0 457959483281
γ_{43} = -0 111208333333	
α_{21} = 0 462	
α_{31} = -0 815668168327E-1	α_{32} = 0 961775150166
$\hat{c}_1$ = -0 717088504499	$\hat{c}_2$ = 0 177617912176E-1
$\hat{c}_3$ = -0 590906172617E-1	
c_1 = 0 217487371653	c_2 = 0 486229037990
c_3 = 0 0	c_4 = 0 296283590357

TABLE 2. ANL BSS-6 Initial Two Group Constants (reference 16)

Constant		Region 1,3	Region 2
D_1	(cm)	1 5	1 0
D_2	(cm)	0 5	0 5
Σ_{r1}	(cm^{-1})	0 026	0 02
Σ_{r2}	(cm^{-1})	0 18	0 08
$\Sigma_{1\rightarrow 2}$	(cm^{-1})	0 015	0 01
$\nu\Sigma_{f1}$	(cm^{-1})	0 010	0 005
$\nu\Sigma_{f2}$	(cm^{-1})	0 2	0 099
χ_1		1 0	1 0
χ_2		0 0	0 0
v_1	(cm/s)	1 0E+7	1 0E+7
v_2	(cm/s)	3 0E+5	3 0E+5

Removal cross section includes capture, fission, and downscatter

Delayed Neutron Parameters

Group	$\bar{\beta}$	λ (s^{-1})
1	0 00025	0 0124
2	0 00164	0 0305
3	0 00147	0 1110
4	0 00296	0 3010
5	0 00086	1 1400
6	0 00032	3 0100

TABLE 3. Comparison of Kaps-Rentrop and Theta Method Performance: 1-D Ramp Transient

Method	Reference[1]	K R Sparse	K-R Full	Theta Method
Number of Nodes	120	120	120	120
Error Tolerance[2]	---	0 01	0 01	0 01
Initial Timestep Size (s)	0 001	0 001	0 001	0 001
Total Number of Timesteps	4000	28	28	41
Total CPU Time[3] (s)	NA	2 7	109 1	81 5
Required Storage (MWords)	NA	0 075	1 86	--[4]
Relative Power				
t = 0 0 s	1 000	1 000	1 000	1 000
t = 0 1 s	1 028	1 028	1 028	1 028
t = 0 2 s	1 063	1 062	1 062	1 061
t = 0 5 s	1 205	1 204	1 204	1 202
t = 1 0 s	1 740	1 738	1 738	1 736
t = 1 5 s	1 959	1 957	1 957	1 956
t = 2 0 s	2 166	2 163	2 163	2 163
t = 3 0 s	2 606	2 602	2 602	2 599
t = 4 0 s	3 108	3 102	3 102	3 096
Regional Power Fractions at t = 4 0 s				
Region 1	0 4424	0 4425	0 4425	0 4424
Region 2	0 4306	0 4303	0 4303	0 4303
Region 3	0 1272	0 1271	0 1271	0 1272

TABLE 4. Comparison of Kaps-Rentrop and Theta Method Performance: 1-D Sinusoid Transient

Method	Reference[5]	K-R Sparse	K-R Full	Theta Method
Number of Nodes	120	120	120	120
Error Tolerance[2]	---	0 01	0 01	0 01
Initial Timestep Size (s)	0 0001	0 001	0 001	0 001
Total Number of Timesteps	40,000	92	92	252
Total CPU Time[3] (s)	15,910	8 8	357 7	373 3

[1]reference for ramp is RAUMZEIT with a fixed 0 001 second timestep (reference 16)

[2]relative error tolerance used in automatic timestep control

[3]single processor on CRAY YMP/8

[4]Theta method not optimized for storage

[5]reference for sinusoid is Theta method with a fixed 0 0001 second timestep

FIGURE 1. Generic Structure of the Time-Dependent Diffusion Equation Coefficient Matrix

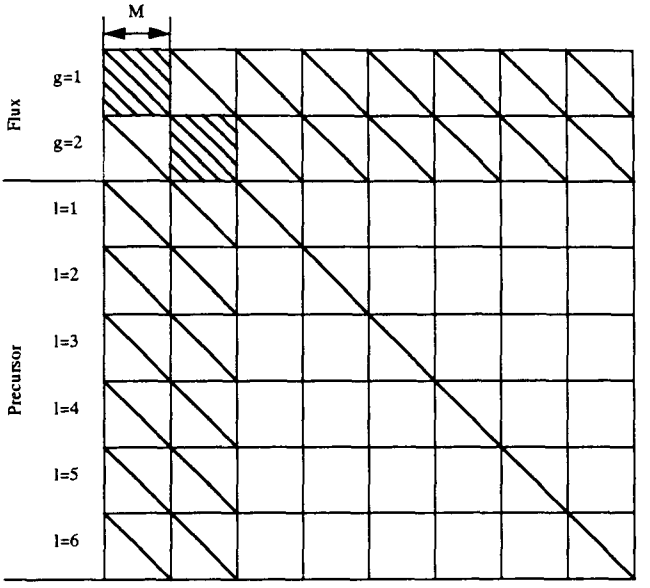

FIGURE 2. Kaps-Rentrop Method Jacobi Matrix in Block Form

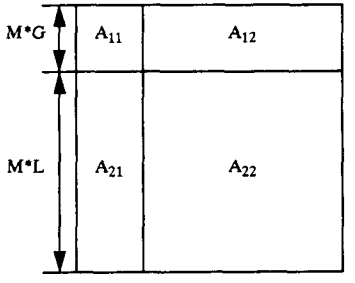

FIGURE 3. ANL-BSS-6 Model Geometry (reference 16)

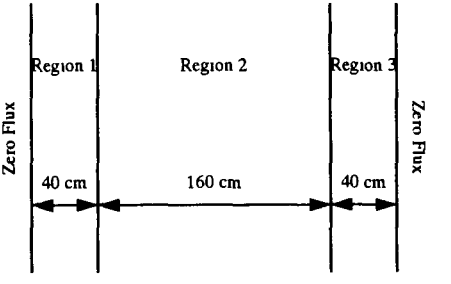

FIGURE 4: ANL BSS-6-A2, RAMP REACTIVITY
120 NODES, 2 FLUX, 6 PRECURSOR GROUPS

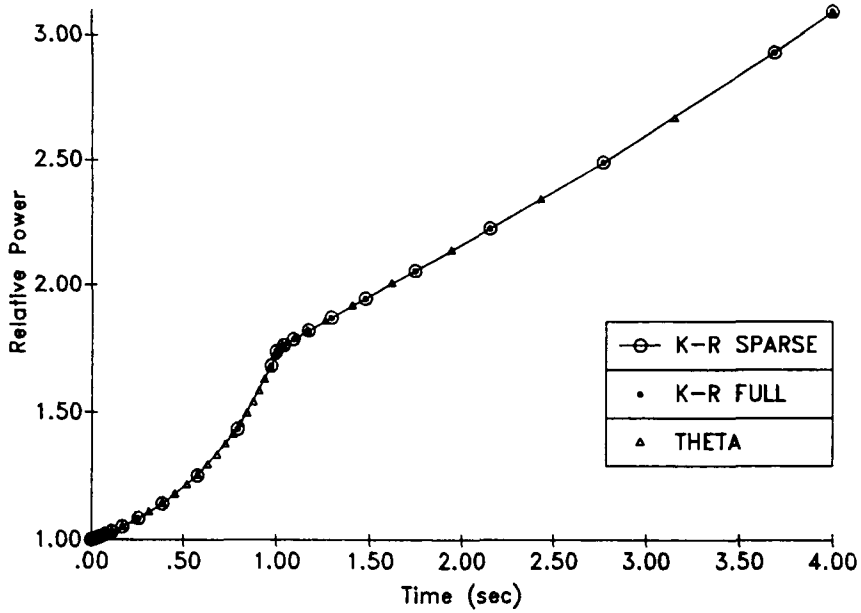

FIGURE 5: ANL BSS-6, SINUSOIDAL REACTIVITY
120 NODES, 2 FLUX, 6 PRECURSOR GROUPS

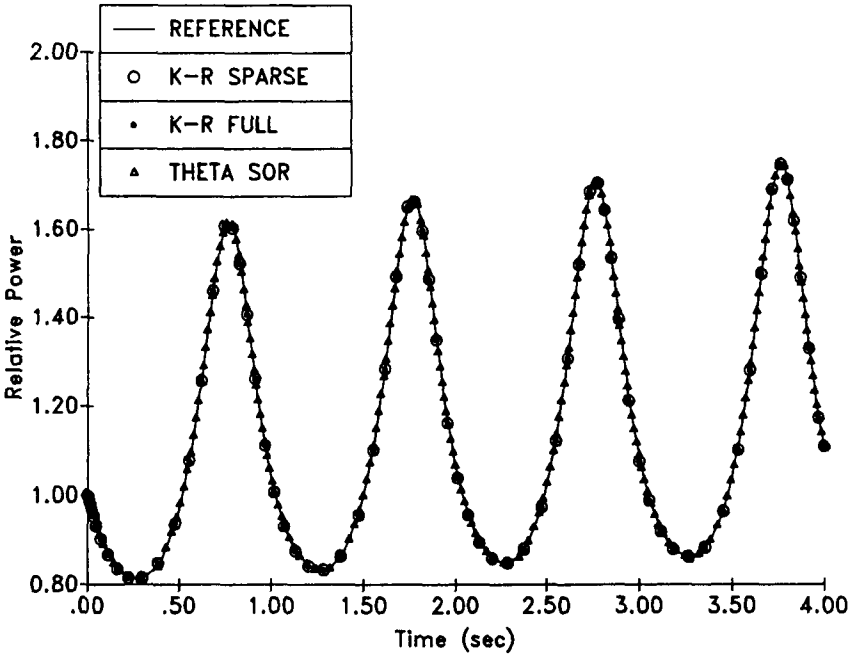

THE MODIFIED SOURCE ITERATION METHOD FOR FEW-GROUP SPACE-TIME DEPENDENT NEUTRON KINETIC EQUATIONS

V.G. Zimin and N.V. Schukin
Moscow Engineering Physical Institute,
31, Kashirskoe shosse, Moscow, 115409, USSR

ABSTRACT

Time-dependent formulations of the few-group space-dependent neutron kinetic equations are obtained using fully-implicit (backward-difference) approximations to the time derivatives. The fully-implicit equations can be solved at each time step using iterative procedures similar to those applied in static calculations. Usually, it's traditional source iteration method based on the standard combination of outer and inner iterations. However, as the results of numerical experiments and the presented analysis have shown, convergence rate of this algorithm in the transient calculations is not satisfactory.

Modified source iteration method with improved characteristics is presented. Results of the executed analysis and numerical experiments show, that presented method is 10-30 times faster than source iteration method. Such essential increase of the proposed method efficiency is due to faster converging iteration process and analytical presentation of the Neumann series sum for the inhomogeneous equation solution.

This method is useful for various techniques of space approximation and permits to use acceleration techniques proved for static calculations.

INTRODUCTION

During the last years substantial efforts have been made in the development of advanced computer codes for the on-line transient analysis of a nuclear power plant. Some of the reasons for this growing interest are increased accuracy of the simulation demands and licensing requirements to analyze off-nominal core conditions. In the most modern computer programs for describing power distribution few-group space-dependent kinetics models are used. As such codes have to operate on the mini-computer at the reactor site, under their development advanced numerical techniques are employed. For the spatial approximation of the neutron kinetic equations a large amount of coarse-mesh and nodal methods are suggested [1-3]. As in multidimensional case, the obtained system of the ordinary differential equations have too many variables, for time

approximation first order fully implicit schemes are used.[2-4] Sometimes, for analysis of the subcritical and delayed critical transients, also "prompt jump" approximation is applied.[5] Then, iteration methods are employed for system solution. As a rule, as outer iterations organization method the source iteration method, the same as for a static problem, is used.

FORMULATION OF PROBLEM

The starting point for both methods is the set of few-group space-time dependent neutron kinetic equations written in matrix form as

$$v^{-1}\frac{d\,\Phi(t)}{dt} = -\,L\,\Phi(t)+(1-\beta)\chi_p F\,\Phi(t)+\sum_{i=1}^{I}\lambda_i\chi_i C_i(t) \qquad (1)$$

$$\frac{dC_i(t)}{dt} = \beta_i F\,\Phi(t) - \lambda_i C_i(t) \qquad (2)$$

The notation is fairly standard.

Integrating equation (2) on time interval $[t_j, t_{j+1}]$, delayed neutron precursors equations are obtained:

$$C_i(t+\Delta t)=C_i(t)\exp(-\lambda_i\Delta t)+\frac{1-\exp(-\lambda_i\Delta t)}{\lambda_i}\beta_i F\Phi(t+\Delta t) \qquad (3)$$

Substitute (3) to (1) and using fully implicit time-differencing scheme, equation (1) is approximated by:

$$\left[L+\frac{1}{\Delta t}v^{-1}\right]\Phi(t+\Delta t)=\left[(1-\beta)\chi_p+\sum_{i=1}^{I}\beta_i\chi_i(1-\exp(-\lambda_i\Delta t))\right]F\Phi(t+\Delta t)$$

$$+\sum_{i=1}^{I}\lambda_i\chi_i\exp(-\lambda_i\Delta t)C_i(t)+\frac{1}{\Delta t}v^{-1}\,\Phi(t) \qquad (4)$$

Equation (4) may be written as follows:

$$\Phi(t+\Delta t) = B\,\Phi(t+\Delta t) + f \qquad (5)$$

Suppose, that space and energy approximation of the equations conducted by such a way, that operator B satisfies the following conditions: B - linear operator; eigenfunctions set of the B-operator is complete; maximum module of the matrix B's eigenvalue λ_o is less than 1.

Then iteration process:

$$\phi^{\iota+1} = B\,\phi^{\iota} + f \qquad (6)$$

converges to equation (5) solution, and as result, to the equation (4) solution, i.e.:

$$\lim_{\iota\to\infty} \phi^{\iota} = \Phi(t+\Delta t)$$

with arbitrary initial vector ϕ^{o}.

TRADITIONAL SOURCE ITERATION METHOD

By using as outer iteration method of the source iteration method there are

$$B = \left[\frac{1}{\Delta t} v^{-1} + L\right]^{-1}\left[(1-\beta)\chi_p + \sum_{\iota=1}^{I} \beta_\iota (1-\exp(-\lambda_\iota \Delta t))\chi_d\right] F \qquad (7)$$

$$f = \left[\frac{1}{\Delta t} v^{-1} + L\right]^{-1}\left[v^{-1}\frac{\Phi(t)}{\Delta t} + \chi_d \sum_{\iota=1}^{I} \lambda_\iota C_\iota(t)\exp(-\lambda_\iota \Delta t)\right] \qquad (8)$$

Evaluate iteration process (6) convergency rate. To do so, from both parts of equation (5) subtract both parts of equation (6). Meaning $\delta^{\iota} = \Phi(t+\Delta t) - \phi^{\iota}$, obtain

$$\delta^{\iota+1} = B\,\delta^{\iota} \qquad (9)$$

Expression (7) corresponds to iteration process for homogeneous equation solution:

$$\lambda\,\delta = B\,\delta. \qquad (10)$$

Initial value of error δ^{o} can be expanded into a operator B eigenfunctions φ_k:

$$\delta^{o} = \sum_{k=0} a_k \varphi_k$$

then:

$$\delta^{\iota} = \sum_{k=o} a_k \, (\lambda_k)^{\iota} \, \varphi_k = (\lambda_o)^{\iota} \, a_o \, \varphi_o + \sum_{k=1} a_k \, (\lambda_k/\lambda_o)^{\iota} \varphi_k$$

Taking only first term obtain:

$$\lim_{\iota \to \infty} \delta^{\iota} \cong (\lambda_o)^{\iota} \, a_o \, \varphi_o \to 0 \, , \text{ that is } \|\delta^{\iota}\| \approx a_o \, |\lambda_o|^{\iota}$$

Evaluate maximum number of iterations T_I, necessary for required error $\varepsilon = e^{-N}$, suggesting, that $a_o \sim 1$:

$$(\lambda_o)^{T} < \varepsilon; \quad T_I > - \frac{N}{\ln(\lambda_o)}$$

Although, in the case of transient on delayed neutrons, fully implicit scheme does not impose essential restrictions on the time step size Δt on stability and accuracy, iteration process converges slowly ($\lambda_o \approx 1$) and for required accuracy achievement e^{-N} the number of iterations required is:

$$T_I > - \frac{N}{\ln(\lambda_o)} \approx N/(1-|\lambda_o|) >> 1. \qquad (11)$$

The large number of iterations in this traditional algorithm is due to very slow speed of approximation to neutron flux amplitude, even if the space-energy distribution has been settled.

MODIFIED METHOD

We propose to modify iteration process, having stayed in the framework of the source iteration method. From both parts of the equation (6), written for i+1th step, both part of equation, written for preceding step are subtracted. Meaning the difference between values of neutron flux on the two next iterations as $\Delta^{\iota} = \phi^{\iota+1} - \phi^{\iota}$, for Δ^{ι} is obtained expression, similar to iteration process (7):

$$\Delta^{\iota} = B \, \Delta^{\iota-1} \qquad (12)$$

As a result

$$\lim_{\iota \to \infty} \Delta^{\iota} = (\lambda_o)^{\iota} \, a_o \, \varphi_o; \quad \| \Delta^{\iota}\| / \|\Delta^{\iota-1}\| \to \lambda_o \qquad (13)$$

Note, that

$$\sum_{k=0}^{i-1} \Delta^k = \phi^i - \phi^0, \qquad (14)$$

i.e.

$$\phi^i = \phi^0 + \sum_{k=0}^{i-1} \Delta^k. \qquad (15)$$

According to that, it is possible to build iteration process as follows. Supposing the initial distribution Φ^0, Φ^1 is calculated:

$$\Phi^1 = B\,\Phi^0 + f, \qquad (16)$$

from this, $\Delta^0 = \Phi^1 - \Phi^0$ will be found. Further, approximated solution from equation (15) is constructed, where Δ^i is defined from iteration process (12). Iteration process is carried out up to required accuracy of the maximum eigenvalue λ_o and eigenfunction of the matrix B is achieved. Finally, it is possible to obtain considerably more accurate approximation to the equation (5) solution, as compared to ϕ^i.
Really,

$$\Phi(t+\Delta t) = \phi^\infty = \phi^i + \sum_{k=i}^{\infty} \Delta^k,$$

$$\text{as } \Delta^k \approx (\lambda_o)^k\, a_o\, \varphi_o, \text{ then } \sum_{k=i}^{\infty} \Delta^k = a_o\, \varphi_o\, \frac{(\lambda_o)^i}{1-\lambda_o} = \frac{\Delta^i}{1-\lambda_o}$$

Therefore, corrected value of ϕ^i_{cor}:

$$\phi^i_{cor} = \phi^i + \frac{\Delta^i}{1-\lambda_o}, \qquad (17)$$

where maximum of the eigenvalue λ_o of the operator B is defined from (13).

Now let's define maximum number of iterations T_H, necessary for required error e^{-N} achievement for homogeneous equation solution. Similarly to above expressions, following is obtained:

$$T_H > - N / \ln(\lambda_1/\lambda_0) << T_I \qquad (18)$$

From this expression can be concluded, that maximum number of outer iterations in modified source iteration method at time step is equal to number of outer iterations during solution this problem in static formulation.

According to our numerical experience the zero vector is the most appropriate as initial approximation of ϕ^0 for solving next equation:

$$\left[L + \frac{1}{\Delta t} v^{-1}\right] \phi^1 = \left[(1-\beta)\chi_p + \sum_{i=1}^{I} \beta_i \chi_i (1-\exp(-\lambda_i \Delta t))\right] F\phi^0$$

$$+ \sum_{i=1}^{I} \lambda_i \chi_i \exp(-\lambda_i \Delta t) C_i(t) + \frac{1}{\Delta t} v^{-1} \Phi(t) \qquad (19)$$

If neutron flux distribution from previous time step $\Phi(t)$ is used as initial approximation ϕ^0, it may cause loosing iteration process convergence.

NUMERICAL RESULTS

Next test calculations are presented to demonstrate the convergence rate of modified source iteration method for different transients. The first of problems include spatially uniform perturbations of a homogeneous reactor. For these problems exist analytical solution as well. Second and third calculations involve a localized perturbation of a homogeneous reactor properties. All calculations were performed with and without "prompt jump" approximation that define influence this approximations on methods convergence rate. The numerical model have the following characteristics:

1. two energy groups
2. one delayed neutron group
3. finite-difference method of space approximation
4. one mesh point per hex in each horizontal plane
5. five axial mesh points
6. fully-implicit scheme of time approximation
7. incomplete Cholesky-conjugate gradient method for the iterative solution of systems of linear equations
8. step change in reactivity at time zero
9. convergence criterion of outer iterations 10^{-6}
10. time step size of test calculations 50 msec.

The few-group macroscopic cross sections and delayed neutron data for these problems are presented in Table 1. Reactor geometry used in test calculations is shown in Fig.1.

TEST 1:

The first series of calculations modeled a bare homogeneous reactor with spatial uniform perturbation in the production cross section. Spatial flux distribution in this transients is constant. These problem can be solved analytically using point kinetic equations. Test calculations were executed for 0.5 β and -0.3 β reactivity perturbation. Number of outer iterations for source iteration method and proposed method for both tests are given in Table 2,3.

TEST 2:

For evaluation of the convergence rate of the modified method in case of change of the flux distribution shape next calculations were carried out. In initial state of homogeneous reactor thermal absorption cross section in region 3 (see Fig. 1) was decreased and in region 2 was increased by 3.5%. Perturbation was an axially uniform step change at time zero. Reactivity of reactor received from static calculation is equal to 0.5 β. Radial distribution of the power is shown in Fig. 2 at steady state and at 3 sec. Difference between the transient power distribution at time 3 sec and asymptotic shape is quite acceptable (error less than 0.3%). Dependence of the central and the surrounding channels power versus time is presented in Fig. 3. Number of outer iterations for source iteration method and proposed method for this test are given in Table 4.

TEST 3:

In order to evaluate convergence rate of iteration process in dependence from value of the perturbation neutron distribution shape was performed test analogous to test 2. But in this test thermal absorption cross sections was changed by 7%, and production cross section was decreased so that reactivity of reactor was equal to 0.5 β. Radial distribution of the power is shown in Fig. 2 at steady state and at 3 sec. Difference between the transient power distribution at time 3 sec and asymptotic shape is less than 0.6%. Power of central and surrounding channels versus time is presented in Fig. 4. Number of outer iterations for source iteration method and proposed method for this test are given in table 5.

CONCLUSIONS

Results of the executed analysis and numerical experiments can conclude, that the presented method is 10-30 times faster than traditional source iteration method. High efficiency of the proposed method is result from the application of faster

converging iteration process and employment of analytical presentation of the Neumann series sum for equation (5) solution. As results of the test calculations show, traditional source iteration method is minimally efficient in cases when the changes of spatial flux distribution are small during time steps. In these cases, a lot of computational work is spent to many times calculate almost identical flux distribution. Modified source iteration algorithm demonstrates in these cases fast convergence rate. Maximum number of outer iterations in modified method at time step is equal to number of outer iterations required to solute this problem in static formulation. It's take place, when shape of neutron flux distribution changes significantly during the transient. Even in these hard transients modified source iteration method is 10 times faster than traditional method.

This method is currently being incorporated in fully coupled, three-dimensional computer code for the on-line transient analysis of РБМК[6]. Results of analysis method in the real transients will be presented in the near future. Finally, we would like to observe that the modified source iteration method has also been applied successfully in other computer code for solving few-group two- and three-dimensional neutron kinetic problems.

REFERENCES

[1] A.M. Sirotkin "Numerical methods of the neutron fields calculation" MEPhI, Moscow, 1989. /In Russian/

[2] W. Werner "Kinetics of Nuclear System: Solution Methods for the Space-Time Dependent Neutron Diffusion Equation" Advances in Nuclear Science & Technology, vol 10., Plenum Press, N.Y., 1977.

[3] R.D. Lawrence "Progress in nodal methods for the solution of the neutron diffusion and transport equations" Progress in Nuclear Energy, Vol.17, No 3, 1986, p. 271.

[4] M.R. Buckner, J.W.Stewart "Multidimensional Space-Time Nuclear Reactor Kinetics Studies - Part 1: Theoretical" Nuclear Science and Engineering, vol 59, 1976, p. 289.

[5] W.M. Stacey "Space-Time Nuclear Reactor Kinetics" Academic Press, N.Y., 1969.

[6] I.V. Zonov, N.V. Schukin, V.A. Hotylev, et al "Dynamic model of a nuclear power plant with РБМК reactor for void coefficient of reactivity calculation" Proceeding VII Nationalwide Scientific Seminar on Reactor Physics on "Nuclear Power Plant Inherent Safety" September 3-7, 1991, Moscow, p.192. /In Russian/

Table 1 Test Reactor Parameters

Heigt core: 100 cm

Radial mesh interval: 15 cm

Number of axial mesh points: 5

Number of radial mesh points: 61 (one per hex)

Number of precursor groups: 1

Precursor constants:

$\lambda = 0.1\ c\ ,\ \beta = 0.0065\ ,$

$\chi_d^1 = 1.0\ ,\ \chi_d^2 = 0.0$

Number of neutron groups: 2

	Group 1	Group 2
χ	1.0	0.0
v(cm/sec)	1.E+07	2.E+05

Material properties:

	Group 1	Group 2
$\nu\Sigma_f\ (cm^{-1})$	1.24493E-03	3.72749E-02
$\Sigma_R\ (cm^{-1})$	1.72327E-02	2.21620E-02
D (cm)	0.70415	0.36902
$\Sigma^{g-g'}\ (cm^{-1})$	1.71254E-02	0.00000

Table 2 Comparison outer iterations organization methods for transient with step perturbation ρ=0.5 β

Outer iterations organization method	Total number of outer iterations	Number outer iterations per time step
Source iteration method	32063/55I6I*	534/9I9
Modified method	958/245	16/4

Table 3 Comparison outer iterations organization methods for transient with step perturbation ρ=-0.3 β

Outer iterations organization method	Total number of outer iterations	Number outer iterations per time step
Source iteration method	14606/I7989	243/300
Modified method	895/I2I	15/2

Table 4.Comparison outer iterations organization methods for test calculation 2.

Outer iterations organization method	Total number of outer iterations	Number outer iterations per time step
Source iteration method	32264/55896	538/932
Modified method	3444/3972	57/66

Table 5. Comparison outer iterations organization methods for test calculation 3.

Outer iterations organization method	Total number of outer iterations	Number outer iterations per time step
Source iteration method	31772/55II2	530/9I9
Modified method	4005/4498	67/75

- - - - -

* without/with "prompt jump" approximation

Figure 1. Reactor geometry for test calculations.

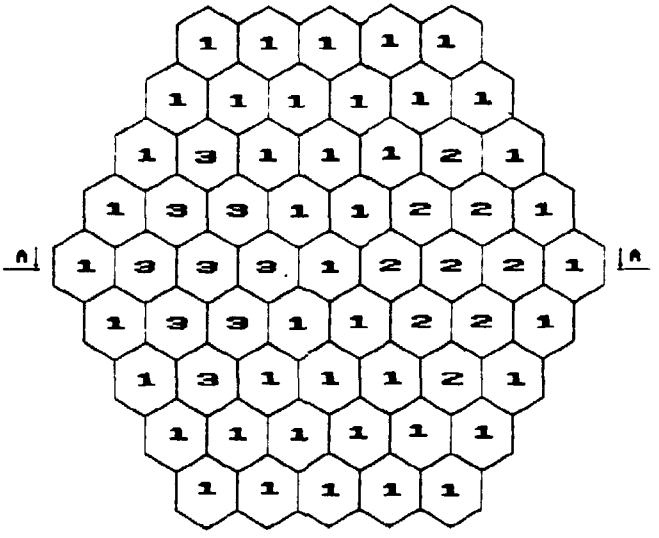

Figure 2 Radial power distribution (section A-A) in test calculations 3 and 4 (normalized to unity in central channel).

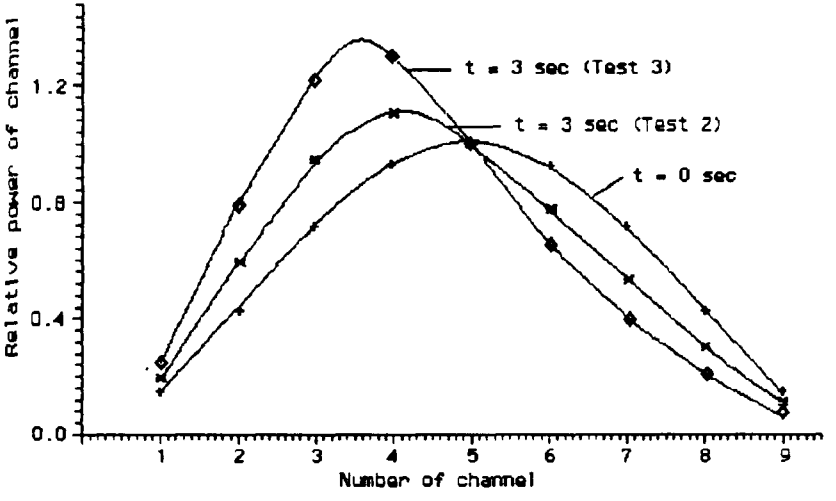

Figure 3. Power of central (5) and surrounding channels (4,6) versus time in the test calculation 2.

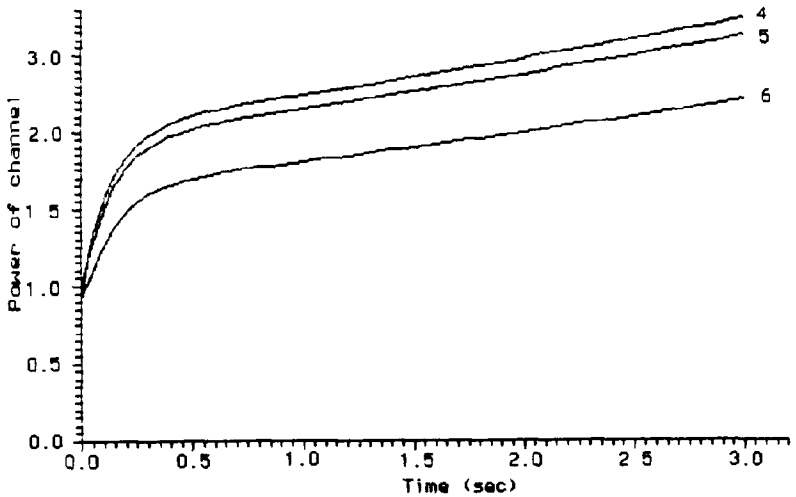

Figure 4. Power of central (5) and surrounding channels (4,6) versus time in the test calculation 3

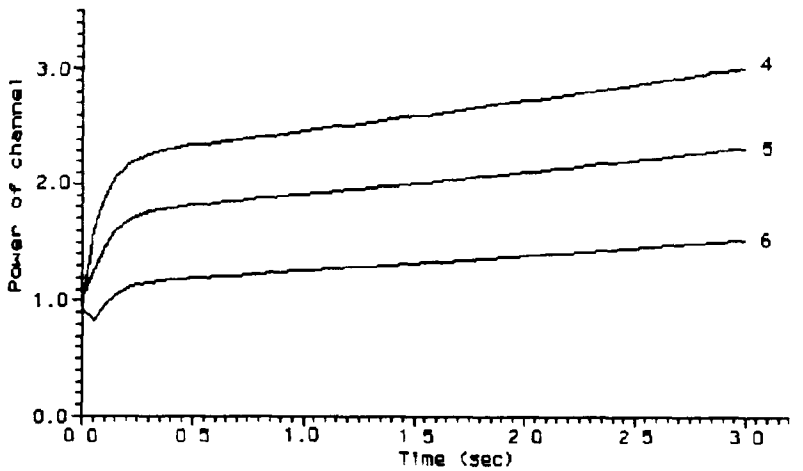

AN IMPROVED QUASISTATIC OPTION FOR THE DIF3D NODAL KINETICS CODE

T. A. Taiwo and H. S. Khalil
Reactor Analysis Division
Argonne National Laboratory
Argonne, Illinois 60439, U.S.A.

ABSTRACT

An improved quasistatic scheme is formulated for solution of the time-dependent DIF3D nodal equations in hexagonal-z geometry. This scheme has been implemented, along with adiabatic and point kinetics solution options, in the DIF3D hexagonal-z nodal kinetics code. The improved quasistatic method is shown to permit significant reduction in computing time, even for transients involving pronounced changes in flux shape. The achievable computing time reduction, in addition to being problem dependent, has also been found to be larger when greater accuracy is required in the computed results.

INTRODUCTION

The formulation of an improved quasistatic scheme [1-3] and other space-time factorization schemes (adiabatic and point kinetics) for solution of the time-dependent DIF3D nodal diffusion equations in hexagonal-z geometry [4,5] is described. The objective of this formulation is to combine the computational efficiency and accuracy of the DIF3D nodal spatial differencing method with the potential efficiency advantage of the quasistatic approach for the analysis of transients in which the flux shape changes more slowly than its amplitude.

The factorization schemes have been implemented along with the theta-method described in reference 5 as a set of options in a time-dependent version of the DIF3D nodal code. This code can be executed either in a "stand-alone" mode with a specified time variation of the input cross sections or as a space-time neutronics module in a reactor dynamics code. The DIF3D nodal kinetics code has been successfully implemented, along with a correlation scheme for representing feedback effects on nodal cross sections, in the SAS-HWR dynamics code [6] being developed at ANL for the analysis of heavy-water reactor transients, including postulated severe accidents.

In this paper, we first derive the expressions for the kinetics parameters appearing in the (point) kinetics equations describing the variation of the flux amplitude; no approximations are introduced in deriving these equations, and their solution would reproduce the "exact" DIF3D nodal space-time results (e.g. obtained with the theta-method using very fine time steps) provided the actual time-dependent flux shape is used to compute the time-dependent kinetics parameters. We then discuss the approximations to the flux shape that distinguish the different space-time factorization options and describe the numerical solution techniques used to determine the flux shape in each case and to compute the flux amplitude. Finally, we compare the efficiency and accuracy of the various DIF3D

nodal space-time factorization options and of the theta method for two types of test problems in hexagonal-z geometry For a 2-D (planar hexagonal) problem, we compare the DIF3D improved quasistatic solution to that obtained using the 2-D finite-difference code FX2-TH [2], which employs a somewhat different improved quasistatic solution scheme

MATHEMATICAL FORMULATION

Time-Dependent Nodal Equations

The principal unknowns in the time-dependent DIF3D nodal equations [5] are the flux moments, partial currents, and the precursor concentration moments The time-dependent equations for the flux moments and the partial currents can be cast into a supermatrix equation of the form

$$\begin{pmatrix} [v]^{-1} & [0] & [0] & [0] & [0] & [0] \\ [0] & [v]^{-1} & [0] & [0] & [0] & [0] \\ [0] & [0] & [v]^{-1} & [0] & [0] & [0] \\ [0] & [0] & [0] & [v]^{-1} & [0] & [0] \\ [0] & [0] & [0] & [0] & [v]^{-1} & [0] \\ [0] & [0] & [0] & [0] & [0] & [0] \end{pmatrix} \frac{d}{dt} \begin{pmatrix} \bar{\phi} \\ \underline{\phi}_{x1} \\ \underline{\phi}_{u1} \\ \underline{\phi}_{v1} \\ \underline{\phi}_{z1} \\ \underline{J}^{out} \end{pmatrix} = \begin{pmatrix} [F_a] & [0] & [0] & [0] & [0] & -[\hat{\epsilon}] \\ [0] & [F_m] & [0] & [0] & [0] & -[\hat{\zeta}_x] \\ [0] & [0] & [F_m] & [0] & [0] & -[\hat{\zeta}_u] \\ [0] & [0] & [0] & [F_m] & [0] & -[\hat{\zeta}_v] \\ [0] & [0] & [0] & [0] & [F_a] & -[\hat{\zeta}_z] \\ [\hat{B}] & [\hat{B}_x] & [\hat{B}_u] & [\hat{B}_v] & [\hat{B}_z] & -[H] \end{pmatrix} \begin{pmatrix} \bar{\phi} \\ \underline{\phi}_{x1} \\ \underline{\phi}_{u1} \\ \underline{\phi}_{v1} \\ \underline{\phi}_{z1} \\ \underline{J}^{out} \end{pmatrix}$$

$$+ \sum_{i=1}^{I} \lambda_i \begin{pmatrix} (\underline{\chi}_i \bar{C}_i) \\ (\underline{\chi}_i C_{i,x1}) \\ (\underline{\chi}_i C_{i,u1}) \\ (\underline{\chi}_i C_{i,v1}) \\ (\underline{\chi}_i C_{i,z1}) \\ (0) \end{pmatrix} \qquad (1)$$

Here $\bar{\phi}$ is a GxK column vector containing the zeroth-moment (node-average) flux for all groups g=1, ,G and all nodes k=1, ,K The GxK column vector $\underline{\phi}_{s1}$ contains for all groups and nodes the first moment of the flux, taken along coordinate direction s (s=x,u,v,z) The vector $\underline{J}^{out}$ is of length 8xGxK and contains the outgoing partial currents for all node-surfaces (8 in 3-D), all groups, and all nodes, the first 8G elements contain the partial currents for the first node The vectors $(\underline{\chi}_i \bar{C}_i)$ and $(\underline{\chi}_i C_{i,s1})$ are of length GxK, they contain for all nodes the node-average precursor concentration $\bar{C}_i^k$ and the s-direction first-moment precursor concentration $C_{i,s1}^k$, respectively, each multiplied by the node volume V^k and by $\underline{\chi}_i$ (a column vector of length G that contains the energy spectrum of neutrons emitted from precursors in family i, i=1, ,I) The parameter λ_i is the decay constant for precursor family i, and I is the number of precursor families The matrix $[v]^{-1}$ is of size GKxGK and contains the products of the nodal volumes and the inverse group velocities The matrices $[F_a]$ and $[F_m]$ are defined as

$$[F_a] = -[\Sigma^r] + [\Sigma^s] + [M_p]$$

and

$$[F_m] = -[\Sigma^r] - [\Sigma^D] + [\Sigma^s] + [M_p],$$

where the GKxGK block-diagonal matrices $[\Sigma^r]$ $[\Sigma^s]$ and $[M_p]$ contain the products of the nodal volumes with the removal cross sections, inscattering cross sections, and production cross sections, respectively The elements of the GKxGK block-diagonal matrix $[\Sigma^D]$, are proportional to the group diffusion coefficient and the nodal axial mesh spacing The matrices $[\hat{B}]$, $[H]$, $[\hat{\epsilon}]$, $[\hat{B}_s]$ and $[\zeta_{s\ell}]$, (s=x,u,v,z) are coupling coefficient matrices $[\hat{\epsilon}]$ and $[\zeta_{s\ell}]$, (s=x,u,v) are GKx8GK block-diagonal matrices, $[\zeta_{z\ell}]$ is a GKx8GK block-tridiagonal matrix (as a result of the quadratic transverse leakage approximation in the axial direction), $[\hat{B}]$ and $[\hat{B}_s]$ are 8GKxGK block-diagonal matrices, and $[H]$ is of size 8GKx8GK These coupling coefficient matrices depend only on the diffusion coefficients and nodal dimensions

Note that Eq (1) does not contain incoming partial currents as unknowns because they have been eliminated in favor of outgoing partial currents by the relation expressing the continuity of partial currents at nodal surfaces

The time-dependent equations for the precursor concentration moments are also cast in supermatrix form as

$$\frac{d}{dt}\begin{pmatrix} (\underline{\chi}\overline{C}_i) \\ (\underline{\chi}C_{ix1}) \\ (\underline{\chi}C_{iu1}) \\ (\underline{\chi}C_{iv1}) \\ (\underline{\chi}C_{iz1}) \end{pmatrix} = \begin{pmatrix} [M_i] & [0] & [0] & [0] & [0] \\ [0] & [M_i] & [0] & [0] & [0] \\ [0] & [0] & [M_i] & [0] & [0] \\ [0] & [0] & [0] & [M_i] & [0] \\ [0] & [0] & [0] & [0] & [M_i] \end{pmatrix} \begin{pmatrix} \underline{\bar{\phi}} \\ \underline{\phi}_{x1} \\ \underline{\phi}_{u1} \\ \underline{\phi}_{v1} \\ \underline{\phi}_{z1} \end{pmatrix} - \lambda_i \begin{pmatrix} (\underline{\chi}\overline{C}_i) \\ (\underline{\chi}C_{ix1}) \\ (\underline{\chi}C_{iu1}) \\ (\underline{\chi}C_{iv1}) \\ (\underline{\chi}C_{iz1}) \end{pmatrix}, \quad i = 1\,2 \qquad ,I \tag{2}$$

where the elements of the GKxGK block-diagonal matrix $[M_i]$ depend on β_i (the fraction of neutrons appearing as delayed neutrons from the decay of precursor family i), χ_{gi} (the energy spectrum of delayed neutrons), the production cross section $\nu\Sigma_g^{fk}$, and the nodal volume V^k

Derivation of the Kinetics Equations

The supermatrix Eqs (1) and (2) are the starting point for the derivation of the space-time factorized DIF3D nodal equations The unknown vector of flux moments and partial currents appearing in Eq (1) is expressed as the product of a normalized shape vector $\underline{S}$ and a global amplitude function T , i e ,

$$\underline{\Psi} \equiv \begin{pmatrix} \underline{\bar{\phi}} \\ \underline{\phi}_{x1} \\ \underline{\phi}_{u1} \\ \underline{\phi}_{v1} \\ \underline{\phi}_{z1} \\ \underline{J}^{out} \end{pmatrix} = \underline{S}T = \begin{pmatrix} \underline{S}_0 \\ \underline{S}_{x1} \\ \underline{S}_{u1} \\ \underline{S}_{v1} \\ \underline{S}_{z1} \\ \underline{S}_J^{out} \end{pmatrix} T \tag{3}$$

The amplitude function is defined as

$$T = \underline{\psi}^{*T} \begin{pmatrix} [v]^{-1} & [0] & [0] & [0] & [0] & [0] \\ [0] & [v]^{-1} & [0] & [0] & [0] & [0] \\ [0] & [0] & [v]^{-1} & [0] & [0] & [0] \\ [0] & [0] & [0] & [v]^{-1} & [0] & [0] \\ [0] & [0] & [0] & [0] & [v]^{-1} & [0] \\ [0] & [0] & [0] & [0] & [0] & [0] \end{pmatrix} \underline{\psi} = \bar{\underline{\phi}}^{*T}[v]^{-1}\bar{\underline{\phi}} + \sum_{s=x\,u\,v,z} \underline{\phi}_{s1}^{*T}[v]^{-1}\underline{\phi}_{s1} \ , \tag{4}$$

where $\underline{\psi}^*$ is the initial state adjoint vector, defined as

$$\underline{\psi}^* = \text{col}\,(\bar{\underline{\phi}} \ , \ \underline{\phi}_{x1}^* \ , \ \underline{\phi}_{u1}^* \ , \ \underline{\phi}_{v1}^* \ , \ \underline{\phi}_{z1}^* \ , \ \underline{J}^{out*}) \ ,$$

and $\underline{\psi}^{*T}$ is its transpose The initial state adjoint vector is computed using the mathematical nodal adjoint scheme in DIF3D [7]

If Eq (3) is used to eliminate the vector of fluxes and partial currents, $\underline{\psi}$, from Eq (4), we obtain the following normalization constraint on the shape vector

$$\bar{\underline{\phi}}^{*T}[v]^{-1}\underline{S}_0 + \sum_{s=x\,u\,v\,z} \underline{\phi}_{s1}^{*T}[v]^{-1}\underline{S}_{s1} = 1 \tag{5}$$

For convenience, we define two vectors $\underline{S}_\phi$ and $\underline{\psi}_\phi^*$ as follows

$$\underline{S}_\phi = \text{col}\,(\underline{S}_0 \ , \ \underline{S}_{x1} \ , \ \underline{S}_{u1} \ , \ \underline{S}_{v1} \ , \ \underline{S}_{z1}) \ ,$$

and

$$\underline{\psi}_\phi^* = \text{col}\,(\bar{\underline{\phi}} \ , \ \underline{\phi}_{x1}^* \ , \ \underline{\phi}_{u1}^* \ , \ \underline{\phi}_{v1}^* \ , \ \underline{\phi}_{z1}^*)$$

These vectors differ from $\underline{S}$ and $\underline{\psi}^*$, respectively, only in the absence of the outgoing partial current components We also define a block-diagonal supermatrix [M] which has the matrix $[M_0] + \sum_{i=1}^{I}[M_i]$ as its diagonal blocks Premultiplying Eq (1) by $\underline{\psi}^{*T}$ and Eq (2) by $\underline{\psi}_\phi^*$, dividing the resulting equations by $\underline{\psi}_\phi^{*T}[M]\underline{S}_\phi$, and using the definitions

$$\Lambda \equiv \frac{\bar{\underline{\phi}}^{*T}[v]^{-1}\underline{S}_0 + \sum_{s=x\,u\,v\,z} \underline{\phi}_{s1}^{*T}[v]^{-1}\underline{S}_{s1}}{\underline{\psi}_\phi^{*T}[M]\underline{S}_\phi} \ , \tag{6}$$

$$\beta_{e,l} \equiv \frac{\underline{\bar{\phi}}^{*T}[M_l]\underline{S}_0 + \sum_{s=X\,U\,V\,Z} \underline{\phi}_{s1}^{*T}[M_l]\underline{S}_{s1}}{\underline{\psi}_{\phi}^{*T}[M]\underline{S}_{\phi}} , \tag{7}$$

$$\beta_e = \sum_{l=1}^{I} \beta_{e,l} , \tag{8}$$

$$\rho \equiv \frac{1}{\underline{\psi}_{\phi}^{*T}[M]\underline{S}_{\phi}} \left\{ \underline{\bar{\phi}}^{*T} \left[\left([F_a] + \sum_{l=1}^{I} [M_l] \right) \underline{S}_0 - [\hat{\varepsilon}]\, \underline{S}_l^{out} \right] \right.$$

$$+ \sum_{s=X\,U\,V} \underline{\phi}_{s1}^{*T} \left[\left([F_m] + \sum_{l=1}^{I} [M_l] \right) \underline{S}_{s1} - [\hat{\zeta}_s]\, \underline{S}_l^{out} \right] + \underline{\phi}_{z1}^{*T} \left[\left([F_a] + \sum_{l=1}^{I} [M_l] \right) \underline{S}_{z1} - [\hat{\zeta}_z]\, \underline{S}_l^{out} \right]$$

$$\left. + \underline{J}^{out*T} \left([\hat{B}]\, \underline{S}_0 + \sum_{s=X\,U\,V,Z} [\hat{B}_s]\, \underline{S}_s - [H]\, \underline{S}_l^{out} \right) \right\} \tag{9}$$

and

$$C_l = \frac{\underline{\bar{\phi}}^{*T}(\underline{\chi}\bar{C}_l) + \sum_{s=X\,U\,V\,Z} \underline{\phi}_{s1}^{*T}(\underline{\chi}\bar{C}_{l,s1})}{\underline{\bar{\phi}}^{*T}[\nu]\,{}^{1}\underline{S}_0 + \sum_{s=X\,U\,V\,Z} \underline{\phi}_{s1}^{*T}[\nu]\,{}^{1}\underline{S}_{s1}} \tag{10}$$

we obtain the conventional form of the kinetics equations, i e ,

$$\frac{d}{dt}T = \frac{(\rho - \beta_e)}{\Lambda} T + \sum_{l=1}^{I} \lambda_l C_l \tag{11}$$

and

$$\frac{d}{dt}C_l = \frac{\beta_{e,l}}{\Lambda} T - \lambda_l C_l , \qquad l = 1, \ldots, I \tag{12}$$

The parameters in these equations have the conventional meaning, i e Λ is the prompt neutron lifetime, $\beta_{e,l}$ is the effective delayed neutron fraction for family l, ρ is the reactivity, and C_l is the adjoint weighted precursor concentration for family l

The kinetics equations, Eqs (11) and (12), are common to all the factorization options and are solved simultaneously for the time variation of the flux amplitude T once the kinetics parameters have been determined We note that no approximations are made in the derivation of these equations from the time-dependent nodal equations, and that it is the use of approximate shape vectors in

place of the exact time-dependent shape function that leads to deviations from exact space-time results (e g by utilizing the initial shape throughout a transient as in the conventional point kinetics model)

Approximation of the Time-Dependent Shape Vector

An approximation to the time-dependent shape vector is required to compute the kinetics parameters in Eqs (6) to (9), as well as to obtain the time-dependent flux and power distributions once the amplitude function has been determined by solution of the kinetics equations The accuracy of the solution depends on the accuracy of the shape vector used to compute the kinetics parameters, especially the reactivity

In implementing the improved quasistatic scheme, we have opted to approximate the flux shape by solving the time-dependent DIF3D nodal equations [5] using the implicit scheme ($\theta = 1$) with large time-step sizes It was shown by Kao and Henry [8] that the use of large time-steps for determining the shape vector provides sufficiently accurate results, even though the associated flux amplitude is quite inaccurate (We have verified the accuracy of this approximate way of determining the shape function Note that the exact shape results when a sufficiently small time-step size is used for the shape calculation) The computed shape is normalized by application of the constraint provided by Eq (5) This approach for determining the shape differs from that originally used by Ott and Meneley wherein an equation derived expressly for the shape vector $\bar{S}$ (as opposed to the equation for the flux, i e the product of the shape and amplitude), is solved with the large time-step

In the adiabatic scheme, the shape is approximated by solving the time-independent DIF3D nodal equations at various instants during the transient, with the time-dependent nodal parameters taking on instantaneous values appropriate to the time at which the calculations are performed Finally, in the point kinetics scheme, the initial shape vector is used to approximate the time-dependent shape for the entire transient duration

SOLUTION TECHNIQUE

Three types of time intervals are defined in implementing the space-time factorization schemes In decreasing order of time-step size, they are the shape step, the reactivity step, and the kinetics solution step, the smaller intervals are nested within the next larger interval Another time interval, called a time domain is also defined independently to facilitate the integration of the DIF3D nodal kinetics code in an integrated dynamics code such as SAS-HWR [6] A time domain corresponds to the main thermal-hydraulic (T-H) step of the dynamics code, and T-H parameters which are calculated at the end of the main T-H step are used to compute new cross sections for the DIF3D kinetics calculation Furthermore, the power densities are edited at the end of a time-domain, which typically consists of one or more reactivity steps On the other hand, a shape interval can span more than one time domain

The DIF3D nodal kinetics code internally computes the kinetics, reactivity, and shape time-step sizes based on user-specified criteria The time-step selection criteria are similar to those used in the FX2-TH code [2] and thus take advantage of previously developed modeling judgements Across each kinetics step within a reactivity interval, the kinetics equations are solved with the modified Kaganove scheme [9,10], using linear or quadratic fits of the kinetics parameters determined at the beginning and end of each reactivity step The solution of the kinetics equation progresses until the end of a reactivity step The Kaganove scheme employs an automatic time-step halving and doubling algorithm to compute the time-step size needed to achieve a user-specified precision

At the end of each reactivity step within a shape interval, new cross sections are calculated by linear interpolation of cross section data evaluated at bracketing time domain endpoints, and they are used along with the appropriate shape vector to compute the kinetics parameters ρ, β_{eff}, and Λ. At a reactivity step endpoint within a shape interval (not corresponding to the endpoint of the shape interval), shape vectors required to compute the power distribution or kinetics parameters are obtained by linear extrapolation of the two preceding shape vectors. This extrapolation scheme can lead to inaccurate reactivity values if the rate of shape variation changes significantly prior to a shape recalculation (i.e. if the specified shape recalculation criteria are inadequate). The extrapolation scheme can optionally be disabled, in which case the shape step is the same as the reactivity step. At the end of each reactivity step, the shape vector is normalized and combined with the amplitude function (at the endpoint) to determine the flux vector and compute the power densities.

The size of a reactivity time-step is determined at the end of the preceding reactivity interval. To determine this reactivity time-step size, three time-step lengths are computed based on user-specified parameters and certain code constraints, and the minimum of these lengths is selected as the reactivity time-step size. The three time-step lengths are:

1. An input maximum reactivity step length.
2. Twice the previous reactivity step length.
3. The reactivity step size for which the estimated amplitude function change, based on quadratic projection of the amplitude function, equals a user-specified maximum value.

The smallest of these time-step lengths is used as the reactivity step size only if it does not contain the endpoint of a time domain, the endpoint of a shape calculation, or the problem end-time. If the smallest time-step contains one of these end-times, the time-step size is adjusted so that the smallest of these times becomes the endpoint of the next reactivity step.

A shape calculation is performed at the end of a shape interval or at the end of an imbedded reactivity step (within the shape interval) if the shape recalculation criteria are met at that point. The fully-implicit option of the theta solution scheme [5] is used to compute the new shape vector. Since a shape interval endpoint also corresponds to the endpoint of the last imbedded reactivity step, kinetics parameters are obtained at this time point with the new shape vector, and the solution of the kinetics equations over this last reactivity step is obtained. The normalized shape vector and the amplitude function (at this endpoint) are then combined and used to obtain the flux and power density distributions. This new flux distribution is used along with information known at the end of the preceding shape interval to compute the precursor concentration moments.

The length of a shape interval is calculated at the end of the preceding shape interval. In order to determine the shape interval duration, three time-step lengths are computed based on user-specified parameters and code constraints, and the minimum of these lengths is selected as the shape interval. The three time-step lengths are:

1. An input maximum shape step interval.
2. Ten times the previous shape interval.
3. The shape step size for which shape change estimated by linear extrapolation equals a user-specified maximum allowable shape change.

The smallest of these time-step lengths is used as the next shape interval size only if it does not contain the transient problem end-time If it does, the time-step size is adjusted so that the problem end-time becomes the endpoint of the shape interval A shape calculation is also enabled at the end of a reactivity step (within the shape interval) if the amplitude change thus far over the shape interval does not satisfy a user-specified value The sizes of the very first reactivity step and shape interval are taken to be the same and are specified by the user as a multiple of the prompt neutron lifetime Λ

NUMERICAL TEST RESULTS

Several test problems have been solved to verify the implementation of the various factorization schemes Results of these problems confirmed that with very small shape time-step sizes, the improved quasistatic scheme reproduces the theta method results As expected, substantial savings in computational time were achieved with the factorization options for problems involving minor shape changes

Results are presented here for two numerical test cases with pronounced space-time effects In each case, the initial core state is a hexagonal-z representation of a heavy-water reactor core [5,11] The first case models the insertion of \$2 7 of (static) reactivity over 0 4 s through the reduction of the thermal capture cross section in the central core patch (central and six surrounding hexagonal cells) by a factor of 1 96 Table 1(a) compares the time evolution of the core power predicted by the improved quasistatic, adiabatic, and point kinetics schemes to the reference results obtained using the fully implicit scheme The point kinetics scheme is seen to be extremely inaccurate for this transient involving a pronounced shape change The adiabatic scheme is also inaccurate because asymptotic shapes are used to approximate the time-dependent shapes (which are not asymptotic in the time period of interest) For example, the adiabatic scheme predicts that the asymptotic reactivity is prematurely reached at 0 4 s, the reference (dynamic) reactivity is 2 % lower than the asymptotic reactivity at this time point The asymptotic reactivity is reached by the reference solution only after 0 5 s has elapsed On the other hand, the improved quasistatic scheme retains the accuracy of the reference solution, while requiring a factor of 8 less computing time It should be noted however that the computing times given in Table 1 can be reduced at the expense of accuracy for both the quasistatic method (by relaxing shape recalculation criteria) and the fully implicit method (by increasing time step sizes) The savings in computing time achievable with the improved quasistatic scheme has been found to depend on the accuracy relative to the reference theta-method solution, as shown in Fig 1, which compares the computation time as a function of accuracy for the improved quasistatic (IQS) and theta schemes It can be seen that the ratio of the computation time for the theta scheme to that for the improve quasistatic scheme decreases as the error in core power increases This suggests that the theta method becomes more competitive as the accuracy requirement is relaxed

The second problem simulates a delayed supercritical transient terminated by the insertion of negative reactivity This transient was modelled by first linearly reducing the thermal capture cross section in the central patch by 28 % over the first 1 0 s, followed by an increase to 0 995 of the initial state value at 2 5 s A reduction of the neutron yield per fission (ν) by 0 8 % was superimposed from 1 0 s to 3 0 s The resulting reference reactivities, obtained with a fully implicit reference calculation, are presented in Table 1(b) This Table also compares the core power results provided by the improved quasistatic, adiabatic, and point kinetics options with the reference results Again, the point kinetics scheme is very inaccurate, underpredicting the maximum core power by 40 6 % The adiabatic scheme appears to be quite accurate for this problem even though it overpredicts the reactivity and the flux amplitude as a function of time (note that the calculated power additionally depends on the shape and benefits in this case from the compensation of the shape and amplitude errors) The improved quasistatic solution is very accurate and requires a factor of 13 less computing time than the reference solution If an error of about 1 5 % in the core power is tolerable, the computation efficiency advantage of the improved quasistatic method is reduced to a factor of about 2

As previously discussed, the DIF3D nodal quasistatic scheme obtains the time-dependent flux shape using the approach of reference 8, i e by solving the fully implicit DIF3D nodal equations with a large time step size The alternative and more conventional approach is to solve an equation specifically derived for the shape, as is done for example in the 2-D finite-difference code FX2-TH [2] To evaluate the implication of this difference in shape calculation approach on the required shape recalculation frequency, comparisons were made between DIF3D and FX2-TH improved quasistatic solutions for the 2-D (planar hexagonal) HWR problem referred to as test-case 2 in reference 5 In that problem, a reactivity increase of 75 cents was introduced over 0 2 s by reducing the absorption cross section in the central part of the core The FX-2 solution was obtained using 24 triangular mesh cells per hexagon and employed the code default parameters [2] for controlling the duration of shape and reactivity intervals The DIF3D improved quasistatic solution was obtained using essentially the same criteria for control of time step sizes (In reference 5, the accuracy of the DIF3D nodal spatial differencing scheme was shown to be comparable to the 24 triangular mesh cells per hexagon finite difference scheme) As shown in Table 2, the two codes yield quasistatic results of comparable accuracy and perform a similar total number of shape calculations, as well as a similar number of shape calculations during each of three portions of the total problem time This result indicates that the DIF3D approach for obtaining the time-dependent shape does not adversely affect the accuracy of the computed results for a given shape recalculation frequency Thus the substantially greater efficiency of the DIF3D nodal spatial differencing approach relative to the finite-difference approach is preserved in the DIF3D nodal quasistatic solution of time-dependent problems

SUMMARY AND CONCLUSIONS

The formulation of three different space-time factorization options for solution of the time-dependent DIF3D nodal diffusion equations in hexagonal-z geometry has been presented These options (point kinetics, adiabatic, and improved quasistatic) have been implemented, along with the existing theta time integration scheme, in the DIF3D nodal kinetics code The availability of all options in one code provides substantial flexibility for minimizing the computational cost of analyzing different types of transients

The space-time factorization options performed, as expected, substantially better than the theta method for problems with relatively mild variations in the flux shape However, even for problems with pronounced space-time effects, the improved quasistatic method outperformed the fully implicit method

The computing efficiency advantage of the improved quasistatic method over the fully implicit method, in addition to being problem dependent, has also been found to depend on the (common) accuracy requirement imposed on the two solutions, as controlled by the respective time step sizes In particular, the efficiency advantage of the improved quasistatic method appears to be greater when higher accuracy in computed power is required More definitive conclusions about the comparative performance of the different transient solution options will become available in the context of analyzing specific transients using the integrated SAS-HWR/DIF3D-nodal dynamics code currently being developed at ANL

REFERENCES

1 K O Ott and D A Meneley, "Accuracy of the Quasistatic Treatment of Spatial Reactor Kinetics," Nucl Sci Eng , 36, p 402, 1969

2 R A Shober, T A Daly, and D R Ferguson, "FX2-TH A Two-Dimensional Nuclear Reactor Kinetics Code With Thermal-Hydraulic Feedback," ANL-78-97, Argonne National Laboratory, October 1978

3 H L Dodds, Jr , "Accuracy of the Quasistatic Method for Two-Dimensional Thermal Reactor Transients With Feedback," Nucl Sci Eng , 59, p 271, 1976

4 R D Lawrence, "The DIF3D Nodal Neutronics Option for Two- and Three-Dimensional *Diffusion Theory Calculations in Hexagonal Geometry*," ANL-83-1, *Argonne* National Laboratory, March 1983

5 T A Taiwo and H S Khalil, "The DIF3D Nodal Kinetics Capability in Hexagonal-Z Geometry -- Formulation and Preliminary Tests," Proceedings of the International Topical Meeting on Advances in Mathematics, Computations, and Reactor Physics, Pittsburgh, Pennsylvania, p 23 2 2-1, American Nuclear Society, April 1991

6 E E Morris, ANL, Private Communication, October 1990

7 R D Lawrence, "Perturbation Theory Within the Framework of a Higher Order Nodal Method," Trans Am Nucl Soc , 46, 402 (1984)

8 P Kao and A F Henry, "Supernodal Analysis of PWR Transients," Proceedings of the Topical Meeting on Advances in Nuclear Engineering Computation and Radiation Shielding, Santa Fe, New Mexico, p 63, Vol 2, American Nuclear Society, April 1989

9 J J Kaganove, "Numerical Solution of the One-Group Space-Independent Reactor Kinetics Equations for Neutron Density Given Excess Reactivity," ANL-6132, Argonne National Laboratory (1960)

10 E L Fuller, "*The Point Kinetics Algorithm for FX2*," ANL-7910, Argonne National Laboratory, p 503, 1976

11 M R Buckner and J W Stewart, "Multidimensional Space-Time Nuclear-Reactor Kinetics Studies-Part I Theoretical," Nucl Sci Eng , 59, p 289, 1976

Table 1(a): Test Case 1 Results

Time (s)	Reference Reactivity[a]	CORE POWER				
		Theta[a]	Improved Quasistatic[b]	Improved Quasistatic[c]	Point Kinetics	Adiabatic[c]
0 00	0 00000	1 0000	1 0000	1 0000	1 0000	1 0000
0 10	0 00908	1 8251	1 8247	1 8256	1 4801	1 8793
0 20	0 01177	8 9447	8 9415	8 9558	2.3334	9 8805
0.30	0 01428	60 295	60 289	60 615	3 1238	70 024
0 40	0 01715	801 63	801 87	810.56	4 0502	999.39
0 50	0 01726	16669	16658	16981	5 0256	21918
No of shape calcs			303	78		78
No of time steps		11076	308	85	9	84
Computation time, s[d]		3616	462	177	23	288

Table 1(b): Test Case 2 Results

Time (s)	Reference Reactivity[a]	CORE POWER			
		Theta[a]	Improved Quasistatic[c]	Point Kinetics	Adiabatic[c]
0 00	0 00000	1 0000	1 0000	1 0000	1 0000
0 10	0 00034	1 0261	1 0261	1 0279	1 0253
0 20	0 00071	1 0782	1 0784	1 0788	1 0774
0 50	0 00207	1 3427	1 3432	1 2851	1 3451
1 00	0 00557	3 1814	3 1831	1 8911	3 2612
1 50	0 00104	1 5448	1 5460	1 2253	1 5615
2 00	00275	0 8245	0 8247	0 7527	0 8283
2 50	00608	0 5919	0 5921	0 5489	0 5957
3 00	00814	0 4926	0 4927	0 4561	0 4958
No of shape calcs			49		52
No of time steps		4549	58	12	61
Computation time, s[d]		1734	133	28	170

[a] Reference solution computed with fully implicit option employing variable time-step size ($\omega\Delta t=10^{-3}$, where ω is the inverse of the local period and Δt is the time-step size)

[b] Shape recalculation based on 2 5 % maximum local shape change

[c] Shape recalculation based on 10% maximum shape change

[d] On the ANL Cray X MP/18 computer

Table 2: Comparison of FX2-TH and DIF3D Improved Quasistatic Solutions

Time (s)	DIF3D Fully Implicit[a]		DIF3D-Improved Quasistatic[b]		FX2-TH[b]	
	Core Power	Reactivity	Core Power	Reactivity	Core Power	Reactivity
0 00	1 0000	0 00000	1 0000	0 00000	1 0000	0 00000
0 01	1 0077	0 00019	1 0068	0 00019	1 0071	0 00019
0 05	1 0991	0 00099	1 0979	0 00099	1 0999	0 00099
0 20	2 4213	0 00527	2 4108	0 00527	2 3990	0 00524
0 50	4 9110	0 00533	4 9425	0 00533	4 8568	0 00531
1 00	7 4772	0 00534	7 4992	0 00534	7 3520	0 00532
1 50	10 862	0 00535	10 890	0 00535	10 626	0 00533
2 00	15 514	0 00535	15 553	0 00535	15 099	0 00533
2 50	21 975	0 00536	22 030	0 00536	21 277	0 00534
3 00	30 986	0 00536	31 063	0 00536	29 843	0 00534
Λ (s) at 0 0 s	1 4865E 04		1 4864E-04		1 4855E-04	
Λ (s) at 3 0 s	1 4685E-04		1 4685E-04		1 4682E-04	
β_e at 3 0 s	7 1804E-03		7 1804E-03		7 1804E-03	
No of Shape Calc in 0 0 - 0 2 s			10		14	
No of Shape Calc in 0 2 - 0 5 s			3		4	
No of Shape Calc in 0 5 - 3 0 s			13		14	
Total No of Shape Calc			26		32	
CPU (s)	111 06[c]		7 22[c]		602 84[d]	

[a] Reference nodal solution computed with time step size Δt=0 0025 s

[b] Improved quasistatic cases employ the default time step selection criteria in FX2-TH [2]

[c] On the ANL Cray X-MP/18 Computer

[d] On the ANL IBM-3084 Computer

Fig. 1: Computation Time Versus Maximum Error

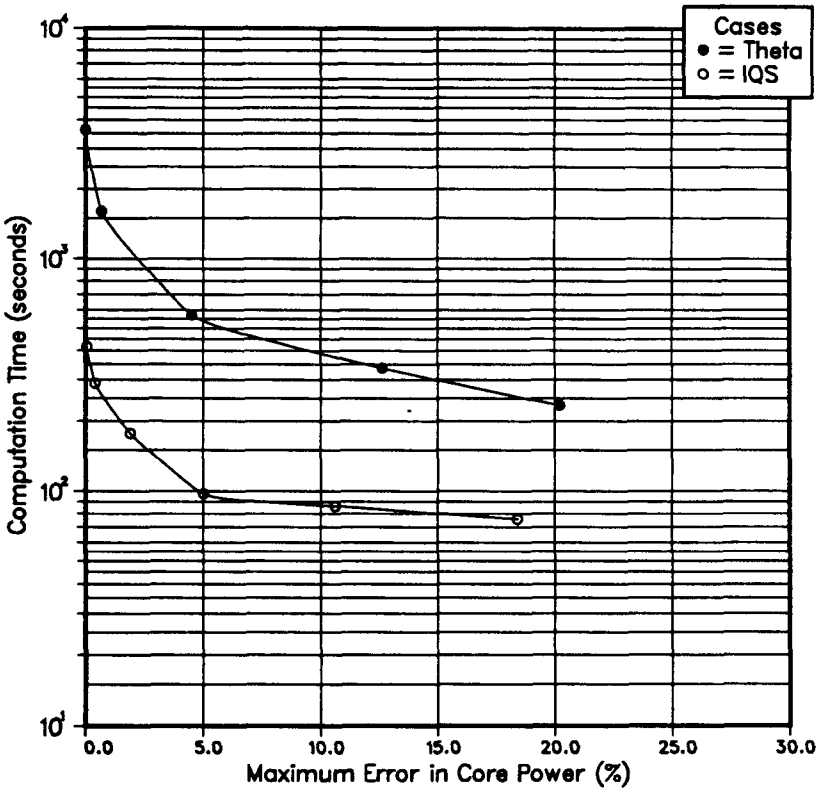

A COUPLED ENERGY ANGLE FOKKER PLANCK DECOMPOSITION SCHEME FOR ION TRANSPORT

L Wayne Brasure
United States Air Force Academy
Colorado Springs, Colorado

Anil K Prinja, J W VanDenburg
University of New Mexico
Albuquerque, New Mexico

B Todd Adams, Jim E Morel
Los Alamos National Laboratory
Los Alamos, New Mexico

ABSTRACT

A method for describing highly forward peaked scattering and transport of ions in random (as opposed to crystalline) solids is presented It is based on a generalized decomposition scheme that separates the singular peaked component of the scattering cross section using a Fokker Planck formalism, leaving a relatively smooth Boltzmann collision integral A suitably modified energy dependent Legendre expansion scheme is introduced to deal with the truncated angular domain in the collision integral resulting from the decomposition A complete library of multigroup cross section moments as well as Fokker Planck coefficients is developed for use with a specially constructed transport code as well as the MCNP Monte Carlo code Outstanding accuracy is achieved for ion implantation profiles and average range when compared with established results

INTRODUCTION

In principle the Boltzmann transport equation (BTE) can be used to describe a general class of linear transport processes, that encompasses both isotropic and anisotropic (or forward peaked) scattering For neutral particle transport, such as neutrons and photons a number of efficient and practical numerical algorithms have been successfully implemented for scattering that is at most moderately anisotropic[1] For charged particle (ion and electron) transport, on the other hand, the situation is drastically different in that highly forward peaked scattering can dominate, i e , the corresponding differential scattering cross sections display a singularity at zero energy transfer Under theses circumstances the naive use of traditional solution methods will result in, e g , an enormous number of Legendre expansion moments with unacceptably high computational cost

A quantitative measure of the forward peaked nature of ion cross sections is provided by the mean cosine of the scattering angle, defined in the laboratory frame by

$$< \mu_L(E) > = \frac{2\pi \int_0^{E_0} dE' \int_{-1}^{1} d\mu_0 \Sigma_s(E \rightarrow E', \mu_0)\mu_0}{2\pi \int_0^{E_0} dE' \int_{-1}^{1} d\mu_0 \Sigma_s(E \rightarrow E', \mu_0)} \quad (1)$$

where $\Sigma_S(E \rightarrow E', \mu_0)$ is the double differential macroscopic scattering cross section[2] In Figure 1 $< \mu_L >$ is plotted as a function of incident ion energy for various ion target combinations, and is seen to be almost unity for a broad energy range, even at low energies This clearly demonstrates the singular nature of ion scattering and the need for a new class of solution methods

THE BOLTZMANN FOKKER-PLANCK APPROACH

The standard BTE approach can be extended to accommodate in a practical manner the highly forward peaked scattering cross section by decomposing the singular kernel into a so called smooth Boltzmann and a singular Fokker Planck component[3] This approach recognizes that extremely forward scattering is associated with very small energy transfers and hence can be accurately described by a continuous slowing down approximation for the energy loss and an angular diffusion operator for the small deflections The 'large angle' scattering is preserved in the Boltzmann (smooth) kernel which is now well behaved and hence amenable to a relatively low order Legendre expansion The resulting Boltzmann Fokker Planck equation for the angular flux then reads, in 1 D

$$\begin{aligned} \mu \frac{\partial \Psi(z, E, \mu)}{\partial z} + \Sigma_s^{smooth}(E)\Psi(z, E\ \mu) &= 2\pi \int_0^{\infty} dE' \int_{-1}^{1} d\mu' \Sigma_s^{smooth}(E' \rightarrow E, \mu_0)\Psi(z\ E\ \mu) \\ &+ \frac{\partial}{\partial E}(S(E)\Psi(z\ E, \mu)) \\ &+ \frac{\alpha(E)}{2} \frac{\partial}{\partial \mu}(1 - \mu^2) \frac{\partial}{\partial \mu} \Psi(z\ E, \mu) \end{aligned} \quad (2)$$

The decomposition into smooth Boltzmann and singular Fokker Planck operators is now evident The problem reduces to accurately obtaining the coefficients associated with the Fokker Planck terms, namely the nuclear stopping power, $S_n(E)$, and the momentum transfer coefficient, $\alpha(E)$ These are, respectively, defined as

$$S_n(E) = \int_0^{\infty} dE'(E - E')\Sigma_s^{singular}(E \rightarrow E') \quad (3)$$

and

$$\alpha(E) = \int_{-1}^{1} d\mu_0(1 - \mu_0)\Sigma_s^{singular}(E, \mu_0) \quad (4)$$

Note that, by definition, only the singular part of the cross section is used in Equations 2 and 4 (see below) Note also that the stopping power in Equation 2 is the sum of the restricted nuclear stopping power given by Equation 3 and the electronic stopping power describing inelastic energy losses with target electrons Below we describe a method for obtaining the Fokker Planck coefficient in a systematic fashion, that does not suffer from the short comings of other methods in the literature

COUPLED ENERGY ANGLE DECOMPOSITION SCHEME

Attempts have previously been made to numerically model ion scattering with the BFP equation using second order accurate diamond difference techniques for the spatial dependence multigroup schemes for the energy dependence and truncated Legendre polynomial expansions for the angular dependence[4,5] Only one of these approaches is complete in the sense that it examines both the angular diffusion and CSDA Fokker Planck terms[5] However the technique it employs to determine the smooth cross section moments and momentum transfer function can exhibit dramatic oscillations about the exact cross section values[6]

We have developed a method of systematically and accurately obtaining the smooth Boltzmann cross section moments, the momentum transfer function and the stopping power for ion scattering applications This new method extends the Partial Range Fitting (PRF) method developed by Landesman and Morel[6] originally to determine the momentum transfer functions for electron scattering applications The PRF method has been previously shown to be very accurate in fitting highly forward peaked electron scattering cross sections[6] however in its original form it was used on cross sections dependent only on scattering angle cosine We have extended the PRF method to accommodate the full energy and angle dependence of ion scattering cross sections, as well as arbitrary mass ratios

The basis of this method is to determine the momentum transfer functions as the difference of the complete and smooth cross sections, since the singular form of the cross sections can be expressed as

$$\Sigma_s^{singular}(E,\mu_0) = \Sigma_s(E,\mu_0) - \Sigma_s^{smooth}(E,\mu_0) \tag{5}$$

where $\Sigma_s(E,\mu_0)$ is the complete cross section Using this result in Equation 4 and integrating gives

$$\alpha(E) = (\Sigma_{s\,0}(E) - \Sigma_{s\,1}(E)) - \left(\Sigma_{s\,0}^{smooth}(E) - \Sigma_{s\,1}^{smooth}(E)\right) \tag{6}$$

The smooth cross section moments are determined by fitting over the partial range However since the Legendre polynomials are defined over the full range of $\mu\epsilon[-1\ 1]$ we must define a new set of polynomials orthogonal over the partial range For ion scattering this entails transforming the Legendre polynomials to the partial range defined over $\mu'\epsilon[\mu_{min}\ \mu_b]$ where μ_{min} is the minimum scattering angle cosine and μ_b is the Fokker Planck cut off value In cases where the incident ion is of smaller mass than the target ion ($m_1 < m_2$) then $\mu_{min} = -1$, since the incident ion can backscatter When $m_1 \geq m_2$ $\mu_{min} \geq 0$ and the maximum angle of scatter for the incident ion cannot exceed $\frac{\pi}{2}$ Hence the transformation that maps μ to μ' is

$$\mu = \frac{2\mu' - \mu_b - \mu_{min}}{\mu_b - \mu_{min}} \tag{7}$$

and

$$\mu' = \left(\frac{\mu_b + \mu_{min}}{2}\right) + \left(\frac{\mu_b - \mu_{min}}{2}\right)\mu \tag{8}$$

Further, the set of polynomials orthogonal over the partial range is given by

$$P_l'(\mu') = P_l\left(\frac{2\mu' - \mu_b - \mu_{min}}{\mu_b - \mu_{min}}\right) \tag{9}$$

The single differential cross section is now fit over the partial range using the expansion

$$\Sigma_s(E,\mu') = \sum_{l=0}^{L} \frac{2l+1}{2}\Sigma_{s\,l}'(E)P_l'(\mu') \tag{10}$$

where

$$\Sigma_{s\,l}' = \frac{2}{\mu_b - \mu_{min}}\int_{\mu_{min}}^{\mu_b} d\mu'\Sigma_s(E,\mu')P_l'(\mu') \tag{11}$$

The partial range cross section moments are transformed to the full range by the expansion

$$\Sigma_{s\,j}(E) = \sum_{l=0}^{L} \frac{2l+1}{2}\Sigma_{s\,l}'\int_{-1}^{1} d\mu P_l'(\mu)P_j(\mu) \quad for \;\; j = 0, L \tag{12}$$

The tremendous accuracy of this method of fitting ion scattering cross sections is depicted in Figure 2 for 100 keV incident Gold ions on a Gold target Both the complete (singular) cross section and the smooth fit are shown here, as well as the Fokker Planck cut off of $\mu_b = 0\,9$ for various order Legendre expansions With this choice of μ_b, we see that a P_7 fit is sufficient to reproduce the complete cross section exactly up to the cut off We also note that the portion of scattering attributed to the Fokker Planck component is simply the area above the smooth curve and below the complete cross section curve in Figure 2 The amount of scatter treated with the Fokker-Planck component can therefore be decreased by increasing the Legendre expansion order or by increasing the value of μ_b

The fitting of the cross section $\Sigma_s(E,\mu_0)$ lies at the heart of the Coupled Ion Recoil Cross Section (CIRXS) method we have developed CIRXS provides multigroup Fokker Planck functions and Boltzmann cross section moments for a BFP version of the Monte Carlo code MCNP[7], as well as for a BFP deterministic code developed separately (ONEBFP)[8] The momentum transfer functions are obtained from Equation 4, whereas the restricted nuclear stopping power and Legendre cross section moments are obtained using the additional relationship

$$\Sigma_s(E' - E, \mu_0) = \Sigma_s(E', \mu_0)\delta(E - g(E', \mu_0)) \tag{13}$$

As a demonstration of the application of the cross-sections library data for realistic problems, we have computed ion ranges and implantation profiles for 100 keV Au ions incident on a Au target The implantation profile is obtained from the number of ions slowing down into the lowest energy group at each spatial location, and is computed from the multigroup from of the slowing down density[2] The corresponding range is defined as the first normalized spatial moment of this distribution Results have been obtained from both MCNP and ONEBFP simulations and compared against predictions from the industry standard code, TRIM[9]

In Figure 3 is contrasted the implantation profile obtained using TRIM and MCNP The agreement is clearly outstanding across the depth of penetration with the peak position

and magnitudes coinciding almost perfectly The corresponding range is 144 angstroms for TRIM and 112 5 angstroms for MCNP which, given the different methodologies of the two codes is quite outstanding

Comparisons of implantation profiles obtained using TRIM and ONEBFP is displayed in Figure 4 While the agreement is not as outstanding as with MCNP it is nevertheless very good The ONEBFP range is 108 angstroms, a less than 5% deviation ONEBFP tends to under predict penetration but also displays some straggling at the end of the range This is the result of numerical straggling following from discretization of the continuous slowing down operator describing inelastic electronic energy losses Such is not the case with the multigroup MCNP predictions wherein continuous slowing down is treated exactly along an ion track The observed straggling in ONEBFP predictions while small in the present application, can become more significant at higher incident energies and lighter mass ions However, it should also be noted that the use of a consistent high order accurate linear continuous discretization in ONEBFP is expected to display superior accuracy to the diamond difference discretization used in some existing approaches[5]

CONCLUSIONS

In conclusion, we have successfully developed and implemented a generalized Boltzmann Fokker Planck decomposition scheme for a class of singular scattering kernels that arise in ion transport A complete library of scattering cross section and Fokker Planck coefficient data has been constructed and coupled with the multigroup MCNP Monte Carlo code as well as with a specially developed ONEBFP transport code Outstanding agreement for ion implantation profiles and the average range of 100 keV Au ions in a Au target was obtained between the two codes and established results, and suggests the application to a broader class of problems that include three dimensional geometry

REFERENCES

1 E E Lewis and W F Miller Jr , Computational Methods of Neutron Transport Wiley New York (1984)

2 L W Brasure, A K Prinja, M S Lazo and J E Morel, Nucl Instr and Meth B53 (1991), p 134

3 J E Morel, Nucl Sci Eng , 79 (1981), p 340

4 T J Hoffman and T Robinson, J Nucl Mat , 85 86 (1979), p 597

5 Patrick Miazza and Jacques Ligou, Nucl Sci Eng , 105 (1990) p 59

6 Mark Landesman and J E Morel Nucl Sci Eng , 103 (1989), p 1

7 Judith F Briesmeister, et al , 'MCNP A General Monte Carlo Code for Neution and Photon Transport, Version 3A," LA 7396 M, Los Alamos National Laboratory Los Alamos New Mexico, September 1986

8 B. Todd Adams, "Solution of the 1-D BFP Equation Using a Linear Discontinuous Galerkin Approximation in Space and Energy," M S Thesis, University of New Mexico, (1990).

9 J F. Ziegler, et al., The Stopping Power and Range of Ions in Solids, The Pergamon Press, New York, (1985).

Figure 1. Average Cosine of scattering angle for several mass ratios.

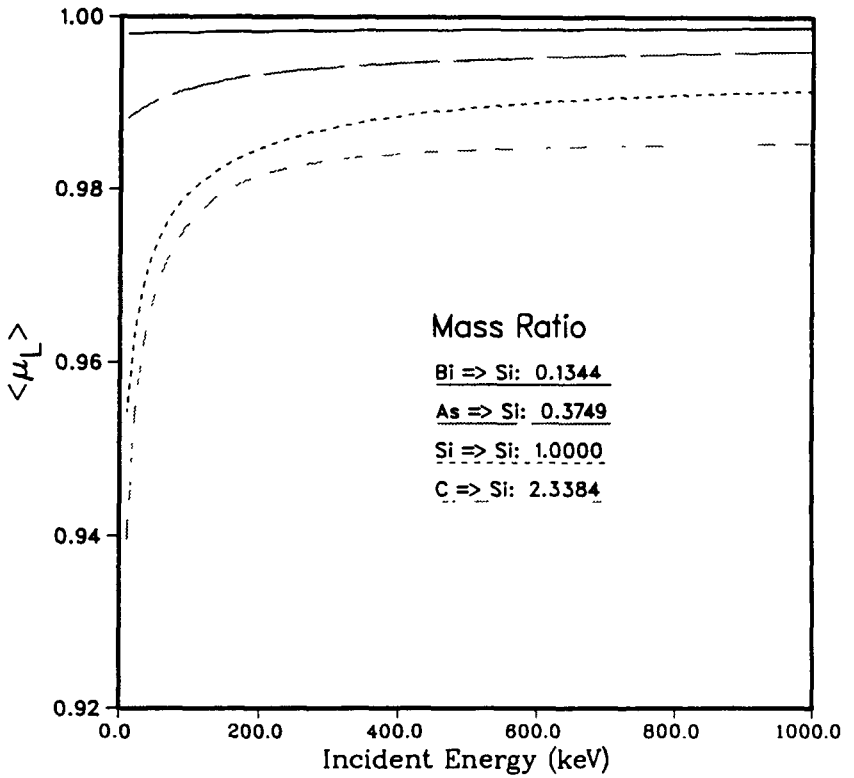

Figure 2. Complete and smooth cross sections for 100 keV Au on Au.

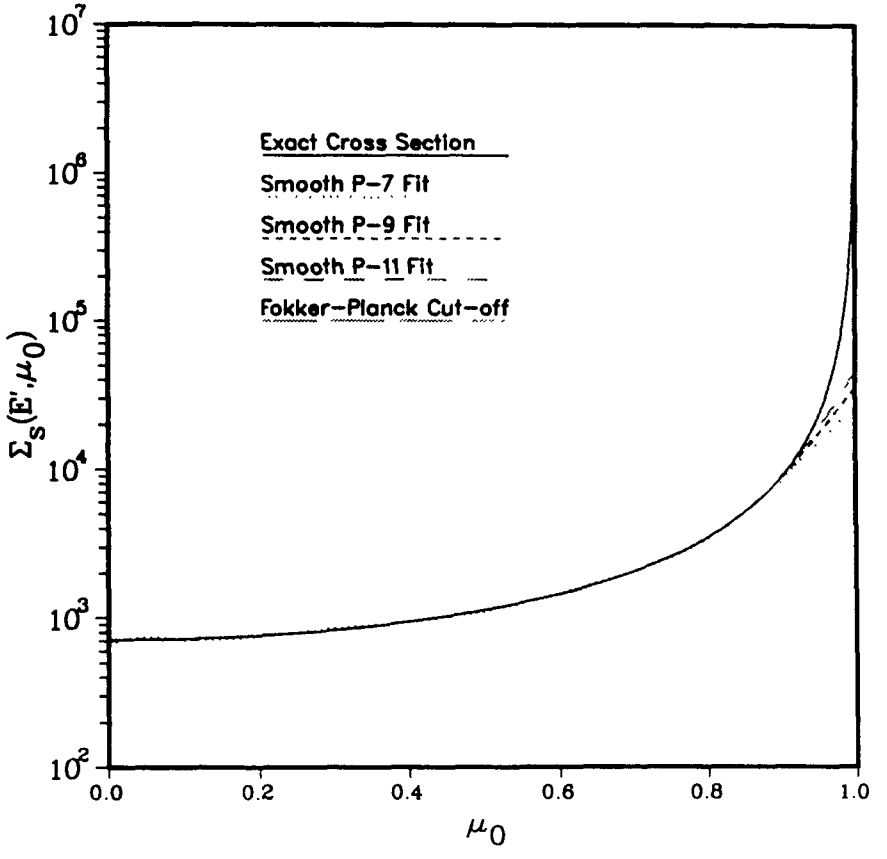

Figure 3 Implantation profile for 100 keV Au ions on Au target
Comparison of TRIM and MCNP code predictions

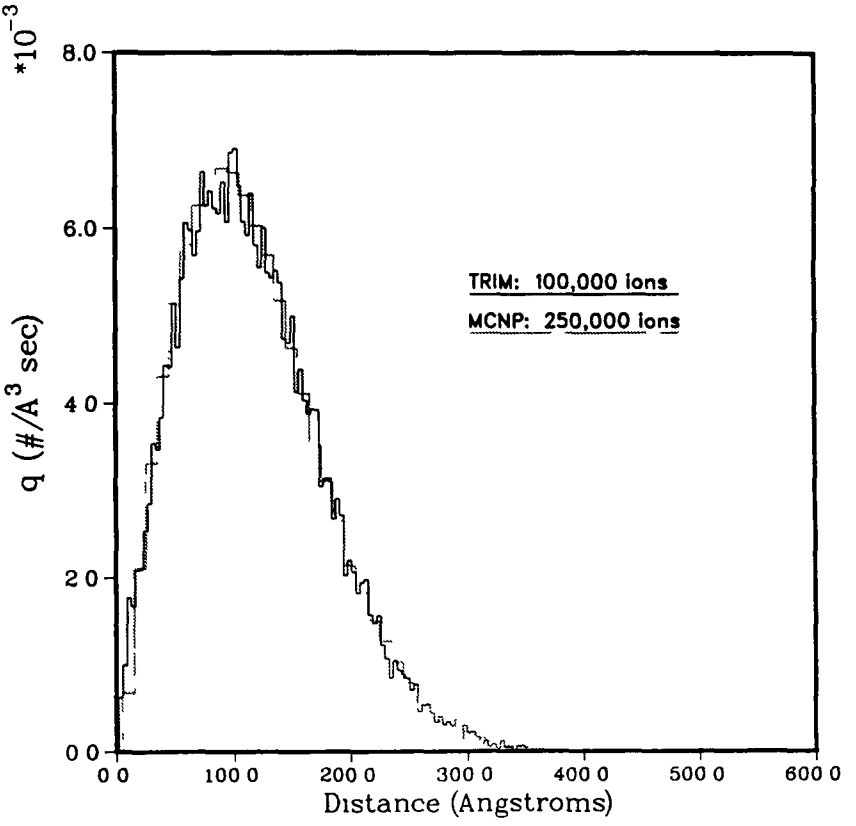

Figure 4. Implantation profile for 100 keV Au ions on Au target Comparisons of TRIM and ONEBFP code predictions.

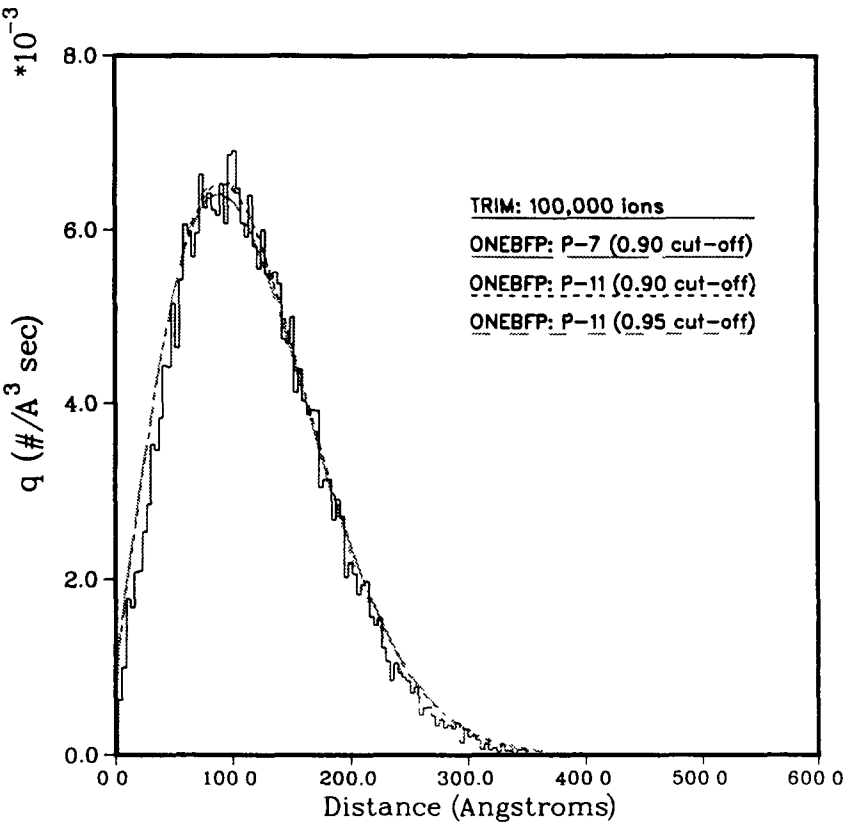

COMPARISON OF THE SEQUENCE FCPM-ICM-NM WITH THE SEQUENCE SPSM-SHM-SHM.

N. I. Laletin, N. V. Sultanov and V. F. Boyarinov
I. V. Kurchatov Institute of Atomic Energy,
Kurchatov Sq., 123182 Moscow, USSR.

ABSTRACT.

A comparison of the two sequence of methods those are used on different stages of neutron-physic calculations is presented. The first sequence - usual one in last time - include a) the first collision probability method (FCPM) on the cell calculation stage; b) the interface current method (ICM) on the assembly calculation stage and c) different nodal methods (NM) on the reactor core calculation stage. The second sequence include for the same stages the surface pseudosource method (SPSM) for cell calculations and the surface harmonic method - different approximations of the method for assembly calculations and reactor core calculation. Advantages of the second sequence are analysed. The numerical examples are demonstrated.

INTRODUCTION.

A natural sequence of stages of the stationary neutron field calculations has formed because each stage requires an individual approximation.

Generally speaking, the necessary answer could be obtained by the direct solution of the exact transport equation. However, this way is not satisfactory for the following reason:

a) Such calculation takes too much computing time and, in our opinion, is unacceptable not only at present, but also in the future, despite of great successes achieved in computer engineering. It is more useful to direct these successes towards extension of calculations for various situations occurring in the course of core burn up, transients, etc.

b) Development of reasonable approximations to the exact transport equation turns out to be closely connected with the qualitative study of the physical processes of interest to us. This work must be made in course of predicting the behaviour of operating reactors and, especially in course of designing the future ones. But when these approximations are developed and studyied, it would be natural to use them in the algorithms of mass calculations.

It is useful to present the established sequence of the neutron-physical calculations by the table.

$r \sim \lambda_{res}$	$r \sim \lambda_{th}$	$r \sim M$	$r \sim R$
$N_g \sim 10^{5-6}$	$N_g \sim 10^2$	$N_g \cong 4-10$	$N_g \cong 1-3$
0) theorems of equivalence	I) FCPM (SPSMD	II) Interface current (SHM-...)	III Nodals methods (SHM-...)

There are dimensions of regions for stages at the line. Here λ_{th}-a mean free path for thermal neutrons, M- a migration lenght, R- a dimension of a core. The numbers of energy groups are indicated at the second line. The usual sequense of methods and the sequense under considerationare demonstated at the third line accordingly.

The zeroth stage - allowance for resonances in the cross-sections - needs such a detailed energetic consideration that this makes undesirable the recalculation of the resonace area in the mass calculations. Fortunately, the same circumstance, namely the narrowness of resonances, that forces to make this detailed division in energy and thereby complicates the problem, simplifies the problem, since every scattering almost by all nuclides (expect the heaviest ones and moreover, for the lower resonaces) removes the neutron from a interval of either resonance. As a result the calculation of the resonance area can be set up as an individual stage. More often the approximating quantities (group resonance integrals dependent on the "dilution" cross-sections and temperatures, and the formulas for calculation of these "dilution" cross-sections) are evaluated in advance and then with the help of them several, usually slightly above ten, group cross-sections for the resonance nuclide are determined.

THE CELL CALCULATION.

I. The next stage is required because the spatial distribution of thermal neutron varies stringly at distances of about the mean free path for neutrons of thermal energies. This results from that in the pin-cell the thermal neutrons are produced (moderated) in the moderator zone, but disappear (are absorbed) in the fuel (or absorber) zone. This stage needs the higher approximations of the transport equation, because a complicated angular distribution corresponds to the fast spatial variation of the neutron flux. The first collision probability method (FCPM) is now used most of all in the stage of pin-cell calculation. This is a basic method in the well-known codes, such as WIMS[1], CASMO[2], PHOENIX[3], APOLLO[4], etc. The surface pseudosource method (SPSMD[5-9] fills this place in the approximation sequence under our consideration. This method is more advantageous than the FCPM for the following reasons.

1) The FCPM is virtually the direct numerical solution of the

Peierls equation with the use of the specific quadrature formula. As a result this method needs a sufficiently fine division of the space zones, that makes this method too cumbersome. It is claimed usually that it is reasonable to divide the cell zones into subzones of approximately the mean free path in size. However, the situations when the subzones of about $0.1\lambda_{th}$[10,11] are required due to vary strong variation of the neutron flux in the "scattering" zones are sufficiently frequent. The example of such situation is given in Tables 1,2.

The SPSM uses the Green functions in an infinite medium and therefore there is no need to divide the "phisical" zones into subzones. Taking into account that the calculation of the Green function moments takes in any case no more time than the calculation of the first collision probabilities for each pair of subzones, it is evident that in achieving the same fixed accuracy the SPSM requires a noticealy less volume of calculations[11] (Table 1)

2) The FCPM is not adapted in principle to calculate the angular distributions of neutrons, because the neutron flux is the unknown quantity in the Peierls equation. But in the improved methods of constructing the finite-difference equations it turns out noticeably more advantageous to use the higher angular momenta together the lowest ones.

The calculation of these quantities is obvious in the SPSM where several angular momenta are continious at the zone interfaces.

Results of calculations of the flux distribution by G_1, G_1^1-approximations (without taking into account of the second angular moments) and by $\tilde{G}_1, \tilde{G}_1^1$-approximations (with taking into account of the second angular moments) are given in Tables 3,4. Results of calculations of the onegroup diffusion coefficient by ORAR-CM code for the some cells with and without taking into account second angular moments are given in Table 5. You can acquaint yourself more detaily with those and another calculations of a cells by SPSM at articles[5,12,13].

3) There is a essential problem in the FCPM. It is a thansition from the Peierls equation which is conventional for this method and in which the isotopic scattering is assumed (usually in the form of transport approximation) to the system of equations where the first and higher angular momenta of the scattering kernel are taken into account.

In the SPSM the allowance for scatterig anisotropy of any order almost does not increase the computing time[10].

4) The calculation of the axial diffusion coefficient $D_\parallel$ (in the case of isotopic scattering or transport approximation) is not difficult in the FCPM, because the "directional" collision probabilities entering in the expressions for $D_\parallel$ are similar to the

ordinary probabilities, calculated by the same way and can be calculated to a great extent parallelly. The situation is different for the transversal diffusion coefficient $D_\perp$. Here a great number of additional integrals describing the correlations between collisions must be calculated besides the "transversal" collision probabilities. As a result, the calculation becomes too labour-consuming and, as far as we know, at present there is no lattice code containing a correct algorithm for calculating $D_\perp$.

In the surface harmonics method (SHM) the calculation of the antisymmetric microstructure needed for $D_\perp$ does not practically differ from the calculation of the symmetric microstructure performed, as a rule, to determine the basic characteristics of cell Σ_a, Σ_f, etc. The calculation of $D_\perp$ carried out by the RADIK code[9].

The advantage of the SPSM over the FCPM manifests itself still more in calculating the group matrix of $D_\perp$ with the non-zero non-diagonal elements which is required for the refines methods of calculation of neutron fields. Table 6 represents calculations of two-group diffusion coefficients for some cells by WIMS-D4 code ("Ariadne" method) and by RADIK code.

THE ASSEMBLY CALCULATION.

II. The second stage of the neutron field calculation results from that the neutron flux smoothened over the cells varies at distances of about the mean free path of neutrons much weaker than the flux inside the cells. This promotes the use of the lower approximations in the angular description of neutron distribution. Since the cross-sections averaged over different cells differ from each, as a rule, much weaker than the cross-sections in different zones of the same cell, for the group presentation of the flux smoothened over cells it is possible to choose fewer groups than in the cell.

The distributions of neutrons inside the assemblies and the characteristics of these assemblies required for calculation of the neutron field in the whole reactor are evaluated in the stage refered to. The assembly-averaged cross-sections for absorption, fission and intergroup transitions appear mostly as such characteristics. The few-group finite-difference fine-mesh equations derived in the diffusion approximation for the homogenized pincells were used earlier for calculation distributions of neutrons inside the assemblies. The dissatisfaction with the accuracy of this approximation has led to that equations of the interface current method (ICM) is used here more and more. The suitable approximation of the SHM ($G_g 3S^\perp$ - approximation) is an alternative in our approach[14-16].

In comparing the above two approaches the following should be noted:

1) In the ICM the one-sided currents join at pincell interfaces while the joining of the resulting currents and the levels (j,l) takes place in the SHM. The advantage of the latter pair of quantities over the former quantities can be felt taking into consideration that the problem for a cell in an infinite homogeneous lattice is a "base" problem for the SHM in virtue of using the pair (j,l), while in the ICM this is a problem about a cell with black boundary conditions. As a consequence the construction of the approximations in the SHM turns out more natural.

2) In the SHM approximation recomended for calculation of the intra-assembly distribution we deal with the finite-difference equation of the same type as the diffusion equation of the homogenization method (but ensuring much higher accuracy in describing the field) (look eq.(1)). This is a well-studied equation for which many iteration methods were developed and which is suitable also for the noniterative solution[17]. In particular, the components of the vector to be calculated in the SHM, unlike the ICM, are always non-negative.

$$\frac{4}{M\,H_r^2}\sum_{i=1}^{M} 2\,\hat{D}_k(\hat{D}_k+\hat{D}_i)^{-1}\hat{D}_i(\vec{\Phi}_i-\vec{\Phi}_k) - \hat{\Sigma}_k\vec{\Phi}_k = 0, \qquad (1)$$

where

$$\hat{\Sigma} = \begin{pmatrix} \Sigma_{a1}+\Sigma_s^{1\to 2}-\dfrac{\nu\Sigma_{f1}}{k_{eff}} & -\dfrac{\nu\Sigma_{f2}}{k_{eff}} \\ -\Sigma_s^{1\to 2} & \Sigma_{a2} \end{pmatrix};$$

M - number of cell sides in the plate;

$\hat{D}$ - matrix of diffusion coefficients;
i,k - cell number;
H_r - lattice pitch.

Equation (1) take place for square (M=4), triangular (M=6) and hexagonal (M=3) lattice.

3) The use of fewer groups than those used at the cell level is more reasonable in the SHM as compared with the ICM, as in this case it is necessary to use the assumption about the spectrum of the resulting current (within a large group) at the cell boundary. The similar assumption in the ICM must be made for the one-side current which is a greater quantity and, therefore, is in need of higher punctuality.

III. The diffusion approximation and few groups, as a rule two groups, are used usually to calculate the neutron field in the whole reactor, i.e. to calculate the neutron distribution smoothened over the assemblies. Various "nodal" methods have been used recently instead of the coarse-mesh finite-difference equations of the diffusion type. Generaly speaking, the term "nodal" methods seems very uncertain, as rather different approaches are associated with it. In comparing these approaches with the SHM approximations we shall imply the most popular ones. The basic differences between the SHM and the nodal approaches are as follows.

1) It is assumed in the nodal methods that the diffusion equation for a homogenized medium is valid inside the assemblies. The SHM does not need such an assumption. The intra-assembly distribution is assumed to be a sum of trial functions calculated in the assumption ensuring a required accuracy. As a result there is no problem with reconstruction of the field within the assembly, whereas in the nodal methods such a reconstruction represents a separate problem[18].

At the SHM it needs to calculate correspondence matrixes $\hat{\sigma}_x$ ("x" - type of functional) in the calculation process of fewgroup cell characteristic. Then unknown fewgroup functional $\vec{F}_x$ can be calculated by formular

$$\vec{F}_x = \sum_{i=0}^{M} \hat{\sigma}_x^i \vec{\Phi}_i ,$$

where vector $\vec{\Phi}$ - solution of equation (1);
M - number of neighbouring cells.

2) In the nodal methods the equations for assemblies of different geometries have to be derived by different ways. In the SHM there exists a common procedure of deriving the equations for all geometries.

3) In the nodal methods every group inside a node (assembly) is characterized by certain cross-sections, that means the invariability of the intragroup neutron spectrum in the node. In the SHM at the same apparent number of groups as if overlapping groups are formed inside the nodes in describing the neutron exchange between the nodes. For example, for the two-group equations each group inside the node has two components whose weights are not predetermined, but obtained after the solution of the entire problem.

As a result, the more high accuracy achieved in describing the neutron field inside the node is coordinated with allowance for the environment of the node (look Table 7 and article[18]).

4) The higher harmonics in the SHM appear by a natural way,

but unlike the nodal methods where the analogous effects are partly taken into account, the number of higher harmonics is unnecessarily divisible by the number of node sides. This ensures the more high flexibility of the calculation procedure in the SHM.

5) The form of SHM equations is similar to that of the coarse-mesh equations of the homogenization method. This allows the use of the well-developed procedures to solve such equations. So the diffusion code JOSHUA [23] was used for the RBMK assemblies calculation (Table 7) because in this code the finite-difference equation of the appeance (1) are solved.

CONCLUSION.

Present here arguments point out in authours opinion the sequence of methods SPSM-SHM-SHM is more perspective one than usual in last time sequence FCPM-ICM-NM for achievment a larger accuracy with fixed expenditures of computer time.

REFERENCES.

1. Askew J., Fayers F., Kemshell P. A General Description of the Lattice Code WIMS. -JBNBC, 1966, Oct., p.564.

2. Edenius M., Forssen B.H., Gragg C.- The Physics Model of CASMO-4. Mtg. Advances in Mathematics Computation and Reactor Physics. Pittsburgh, USA, v.2, p.10.1 1-1, 1991.

3. Lee D.K. Benchmark of the PHOENIX P/ANC Computer Code for Common Wealth Edison PWRs. ibid, v.3, p.14.1 4-1, 1991.

4. Coste M., Sanchez R ., Stankovski Z., VanDer Gucht C., Zmijarevic I. APOLLO-II Assembly Spectrum Code: New Features. ibid, v.2, p.10.1 4-1.1991.

5. Laletin N.I. The Surface Pseudosource Method for Solution of the Equation of Neutron Transport (G_N-approximation) In book The methods for calculation of thermal neutron fields in the reactor lattices. Ed. Ya. V. Shevelev, M., Atomizdat, 1974, p.187-215.

6. Laletin N.I. Use of Operator Fragmentation Method for Separation of Energy and Spatial Problems under Calculation of Neutrons Distribution in a Reactor Cell. Voprosy Atomnoy Nauki i Tekhniki. Series: Phisika i Tekhnika Yadernyh Reaktorov, 5(18), p.63, 1981.

7. Sultanov N.V. Multigroup Calculation of Cylindrical Cells with Efficiently Absorbing Ring Zones by Surface Pseudosources Method. "Atomnaya Energiya", v.58, p.410, 1985.

8. Sultanov N.V. Multigroup Calculation of Cluster Cells with Use of Surface Pseudosources Method. "Atomnaya Energiya", v.58, p.414, 1985.

9. Boyarinov V.F. Multigroup Calculation of Antisymmetrical Distributions of Neutrons in a Cylindrical Cell. "Atomnaya Energiya"

v. 61, p. 324, 1986.

10. Laletin N.I., Sultanov N.V., Boyarinov V.F. The Anisotropic Scattering Effect in Calculation of the Nuclear Reactor Cells by the Surface Pseudosource Method. Mtg. Advances in Mathematics Computation and Reactor Physics. Pittsburgh, USA, v. 4, p. 20.1 3-1, 1991.

11. Sultanov N.V. A Comparison of Some Codes for the Calculation of Cell Characteristics in Nuclear Reactors. Voprosy Atomnoy Nauki i Tekhniki. Series: Physika Yadernyh Reactorov, v. 1, p. 42. 1990.

12. Laletin N.I., Sultanov N.V. Development of Surface Pseudosources Method for Calculation Neutron Fields in Cells with a Cluster of Fuel Elements. "Atomnaya Energiya", v. 46, p. 148, 1979.

13. Laletin N.I., Boyarinov V.F. An Effective One Group Diffusion Coefficient of Neutrons in the Reactor Lattices. "Atomnaya Energiya", v. 59, p. 91, 1985.

14. Laletin N.I. Basis Principles for Developimg Equations for Heterogeneous Reactors - A Modification of the Homogenization Method. Nucl. Sci. and Engng. v. 88, N2, p. 133, 1983.

15. Laletin N.I., El'shin A.V. The Refinement of the Homogenization Method of Heterogeneous Reactor. "Atomnaya Energiya", v. 43, p. 247, 1977.

16. Laletin N.I., Sultanov N.V., Boyarinov V.F. Surface Harmonics and Surface Pseudosource Method. Proc, PHYSOR-90, ANS/ENS, vol. 2, XII, Marseille, April, 1989.

17. Weiss Z., Jonbert W. Alternative Method of Solution Response Matrix Equations. Mtg. Advances in Mathematics Computation and Reactor Physics. Pittsburgh, USA, v. 5, p. 21.2 2-1, 1991.

18. Zhang H., Rizwan-uddin, Dorning J.J. Systematic Cell and Assembly Homogenization and Local Flux Reconstruction for Nodal Diffusion Methods. ibid, v. 4, p. 16.2 4-1, 1991.

19. Smith K., Greenman G., and HenryA.F. Resent Advances in an Analitic Nodal Method for Static and Transient Analysis. Proc. ANS Topl. Mtg. on Computational Methods in Nuclear Science and Engineering, Williamsburg, va., 1, p. 3-49. (1979).

20. Derning J.J. Modern Coarse-Mesh Method - A Development of the 70's. Proc. ANS Topl. Mtg. on Computational Methods in Nuclear Science and Engineering, Williamsburg, v. 1, p. 3-1. (1979).

21. Arkuszewski J. SIXTUS-A 2D Diffusion Theory Nodal Code in Hexagonal Geometry. EIR-410, Eidg. Institute fur Reactoforschung, Wurenlingen (1980).

22. Siltanen P., Terasvieta R. and Anttila M. HEXBU -A 2D Core Power Distribution, Burnup and Fuel Assemblies. Report 14, Technical Research Centre of Finland, (1974).

23. Roth M.J., Thompson Mrs. M.A. The Facade Version JOSHUA. AEEW-R1186, 1978.

24. Marchuk G.I., Lebedev V.I. The Numerical Methods in the

heory of Neutron Transport. Atomizdat, M., 1981.

25. Takeda T., Azekura K., Sekiya T. Effect of Higher Order Anisotropy on Disadvantage Factor in a Cell. J. Nucl. Sci. and Tech. v. 9, N4, p. 249.

26. Gomin E. A., Mayorov L. V. Annotation of the WERTER Code. Voprosy Atomnoy Nauki i Tekhniki. Series: Phisika i Tekhnika Yadernyh Reaktorov, M., NIKIET, v. 5(27), p. 83, 1982.

Table 1. Two-group constants for the RBMK cell.

Cons-	Codes, approximations		
tants	KLARA	WIMS-D4,	PIJ
	G_3^1	13 subzone	42 subzone
k_∞	1,2971	1,3025	1,3000
		(0,4)*)	(0,2)
Σ_a^2	0,004654	0,005057	0,004708
		(8,8)	(1,2)
Σ_a^1	0,001291	0,001292	0,001299
		(0,1)	(0,6)
$\nu\Sigma_f^2$	0,006775	0,007449	0,006872
		(9,9)	(1,5)
$\nu\Sigma_f^1$	0,0007731	0,0007601	0,0007741
		(-1,7)	(0,1)
$\Sigma_{s1\to 2}$	0,005693	0,005831	0,5737
		(2,4)	(0,8)
$t_{(min)}$**)	3,2	6,5	111
$(\Delta r/\lambda_{th})_{min}$		~ 1	~ 0,1

*) In brackets the percentage difference between the given results and the G_3^1-approximation data is shown.

**) The ES-1055 computer time is given.

Table 2. The disadvatage factors in the two-zone cylindrical cells.

Method approxi-mations	r_1 r_2=3,0 (sm)	Number of members K in the scatering kernal. 0	1	2	4	Trasport approximation
FPCM[25]	0,5	1,3556	1,2680	1,2794	-----	------
SPSM		1,3870	1,2635	1,2839	1,2833	1,3115
FPCM[25]		2,2813*)	2,0269	2,0620	------	------
	2,0	2,3373**)				
SPSM		2,3438	2,0548	2,1074	2,1061	2,1869

*) 5 subzone division with $\Delta r/\lambda_{th}$~0,3.

**) 20 subzone division in the WERTER code[26] with $\Delta r/\lambda_{th}$<0,1.

Table 3. The flux distribution in the three-zone cylindrical cell.

Zone number	r (sm)	Σ_a (1/sm)	Σ_{tot} (1/sm)	q (n/sm^3)	The method of characteristics	SPSM G_1	$\tilde{G}_1$	G_3
1	1,75	0,7	2,0	0,52	1,9678	1,7634 (-11%)	1,9470 (-1,1%)	1,9562 (0,6%)
2	2,0	1,8	2,0	0,0	3,5423	3,8074 (7,6%)	3,5835 (1,2%)	3,5633 (0,6%)
3	4,0	0,02	2,0	1,0	14,077	14,1131 (0,2%)	14,048 (-0,2%)	14,094 (0,1%)

Table 5. Onegroup diffusion coefficients of cells with and without taking into account second angular moments.

Cell number	Zone number	Radius sm	Σ_{tr} sm^{-1}	Σ_a sm^{-1}	D (without)	D (with)
1	1	0.68	0.6114	0.2455	0.2940	0.3089
	2	0.864	2.1318	0.0075		
2	1	0.38	0.15604	0.01962	5.7996	2.4290
	2	1.27	0.13655	0.109716		
1	1	4.4	1.117	0.11	0.85275	0.8527
	2	14.105	0.38091	0.00001		

Table 4. The flux distribution in the cluster cell.

Zone number	Material	$(\Phi-\Phi_{m-c})/\Phi_{m-c}*100\%$ G_1^1	$\tilde{G}_1^1$	G_3^1	Φ_{m-c}
1	Zr	-22	-12	-3	$1,34(1\pm1,3*10^{-2})$
	H_2O	-12	-5	-0,6	$1,52(1\pm0,6*10^{-2})$
2	UO_2	-13	-6	-0,8	$1,34(1\pm0,7*10^{-2})$
3	H_2O	6	2	0,3	$2,08(1\pm0,3*10^{-2})$
	UO_2	3,1	2,1	0,2	$2,36(1\pm0,3*10^{-2})$
4	Zr	6,2	2,1	0,2	$4,64(1\pm0,2*10^{-2})$
5	C	7,8	2,0	1,2	$5,10(1\pm0,2*10^{-2})$
6	C	8,2	1,2	1,2	$5,60(1\pm0,2*10^{-2})$
7	C	8,0	0,5	0,3	$6,09(1\pm0,2*10^{-2})$
8	C	9,3	1,2	1,1	$6,47(1\pm0.1*10^{-2})$

Table 6. Twogroup diffusion coefficients of RBMK cells.

Cell type	RADIK		WIMS-D4 ("Ariadne")	
cell with fuel assembly with H_2O	1.2845	-0.0287	1.1139	0.
	-0.1636	0.8605	0.	0.8111
cell with fuel assembly without H_2O	1.2695	-0.0248	1.1628	0.
	-0.1591	0.9047	0.	0.8970
cell with empty channel	1.3697	-0.6E-5	1.1101	0.
	-0.1476	0.9596	0.	0.8855
cell with CR channel	1.3205	-0.8E-5	1.2273	0.
	-0.1481	0.9214	0.	0.8707
cell with SA with H_2O	1.3217	-0.7E-5	1.2027	0.
	-0.1822	0.8031	0.	0.8237
cell with SA without H_2O	1.3198	-0.7E-5	1.0865	0.
	-0.1495	0.9555	0.	0.8201

*) CR - control rod

**) SA - supplementary absorber

Table 7. Reactivity of fuel assemblies of RBMK.

$(K_{calc} - K_{exp})*100$

Number of assembly	1	2	3	4	5	6	7	8	9	10
Traditional homogenization method	2.41	2.66	2.71	2.27	2.30	2.13	1.59	2.38	2.07	2.75
SHM	-0.26	-0.02	-0.03	0.10	0.12	-0.36	-0.31	-0.36	0.00	-0.23
Composition of assemblies	23 TBC WITH H_2O 301 PK PK	45 TBC WITH H_2O 4DP WITH H_2O 275 PK	44 TBC WITH H_2O 4DP WITHOUT H_2O 276 PK	49 TBC WITH H_2O 4DP WITHOUT H_2O 271 PK	48 TBC WITH H_2O 4DP WITHOUT H_2O 272 PK	56 TBC WITH H_2O 12DP WITH H_2O 256 PK	71 TBC WITH H_2O 12DP WITHOUT H_2O 241 PK	89 TBC WITH H_2O 32DP WITH H_2O 203 PK	18 TBC WITH H_2O 306 PK	22 TBC WITH OUT H_2O 302 PK

TBC - fuel assembly; DP - an extra absorber;

PK - "void channel" (without fuel rods and coolant)

NEUTRON DISTRIBUTION MODELLING BASED ON INTEGRO-PROBABILISTIC APPROACH OF DISCRETE ORDINATES METHOD

V.V.Khromov, E.F.Kryuchkov, G.V.Tikhomirov

Moscow Engineering Physics Institute
Kashirskoe Shosse 31, Moscow M-409, U S S R

Abstract

In this paper it is described the universal nodal method for the neutron distribution calculation in reactor and shielding problems, based on using of influence functions and factors of local-integrated volume and surface neutron sources in phase subregions. This method permits to avoid the limited capabilities of collision-probability method concerning with the detailed calculation of angular neutron flux dependence, scattering anisotropy and empty channels. The proposed method may be considered as modification of S_n - method with advantage of ray-effects elimination. There are presented the description of method theory and algorithm following by the examples of method applications for calculation of neutron distribution in three-dimensional model of fusion reactor blanket and in highly heterogeneous reactor with empty channel.

1. Influence functions and factors of local-integrated neutron sources and discrete analogues of neutron distribution equations

Neutron distribution in global system volume V with external boundary S may be described in term of group neutron flux function $\phi_g = \phi_g(x)$, where x - generalized combination of space-anqular phase variables $(\vec{r}, \vec{\Omega})$. The domain U of group neutron fluxes is subdivided by the non-crossing local phase subregions $U_{m,k} = V_m \times \Delta\Omega_k$ in process of separation the local (heterogeneous, in general case) volumes V_m and angular diapazones $\Delta\Omega_k$.

Transport and neutron-nuclei interactions are described by the equation:

$$\vec{\Omega}\,\nabla\phi_g + \Sigma_g\phi_g = q_g\,, \qquad (1)$$

where Σ_g - total cross-section of neutron-nuclei interaction;

q_g - volume neutron source in energy group g.

Equation (1) must be added by the respective boundary conditions on external boundary S.

For noting simplification it is supposed that V_m is regular polygon with plane boundary sides $S_j^{(m)}$, having outer normal $\vec{n}_j$; the volume sides did not intersect the angular diapazones boundary. The phase subregion $S_j^{(m)} \times \Delta\Omega_k$ with $(\vec{\Omega}\cdot\vec{n}_j)<0$ will be referenced as $U_{j,k}^{(-)}$ (in opposite case with $(\vec{\Omega}\cdot\vec{n}_j)>0$, it will be $U_{j,k}^{(+)}$).

Neutron flux in volume V_m may be determined by the quadrature formula:

$$\phi_g(\vec{r},\vec{\Omega}) = \int_{V_m} d\vec{r}\,' G^{(v)}(\vec{r}\leftarrow\vec{r}\,',\vec{\Omega},g)\cdot q_g(\vec{r}\,',\vec{\Omega}) + \sum_{j'}\int_{S_{j'}} dS\; G^{(s)}(\vec{r}\leftarrow\vec{r}_s,\vec{\Omega},g)\cdot {}^{(-)}I_g(\vec{r}_s,\vec{\Omega}), \qquad (2)$$

where ${}^{(-)}I(x)$ $(x\in U_{j,k}^{(-)})$ - intensity of surface neutron sources on $S_j^{(m)}$ side of V_m volume.

Volume Green's function is determined by the equation:

$$G^{(v)}(\vec{r}\leftarrow\vec{r}\,',\vec{\Omega},g) = \frac{1}{|\vec{r}-\vec{r}\,'|^2}\exp\left\{-\int_0^{|\vec{r}-\vec{r}\,'|} d\xi\Sigma_g(\xi)\right\}\delta\left[\frac{\vec{r}-\vec{r}\,'}{|\vec{r}-\vec{r}\,'|}\cdot\vec{\Omega}\right] \qquad (3)$$

and related with the surface function by the reciprocity relationship:

$$G^{(s)}(\vec{r}\leftarrow\vec{r}_s,\vec{\Omega},g) = G^{(v)}(\vec{r}_s\leftarrow\vec{r},-\vec{\Omega},g) \quad . \qquad (4)$$

Basing on the quadrature formula (2) the transfer to discrete analoque of neutron transport equation is carried out. The discrete analoque is the system of equalities which relates the flux functionals:

$$\Phi_{mkg} = \langle\phi_g(x)\rangle_{U_{m,k}} ; \qquad {}^{\{+\}}I_{mkg}^{(j)} = \langle|\vec{\Omega}\cdot\vec{n}_j|\phi_g\rangle_{U_{j,k}^{(+)(-)}} \quad , \qquad (5)$$

where brackets mean the integration of included functions on phase subregions. In result of the substitution (2) in (5) one may receive the following system of equalities:

$$\begin{aligned} \Phi_{mkg} &= F(m\leftarrow m,k,g)\; q_{mkg} + \sum_{j'} F(m\leftarrow j',k,g)\; {}^{(-)}I_{mkg}^{(j')} \\ {}^{(+)}I_{mkg}^{(j)} &= I(j\leftarrow m,k,g)\; q_{mkg} + \sum_{j'} I(j\leftarrow j',k,g)\; {}^{(-)}I_{mkg}^{(j')} \quad , \end{aligned} \qquad (6)$$

where $q_{mkg}=\langle q_g\rangle_{U_{m,k}}$; factors F and I have the meaning of the discrete probabilities (on angular diapazones) of influence of local-integrated volume and surface sources on integrated in $U_{m,k}$ flux and integrated in $U_{j,k}^{(-)}$ currents of collisionless neutrons.

These factors are determined by the following system of

equalities:

$$
\begin{aligned}
F(m\leftarrow m,k,g) &= \langle \phi^{(v)}(x\leftarrow m,k,g)\rangle_{U_{m,k}} \\
F(m\leftarrow j',k,g) &= \langle \phi^{(s)}(x\leftarrow j',k,g)\rangle_{U_{m,k}} \\
I(j\leftarrow m,k,g) &= \langle |\vec{\Omega}\cdot\vec{n}_j|\ \phi^{(v)}(x\leftarrow m,k,g)\rangle_{U^{(+)}_{j,k}} \\
I(j\leftarrow j',k,g) &= \langle |\vec{\Omega}\cdot\vec{n}_j|\ \phi^{(s)}(x\leftarrow j',k,g)\rangle_{U^{(+)}_{j',k}} \ .
\end{aligned}
\tag{7}
$$

where $\phi^{(v)}$ and $\phi^{(s)}$- influence functions of local-integrated neutron sources on the neutron flux in the phase point x . These functions are related with Green's functions by the equations:

$$
\begin{aligned}
\phi^{(v)}(\vec{r},\vec{\Omega}\leftarrow m,k,g) &= \int_{V_m} d\vec{r}\,' G^{(v)}(\vec{r}\leftarrow\vec{r}\,',\vec{\Omega},g)\ q_g(\vec{r}\,',\vec{\Omega})\ /\ \langle q_g\rangle_{U_{m,k}} \\
\phi^{(s)}(\vec{r},\vec{\Omega}\leftarrow j',k,g) &= \int_{S_{j'}} d\vec{r}_s' G^{(s)}(\vec{r}\leftarrow\vec{r}_s',\vec{\Omega},g)\ {}^{(-)}I_g(\vec{r}_s',\vec{\Omega})\ /\ \langle {}^{(-)}I_g\rangle_{U^{(-)}_{j',k}} \ .
\end{aligned}
\tag{8}
$$

According with definition the function $\phi^{(v)}$ in volume V_m is satisfied by the equation (1) with $q_g = q_g(\vec{r},\Omega)\cdot\delta(\vec{r},V_m)\cdot\delta(\Omega,\Delta\Omega_k)\ /\ \langle q_g\rangle_{U_{m,k}}$ provided the homogeneous boundary conditions for incoming neutron currents on the surface $S_j^{(m)}$, and function $\phi^{(s)}$- is satisfied by the homogeneous equation (1) with non-homogeneous boundary conditions

$$
|\vec{\Omega}\cdot\vec{n}_j|\phi^{(s)}(\vec{r}_j,\vec{\Omega}\leftarrow j',k,g) = {}^{(-)}I_g(\vec{r}_j,\vec{\Omega})\cdot\delta(\vec{r}_j,S_j^{(m)})\cdot\delta(\vec{\Omega},\Delta\Omega_k) \ ,
$$

where $\delta(y,\Delta y)$ equals to unity when $y\in\Delta y$ and zero when $y\notin\Delta y$.

Quadrature formula (2) may be written in terms of $\phi^{(v)}$ and $\phi^{(s)}$ in following form:

$$
\phi_g(\vec{r},\vec{\Omega}) = \phi^{(v)}(\vec{r},\vec{\Omega}\leftarrow m,k,g)\cdot q_{mkg} + \sum_{j'}\phi^{(s)}(\vec{r},\vec{\Omega}\leftarrow j',k,g)\cdot {}^{(-)}I^{(j')}_{mkg} \ . \tag{9}
$$

It may be considered as formula of neutron flux reconstruction (and currents of neutrons outcoming from V_m by the $S_j^{(m)}$) in terms of known local-integrated volume and surface sources and its influence functions.

From equations for $\phi^{(v)}$ and $\phi^{(s)}$ the balance relations may be received which invarianted to distributions of volume and surface sources:

$$
\begin{aligned}
\sum_j I(j\leftarrow m,k,g) + \langle\Sigma_g\phi^{(v)}\rangle_{U_{m,k}} &= 1 \\
\sum_j I(j\leftarrow j',k,g) + \langle\Sigma_g\phi^{(s)}\rangle_{U_{m,k}} &= 1 \ .
\end{aligned}
\tag{10}
$$

The joint consideration of 2-nd equation of system (6) with equalities (9) and (10) leads to the balance relation for reaction rates

in phase subregions $U_{m,k}$, in energy group g:

$$\sum_j \left({}^{(+)}I^{(j)}_{mkg} - {}^{(-)}I^{(j)}_{mkg} \right) + \langle \Sigma_g \phi_g \rangle_{U_{m,k}} = q_{mkg} \quad . \qquad (11)$$

The second term of the left part of equation (11) determines the way of averaging (homogenization) of total cross-section within the heterogeneous volume V_m:

$$\bar{\Sigma}_{g,k} = \langle \Sigma_g \phi_g \rangle_{U_{m,k}} / \langle \phi_g \rangle_{U_{m,k}} \quad . \qquad (12)$$

In general case volume neutron sources in V_m depend on neutron flux. So local-integrated sources q_{mkg} are presented by the linear functionals of neutron flux. For the condition-critical reactor the following equation may by written:

$$q_{mkg} = \sum_{k'} \sum_{g'} \left[\bar{\Sigma}_{s,m}(k, g \leftarrow k', g') + \frac{\omega_k}{k_{ef}} \frac{\chi_{g,m}}{4\pi} (\overline{\nu_f \Sigma_f})_{mg'} \right] \phi_{mk'g'} \quad , \qquad (13)$$

where $\omega_k = \int_{\Delta\Omega_k} d\vec{\Omega}$; k_{ef} - effective neutron multiplication factor. Homogenized macro-constants for volume V_m are determined by the equation:

$$\bar{\Sigma}_{s,m}(k, g \leftarrow k', g') = \langle \int_{\Delta\Omega_{k'}} d\vec{\Omega}' \Sigma_s(\vec{r}; \vec{\Omega}, g \leftarrow \vec{\Omega}', g') \phi_{g'}(\vec{r}, \vec{\Omega}') \rangle_{U_{m,k}} / \langle \phi_{g'} \rangle_{U_{m,k'}}$$

$$(\overline{\nu_f \Sigma_f})_{mg} = \langle (\nu_f \Sigma_f)_g \phi_g(x) \rangle_{U_{m,4\pi}} / \langle \phi_g(x) \rangle_{U_{m,4\pi}} \qquad (14)$$

$$\bar{\chi}_{mg} = \int_{V_m} d\vec{r}\, \chi_g(\vec{r}) \sum_{g'} \int_{4\pi} d\vec{\Omega}' (\nu_f \Sigma_f)_{g'} \cdot \phi_{g'}(\vec{r}, \vec{\Omega}') / \langle (\nu_f \Sigma_f)_{g'} \cdot \phi_{g'} \rangle_{U_{m,4\pi}} ,$$

where $U_{m,4\pi} = V_m \times 4\pi$.

If external surface sources absent on $S^{(m)}_j$ the following condition of continuity may by written:

$${}^{(-)}I^{(j)}_{mkg} = {}^{(+)}I^{(j)}_{m(j)kg} \quad , \qquad (15)$$

where m(j) is the numbers of neighbours to volume V_m with the joint side S_j.

The system of equalities (6),(13),(15) with homogeneous boundary conditions for currents of incoming neutrons is the exact discrete analogue of neutron transport equation in condition-critical reactor.

If the factor F, I of equation (7) are assumed to be apriori known along with the homogenized parametrs (equations (14)) then system (6), (13), (15) is closed system of equations of condition-critical reactor for local-integrated fluxes and partial neutron currents.

The different ways of apriori evaluation of influence factors and macro-characteristics discover the different approximated algorithms for neutron flux calculation with discrete analogues of transport equation. One of these will be considered in respective section of present paper.

Simultaneously the above written equation permits to organize the closed on phase subregions iterative algorithm for detailed neutron flux calculation. In this algorithm the equations (6),(13), (15), factors and macro-characteristics must determine the phase subregion-integrated neutron fluxes and currents (global distribution), formula (9) may reduce the detailed distributions of volume and surface sources (local distribution).

Basing on these distributions one may correct factors F , I and averaged macro-characteristics for the next iterations of global calculation. Such algorithm has familiar structure with algorithm of neutron rebalance method applied for the improvement of iterative processes convergence.

2. Approximation of the plane fluxes in phase subregious.

Suppose that volumes V_m are homogeneous and its optical thicknesses $\Sigma \cdot d$ (d-diameter of the volume) are rather small. Then using the equations (6), (11), (13) one may receive the closed algorithm for calculation of functionals Φ^{mkg}_k and $I^{(+)}_{(j)}$ if the following assumption are made in determination of factors F, I and in averaging of system macro-characteristics:

$$\phi_g(\vec{r},\vec{\Omega})=\text{Const}, \text{ if } (\vec{r},\vec{\Omega})\in U_{m,k}; \qquad \phi_g(\vec{r}_j,\vec{\Omega})=\text{Const}, \text{ if } (\vec{r}_j,\vec{\Omega})\in U^{(-)}_{j,k} .$$

Such approximation may be called by the plane flux approximation. This approximation differs significantly from the analogous one of collision probability method by the discrete procedure of angular neutron distribution accounting for the volume V_m and its surface. Presented approximation leads to the following relation:

$$q_g(\vec{r},\vec{\Omega})=\text{Const}, \quad (\vec{r},\vec{\Omega})\in U_{m,k}$$

in factors calculation, and so from the reciprocity equation (5) one may receive:

$$I(j\leftarrow m,k,g)\cdot V_m \cdot \omega_k = F(m\leftarrow j,k,g)\cdot S_j \cdot \mu_{jk} , \qquad (16)$$

where $\mu_{jk} = \int_{\Delta\Omega_k} d\vec{\Omega}|\vec{\Omega}\cdot\vec{n}_j|$; and balance relations (10) transfer into the equations:

$$\begin{aligned} &\sum_j I(j\leftarrow m,k,g) + \Sigma_g F(m\leftarrow m,k,g) = 1 \\ &\sum_j I(j\leftarrow j',k,g) + \Sigma_g F(m\leftarrow j',k,g) = 1 \end{aligned} \qquad (17)$$

The theoretical estimates show that presented algorithm has second order of approximation for space-angular functions in phase subregions with rather smooth solutions

Determination of the factors-probabilities is key problem of the method In this method it is enough to calculate the factor $I(j\leftarrow j',k,g)$, and using these factors it is possible to determine all other factors by the formulas (16),(17) However here there are some difficulties The first, if $\Sigma=0$ then the relations controlled by the egualities (17) are interrupted So calculation of above mentioned factors for empty channels requires the special consideration The second, calculation of factors $I(j\leftarrow j',k,g)$ determined in general case by the following equation

$$I(j\leftarrow j',k,g)=\frac{1}{S_{j'}\mu_{j'k}}\int_{S_j}d\vec{r}_s\int_{S_{j'}}d\vec{r}'_s\int_{\Delta\Omega_k}d\vec{\Omega}\,\varkappa_{jj'k}(\vec{r}_s,\vec{r}'_s,\vec{\Omega})\cdot\exp\left\{-|\vec{r}_s-\vec{r}'_s|\cdot\Sigma_g\right\} \tag{18}$$

where

$$\varkappa_{jj'k}(\vec{r}_s,\vec{r}'_s,\vec{\Omega})=\frac{|\vec{\Omega}\,\vec{n}_j|\cdot|\vec{\Omega}\,\vec{n}_{j'}|}{|\vec{r}_s-\vec{r}'_s|^2}\cdot\delta\left[\frac{\vec{r}_s-\vec{r}'_s}{|\vec{r}_s-\vec{r}'_s|}\cdot\vec{\Omega}\right],\quad\vec{\Omega}\in\Delta\Omega_k \tag{19}$$

requires the numerical integration

The function $\varkappa_{jj'k}(\vec{r}_s,\vec{r}'_s,\vec{\Omega})$ may be interpreted as distribution function of neutron trajectories travelling in vacuum in angular diapazone $\Delta\Omega_k$ from $S_{j'}$ side to S_j one (for isotropic flux in ${}^{(-)}U_{j',k}$)

Then functional

$$\overline{\ell^n_{jj'k}}=\frac{1}{\varkappa^{(0)}_{jj'k}}\int_{S_j}d\vec{r}\int_{S_{j'}}d\vec{r}'\int_{\Delta\Omega_k}d\vec{\Omega}\,|\vec{r}_s-\vec{r}'_s|^n\cdot\varkappa_{jj'k}(\vec{r}_s,\vec{r}'_s,\vec{\Omega}) \tag{20}$$

where $\varkappa^{(0)}_{jj'k}$ – integral of eguation (20) at n=0, will determine at n=1 the average distance of neutron travelling in vacuum between S_j and $S_{j'}$ sides in angular diapazone $\Delta\Omega_k$, at n=2 – average square of this distance etc

Let us use the asterisk (*) for the factors F and I at $\Sigma=0$ The following equations may by written

$${}^{(*)}I(j\leftarrow j',k,g)=\frac{1}{S_{j'}\mu_{j'k}}\varkappa^{(0)}_{jj'k},\qquad I(j\leftarrow m,k,g)=\frac{1}{V_m\omega_k}\sum_{j'}(\bar{\ell}\cdot\varkappa^{(0)})_{jj'k}$$

$${}^{(*)}F(m\leftarrow j',k,g)=\frac{1}{S_{j'}\mu_{j'k}}\sum_{j'}(\bar{\ell}\cdot\varkappa^{(0)})_{jj'k} \tag{21}$$

$${}^{(*)}F(m\leftarrow m,k,g)=\frac{1}{2V_m\omega_k}\sum_j\sum_{j'}(\overline{\ell^2}\cdot\varkappa^{(0)})_{jj'k}$$

The following normalization conditions must be fulfilled:

$$\sum_k \sum_j \sum_{j'} (\bar{\ell} \cdot K^{(0)})_{jj'k} = 4\pi V_m; \qquad \sum_k \sum_j \sum_{j'} K^{(0)}_{jj'k} = S^{(m)}\pi \quad . \qquad (22)$$

From these equations one may receive the well known formula for the mean chord of volume V_m: $\bar{\ell}_m = 4\, V_m / S^{(m)}$.

For the rather small $\Sigma\bar{\ell}_{jj'k}$ the explicit I factor dependence on Σ may be presented by the series:

$$\frac{S_{j'} \cdot \mu_{j'k}}{K^{(0)}_{jj'k}} I(j \leftarrow j', k, g) = \left[1 - \Sigma\bar{\ell} + \frac{1}{2}(\Sigma\bar{\ell})^2 \frac{\overline{\ell^2}}{(\bar{\ell})^2} - \frac{1}{6}(\Sigma\bar{\ell})^3 \frac{\overline{\ell^3}}{(\bar{\ell})^3} + \ldots \right]_{jj'k}.$$

The explicit factor I dependence on Σ and $\overline{\ell^n}$ which permits to evaluate this factor within the more wide diapazone of optical thicknesses is formed with use of different approximated formulas.

3. Realization of method in the computer code. Results of modelling problems calculations.

The above described algorithm was realized in the computer codes for three-dimensional neutron distribution calculations in (X, Y, Z) - geometry. Code can resolve the following problems:

- the calculational support of the experimental investigations of the fusion reactor blanket zones (neutron propagation problem for finite heterogeneous media with external source);
- the calculation of the heterogeneous cells and reactors (eigenvalue problem) - code "PRIZMA".

The peculiarities of the first problem are related with the need of correct accounting for the elastic and inelastic scattering anisotropy and with difficulties of neutron field calculations in empty channels. The results of benchmark experiments performed at "Neutron Generator" laboratory of MEPhI[1] were used for verification of code.

The experimental installation was a graphite assembly consisting of separate blocks. The front wall of this assembly was irradiated by the external source of fusion neutrons (E=14.75 MeV). Source was installed along with the symmetry axis of the assembly. The measurements of threshold process rates was carried out by the activation detectors positioned along the source axis in channel on the different distances from the front wall of assembly. In one case the instrumented channel with detector was filled by the graphite and in another case - detectors were placed in the empty channel. More detailed description of the experimental installation and method of investigation may be found in [1].

The mathematical model of the experimental assembly presents the system of non-crossing calculational cells having the form of rectangular prisms with different sizes. External source of fusion

neutrons was assumed to be point and isotropic. To account the peculiarities of the problem the directions sphere was divided on 16 angular diapazones in forward from source and on 4 angular diapazones in backward. In calculations it was used the multi-group cross-sections library VITAMIN-C in AMPX format. It is supposed that the energies of external source neutrons belong to the interval from 14.918 to 14.55 MeV (4-th energy group in VITAMIN-C library).

The result of calculations are presented in Table 1 and Figures 1,2. The reaction thresholds of activation detectors covered the energy region from 3 MeV to energy of source. This energy region is interesting by the fact that here the processes of elastic and inelastic scattering on carbon nuclei have pronounced anisotropic character. All 4 moments of cross-sections of anisotropic group transfers of VITAMIN-C library were used in calculations.

For testifying of code "PRIZMA" it was performed the calculation one of the benchmark problem described in [2]. Geometrical parameters of the test problem presented in Fig.3, the macroconstants - in Table 2.

The calculation were performed with recommended[2] space mesh 1x1x1 sm for two variants:
variant 1 - rod absents in physical zone 3 (composition 3);
variant 2 - rod presents in physical zone 3 (composition 4)
with saturation on angular mesh.

As standard the results of code MCU (Monte-Carlo method) calculations performed in Kurchatov Atomic Energy Institute were used.

The results of code "PRIZMA" calculations are presented in Tables 3,4,5. Values L in Tables mean a number of sectors of directions sphere divided by the typical for S_n-method procedure.

Note that for overcoming of disagreement of values calculated by the two codes in 2-nd energy group it is necessary to perform additional computations with space mesh more detailed than recommended. This fact is related with sharp gradients of neutron flux in calculational cell of reflector.

Conclusion.

In the paper the universal nodal method of neutron distribution calculations for reactor and shielding problems based on using of influence functions and factors of local-integrated volume and surface neutron sources in phase subregions is presented in general form. Effectiveness of the simplest method approximation - plane flux approximation - was illustrated by the examples of test problems calculations.

The main efforts of the authors now concentrated on development and realization of algorithm of interrelated local and global neutron flux calculation with correction of influence factors and constants homogenization on different stages of computation.

References.

1. V.L.Romodanov, V.V.Khromov "Experimental and Calculation Provision of Neutron Field Functional Investigation of Fusion Reactors Blankets", Proceeding of the 19-th International Symposium of Nuclear Physics - Nuclear Processes in Fusion Reactors - November 6-10, 1989 in Castle Gaussing (Germany), p.19.

2. T.Takeda, M.Tamitani, H.Unesaki "Proposal of 3-D Neutron Transport Benchmark Problems NEACRP-A-953 (Revision-2)", January 1989.

Table 1.

Absolute activation rates of threshold detectors on 50 mm from the front wall, 10^{28} (neutron/nucleus × source neutron)

Reaction	E*, MeV	Homogeneous graphite			Empty channel		
		Exper.	Calc.	δ%	Exper.	Calc.	δ%
$Cu^{63}(n,2n)$	12.2	0.84(2)**	0.83	1.2	1.10(3)	1.14	3.6
$Cu^{65}(n,2n)$	11.0	1.52(4)	1.49	2.0	2.01(6)	2.02	0.5
$Fe^{56}(n,p)$	6.8	0.210(5)	0.194	8.2	0.255(8)	0.244	4.3
$Al^{27}(n,p)$	4.7	0.156(5)	0.149	4.5	0.181(5)	0.175	3.3
$Zn^{64}(n,p)$	3.0	0.37(1)	0.393	5.6	0.42(1)	0.466	9.9
$Pb^{204}(n,n')$	4.0	0.235(7)	0.245	4.3	0.239(7)	0.245	2.3

* - the physical threshold of reaction
** - means 0.84 ± 0.02
δ%-relative deviation of calculational and experimental values.

Table 2.

Macroconstants of the test problem.

Composition	Group	Σ_{tr}	Σ_a	$\nu\Sigma_f$	χ	$\Sigma^{1\to2}$
Core	1	0.223775	8.52709^{-3}*	9.09319^{-3}	1.0	2.28253^{-2}
	2	1.038640	1.58196^{-1}	2.90183^{-1}	0.0	
Reflector	1	0.250367	4.16392^{-4}	0.0	---	5.65042^{-2}
	2	1.644820	2.02999^{-2}	0.0	---	
3	1	1.28407^{-2}	4.65132^{-5}	0.0	---	2.40997^{-5}
	2	1.20676^{-2}	1.32890^{-3}	0.0	---	
4	1	8.52325^{-2}	1.74439^{-2}	0.0	---	6.45461^{-5}
	2	0.217460	0.182224	0.0	---	

* - means 8.52709×10^{-3}

Table 3.

Effective multiplication factor of system.

Var.	MCU	PRIZMA		
		L=8	L=24	L=48
1	0.975 ∓ 0.002	1.024	0.9864	0.9758
2	0.961 ∓ 0.002	1.009	0.9695	0.9596

Table 4.

Leakage from the system.

Var.	Group	MCU	PRIZMA		
			L=8	L=24	L=48
1	1	0.1272 ∓ 0.0005	0.09373	0.11674	0.1203
	2	0.0754 ∓ 0.0004	0.09185	0.09314	0.0928
2	1	0.1158 ∓ 0.0006	0.0867	0.10675	0.1100
	2	0.0648 ∓ 0.0004	0.0795	0.08135	0.0809

Table 5.

Averaged in physical zones fluxes , 10^3

Zone	Group	Var.	MCU	PRIZMA		
				L=8	L=24	L=48
Core	1	1	4.778 ∓ 0.008	4.768	4.755	4.751
		2	4.907 ∓ 0.007	4.910	4.893	4.891
	2	1	0.875 ∓ 0.003	0.871	0.872	0.872
		2	0.871 ∓ 0.001	0.867	0.868	0.868
Reflector	1	1	0.598 ∓ 0.001	0.574	0.590	0.597
		2	0.593 ∓ 0.001	0.567	0.587	0.593
	2	1	0.918 ∓ 0.003	0.794	0.810	0.817
		2	0.887 ∓ 0.003	0.755	0.776	0.782
3	1	1	1.444 ∓ 0.008	1.520	1.481	1.470
		2	1.229 ∓ 0.007	1.257	1.251	1.251
	2	1	0.965 ∓ 0.009	0.906	0.907	0.908
		2	0.243 ∓ 0.002	0.254	0.263	0.266

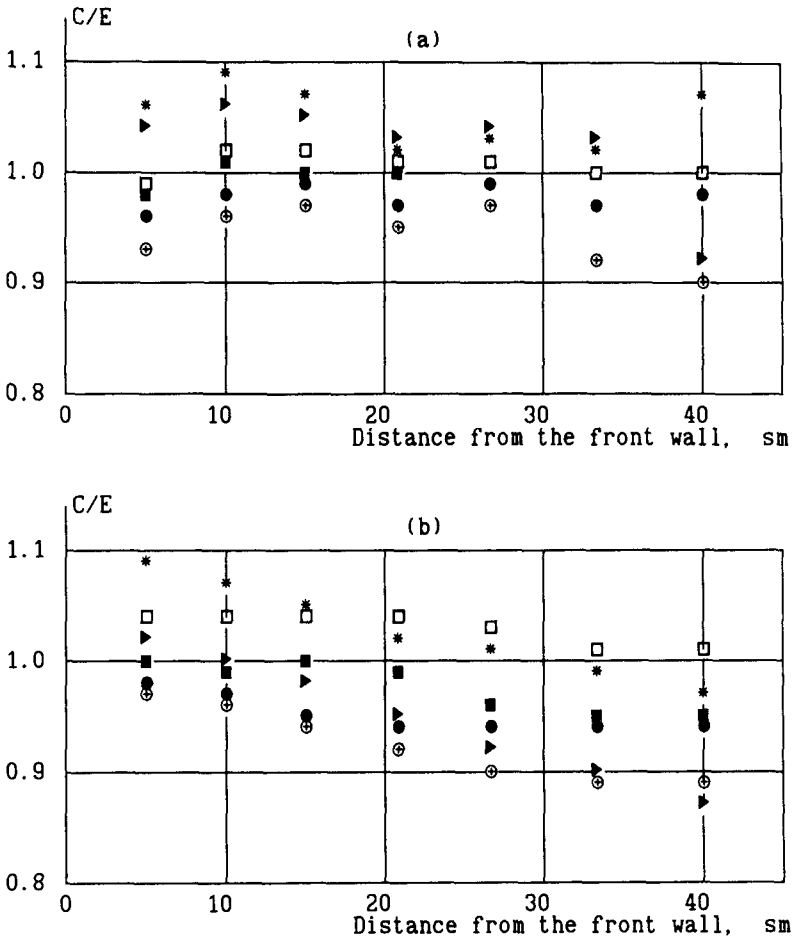

Fig.1 Calculational and experimental data ratio (C/E) for the absolute activation rates of threshold detectors.
(a) - homogeneous graphite assembly
(b) - graphite assembly with empty channel

* - $Zn^{64}(n,p)$, ▶ - $Pb^{204}(n,n')$, □ - $Cu^{63}(n,2n)$,
■ - $Cu^{65}(n,2n)$, ● - $Al^{27}(n,p)$, ⊛ - $Fe^{56}(n,p)$

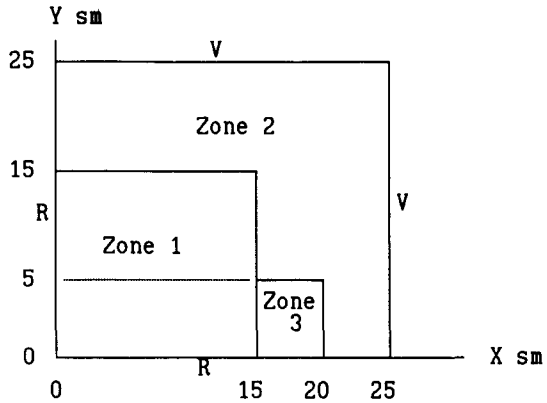

Boundary conditions:
V - vacuum
R - reflection

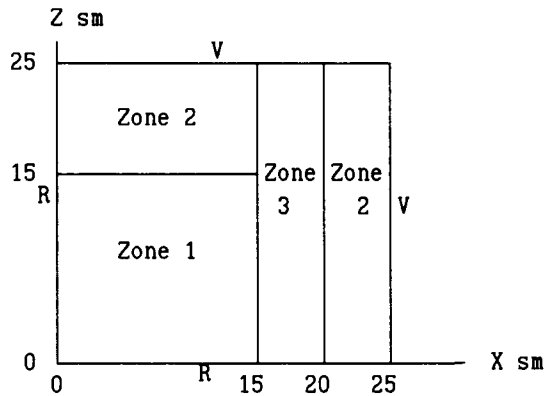

Fig.2 Geometry of test problem.

Zone 1 - Core
Zone 2 - Reflector
Zone 3 - Absorbing rod absents (variant 1)
- Absorbing rod presents (variant 2).

THE CODE GETERA FOR CELL AND POLYCELL CALCULATIONS. MODELS AND CAPABILITIES.

Belousov N.,Bichkov S.,Marchuk Y.,Prianichnikov A.,
Savander V.,Fyodorov I.
Moscow Physical Engineering Institute, USSR

ABSTRACT

The GETERA code is intended for calculation of neutron space-energy distribution in nuclear reactor cells and polycells and various neutron flux functionals by the collision probability method in multigroup approximation. The code uses the 26-group BNAB nuclear data library for slowing down diapason. In the Ø to 2.15 eV thermalization range the code uses a special 1ØØ-group neutron cross-section library based on the ENDF/B-IV and JENDL-2 evaluated nuclear data files.

GENERAL DESCRIPTION

The GETERA computer code is developed for the nuclear reactor cell and polycell calculations using collision probability method. The neutron flux density distribution in down-scattering energy range of 1Ø.5 MeV to 2.15 eV is calculated in a 22-group approximation on the basis of the BNAB neutron cross section library. The computation of neutron spectrum in the 2.15 to Ø eV thermalization energy range is performed through the Cadillac differential model on the basis of microscopic neutron cross sections obtained from the ENDF/B-IV data files. The code permits to calculate the neutron flux distribution, multiplication factors, void effects, to prepare the multi-group neutron cross section, and to compute reaction rates and a number of other functionals in nuclear reactor cells and polycells for various types of boundary conditions. The present GETERA code version envisages simulating the following systems:

- the unit cell with arbitrary albedo boundary conditions and arbitrary axial buckling; it is possible to adjust multiplication factor of the unit cell through albedo or buckling changes;

- the unit cell in cell's surroundings; this model can be used to prepare the neutron cross section for cells without multiplication surrounded with the fissile cells; or to evaluate the fissile cell's reactivity effects when the surplus reactivity is partly compensated with cells having additional absorbers or control rods; or to calculate more precisely some other functionals of the analyzed cell with respect to its surroundings;

- the core fraction with arbitrary cell surroundings,

- the polycell with arbitrary albedo boundary conditions

The geometry for both non-fissile cell and its surrounding can generally be described as cylinder, sphere or slab The neutron currents between cells under consideration are set according to their reciprocal location

Another original feature of the GETERA code is its capability to calculate the cells with the HTGR type dispersed fuel There are depletion modules in the GETERA, which permit to evaluate the reactivity effects, to prepare small-group neutron cross section and to compute a number of other functionals for cells with different burn-up

A special data-base management system with an advanced user interface enables to create and develop libraries of input and output data, and to analyse the data through tables and graphs

The GETERA code was created as a combination of independent modules exchanging information through the common data field It enables to change flexibly the calculation approach and on the other hand to provide a comfortable interface with the customer s codes

The Table 1 presents the calculation results for the known uranium-water benchmark lattices (NB-1,NB-2,NB-4,NB-5) The depleted cells were compared with test results obtained at the Japan Atomic Energy Research Institute (JAERI-M 88-200) (Table 2) It can be shown that the GETERA methods and neutron cross sections correspond on the demands for multiple calculations of increased safety nuclear reactor core It is useful for the reactivity effects calculations, preparation of small-group neutron cross sections, for experimental data analysis and for a number of other problems connected with neutron spectrum calculation of heterogeneous parts of nuclear reactor core The existing data discrepancies are within the cross sections errors for the ENDF/B-IV, ENDF/B-V libraries

A SAMPLE OF THE GETERA CODE USE

To evaluate numerically the void effects for RBMK reactor cells the fuel, moderator and coolant location was simulated in the following ways

- as a Wigner-Seitz cell with circular zones (Fig 1),
- as chess polycell (Fig 2), and
- as complex polycell (Fig 3)

The Table 3 presents calculation results of the multiplication factors and the void effect for each of the three models The discrepancy in the results between the models can be evaluated as the error accompanying simulation of a real process

Evaluation of void effect in conditionally critical problems is known to have only restricted application because in real systems neutron currents compensate for the positive or negative reactivity The first evaluation in Table 3 shows that involving the neutron intercurrents for cells with K inf other than 1 gives a neutron spectrum different from that of the conditionally critical problem This difference influences essentially void effect evaluation Table 4 presents the void effects for unit cell in cases when surplus reactivity is compensated

a) by radial leakage,
b) by axial leakage,
c) by neutron intercurrents from cell under consideration to cell with control rod

CONCLUSION

The GETERA code is used for computation of cell systems Their multiple simulation provides for evaluation of functionals errors and increases the reliability of the modeling

Table 1.Integral Parameter Results for NB Lattices.

Lattice	Parameter	EPRI-CELL ENDF/B-V	Monte-Carlo ENDF/B-V	GETERA ENDF/B-IV
NB-1	K inf.	1.1449	1.1471	1.1426
	R28	1.360	1.363	1.383
	D25	0.0814	0.0803	0.0857
	D28	0.0705	0.0722	0.0704
	CR	0.796	0.798	0.7961
NB-4	K inf.	1.3415	1.3424	1.3407
	R28	2.632	2.654	2.727
	D25	0.157	0.159	0.1663
	D28	0.0612	0.0617	0.0609
	CR	0.548	0.549	0.5521
NB-5	K inf.	1.1421	1.1456	1.1328
	R28	8.534	8.503	9.012
	D25	0.550	0.548	0.570
	D28	0.132	0.133	0.131
	CR	1.006	1.006	1.014
NB-2	K inf.	1.1698	1.1748	1.1861
	R28	2.613	2.612	2.542
	D25	0.152	0.151	0.154
	D28	0.297	0.297	0.270
	CR	2.148	2.148	2.081

Table 2.K infinity for different void fraction
(JAERI test ,Vn/Vf=1.1,30 GWd/t)

Progr. \ Void (%)	0	45	90	99
ANSTO	0.999	0.968	0.980	0.987
HITACHI(B4)	1.013	0.980	0.985	0.979
HITACHI(J2)	1.013	0.977	0.985	0.978
IKE	1.010	0.976	0.990	0.985
JAERI(SRAC)	1.006	0.969	0.978	0.989
KFK(NEWEST)	1.005	0.968	0.973	0.991
KFK(1985LIB.)	0.980	0.949	0.972	1.022
MAPI-CRC	1.006	0.978	1.003	0.993
NAIG	1.008	0.980	0.996	0.993
PNC	1.010	0.983	1.002	0.993
PSI(BOXER)	1.003	0.977	1.006	1.023
PSI(DANDE)	0.998	0.971	1.000	1.003
STUDSVIK	1.006	0.983	1.008	1.013
TUBS(DATUBS4)	1.021	0.992	1.003	1.004
TUBS(DATUBS5)	1.002	0.971	0.992	1.003
WINFRITH	1.002	0.988	1.025	1.006
GETERA	1.012	0.972	0.994	1.009

Table 3. K infinity for different void fraction (different models)

Type of model	K inf. Void = Ø (%)	K inf. Void = 1ØØ (%)	Δ K
Cell of Wigner-Seitz	1.2835	1.345Ø	6.15e-2
Chess cell	1.2855	1.3545	6.9Øe-2
Polycell model	1.3Ø23	1.34Ø2	4.21e-2

Table 4. K infinity for different void fraction (different types of compensation)

Type of model	K inf. Void = Ø (%)	K inf. Void = 1ØØ (%)	Δ K
Bukling	1.	Ø.893Ø	-1.Ø7e-1
Albedo	1.	Ø.95ØØ	-5.ØØe-2
1 Cell with control rod on 4.9 Cell with fuel	Ø.9979	Ø.9757	-2.22e-2

Figure 1. Transformation cell of RBMK to Wigner-Seitz cell

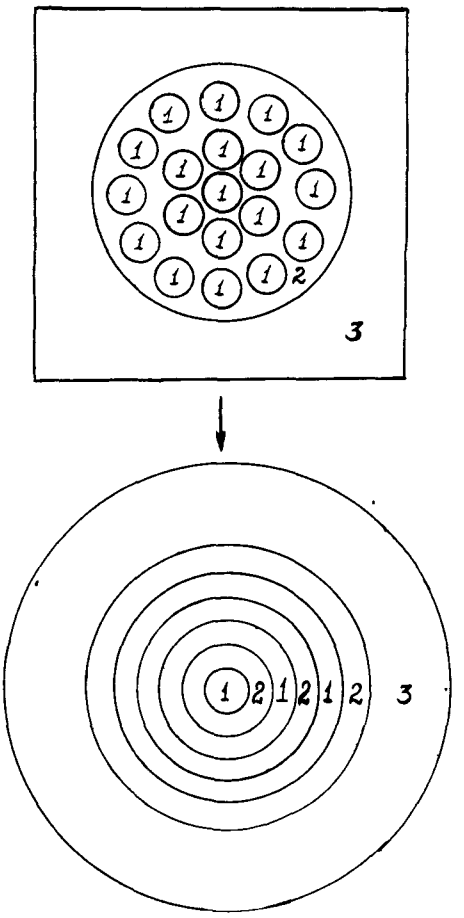

1 - fuel
2 - coolant (H2O)
3 - moderator (C12)

Figure 2. Transformation cell of RBMK to chess cell

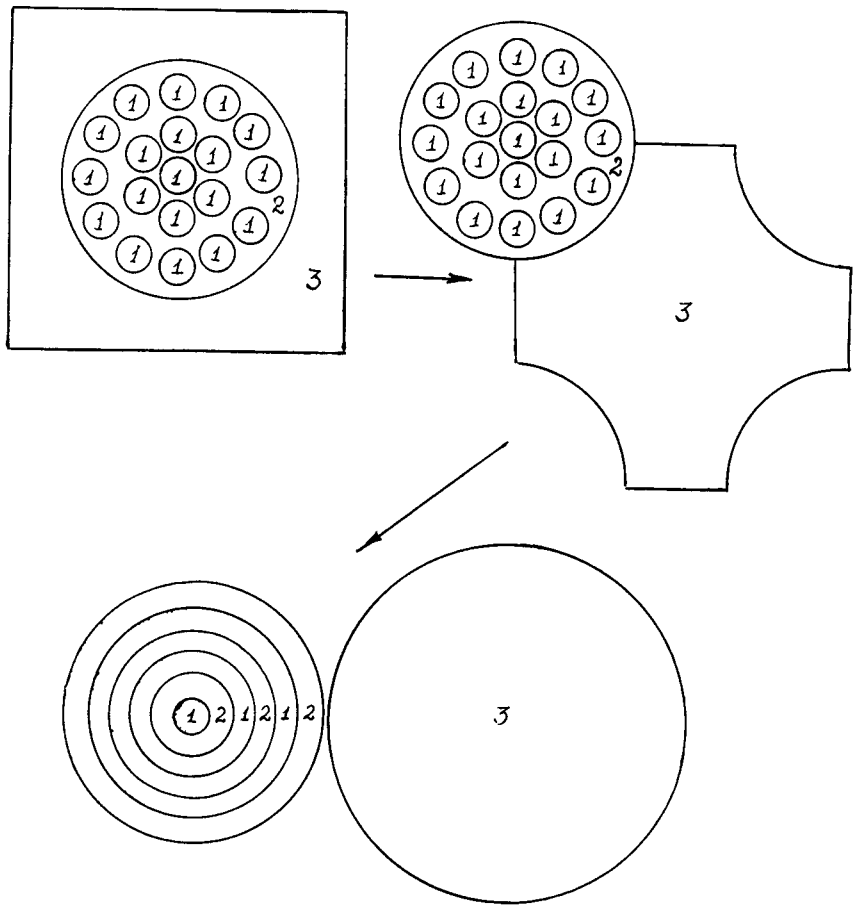

1 - fuel
2 - coolant (H2O)
3 - moderator (C12)

Figure 3. Transformation cell of RBMK to complex polycell

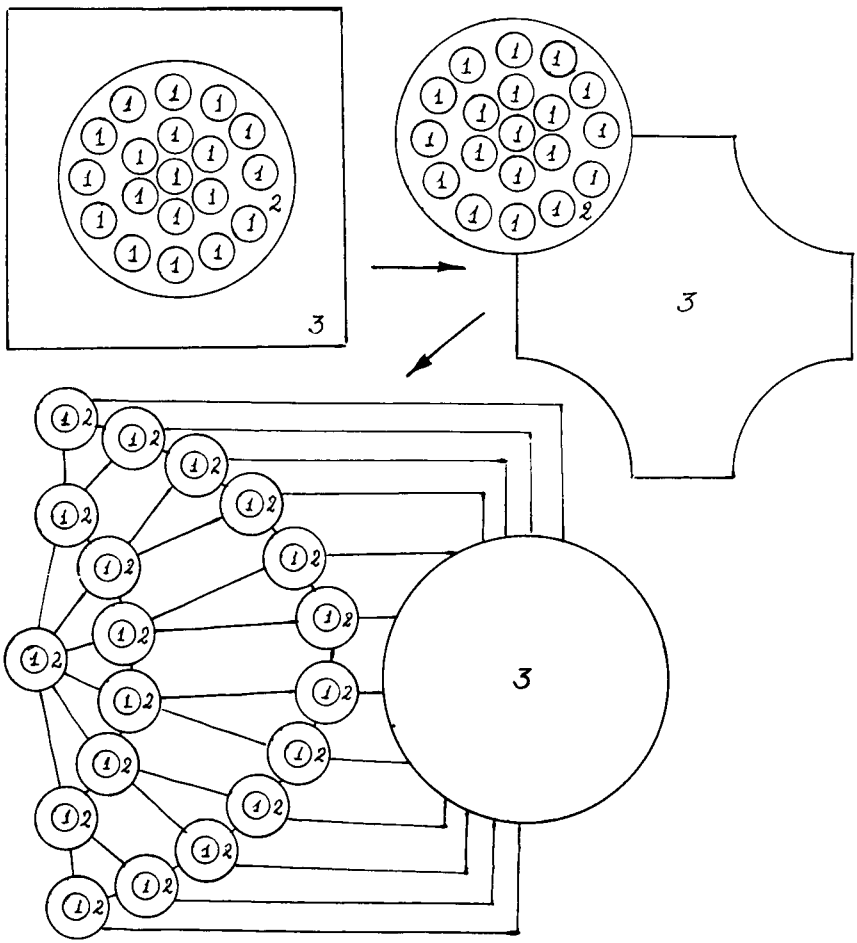

1 - fuel
2 - coolant (H2O)
3 - moderator (C12)

QUASI - ANALYTICAL SOLUTION OF GAMMA - RAYS TRANSPORT EQUATION IN ONE - DIMENSIONAL GEOMETRIES WITH USING INTEGRAL TRANSFORM

S. D. Romanin, V. B. Troyanskiy
Moscow Engineering Physics Institute
Kashirskoe shosse 31, Moscow, 115409, USSR.

ABSTRACT

Quasi-analytical or semi numerical method for solving gamma rays transport equation is described. The technique is based on some combination of integral transform and the method of successive collisions. This method makes it possible to derive a transport equation solution in analytical form with continuous energy dependence. To compare the solution with other methods and experimental data, calculations of gamma rays from plane source, penetrating varying thicknesses of steel, lead and uranium shields were done. Numerical results and experimental data and results obtained from the one-dimensional discrete-ordinates transport code P03-6.3 were compared. There are clearly discrepancies between the calculated values and experimental data. The described method results and the results of calculation by polynomial expansion are in good agreement at energy range from 0.5 to 10 MeV. This technique may be used to solve gamma ray transport problem for estimation of value of gamma ray flux.

ALGORITHM

The algorithm for solving gamma rays transport equation, based on integral transform and method of successive collisions, allows to derive a solution of gamma-rays transport equation as a comparatively simple formula, and the calculations can be done by simple computer code.

For simplicity we consider this method for plane geometry. The gamma-rays transport equation for plane geometry can be written as:

$$\omega \frac{\partial I(z,\omega,\lambda)}{\partial z} + \mu(\lambda) I(z,\omega,\lambda) =$$

$$= \int d\lambda' \int I(z,\vec{\Omega}',\lambda') K(\lambda',\lambda) \frac{\delta(1+\lambda'-\lambda-\vec{\Omega}'\vec{\Omega})}{2\pi} d\vec{\Omega}' + S(z,\omega,\lambda), \quad (1)$$

where $I(z,\omega,\lambda)$ - intensity of gamma-rays (angular flux of energy of gamma quantum); λ', λ - wave length of gamma quantum before and after scattering, respectively, in units of Compton wave of electron; ω - cosine of polar angle; $\mu(\lambda)$ - linear coefficient of absorption (total macroscopic cross section); $S(z,\omega,\lambda)$ - distribution of external sources; delta function describes Compton scattering; $K(\lambda',\lambda)$ - function, describing scattering, according to Klein - Nishina formula:

$$K(\lambda',\lambda) = \begin{cases} \frac{3}{8}\frac{\lambda'}{\lambda}\left[\frac{\lambda}{\lambda'} + \frac{\lambda'}{\lambda} + 2(\lambda'-\lambda) + (\lambda'-\lambda)^2\right], & \lambda \le \lambda' \le \lambda + 2 \\ 0, \text{ otherwise}. \end{cases}$$

We define Fourier-transform as:

$$g(k,\omega,\lambda) = \int_{-\infty}^{\infty} I(z,\omega,\lambda)\exp(ikz)dz$$

and, respectively, inverse integral transform:

$$I(z,\omega,\lambda) = \frac{1}{2\pi}\int_{-\infty}^{\infty} g(k,\omega,\lambda)\exp(-ikz)dk$$

Fourier transform of Equation 1 yields:

$$\left[\mu(\lambda) - ik\omega\right] g(k,\omega,\lambda) =$$

$$= \int d\lambda' \int g(k,\omega',\lambda')K(\lambda',\lambda)\frac{\delta(\eta - \vec{\Omega}\vec{\Omega}')}{2\pi} d\vec{\Omega}' + Q(k,\omega,\lambda), \quad (2)$$

where $\eta = 1+\lambda'-\lambda$, $Q(k,\omega,\lambda) = \int S(z,\omega,\lambda)\exp(ikz)dz$.

To simplify Equation 2 we make assumption that gamma-quantum have near-forward scattering, likewise assumption was made by Fano[1], i.e. $\omega \simeq \omega'$, which results in elimination of angular integration in Equation 2.

$$\left[\mu(\lambda) - ik\omega\right] g(k,\omega,\lambda) = K\int g(k,\omega,\lambda)d\lambda' + Q(k,\omega,\lambda) \quad (3)$$

where $K = K(\lambda,\lambda) = \text{const}$ is independent of the wave length, because the assumption was made.

After derivation with respect to λ of the last equation we obtain

$$\frac{\partial g(k,\omega,\lambda)}{\partial\lambda} + \frac{\frac{\partial\mu(\lambda)}{\partial\lambda} - K}{\mu(\lambda) - ik\omega} g(k,\omega,\lambda) = \frac{\frac{\partial Q(k,\omega,\lambda)}{\partial\lambda}}{\mu(\lambda) - ik\omega}.$$

The solution of this differential equation for monochromatic source, localized in spatial coordinate $z = 0$ is

$$g(k,\omega,\lambda) = \frac{K}{2} Q(\omega)\exp\left[K\int_{\lambda_0}^{\lambda}\frac{d\lambda'}{\mu(\lambda')-ik\omega}\right] / \left[(\mu-ik\omega)(\mu_0-ik\omega)\right] +$$

$$+ Q(\omega)\frac{\delta(\lambda-\lambda_0)}{\mu - ik\omega}, \quad (4)$$

where μ_0 is a total absorption coefficient at the incident wave length λ_0.

We have to make linear approximation of $\mu(\lambda)$ for integration in exponent can be done analytically. Inverse Fourier transform of last equation yields solution of Equation 1 for infinite homogeneous medium, monochromatic, monodirectional external source, localized in coordinate $z = 0$, at simplifying assumption about near-forward scattering and linear approximation of total macroscopic cross section $\mu(\lambda)$

$$I(z,\omega,\lambda) = \frac{K}{2\omega^2} \exp\left(-\frac{\mu z}{\omega}\right) z\, {}_1F_1[\alpha,2,\beta]\, \delta(\omega - 1) + \\ + \exp(-\mu z/\omega)\, \delta(\lambda-\lambda_0)\, \delta(\omega-1)/\omega \qquad (5)$$

where $\alpha = 1 + K / \dot{\mu}_0$, $\dot{\mu}_0 = \left.\frac{\partial\mu(\lambda)}{\partial\lambda}\right|_{\lambda=\lambda_0}$, $\beta = z\cdot(\mu(\lambda) - \mu_0)$, $z>0$, $\omega>0$;

${}_1F_1[\alpha,2,\beta]$ is confluent hypergeometric function.

The essence of the presented method is to use Equation 5 in the method of successive collisions instead of the solution for noncollided component. We substitute function $I(z,\omega,\lambda)$, given by Equation 5 to integral in Equation 1, instead of unknown function $I(z,\Omega',\lambda')$. After this substitution we obtain the differential equation from integrodifferential Equation 1.

$$\frac{\partial I(z,\omega,\lambda)}{\partial z} + \frac{\mu(\lambda)}{\omega} I(z,\omega,\lambda) = \frac{1}{\omega} Q(z,\omega,\lambda), \qquad (6)$$

where $Q(z,\omega,\lambda)$ is a sum of the integral and the source.

The solution of Equation 6, after integration over cosine of polar angle ω, is

$$I(z,\lambda) = \pi K \int \frac{K(\lambda',\lambda)}{\eta'} \exp\left(- \frac{\mu(\lambda)\, z}{\eta'}\right) d\lambda' \quad \times$$

$$\times \int_0^z {}_1F_1[\alpha,2,\xi]\; z' \exp\left[\left(\frac{\mu(\lambda)}{\eta'} - \mu(\lambda')\right) z'\right] dz' +$$

$$+ 2\pi K(\lambda_0,\lambda) \frac{\exp(-\mu_0 z) - \exp(-\mu z/\omega)}{\mu - \mu_0\eta_0} + \exp(-\mu z)\delta(\lambda-\lambda_0). \quad (7)$$

In this expression $\eta_0 = 1 + \lambda_0 - \lambda$, $\eta' = 1 + \lambda' - \lambda$,

$$\xi = z\,(\mu(\lambda') - \mu_0).$$

Integration in Equation 7 must be done numerically.

The first, the second, and the third terms in Equation 7 are multiple scattering, single scattering, and nonscattering components of gamma rays flux, respectively.

We obtain the solution of Equation 1 in case of plane geometry and plane isotropic source and solution of gamma rays transport equation for spherical geometry and point source, too. The solutions were derived by the method, which is analogous to that used in the case of plane monodirectional source. The calculations of penetration of gamma rays with using the derived solutions were made and compared with the calculations made by Goldstein and Wilkins by polynomial expansion method[2].

We have made an attempt to apply the described integral transform method to multilayer medium plane geometry. The Equation for this case is:

$$\omega \frac{\partial I(z,\omega,\lambda)}{\partial z} + \mu(z,\lambda) I(z,\omega,\lambda) =$$

$$= \int d\lambda' \int I(z,\vec{\Omega}',\lambda') n_e(z) \sigma_k(\lambda',\lambda) \frac{\delta(\eta - \vec{\Omega}'\vec{\Omega})}{2\pi} d\vec{\Omega}' + S(z,\omega,\lambda), \quad (8)$$

where: $n_e(z)$ - electron density, $\sigma_k(\lambda',\lambda)$ - function, which describes scattering according to Klein-Nishina formula (differential scattering formula for one electron or microscopic

cross section for Compton scattering).

We define optical distance as

$$\rho = \int_0^z \mu(z',\lambda)dz'$$

and denote $\tilde{\sigma}(\lambda',\lambda) = \sigma_k(\lambda',\lambda)/(2\pi\sigma(\lambda))$; $\tilde{S}(\rho,\omega,\lambda) = S(z,\omega,\lambda)/\mu(z,\lambda)$. After that Equation 8 may be rewritten as

$$\omega \frac{\partial I(\rho,\omega,\lambda)}{\partial\rho} + I(\rho,\omega,\lambda) =$$

$$= \int d\lambda' \int I(\rho,\vec{\Omega}',\lambda')\tilde{\sigma}(\lambda',\lambda)\delta(\eta - \vec{\Omega}\vec{\Omega}')d\vec{\Omega}' + \tilde{S}(\rho,\omega,\lambda). \quad (9)$$

The solution of Equation 9 can be obtained in analytical form by applying to it integral transform which is analogous to that used for Equation 1. In this case we have made the same assumptions as in the case of Equation 1.

$$I(\rho,\omega,\lambda) = \frac{S_0\,\tilde{\sigma}(\lambda)}{2\pi\,\mu_1(\lambda_0)} \int \frac{\exp(-ik\rho)}{(1-ik\omega)^2} \left[\frac{\sigma(\lambda)}{\sigma(\lambda_0)}\right]^{\frac{c}{\dot{\sigma}_0(1-ik\omega)}} dk +$$

$$+ S_0 \frac{\exp(-\rho/\omega)}{\mu_1(\lambda)\,\omega}\delta(\lambda - \lambda_0). \quad (10)$$

In this expression $\mu_1(\lambda)$ is linear coefficient of absorption near boundary of semi-infinite medium; S_0 is a magnitude of the external source; $c = \sigma_k(\lambda,\lambda)$; $\tilde{\sigma}(\lambda) = c/\sigma(\lambda)$.

In special case, if $\omega > 0$, $\dot{\sigma}_0 < 0$, $\sigma(\lambda) > \sigma(\lambda_0)$, integration in Equation 10 can be done analytically.

$$I(\rho,\omega,\lambda) = S_0 \frac{\exp(-\rho/\omega)}{\mu_1(\lambda_0)\,\omega} \left\{ \tilde{\sigma}(\lambda) \sqrt{-\frac{\omega\, c}{\rho\, \dot{\sigma}_0} \ln\left[\frac{\sigma(\lambda)}{\sigma(\lambda_0)}\right]} \times \right.$$

$$\left. \times\, I_1\left(2 \sqrt{-\frac{\rho\, c}{\omega\, \dot{\sigma}_0} \ln\left[\frac{\sigma(\lambda)}{\sigma(\lambda_0)}\right]} \right) + \delta(\lambda - \lambda_0) \right\}, \qquad (11)$$

where $I_1(\ldots)$ is Bessel function.

It is necessary to say, that to derive Equation 10 we assume the function $\tilde{\sigma}(\lambda)$ is independent of the spatial variable, i.e. the cross section $\tilde{\sigma}(\lambda)$ per electron does not depend on the material. This assumption can be accepted in some degree for chemical elements with atomic weight above hundreds and for energy above MeV. In this energy range total microscopic cross sections per electron for heavy atoms differ no more than about 10%. Moreover, the assumption about near-forward scattering results in elimination of backward scattered gamma-quanta.

NUMERICAL RESULTS

The results of the calculations of the penetrations of gamma rays by derived formulas and the comparisons with the calculations by other methods are presented. For the purposes of comparison of the solution with other methods solutions and experimental data, computations of gamma rays penetration from monochromatic monodirectional and isotropic sources were done. Equation 7 and Equation 11 were used for obtaining numerical results for semi-infinite homogeneous and two-layer shield slabs. The results were compared with the results obtained by Goldstein and Wilkins[2], the experimental data of Bishop and Banai[3] and the ones from the one-dimensional discrete-ordinates transport code ROZ-6.3[4]. The

values of linear coefficient of absorption, used in calculations by Equation 7 and Equation 11, were taken from reference 2. The results of the comparison are shown at Figures 1- 4.

The results of calculations by Equation 7 and the ones by polynomial expansion from reference 2, presented in Figure 1 - 2, are in satisfactory agreement. It may be explained by using the same total cross sections and infinite media and source in both calculations. The main contributions to the discrepancies between calculated spectra are due to the assumption about near-forward scattering, that results in omission of backward scattered gamma-quanta, and linear approximation of total cross section $\mu(\lambda)$ in integrand in Equation 4.

Figure 3 shows the calculated spectrum by using Equation 11 (smooth curve) and the experimental data from reference 3 (histogram). The dashed line above and below the histogram represents standard deviation. For the purposes of comparison all the spectra have been normalized to the uncollided flux. There are clearly discrepancies between the measured and calculated values. The differences in the lower energy range result from the omission of backward scattered flux, positron annihilation and bremsstrahlung sources in the calculated values. It is also since calculations by Equation 11 use a source of infinite lateral dimensions which will give higher values for the uncollided flux and has some effect on the structure of the scattered spectrum. Calculated values for energy above 3 MeV can't be considered as absolutely correct, because conditions of using Equation 11, i. e. $\dot{\sigma}_0 < 0$ and $\sigma(\lambda) > \sigma(\lambda_0)$, not provided for lead in this energy range.

Figure 4 shows comparison of scalar flux spectra from two layer plane shield, calculated by Equation 11 with that obtained using ROZ-6.3 code. There are many reasons for the discrepancies between the derived spectra. As already stated, the Equation 11 apply only to infinite source and shielding slabs, and omit secondary sources of photons.

CONCLUSIONS

The presented algorithm makes it possible to derive a solution of gamma rays transport equation in analytical form with continuous energy dependence. The solution of the transport equation is a comparatively simple formula, so the calculations can be done by a simple computer code. The numerical inverse Fourier transform in Equation 10 is regarded as a significant improvement to the accuracy of the calculations.The algorithm can be used to solve gamma ray transport calculating problems which concern to reactor shield, blanket of fusion reactor and others,in case time of calculations and computer memory are limited but accuracy is not of much importance.

REFERENCES

[1] U.Fano,L.V.Spenser and M.J.Berger. Penetration and Diffusion of X Rays. Handbuch der Physik. Band XXXVIII/2. Neutronen und Verwandte Gammstrahlprobleme. Berlin-Gottingen-Heidelberg,1959.

[2] Goldstein H.,Wilkins J.,Jr. Calculations of the Penetration of Gamma Rays, USAEC, Rept. NO-3075, June 30, 1954.

[3] G. B. Bishop and J. Banai," Angular Benchmark Data for 6.13 MeV Source Photons of Disc Geometry Penetrating Lead, Steel and Concrete", Ann. nucl. Energy, Vol.12, No.11, pp.593-612, 1985.

[4] A. M. Voloschenko, A. A. Dubinin, "The one-dimensional discrete ordinates transport code ROZ-6.3", Nuclear Reactor Physics and Calculational Methods, Vol. 6(43), pp.30-39, 1984.

Figure 1 Comparison of scalar flux of energy from monodirectional monochromatic source energy 1 0 MeV in uranium thickness 1 m f p $\underline{I}(z,E)\ \exp(\mu_o z)$ in (MeV/s/cm**2)

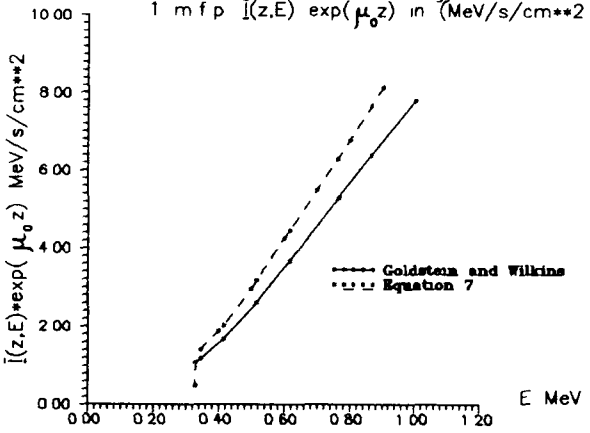

Figure 2 Comparison of scalar flux of energy from monodirectional, monochromatic source energy 10 MeV in uranium thickness 1 m f p $\underline{I}(z,E)\ \exp(\mu_o z)$ in (MeV/s/cm**2)

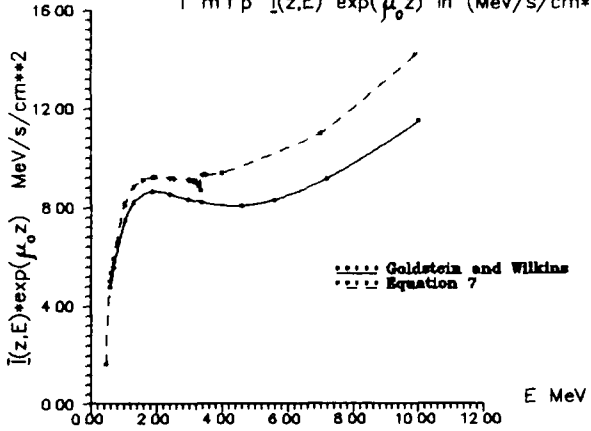

Figure 3 Comparison results obtained by Bishop & Banai (histogram) and results obtained by Equation 11 (smooth curve) (Pb, 3 77 m f p , source energy 6 13 MeV)

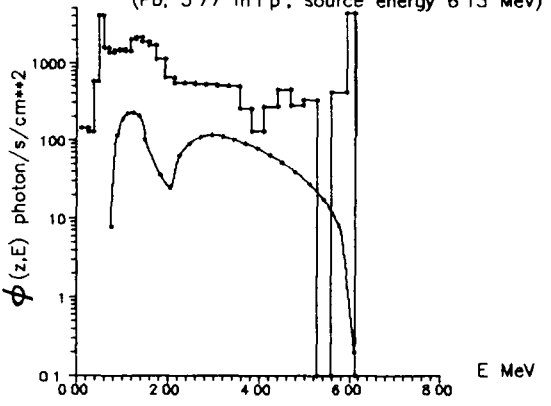

Figure 4 Comparison results obtained by Equation 11 (smooth curve) and results obtained by code ROZ-6 3 (histogram), 5 cm Pb + 5cm Fe source 6 13 MeV, (in photon/s/cm**2)

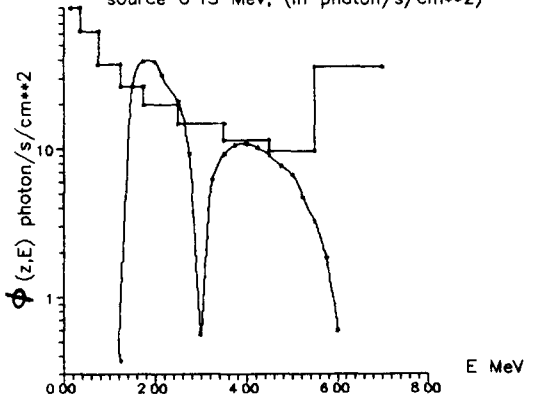

SPACE-DEPENDENT EFFECTS IN FAST REACTOR DYNAMICS AND THEIR ANALYSIS USING THREE-DIMENSIONAL KINETICS CODE WIND-3D

Podobed S.S., Shmelev A.N., Shkolnik V.S.

Moscow Engineering Physics Institute
Kashirskoe shosse 31, Moscow, 115409, USSR

ABSTRACT

The computer code intended for fast reactor 3D dynamics analysis is described. The code is used in routine practice of calculational support of BN-350 fast breeder reactor operation. It was shown that substantional 3D effects can be induced by asymmetrical reactivity perturbations to the system. Some divergence factor was introduced to describe the difference between the point kinetics model results and results obtained in reactor measurements.

The computation procedures currently applied for fast reactor dynamics analysis (including preliminary safety analysis) are mainly based on the point kinetics model. In these cases the fast reactor core is assumed to be fairly tight coupled. It is well known however that there are many situations when spatial effects may be of great significance for safety analysis and operation support of fast reactor. The computer code WIND-3D was created for the mathematical simulation of the LMFBR dynamics and is used in routine practice of calculational support and safety analysis of the BN-350 prototype fast breeder reactor. It has a medium size core with the height of approximately 1.06 metres and the diameter of approximately 1.58 metres and the oxide type of fuel is used in the core and in the blankets. This reactor is considered to be tight coupled so the point kinetics model was widely used to predict its global performance characteristics.

Nevertheless, the operational experience clearly showed that there were regimes accompanied by neutron field distribution distortion. So it was considered to be interesting to estimate these effects and their influence on the reactor dynamics.

The dynamical model used in calculations includes the algorithm of space-time dependent neutron flux calculations in 3-D hexagonal geometry, coupled with algorithm of thermohydraulic and feedback calculations.

Model takes into account the following requirements:

- transient calculations must consider the real geometrical and constructive peculiarities of reactor;
- it is necessary to have a possibility to calculate detailed space-time behavior of power and temperature, to evaluate the

effects of feedbacks and coolant flow variations in reactor zones.

The main principles of dynamical model are as follows:
- neutron transport equation is solving by one-group diffusion approximation in 3-D hexagonal geometry along with equations for delayed neutron precursor groups;
- energetic distribution of neutron flux density is simulated by the set of space-dependent catalogues of one-group effective microconstants accounting the nonuniformity of neutron spectra in reactor zones.
- the prompt jump approximation is used.

Application of the prompt jump approximation leads to the constraints on the processes that may be considered in the model frameworks. The main condition is as follows:

$$K_{eff} < 1 + \delta$$

where δ is effective fraction of delayed neutrons.

One-group diffusion equation is solved by the iterative synthesis method with neutron flux density expansion in form (1) using continuous trial functions. Method was specified for non-homogeneous problem solution.

$$F(\vec{r},z) = \sum_{n=1}^{N} a_n R_n(\vec{r}) Z_n(z) \quad , \qquad (1)$$

$\{R_n(\vec{r})\}_{n=1}^{N}$ and $\{Z_n(z)\}_{n=1}^{N}$ - continuous ortonormalized functions of hexagonal and axial coordinates, a_n - factor of normalization.

The procedure of preparation of space-dependent catalogues of one-group microconstants is based on the solution of multy-group diffusion equations for 2-D (r,z) reactor model by the iterative synthesis method with discontinuous trial functions followed by the the averaging of multy-group microconstants with weight of integral in zones neutron spectra.

For more precision evaluation of the neutron cross-sections near the points of experimental measurements and control rod assemblies there is a possibility of using the model based on the local diffusion calculation. This model uses the iterative finite difference method for multy-group equations solution with using of non-regular set of the space points.

Accounting of the feedbacks in transient analysis is carrying out by means of preliminarily calculated factors for temperature dependence of microconstants in each reactor zone. Temperature dependence of nuclide concentrations is described by the thermal expansion coefficients of fuel, coolant and construction materials.

The calculation of the reactor components temperatures is

based on the method considering the dynamics of average (for axial layers) temperatures for fuel, coolant and cladding in each assembly. Difference of the fuel thermophysical properties in reactor zones is taken into account by the effective fuel time constants. Additionally, the reactor core is divided on regions with coolant flow profiling.

Also, there is a possibility of using alternative subroutines:
TEMP - 3-D channel-by-channel calculation of stationary temperature distributions in fuel assembly of fast reactor;
TVEL - 2-D non-stationary calculation of temperature distribution for one fuel element in (r,z) geometry.

The control rods movement is simulated by recalculating of the nuclide concentrations in the proper axial zones with accounting to the rods velocity.

Described algorithm was realized in dynamics code WIND-3D which is integrated into the program support system of multyfunctional reactor operation.

The code uses the data file containing the information about reactor states in any time period of operation. This fact allows the flexible organization of calculational process. The data obtained are accumulated in the above mentioned reactor states archives and special dynamical archives. The model uses the cross section data library of ABBN type.

Typical fast reactor calculational model includes 817 fuel assemblies, 256 spectral zones, 98 axial meshpoints and approximatelly 80000 of total amount of meshpoints.

The percentage of time used within one time-step is as follows: neutron parameters calculations ~ 65%; calculations of temperatures changes ~ 10%; feedbacks, hydraulics and rods positions changes ~ 18%; storage of obtained information in archives and intermediate temporary files ~ 7%. This relations can slightly be changed depending on the problem considered.

The code WIND-3D permits using of delayed neutrons constants with different degree of detailisation: the same in the whole core of the reactor; each spectral zone has its own set of parameters; each of the axial zone in each assembly or each meshpoint has its own set of delayed neutrons parameters.

There is a possibility to use recurrent calculatons with reduced time-steps due to find some local (in time) perculiarities in reactor dynamics. That are local maxima and minima in power, temperatures and so on.

The code uses ~ 12.7 times less CPU resources per time step in case of a modular type reactor containing 91 assemblies than in case with 817 assemblies (typical BN-350 calculations).

The main efforts in calculation with code WIND-3D center on

the problem of BN-350 safety performance. One of the problem considered concerned the accident with the loss of equipment power supply along with failure of reactor shutdown system. In this case the gradual slow relaxation of main circulation pumps (MCP) action provides the forced sodium circulation during 70-90 sec. After pumps stop the decay heat removal is possible only by natural circulation (NC) regime.

The code WIND3D was used for the calculation of power, fuel and sodium temperatures behaviour for 15 sec period after the accident initiation. Supposed that the sodium flow decreases in accordance with the hyperbolic rule $b/(t+b)$, b - time constant (b=4 sec). Time behaviour of reactor power and sodium temperature on the exit of assembly with maximum heating up are presented in Fig.1 (curve 1). Sodium temperature in that assembly reaches the boiling point at 12 sec. Fuel temperature in that assembly didn't reach the melting point at the moment of sodium boiling initiation. The results obtained didn't show any substantial neutron or temperature fields distortion during the process.

The picture is quite different when one asymmetric scram rod inserts simultaneously with the MCP turning off. In such a case the time behaviour of sodium temperature considerably changes. This time dependence has a local maximum (1 sec) and local minimum (5 sec) followed by the monotonous increasing (curve 2). It is shown that sodium boiling didn't occur before the formation of NC regime. Non-monotonous sodium temperature behaviour was explained in terms of uncorrelated relaxation of sodium flow and reactor power. Moreover, this process is accompanied with spatial effects. The coordinate of assembly with maximum outlet sodium temperature in time moment T=0 sec is shifting during the process as shown by arrow in Fig.1. Curve 3 represents outlet sodium temperature from this new maximum assembly. The curves don't differ greatly in appearance, but there is obvious delay in their behaviour.

The change in ratio of integral neutron fluxes in the directions of symmetrically placed ionization chambers was approximately 9% to the end of the scram rod movement (that is 0.8 sec). This ratio was used in the form of following relation

$$R = \int_{S\ right} F(\vec{r},z)\ dS \ \Big/ \int_{S\ left} F(\vec{r},z)\ dS$$

and it can be used as a point model and real reactor divergence parameter in a concrete dynamical process (such as control rod weighting). The curve representing R is shown on Fig.2.

Axial distortion of the neutron distribution during this process is shown on Fig.3. The curve represents the ratio of the energy release in upper and lower parts of the core during the rod scram. The minimum of the curve corresponds to the approximately half of the rod inserted into the core.

Figure 4 represents the ratio of the neutron flux on the

60-th axial meshpoint level (curve 1) and on the 40-th axial meshpoint level (curve 2) at t = 0.4 sec. These ratios were calculated along the diagonal that runs through the moving rod. The ratio was taken in the form of:

$$\alpha = \frac{F(r_i, z_i)\ t=T}{F(r_i, z_i)\ t=0\ sec}$$

where r_i is the assembly coordinate along the diagonal; z_i is number of axial meshpoint (in our case z_i is 60 and 40 respectively and T=0.4 sec). The axial meshpoint number 1 is situated at the lower end of assembly.

The curves on Fig.2 and 3 are normalized on 1.0 in time moment T=0 sec.

Space-time effects in the dynamic behavior of small prototype LMFBR BN-350 were examined in this paper using dynamical code WIND-3D. It was shown that these substantial 3-D effects can be induced by asymmetrical reactivity perturbations to the system. The difference between real dynamical parameters and parameters obtained using point kinetics model may be estimated with the help of some divergence factor, as that described above. These dynamical peculiarities may be of interest for safety performance of large LMFBRs.

Figure 1. The dependence of reactor power and sodium temperature on the time

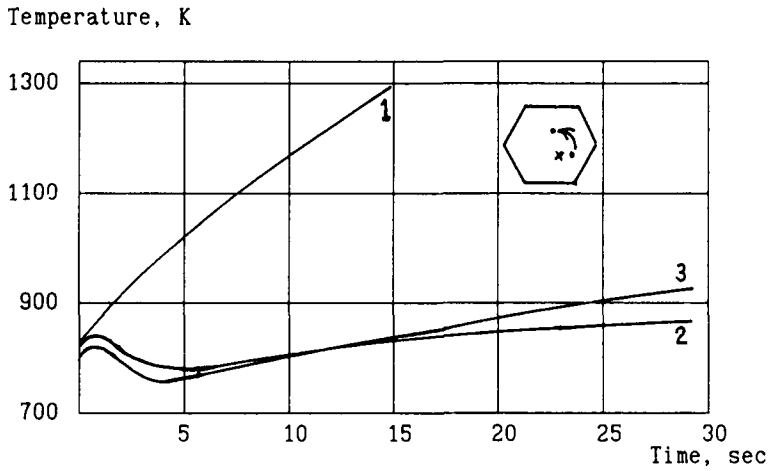

Figure 2. The ratio of integral neutron fluxes

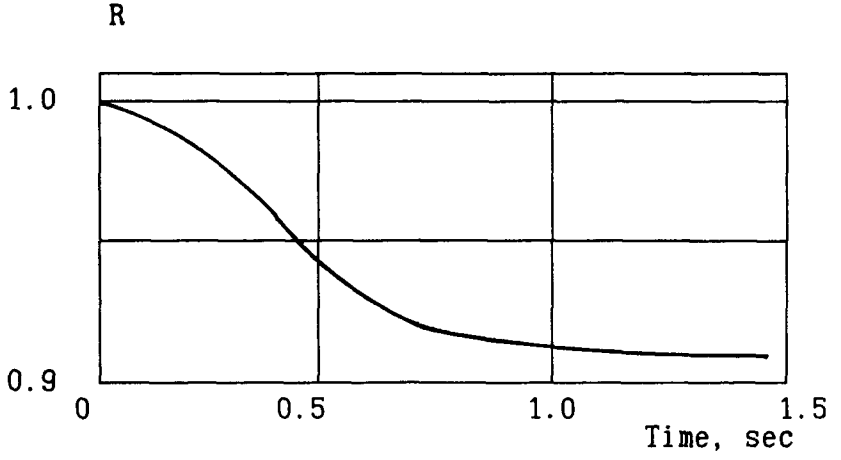

Figure 3. The ratio of energy release

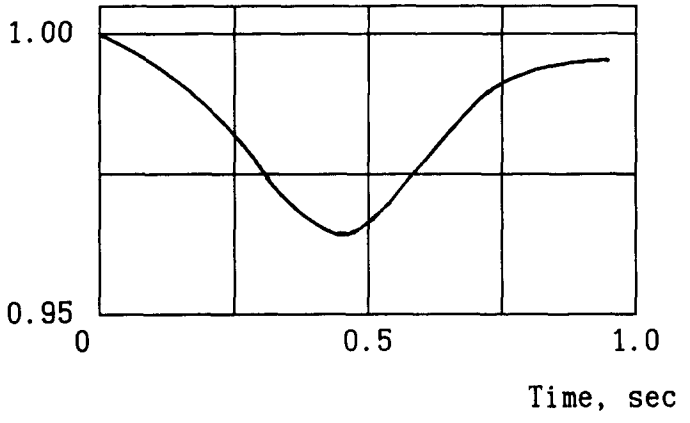

Figure 4. Neutron flux ratio along the diagonal on the 60-th and 40-th meshpoints level.

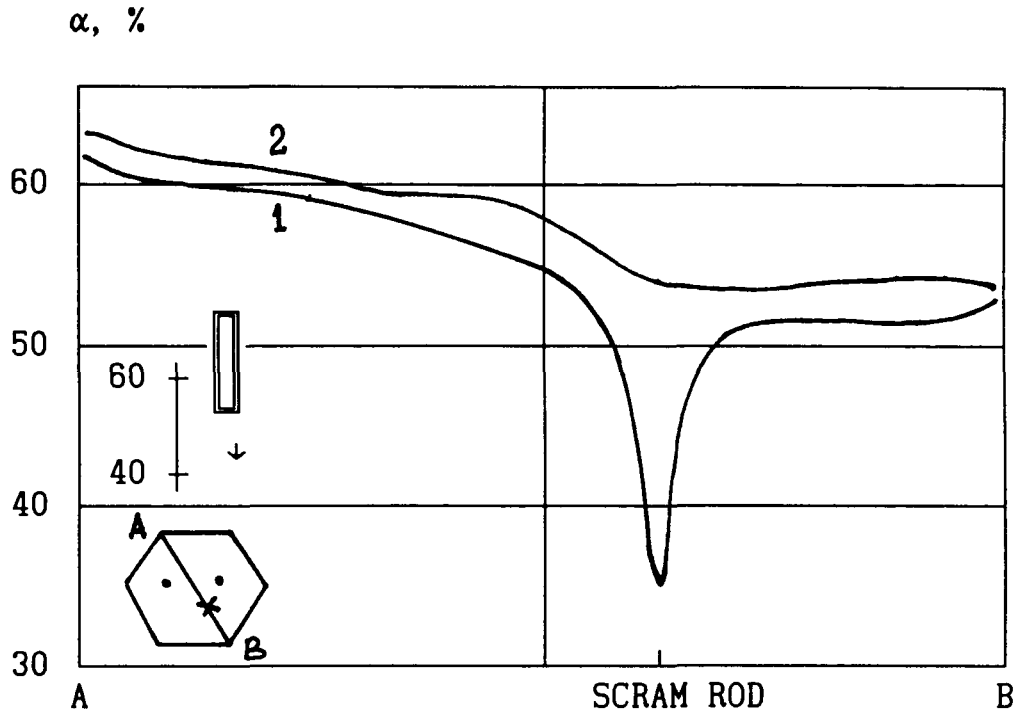

FEEDBACK COMPONENTS OF A U20Pu10Zr-FUELED COMPARED TO A U10Zr-FUELED EBR-II*

D Meneghetti and D A Kucera
Argonne National Laboratory
Argonne, Illinois 60439

ABSTRACT

Calculated feedback components of the regional contributions of the power reactivity decrements (PRDs) and of the temperature coefficients of reactivity of a U20Pu10Zr-fueled and of a U10Zr-fueled Experimental Breeder Reactor II (EBR-II) are compared The PRD components are also separated into power-to flow dependent and solely power dependent parts The effects of these values upon quantities useful for indicating the comparative potential inherent safety characteristics of these EBR-II loadings are presented

INTRODUCTION

Calculational comparisons of detailed reactivity feedback components in regions of a U20Pu10Zr-fueled Experimental Breeder Reactor II (EBR-II) with the corresponding components of an analogous U10Zr-fueled EBR-II are made These are of interest because of the planned conversion of the core to plutonium-containing fuel

The linear and Doppler components comprising the power reactivity decrement (PRD) and the corresponding temperature coefficients of reactivity are calculated The PRD at a power is here the negative of the reactivity required to bring the reactor from zero power hot-critical to that power The PRD components are also separately delineated into power-to-flow dependent and into solely power dependent parts These delineations together with the components of the temperature coefficients of reactivity are useful for indicating relative potential inherent safety characteristics [1]

For each of the two fuel types three sets of components are calculated These correspond at zero power, to bond-sodium gap fully open bond-sodium gap fully closed, the fuel not adhering to the clad, and no sodium in the fuel porosity, and bond sodium gap fully closed, the fuel adhering to the clad such that the fuel axial expansion is that of the clad, and about one-third of the fuel porosity contains sodium

*Work supported by the U S Department of Energy, Reactor Systems, Development and Technology, under contract W-31-109-ENG-38

REACTOR LOADINGS

In these analyses the descriptions for the reactor are the same except for the fuel type the cladding type and a thicker cladding with a concomitant smaller radial dimension for the U20Pu10Zr fuel Rows 1 to 6 of the reactor description constitute the core rows 7 to 10 the radial steel reflector, and rows 11 to about 15 the radial blanket of essentially depleted uranium The 91 subassembly locations in the cores contain 61 drivers 10 half drivers 8 operational control rods (7 high worth and 1 standard) 1 non operational control rod experiment and 2 safety rods Also included in the six rowed cores are 1 fuel-type experiment, 3 structural-type experiments and 5 dummy structural subassemblies

The U20Pu10Zr driver fuel has 75% smear density (percentage of inner area of clad occupied by fresh fuel) and the Pu contains 81% Pu 239 18% Pu-240 and 1% Pu-241 The fuel of 343 mm (13 5 in) length is contained in 5 84 mm (0 230 in) O D cladding having radial thickness 0 457 mm (0 018 in) The cladding of length 749 mm (29 5 in) and the 1 067 mm (0 042 in) diameter wire wrap are assumed to be made of HT 9 a ferritic steel There are 61 fuel elements per driver subassembly There are 31 fuel elements plus 30 steel elements per half-driver subassembly

The U10Zr driver fuel has 75% smear density and a uranium enrichment of 67% The fuel of 343 mm (13 5 in) length is contained in 5 84 mm (0 230 in) O D cladding having instead radial thickness of 0 381 mm (0 015 in) The 749 mm (29 5 in) long cladding and 1 067 mm (0 042 in) diameter wire wrap are assumed to be made of D9 an austenitic steel

For both loadings the 61 elements of the control and safety rods are fueled by U10Zr with a uranium enrichment of 78% The clad O D is 4 42 mm (0 174 in), with radial thickness 0 305 mm (0 012 in) The fuel smear density is 75% The remaining in core and out of core subassemblies are also considered to be identical in the two loadings

METHODS

The linear and Doppler components of the PRDs are calculated using the EBRPOCO program[2] together with an addition (RODCO) to the program which estimates the PRD effects of axial positions of control rods By repeating the calculation assuming all thermal conductivities to be infinite the power to flow dependent components are obtained (Setting the thermal conductivities in EBRPOCO to infinity causes the temperatures of all regions of a subassembly at a given axial level to have the same temperature above inlet as does the coolant at that axial level in the subassembly Axial heat transfer in EBRPOCO is only by axial coolant flow) The components of the power dependent part are obtained by subtraction of the calculated power to flow components from the corresponding components of the calculated PRD

The components of the temperature coefficients of reactivity are calculated using the TEMCO addition[3] to the EBRPOCO code The grid plate radial expansion component of the temperature coefficient and some aspects of the net rod-bank suspension components of the temperature coefficient which are additional

components of inlet temperature coefficients are calculated separately from the EBRPOCO and TEMCO programs

PRD COMPONENTS

For each core, steel radial reflector and uranium radial blanket subassembly of a loading, the subassembly area averaged axial distributions of the temperatures of sodium coolant, fuel-and blanket element claddings, structural rods and steel reflectors, sodium in gaps, and fuel are calculated Axially delineated PRD components for every subassembly and control rod location are calculated and then summed to obtain the regional components resulting from coolant density (density reduction of Na due to temperature) coolant displacement (displacement of Na coolant by thermal expansion of cladding structural rods subassembly ducts and lower and upper axial reflector regions) steel density (density reduction of these steel components due to axial expansions with temperatures), bond Na (resultant of displacement of bond Na if present in the open gaps, by differential thermal expansions of fuel and cladding and of density reduction of bond Na due to temperature or resultant of displacement of above-fuel bond Na, if present in close gap situations by thermal expansion of cladding and of density reduction of the above-fuel bond Na due to temperature), fuel and blanket axial expansions (free axial expansions if unrestricted by cladding or restricted axial expansion of fuel determined by axial expansion of cladding), Doppler (in fuel and blanket) and the rod-bank suspension (downward expansion of the control rods relative to core because of their being suspended from above)

The reactivity change resulting from a unit change in the core to rod-bank relative axial displacement, at the assumed rod bank positions, is also calculated It is subsequently used to obtain the net rod bank suspension component of the inlet temperature coefficient by auxiliary calculations

TEMPERATURE COEFFICIENT COMPONENTS

Because calculations of the components of the PRD using EBRPOCO require corresponding calculated axially delineated temperatures of the intra-subassembly components, the temperatures are available for the calculations of corresponding temperature coefficients in the TEMCO addition to the program In this manner temperature coefficients are calculated using a unified method following the EBRPOCO calculations of the PRD components Temperature coefficients calculated by TEMCO correspond to average temperature coefficients between the coolant inlet temperature and the applicable positional temperatures at the power and coolant flow rate of the reactor

NET ROD-BANK SUSPENSION COMPONENT

The effective rod-bank suspension component is the net reactivity resulting from the net effects of the axial movements of the control rods (because of their structural suspensions from above the reactor) the below core steel-containing regions and the surrounding sodium-containing pool tank (which is also suspended from above) This is a component of the coolant inlet temperature coefficient

In EBR-II a steel vessel encloses the reactor subassemblies through which the primary coolant flows upward The enclosed subassemblies rest upon a grid-plate region through which flows the inlet coolant pumped from the sodium pool

of the large surrounding overhead suspended steel tank The outer side of this tank is thermally insulated so that the tank wall at equilibrium is essentially at the temperature of the adjacent pool sodium The vertical structural dimensions involved in these simplified and idealized analyses of the net rod-bank suspension components are schematically shown in Fig 1 The arrows are directed to indicate directions of structural expansions resulting from temperature increases of the structures For a change in coolant temperature due solely to change in inlet temperature and assuming the idealized equilibrium conditions that the temperature change occurs everywhere including the pool sodium and the tank wall the net rod bank suspension coefficient in this situation is small because only the protrusion length of the fueled portion of the control rod is effective i e $(l_u+l_v+l_p+l_a+l_s+l_s\ l_t) = l_p$ (At the "11 in" rod bank position the values of l_p are about 159 mm (6 25 in) for a high worth control rod and 82 6 mm (3 25 in) for a standard control rod)

The values of the reactivity changes resulting from unit change in the rod bank to core net axial displacement at this banking (0 1Δk/k per meter as calculated by RODCO) are used together with the effective averaged value of l_p and the thermal expansion coefficient of the steel to obtain the reactivity change per degree

GRID-PLATE COMPONENT

The reactivity change resulting from radial expansion of the grid plate caused by a uniform change in its temperature is calculated by differences of the eigenvalues of the reference system and that of a uniform radial expansion of the system The expansion of the grid plate causes voids in the system (everywhere above the grid plate) which are replaced by Na coolant of equivalent volumes The grid plate temperature coefficient component is the reactivity resulting from a one degree increase (only in its temperature) which causes the subassemblies to move radially outward because they set upon the grid plate as a support This component contributes to the coolant inlet temperature coefficient

CONDUCTIVITIES AND EXPANSIONS

The thermal conductivities of the fuels over the temperature range of interest for these calculations are quadratic fits (as required by the EBRPOCO program) of estimates made from available data For the U20Pu10Zr case these data are measured values[4] for U18 4Pu11 5Zr For the U10Zr case these are interpolations of measured values[5] for U5Zr and U20Zr Comparative values used herein for fresh fuels are listed in Table 1 at three temperatures The fresh U20Pu10Zr conductivity is about 30 percent smaller than the fresh U10Zr conductivity

The thermal conductivity of stainless steel assumed throughout these calculations is 12 0 BTU hr^{-1} ft F (20 8 W m^{-1} C^{-1}) except in the axial regions of subassemblies having predominantly non austenitic HT-9 steel In the latter axial regions of those subassemblies the conductivity is increased to 15 0 BTU hr^{-1} ft^{-1} F^{-1} (26 0 W m^{-1} C^{-1}) This is an averaged value over the temperature range of interest deduced from measured[6] data Thus the 25% increased value is used only in core and pintop axial regions of the U20Pu10Zr fueled subassemblies in these analyses

The fuel temperature coefficients of linear expansion assumed in these calculations are listed in Table 2 for the indicated temperature ranges These are piecewise-constant approximate values (as required by the EBRPOCO program) deduced from expansion data[7] of U15Pu10Zr and U10Zr, respectively

The temperature coefficient of linear expansion of stainless steels assumed in these calculations is 11 x10 $^{6}F^{-1}$(20x10 $^{6}C^{-1}$) except in the axial regions of subassemblies having predominantly non-austenitic HT-9 steel In the latter axial regions of those subassemblies the coefficient is reduced to 7 7x10 ^{6} F^{-1}(14 x10$^{-6}C^{-1}$) This value is an estimated average for the range of interest, deduced from measured° data Thus, the reduced value is used only in core and pintop axial-regions of the U20Pu10Zr fueled subassemblies in these analyses

FEEDBACKS BY COMPONENTS AND REGION

The values are given in units of 10^{-5} $\Delta k/k$ and 10^{-7} $\Delta k/k$ per degree C for the reactivity components and the temperature coefficient components respectively The reactivity components are for a power of 62 5 MWt and total intrasubassembly (and intrarod) coolant flow of 8880 gpm (0 560 m^3 s^{-1}) corresponding to a discharge of about 9340 gpm (0 590 m^3 s^{-1}) from the primary pumps The operational control rods are assumed at the "11 in" position For conversions to β_{eff}-sensitive units values of 0 0053 and 0 0070, respectively can be used for β_{eff} In the tables the values in parentheses apply if at all powers the fuels in core are assumed to have the bond-sodium gaps fully closed (instead of fully open), however with the fuels not adhering to the clads and with no bond-sodium in the fuel porosities The values in brackets apply if at all powers the fuels are assumed to be fully adhering to the clads, such that the axial expansions of the fuels are those of the clads, and about one-third of the resulting fuel porosities contain bond sodium

PRD COMPONENTS

The regional contributions of the components of the PRDs are shown in Table 3 for the two fuel types designated as Pu and U Except for core and above core regions the corresponding components are similar The core values of fuel axial expansion components are larger in magnitude for the Pu-case than the corresponding U-case if the gaps are open or if the gaps are closed with fuels free to axially expand because of the smaller thermal conductivities for the Pu-case If fuels are adhered to the clads this component is smaller in magnitude for the Pu-case because the temperature coefficient of the HT-9 steel clad is less than that of the austenitic steel clad of the U-case The smaller negative values of the steel density component and the coolant displacement component also result largely from the same cause These latter two components are analogously affected in the above core regions also because of the differing steel assumptions in the pintop axial-position of the overall above core region For both the Pu- and U- cases the fuel axial expansion components are larger in magnitudes if the fuels are assumed to be expanded to the clads but not adhering thereto This is especially noted for the Pu-case These are because the porosities (due to burnup expansions) reduce the fuel conductivities and thereby increase the axial expansions

The small negative Doppler values are relatively larger in magnitude for all three gap situations of the Pu case relative to the corresponding U case because of the larger U 238 content and larger temperatures of the fuel

Sums over all components and regions result in ratios of the Pu case values of the total linear (and Doppler) PRD relative to the values of the U case of about 1 08 (1 23) and [0 95] for the three respective gap situations

POWER TO FLOW COMPONENTS

The regional contributions of the power to flow components of the PRDs are shown in Table 4 The coolant density components being solely power to flow dependent are identical to those in Table 3 The rod bank suspension components are assumed herein as essentially also power to flow dependent The values of other components are smaller in magnitude relative to corresponding quantities of Table 3 because they represent reactivity losses resulting only from effects of the component temperature increases from inlet to the coolant temperatures at the various axial levels of the subassemblies For the same reason the in core power to flow values of the Doppler components for the Pu cases or the U cases are not affected by closures of the bond sodium gaps and the power to flow values of the fuel axial expansion components are also not affected by gap closures if the fuels however are not adhered to the clads

It is noted that although various components of the Pu case can noticeably differ from the U case values the sums over all components and regions result in ratios of the Pu case to the U case of only about 1 00 (1 00) and [0 9b] respectively

POWER COMPONENTS

The regional contributions of the power components of the PRDs are shown in Table 5 The power components of fuel axial expansion of core fuel (and associated bond sodium component if present) and Doppler are significantly larger than values of corresponding power to flow quantities shown in Table 4 Values of coolant displacement and steel density quantities of power components for the radial steel reflector region are essentially as large as the corresponding power to flow quantities in Table 4 (This is because in EBR II the steel in a radial reflector subassembly is in the form of a large hexagonal shaped block inserted into the hexagonal shaped subassembly duct with the coolant flowing axially between the block and the duct This results in sizeable radial edge to peak temperature differences which enhances the power components)

Comparisons of the in core power components of the fuel axial expansion quantities for the Pu case relative to corresponding U case in Table 5 indicate ratios of about 1 5 if the gaps are assumed fully open These result from the larger fuel temperature in the Pu case because of the relatively smaller conductivity If the gaps are assumed closed but the fuels not adhering to the clads this ratio becomes 2 3 This is larger than the former ratio because the increased fuel temperature for the Pu case increases the effective temperature coefficient of thermal expansion of that fuel more than for the U case The larger temperature encompasses a larger fraction of the expansion coefficient in the larger valued transitional region If the fuels are assumed adhered to the clads then the power component of the fuel axial expansion of the Pu case is

less than that of the U-case because of the lesser value of the temperature coefficient of the HT-9 steel clads relative to the austenitic steel clads

Although sums of the power components over all regions moderate the effects of the large differences in the fuel components significant differences can remain Thus the ratios of the total linear (and Doppler) power components for the Pu-case relative to the U-case are about 1 3, (1 9), and [0 9] respectively

TEMPERATURE COEFFICIENT COMPONENTS

The regional contributions of the components of the temperature coefficients of reactivity are shown in Table 6 Examination of the in core values for the Pu-cases relative to the U-cases show less negative coolant density component due to the relatively smaller worth of sodium, less negative steel density component due to the presence of the smaller expansion of the HT-9 steel, less negative coolant displacement component due to the composite of the smaller expansion of the HT-9 steel and the lesser worth of the displaced sodium coolant, larger negative values of the fuel axial expansion with fuels not adhering to the clads, due to the relatively larger fuel temperatures encompassing temperature ranges having the larger expansion rate with temperature, and more negative Doppler values due to the fuel composition having a larger U-238 content and which also then enhances the lower energy spectral shape by the increased inelastic-scattering The effective net-rod-bank inlet-temperature coefficients are small, whereas, the grid-plate coefficients are large

The values of the total inlet temperature coefficients of the Pu cases relative to the U-cases are only 1 03 (1 06) and [0 99] because of compensations of increasing and decreasing components

INTEGRAL COEFFICIENTS AND FEEDBACK RELATIONS

Divisions of the sums of the components from Tables 3, 4, and 5, respectively, by the power give the integral coefficients of power (A+B), of power-to-flow (B), and solely of power (A) These together with the sums of the temperature coefficient components (C), from Table 6, are shown in Table 7 These integral coefficients enable the reactivity change $\Delta\rho$ due to a power increment ΔP, a power-to-flow increment $\Delta(P/Q^*)$, and a change ΔT_1 in inlet-temperature to be approximated by $\Delta\rho \cong A\Delta P+B\Delta(P/Q^*) + C\Delta T_1$ where Q^* is the fraction of the reference flow Listed are also corresponding quantities of interest in loss-of-flow-without-scram (LOFWS) and loss-of-heat-sink-without-scram (LOHSWS) situations assuming these loadings For LOFWS the quantity A/B is significant because the ratio of the final coolant-temperature increment through the system at equilibrium conditions can for purposes of these intercomparisons be approximated by $\Delta T_f/\Delta T_0 \cong 1+A/B$ where ΔT_f and ΔT_0 are the final and initial coolant-temperature increments across the system For LOHSWS the quantity (A+B)/C is significant because the increase in coolant inlet-temperature required so that the negative reactivity will compensate for the otherwise positive reactivity resulting from the return of the PRD due to the power decrease to zero can be approximated by $\Delta T_1 = (A+B)\ P/C$ (Non-inclusion of a subassembly bowing component in B should not significantly affect the LOFWS quantities Non-inclusion of a subassembly-bowing component in B however, most likely would cause the listed inlet coolant temperature increases, ΔT_1 to be too

large because in EBR-II the bowing component of the PRD is usually positive) The quantity ϕ_0 (see footnote e of Table 7) is significant because it is an indicator of the relative peak temperature overshoot in LOFWS situations in that if ϕ_0 is smaller the relative overshoot is larger and vice-versa [1]

Thus, for situations having fuels not adhering to clads the U20Pu10Zr case has relatively larger $\Delta T_f/\Delta T_0$ (in LOFWS) and ΔT_1 (in LOHSWS) values but for this case the relative values of ϕ_0 indicate less peak temperature overshoot in LOFWS For situations having fuels adhering to clads, however the respective values of these quantities are essentially the same for the two cases

CONCLUSIONS

Comparison of the feedbacks of the Pu case relative to those of the U fueled case result in the following main conclusions (Percentage values in parentheses refer to approximate comparisons in β_{eff} units for the three assumed gap-situations)

The PRD is about 20 percent larger for situations having fuels completely expanded to clads but not adhering to clads, but, the corresponding PRDs are within 10 percent for fully open gaps or for fuels adhering to the clads (+40%, (+60%), [+25%])

The power-to-flow parts of the PRDs are similar for the corresponding gap situations (+30% (+30%), [+30%])

The power parts of the PRDs are 30 percent larger for the fully open gaps, 100 percent larger for the closed gaps having fuel free, and 10 percent smaller if the fuels are adhered to the clads (+70%, (+150%), [+20%])

The inlet temperature coefficients of reactivity are similar (+35%, (+40%), [+30%])

The LOFWS ratios $\Delta T_f/\Delta T_0$ are essentially similar except for the closed-gap fuel-free situations which indicate about a 20 percent increase

The LOHSWS values of ΔT_1 are similar except for the closed-gap fuel free situations which indicate about a 15 percent increase

The relative values of ϕ_0 indicate less peak-temperature overshoots during LOFWS

REFERENCES

1 H P Planchon J I Sackett G H Golden and R H Sevy 'Implications of the EBR-II Inherent Safety Demonstration Test,' Nucl Erg Des , 101 75 (1987)

2 D Meneghetti and D A Kucera, EBRPOCO A Program to Calculate Detailed Contributions of Power Reactivity Components of EBR-II " Proc Int Topl Mtg Advances in Mathematical Methods for the Solution of Nuclear

Engineering Problems, Munchen, FRG, April 27-29, 1981, Vol 2, p 225, Kernforschungszentrum Karlsruhe (1981)

3 D Meneghetti and D A Kucera, "Calculation of the Temperature Coefficients of Reactivity for EBR-II Kinetic Analysis," Ann Nucl Energy, 14, 12, 663 (1987)

4 Reactor Development Program Progress Report ANL-7230, 10 (1966)

5 Y S Touloukian, R K Kirby, R E Taylor, and P D Desai, "Thermophysical Properties of Matter, 1, Thermal Conductivity, Metallic Elements and Alloys", IFR/Plenum, New York (1970)

6 L Leibowitz and R A Bloomquist, "Thermal Conductivity and Thermal Expansion of Stainless Steels D9 and HT9", Int Journal Thermophysics, 9, No 5, 873 (1988)

7 Y S Touboulian, R K Kirby, R E Taylor, and P D Desai, 'Thermophysical Properties of Matter, 12, Thermal Expansion, Metallic Elements and Alloys," Plenum, New York (1975)

Table 1 U20Pu10Zr and U10Zr Thermal Conductivities
BTU s^{-1} ft^{-1} F^{-1} (W m^{-1} C^{-1})

Fuel	700 F(371 C)	950 F(510 C)	1200 F(649 C)
U20Pu10Zr	0 0027(16 8)	0 0033(20 6)	0 0037(23 0)
U10Zr	0 0039(24 3)	0 0045(28 0)	0 0052(32 4)

Table 2 U20Pu10Zr and U10Zr Temperature Coefficients of Linear Expansion

Fuel	Temperature Range F(C)	Coefficient, Units 10^{-5} $F^{-1}(C^{-1})$
U20Pu10Zr	T<1112(600)	1 1(2 0)
	1112(600)≤T≤1224(662)	4 7(8 5)
	T>1224(662)	1 1(2 0)
U10Zr	T<1160(627)	1 0(1 8)
	1160(627)≤T≤1250(677)	6 0(10 8)
	T>1250(677)	1 2(2 2)

Table 3 Linear (and Doppler) PRD Components of a U20Pu10Zr-Fueled and a U10Zr-Fueled EBR-II, 10^{-5} $\Delta k/k$ Units

Region	Fuel	Coolant Density	Coolant Displ	Steel Density	Bond Sodium	Fuel Axial Exp	Doppler	B_4C-Fuel	Sum
Core	Pu	-45 0	-9 7	-5 2	-15 1	-84 2	-6 7	0	-166 0
					(0)	(-146 3)	(-8 4)		(-214 6)
					[0]	[-23 6]	[-7 0]		[-90 5]
	U	-47 2	-13 6	-6 2	-14 2	-58 1	4 8	0	-144 0
					(0)	(-72 3)	(-5 7)		(-145 0)
					[0]	[-30 4]	[-5 0]		[-102 3]
Above Core	Pu	-41 9	-6 7	-4 8	0	0	0	+1 2	-52 2
					(-16 0)				(-68 1)
					[-11 1]				[-63 3]
	U	-40 8	-9 0	-6 0	0	0	0	+1 2	-54 5
					(-16 2)				(-70 8)
					[-11 4]				[-65 9]
Below Core	Pu	-0 7	-0 5	-0 6	-0 2	-1 6	+1 5	0	-2 0
					(0)	(-2 0)	(+1 9)		(-1 9)
					[0]	[-1 7]	[+1 6]		[-1 9]
	U	-0 6	-0.5	-0 6	-0 1	-1 3	+1 2	0	-1 9
					(0)	(-1 6)	(+1 5)		(-1 8)
					[0]	[-1 4]	[+1 3]		[-1 7]
Rad Refl.	Pu	-4 4	-6 8	-10 5	0	0	0	--	-21 7
	U	-4 4	-7 0	-10 5	0	0	0	--	-21 8
Rad. Blkt.	Pu	-0 3	-0 2	- 0 1	-0 1	-0 5	-1 7	--	-3 1
	U	-0 3	-0 2	-0 1	-0 1	-0 5	-1 6	--	-2 8
Sum	Pu	-92.3	-23 9	-21 2	-15 4	-86 4	-6 9	+1 2	-244 9
					(-16 1)	(-148 8)	(-8 3)		(-309 4)
					[-11 2]	[-25 9]	[-7 1]		[-180 4]
	U	-93 3	-30 2	-23 3	-14 5	-59 9	-5 1	+1 2	-225 1
					(-16 4)	(-74 5)	(-5 7)		(-242 1)
					[-11 5]	[-32 3]	[-5 3]		[-194 6]

Rod-bank Suspension Pu -57.3 U -56 0

Total Pu -302 2 (-366 7)[-237 7] U -281 1 (-298 1) [-250 6]

Table 4 Linear (and Doppler) Power to Flow Components of the PRDs of a U20Pu10Zr-Fueled and a U10Zr Fueled EBR-II

Region	Fuel	Coolant Density	Coolant Displ	Steel Density	Bond Sodium	Fuel Axial Exp	Doppler	B_4C-Fuel	Sum
Core	Pu	-45 0	-7 3	-4 3	-6 4	23 6	2 2	0	88 8
					(0)	(23 6)	(-2 2)		(82 4)
					[0]	[16 1]	[-2 2]		[-74 9]
	U	-47 2	-9 9	-5 0	-6 1	-18 3	-1 7	0	88 2
					(0)	(-18 3)	(-1 7)		(-82 1)
					[0]	[-20 4]	[-1 7]		[-84 1]
Above Core	Pu	-41 9	-6 7	4 8	0	0	0	+1 2	-52 2
					(-16 0)				(-68 1)
					[-11 1]				[-63 3]
	U	-40 8	-9 0	-6 0	0	0	0	+1 2	-54 5
					(-16 2)				(-70 8)
					[-11 4]				[65 9]
Below Core	Pu	-0 7	-0 1	-0 1	-0 1	-0 4	+0 3	0	-1 0
					(0)	(-0 4)	(+0 3)		(-0 9)
					[0]	[-0 4]	[+0 3]		[-0 9]
	U	-0 6	-0 1	-0 1	0 0	-0 3	+0 3	0	-0 8
					(0)	(-0 3)	(+0 3)		(-0 8)
					[0]	[-0 3]	[+0 3]		[0 8]
Rad. Refl	Pu	-4 4	-3 4	-5 4	0	0	0	--	-13 1
	U	-4 4	-3 4	-5 3	0	0	0	--	-13 0
Rad. Blkt.	Pu	-0 3	-0 2	-0 1	-0 1	-0 5	-1 6	--	2 9
	U	-0 3	-0 2	-0 1	-0 1	-0 5	-1 4	--	-2 7
Sum	Pu	-92.3	-17 7	-14 7	-6 5	-24 5	-3 5	+1 2	-157 9
					(-16 1)	(-24 5)	(-3 5)		(-167 5)
					[-11 2]	[-17 0]	[-3 5]		[-155 1]
	U	-93 3	-22 6	-16 4	-6 2	-19 1	-2 9	+1 2	-159 3
					(-16 3)	(-19 1)	(-2 9)		(-169 4)
					[-11 5]	[-21.1]	[-2 9]		[-166 5]

Rod-bank Suspension Pu -56 6 U -55 3

Total Pu -214 5(-224.1)[-211 7] U -214 6(-224 7) [-221 8]

Table 5 Linear (and Doppler) Power Components of the PRDs of a U20Pu10Zr Fueled and a U10Zr-Fueled EBR-II, 10^{-3} $\Delta k/k$ Units

Region	Fuel	Coolant Density	Coolant Displ	Steel Density	Bond Sodium	Fuel Axial Exp	Doppler	B_4C-Fuel	Sum
Core	Pu	0 0	-2 4	-0 9	-8 7	-60 6	4 5	0	-77 2
					(0)	(-122 7)	(6 2)		(-132 2)
					[0]	[-7 5]	[4 8]		[-15 6]
	U	0 0	-3 7	-1 2	-8 1	-39 8	-3 1	0	-55 8
					(0)	(-54 0)	(-4 0)		(62 9)
					[0]	[-10 0]	[-3 3]		[-18 2]
Above Core	Pu	0 0	0 0	0 0	0	0	0	0 0	0 0
					(0 0)				(0 0)
					[0 0]				[0 0]
	U	0 0	0 0	0 0	0	0	0	0 0	0 0
					(0 0)				(0 0)
					[0 0]				[0 0]
Below Core	Pu	0 0	-0 4	-0 5	-0 1	-1 2	+1 2	0	-1 0
					(0)	(-1 6)	(+1 6)		(-1 0)
					[0]	[-1 3]	[+1 3]		[-1 0]
	U	0 0	-0 4	-0 5	-0 1	-1 0	+0 9	0	-1 1
					(0)	(-1 3)	(+1 2)		(-1 0)
					[0]	[-1 1]	[+1 0]		[-0 9]
Rad. Refl.	Pu	0 0	-3 4	-5.1	0	0	0	--	-8 6
	U	0 0	-3 6	-5 2	0	0	0	--	-8 8
Rad Blkt.	Pu	0 0	0 0	0 0	0 0	0 0	-0 1	--	-0 2
	U	0.0	0 0	0 0	0 0	0 0	-0 2	--	-0 1
Sum	Pu	0 0	-6 2	-6 5	-8 9	-61 9	-3 4	0 0	87 0
					(0 0)	(-124 3)	(-4 8)		(-141 9)
					[0 0]	[-8 9]	[-3 6]		[-25 3]
	U	0 0	-7 6	-6 9	-8 3	-40 8	-2 2	0 0	-65 8
					(-0 1)	(-55 4)	(-2 8)		(-72 7)
					[0 0]	[-11 2]	[-2 4]		[-28 1]

Rod-bank Suspension Pu -0 7 U -0 7

Total Pu -87 7(-142 6)[-26 0] U -66 5(-73 4)[-28 8]

Table 6 Components of Temperature Coefficients of Reactivity for a U20Pu10Zr-Fueled and a U10Zr-Fueled EBR-II, 10^{-7} $\Delta k/k$ per °C Units

Region	Fuel	Coolant Density	Coolant Displ	Steel Density	Bond Sodium	Fuel Axial Exp	Doppler	B_4C-Fuel	Sum
Core	Pu	-77 2	-11 6	-7 00	-13 7	-45 4	-3 87	+1 07	-158
					(0)	(58 5)	(3 74)		(-157)
					[0]	[-30 8[c]]	[-3 85]		[129]
	U	-82 3	-15 9	-8 03	12 5	-34 6	-3 02	+1 25	155
					(0)	(-35 1)	(-2 97)		(-143)
					[0]	[-38 0[d]]	[-3 01]		[-146]
Above Core	Pu	-38 3	-6 12	-4 63	0	0	0	+0 141	-49 0
					(-13 7)				(-62 6)
					[9 52]				[-58 5]
	U	37 1	-7 99	-5 72	0	0	0	+0 165	50 6
					(-13 6)				(-64 3)
					[-9 56]				[-60 1]
Below Core	Pu	34 6	-4 23	-5 96	-0 27	+1 32	+1 87	+0 490	-41 4
					(0)	(+1 32)	(+1 84)		(-41 2)
					[0]	[+1 32[b]]	[+1 85[b]]		[-41 0]
	U	34 2	-4 18	-5 80	-0 266	+1 70	+1 76	+0 574	-40 3
					(0)	(+1 70)	(+1 74)		(-40 1)
					[0]	[+1 70[b]]	[+1 76[b]]		[-40 1]
Rad Refl	Pu	-17 1	-11 5	-18 0	0	0	0	-	-46 6
	U	-17 3	-11 7	18 0	0	0	0	-	47 0
Rad Blkt [a]	Pu	-0 727	-0 547	-0 342	-0 293	-1 09	-3 65	-	-6 65
	U	0 763	-0 576	-0 355	-0 308	-1 11	-3 58	-	-6 69
Sum	Pu	-168	-34 0	-36 0	-14 2	-45 2	-5 65	+1 70	-301
					(-14 0)	(-58 3)	(-5 55)		(-315)
					[-9 81]	[-30 6]	[-5 65]		[-283]
	U	-172	-40 3	-38 0	13 1	-34 0	-4 84	+1 99	-301
					(-13 9)	(-34 4)	(-4 81)		(-301)
					[-9 87]	[-37 4]	[-4 83]		[-301]

Effective Net-rod-bank Inlet-temperature Coeff Pu -3 24 U -3 24

Grid-plate Inlet-temperature Coeff Pu -174 U -160

Total Pu -478(-492)[-460] U -464(-464)[-464]

[a]Open-gaps assumed in blanket elements
[b]Gaps-closed fuels-free and Na in one-third of porosities assumed in control rod fuels.
[c]Relative to clad temperature (Relative to fuel temperatures this would effectively be -12 9)
[d]Relative to clad temperature (Relative to fuel temperatures this would effectively be -17 2)

Table 7 Power, Power-to-Flow, and Inlet-Temperature Integral Coefficients and Pertinent LOFWS and LOHSWS Quantities

Case	Coefficient or Quantity	Open-Gap	Closed-Gap Fuel-Free	Closed-Gap Fuel-Restr Na in ⅛ Pores
U20Pu10Zr-Fueled (β_{eff} = 0 0053)	(A+B)[a]	-4 83 (-0 91)	5 87 (-1 11)	3 81 (-0 72)
	B[a]	-3 44 (-0 65)	-3 58 (-0 68)	3 39 (-0 64)
	A[a]	-1 39 (-0 26)	-2 29 (-0 43)	-0 42 (-0 08)
	C[b]	-4 78 (-0 90)	-4 92 (-0 93)	-4 60 (-0 87)
	$(\Delta T_f/\Delta T_0)$[c]	1 40	1 64	1 12
	ΔT_i[d]	63	75	52
	ϕ_0[e]	0 45	0 64	0 28
U10Zr-Fueled (β_{eff} = 0 0070)	(A+B)	-4 50 (-0 64)	4 77 (-0 68)	4 01 (-0 57)
	B	-3 44 (-0 49)	-3 60 (-0 51)	-3 55 (-0 51)
	A	-1 06 (-0 15)	-1 17 (-0 17)	-0 46 (-0 06)
	C	-4 64 (-0 66)	-4 64 (-0 66)	-4 64 (-0 66)
	$(\Delta T_f/\Delta T_0)$	1 31	1 33	1 13
	ΔT_i	61	64	54
	ϕ_0	0 29	0 32	0 23

[a]Units of 10^{-5} $\Delta k/k$ per MWt (Units of cents per MWt)

[b]Units of 10^{-5} $\Delta k/k$ per °C (Units of cents per °C)

[c]$\Delta T_f/\Delta T_0 = 1 + (A/B)$

[d]$\Delta T_i = (A+B)P/C$ in °C, P = 62 5 MWt

[e]$\phi_0 = \frac{-\lambda\tau}{\beta_{eff}} \frac{(A+B)^2 P}{B}$ in \$, λ=0 08s^{-1}, and τ=7s

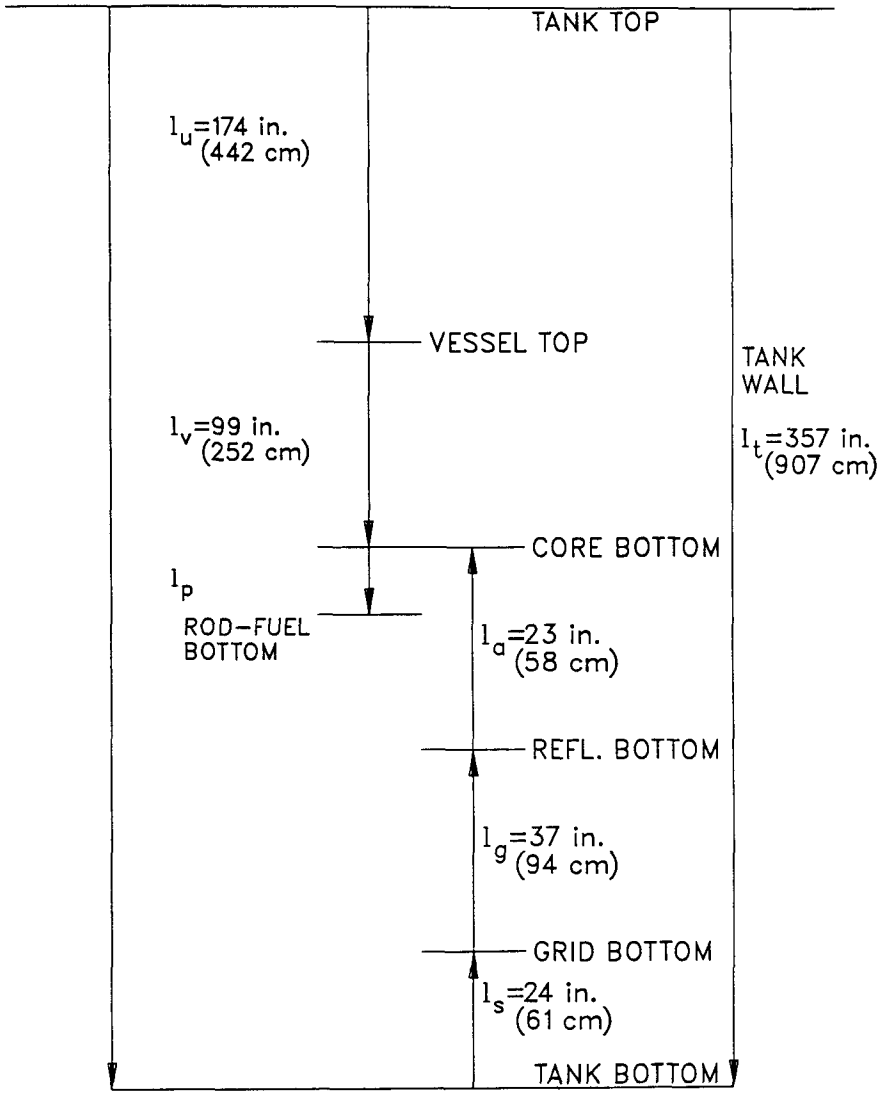

Fig. 1. Schematic diagram of vertical dimensions effective in net rod-bank suspension component (not to scale).

FBR CORE DESIGNS LEADING TO LOW SODIUM VOID WORTH

J. Tommasi - C. Girard - A. Zaetta

Commissariat à l'Energie Atomique - DRN
CEN Cadarache - DER/SPRC - Bât. 212
13108 - ST PAUL LEZ DURANCE CEDEX - FRANCE

ABSTRACT

A better intrinsic safety of fast reactors relies to some extent on the reduction of sodium voiding reactivity effects. Firstly, this paper recollects physical explanations about void reactivity effects and their variations, according to simple typical design changes, so as to point out the most promising directions to investigate to ensure the best void reactivity reductions. But out of equivalently void reactivity reducing changes, those of best economical characteristics must be sorted out ; only fuel cycle costs will be taken here into account, the parameter taken as representative of fuel cycle cost being the core reactivity loss rate, directly correlated with the fuel elements residence time. Finally, to make this study profitful, the preceding results will be used to get alternative EFR core designs with low sodium void worth. Fixed parameters will be here EFR thermal output and, as far as possible, core radial bulk.

1 - CALCULATION METHODS

All calculations in parts 2 and 3 have been performed using the MECONG code designed at CEA to combine CCRR modules flexibly according to the purpose of the calculations required (CCRR is the french code system for fast reactors). MECONG can perform enrichment ratio of mean enrichment searches, evolution calculations with either time, burn-up, damage dose, or reactivity as end criteria, or simple diffusion calculations. The geometrical model used is a R-Z representation ; there can be up to 25 energy groups. MECONG can also design assemblies (pins and wrappers) according to design basis constraints.

Three core designs have been chosen to obtain and/or check the results and reasonings quoted in parts 2 and 3 : three volumes (1.5, 6, and 12 m^3) with the same cylindrical shape (H/D = 0.35), with assemblies designed to withstand 450 W/cm maximum linear power, 150 GWd/t maximum burn-up and 180 dpaNRT maximum damage. In part 3 calculations, enrichments have been adjusted to provide the same reactivity at beginning of life (BOL). For sodium void worth ($\Delta\rho_{Na}$) calculations, as this is only a sensitivity study, a 6 group energetical mesh has been chosen to reduce computation times without spoiling accuracy too much.

2 - PHYSICAL EXPLANATIONS OF REACTIVITY VARIATIONS

Calculations using multigroup diffusion perturbation formalism yield the following splitting of the reactivity variation between two core configurations (standard and primed notations, $\delta x = x' - x$) : $\Delta\rho = L + S + A + P$, with :

$$L = \frac{1}{N}\int \sum_i \delta D_i \Phi_i^* \nabla^2 \Phi_i' \qquad \text{(leakage term)}$$

$$S = \frac{1}{N}\int \sum_{i,j} \delta\Sigma_{j\to i}(\Phi_i^* - \Phi_j^*)\Phi_j' \qquad \text{(spectral or scattering term)}$$

$$A = -\frac{1}{N}\int \sum_i \delta\Sigma_i^a \Phi_i^* \Phi_i \qquad \text{(absorption term)}$$

$$P = \frac{1}{N}(1-\rho)\int \sum_i \chi_i \Phi_i^* \sum_j \delta(\nu\Sigma_f)_j \Phi_j' \qquad \text{(production term)}$$

the normalization factor being :

$$N = \int \sum_i \chi_i \Phi_i^* \sum_j (\nu\Sigma_f)_j' \Phi_j' \qquad \text{(normalization on productions)}$$

A word on the signs and magnitudes of these components : L is negative, as in a critical system the flux shape has its concavity mainly turned down (its curvature is globally negative) ; the sign and magnitude of S depend on the shape of the production/disparition cross-section ratio vs energy curve : S is positive in the case of Pu^{239} fuels ; A is positive, as Σ_a decreases when the coolant is removed ; finally, the $\delta(\nu\Sigma_f)_i$ are only due to autoprotection changes and cross-section condensation effects : P would be 0 in infinitely fine spatial and energetic mesh calculations and, from a physical point of view, we can neglect this term is qualitative reasoning.

2.1 - VARIATIONS ON CORE COMPONENTS

As long as there are no geometry changes, we can interpret the precedent formulations in this way : in first approximation, the variations in these components are mainly due to the non-normalized, variable terms which appear in them. That is, δD_i in L, $\delta\Sigma_{j\to i}$ and $(\Phi_i^* - \Phi_j^*)$ in S, $\delta\Sigma_i^a$ in A, and $(\nu\Sigma_f)_j$ in N.

An approximate expression for the diffusion coefficient is $D \approx \frac{1}{3\Sigma_t} = \frac{1}{3(\Sigma_0 + \Sigma_{Na})}$

where Σ_0 and Σ_{Na} are the total non-sodium and sodium-only total cross-sections. This gives $\delta D \approx \frac{\Sigma_{Na}}{3\Sigma_0(\Sigma_0 + \Sigma_{Na})}$.

* Volume fractions (single parametric variations)

. Steel : The prominent variations are here those of δD in L and of $|\Phi_i^* - \Phi_j^*|$ in S. If the steel volume fraction (X_S) increases, then Σ_0 goes up, and D goes down : as L is negative this means an increase in $\Delta\rho_{Na}$. As when X_S goes up, the importance vs energy curve becomes less steep (because of the absorption

of steel at low energy, where importance increases with lethargy), S goes down, which means a decrease in $\Delta\rho_{Na}$. The balance between these two antagonistic effects depends on the initial core leakage level : in a high leakage core, the positive effect dominates, while in a low leakage core it can be offset by the negative one (cf. fig. 1a)*.

. Sodium : The variations are here mainly due to δD in L, $\delta\Sigma_{j\to i}$ and $|\Phi_i^* - \Phi_j^*|$ in S, and $\delta\Sigma_i^a$ in A. When the sodium volume fraction (X_{Na}) goes up, δD increases then saturates ; this means a negative effect on $\Delta\rho_{Na}$ with saturation for high W_{Na} values. When X_{Na} goes up, $\delta\Sigma_a$ and thus A increase ; this means a positive effect on $\Delta\rho_{Na}$.

Finally, the $\delta\Sigma_{j\to i}$ increase with X_{Na}, while the $|\Phi_i^* - \Phi_j^*|$ remain quite unchanged (as the increase in absorption which tends to decrease absorption at low energy is compensated by the increase in moderation which tends to decrease importance at high energy). This means again a positive effect on $\Delta\rho_{Na}$. Here again the net effect depends on the initial core leakage level : in a high leakage core the initial slope of the $\Delta\rho_{Na} = f(X_{Na})$ curve is negative, then saturates and may become positive ; in a low leakage core, this slope is always positive (cf. fig. 1b).

. Fuel : We must take here into account the variation of the $\nu\Sigma_f$. When the fuel volume fraction (X_f) goes up, Σ_a and $\nu\Sigma_f$ increase : L gives a positive effect on $\Delta\rho_{Na}$. The $|\Phi_i^* - \Phi_j^*|$ increase (because of the increase of production cross-sections at high energy and the competition at low energy between the increase of fissions in Pu and of absorptions in U), but $\nu\Sigma_f$ goes up even faster, and the global effect on S is negative. As the $\nu\Sigma_f$ increase, there is a negative effect of A too. The balance is dominated by the fact that the increase in L is due to the multiplication of two increasing factors ; one expects then L to impose its behaviour, except on very low leakage cores (cf. fig. 1c).

* Mean enrichment

The replacement of U by Pu lessens more the captures in U than it increases the Pu cross-sections : Σ_a goes down and δD increases. But an antagonistic and more important effect is the increase of $\nu\Sigma_f$, and finally L gives a positive contribution to $\Delta\rho_{Na}$. The $|\Phi_i^* - \Phi_j^*|$ go down and the $\nu\Sigma_f$ go up when the mean enrichment (E_m) increases : these two variations contribute to a negative effect on $\Delta\rho_{Na}$ by means of R, the second to a negative effect by means of A. Generally, the negative effect on S and A is predominant, there is an increase followed by a decrease (when the variations of L saturate) in $\Delta\rho_{Na} = f(E_m)$, which comes sooner in a low leakage core than in a high leakage one (cf. fig. 1d).

* Enrichment ratios

. Radial : E_1 is the inner zone enrichment, E_2 the outer zone one. If E_1/E_2 becomes very small, one gets an annular core of great and increasing enrichment E_2:$\Delta\rho_{Na}$ will decrease. Thus, for small values of E_1/E_2, $\Delta\rho_{Na}$ goes

---

* Throughout this paper, reactivities will be expressed in pcm (1 pcm = 10^{-5} $\frac{\Delta K}{K}$). High leakage core means the 1.5 m^3 core quoted before, and low leakage core the 12 m^3 one.

up with E_1/E_2. If E_1/E_2 becomes very large, one gets a small core of great and increasing enrichment E_1, where $\Delta\rho_{Na}$ will decrease. Thus, for large values of E_1/E_2, $\Delta\rho_{Na}$ decreases when E_1/E_2 increases.

The position of the maximum depends on the core shape, more precisely on the ratio between initial leakages in the two zones. One can express (by using *area-to-volume ratios to approximate leakage levels*) an approximation of this ratio in terms of α and H/D, where α is the ratio between external and internal radii, and H/D the height to diameter ratio of the core. This shows that when H/D goes up the maximum shifts towards low E_1/E_2 values, while when α increases, the maximum shifts towards high E_1/E_2 values (cf. fig. 1e).

. Axial : E_1 is the inner zone enrichment, E_2 the double outer zone one. The reasoning is the same as above, and leads to the following behaviour : when H/D or α increase, the maximum shifts towards high values of E_1/E_2 (the roles of H and D having been inverted with respect to the above reasoning).

* Plutonium isotopic composition

There are two main points affecting $\Delta\rho_{Na}$ when the isotopic composition of the plutonium changes ; the increase of fertile Pu isotopic proportions is analogous to an enrichment diminution, but the absorption cross-sections of these fertile isotopes being greater than those of U_{238}, there will be a more important positive effect on L, and so a degradation on $\Delta\rho_{Na}$ values. As for fissile isotopes, Pu_{241}, like U_{235}, has a production-to-disparition cross-section ratio less increasing at middle and high energies than that of Pu_{239}, so that S is much lesser in Pu_{241} fuel than in Pu239 fuel. In short terms, the more aged the Pu is before core operation or the more spent is the fuel it originates from, the worse is the $\Delta\rho_{Na}$.

. Other fuel : The purpose is to use dense fuels (nitride, carbide, metal alloys) in order to achieve greater breeding gains and lesser reactivity losses during operation. The calculations show that from the $\Delta\rho_{Na}$ point of view the best choice is nitride fuel followed by carbide and then by metallic fuel. Due to the disparition of the cross-section peak of oxygen and to the higher density of heavy atoms, the spectrum becomes harder, with, in order of hardness : nitride, carbide, and metal (lesser slowing down of zirconium) ; the worsening on $\Delta\rho_{Na}$ is in the same order : nitride, carbide, metal. More details on alternative fuels are given in another paper presented at this meeting[1].

. In-core moderator : If there were a fixed (unlike sodium) moderator present in the core, the voiding effect might be lessened. The introduction of beryllium oxide in fuel assemblies suits this purpose. The effect on S is that the high moderation diminishes the importance at high energies and so flattens the importance curve : S will decrease. As for L, δD will decrease due to the increase of the total sections : the effect on $\Delta\rho_{Na}$ will be positive, with a greater amplitude in high leakage cores. Thus the introduction of in-core moderator will be more efficient in low-leakage cores, which are precisely those that suffer the greatest $\Delta\rho_{Na}$ values.

. Other coolants. A more radical approach of the problem is to change the coolant ; calculations have been done with lead as coolant. Lead being a heavy atom has low slowing down and high capture sections with respect to sodium. This means that δD is greater in the case of lead (this gives a negative effect on $\Delta\rho_{cool}$). The $|\Phi_i^* - \Phi_j^*|$ increase due to the lesser slowing down at high energies and the greater absorption at low energies (the importance curve gets steeper) ; but there is an antagonistic effect on S due to the

lower $\delta\Sigma_s$ A goes up with the $\delta\Sigma_a$ The gain on $\Delta\rho_{cool}$ goes up with the leakage level in the core the substitution will be more efficient in a core having yet a low $\Delta\rho_{cool}$ due to high leakage (cf fig 1f)

Effect of burn-up As the fission products created during reactor operation are absorbing at low energies, the spectral hardening due to voidage will be more important, and so $\Delta\rho_{Na}$ The $\nu\Sigma_f$ go down during reactor operation A goes up , as δD goes down due to the increase of Σ_0, the effect on L results of two antagonistic causes , the importance curve gets steeper due to greater absorptions at low energies the positive effect on S results from two coherent causes. One expects then a positive effect on $\Delta\rho_{Na}$, mainly of a spectral nature

2 2 - GEOMETRY CHANGES

The geometry changes aiming at reducing $\Delta\rho_{Na}$ all result in an increase of the part of leakage in the neutronic balance This increase can be seen in the variations of L, but also in those of S (from the $\Delta\rho_{Na}$ splitting for the two configurations) , in fact, as $\Phi_i^* = \frac{\frac{(\nu\Sigma_f)_i}{k} + \sum_{j \neq i} \Sigma_{i \to j} \phi_j^*}{\Sigma_i^R + D_i B^2}$, if the leakage ($D_i B^2$) goes up, the importance goes down, the most affected groups being those of high energy where D_i is large · the steepness of the importance curve decreases, and so does S , while L increases simply due to the greater flux curvatures in high leakage systems

The weight of leakage in the neutronic balance can be approximated, in its sense of variation, by the ratio of the core external area to the core volume, for a convex core For a classical, cylindrical core, here are two expressions of this ratio (H, D, R, V are respectively the core height, diameter, radius, volume), which will help the interpretation of some of the results presented in the second part of the paper

$$\frac{S}{V} = 2\left[\frac{1}{R} + \frac{1}{H}\right] = \left[\frac{2\pi}{V}\right]^{\frac{1}{3}}\left[2\left[\frac{H}{D}\right]^{\frac{1}{3}} + \left[\frac{H}{D}\right]^{-\frac{2}{3}}\right] \qquad \text{(Equ 1)}$$

By giving up the compact cylindrical shape of the core, we can get to the so-called H or diabolo cores in which the external zone is higher than the inner one, or to heterogeneous cores However, it can be shown that axial heterogeneity (i.e the introduction of horizontal non-fissile slabs into the core), brings no significant amelioration to $\Delta\rho_{Na}$ Radial heterogeneity, to the contrary, proves very interesting according to this point of view (see part 2). To the end, this logic leads to modular cores, i e several small cores embedded in a decoupling matrix inside the same vessel , studies are underway at CEA to optimize such designs

Another way is to modify the core surroundings albedo (lightened or absent blankets) For example, for an EFR-type core, a reduction of about 1 $ in $\Delta\rho_{Na}$ is possible by removing the axial blankets and by reducing the steel concentration of outer axial core structures This does not modify radial core bulk, but problems of protection of upper core structures arise

3 - COMPARED ECONOMICAL WORTH OF SOME DESIGN CHANGES

Three kinds of design changes have been chosen (to be studied on the three core volumes already mentioned) : core shape (H/D), in-core moderator (BeO), radial heterogeneity (central fertile slab). The volume fractions, which depend on design basis constraints, will be fixed during this parametric studies. The parameter representative for fuel cycle cost will be the reactivity loss rate ($\Delta\rho_{/EFPD}$), which is directly linked to the fuel elements residence time in the core.

Figure 2 gives the variation of $\Delta\rho_{Na}$ with H/D (fig. 2a), in-core moderator fraction (fig. 2b) and radial heterogeneity fraction, i.e. in-core fertile volume/core volume ratio (fig. 2c). This confirms the trends given in part 1 :

- H/D variations. The curve has a maximum for H/D = 1 and a steep slope for low H/D values, according to (Equ. 1). The discrepancy for V = 1.5 m^3 is explained mainly by the fact that the mean enrichment being adjusted to maintain the same initial reactivity, it increases as H/D goes down, and for such a high leakage core $\Delta\rho_{Na}$ increases with E_m, and, secondly by the fact that (Equ. 1) expression assumes that no core dimension gets too much close to the neutron mean free path in the core. These effects offset the predicted behaviour,
- in-core moderator fraction. The $\Delta\rho_{Na}$ reduction rate is greater in low leakage cores, as predicted,
- radial heterogeneity. This proves to be a very efficient means to reduce $\Delta\rho_{Na}$. But it calls for design basis changes (increase of pin number per assembly) to keep linear ratings within their allowed limit.

This shows that it is difficult to bring the sodium void worth of large cores to very low values. According to this point of view, an intermediate volume core (such as the 6 m^3 one, with ≈ 1600 MWth output) would allow low $\Delta\rho_{Na}$ values with moderate design changes from a compact, homogeneous design.

Figure 3 gives $\Delta\rho_{/EFPD}$ vs $\Delta\rho_{Na}$ curves relative to these design changes for the three core volumes : 1.5 m^3 (fig. 3a), 6 m^3 (fig. 3b) and 12 m^3 (fig. 3c). According to this point of view only, H/D reduction is the best means to reduce $\Delta\rho_{Na}$, followed by radial heterogeneity and then by in-core moderator introduction.

Core flattening is very expensive in terms of radial bulk, and presents acute problems of power distribution control if the core volume is kept constant (if the core radius is kept constant the same design basis changes as for radial heterogeneity should apply). Radial heterogeneity can give birth to thermal stripping problems if the decoupling material is fertile, so inert material would be preferred, providing a light penalty on $\Delta\rho_{/EFPD}$. As for moderator introduction, the problems are those of its activation and its progressive disappearance with burn-up, while $\Delta\rho_{Na}$ increases with burn-up.

4 - APPLICATION TO LOW VOID DESIGNS FOR EFR

The First Consistent Design (FCD) of EFR (fissile volume 16 m^3, fissile height 1.4 m) presented a too high value of $\Delta\rho_{Na}$, of about 2350 pcm at BOL conditions. Investigations aiming to reduce this value led to the Consistent Design (CD), with a reduced fissile height of 1 m, the number of pins per assembly being increased from 271 to 331 to keep on meeting the requirements

about maximum linear rating, and the greater reactivity loss rate leading to a 6-batch management instead of a 3-batch one This allows a substantial reduction of $\Delta\rho_{Na}$ of roughly 35 %, leading to a BOL value of about 1510 pcm A separate way to reduce $\Delta\rho_{Na}$, starting from FCD is to introduce a radial heterogeneity in the core

The radial heterogeneity fraction retained being of 20 % three cases have been taken into account (3D hexagonal calculations)

case 1 a fertile cylindrical slab,
case 2 the same fertile cylindrical slab + a fertile horizontal slab (this in order to reduce clad corrosion),
case 3 a steel cylindrical slab (in order to get rid of thermal stripping problems due to the power level time evolution in a fertile slab) + a fertile horizontal slab

The results are summarized in table 1 In the third case the $\Delta\rho_{Na}$ reduction at SOL is of about 45 %

TABLE 1

	FCD	CD	case 1	case 2	case 3
BOL volumic output (W cm^{-3})	460	510	450	510	510
BOL void worth (pcm)					
- fissile zone	2350	1510	1350	1000	1030
- fissile zone + radial slab			1370	1060	1100
- fissile zone + radial and axial slabs				1240	1330

REFERENCES

1 J C GARNIER, Ph BERGEONNEAU, A ZAETTA "Comparative performances of FBR advanced cores with dense fuels", this meeting proceedings

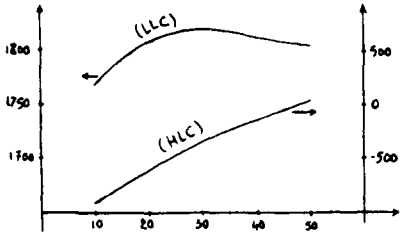

1a. $\Delta\rho_{Na}$ (pcm) vs steel volume fraction (%)

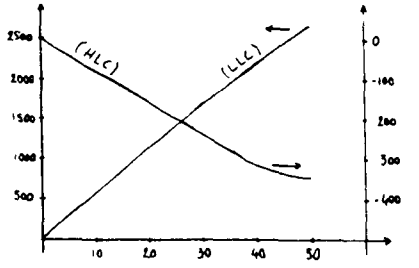

1b. $\Delta\rho_{Na}$ (pcm) vs sodium volume fraction (%)

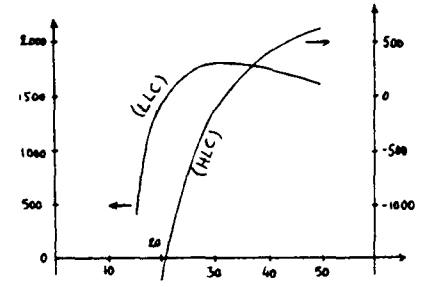

1c. $\Delta\rho_{Na}$ (pcm) vs fuel volume fraction (%)

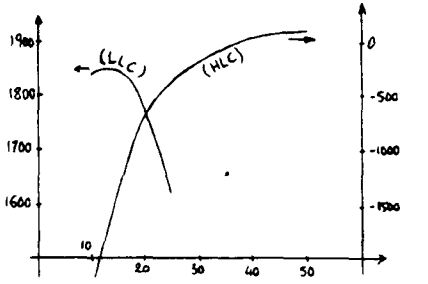

1d. $\Delta\rho_{Na}$ (pcm) vs mean enrichment (%)

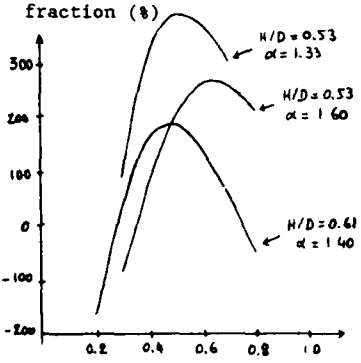

1e. $\Delta\rho_{Na}$ (pcm) vs E_1/E_2 for different near-PHENIX designs

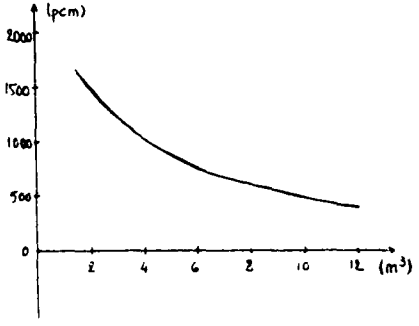

1f. Void worth gain (Na → Pb) vs core volume (at constant H/D)

Figure 1. Void worth variations with several one-parameter variations in low leakage cores (LLC) and high leakage cores (HLC)

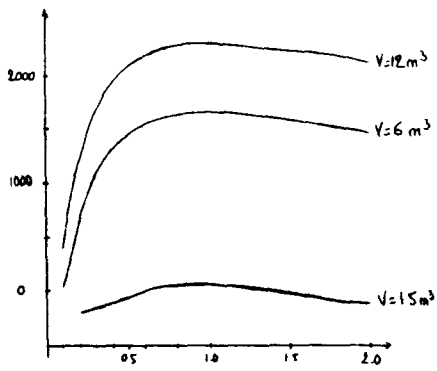

2a. $\Delta\rho_{Na}$ (pcm) vs H/D

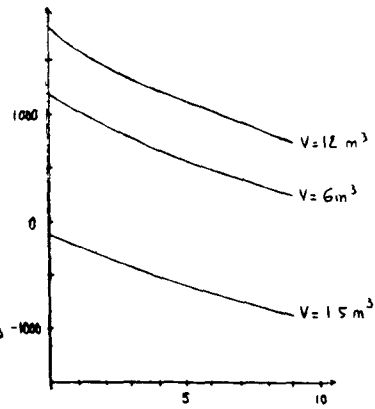

2b. $\Delta\rho_{Na}$ (pcm) vs BeO volume fraction (%)

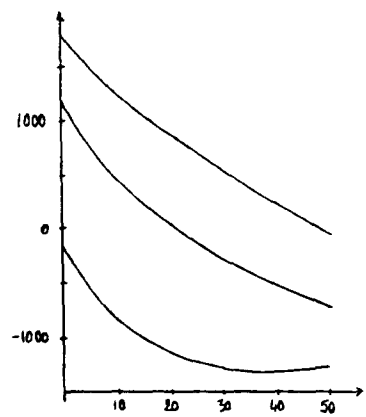

2c. $\Delta\rho_{Na}$ (pcm) vs radial heterogeneity (%)

Figure 2. $\Delta\rho_{Na}$ variations with mean enrichment adjusted to keep initial reactivity constant

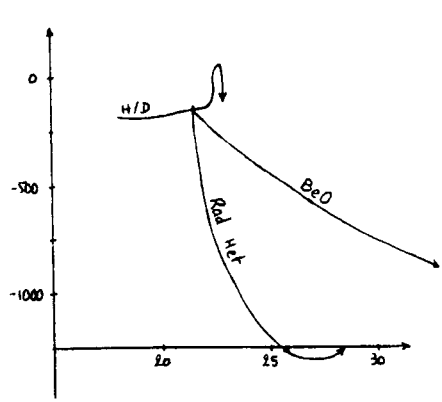

3a. For the 1.5 m^3 core

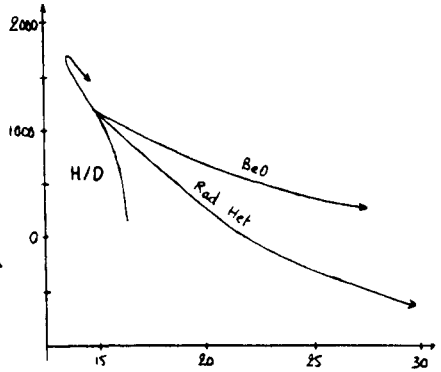

3b. For the 6 m^3 core

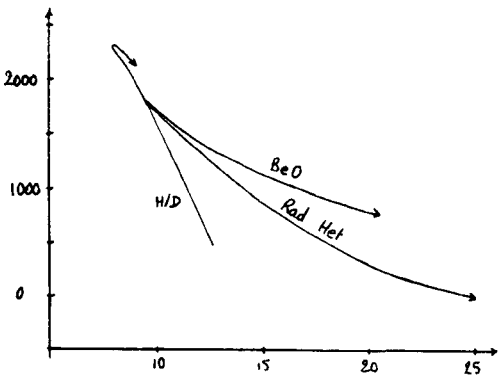

3c. For the 12 m^3 core

Figure 3. $\Delta\rho_{Na}$ vs $\Delta\rho_{IEFPD}$ comparisons

COMPARATIVE STUDY OF THE NEUTRONIC PERFORMANCES OF LMFBR USING OXIDE AND ALTERNATIVE FUELS

J.C. Garnier, R. Casimir, P. Bergeonneau, A. Zaetta

Commissariat à l'Energie Atomique - DRN
CEN Cadarache - DER/SPRC - Bât. 212
13108 - ST PAUL LEZ DURANCE CEDEX - FRANCE

ABSTRACT

A primary study has been carried out on the respective merits of oxide, nitride, carbide and metallic fuels used in a fast breeder reactor. Differences concerning burn-up reactivity loss, damage rate, Doppler and sodium void reactivities are evaluated and physically explained. The sensitivity of the different fuels to design parameter variations is also examined.

INTRODUCTION

LMFBR development remains closely dependent on significant economics and safety improvements. Pursuing that goal, the CEA core design studies have been enlarged to nitride fuel (UN, PuN), metallic fuel ([U, Pu] 10 % Zr) and carbide fuel (UC, PuC) considered for the long term as possible alternatives to oxide fuel (UO_2, PuO_2).

In a preliminary phase, a neutronic comparison between an oxide fuelled core taken as reference and cores with the three alternative fuels has been made using a two enrichment zone homogeneous core design optimized for oxide fuel. Two reference cores have been concidered : a PRISM-type and an EFR-type. Then, variations of the performances with smear density has been examined. Results discussed in this paper are related to this work.

CORE DESIGN DESCRIPTION

The main characteristics of the two cores studied are outlined in table 1 and cores layouts are given in fig. 1.

The three alternative cores are assumed to be identical to the oxide one, except with regard to smear density and gas plenum, those differences being justified by the swelling properties specific to each fuel.

METHODOLOGY

The basic cross section data used for the neutronic calculations were CARNAVAL IV. Twenty-five group cross section sets were generated for general use. Code calculations were carried out in RZ geometry using the CCRR code system and a diffusion theory methodology.

Enrichments of the fresh fuel have been chosen to obtain a zero end-of-equilibrium cycle excess reactivity, the ratio between the two enrichments being equal to 0.8.

The cycle length was adjusted to achieve a burn-up as close as possible to 150000 MWd/t for the oxide fuel.

Both Doppler and sodium void reactivities were obtained by direct calculation. The Doppler reactivity was performed between 180°C and nominal operating temperatures (843°C for the metallic fuel, 1227°C for the other fuels) and the sodium void reactivity was performed for a complete voiding of the fissile plus axial breeder zones.

PRISM CORE PERFORMANCE CHARACTERISTICS

Main results can be found in table 2.

The fresh fuel mass inventory makes clear the higher heavy atom content of alternative fuels (also called dense fuels). The additional mass is mainly supplied by depleted uranium, leading to a better breeding gain and accordingly to a smaller reactivity loss. Carbide and nitride have a very close reactivity loss, metallic fuel a little higher one, though far lower than oxide's.

The peak discharge burn-up is inexorably lower in the alternative cores, mainly because of the higher initial heavy atom mass. The carbide fuelled core is the least indranced, but burn-ups of the three cores are not radically different.

As for the damage rate, the three fuels have not the same behaviour. The metal damage rate is higher than oxide's, when nitride's and carbide's are lower. This disadvantage of metallic fuel could partly compensate the possibility of having longer cycle length induced by the smaller reactivity loss.

Doppler reactivity remains the same for nitride fuel, increases for carbide fuel and decreases considerably for metallic fuel (factor 2), inducing a penalty on metal safety aspect.

The sodium void reactivities increase for the three alternative fuels. This variation is moderate for the nitride fuel, the reactivity remaining strongly negative ; it's greater in the carbide fuel, but stay hardly negative. In the metallic fuel, this increase is enormous, the reactivity becoming strongly positive.

PHYSICAL ANALYSIS OF THE PHENOMENA

Having seen the compared performances of the different cores, the second part of this study will consist in trying to understand the phenomena involved in the variations of the main characteristics of the cores.

DAMAGE RATE

The damage rate is mainly due to the average flux in the fuel zone and the one group equivalent cross section of damage σ(DPA) The relative variations of those parameters with respect to oxide are shown below

	$\Delta\Phi$	$\Delta\sigma$(DPA)
METAL/OXIDE	+3 2 %	+4 5 %
NITRIDE/OXIDE	-12 6 %	+6 6 %
CARBIDE/OXIDE	-8 3 %	+1 4 %

The variation of the average flux results of a competition between a spectrum and a mass effect The more important heavy atom mass in the alternative fuels tends to diminish the average flux, but the decrease of the microscopic cross sections, thanks to the hardening of the spectrum in those fuels, tends to enhance it

Nitride and carbide spectrums are relatively close to oxide's, thus the preponderant effect is the heavy atom mass

In opposition, the metal spectrum is so hard that it does drive the variation of the average flux

The variation of the one group equivalent cross section is due to a spectrum effect This section is calculated by balancing the flux normalized to one by the pseudo cross section of damage (given in table 3), which decreases with energy We could then expect the one group equivalent section to be greater for the metallic fuel , but not only the hardening of the spectrum must be taken in consideration, but also it's repartition group by group The important groups of energy for the calculation of the equivalent cross section are the first ten groups, energies from 67 Kev to 14 5 Mev But the flux of the alternative fuels don't behave the same way in those groups

From the group 4 (2 Mev) to the group 10 (67 Kev), the flux of the metal fuelled core is much higher than the other's, the flux of the carbide fuelled core being close to oxide's and the flux of the nitride fuelled core being intermediate

In the first three groups (2 Mev to 14 5 Mev), the most important in the equivalent cross section calculation, the metal flux is the lowest The competition between the negative effect of the variation of the flux (compare to oxide) of these three groups and the positive effect of the seven others leads to a global positive effect

In the nitride, the effect of the first three groups is nearly zero, leading with the positif effect of the seven other groups to a global positive effect even greater than in the metal core

The effect of the first three groups for the carbide is hardly negative and hardly positive for the seven others, leading to a very little positive effect

The combination of the two phenomena we have just discussed, average flux and equivalent cross section of damage, leads to a positive variation of the damage rate +4 8 % for the metallic fuelled core and a negative variation for the two others core -4 1 % nitride, -3 4 % carbide The differences discussed above clearly come from of a competition between a mass effect (average flux) and spectral effects (average flux and cross section), but they are not significant enough to induce big penalties or advantages for any of the alternative fuels for this size of core

DOPPLER REACTIVITY

Doppler reactivity has been calculated between 180°C and the nominal fuel temperature 843°C for the metal (due to its low melting point) and 1227°C for the other fuels This difference in the fuel nominal temperature explains partly the very low Doppler reactivity of metallic fuelled core To explain the remaining part of the effects we have worked on the Doppler coefficient K defined as

$$K = \delta\rho/\log(T/T0)$$

$\delta\rho$ = reactivity above described
T0 = 453 K (= 180°C)
T = nominal fuel temperature in K

Using a perturbation calculation, it has been possible to divide K in three components The results of this calculation are shown below

	Capture + absorption pcm	Production pcm	Leackage pcm	K pcm
Oxide	-768	+157	+5	-606
Metal	-439	+57	+7	-375
Nitride	-762	+132	+5	-625
Carbide	-834	+136	+7	691

The leackage component can be neglected in any cases

In the metal fuelled core, the negative contribution of the "capture plus absorption" component diminishes strongly due to the decrease of the U238 effective capture cross section, explaining the very low value of Doppler reactivity This is partially compensated by the diminution of the positive production component, thanks to the decrease of the Pu239 effective fission cross section, preventing the Doppler reactivity from being even lower

The nitride behaviour is very close to oxide's

The capture plus absorption component for the carbide fuel increases a little, leading to a better Doppler reactivity

These differences are mainly the consequence of a spectral effect (fig 2) In the zone of the U238 capture resonances (centred on the group 18 at 1 Kev), the metal core flux is much lower than the others because of the presence of an heavy element in the fuel matrix, Zr(91,40) This is the fundamental difference between metal and the other fuels (composed of light elements O(16,8), N(14,7) and C(12,6) The U238 mass effect, that tends to increase the Doppler coefficient (more U238 atoms in alternative fuels), is entirely dominated by the spectral effect of the metal, inducing the very low reactivity for the metal core, when it balances this effect in nitride and carbide cores, leading to reactivities close to oxide's

SODIUM VOID

The sodium void reactivity is the consequence of a competition between four effects leackage, spectrum, absorption and fission The last three are gathered in a single effect the so called central component (C C) The repartition of the reactivity in leackage and central component (in pcm) for each fuel is shown in the following table and given for the Axial Breeder (A B), the Inner Fuel (I N) and the Outer Fuel (O F)

		OXIDE	METAL	NITRIDE	CARBIDE
A B	C C	+235	+430	+213	+199
	Leackage	-379	-602	-345	357
	Total	-144	-172	-132	-158
I F	C C	+1394	+2546	+1343	+1769
	Leackage	-1095	1550	-1055	-1229
	Total	+239	+996	+288	+540
O F	C C	+319	+664	+305	+400
	Leackage	-730	-1048	-704	-823
	Total	-411	+384	-399	423
SODIUM VOID REACTIVITY		-316	+440	-243	-41

The global reactivity balance is a competition between the positive effect of the central component and the negative effect of leackage The central component is the most important one in the inner zones of the cores, the leackage becoming preponderant in the outer zones The contribution of the axial breeder is approximately the same in any case

The increasing of the sodium void reactivity in the metal fuelled core is due to a strong increase of the central component only partially balanced by a smaller increase of leackage

The phenomena in the carbide and nitride fuelled cores are the same, but with smaller amplitudes, inducing smaller augmentations of the reactivities

Having settled that the variations of reactivities are mainly driven by the central component, we try to explain the variations of this component by an analysis of the neutronic balance characteristics calculated in infinite medium (without leackage), with and without sodium (table 4) The results of this analysis are the followings

In the oxide fuel, the contribution of the oxygen captures can be neglected The hardening of the spectrum during the voiding induces a diminishing of the production term due to the decrease of the fission cross section of Pu239, and an even greater diminishing of the absorption term due to the decrease of the captures of U238, leading to a small increase of the multiplier coefficient

In the metal fuelled core, the hardening of the spectrum is so important that the decrease of the fissions of Pu239 is balanced by the increase of the fissions of U238 The decrease of absorptions being the same than in oxide, this leads to a positive reactivity effect

In the nitride fuel, the contribution of the captures of nitrogen 14 can't be neglected (around 10 % of the total captures) This contribution increases during the voiding, thanks to the spectral hardening which opens the (n,p) and the (n,α) reactions on N14 This tends to decrease the diminishing of absorptions and improve the reactivity effect But the spectral hardening also leading to a smaller decrease of productions the global effect is a little worse than oxide's

In the carbide fuel, productions diminish less than in oxide because of the augmentation of U238 fissions This phenomenon not being compensated induces a far worse effect than oxide's or nitride's, but better than metal's as carbide's spectral hardening is less important than metal's

SENSITIVITY TO PARAMETER VARIATIONS

Two parameters will be discussed here smear density and size of core

SMEAR DENSITY

The present knowledge on use of alternative fuels in LMFBR being far from the one achieved for oxide fuel, uncertainties affecting design parameters are obviously larger Particularly because of swelling characteristics of each fuel, the smear density capable of achieving high discharge burn-up could not exactly be the values previously mentioned So it was interesting to evaluate alternative core performances considering a variation of smear density of more or less five percent

Increasing smear density clearly allows gains on burn-up reactivity variations, but induces penalties on sodium void reactivities Those penalties, compared to the gains, don't justify the increase of the smear density, especially in the metal core which has already a bad sodium void effect

The decrease of smear density induces of course opposite consequences gain on sodium void effects and loss on reactivity variations The low value of sodium void in nitride fuelled core doesn't justify the decrease of smear density, the value chosen appearing to be the appropriate one To have larger margin for carbide and above all to improve safety aspect for metal, a small diminishing of smear density will contribue to decrease sodium void reactivity without too much loss in performances, which will remain far better than oxide's

The nitride, which already has good performances, could then be really advantaged compared to the other fuels

CORE SIZE

To study core size variation, the same calculation as previously described are done on a large size core, EFR type Results are gathered in table 5

The reactivity loss is enormously improved (greater heavy atom mass), especially for metal core in which the goal of a zero reactivity loss is near from being achieved

Doppler reactivities improve too, the relative differences between fuels remaining unchanged This variations of Doppler reactivities are due to an increase of the disparition component thanks to the enormous augmentation of U238 mass, the other components remaining the same as they were in PRISM core

The variations of damage rates are more pronounced than they were in PRISM better improvement in nitride and carbide cores, greater penalties in metal core Those differences came from the augmentation of the mass and the spectral softening The differences weren't significant in a PRISM size core, they can't be neglected any more in an EFR size one The damage rate in the metallic fuelled core is 15 % higher than in oxide and this could balance the improvement of the burn-up reactivity loss Nitride and carbide cores, with a variation of -10 %, could then have better performances than metallic one

The sodium void reactivity becomes positive for all the fuels It results of a diminishing of the leackage component due to the augmentation of core size, and of an increase of the central component induced by the augmentation of the U238 mass then the spectral hardening in the voiding induces more fissions of U238 than it does in a smaller core The augmentation of the central component is more important in the metal fuelled core, inducing a bigger penalty for this fuel

CONCLUSIONS

This study identifies the main characteristics of alternative fuels and the main physical phenomena explaining these characteristics, i e the heavy atom mass and the spectrum Nitride and carbide appear to be close from each other, the only neutronic aspect not being sufficient to choose among them The metal seems to have big safety penalties, but can't be definitely cancelled without further investigations

The next step of the study, which is underway, is to compare the behaviour of these fuels in the main transients, in order to quantify the safety level of the two sizes of core considered when they are using one or the other of these fuels Finally geometrical and conceptual improvements will be examined in order to achieve an optimization of the cores fuelled with the fuels that will successfully pass this safety study

REFERENCES

1 Ph Bergeonneau, G Flamenbaum, J Graveleau, P Marmonier, P Millet, J Rouault et X Talmont, "ETUDE critique du concept de reacteur rapide a combustible metallique preconise par Argonne National Laboratory" (1987)

2 "The prism reactor project", ENS, Genève (1984)

3 U Wehmann, R de Wouters, R Suderland and H Sztark, "Core optimization studies for the European Fast Reactor EFR", International conference on the physics of reactors Marseille (1990)

4 Ph Bergeonneau, "Reactivity effects and dynamic behaviour comparative performances of large LMFBR's oxide and metallic fuel cores", 32nd NEACRP meeting, Argonne (1989)

Table 1. Core characteristics

	PRISM type	EFR type
Fissile volume (m^3)	1 27	11 51
Fissile height (cm)	101	100
Thermal power (MWth)	425	3600
Number of fuel subassemblies	76	376
Number of fuel enrichment zone	2	2
Subassembly pitch (mm)	138 2	188.0
Pin outer diameter (mm)	7 16	8 13
Number of refuelling batches	6	6

Figure 1. Core layouts

PRISM core

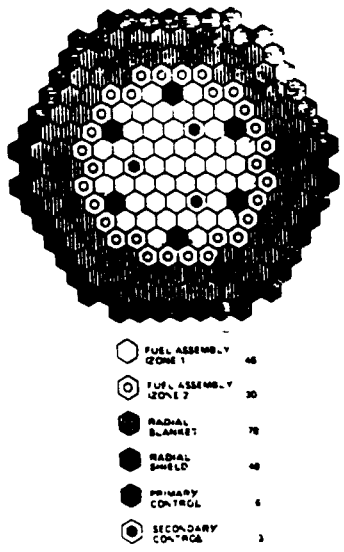

EFR core

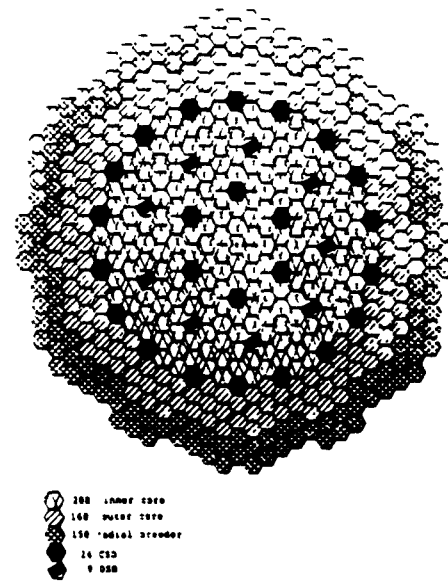

Table 2. PRISM core performances

	OXIDE	METAL	NITRIDE	CARBIDE
Smear density (%)	0 83	0 70	0 80	0 80
Average enrichment (% vol)	23 94	19 76	20 94	20 50
Initial Pu loading (Kg)	939	956	1053	991
Initial U+Pu loading (Kg)	3783	4705	5045	4834
Cycle length (EFPD)	141	141	141	141
Reactivity at BOEC (pcm)*	2683	1945	1963	1792
Reactivity at EOC (pcm)*	-11	-38	+79	-78
Burn up reactivity loss (pcm/EFPD)	19 06	14 03	13 33	13 24
Peak linear rating at BOEC (W/cm)	431	425	447	445
Average discharge BU (MWd/t)	78510	63774	63132	66096
Peak discharge BU (MWd/t)	147978	118840	122032	128069
Peak damage rate (DPA NRT, Fe)	145	152	139	140
Sodium void reactivity at BOEC (pcm)	-316	440	-243	-41
Doppler reactivity at BOEC (pcm)	-725	-339	-748	-827

Table 3. Pseudo cross sections of damage

Group	1	2	3	4	5	6	7	8	9
Energy (KeV)	14 5E3	3 68E3	2 23E3	1 35E3	821	498	302	183	111
Sections	1751	1289	879 8	511 2	378 7	295	221 8	150 1	120 6
Group	10	11	12	13	14	15	16	17	18
Energy (KeV)	67 4	40 9	24 8	15	9 12	5 53	3 36	2 04	1 23
Sections	74 3	84 2	27 9	29 5	32 2	16 3	5 6	3 7	3
Group	19	20	21	22	23	24	25		
Energy (KeV)	0 748	0 454	0 275	0 101	0 0226	0 00306	Th		
Sections	0 4	0 1	0 2	0 5	1 6	4 9			

* BOEC = Beginning Of Equilibrium Cycle
* EOC = End Of Cycle

Table 4. Neutronic balance without leackage

	OXIDE		METAL	
	With Na	Without Na	With Na	Without Na
R	0 381	0 447 (+17 %)	0 478	0 623 (+30 %)
$\Sigma c(P)$	0 014	0 015	0 040	0 033
Σc	2 503	2 181 (13 %)	2 330	1 919 (-18 %)
$\Sigma c(P)/\Sigma c$ (%)	0 6	0 7	1 7	1 7
Σf	2 583	2 515 (-3 %)	2 534	2 528 (~ 0)
$\nu\Sigma f$	7 611	7 427 (-2 %)	7 466	7 471 (~ 0)
Σa	5 088	4 698 (-8 %)	4 864	4 447 (9 %)
$K^* = \nu\Sigma f/\Sigma a$	1 496	1 581 (+6 %)	1 535	1 680 (+9 %)
$\Delta\rho$ (pcm)	+3594		+5623	
	NITRIDE		CARBIDE	
	With Na	Without Na	With Na	Without Na
R	0 427	0 504 (+18 %)	0 390	0 466 (+19 %)
$\Sigma c(P)$	0 276	0 298	0 00	0 00
Σc	3 132	2 821 (-10 %)	2 901	2 510 (13 %)
$\Sigma c(P)/\Sigma c$ (%)	8 8	10 6	0 0	0 0
Σf	2 953	2 910 (-1 %)	2 790	2 729 (-2 %)
$\nu\Sigma f$	8 701	8 594 (-1 %)	8 215	8 053 (-2 %)
Σa	6 087	5 729 (-6 %)	5 693	5 239 (-8 %)
$K^* = \nu\Sigma f/\Sigma a$	1 430	1 500 (+5 %)	1 443	1 537 (+7 %)
$\Delta\rho$ (pcm)	+3263		+4238	

Avec

R - spectral characteristic parameter (R increase ⟹ spectrum hardens)

$\Sigma c(P)$ - section macroscopic of capture of O in oxide, Zr in metal, N in nitride, C in carbide

Σc - section macroscopic of capture

Σf - section macroscopic of fission

$m\Sigma f$ - section macroscopic of production

Σa - section macroscopic of absorption

$K^* = \nu\Sigma f/\Sigma a$ - multiplier coefficient

$\Delta\rho$ - sodium void reactivity without leakage

Table 5. EFR core performances

	OXIDE	METAL	NITRIDE	CARBIDE
Smear density (%)	0.83	0.70	0.80	0.80
Average enrichment (% vol.)	17.08	13.82	15.20	14.90
Initial Pu loading (Kg)	6573	6534	7472	7044
Initial U+Pu loading (Kg)	36996	45905	49338	47266
Cycle length (EFPD)	200	200	200	200
Reactivity at BOEC (pcm)	1818	304	771	549
Reactivity at EOC (pcm)	83	13	1	28
Burn up reactivity loss (pcm/EFPD)	8.67	1.45	3.85	2.60
Peak linear rating at BOEC (W/cm)	419	414	431	432
Average discharge BU (MWd/t)	98458	80518	79166	83152
Peak discharge BU (MWd/t)	150059	125294	122305	128623
Peak damage rate (DPA NRT, Fe)	171	197	154	153
Sodium void reactivity at BOEC (pcm)	1331	3383	1326	1750
Doppler reactivity at BOEC (pcm)	-1254	-608	-1197	-1334

Figure 2. Spectra in PRISM core

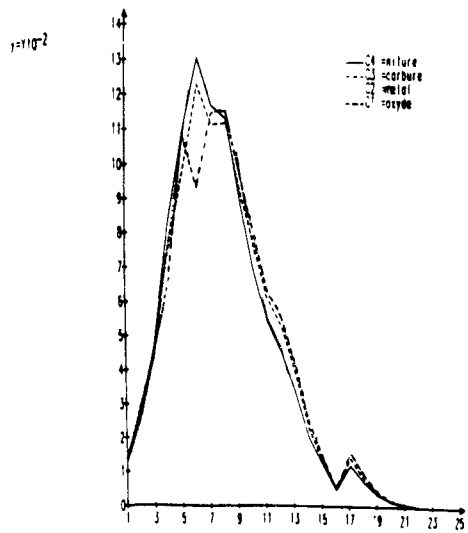

COMPARATIVE NEUTRONIC ANALYSIS OF PB- VERSUS NA-COOLED LMR CORES

J R Liaw, E K Fujita, and D C Wade
Reactor Analysis Division
Argonne National Laboratory
9700 South Cass Avenue
Argonne, Illinois 60439 USA

ABSTRACT

A comparative neutronic study has been conducted on several LMR cores using both lead-magnesium eutectic alloy(97 7% Pb - 2 3% Mg) and sodium as coolant In order to have a consistent comparison for these two coolants on a common basis, i e interchangeable designs, this study used exactly the same reactor core layout, assembly design parameters, and compositions for structure material Only driver fuel enrichments were adjusted respectively for these two coolants in order to meet the same set of requirements for specified burnup cycles Equilibrium cycle performance and coolant void worth were calculated for five different lattice designs, first for sodium coolant and then for Pb-Mg coolant Our results indicated a better neutron economy is achieved in cores using Pb-Mg as coolant which generally have higher breeding performance, smaller burnup reactivity swing, and lower fissile enrichment On the otherhand, linear heat rate goes up, power peaking worsens, and peak fast fluence increases in Pb-Mg cooled cores Some of these problems may be mitigated if the design constraint of interchangeability were relaxed Special emphasis has been put on the void worth comparison between Na and Pb-Mg coolant Quite large negative void worths were obtained for several cases using Pb-Mg as coolant where the Na coolant would have otherwise yielded positive values The differences in void worths were explained from basic physical principles involved in voiding these two coolants The large negative void worth with Pb-Mg coolant is mainly caused by the enhanced leakage component rather than the direct spectral hardening effects of heavy coolants

I. INTRODUCTION

In the early days of fast reactor development, various kind of liquid metals have been considered as coolant [1] Liquid sodium (or NaK eutectic) has been chosen as the preferred coolant for fast reactors worldwide mainly because of its low neutron capture cross section, low melting point, high thermal conductivity, low pumping power requirements, compatibility with fuel and structure materials, and ready availability at low cost Unfortunately, sodium is extremely chemically active, it burns readily in the air and reacts with water violently Furthermore, voiding the sodium from a large Pu-fueled fast reactors usually adds positive reactivity promptly that must be adequately compensated or controlled to prevent possible core damages Consequently, it remains as a prime design goal to reduce the sodium void reactivity to as low as possible level that is still compatible with other performance requirements

Feasibility studies of non-positive void worth in sodium-cooled fast reactors have been reported by Alekseev et al [2] In their studies, the sodium void worth was reduced in a reactor by increasing the contribution from the leakage component They found that non-positive sodium void worths can be achieved in their proposed new generation of high safety LMR cores which use intra-subassembly oxide-metal fuel heterogeneity and ductless lattice designs [3] Enhanced leakage effect that leads to

negative void worth was obtained mainly by reducing both core height and axial blanket or reflector thickness A very extensive evaluation of LMR design options for reducing sodium void worth was also conducted recently by Hill and Khalil [4] In that study, a self-consistent evaluation on a common design basis has been made so that void worth reduction achieveable by various design options were considered at the same time with other associated core physics tradeoffs Their results indicated that a tightly coupled, radially heterogeneous configuration can be designed to yield an acceptably low void worth with some compromise in breeding gain and fissile loading requirement. However, the sodium void worth, though being reduced substantially in many ways, generally remains finite and positive Design options seemed exhausted in order to reduce the sodium void worth any further without deviating too far from the conventional large sodium-cooled Pu-fueled fast reactor design concepts

The positive reactivity worth of voiding sodium is caused mainly by eliminating its moderating power thus hardens the spectrum This effect might be alleviated with the use of heavy coolants which will not slow down neutrons during collisions as much as light coolants Therefore voiding the heavy coolants will not harden the spectrum as much as if sodium is voided Calculations made in 1960 by Yifta and Okrent [5] indicated that negative void worths were obtained for Pb-Bi eutectic (44 5% Pb - 55 5% Bi) cooled large reactors which the conventional sodium coolant would normally produce highly positive values Recently a renewed interest has also been expressed by the Russian designers [2,6] to replace sodium by lead as coolant which they hope might reduce the void worth to nearly zero or even negative values Furthermore, lead is chemically benign with air and water, thus avoiding sodium fire and explosion concerns in the conventional LMR designs Lead is also much heavier than sodium so that its inertia might enable a better natural circulation when pumps are tripped

In recent years, the emphasis on the design of LMRs has been placed upon its inherent safety rather than maximizing its breeding performance Hence stringent thermal-hydraulic requirements for a tight lattice and compact core in conventional LMR designs can be relaxed It is appropriate to re-evaluate the non-conventional concept of using heavy metals such as lead or its eutectic as coolant in LMR designs This paper summarizes a comparative neutronic study conducted on typical LMR designs using both lead-magnesium eutectic (97 7% Pb - 2 3% Mg) and sodium as coolant In order to have an objective comparison between these two coolants, this study used exactly the same reactor core geometries, assembly design parameters, and compositions for structure material Only coolant sodium is replaced by Pb-Mg eutectic composition and the fissile enrichment of the drivers is adjusted for each design accordingly Special emphasis has been put on void worth comparison between Pb-Mg and Na coolant Other performance parameters will also be analyzed in order to see the associated core physics performance differences between these two coolants

II. PROPERTIES OF PB-MG AS REACTOR COOLANT

The small amount of Mg in the Pb-Mg eutectic lowers the melting point of the alloy to ~ 250C (482F) from that of pure lead at ~ 327C (621F) Its contribution to the neutronic performance is relatively insignificant Therefore we will focus our attentions on the comparisons between Pb and Na, without paying much attention to Mg even though it is included in all of our calculations

The density of Pb is ~ 13 times that of Na and the atomic weight of Pb is ~ 9 times that of Na For a fixed geometry (or volume), the lead coolant will have ~ 40 % more atoms per cm^3 than that for sodium coolant Furthermore, the melting point of Pb is 621F and the boiling point is ~ 3159F, both are much higher than that for Na, giving it a substantially larger working fluid range (melting to boiling) than does sodium According to a thermal-hydraulic comparison analysis for Pb and Na coolant, [7] it is found that he Pb-cooled reactor will have much higher (~ 17 times) pumping power requirements, higher natural circulation velocity at higher clad temperature, more severe fluid

hammer effects due to sudden velocity changes, and harder to design a guard heating system to keep the coolant temperature above the melting point in order to prevent local freezing

Since Pb atom is heavy, the energy loss of a neutron colliding with Pb nucleus will be very small The maximum fractional energy loss per collision for neutrons with Pb is ~ 2% whereas that for Na is ~ 16% Therefore, for a fixed fuel and structure composition, a reactor with Pb coolant will have a harder neutron spectrum than that with Na coolant. Consequently its fertile fission bonus will be higher, thus its breeding performance will be enhanced In this study we fixed the lattice geometry and structure compositions, but the fissile enrichment is adjusted for each coolant. So the benefit of harder neutron spectrum using Pb as coolant is realized by reducing the fissile enrichment Consequently a core using Pb coolant does not necessarily have a significantly harder spectrum than that using Na coolant as we shall see later

In the energy range between 50 keV and 1 MeV where most of the neutrons will have in a typical LMR design, the capture cross section of Pb is ~ 10^{2} to 10^{3} barns, which is ~ 5 to 10 times larger than that for Na. The transport cross section in that same energy range for Pb is ~ 5 to 10 barns, which is ~ 2 to 3 times that for Na. Consequently, the substitution of Na by Pb will increase the coolant capture reaction rate slightly (due to a small value of σ_c of Pb) and reduce the leakage rate more significantly (smaller diffusion coefficient due to larger value of σ_{tr} of Pb) Both the spectral and the leakage effects contribute to a better neutron economy for the Pb-cooled LMRs However, neutron leakage rate is greatly enhanced by a larger δD and a larger flux gradient $\nabla\phi$ when Pb coolant is voided More discussions on the effects of Pb-coolant voiding will be given in later sections

III. DESCRIPTIONS OF LMR CORES AND CALCULATIONS

In this study, the LMR reference design is a 900 MWt, tightly coupled, radially heterogeneous core which has been analyzed in reference 4 The core layout is shown in Fig 1 This design has an equivalent core diameter of ~ 90 in for the 199 subassemblies inside the radial blankets and the steel shields interface The active driver fuel height is 38 in with no axial blanket extension Both internal and radial blankets have active fuel height of 38 in. as well

A systematic variations from the reference case were made on the assembly mechanical designs to investigate their effects on neutronic performance parameters A total of five different cases as shown in Table 1 were studied Three driver pin sizes (0 25, 0 285, and 0 32 in) and three pitch to diameter (P/D) ratios (1 18, 1 36, and 1 54) were chosen Such changes redistribute the core volume between the existing three materials fuel, structure, and coolant In each design, the structural material is HT-9 steel The duct wall thickness is fixed at 0 14 in and the cladding thickness is set to 0 077 x driver pin diameter to conserve the hoop stress The blanket pin diameter is proportional to the driver pin diameter The interassembly gap sizes were determined by standard assembly design calculations For smaller P/D bundles, the pressure drop is larger thus a larger interassembly gap is needed to accommodate the larger duct dilation As P/D increases, the fuel volume fraction is reduced and the coolant volume fraction increases while the structure volume fraction remains nearly constant. The core size changes from ~ 90 in (case #2) to ~ 129 in (case #5) as the lattice pitch changes Case #2 is the reference LMR design which has a small pitch-to-diameter ratio and a large pressure drop (57 psi) due to tight lattice design When the P/D increases, the coolant volume fractions increases significantly (from less than 30% in case #2 to more than 45% in case #5) Therefore we anticipate a larger impact will result when increased amount of coolant is voided Sodium bond was assumed for all cases Only the flowing sodium and the interassembly gap sodium were replaced by Pb-Mg in this comparative study

Equilibrium cycle performance and coolant void worth calculations were performed for each case, first for sodium coolant and then for the Pb-Mg coolant The refueling cycle length is 365 days and the capacity factor is 80% Fissile enrichments and fuel residence times were adjusted in each case so that the discharge burnup would be roughly the same The equilibrium cycle performance parameters were calculated by REBUS-3 code [8] using the nodal option in hex-z 3-D geometry with a 9-group ENDF/B-V neutron cross section set Coolant void worths were calculated for the End-of-Equilibrium-Cycle (EOEC) core compositions with a 21-group ENDF/B-V neutron cross section set Real fluxes were calculated for the flooded states and adjoint fluxes were calculated for the voided states Exact perturbation theory was assumed and the edits of coolant void reactivity worths were given by regions as well as by reaction types or components

IV. EQUILIBRIUM CYCLE PERFORMANCE PARAMETERS

Table 1 shows the key performance parameters for the LMR cores for the five cases with both Na and Pb-Mg as coolant side by side for easy comparison The impacts and interpretations of the lattice design variations on performance parameters have been addressed in detail in reference 4 for sodium coolant and therefore would not be repeated here Only the differences in performance parameters between the Na coolant and the Pb-Mg coolant will be highlighted and analyzed in the following paragraphs

For the reasons mentioned in Section II, a lead cooled core will have better neutron economy for breeding, thus leads to a smaller burnup reactivity swing and a lower fissile loading requirement This can easily be seen in comparing the results between Na and Pb-Mg coolants in the reference design (case #2) for the following items: (i) the breeding ratio with Na is 1 055 versus 1 138 with Pb-Mg, (ii) the burnup swing with Na is 0 599% versus -0 285% $\delta k/kk'$ with Pb-Mg, (iii) the fissile loading with Na is 367 1 versus 329 1 kg/y with Pb-Mg, and (v) the neutron leakage out of the driver, internal and radial blankets is 23 8% with Na versus 20 3% with Pb-Mg

Since our design approach is based on a fixed lattice geometry and searching for the fuel enrichment to sustain a burnup cycle, a core with better neutron economy will have lower fissile enrichment Consequently, a higher flux level will be required in order to produce the same power output In general the flux levels in lead cooled core are roughly 20-30% higher than that cooled by sodium This higher flux level in lead cooled core shifts power to the blanket regions, causes higher power peaking and larger flux gradients in outer core regions, and enhances the leakage component of coolant void reactivity worths However, optimizing the core layouts for the Pb-Mg coolant would alleviate the power peaking problem

The variation of fissile enrichments versus P/D (cases #2, #3, #4) for a fixed pin diameter of 0 285 in using Na or Pb-Mg as coolant are shown in Fig 2 A difference of ~ 2 to 3 % in fissile enrichments is found between Na and Pb-Mg coolant As P/D increases for a fixed pin diameter, the coolant volume fractions increase at the expense of fuel volume fractions This leads to a higher fissile enrichments for the drivers The two curves in Fig 2 are very similar indicating that the variations in P/D for both coolants will have similar impacts on core performance parameters

For a fixed pitch to diameter ratio (P/D = 1 54), the variation of fissile enrichments versus pin diameter from 0 25, 0 285, to 0 32 in (cases #1, #4, #5) can be found in Table 1 Such a variation reduces coolant fraction and increases fuel fraction, just the opposite to the previous variation The neutron economy improves in these cases as pin diameter increases and the breeding performance gets better This leads to lower annual fissile makeups and smaller burnup reactivity swings as pin diameter increases Of course the initial fissile requirement will increase as the pin diameter increases in these cases The advantage of Pb-Mg over Na as coolant in neutron economy is still clearly being maintained

V. COOLANT VOID WORTH COMPARISON

Coolant void worths were calculated for the EOEC core compositions and the results are summarized in Table 1 for the five cases with both Na and Pb-Mg as coolant. As expected the coolant void worth does become smaller when Na is substituted by Pb-Mg in all cases In several cases where coolant volume fraction is large (cases #1, #4, and #5 with P/D = 1 54), the void worths turn into negative values as postulated for Pb-Mg coolant The trends of coolant void reactivity worths versus lattice design parameter changes will be discussed in this section The differences in void worth resulting from differences in the nuclear properties of the coolants will be discussed in the next section

For a fixed pin diameter of 285 in , the impact of varying P/D from 1 18, 1 36 to 1 54 (cases #2, #3, and #4) on the void worth can be seen in Fig 3 As the P/D ratio increases, larger amount of coolant will be voided and one may anticipate a larger impact on the reactivity worths For Na coolant, the void worths exhibit some non-linear behavior and its explanation has been given in reference 4 However, the void worths for Pb-Mg coolant show a steady decline trend as the P/D increases The margin in void worth between Na and Pb-Mg coolant widens from ~ 10 to ~ 30 (x 10^{-3} $\delta k/kk'$) as P/D increases from 1 18 to 1 54 As shown in Table 1, most of the difference is contributed by the drivers and the radial blankets with small contribution by the inner blankets

For a fixed P/D ratio, the impact of varying pin diameter from 0 25, 0 285, to 0 32 in (cases #1, #4, and #5) on the void worth can be seen in Fig 4 As the pin diameter increases, the assembly size and core size increase proportionally But the fuel and coolant volume fractions remain relatively invariant The increase in core size will affect the spectral and capture components of the void worth more significantly than the leakage component which comes predominantly from the peripheral regions of the reactor As can be seen in Table 1, the Pb-Mg coolant void worths are negative for all three cases where otherwise the Na void worths are highly positive The increasing trends of void worths for Na and Pb-Mg as coolant are similar, with a fixed margin of ~ 30 x 10^{-3} $\delta k/kk'$ being maintained for all three cases Again, most of the difference comes from the radial blankets, some from the drivers, and very small difference is from the internal blankets The trends of void worths in Figs 3 and 4 due to varying lattice parameters are fairly similar for both the Na coolant and the Pb-Mg coolant The interpretation of these trends for Na coolant in reference 4 is generally applicable to the Pb-Mg coolant. Therefore we will focus our attention in next section mainly on the differences (margins) in void reactivity worths between Na and Pb-Mg as coolant for the reference LMR design (case #2)

VI. PHYSICAL INTERPRETATIONS OF VOID WORTH DIFFERENCES

In order to fully understand these trends observed in Figs 3 and 4, especially what causes the large margins between Na and Pb-Mg coolants, one needs to look into the basic physical reasons involved in coolant void reactivity worth According to Hummel and Okrent, [9] there are three major components that make up the bulk of coolant void reactivity worth They are the capture, spectral, and leakage component Relatively smaller contributions from fission reactions and the fission source (nu-fission) terms are also found when coolant is voided They can be neglected in most cases in this study (see Table 2) Reactivity contributions from each of these three major components may be positive or negative with varying magnitudes depending on which regions are voided The intricate interplay of these components from various regions of the reactor determines the total void reactivity worth

In the next few paragraphs, we will use the same notations for void worth formula as those found in reference 9 without further clarifications However, it is important to note here that the perturbation denominator N defined as following

$$N = \int_V (\sum_k \chi_k \phi^*_k) \sum_j (\nu\Sigma_f)_j \phi_j dV \quad (1)$$

remains relatively invariant for this comparative study It is a normalization constant depending mainly on the reactor power Therefore for a fixed reactor power at 900 MWt, its value changes very little (< 5 %) between cases in this study Thus we can assume the perturbation denominator N to be a constant in the following discussions so that it does not complicate the analysis unnecessarily

VI.1 Spectral Component

The increase of η (ratio of neutron production to absorption) with neutron energy enables the production of excess neutrons for breeding in a fast reactor However, this increase of η with energy leads to an increase in the excess neutrons produced when the coolant is voided and the spectrum hardens, thus adding a positive reactivity to the reactor This effect can be quantified as the spectral component of void reactivity worth as following

$$\delta k_j^{spec} = \frac{1}{N} \int_V \phi_j \sum_{k \neq j} (\phi^*_k - \phi^*_j) \delta\Sigma_s(j \rightarrow k) dV \quad (2)$$

where $\delta\Sigma_s$ is the change in the total scattering cross section caused by voiding the coolant, ϕ^* is the perturbed adjoint flux, N is the perturbation denominator, and j and k are energy group indices The spectral component can become increasingly dominant if the core volume V is allowed to increase, thus leading to a positive coolant void worth in large conventional LMRs

When Na coolant is substituted by the Pb-Mg coolant, major impacts on the spectral component are the following (i) increased flux level ϕ_j which is needed to maintain the same total reactor power output due to the reduced fissile enrichment, and (ii) increased magnitude of perturbation $\delta\Sigma_s$ due to more Pb-Mg atoms are removed and larger scattering cross section of Pb than Na Both of these factors make the spectral component of void worth of Pb-Mg coolant larger than that of Na coolant in the interior regions of the reactor where spectral component is most important As can be seen from Table 2, the spectral component from Pb coolant is roughly 30% higher than that from the Na coolant in the interior regions such as inner core and internal blankets Whereas in the peripheral regions of the reactor such as gas plena, radial blankets and radial shields, the Na coolant has higher spectral component than the Pb coolant

Comparison of the neutron spectra for the inner core region, either flooded or voided, revealed that both Na and Pb-Mg coolants have quite similar neutron energy characteristics The hardening of the spectrum due to voiding was observed for both coolants As P/D increases for a fixed pin diameter, the hardening of neutron spectrum is more enhanced which should also make the capture and spectral components of void worth more positive But the increase in leakage component (negative) in the peripheral regions is even larger, thus make it overshadow the spectral contribution and hence dominating the total coolant void worth as we shall see in the next section

VI.2 Leakage Component

The leakage component of coolant void worth can be expressed as follows

$$\delta k_j^{leak} = -\frac{1}{N}\int_V \delta D_j \nabla\phi_j \nabla\phi_j^* dV \tag{3}$$

which accounts for the fact that loss of coolant allows more neutrons to escape the core leading to a reactivity loss This component may dominate for small and leaky LMRs leading to a negative void worth

The difference in the leakage component when Na is substituted by Pb-Mg is caused by the following (i) increased magnitude of perturbation on the diffusion coefficient of a region δD_j, and (ii) increased spatial gradient of the flux ϕ_j and/or adjoint ϕ_j^* due to higher flux levels that are needed in Pb-Mg cooled cores to maintain same power level with lower fissile enrichments These fluxes must vanish at the extrapolation distances for a fixed core boundary for both coolants respectively It is important to note that the leakage component is dependent on the spatial flux shape, i e , the gradient Thus, the effect comes predominantly from the core boundaries where the gradient is usually the largest The bulk of the difference in total coolant void reactivity worths between Na and Pb-Mg coolant is caused by the leakage components near the core boundaries, i e , outer core and radial blanket regions

The leakage component for Pb coolant is roughly a factor of 2 to 3 of that for Na coolant in almost every region of the core, even the central regions where the flux gradients are very small This difference is mainly caused by the perturbation in diffusion coefficient between these two coolants The perturbation δD_j can be calculated as follows

$$\delta D_j^{void} = \frac{\delta\Sigma_{tr}}{3\Sigma_{tr}\Sigma_{tr}} \tag{4}$$

where Σ_{tr} is the transport cross section of the perturbed (or voided) state The macroscopic transport cross section Σ_{tr} consists of three components

$$\Sigma_{tr} = N_c\sigma_{trc} + N_s\sigma_{trs} + N_f\sigma_{trf} \tag{5}$$

where the first term represents coolant, the second term represents structure, and the third term represents fuel Most of the contribution to Σ_{tr} comes from the structure (~ 65 %), followed by that from fuel (~ 20 %), and then by coolant (~ 15 %) Since the bulk (~ 85 %) of Σ_{tr} will not be affected when Na is substituted by Pb-Mg in this study, the denominator in Equation 4 remains roughly constant for both coolants Therefore the perturbation in diffusion coefficient is mainly determined by $\delta\Sigma_{tr}$

To a good approximation, we can express the perturbation on the transport cross section as

$$\delta\Sigma_{tr} = \delta N_c\sigma_{trc} + N_s\delta\sigma_{trs} + N_f\delta\sigma_{trf} \tag{6}$$

where the first term accounts for the change in coolant number density, the second and third term account for the transport cross section changes in structure and fuel due to spectral hardening of voiding the coolant Due to larger number of Pb-Mg atoms are removed and the transport cross section of Pb is larger than that for Na by a factor of two or more, the first term for Pb coolant is therefore larger than that for Na coolant in proportion The differences in the second and third term between Pb and Na coolant are relatively smaller when compared to the first term Thus the perturba-

tion in $\delta\Sigma_x$ due to coolant voiding on the leakage components is a multiplier to the flux gradients $\nabla\phi$ and $\nabla\phi^*$ in equation 3 This fact can be seen from the data shown in Table 2 where the leakage components from almost all regions of the reactor are a factor of two or more for Pb coolant than that for Na coolant, even in the core central regions where the flux gradients are small

VI.3 Capture Component

The capture component of coolant void reactivity worth is calculated from the expression

$$\delta k_j^{capt} = -\frac{1}{N}\int_V \delta\Sigma_{cj}\phi_j\phi^*_j dV \qquad (7)$$

which is the reactivity gain caused by the elimination of coolant capture as well as the reduction of capture by other materials due to the hardening of the neutron spectrum when coolant is voided

The difference in the capture component when Na is substituted by Pb-Mg are the following (i) increased magnitude of perturbation in $\delta\Sigma_{cj}$ due to more Pb-Mg atoms are removed and higher capture cross section for Pb-Mg coolant than Na coolant, a factor of 3 larger (more negative) can be seen in Table 2 for Pb coolant in most regions, and (ii) increased flux level ϕ_j in the driver regions needed to maintain the same total reactor power output due to reduced fissile enrichment Both of these factors make the capture component larger for the Pb coolant than the Na coolant Compared to the spectral and leakage components, the capture component contributes rather small amount of reactivity to the total coolant void worth in all cases in this study

VII. CONCLUSIONS AND DISCUSSIONS

Based on the analysis performed and the results obtained in this study, we concluded the following

1 Major differences in basic nuclear data between Pb and Na are the following (i) the transport cross section for Pb is ~ 2 to 3 times that for Na, (ii) the capture cross section of Pb is ~ 5 to 10 times that for Na, but the magnitude is relatively small, and (iii) for a fixed lattice design, there are 40% more Pb atoms than Na atoms These differences manifest themselves in equilibrium cycle performance parameters as well as coolant void worths rather directly

2 Equilibrium cycle analysis indicated that the Pb-Mg cooled LMR cores in general have better neutron economy over the Na cooled cores Higher breeding ratios, lower burnup reactivity swings, and lower fissile loadings are obtained for the Pb-Mg cooled cores However, power peaking, linear heat rates, discharge burnups, and fast fluences suffered degradation in the Pb-Mg cases (The power peaking and linear heat rating can be improved if the design constraint of interchangeability were relaxed) Such results are the consequences of higher flux levels in Pb-Mg cooled cores that are required to maintain the same power output with reduced fissile enrichment for a fixed core geometry Spectral effects from substituting Na by Pb-Mg do not have dramatic and direct impacts on neutronics as one have anticipated intuitively

3 Coolant void worths are reduced substantially in the Pb-Mg cases over the Na cases Negative values were achieved in three cases where the coolant fractions are large (P/D = 1 54) with Pb-Mg coolant where otherwise Na coolant would have yield large positive void worths The trends of void worths versus lattice design parameters are fairly similar between Pb-Mg and Na coolant A favorable margin of void worth is maintained for Pb-Mg over Na as coolant in all cases

4 The bulk (> 80%) of differences in coolant void worths between Pb-Mg and Na coolant is caused by the leakage component from outer regions of the reactor There are two main reasons for the enhanced leakage effect in Pb-Mg coolant (i) the magnitude of perturbation in diffusion coefficient due to voiding Pb-Mg is ~ twice as large as that for Na coolant, and (ii) the flux gradients are larger for Pb-Mg coolant due to higher flux levels needed to maintain the same power density with lower enrichment fuel in drivers

5 The lattice design and core configuration are based on the LMR design which was optimized for the Na coolant. Therefore the neutronic performance of these cases may be improved for the Pb-Mg coolant if we re-optimize the LMR design

6 Some other heavy liquid metal coolants which have similar neutronic properties as the Pb-Mg eutectic but lower melting points may worth our consideration in future studies One is lead-bismuth (44 5% Pb - 55 5% Bi) which has a melting point of 257F (125C) and the boiling point of 3038F (1670C) The other one is the lead-bismuth-tin ternary alloy (50% Bi - 31 2% Pb - 18 8% Sn) which has a melting point of only ~ 94C (201F)

7 Although Pb-Mg cooled LMRs have improved coolant void reactivity worths over the sodium cooled LMRs, several thermal-hydraulic design issues need to be addressed Some of the key concerns are (i) pumping power requirement, (ii) higher natural circulation velocity at higher clad temperature, (iii) more severe fluid hammer effect, and (iv) guard heating system to prevent local freezing Finally, the chemical compatibility of Pb-based coolants were not addressed at all in this neutronics scoping study

REFERENCES

1 L E Crean & W E Parkins, "Liquid Metal Cooled Reactors," Reactor Handbook, Vol IV, 2nd Edition, John Wiley & Sons, Inc , 1964

2 P N Alekseev, et al , "Feasibility of Nonpositive Void Reactivity Effect in the Fast Sodium Reactors of Enhanced Self-Protection," NEACRP-A-1014, 32nd NEACRP Meeting in Chicago, October 1989

3 P N Alekseev, et. al , "Concept of the New Generation High Safety Liquid Metal Reactor (LMFR)," Proc Intl Conf on Safety of New Generation Power Reactors, Seattle, May 1988

4 R N Hill & H Khalil, "An Evaluation of LMR Design Options for Reduction of Sodium Void Worth," Proc Intl. Conf on the Physics of Reactors Operation, Design and Computation, Marseille, Vol II 19, April 1990

5 S Yifta & D Okrent, "Some Physics Calculations on the Performance of Large Fast Breeder Power Reactors," USAEC Report ANL-6212, Argonne National Laboratory, December 1960

6 E P Velikhov, et al , "The High Safety and Economy NPP With Liquid Lead-Cooled Reactors," Nuclear Power and Industry Ministry, USSR, Moscow 1990

7 Ralph M Singer, Argonne National Laboratory, private communications, March 1990

8 B J Toppel, "A User's Guide to the REBUS-3 Fuel Cycle Analysis Capability," ANL-83-2, Argonne National Laboratory, March 1983

9 H H Hummel & D Okrent, Reactivity Coefficients in Large Fast Power Reactors, Chapter 4, "Sodium-Void Effect," American Nuclear Society, 1970

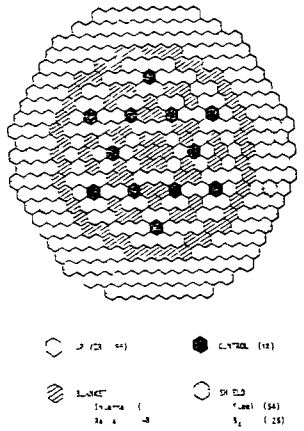

Fig. 1. Reference LMR core layout

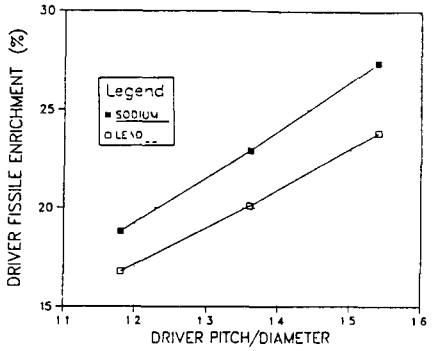

Fig. 2. Driver fissile enrichment versus P/D ratio for 0.285 in. pin

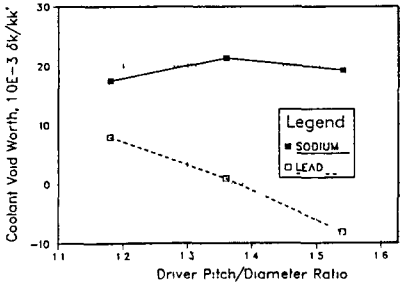

Fig. 3. Coolant void worth versus P/D ratio for 0.285 in. pin

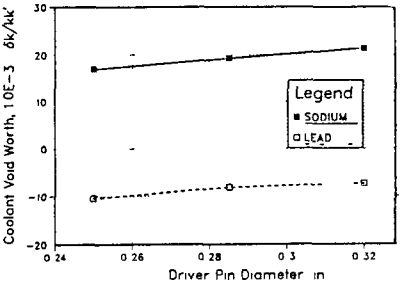

Fig. 4. Coolant void worth versus pin diameter for P/D = 1.54

TABLE 1. PERFORMANCE CHARACTERISTICS FOR LMR CORES

	Case #1		Case #2		Case #3		Case #4		Case #5	
DRIVER PIN DIAMETER, in	.25		.285		.285		.285		.320	
DRIVER PIN P/D	1.54		1 18		1 36		1.54		1 54	
LATTICE PITCH in	6 9		6 1		6 9		7 7		8 7	
DRIVER RESIDENCE TIME, Cycles	3		4		4		4		5	
COOLANT	Na	Pb	Na	Pb	Na	Pb	Na	Pb	Na	Pb
BURNUP REACTIVITY SWING %Δk	3 535	3 051	0 599	-0 285	1 810	1 147	2 667	2 302	2 117	1 860
BREEDING RATIO										
Driver	2993	.3579	4474	4944	.3805	4365	.3224	.3829	.3419	4052
IB	2930	.3347	.3979	4348	.3493	.3884	.3036	.3413	.3096	.3431
RB	1563	1704	2097	.2091	1923	1934	1726	1759	1771	1801
Total	7585	8630	1 0550	1 1382	9223	1 0184	7985	9001	8235	9284
PEAK LINEAR POWER, kw/ft										
Driver (BOL)	14 9	15 9	14 4	14 8	14 7	15.5	15 1	16 2	15.3	16 1
Blanket (EOL)	9 0	10 9	14 4	16 1	11 5	13 5	9 6	11 6	10 0	11 9
POWER PEAKING FACTOR	1.576	1 682	1 701	1 744	1 621	1 713	1 614	1 726	1 644	1 722
PEAK/AVG DISCHARGE BURNUP, MWd/kg										
Driver	150/110	155/109	150/104	151/102	149/108	154/107	153 112	161/110	154 111	163/110
IB	30/19	35/21	49/31	55/34	40/25	46/27	33 21	36/22	34/20	39 22
RB	15 6.3	15/5 6	23/8 7	22/8 0	19/7 7	19/7 0	17/6 6	17/6 0	17 6 6	17/5 9
PEAK FAST FLUENCE, 10^{23}n/cm^2	2 29	2 77	3 51	3 96	2 93	3 45	2 48	3 02	2.59	3 16
MASS FLOWS, kg/y										
Fissile (driver)	586 1	507 9	367 1	329 1	447 6	394 0	537.3	466 8	515 4	448 0
DRIVER FISSILE ENRICHMENT, % HM	29 2	25 3	18 8	16 8	22 9	20 1	27 4	23 8	26 1	22 7
HEAVY METAL LOADING, kg/y										
Driver	2008 8		1958 1		1958 0		1958 1		1974 8	
IB	1336.3		1295 8		1308 3		1302 9		1314 4	
RB	1491 6		1446 4		1460 4		1454 4		1467.3	
Total	4836 7		4700 3		4726 7		4715 4		4756.5	
NEUTRON LEAKAGE[a]										
BOEC	27 8	22 7	23 8	20 3	25 4	21 0	26 8	21 7	25 9	20 8
EOEC	29 4	23 9	24 0	20 1	26 1	21 2	27 9	22 4	26 8	21.3
COOLANT VOID WORTH, 10^{-3} Δk/(kk')										
Driver	9 95	- 5 04	11 18	4 90	12 93	2 16	11 42	- 2 47	12 68	- 0 89
IB	13 23	10 25	8 20	7 77	12 48	11 12	13 94	10 72	14 22	10 63
RB	3 48	-14 80	0 52	- 4 09	- 1 65	9.58	- 2 87	13 46	- 2 43	12 51
Total[b]	17 00	-10 04	17 51	7 95	21 38	0 92	19 27	- 8 18	20 58	7 36

[a]Neutron leakage out of the Driver, IB, and RB regions.
[b]Drive plus IB, includes their upper plenum regions.

Table 2. Comparison of coolant void worth by regions and components for the reference LMR core

COOLANT	REGION	REACTION / COMPONENT						SUM OF REACTIONS
		CAPTURE	FISSION	NU-FISSION	SPECTRAL	R-LEAKAGE	Z-LEAKAGE	
NA	ICORE	1 84E-04	1 42E-05	-5 75E-05	3 97E-03	-1 07E-04	-9 17E-04	3 09E-03
PB	ICORE	5 81E-04	8 69E-06	-3 29E-05	5 17E-03	-2 60E-04	-2 42E-03	3 06E-03
NA	MCORE	3 85E-04	2 12E-05	-8 66E-05	7 88E-03	-3 68E-04	-1 97E-03	5 86E-03
PB	MCORE	1 21E-03	8 20E-06	-3 02E-05	1 01E-02	-1 00E-03	-5 08E-03	5 20E-03
NA	OCORE	3 57E-04	-5 04E-06	2 68E-05	7 15E-03	-3 37E-03	-1 92E-03	2 24E-03
PB	OCORE	1 05E-03	-5 71E-06	3 26E-05	8 76E-03	-8 83E-03	-4 36E-03	-3 35E-03
NA	TCORE	9 26E-04	3 03E-05	-1 17E-04	1 90E-02	-3 84E-03	-4 81E-03	1 12E-02
PB	TCORE	2 85E-03	1 12E-05	-3 05E-05	2 40E-02	-1 01E-02	-1 19E-02	4 90E-03
NA	ICPL	5 51E-06	0 0	0 0	1 77E-04	-1 81E-05	-3 93E-04	-2 28E-04
PB	ICPL	1 11E-05	0 0	0 0	1 03E-04	-4 69E-05	-7 05E-04	-6 37E-04
NA	MCPL	9 36E-06	0 0	0 0	3 57E-04	-4 77E-05	-8 78E-04	-5 60E-04
PB	MCPL	2 07E-05	0 0	0 0	2 02E-04	-1 10E-04	-1 52E-03	-1 41E-03
NA	OCPL	1 09E-05	0 0	0 0	3 18E-04	-2 04E-04	-8 29E-04	-7 04E-04
PB	OCPL	2 00E-05	0 0	0 0	1 75E-04	-3 52E-04	-1 35E-03	-1 51E-03
NA	TCPL	2 57E-05	0 0	0 0	8 52E-04	-2 70E-04	-2 10E-03	-1 49E-03
PB	TCPL	5 18E-05	0 0	0 0	4 81E-04	-5 09E-04	-3 58E-03	-3 56E-03
NA	IBLKT	9 12E-05	1 92E-06	-5 73E-06	1 84E-03	-4 25E-05	-2 14E-04	1 67E-03
PB	IBLKT	2 38E-04	1 06E-06	-1 16E-07	2 13E-03	-1 10E-04	-6 07E-04	1 65E-03
NA	MBLKT	2 35E-04	2 00E-06	-5 96E-06	4 28E-03	-4 51E-05	-5 50E-04	3 92E-03
PB	MBLKT	6.15E-04	-1 07E-06	1 18E-05	5 02E-03	-1 26E-04	-1 59E-03	3 93E-03
NA	OBLKT	1 67E-04	-8 73E-07	3 27E-06	3 08E-03	-2 03E-04	-4 34E-04	2 61E-03
PB	OBLKT	4 34E-04	-2 23E-06	1 07E-05	3 55E-03	-6 59E-04	-1 14E-03	2 19E-03
NA	INBKT	4 94E-04	3 05E-06	-8 43E-06	9 21E-03	-2 91E-04	-1 20E-03	8 20E-03
PB	INBKT	1 29E-03	-2 25E-06	2 24E-05	1 07E-02	-8 95E-04	-3 34E-03	7 77E-03
NA	IBPL	2 62E-06	0 0	0 0	7 23E-05	-1 01E-06	-1 28E-04	-5 43E-05
PB	IBPL	4 53E-06	0.0	0 0	4 09E-05	-1 83E-06	-2 41E-04	-1 97E-04
NA	MBPL	4 47E-06	0 0	0 0	1 79E-04	-1 68E-05	-3 44E-04	-1 78E-04
PB	MBPL	9 22E-06	0 0	0 0	9 63E-05	-4 13E-05	-6 13E-04	-5 48E-04
NA	OBPL	3 78E-06	0 0	0 0	1 19E-04	-1 89E-05	-2 59E-04	-1 54E-04
PB	OBPL	7 09E-06	0 0	0 0	6 52E-05	-3 00E-05	-4 58E-04	-4 16E-04
NA	INPL	1 09E-05	0 0	0 0	3 71E-04	-3 67E-05	-7 31E-04	-3 86E-04
PB	INPL	2 08E-05	0 0	0 0	2 02E-04	-7 32E-05	-1 31E-03	-1 16E-03
NA	RBLKT	1 07E-04	-2 87E-06	1 66E-05	1 89E-03	-2 34E-03	-1 94E-04	-5 24E-04
PB	RBLKT	2 08E-04	-1 95E-06	1 22E-05	1 73E-03	-5 61E-03	-4 39E-04	-4 09E-03
NA	RDPL	3 44E-06	0 0	0 0	9 14E-05	-1 50E-04	-1 45E-04	-2 00E-04
PB	RDPL	4 79E-06	0 0	0 0	4 33E-05	-2 41E-04	-2 26E-04	-4 19E-04
NA	REACT	1 53E-03	3 05E-05	-1 09E-04	3 01E-02	-6 47E-03	-6 20E-03	1 89E-02
PB	REACT	4 34E-03	6 98E-06	4 05E-06	3 65E-02	-1 66E-02	-1 56E-02	8 57E-03
NA	TOTAL	1 57E-03	3 05E-05	-1 09E-04	3 14E-02	-6 93E-03	-9 18E-03	1 68E-02
PB	TOTAL	4 42E-03	6 98E-06	4 05E-06	3 72E-02	-1 74E-02	-2 08E-02	3 43E-03

REGION DEFINITION

ICORE = INNER CORE
MCORE = MIDDLE CORE
OCORE = OUTER CORE
TCORE = TOTAL CORE

ICPL = INNER CORE PLENUM
MCPL = MIDDLE CORE PLENUM
OCPL = OUTER CORE PLENUM
TCPL = TOTAL CORE PLENUM

IBPL = INNER BLKT PLENUM
MBPL = MIDDLE BLKT PLENUM
OBPL = OUTER BLKT PLENUM
INPL = TOTAL BLKT PLENUM

IBLKT = INNER BLKT
MBLKT = MIDDLE BLKT
OBLKT = OUTER BLKT
INBKT = TOTAL BLKT

RBLKT = RADIAL BLKT
RDPL = RADIAL BLKT PLENUM
REACT = TCORE + INBKT + RBLKT
TOTAL = REACT + TCPL +INPL + RDPL

AUTHOR INDEX

APPENDIX

BELGIAN EXPERIENCE WITH START-UP WITHOUT SECONDARY NEUTRON SOURCES

N. A. Hollasky

AIB-VINCOTTE Nuclear

Brussels, Belgium

ABSTRACT

A belgian Utility observed a contamination of the primary system of its plant in Antimony 124 and concluded that one or more secondary source rods were damaged.
The presence of secondary source assemblies in the cores of the power plants was questioned and start-ups without sources envisaged.
Information allowing to estimate the feasibility of such start-ups was collected, many measurements were performed in several plants and it was concluded that start-ups without secondary neutron sources present advantages.
Neverthless, some rules and recommendations were expressed.

INTRODUCTION

Since there is low neutron activity during loading, refueling, shutdown and approach to criticality, neutron sources are placed in the reactor to provide a positive neutron count on the source range detectors.
The function of the secondary sources is limited to those time intervals when the reactor is in a subcritical state i.e. when the neutron flux is within the source range.
This corresponds to refueling conditions ($k<.95$), to cold and hot shutdown ($k<.99$) and to approach to criticality ($k<1.0$).
Reactivity monitoring during these reactor states is accomplished through monitoring of the multiplication of neutrons from the secondary sources (and from the spent elements if present in the core) using the source range detectors (counting rate $<10^5$ c/sec).
This allows detection of changes in the core multiplication factor due to addition of fuel assemblies while loading the core but also detection of changes in control rod positions or in boron concentration (for instance : uncontrolled dilution).
The secondary neutron sources also contributes to keep under control the approach to criticality since the counting rate of the source range detectors is in direct ratio to the subcritical multiplication.

During cycle 12 of Tihange 1, the Utility observed a contamination of the primary system in Antimony 124 and concluded that one or more secondary source rods were damaged.
The presence of secondary source assemblies in the core was questioned and start-up without sources envisaged for the ulterior cycles.
In this point of view, information allowing to estimate the feasibility of such a start-up, i.e. with only the spontaneous fissions and the reactions (γ , n) from the irradiated fuel as neutron source in the core, was collected.
Many measurements were performed and a "point" model was developed by Tractebel to solve the kinetic equations with source.
Several reactivity transients were simulated, initiated from subcritical conditions in order to evaluate the time required by the operator to detect them.
Some time later, other Utilities, on account of the potential problems which could occur in case of damaged source rod, also envisaged to operate without secondary sources.
The purpose of this paper is to summarize the Belgian experience in that field and to draw the rules and recommendations which were derived from it.

LEGAL ASPECTS

The minimal requirements with regard to the source range detectors for an initial loading are specified by the NRC in the Regulatory Guide 1.68 Rev. 2 :
- the net counting rate must be above 0.5 c/sec
- the ratio signal/noise must be above 2.

According to Westinghouse and Siemens recommendations, the plants which work without secondary sources have introduced the following criteria in their technical specifications :
- the net counting rate must be above 2 c/sec
- the ratio signal/noise must be above 2

when they are three or more fuel assemblies in the core.

DESCRIPTION OF THE SECONDARY NEUTRON SOURCE ASSEMBLIES (fig. 1)

A secondary source assembly contains a symmetrical grouping of four secondary source rods
Locations not filled with a source rod (16 in Tihange 1 and 20 in the other plants) contain a thimble plug.
The secondary source rod is in stainless steel about half-filled with stacked Sb-Be pellets.
The stable material (Sb) is activated by neutron bombardment during reactor operation.
The activation results in the subsequent release of neutrons through the reactions

$$Sb^{124} \xrightarrow{\gamma} Te^{124} + e$$

$$Be^{9}_{4} + \gamma \longrightarrow Be^{8}_{4} + n$$

This becomes the source of neutrons during periods of low neutron flux.
The period of the Sb 124 is about 60 days.
After a stay of one year in a reactor operating at nominal power, one gram of mixed Sb-Be emits 10^7 neutrons/sec.

Neutron source assemblies are employed at diametrically opposite sides of the core.
The assemblies are inserted into the rod cluster control guide thimbles in fuel assemblies at selected unrodded locations.
The rods in the secondary source assembly are permanently fastened at the top end to a spider assembly which is similar to that of a control rod assembly.
This allows permutation between assemblies during refueling to be performed in the reactor cavity using the same handling machine as for control rod permutation.

TIHANGE 1 EXPERIENCE

Tihange 1 operates with extended cycles and has adopted a reload strategy type "third of core - fresh assemblies in periphery".
Two secondary source assemblies emit about 3.4 10^{10} neutrons/sec at the moment of stop for unloading (2.4 10^{10} neutrons/sec after a stop period of 30 days).
The amplitude of the neutron source in the irradiated fuel, which is mainly due to the spontaneous fissions of the Cm^{242}, has been evaluated by means of the code ORIGEN 2 and reaches about 10 % of this value.
It is strongly dependent on the loading pattern and thus varies from one cycle to the other.
In this evaluation, the initial enrichment, the burn up and the stay in pool time of each fuel assembly have been taken into account; by conservatism, the reactions (γ ,n) have been neglected.
The number of neutrons emitted by an assembly is proportional to the power 3.5 of its burn up.

In February 1989, at the end of cycle 12, when opening the vessel for reloading, there were three secondary source assemblies in the core (respectively located in H13, F07 and H03) and the fuel assemblies situated nearest the source range detectors had burn up rates varying between 8,700 and 10,000 MWd/T for the first row (lines 1 and 15) and between 10,000 and 40,000 MWd/T for the second one (lines 2 and 14) (See figure 2).
During the reloading operations, the secondary sources were withdrawn and the counting rates summarized in table 1 have been observed.

These results, together, with others coming from foreign plants, lead to the following conclusions :

. The withdrawal of a secondary source located "in the front" of a source-range detector only affects the count rate of this detector.

- *The withdrawal of a secondary source located in the center of the core does not affect the count rate of any detector.*

- *The moving, core loaded, of a secondary source from position G01 to position H03 (or from J15 to H13) reduces the count rate of the nearest source range detector by a factor 10 to 15.*

- *The signal of a source range detector for a fully loaded core is 2 to 10 times higher than for an isolated, irradiated assembly, located in the periphery of the core, near a detector (Siemens result).*

REACTIVITY TRANSIENTS SIMULATION

A "point" model, solving the kinetic equations with sources, shows that when a transient is initiated from subcritical stable conditions, the kinetic behaviour of the core is only dependent on the variation law of the reactivity with time.
In particular, the source level does not influence the core power variation.
Tractebel has simulated reactivity ramps of .25 to 10 pcm/sec in order to evaluate the time the operators in the control room would dispose of to act if such a transient would occur during reloading operations without secondary sources in the core.
The table hereafter shows the values of the different parameters when criticality is reached.
(The initial subcriticality of the core was - 5000 pcm and the initial neutron flux ϕ_o was normalized to 1).

Reactivity ramp (pcm/sec)	*Time (sec)*	*Flux (ϕ/ϕ_o)*	*Flux variation $\partial\phi/\partial t$ (dec/min)*
10	*500*	*34.15*	*1.27*
5	*1,000*	*44.22*	*0.84*
2.5	*2,000*	*57.69*	*0.55*
1	*5,000*	*84.89*	*0.31*
.5	*10,000*	*116.45*	*0.21*
.25	*20,000*	*154.39*	*0.15*

If we consider, for instance, a reactivity ramp of 0. 5 pcm/sec (which corresponds to an uncontrolled boron dilution with maximum dilution flow), the detection in the control room will become possible when the flux level will have been multiplied by a factor 10 i.e. 150 minutes after the beginning of the transient
The variation of the flux will at that moment be 0.025 decade/minute and the reactor trip will occur more than 20 minutes later.

DOEL 4 MEASUREMENTS

At the end of cyle 5, the Utility of Doel 4 envisaged in his turn to withdraw the secondary neutron sources from the core.
Doel 4, as opposed to Tihange 1, has chosen to operate with annual cycles and has adopted a reload strategy type "quarter of core - low leakage (irradiated assemblies in periphery)".
The presence of irradiated fuel assemblies in the periphery of the core, and in particular in front of the source range detectors, has the following advantages :

- they are nearer the source range detectors than the source assembly (H3 and H13) what increases the counting rate by a factor 10 to 15
- there is no control rod between the fuel assembly and the detector what increases the counting rate by a factor 2
  (This is not the case for the source assembly : there is a control rod in H2 and in H14).

A secondary source at the moment of shutdown for refueling produces 10^{10} neutrons/sec.
An irradiated assembly of 27,000 MWd/T at the same moment provides 10^{8} neutrons/sec i.e. 100 times less.
Although the secondary source is 100 times more efficient, the above-mentioned compensating effects should reduce this ratio by 5.

Table 2 summarizes the measurements performed in Doel 4.

As we can see from these measurements, when the secondary sources are withdrawn, the neutrons counted by the detectors come almost solely from the two assemblies strongly irradiated located near the detectors and not from the rest of the core assemblies.
Therefore, by complete unloading the counting rate will respect the criterion if we take the precaution for always keeping sufficiently irradiated (25,000 MWd/T) assemblies in positions G15, H15 or J15 and G1, H1 or J1.

The same conclusions can be drawn from the measurements performed in Doel 1 at end of cycle 16 and in Doel 2 at end of cycle 15 (see table 3 and figure 3).

DOEL 3 RESULTS (Begin of cycle 9)

The situation in Doel 3 is quite different from the one of Doel 4.
Doel 3 also operates with annual cycles and a reload strategy type "quarter of core -low leakage" but the irradiated assemblies situated nearest the source range detectors at begin of cycle 9 came from cycle 4 and had therefore stead in desactivation pool during about four years before being reloaded.
The neutrons still emitted by such assemblies in absence of secondary source only result from the decrease of Cm 244 (Cm 242 has a half life period of 162.8 days and has consequently almost completely disappeared after four years) and represent 34 % of the total initial emission rate (due to Cm 242 and Cm 244)

If we take the results of Doel 4 as a basis, we may expect these assemblies to provide at least 2.4 c/sec. and therefore the criteria (see LEGAL ASPECTS) to be satisfied.
Several measurements for different configurations were performed in Doel 3 before the start-up of cycle 9 (see table 4); the observed effects can be summarized as follow:

Fuel element	Effect (c/sec)	
	With secondary source	Without secondary source
Fresh	65 (c-d)	6 (l-m)
One cycle irradiated	50 (b-c)	6 (k-l)
Three cycles irradiated	58 (d-e)	34 (i-j)
Three cycles irradiated - four years in desactivation pool	31 (a-b)	8 (j-k) 9 (f-g)

As foreseeable, when a secondary source is present, the neutrons emitted by a fresh or by a "young" element mainly result from the fissions of the U-235.
For a three cycle irradiated element, about one half of the emmitted neutrons are coming from the fissions of the U-235 and the other half from the decrease of the Cm.
After a stay of four years in a desactivation pool, this last quantity is reduced to about 30 % of its value, while the first one decreases of about a factor 2.

CONCLUSION AND RECOMMENDATIONS

The start-up without secondary neutron sources presents many advantages: it increases the core design flexibility improving fuel utilization, reduces probability of fuel assembly damage and of primary system contamination and shortens time requirements for refueling.
Our experience allows us to systematically adhere to this practice; nevertheless, we express some recommendations, principally for the plants which operate with extended cycles and a reload strategy type "third of core - fresh assemblies in periphery".
Indeed, with this type of strategy, it is in most cases not possible to assign peripherical locations to irradiated assemblies.
Consequently, we recommend:

- *to load temporarily irradiated fuel assemblies (about 30,000 MWd/T) in the front of the source range detectors (lines 1 and 15) and to replace them by fresh ones when the refueling operations are terminated.*
- *to respect as well as possible the minimum boron concentration required for refueling operations (400 ppm boron more reduces the counting rate by a factor 2)*

- if the counting rate criterion is not satisfied, to sheathe momentarily the detector with a moderator (increases the counting rate by a factor 1.5 or 2)
- by low values, to integrate the counting rates over 10 minutes
- to withdraw the control rods (except group D) before beginning the dilution process

ACKNOWLEDGMENTS

We thank Mr. M. Melice and J.J. Jadot from Tractebel for their collaboration in discussing this paper.

Table 1. Counting rates observed in Tihange 1

State of the reactor	Stop and control rods	Pressure (b)	Temperature (°C)	Boron concentration (ppm)	Loading pattern	Secondary sources	Source range detectors F11 (c/sec)	Source range detectors F12 (c/sec)
Shutdown for refuelling				2010	Cy 12 (fig 3)	SS4 in H13 SS5 in F7 SS3 in H3	24	18
					Depleted assemblies in front of the source range detectors.	SS5 in F7 SS3 in H3	5	19
						SS3 in H3	5	18
						without	5	4
Shutdown for refuelling				2020	Cy 13	without	2.5 - 3	2.5 - 3
Intermediate shutdown	ARI	30	180	2400	Fresh assemblies in periphery of the core. One depleted assembly in the second row.	without	1	1 - 2
Hot shutdown	Stop ARO Control ARI	154	286	2250		without	1.8	3.4
Hot shutdown	Stop ARO Control ARI	154	286	2040		without	2.5	4.7
Hot shutdown	Stop ARO Control ARI	154	286	1554		without	4.43	9.75
Approach to criticality	A at 100 steps						9	15
	D at 25 steps						25	45
	D at 100 steps						80	140
	D at 170 steps						975	1685

Table 2. Counting rate of the source range detectors in Doel 4

Core configuration in the proximity of the detectors	Source range detectors IE001 (c/sec)	Source range detectors IE004 (c/sec)	Comments
1. *During the complete unloading after cycle 5*			
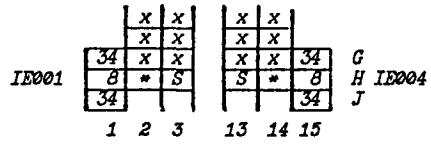	19.81	26.02	
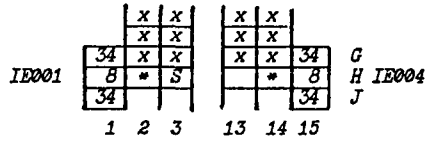	19.89	16.29	
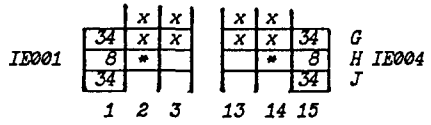	12.31	14.38	about 60 % of the initial values
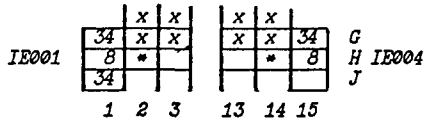	12.12	8.18	
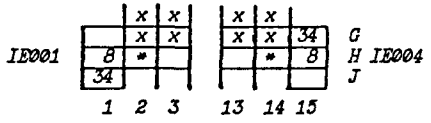	5.58	6.43	about 30 % of the initial values
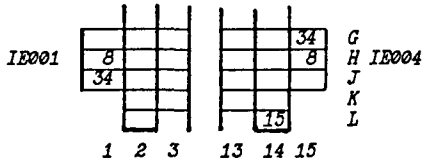	5.10	6.84	no change in the counting rate (no more than 5 assemblies in the core)
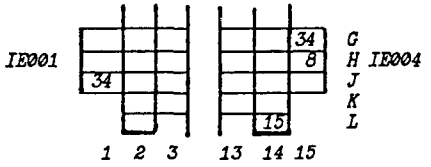	4.12	6.78	

Core configuration in the proximity of the detectors	Source range detectors IE001 (c/sec)	Source range detectors IE004 (c/sec)	Comments
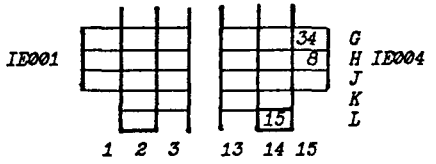	0.17	6.80	
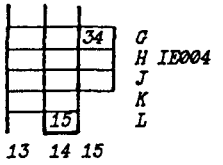	0.15	4.34	
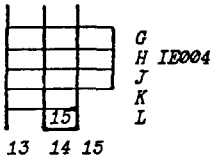	0.19	0.25	
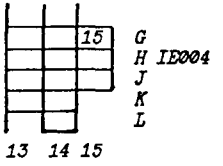	0.17	0.77	
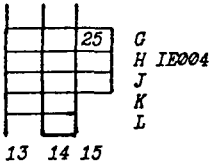		2.51	

2. *During the loading for cycle 6*

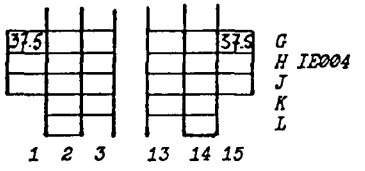	6.37	6.47	

x fuel assembly
* fuel assembly with control rod
nn burn up of the fuel assembly in GWd/T
S Secondary Source

Table 3. Doel 1 and 2 Results

Core configuration	Source range detectors			
	NI1 (c/sec)		NI2 (c/sec)	
	Doel 1	Doel 2	Doel 1	Doel 2
Fully loaded with secondary sources	212	253	199	176
Fully loaded without secondary sources	21	38	22	26
After withdrawal of F1 element (Doel 1: 39257 MWd/T, Doel 2: 36524 MWd/T)	11.5			16
After withdrawal of G1 element (Doel 1: 7033 MWD/T, Doel 2: 7191 MWd/T)	9.2			12
After withdrawal of H1 element.2 (Doel 1: 39172 MWd/T, Doel 2: 36527 MWd/T)	1.02			1.2
After withdrawal of F13 element (Doel1: 39203 MWd/T, Doel 2: 34092 MWd/T)		22	11.8	
After withdrawal of G13 element (Doel 1: 6988 MWd/T, Doel 2: 7105 MWd/T)		17	9.2	
After withdrawal of H13 element (Doel 1: 39263 MWd/T, Doel 2: 36559 MWd/T)		1.3	1.5	

Table 4. Doel 3 Results: Start-up of cycle 9 (2560 ppm boron)

Core configuration nearest the source range detectors		Source range detectors (c/sec)	Comments
		INS 1	
with s.s.	[36][8][36]	141.2	
with s.s.	[36][8][ ] (a)	91.3	
		(~31c/sec)	effect of an irradiated fuel element whish has stead in desactivation pool during 4 years
with s.s.	[36][8][32] (b)	122.0	
		(~50c/sec)	effect of a "young" fuel assembly
with s.s.	[36][ ][32] (c)	69.3	
		(~65c/sec)	effect of a fresh fuel assembly
with s.s.	[36][0][32] (d)	134.2	
		(~58c/sec)	effect of an irradiated fuel.
with s.s.	[ ][0][32] (e)	76.2	
		(~64c/sec)	effect of a secondary source
with s.s.	[ ][0][32] (f)	11.6	
		(~9c/sec)	effect of an irradiated fuel element which has stead in desactivation pool during 4 years
with s.s.	[32][0][32] (g)	21.3	

Core configuration nearest the source range detectors		Source range detectors (c/sec)	Comments
		INS 2	
with s.s.	36 | 8 | 36	127.6	
with s.s.	| 8 | 36	81.4	
with s.s.	32 | 8 | 36 (h)	113.4	
		(~70c/sec)	effect of a secondary source
	32 | 8 | 36 (i)	45.9	
		(~34c/sec)	effect of an irradiated fuel element
	32 | 8 | 36 (j)	12.6	effect of an irradiated fuel
		(~8 c/sec)	element which has stead in desactivation pool during 4 years
	32 | 8 | 32 (k)	21	
		(~5 c/sec)	effect of a "young" fuel element
	32 | | 32 (l)	14.8	
		(~6 c/sec)	effect of a fresh fuel element
	32 | 0 | 32 (m)	20.8	

36 36 MWd/T irradiated fuel element

0 fresh fuel element

32 32 MWd/T irradiated fuel element coming from cycle 4

s.s. secondary source

Figure 1. Secondary Source Assembly

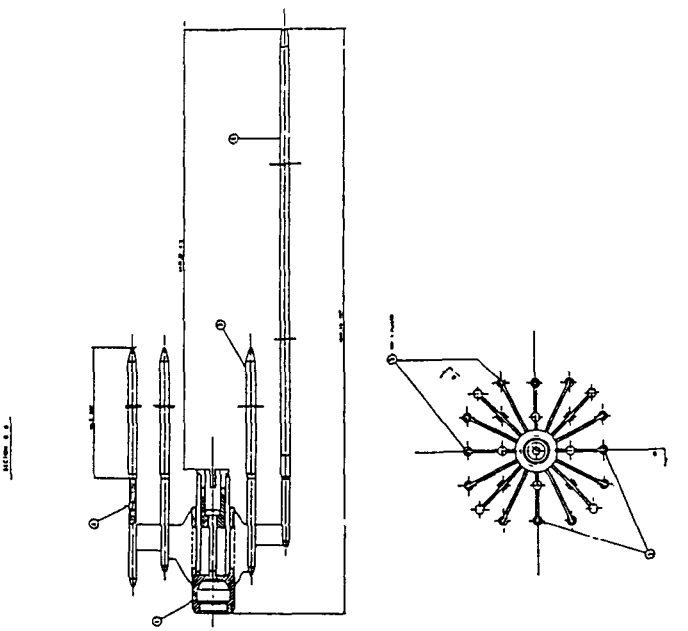

Figure 2. Tihange 1 Localisation Map

FI1 and 2 : Source range detector

FI3 and 4 : Intermediate range detector

FI5 to 8 : Power range detector

: Secondary source

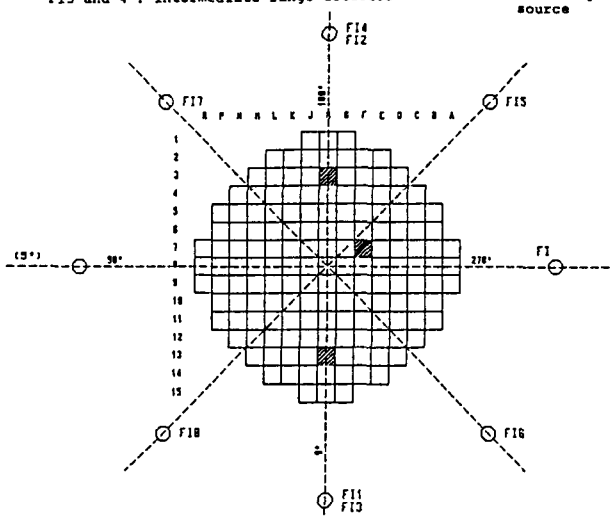

Fuel assemblies burn up rates

	MWd/T		MWd/T
J1	8744	J2	12482
H1	9895	H2	39201
G1	8786	G2	13046
J15	8807	J14	13104
H15	9908	H14	39414
G15	8743	G14	12961

Figure 3 : Doel 1 and 2 : Layout of the cores